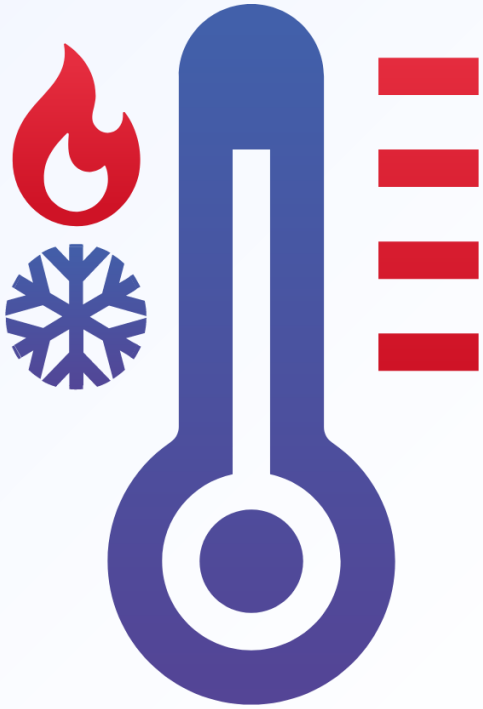
Vol. 47 No. 3 (2026)

ARCHIVES OF THERMODYNAMICS

ISSN: 1231-0956
ISSN: 2083-6023 (Online)



Co-published by

Institute of Fluid Flow Machinery
Polish Academy of Sciences

Committee on Thermodynamics and Combustion
Polish Academy of Sciences

WYDAWNICTWO IMP PAN

Aims and Scope

The aim of the quarterly journal Archives of Thermodynamics (AoT) is to disseminate knowledge between scientists and engineers worldwide and to provide a forum for original research conducted in the field of thermodynamics, heat transfer, fluid flow, combustion and energy conversion in various aspects of thermal sciences, mechanical and power engineering. Besides original research papers, review articles are also welcome.

The journal scope of interest encompasses in particular, but is not limited to:

- Classical and extended non-equilibrium thermodynamics
- Thermodynamic analysis including exergy
- Thermodynamics of heating and cooling
- Thermodynamics of nuclear power generation
- Thermodynamics in defence engineering
- Advances in thermodynamics
- Experimental, theoretical and numerical heat transfer
- Thermal and energy system analysis
- Renewable energy sources including solar energy
- Secondary fuels and fuel conversion
- Heat and momentum transfer in multiphase flows
- Nanofluids
- Energy transition
- Advanced energy carriers
- Energy storage and efficiency
- Energy in buildings
- Hydrogen energy
- Combustion and emissions
- Turbomachinery
- Thermal and energy system analysis
- Integrated energy systems
- Distributed energy generation
- Thermal incineration of wastes
- Waste heat recovery.

Supervisory Editors

- K. Badyda, Warsaw University of Technology, Poland
- M. Lackowski, Institute of Fluid Flow Machinery, Gdańsk, Poland

Honorary Editor

- J. Mikielewicz, Institute of Fluid Flow Machinery, Gdańsk, Poland

Editor-in-Chief

- P. Ocłoń, Cracow University of Technology, Cracow, Poland

Section Editors

- P. Lampart, Institute of Fluid Flow Machinery, Gdańsk, Poland
- S. Polesek-Karczewska, Institute of Fluid Flow Machinery, Gdańsk, Poland
- I. Szczygieł, Silesian University of Technology, Gliwice, Poland
- A. Szlęk, Silesian University of Technology, Gliwice, Poland

Technical Editors

- J. Frączak, Institute of Fluid Flow Machinery, Gdańsk, Poland
- S. Łopata, Institute of Fluid Flow Machinery, Gdańsk, Poland

Members of Programme Committee

- D. Kardaś, Inst. Fluid Flow Mach., Gdańsk, Poland (Chairman)
- J. Badur, Inst. Fluid Flow Mach., Gdańsk, Poland
- T. Chmielniak, Silesian Univ. Tech., Gliwice, Poland
- P. Furmański, Warsaw Univ. Tech., Poland
- R. Kobyłecki, Częstochowa Univ. Tech., Poland
- S. Pietrowicz, Wrocław Univ. Sci. Tech., Poland
- J. Wajs, Gdańsk Univ. Tech., Poland

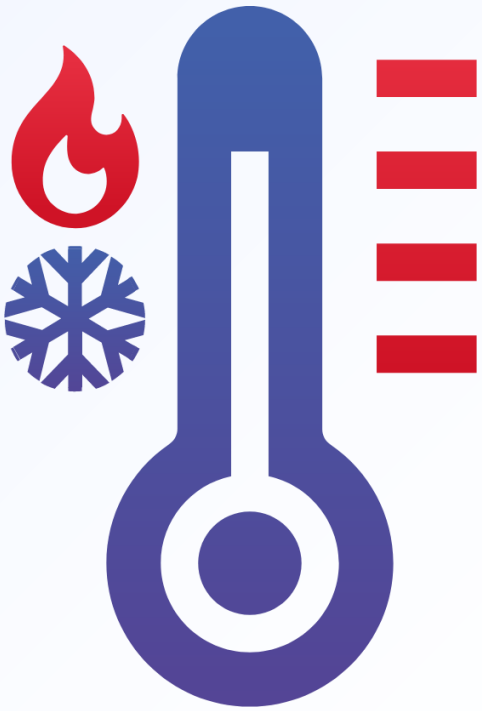
International Advisory Board

- J. Bataille, Ecole Centr. Lyon, France
- W. Błasiak, Royal Inst. Tech., Stockholm, Sweden
- A.C. Benim, Univ. Appl. Sci., Duesseldorf, Germany
- G.P. Celata, ENEA, Rome, Italy
- L.M. Cheng, Zhejiang Univ., Hangzhou, China
- M. Colaco, Federal Univ. Rio de Janeiro, Brazil
- J.M. Delhaye, CEA, Grenoble, France
- M. Giot, Univ. Catholique Louvain, Belgium
- K. Hooman, Univ. Queensland, Australia
- D. Jackson, Univ. Manchester, UK
- D.F. Li, Kunming Univ. Sci. Tech., China
- K. Kuwagi, Okayama Univ. Science, Japan
- J.P. Meyer, Univ. Pretoria, South Africa
- S. Michaelides, Texas Christian Univ., USA
- W. Muschik, Tech. Univ., Berlin, Germany
- I. Müller, Tech. Univ., Berlin, Germany
- H. Nakayama, JAEA, Japan
- S. Nizetic, Univ. Split, Croatia
- H. Orlande, Federal Univ. Rio de Janeiro, Brazil
- M. Podowski, Rensselaer Polyt. Inst., USA
- R.V. Rao, Sardar Vallabhbhai Nat. Inst. Techn., India
- A. Rusanov, Inst. Mech. Eng. Probl., Kharkiv, Ukraine
- A. Vallati, Sapienza Univ. Rome, Italy
- M.R. von Spakovsky, Virginia Polyt. Inst., USA
- H.R. Yang, Tsinghua Univ., Beijing, China

Vol. 47 No. 3 (2026)

ARCHIVES OF THERMODYNAMICS

ISSN: 1231-0956
ISSN: 2083-6023 (Online)



Co-published by

Institute of Fluid Flow Machinery
Polish Academy of Sciences

Committee on Thermodynamics and Combustion
Polish Academy of Sciences

WYDAWNICTWO IMP PAN

Editorial Office
IMP PAN Publishers
Institute of Fluid Flow Machinery, Fiszera 14, 80-231 Gdańsk, Poland,
Phone: (+48) 58-341-12-71 int. 230, e-mail: redakcja(at)imp.gda(.)pl
https://www.imp.gda.pl/archives-of-thermodynamics/
Journals PAS – Electronic Library Polish Academy of Sciences
https://journals.pan.pl/ather

Subscription outside Poland
From 2024, Archives of Thermodynamics appear only in electronic version as an open access journal. However, printed archive volumes or issues are still available. The price of a full volume outside Poland is **120 EUR**. The price of a single issue is **30 EUR**. Archived volumes or issues are available on request. Orders should be sent directly to IMP PAN Publishers:
Institute of Fluid-Flow Machinery,
Fiszera 14, 80-231 Gdansk, Poland,
e-mail: redakcja(at)imp.gda.pl or jfrk(at)imp.gda(.)pl or jrybka(at)imp.gda(.)pl.
Payments should be transferred to the bank account of IMP PAN:
IBAN 28 1130 1121 0006 5498 9520 0011 at Bank Gospodarstwa Krajowego; Code SWIFT: GOSKPLPW.

Prenumerata w Polsce
Od 2024, czasopismo ukazuje się tylko w formie elektronicznej otwartej. Osiągalne są jednak wydania papierowe archiwalne. Cena pojedynczego numeru wynosi **50 PLN**. Cena rocznika **200 PLN**. Zamówienia z określeniem numeru (rocznika), nazwiskiem i adresem odbiorcy należy kierować bezpośrednio do Wydawcy:
Instytut Maszyn Przepływowych PAN
ul. Fiszera 14, 80-231 Gdańsk,
e-mail: redakcja(at)imp.gda(.)pl lub jfrk(at)imp.gda(.)pl lub jrybka(at)imp.gda(.)pl.
Wpłaty prosimy kierować na konto Instytutu Maszyn Przepływowych PAN:
nr 28 1130 1121 0006 5498 9520 0011 w Banku Gospodarstwa Krajowego.

Articles in Archives of Thermodynamics are abstracted and indexed within:
Arianta • Baidu Scholar • BazTech • Cabell's Directory • Chemical Abstracts Service (CAS) – CAplus • CNKI Scholar (China National Knowledge Infrastucture) • CNPIEC • EBSCO • Elsevier – SCOPUS • Genamics JournalSeek • Google Scholar • Inspec • Index Copernicus • J-Gate • Journal Citation Reports (ESCI) • Journal TOCs • Naviga (Softweco) • POL-index • Polymer Library • Primo Central (ExLibris) • ProQuest • ReadCube • SCImago (SJR) • TDNet • TEMA Technik und Management • Ulrich's Periodicals Directory/Ulrichsweb • Web of Science (Core Collection) • WorldCat (OCLC)

ISSN 1231-0956
ISSN 2083-6023 (Online)
Copyright © 2026 by the Authors under license CC BY-NC-ND 4.0.
Publication funding of this journal is provided by resources of the Polish Academy of Sciences and the Institute of Fluid Flow Machinery

Contents

1) Adam Pawłowski, Wiesław Zima, Sławomir Grądziel, Artur Cebula, Monika Piwowarczyk, Ewa Kozak-Jagieła
Experimental verification of the effectiveness of CO2 capture from flue gas after pulverised coal combustion 5–14

2) Katarzyna Katana, Andrzej Grzebielec, Adam Szelągowski, Maksymilian Kruk, Krzysztof Bruzi
Experimental study of a reversible ventilation – heat pump system with a ceramic regenerator 15–24

3) Nadiya Philip, Prakash Chandra Ghosh
Phase change material for thermal management of high-temperature proton exchange membrane fuel cells in electric vehicle 25–30

4) Robert Szczepaniak, Andrzej J. Panas, Łukasz Omen, Maciej Starczewski, Maciej Kowalski
Comparative experimental studies of the specific heat of Fe and Ni using scanning calorimetry methods 31–39

5) Youcef Lakahal, Houssem Laidoudi
Rheological and porous effects on mixed convection: Power-law fluid flow in a finned annular configuration 41–55

6) Seweryn Szultka, Stanislaw Czapp, Adam Tomaszewski, Marian Czapp
A method for determining the current-carrying capacity and durability of power cables based on variable ambient temperature and solar radiation 57–67

7) Aed Ibrahim Owaid, Sabah M. Hadi, Husam Sabeeh Al-Arab
A novel passive solar energy space heating design of an emergency tent 69–77

8) Emad Jaleel Mahdi, Hussein Fawzi Hussein, Ali Isam Ata
Dual-use PV canopies for public gardens: Performance, techno-economic feasibility, and CO_2 mitigation of an 84.5 kWp grid-tied system in Baghdad, Iraq 79–88

9) Tuba Fatima, Saurabh Patel
Numerical investigation of heat transfer in a partially porous-filled channel with core and wall configurations 89–98

10) Chegu Ramprasad, Chundru Maheswari, Bhavanam Naga Lakshmi, Tadavarthi Madhu Mohan, Ravuri Mohana Ramana
Mixed convective chemically reacted hybrid nanofluid flowing over a non-isothermal/non-isosolutal cone/wedge with heat generation/absorption: A numerical study 99–110

11) Syed Shahzad Ali, Muhammad Imran Khan, Mohammed Almakki, Ahmed Zeeshan
Physics-Informed Deep Learning Optimisation for Heat Transfer Analysis of Non-Similar Flow over Porous Moving Surface 111–123

12) Muhammad Yousuf Rafiq, Zaheer Abbas, Ayesha Naeem
Analysis of oscillatory flow and heat transfer of Maxwell fluid through a porous circular microchannel with Hall effects 125–137

13) Ali K. Abdul Razzaq, Khudheyer S. Mushatet, Riyam Ali Khaled
Numerical investigation of a double twisted tube heat exchanger in different configurations 139–146

14) Akashdeep Negi, Lalit Ranakoti, Kapil Kumar Sharma, Adhirath Mandal, Mansi Sharma, Deepak Kumar, Jeetendra Mohan Khare, Shobhit Sharma, Prabhakar Bhandari, Sneha Singh
Enhancing Solar Still Productivity through Fin, Solar Collector and Wick Modifications: A Comprehensive Review 147–156

15) Asmaa Nadia Bouguesri, Houssem Laidoudi, Abderrahmane Aissa
Enhancement of buoyancy-driven flow in an annular system by using nano-encapsulated phase change material fluid 157–172

16) Liliana Mirosz
Experimental validation of the CFD model of heat losses from the horizontal rectangular flue gas duct exposed to wind and solar radiation 173–186

17) Kinga Strąk, Dariusz Strąk
Experimental investigation of flow boiling heat transfer in a minichannel heat exchanger with countercurrent hot and cold fluid circuits 187–197

18) Katarzyna Stolecka-Antczak, Andrzej Rusin
Safety aspects of the use of ammonia and an ammonia-hydrogen mixture 199–211

19) Veljko Minic, Nikola Bojanic, Milena Zecevic, Aleksandar Djordjevic, Dragan Manasijevic, Milan Kolarevic
Experimental test and simulation of properties from ternary Bi-Ni-Pb system: microstructural, mechanical, electrical properties, Scheil and Lever simulation 213–232

20) Salma Seham Jameel, Ali Rahim Ali, Hussein Fawzi Hussein, Alaa Hussein Ali, Shaalan Bdaiwi Ahmed
Experimental Investigation of Microplastic Removal from Drinking Water Using Aluminium Electrocoagulation: Process Performance and Operating Parameters 233–240

21) P. Sudarsana Reddy, P. Sreedevi
Impact of activation energy and Deborah number on heat and mass transfer of three dimensional rotating magnetic nanofluid over a stretching surface 241–252

22) Heyu Jia, Wenzhe Dang, Xiaopo Wang
Analysis of phase behaviour of R1243zf/lubricant oil mixtures and its impact on the performance of vapour-compression refrigeration cycle 253–260

23) Łukasz Omen, Maciej Kowalski, Robert Szczepaniak, Andrzej J. Panas
Experimental Studies of Heat Diffusion in a Bulk Bed at Coupled Energy Transport and Phase Change Effects 261–268

Co-published by
Institute of Fluid-Flow Machinery
Polish Academy of Sciences
Committee on Thermodynamics and Combustion
Polish Academy of Sciences

Copyright©2026 by the Authors under licence CC BY-NC-ND 4.0

http://www.imp.gda.pl/archives-of-thermodynamics/

Experimental verification of the effectiveness of CO_2 capture from flue gas after pulverised coal combustion

Adam Pawłowski*, Wiesław Zima, Sławomir Grądziel, Artur Cebula, Monika Piwowarczyk, Ewa Kozak-Jagieła

Faculty of Environmental Engineering and Energy, Department of Energy, Cracow University of Technology, Warszawska 24, 31-155 Cracow, Poland
*Corresponding author email: adam.pawlowski@pk.edu.pl

Received: 28.02.2026; revised: 02.07.2026; accepted: 21.07.2026

Abstract

This article presents experimental verification of CO_2 capture from flue gases generated in a pulverised coal-fired power boiler. The tests were carried out using a pilot-scale moving bed temperature swing adsorption system installed in an operating coal-fired power plant (Skawina Power Plant). Activated carbon in the form of beads was used as the adsorbent due to its developed microporous structure, large specific surface area and excellent mechanical resistance under conditions of continuous circulation. The installation enables treatment of a flue gas stream with a volumetric flow rate of up to 50 m³/h. The supplied flue gas, composed mainly of N_2 and CO_2, was extracted downstream of the plant's gas-cleaning system. Two recent measurement campaigns were analysed under variable inlet CO_2 concentrations (4.81–7.16 vol.%; it depends on the operation of the power plant, so it cannot be controlled by researchers), different flue gas flow rates and varying sorbent mass flow rates. Under quasi-steady-state operating conditions, a capture efficiency of 50–60% was achieved at an inlet CO_2 concentration of 6–7% by volume, with an average energy consumption of 55.3 MJ/kgCO_2. A second series of measurements confirmed the high sensitivity of capture efficiency to the ratio of sorbent mass flow rate to flue gas flow rate and to regeneration conditions. The results demonstrate the technical feasibility of moving bed temperature swing adsorption operation under actual coal-fired power plant conditions; however, significant optimisation of heat integration, process configuration and sorbent management is necessary to reduce energy requirements to a level compatible with industrial implementation.

Keywords: Experimental tests; CO_2 capture; Research facility; Moving bed temperature swing adsorption

Vol. 47(2026), No. 3, 5–14; doi: 10.24425/ather.2026.3648

Cite this manuscript as: Pawłowski, A., Zima, W., Grądziel, S., Cebula, A., Piwowarczyk, M., & Kozak-Jagieła, E. (2026). Experimental verification of the effectiveness of CO_2 capture from flue gas after pulverised coal combustion. *Archives of Thermodynamics*, 47(3), 5−14.

1. Introduction

Anthropogenic carbon dioxide (CO_2) emissions remain a primary driver of climate change and continue to pose a direct challenge for the power sector and other energy intensive industries. Even under accelerated deployment of renewable energy and electrification, large stationary point sources such as coal and gas fired power plants, cement kilns, steelworks and refineries are expected to contribute substantially to residual emissions over the coming decades. For this reason, carbon capture, utilisation and storage (CCUS) is widely recognised as a key bridging technology to enable deep decarbonisation while maintaining security of supply and industrial competitiveness. A comprehensive review by Markewitz et al. [1] emphasised that CCUS deployment must be assessed not only in terms of capture efficiency, but also in terms of system integration, energy penalty and the implications for the entire energy chain.

From an engineering and policy perspective, the major barrier to large-scale CCUS implementation has consistently been the cost and energy demand of capture, particularly for post-

Nomenclature

CO_2– CO_2 concentration in the flue gas, %
m_{CC}– mass of CO_2 captured from the flue gas, kgCO_2
Q – thermal energy supplied via steam for sorbent regeneration, MJ

Greek symbols

ζ – energy consumption of CO_2 capture, MJ/kgCO_2
η – CO_2 capture efficiency, %

Subscripts and Superscripts

in – before contact with adsorbent
out – after contact with the adsorbent

Abbreviations and Acronyms

BAC – ball-shaped activated carbon
CCS – carbon capture and storage
CCUS – carbon capture, utilisation and storage
CO_2 – carbon dioxide
IGCC – integrated gasification combined cycle
MBTSA– moving bed temperature swing adsorption
MEA – monoethanolamine
MOF – metal-organic frameworks
PSA – pressure swing adsorption
SCADA– supervisory control and data acquisition
TSA – temperature swing adsorption
VSA – vacuum swing adsorption
VTSA – vacuum temperature swing adsorption

combustion flue gas streams where CO_2 is diluted in nitrogen, and where the treated gas flow rates are large. Rubin et al. [2] showed that capture dominates the levelised cost of carbon capture and storage (CCS) for power generation and that cost reductions depend strongly on both process intensification and integration opportunities at the plant level. For pulverised coal units, retrofitting post-combustion capture remains an attractive route because it can, in principle, be implemented without radical modifications to the boilers and turbines system.

Aqueous amine absorption (most commonly monoethanolamine (MEA) based) remains the benchmark technology for post-combustion CO_2 capture due to its technological maturity and demonstrated performance. Rochelle's [3] widely cited review pointed out that amine scrubbing is robust and industrially proven, but also highlighted the fundamental thermodynamic minimum work and the practical need to reduce energy consumption through solvent and process improvements. In practice, the regeneration duty and the associated steam extraction reduce power output and may complicate part-load operation. These limitations motivate continuous research into alternative capture concepts that could reduce the energy penalty, mitigate solvent degradation, and simplify operation and maintenance.

At the industrial scale, the Shell CANSOLV process provides an important reference point for post-combustion CO_2 capture based on regenerable amine absorption. The first commercial applications of this technology demonstrated high CO_2 capture performance and high product purity [4].

Post-combustion capture options include chemical absorption, physical adsorption, membrane separation, and hybrid configurations combining several mechanisms. In a broad review of post-combustion carbon capture, Chao et al. [5] underlined that no single technology is universally optimal; instead, performance depends on flue gas composition, required CO_2 purity and recovery, integration constraints, and site-specific economics. Within this landscape, adsorption-based approaches have attracted increasing attention because regeneration can be driven by temperature and/or pressure changes, and because solid sorbents can potentially avoid some drawbacks of liquid solvents (corrosion, solvent losses, and oxidative/thermal degradation).

The viability of adsorption-based CO_2 capture depends on two coupled elements: the intrinsic properties of the sorbent (capacity, selectivity, kinetics, stability) and the process design (contactor configuration and regeneration strategy). Choi et al. [6] provided an early, influential review of sorbent classes for large point sources, discussing activated carbons, zeolites, alkaline oxides, hydrotalcites, amine-functionalised solids and metal-organic frameworks (MOFs), and highlighted that process design constraints often dominate material selection when moving from laboratory to industrial scales. In a later review focused specifically on post-combustion capture using solid sorbents, Samanta et al. [7] stressed the importance of cyclic stability, tolerance to moisture and impurities, and the practical challenges of scaling fixed-bed systems, including pressure drop and heat management. More recently, Raganati et al. [8] summarised the state of adsorption-based post-combustion capture, emphasising that regeneration strategy and heat integration determine much of the overall energy penalty and capture cost.

The development of advanced sorbents remains an active area of research, especially for low CO_2 partial pressures where high selectivity is required. D'Alessandro et al. [9] discussed the prospects and limitations of new porous materials for CO_2 separation, noting that improved materials must be evaluated under realistic operating conditions, including temperature, humidity and exposure to contaminants. In a recent review, Kong et al. [10] compared carbon sorbents, zeolites and MOFs for post-combustion capture, highlighting recurring trade-offs: zeolites and some MOFs exhibit high efficiency and selectivity but can be sensitive to water, while carbonaceous materials are generally more resistant to moisture and contamination but may exhibit lower selectivity and operating efficiency under flue gas conditions.

From a process standpoint, adsorption cycles can be broadly classified as pressure swing adsorption (PSA), vacuum swing adsorption (VSA), temperature swing adsorption (TSA), and combined VTSA cycles. TSA is particularly relevant for near-atmospheric flue gas because it avoids deep vacuum operation and can allow us to use waste heat; yet, TSA can suffer from slow heating and cooling rates, large thermal inertia and high heat demands. Clausse et al. [11] performed a numerical parametric study on indirect TSA for post-combustion capture, and demonstrated that cycle performance is strongly affected by the regeneration temperature, purge conditions and heat transfer characteristics, with energy consumption being a central constraint for industrial relevance. Earlier, Bonjour et al. [12] investigated a TSA process with indirect heating and cooling, and dis-

cussed how internal heat exchanger design and scaling influence specific heat consumption, providing a process-intensification perspective directly relevant to pilot- and industrial-scale systems.

Thermodynamic analyses of integrated gasification combined cycle (IGCC) systems with pre-combustion, post-combustion and oxy-fuel configurations make a significant contribution to the assessment of the efficiency of coal-fired power plants integrated with CCS systems. Kindra's et al. [13] work provides a comparative analysis of these variants using simulation models, showing that the highest net efficiency (47.2%) can be achieved in an IGCC system with pre-combustion capture, assuming effective thermal integration of the synthesis gas preparation section, while the oxy-fuel configuration minimises CO_2 emissions (approx. 9 g/kWh), but at the cost of a significant drop in efficiency to 36.3%. These results clearly indicate that the competitiveness of CCS technology is primarily determined by the energy balance of the system and the extent of heat recovery. However, it should be emphasised that the presented analyses are model-based and refer to fixed operating conditions, which justifies the need for experimental research conducted under real conditions, allowing for the verification of the assumptions made and the assessment of operational limitations, in particular with regard to adsorption processes.

Beyond the choice of the cycle, it is increasingly recognised that meaningful comparisons between the capture technologies require consistent performance metrics: capture rate, product purity, productivity and specific energy consumption (thermal and/or electrical), ideally evaluated under comparable boundary conditions. Zhao et al. [14] proposed performance analysis frameworks for TSA systems and emphasised the role of thermodynamic benchmarking when interpreting reported energy demands. In a comprehensive evaluation of TSA for post-combustion capture, Zhao et al. [15] further highlighted that the apparent energy penalty depends not only on the heat of adsorption but also on the heat capacity of the sorbent and the overall heat management of the contactor and auxiliaries. This is particularly important for systems aiming at continuous or quasi-continuous operation, where thermal integration is an explicit design objective.

Moving bed temperature swing adsorption (MBTSA) has been proposed as an approach to overcome some intrinsic limitations of fixed-bed TSA. The key concept is continuous circulation of the adsorbent through spatially separated sections for adsorption, heating (desorption) and cooling, which can reduce pressure drop in the adsorption zone and potentially improve heat transfer by decoupling the thermal front from the gas-phase pressure constraints. Mondino et al. [16] developed and analysed MBTSA configurations for post-combustion capture in a coal-fired power plant context and showed that process modifications, particularly gas recirculation from the desorption section, can substantially improve CO_2 purity and capture rate compared to simple baseline configurations. In a later study, Mondino et al. [17] investigated MBTSA as an alternative to absorption for natural gas combined cycle plants, where the CO_2 partial pressure is typically low, demonstrating that MBTSA can be competitive when integrated at the plant level and when the capture process auxiliaries are fully accounted for. More recently, MBTSA was assessed for a waste-to-energy application, with a clear focus on internal heat recovery and experimentally informed heat-transfer correlations, reinforcing that heat transfer and thermal integration remain decisive factors for the practical feasibility of the concept [18].

A concept utilising a fixed sorbent in continuous mode for CO_2 capture has also been developed by Kawasaki; in this system, the process relies on a porous, amine-impregnated material regenerated with low-temperature steam, which differs significantly from the spherical activated carbon used in the current MBTSA plant. In early moving-bed tests, CO_2 was captured from coal-combustion exhaust gas using steam at approximately 60°C, with a reported CO_2 product concentration of at least 95%, whereas later parametric tests were performed on a 5 t_{CO_2}/day moving-bed unit [19,20]. These studies indicate that the moving-bed configuration itself can be technically feasible, but they also show that process performance is strongly dependent on sorbent chemistry, regeneration strategy and heat integration.

While modelling studies provide critical insights into process design space, experimental evidence under real flue gas conditions remains essential. Flue gas contains water vapour and trace contaminants, exhibits temporal variability and imposes operational constraints that are often simplified or ignored in simulations. Pilot scale adsorption capture using multi-layer VSA/VPSA or MBTSA configuration (described in the next chapters) has been demonstrated at coal-fired power plants, providing valuable benchmarks for actual performance. Liu et al. [21] reported on onsite CO_2 capture from coal-fired flue gas using an adsorption process after dehydration, demonstrating high CO_2 purity and recovery in a multi-bed cycle and reporting experimentally measured energy consumption under plant integrated conditions. In a related short communication, Wang et al. [22] experimentally evaluated adsorption capture in an existing coal-fired power plant and showed that dehumidification and real-gas operation are central to stable performance and energy consumption. These studies underscore the importance of plant-level constraints and provide context for interpreting energy metrics obtained in pilot systems.

For adsorption-based capture from flue gas, moisture is a dominant factor affecting cycle performance. Activated carbons are often considered advantageous in wet conditions due to their relatively hydrophobic character compared to many zeolites. Xu et al. [23] investigated the effects of water vapour on CO_2 capture using activated carbon in VSA operation and demonstrated that, even when CO_2/N_2 separation remains feasible, moisture can increase energy consumption and complicate cycle optimisation. Consequently, pilot-scale evaluation under real flue gas conditions should clearly consider humidity management, thermal inertia and the stability of the sorbent under repeated cycling.

Another central but frequently underestimated contributor to energy penalty in TSA/MBTSA systems is the sensible heat required to raise and lower the temperature of the circulating solid phase. Even when the heat of adsorption is moderate, a high sorbent heat capacity or excessive thermal mass in the contactor can lead to large regeneration duties. Querejeta et al. [24] sys-

tematically measured heat capacities of activated carbons in the temperature range relevant for TSA-based CO_2 capture and concluded that selecting and/or modifying carbon materials to reduce heat capacity can be an effective strategy to lower regeneration energy demand. This insight is directly relevant for moving bed concepts, where continuous sorbent circulation amplifies the impact of solid-phase thermal properties.

In addition to the international studies discussed above, Polish pilot and demonstration projects provide important quantitative benchmarks for assessing post-combustion CO_2 capture processes under real-world flue gas conditions. Pilot tests based on the amine process, carried out at the Łaziska Power Station, enabled the removal of over 19 000 kg of CO_2 over approximately 550 hours of operation and demonstrated the practical significance of mobile pilot installations integrated with coal-fired units [25]. Earlier Polish studies on amine-based post-combustion CO_2 capture reported a pilot plant capacity of up to 200 Nm³/h of flue gas [26].

These studies are complemented by national energy and economic analyses of CO_2 capture installations using monoethanolamine and ammonia, which indicate that the choice of absorbent significantly affects the heat demand for regeneration and the cost of the process [27]. In the case of adsorption-based capture methods, Polish research into DR-VPSA was carried out using actual flue gases, a four-column adsorption system and a complete gas pre-treatment line, comprising dust removal, cooling, desulphurisation, denitrification, drying and compression [28]. The long-term performance of activated carbon in a pilot DR-VPSA plant was also analysed over 808 hours under real flue gas conditions [29]. These results are relevant to the present MBTSA study, as they show that capture efficiency must be interpreted in conjunction with gas conditioning, sorbent durability, regeneration stability, pressure drops, heat recovery and auxiliary energy requirements.

In the next chapters, this paper presents an experimental performance of CO_2 capture using a pilot MBTSA system installed in an operating pulverised coal-fired power plant (Skawina Power Plant, Poland). The installation processes actual flue gas taken from the end of the existing purification installation and uses ball-shaped activated carbon (BAC) as a mechanically robust sorbent suitable for continuous circulation. The scope of the experiment focuses on determining the capture efficiency at different CO_2 inlet concentrations and flow conditions, and calculating the energy consumption associated with thermal regeneration using a heat source integrated with the power plant and operating data recorded by the SCADA system. This experimental analysis complements previous work comparing MBTSA simulations with experimental observations for the same installation [30].

2. Description of the research facility

As part of the conducted research, a specially designed pilot installation for CO_2 capture from flue gas was employed. The system enables treatment of a flue gas stream with a volumetric flow rate of up to 50 m³/h. The process was implemented using the MBTSA technology. The installation was connected to the flue gas duct of a pulverised coal-fired boiler downstream of the existing gas-cleaning units. As a result, the supplied gas stream consisted predominantly of N_2 and CO_2. A specially prepared ball-shaped activated carbon (BAC), manufactured by Kureha [31], was used as the adsorbent. The sorbent circulates continuously between three main process sections: the adsorption section, where CO_2 and partially N_2 are captured; the regeneration section, in which the sorbent undergoes thermal desorption; and the cooling section. Material transport between the columns is carried out by insulated belt conveyors, which receive the sorbent after its passage through each process section.

2.1. Description and purpose of individual sections of the facility

The pilot installation consists of three main process sections enabling continuous CO_2 capture from flue gas using the temperature swing adsorption concept. Each section is equipped with a rotary valve that ensures controlled sorbent flow by allowing gradual discharge at the bottom of the column. The combination of bed level sensors and frequency inverters enables automatic adjustment of the rotational speed of the rotary valves. Since the belt conveyors operate at constant speed, regulation of sorbent dosing via the rotary valves makes it possible to vary the sorbent mass flow rate while maintaining predefined filling levels in each process section.

The three principal sections of the installation (Fig. 1) are described below in the order corresponding to sorbent circulation, excluding mechanical transport elements:

1. Adsorption section (reactor).
   The adsorption section consists of a sealed, cylindrical column with plastic walls and filled with Mellapak™ structured packing. Within the column, upward-flowing flue gas comes into contact with adsorbent particles descending under gravity, resulting in adsorption of CO_2 onto the sorbent surface. The flue gas is introduced at the bottom of the column and, under slight overpressure, exits at the top. The sorbent is supplied from the top and flows downward to the bottom of the column. The application of Mellapak™ structured packing ensures uniform distribution of both gas and solid phases and extends gas–solid contact time.
2. Regeneration/heating section.
   The regeneration section consists of a thermally insulated column in which the sorbent undergoes thermal desorption at a temperature of approximately 180°C, required for effective regeneration of the activated carbon. Three shell and tube heat exchangers are installed inside the column. The upper heat exchanger forms part of a closed internal heat recovery loop. It transfers energy between the regeneration and cooling sections, enabling preheating of the incoming sorbent while simultaneously recovering heat from the cooling column. The remaining two heat exchangers operate in series. Saturated steam extracted from the turbine, with parameters of approximately 190°C and 1.3 MPa, is supplied to the lower exchanger. The steam condenses while transferring heat to the sorbent. The resulting condensate is then directed to the middle exchanger, where its temperature decreases to approximately 121°C. The desorbed gas stream, consisting primarily of CO_2 and

N_2, is removed through an outlet equipped with a fan generating slight underpressure, ensuring stable evacuation of the desorption gases from the system.

3. Cooling section.
   The final section of the installation is a thermally insulated column designed to reduce the sorbent temperature to restore its adsorption capacity prior to re-entry into the adsorption section. Two shell and tube heat exchangers are installed within this column. The upper exchanger is integrated into the previously described internal heat recovery loop, while the lower exchanger provides direct cooling of the sorbent. Cooling water at approximately 15°C flows through the lower heat exchanger, enabling reduction of the sorbent temperature to below 25°C before it returns to the adsorption section.

Figure 1 presents the pilot installation viewed from the conveyor connecting the cooling section, visible as the insulated column on the left, with the adsorption section, visible as the column on the right. The regeneration section is located on the opposite side of the facility and is only partly visible in the photograph. One belt conveyor transfers the activated carbon from the adsorption section to the regeneration section, while another conveyor transports the regenerated sorbent from the regeneration section to the cooling section. The silver-coloured cladding visible on the regeneration section, the cooling section and the conveyor between these sections protects and stabilises the mineral-wool insulation, ensuring continuity and high effectiveness of thermal insulation. Due to the presence of supporting structures and other power plant equipment, capturing a complete view of the installation in a single photograph is not feasible.



Fig. 1. Illustrative photograph of research facility.

A simplified process scheme of the installation is shown in Fig. 2. The scheme illustrates the main circuits present in the CO_2 capture system, including the flue gas path, sorbent circulation loop, heating medium circuit, cooling-water circuit and CO_2-rich gas outlet. The sections connecting the bottom of one column with the top of the next column represent belt conveyors used for transporting the activated carbon between the process sections.

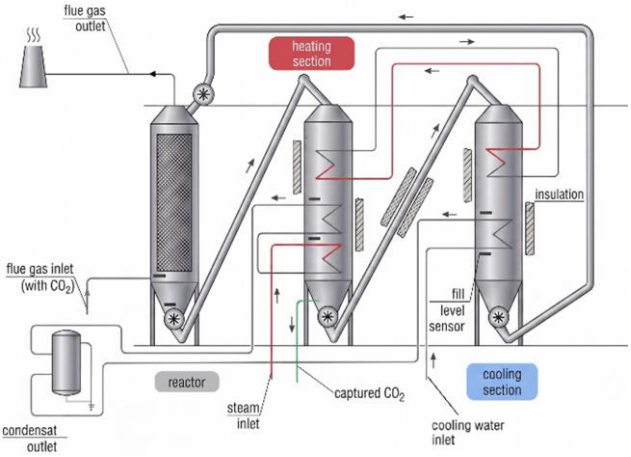


Fig. 2. Scheme of research facility.

The flue gas is introduced into the lower part of the adsorption reactor and is withdrawn from the upper part of the reactor under a slight negative pressure. In the upper parts of the regeneration and cooling sections, heat exchangers filled with circulating water form an internal heat-recovery loop between these two sections. In the middle and lower parts of the regeneration section, additional heat exchangers are installed. Saturated steam extracted from the turbine is supplied to the inlet of the lower heat exchanger, where it condenses while transferring heat to the activated carbon. The condensate then flows through the middle heat exchanger and is subsequently discharged to the condensate tank, where it is cooled before being released to the drainage system. The CO_2-rich gas released from the activated carbon during thermal desorption is extracted by a small fan and discharged from the installation. In the lower part of the cooling section, a heat exchanger supplied with cold water is used to reduce the temperature of the regenerated sorbent before it returns to the adsorption section. After leaving the cooling section, the water is directed to the condensate tank, where it assists in reducing the condensate temperature before discharge to the drainage system.

2.2. Structural layout of the research facility

The pilot installation was designed in a triangular configuration, in which the three main process sections (adsorption, regeneration and cooling) are located at the vertices of a triangle, while the sorbent transport system forms its sides. This arrangement enabled efficient utilisation of the available space and ensured compliance with structural constraints associated with installing the system inside an existing building. The adopted layout also provides protection of the installation components against adverse environmental conditions and facilitates operation and maintenance. A vertically stacked configuration was initially considered, as it would have theoretically reduced the number of required belt conveyors. However, this option exceeded the available floor height and permissible structural load limits, and was therefore rejected at the design stage.

2.3. Characteristics of flue gases feeding the system

The flue gas supplied to the adsorption section originated from a power boiler operating under real plant conditions. Consequently, its chemical composition exhibited continuous variability, resulting in significant fluctuations in the carbon dioxide (CO_2) concentration within the analysed stream. The recorded volumetric CO_2 concentrations ranged from 4,81% to 7.16%, which is considerably lower than the values assumed at the design stage of the pilot installation. The CO_2 concentration in the flue gas was measured using a Vaisala CARBOCAP® GMP251 probe based on infrared (IR) absorption technology.

2.4. Information about the adsorbent

Activated carbon was selected as the sorbent material primarily due to its favourable thermo-physical properties, in particular its relatively high heat transfer coefficient on the solid side, reported in the range of 69–117 W/(m^2·K) [17]. An additional factor influencing this choice was its superior mechanical strength compared with alternative sorbents such as zeolite 13X.

Although zeolites exhibit more favourable adsorption characteristics, resulting in lower specific energy consumption in MBTSA processes, their practical applicability remains limited. Simulation studies indicate that the specific energy demand for zeolite 13X may reach approximately 2.3 MJ/kg CO_2 [16], whereas for activated carbon it is estimated at approximately 5.7 MJ/kg CO_2 [17]. However, commercially available zeolites are characterised by relatively low mechanical strength and high brittleness, leading to rapid degradation under continuous circulation conditions. This makes their application in MBTSA systems currently impractical.

The thermo-physical properties of the activated carbon have been reported in the literature [17,31]. Its principal characteristics are summarised in Table 1, while a photograph of the material in its original packaging is presented in Fig. 3.

Table 1. Selected parameters of activated carbon [32].

Shape	Specific surface area	Average particle diameter	Hardness
Spherical	1100-1300 m^2/g	≈0,7 mm	≥95%



Fig. 3. BAC-type activated carbon: a) in its original packaging; b) spilled out on a paper.

3. Analysis of experimental results

The experimental results are presented in graphical form and include both direct measurements obtained from the pilot installation and values calculated on the basis of these measurements. All data were acquired and archived using a SCADA (supervisory control and data acquisition) system, which enables continuous monitoring of process parameters based on signals from sensors installed throughout the installation.

Figures 4 and 5 present selected measurement data recorded during operation of the pilot unit, including:

- CO_2 concentration in the flue gas at the inlet and outlet of the adsorption section (Figs. 4a and 5a),
- mass flow rate of the activated carbon (Figs. 4b and 5b),
- volumetric flow rate of the supplied flue gas (Figs. 4b and 5b).

In addition, two key performance indicators were determined based on the recorded data:

- CO_2 capture efficiency (η), defined as the relative reduction in CO_2 concentration in the flue gas after contact with the sorbent. This parameter was calculated according to the following equation:

$$\eta = 1 - \frac{CO_{2,out}}{CO_{2,in}}, \quad (1)$$

where: η – CO_2 capture efficiency [%], $CO_{2,out}$ – CO_2 concentration in flue gas after contact with the adsorbent [%], $CO_{2,in}$ – CO_2 concentration in flue gas before contact with the adsorbent [%],

- energy consumption of the CO_2 capture process (ζ), defined as the ratio of the total heat supplied for sorbent regeneration to the mass of captured CO_2:

$$\zeta = \frac{Q}{m_{CC}}, \quad (2)$$

where: ζ – energy consumption of CO_2 capture [MJ/kgCO_2], Q – thermal energy supplied via steam for sorbent regeneration [MJ], m_{CC} – mass of CO_2 captured from the flue gas [kgCO_2].

Figure 4 presents the results of measurements and calculations performed on 8 March 2024. Although these are not the earliest available datasets, it should be noted that the activated carbon used during this campaign had already been subjected to significant prior operation (several dozen hours of circulation within the system). Consequently, partial sorbent degradation and a reduction in adsorption performance were expected.

The results presented correspond to an approximately 30-minute segment of measurement data selected from the analysed day. This period was chosen because it represented the longest uninterrupted operation of the installation under a constant activated carbon mass flow rate and a relatively stable flue gas volumetric flow rate (Fig. 4b). This approach limited the influence of transient operating conditions on CO_2 capture efficiency and specific energy consumption. As shown in Fig. 4a, the CO_2 concentration in the flue gas entering the adsorption column varied within the range of 6–7%, while the outlet concentration averaged approximately 3%. This corresponded to a capture effi-

ciency of 50–60% during most of the analysed interval. At the same time, a high specific energy consumption was observed (Fig. 4c), with a median value of 55.3 MJ/kgCO_2, which must be considered unfavourable from the standpoint of energy performance.

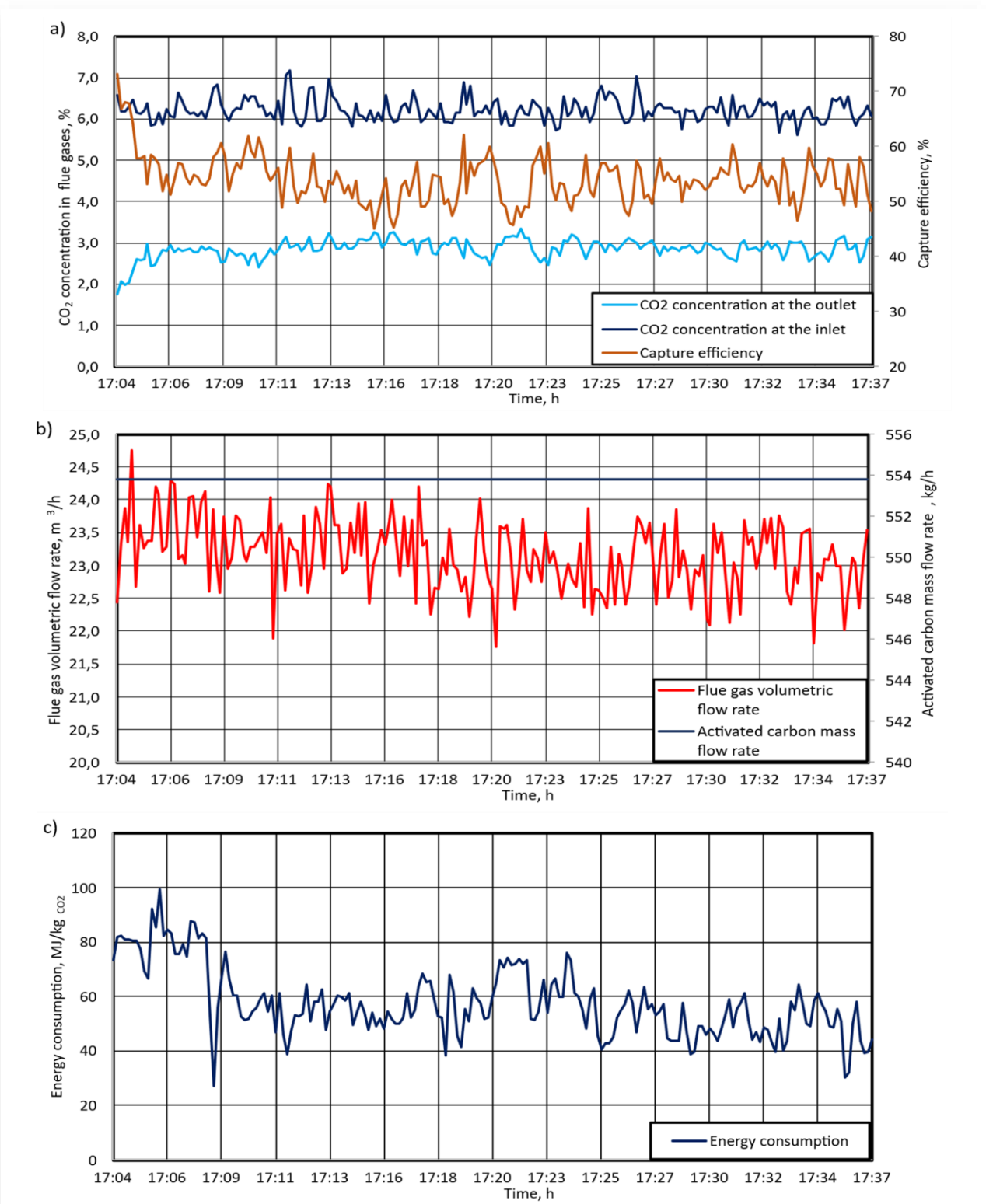
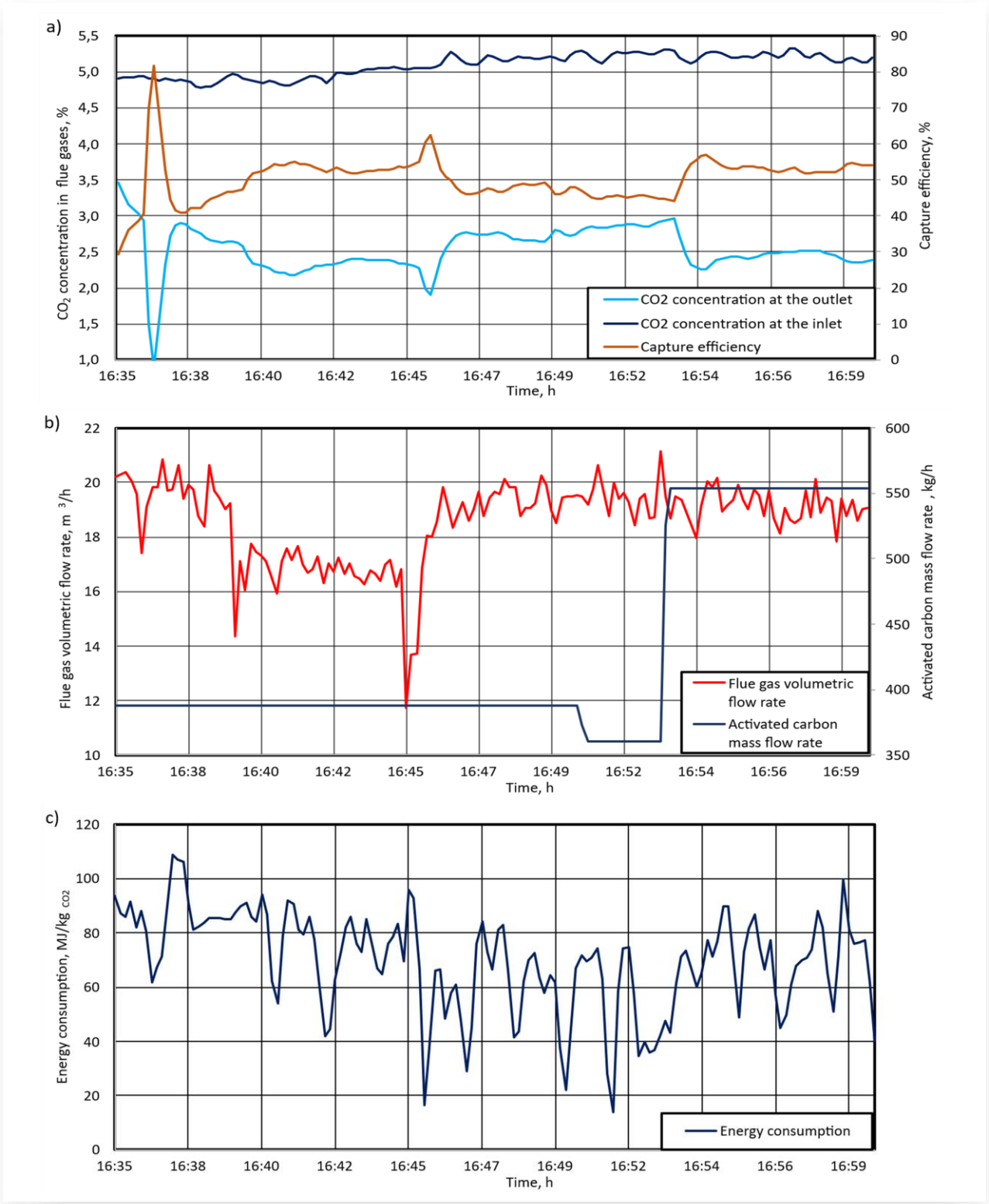


Fig. 4. Results obtained on 8 March 2024: a) CO_2 concentration in the inlet and outlet flue gas streams and corresponding capture efficiency; b) volumetric flow rate of the flue gas and mass flow rate of the activated carbon; c) specific energy consumption of the capture process.

Figure 5 presents the results obtained on 17 April 2024. During the period between the two measurement campaigns, the installation remained inactive, and no fresh sorbent was introduced into the circulation loop, implying further physico-chemical degradation of the activated carbon. In contrast to the relatively stable conditions shown in Fig. 5, the time interval pre-

sented in Fig. 5b exhibits noticeable variability in both the activated carbon mass flow rate and the flue gas volumetric flow rate. These variations directly affected the CO_2 concentration at the reactor outlet. A decrease in flue gas flow rate or an increase in sorbent feed resulted in improved capture efficiency, whereas the opposite changes led to a reduction in performance.

Pronounced changes in specific energy consumption were also observed (Fig. 5c); however, its response was less immediate. The specific energy demand exhibited a delayed reaction to variations in the sorbent mass flow rate, which can be attributed to system inertia, including gradual sorbent dosing through the rotary valve and the dynamic behaviour of the internal heat recovery loop.



Significant variations in the operating parameters of the installation may substantially affect data interpretation, particularly when datasets covering periods longer than two hours are analysed with a time resolution of 30 s. In contrast, results

obtained over shorter intervals with a 15 s sampling step allow for more detailed analysis of transient effects occurring after changes in key operating conditions.

4. Conclusions

The analysis of results obtained from the two measurement series clearly indicates a significant influence of the activated carbon mass flow rate on the efficiency of the CO_2 adsorption process. Although increasing the sorbent feed appears to be a straightforward method for improving capture efficiency, it may simultaneously lead to higher specific energy consumption and an increased risk of insufficient heating of the sorbent to the required regeneration temperature. Under the investigated experimental conditions, the specific energy demand reached very high values, representing a major barrier to potential industrial implementation of the technology. For this method to become attractive from both economic and environmental perspectives, a substantial reduction in regeneration energy consumption is essential. Inadequate heating of the activated carbon results not only in incomplete sorbent regeneration, leading to reduced adsorption capacity, but also in gradual cooling of the internal heat recovery circuit. This effect may further deteriorate the overall energy balance of the installation and hinder the achievement of stable operating conditions.

It should also be pointed out that the presented results were obtained using the sorbent that had already operated in the circulation loop for several hours, implying a reduction in its initial adsorption performance. Previous studies [31] have reported significantly higher CO_2 capture efficiencies, reaching approximately 76%, together with lower specific energy consumption of about 25 MJ/kgCO_2, when partial replacement of activated carbon was implemented during operation.

In light of these observations, further optimisation of the MBTSA technology appears justified, both in terms of installation design and sorbent selection. One potential development pathway is the reconstruction of the system into a vertically stacked configuration, in which the individual process sections would be arranged one above another. Such a layout could reduce heat losses associated with sorbent transport between sections and decrease the risk of leakage through flexible components (e.g. seals), which may allow ingress of cold and humid ambient air. In parallel, further investigations of alternative commercial sorbents are recommended, particularly those offering lower regeneration energy demand, higher CO_2 selectivity, and mechanical durability comparable to that of activated carbon.

The obtained results should also be considered in the broader context of Polish pilot and demonstration experience. Compared with Polish pilot tests based on amine processes, in which CO_2 removal above 90% and large cumulative amounts of captured CO_2 were reported [25], the results obtained in the present MBTSA study confirm the technical feasibility of conducting an adsorption-based CO_2 capture process using real flue gas from coal combustion. At the same time, however, they indicate much stronger limitations related to regeneration energy and solid-phase heat management. The measured capture efficiency of approximately 50–60% at an inlet CO_2 concentration of 6–7 % vol. and the median specific energy consumption of 55.3 MJ/kgCO_2 indicate that the investigated configuration is not yet energetically competitive with mature absorption-based processes. At the same time, the previous result of approximately 76% capture efficiency and about 25 MJ/kgCO_2 after partial replacement of the activated carbon shows that this technology is highly sensitive to sorbent condition, heat recovery efficiency and operating parameters. Therefore, the practical assessment of MBTSA technology should include not only instantaneous capture efficiency, but also sorbent ageing, regeneration completeness, steam parameters, cooling demand, heat losses during sorbent transport, internal heat recovery, leaks leading to the intake of cold and humid ambient air, and long-term operational stability [30].

Against the background of the international literature, it should only be noted that mature amine absorption processes, such as Shell CANSOLV [4] and moving-bed systems developed by Kawasaki [19,20], confirm the key importance of sorbent type, regeneration strategy and thermal integration for the achieved CO_2 capture performance.

At the same time, the results obtained in the present MBTSA installation cannot be directly compared on a one-to-one basis with results reported for other pilot and demonstration CO_2 capture installations [25−30]. These installations were based on different capture methods, including primarily amine absorption and cyclic adsorption processes, and they also differed in process configuration, scale, operating pressure, regeneration strategy, heat source, gas pretreatment requirements and performance assessment indicators. Moreover, the experimental campaign described in this study revealed a number of design and construction imperfections in the investigated installation that may have adversely affected the measured capture efficiency and specific energy consumption. These include excessive heat losses during sorbent transport, possible air intake through flexible connections and sealing elements, non-uniform heating of the circulating activated carbon, incomplete regeneration, limitations of the internal heat recovery system and process sensitivity to sorbent ageing and dosing stability. Therefore, before the obtained results can be used for a reliable quantitative comparison with other demonstration studies, the identified design and construction problems should be eliminated, and the installation should be retested under repeatable operating conditions with clearly defined boundary parameters.

Acknowledgements

The research that led to these results received funding from the Norway Grants 2014−2021 through the National Centre for Research and Development (grant NOR/POLNORCCS/0015/2019-00).

References

[1] Markewitz, P., Kuckshinrichs, W., Leitner, W., Linssen, J., Zapp, P., Bongartz, R., Schreiber, A., & Müller, T.E. (2012). Worldwide innovations in the development of carbon capture technologies and the utilization of CO_2. *Energy & Environmental Science*, 5, 7281–7305. doi: 10.1039/C2EE03403D

[2] Rubin, E.S., Davison, J.E., & Herzog, H.J. (2015). The cost of CO_2 capture and storage. *International Journal of Greenhouse Gas Control*, 40, 378–400. doi: 10.1016/j.ijggc.2015.05.018

[3] Rochelle, G.T. (2009). Amine scrubbing for CO_2 capture. *Science*, 325(5948), 1652–1654. doi: 10.1126/science.1176731

[4] Singh, A., & Stéphenne, K. (2014). Shell Cansolv CO_2 capture technology: Achievement from First Commercial Plant. *Energy Procedia*, 63, 1678–1685. doi:10.1016/j.egypro.2014.11.177

[5] Chao, C., Deng, Y., Dewil, R., Baeyens, J., & Fan, X. (2021). Post-combustion carbon capture. *Renewable and Sustainable Energy Reviews*, 138, 110490. doi: 10.1016/j.rser.2020.110490

[6] Choi, S., Drese, J.H., & Jones, C.W. (2009). Adsorbent materials for carbon dioxide capture from large anthropogenic point sources. *ChemSusChem*, 2(9), 796–854. doi: 10.1002/cssc.200900036

[7] Samanta, A., Zhao, A., Shimizu, G.K.H., Sarkar, P., & Gupta, R. (2012). Post-combustion CO_2 capture using solid sorbents: A review. *Industrial & Engineering Chemistry Research*, 51(4), 1438–1463. doi: 10.1021/ie200686q

[8] Raganati, F., Miccio, F., & Ammendola, P. (2021). Adsorption of carbon dioxide for post combustion capture: A review. *Energy & Fuels*, 35(16), 12845–12868. doi: 10.1021/acs.energyfuels.1c01618

[9] D'Alessandro, D.M., Smit, B., & Long, J.R. (2010). Carbon dioxide capture: Prospects for new materials. *Angewandte Chemie International Edition*, 49(35), 6058–6082. doi: 10.1002/anie.201000431

[10] Kong, M., Song, L., Liao, H., Zhang, S., Wang, Y., Deng, X., & Feng, W. (2024). A review on development of post combustion CO_2 capture technologies: Performance of carbon based, zeolites and MOFs adsorbents. *Fuel*, 362, 132103. doi: 10.1016/j.fuel.2024.132103

[11] Clausse, M., Merel, J., & Meunier, F. (2011). Numerical parametric study on CO_2 capture by indirect thermal swing adsorption. *International Journal of Greenhouse Gas Control*, 5(5), 1206–1213. doi: 10.1016/j.ijggc.2011.05.036

[12] Bonjour, J., Clausse, M., & Meunier F. (2005). A TSA process with indirect heating and cooling: parametric analysis and scaling-up to practical sizes. *Chemical Engineering and Processing: Process Intensification*, 44(9), 969–977. doi: 10.1016/j.cep.2005.01.002

[13] Kindra, V.O., Milukov, I.A., Shevchenko, I.V., Shabalova, S.I., & Kovalev, D.S. (2021). Thermodynamic analysis of cycle arrangements of the coal-fired thermal power plants with carbon capture. *Archives of Thermodynamics*, 42(4), 103–121. doi: 10.24425/ather.2021.139653

[14] Zhao, R., Deng, S., Zhao ,L., Li, S., Zhang, Y., & Liu, B. (2017). Performance analysis of temperature swing adsorption for CO_2 capture using thermodynamic properties of adsorbed phase. *Applied Thermal Engineering*, 123, 205–215. doi: 10.1016/j.applthermaleng.2017.05.042

[15] Zhao, R., Liu, L., Zhao, L., Deng, S., Li, S., & Zhang, Y. (2019). A comprehensive performance evaluation of temperature swing adsorption for post combustion carbon dioxide capture. *Renewable and Sustainable Energy Reviews*, 114, 109285. doi: 10.1016/j.rser.2019.109285

[16] Mondino, G., Grande, C.A., & Blom, R. (2017). Effect of gas recycling on the performance of a moving bed temperature swing (MBTSA) process for CO_2 capture in a coal fired power plant context. *Energies*, 10(6), 745. doi: 10.3390/en10060745

[17] Mondino, G., Grande, C.A., Blom, R., & Nord, L.O. (2019). Moving bed temperature swing adsorption for CO_2 capture from a natural gas combined cycle power plant. *International Journal of Greenhouse Gas Control*, 85, 58–70. doi: 10.1016/j.ijggc.2019.03.021

[18] Mondino, G., Grande, C.A., Blom, R., & Nord, L.O. (2022). Evaluation of MBTSA technology for CO_2 capture from waste to energy plants. *International Journal of Greenhouse Gas Control*, 118, 103685. doi: 10.1016/j.ijggc.2022.103685

[19] Okumura, T., Ogino, T., Nishibe, S., Nonaka, Y., Shoji, T., & Higashi, T. (2014). CO_2 Capture Test for a Moving-bed System Utilizing Low-temperature Steam. *Energy Procedia*, 63, 2249−2254. doi:10.1016/j.egypro.2014.11.243

[20] Okumura, T., Yoshizawa, K., Nishibe, S., Iwasaki, H., Kazari, M., & Hori, T. (2017). Parametric Testing of a Pilot-scale Design for a Moving-bed CO_2 Capture System Using Low-temperature Steam. *Energy Procedia*, 114, 2322–2329. doi: 10.1016/j.egypro.2017.03.1369

[21] Liu, Z., Wang, L., Kong, X., Li, P., & Yu, J. (2012). Onsite CO_2 capture from flue gas by an adsorption process in a coal fired power plant. *Industrial & Engineering Chemistry Research*, 51, 7355–7363. doi: 10.1021/ie3005308

[22] Wang, L., Liu, Z., Li, P., & Yu, J. (2013). Experimental evaluation of adsorption technology for CO_2 capture from flue gas in an existing coal fired power plant. *Chemical Engineering Science*, 101, 615–619. doi: 10.1016/j.ces.2013.07.028

[23] Xu, D., Xiao, P., Zhang, J., Li, G., Xiao, G., Webley, P.A., & Zhai, Y. (2013). Effects of water vapour on CO_2 capture with vacuum swing adsorption using activated carbon. *Chemical Engineering Journal*, 230, 64–72. doi: 10.1016/j.cej.2013.06.080

[24] Querejeta, N., García, S., Álvarez-Gutiérrez, N., Rubiera, F., & Pevida, C. (2019). Measuring heat capacity of activated carbons for CO_2 capture. *Journal of CO_2 Utilization*, 33, 148−156. doi: 10.1016/j.jcou.2019.05.018

[25] Stec, M., Tatarczuk, A., Więcław-Solny, L., Krótki, A., Spietz, T., Wilk, A., & Śpiewak, D. (2016). Demonstration of a post-combustion carbon capture pilot plant using amine-based solvents at the Łaziska Power Plant in Poland. *Clean Technologies and Environmental Policy*, 18, 151–160. doi: 10.1007/s10098-015-1001-2

[26] Więcław-Solny, L., Stec, M., Tatarczuk, A., Krótki, A., Spietz, T., & Wilk, A. (2013). First Polish Pilot Plant for CO_2 Post Combustion Capture. *Proceedings of the 2nd Post Combustion Capture Conference*, September 17–20, Bergen, Norway.

[27] Bochon, K., & Chmielniak, T. (2015). Energy and economic analysis of the carbon dioxide capture installation with the use of monoethanolamine and ammonia. *Archives of Thermodynamics*, 36(1), 93–110. doi: 10.1515/aoter-2015-0007

[28] Wawrzyńczak, D., Majchrzak-Kucęba, I., Srokosz, K., Kozak, M., Nowak, W., Zdeb, J., Smółka, W., & Zajchowski, A. (2019). The pilot dual-reflux vacuum pressure swing adsorption unit for CO_2 capture from flue gas. *Separation and Purification Technology*, 209, 560–570. doi: 10.1016/j.seppur.2018.07.079

[29] Majchrzak-Kucęba, I., Wawrzyńczak, D., Ściubidło, A., Zdeb, J., Smółka, W., & Zajchowski, A. (2019). Stability and regenerability of activated carbon used for CO_2 removal in pilot DR-VPSA unit in real power plant conditions. *Journal of CO_2 Utilization*, 29, 1–11. doi: 10.1016/j.jcou.2018.11.003

[30] Zima, W., Pawłowski, A., Grądziel, S., Cebula, A., Piwowarczyk, M., & Kozak-Jagieła, E. (2025). CO_2 capture from flue gases in a temperature swing moving bed – simulation results vs. the experiment. *Energy*, 327, 136445. doi: 10.1016/j.energy.2025.136445

[31] Kureha. *Bead-Shaped Activated Carbon*. https://www.kureha.co.jp/en/business/material/bac.html [accessed 22 Feb. 2025].

Co-published by
Institute of Fluid-Flow Machinery
Polish Academy of Sciences
Committee on Thermodynamics and Combustion
Polish Academy of Sciences

Copyright©2026 by the Authors under licence CC BY-NC-ND 4.0

http://www.imp.gda.pl/archives-of-thermodynamics/

Experimental study of a reversible ventilation – heat pump system with a ceramic regenerator

Katarzyna Katana[a], Andrzej Grzebielec[a*], Adam Szelągowski[a], Maksymilian Kruk[a], Krzysztof Bruzi[b]

[a]Warsaw University of Technology, pl. Politechniki 1, 00-665 Warszawa, Poland
[b]Respireco sp. z o.o., Piaski 39, 63-300 Pleszew, Poland
*Corresponding author email: andrzej.grzebielec@pw.edu.pl

Received: 07.02.2026; revised: 23.05.2026; accepted: 29.05.2026

Abstract

Mechanical supply-exhaust ventilation systems are increasingly required in newly constructed residential buildings, yet their higher primary energy consumption remains a key challenge, particularly given the growing demands of energy efficiency and unchanged fresh air requirements. Existing solutions based on recuperators achieve heat recovery efficiencies of 40−70%, whereas regenerative systems can exceed 90%, but their performance under real operating conditions and integration with heat pump technology has not been sufficiently investigated. This study presents an experimental analysis of a compact ventilation unit, dedicated to classrooms, operating in reversible mode with a rotary regenerator and an integrated R290 (propane) air-to-air heat pump. Measurements were conducted across an outdoor temperature range from 0.6°C to 8.6°C. The regenerator-only mode achieved heat recovery efficiency exceeding 90% throughout the entire tested temperature range. When the R290 heat pump was activated to sustain operation during periods of lower outdoor temperatures without an auxiliary heat source, the system yielded COP values between 3.70 and 4.31, substantially higher than 2.0−2.5 values typically reported for conventional air-to-air heat pumps. These results demonstrate that the proposed integration of regenerative heat recovery with a dedicated R290 heat pump constitutes a technically viable and energy-efficient solution for both heating and ventilation needs.

Keywords: Ventilation; Ceramic regenerator; Heat recovery; Heat pump; Energy efficiency

Vol. 47(2026), No. 3, 15–24; doi: 10.24425/ather.2026.3650

Cite this manuscript as: Katana, K., Grzebielec, A., Szelągowski, A., Kruk, M., & Bruzi, K. (2026). Experimental study of a reversible ventilation – heat pump system with a ceramic regenerator. *Archives of Thermodynamics*, 47(3), 15−24.

1. Introduction

All buildings occupied by people must be equipped with a ventilation system, whose primary function is to supply fresh air and remove used one [1,2]. However, the requirements for ventilation performance vary depending on building function and occupancy characteristics [3]. Providing adequate indoor air quality (IAQ) represents one of the central challenges of contemporary building engineering. High occupant density combined with extended occupancy periods leads to rapid deterioration of indoor air quality, manifested primarily through elevated concentrations of CO_2 and particulate matter. Transitioning to mechanical supply-and-exhaust ventilation resolves the IAQ problem but introduces substantial heating energy penalties, which can reach 35−40 kWh/m² annually at the building level [4]. Among available heat recovery technologies, fixed bed regenerators (FBR) based on ceramic fill represent an alternative to the widely used rotary and crossflow plate heat exchangers [5,6]. The effectiveness of heat exchangers in heat recovery systems depends on airflow rate, temperature differences, and the moisture content of the air streams [7]. Figures 1 and 2 show the actual heat recovery effectiveness for crossflow and rotary heat exchangers, respectively, for the full ranges of available products [8].

Nomenclature

i – specific enthalpy, J/kg
$\dot{m}$ – air mass flow rate, kg/s
p – gauge pressure, bar
P – electrical power, W
q – air mass flow rate
Q – heat, J
$\dot{Q}$ – heat capacity, W
RH – relative humidity, %
t – time, s
W – electrical energy, J

Greek symbols

η – regenerator effectiveness,
θ – air temperature, °C
τ – time period, s

Subscripts and Superscripts

1,2,3,4 – process periods
11 – exhaust at inlet of regenerator
21 – supply at inlet of regenerator
22 – supply at outlet of regenerator
I – indoor air
II – condenser air side
III – outdoor air
IV – evaporator air side
cycle – amount for one cycle
el – electric
n – number of cycles

Abbreviations and Acronyms

IAQ – indoor air quality
COP – coefficient of performance
FBR – fixed bed regenerators
R290 – propane refrigerant

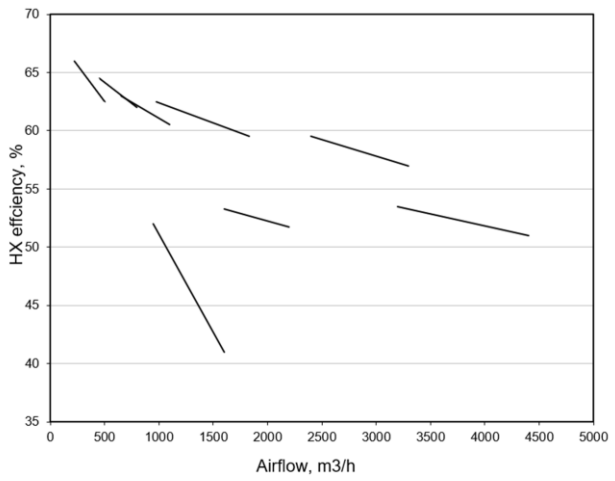


Fig. 1. Crossflow heat exchangers effectiveness (each line corresponds to one heat exchanger from the product range) [18].

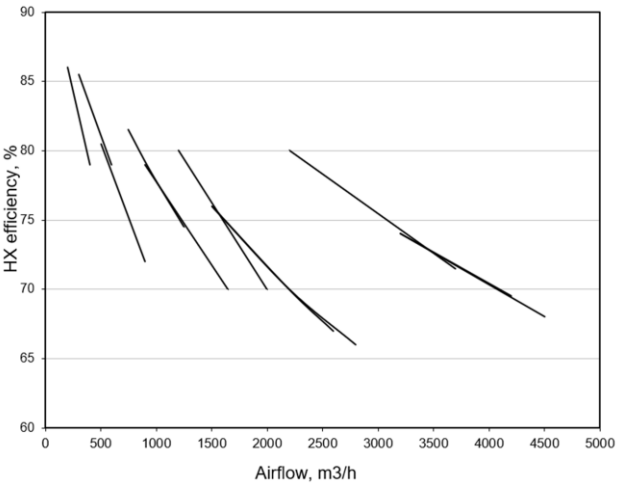


Fig. 2. Rotary heat exchangers effectiveness (each line corresponds to one heat exchanger from the product range) [18].

Each line corresponds to one heat exchanger from the product range. Results show that for rotary heat exchangers, effectiveness ranges from 40% to 66%. For each heat exchanger in the product range, effectiveness decreases when airflow increases (thus airflow speed). Similar results are obtained for rotary heat exchangers, but with higher effectiveness levels ranging from 65% to 86%.

Ceramic regenerators are characterised by a significantly greater heat transfer surface area per unit volume compared with recuperators, combined with the ability to recover both sensible and latent heat through adsorption and desorption of moisture on the porous ceramic surface [9]. The reversible operation of such devices, in which a single duct alternately serves as supply and exhaust, driven by a reversing fan, allows deployment without the need for separate supply and exhaust duct networks, making them particularly well-suited for retrofit applications in existing buildings. Commercial implementations of ceramic FBR ventilation units are currently offered by many manufacturers; however, systematic experimental characterisation of their performance under controlled conditions remains limited in the open literature.

A further improvement in energy efficiency can be achieved by integrating the ceramic regenerator with a heat pump. Exhaust air heat pumps (EAHP), which utilise the warm exhaust air stream as the heat source for the refrigeration circuit, represent an emerging class of ventilation and heating systems capable of simultaneously fulfilling the ventilation and space heating functions of a building [10]. The use of exhaust air at approximately 20°C as the heat source, rather than cold outdoor air, results in significantly more favourable evaporator operating conditions compared to conventional air-source heat pumps (ASHP), which translates directly into higher coefficients of performance [11]. The refrigerant R290 (propane) is an increasingly preferred working fluid for such applications due to its favourable thermodynamic properties and near-zero global warming potential (GWP) [12].

Despite the growing commercial interest in integrated ventilation – heat pump systems, published experimental data on systems combining a ceramic FBR regenerator with a heat pump

circuit are scarce. Niemierska and Jadwiszczak [5] investigated a ceramic FBR regenerator in a decentralised reversible ventilation system, reporting temperature effectiveness values above 80%, but without integration with a heat pump. Aktershev et al. [6] conducted a parametric numerical study of regenerative heat exchangers with periodic flow reversal. To the authors' knowledge, no experimental study has so far reported the combined performance of a ceramic fixed-bed regenerator integrated with an R290 air-to-air heat pump. The present paper addresses this gap. A laboratory test stand was constructed at the Institute of Heat Engineering, Warsaw University of Technology. The system was tested in both regenerator-only mode and heat pump mode. The primary objectives of this study were to develop a method for determining the temperature and total effectiveness of the ceramic FBR regenerator that accounts for the cyclic nature of its operation, and to experimentally characterise the heating capacity and coefficient of performance of the integrated system under varying outdoor conditions.

2. Materials and methods

Figure 3 shows the experimental laboratory setup and the locations of the temperature and relative humidity sensors. The purpose of the stand was to test the heat regeneration effectiveness of ceramic blocks and the operation of a heat pump with an incorporated regenerator. Propane (R290) was used as the working refrigerant. The total charge of propane was equal to 800 g. Although R290 is classified as a class A3 flammable refrigerant according to the PN-EN 378 standard, this charge quantity is permissible for rooms that meet the minimum space requirements or are equipped with a leak detection system that activates additional ventilation [13].

The stand is composed of:

- ventilation duct, inside of which is a reversible fan (which allows for the airflow to alternate between directions using a specialised guide vane);
- heat regenerator in a form of ceramic blocks;
- two heat exchangers associated with a heat pump;
- compressor with an inverter;
- 4-way valve;
- an expansion valve;
- refrigerant receiver;
- air filters at the inlet and outlet of the duct.

The test stand is equipped with an automation system that enables changing airflow direction, airflow rate, compressor rotational speed, heat exchangers operating mode (evaporator/condenser) and storing the refrigerant in a receiver.

Inside the device, there are two rows of ceramic blocks, 30 in total. The top row consists of 15 blocks with dimensions of 150 × 150 × 300 mm, whereas the bottom row has 15 shorter blocks measuring 150 × 150 × 72 mm. The masses are equal to 6.15 kg and 1.39 kg, respectively. The blocks are supported by thin-walled metal tubes. The total mass of the regenerator amounts to 113.1 kg, whereas the theoretical thermal capacity amounts to 99 528 J/K. The open flow area through each ceramic block is equal to approximately 0.01778 m². The physical layout of the ceramic blocks is presented in Fig. 4, while a photograph of the ceramic regenerator is shown in Fig. 5.

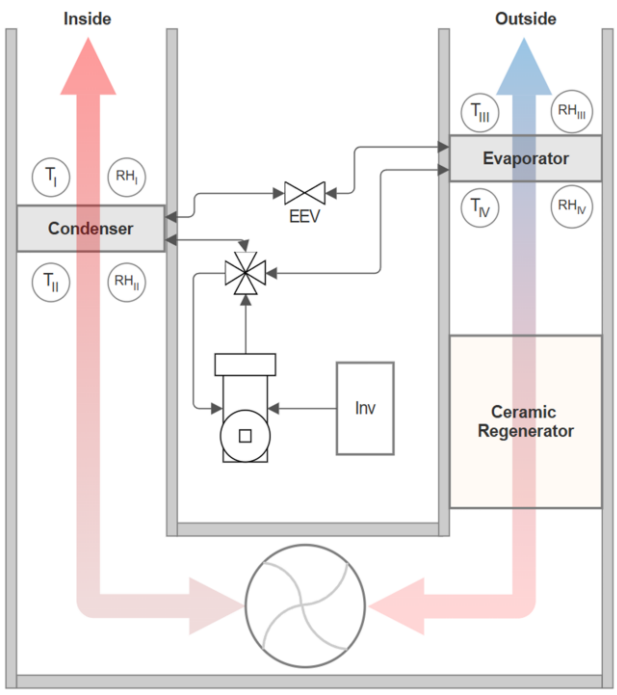


Fig. 3. Schematic diagram of the laboratory setup.

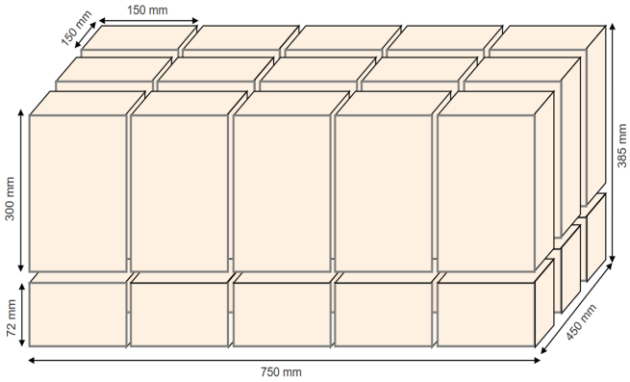


Fig. 4. Physical layout of ceramic blocks.



Fig. 5. Ceramic regenerator.

The device operates in two alternating modes. In an air supply phase, outdoor air flows through the ceramic regenerator, previously heated by the exhaust air removed from the room. As a result, the air supplied to the indoor space is preheated. During the air exhaust phase, indoor air is discharged to the outside while flowing through the said regenerator, which results in charging the heat storage. Additionally, incorporating a four-way valve allows the heat pump to operate in cooling mode during summer months.

NTC thermistors of accuracy class B were used for measuring temperature. In accordance with IEC 60539-1, the measurement tolerance of these sensors does not exceed ±0.425°C over the temperature range investigated in the device (from −10°C to 25°C) [14]. The relative humidity measurement accuracy is ±3% over the range of 20–80%, increasing linearly to ±4.5% for values outside this interval. An Iris-type damper (IRIS 250) was used to measure the airflow rate. The pressure difference was defined by two HK Instruments DPT250-R8 differential pressure transmitters, for which the measurement error is ±1%, corresponding to a maximum of ±8 Pa. The device also incorporated two Carel SPKT0041-DO pressure transducers on the refrigerant side, positioned at the discharge and suction ports of the compressor, corresponding to the condensation and evaporation pressures, respectively. Knowledge of the phase-transition pressures allows unambiguous determination of the condensation and evaporation temperatures. For this type of transducer, the measurement error does not exceed ±1%, which translates to a deviation of ±0.182 bar. To quantify the energy consumption of the control system, a Lumel N27P energy meter was employed, offering a measurement accuracy of 0.2% of the measuring range for active power, corresponding to approximately 2–3 W. The measurement instruments used in the experimental setup and their associated uncertainties are presented in Table 1.

Table 1. Measurement instruments and associated uncertainties used in the experimental setup.

Quantity	Instrument	Limit error	Standard uncertainty
Temperature	NTC class B	±0.425°C	0.245°C
Relative humidity	SHT20	±3% *RH* (20–80%), ±4.5% outside this range	1.732% RH
Airflow rate	IRIS250	±5%	2.887%
Air differential pressure	DPT250-R8	±1% of range	±8 Pa
Refrigerant pressure	Carel SPKT0041-DO	±1%	±0.182 bar
Electrical power	Lumel N27P	±0.2% of range	1.732 W

2.1. Ceramic regenerator effectiveness

In the first step, regenerator's effectiveness was tested for different temperature levels. Research was conducted in accordance with the norm: PN-EN 13141-8:2014-09 „Ventilation of buildings — Testing of performance of components/products for residential ventilation — Part 8: Testing of performance of ductless mechanical supply and exhaust units (including heat recovery) for mechanical ventilation systems" [10]. The device works periodically (supply/exhaust modes), and its cycle stages are shown in Fig. 6, where: τ_1 – time of air flow from the building to the outside, [s]; τ_2 – dwell time, [s]; τ_3 – time of air flow from the outside into the building, [s]; τ_4 – dwell time, [s]; $\dot{m}_{22}$ – mass flow rate of supply air at the outlet, [kg/s]; $\dot{m}_{11}$ – mass flow rate of exhaust air at the inlet, [kg/s].

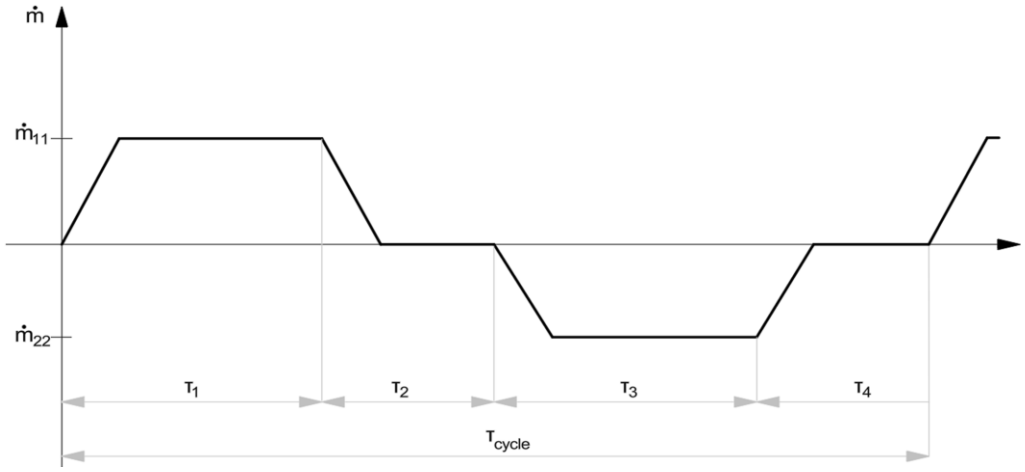


Fig. 6. Changes in the air mass flow rate as a function of time during one full cycle [19].

Times τ_1 and τ_3 correspond to the half time required for the fan guide vane to turn. The measured dwell time is equal to 4 s, therefore: τ_2 = 2.0 s and τ_4 = 2.0 s. This is the result of the device's design. The fan runs continuously, while the direction of airflow is changed by a guide vane; the fan is not turned off.

Therefore, the time to complete one full cycle is expressed as:

$$\tau_{cycle} = \tau_1 + \tau_2 + \tau_3 + \tau_4, [\text{s}]. \quad (1)$$

For this type of device, regenerator's effectiveness is defined by [15]:

$$\eta_\theta = \frac{\int(\theta_{22}-\theta_{21})\mathrm{d}t}{\int(\theta_{11}-\theta_{21})\mathrm{d}t} \cdot \frac{\dot{m}_{22}}{\dot{m}_{11}}, \quad (2)$$

where: θ_{22} – supply air temperature at the outlet of the heat recovery component, [°C]; θ_{21} – supply air temperature at the inlet of the heat recovery component, [°C]; θ_{11} – exhaust air temperature at the inlet of the heat recovery component, [°C].

Figure 7 presents regenerator's effectiveness results obtained during laboratory tests in accordance with Eq. (2) for the outside temperatures: −15°C, −7°C, +2°C, +7°C, and inside temperature equal to +20°C.

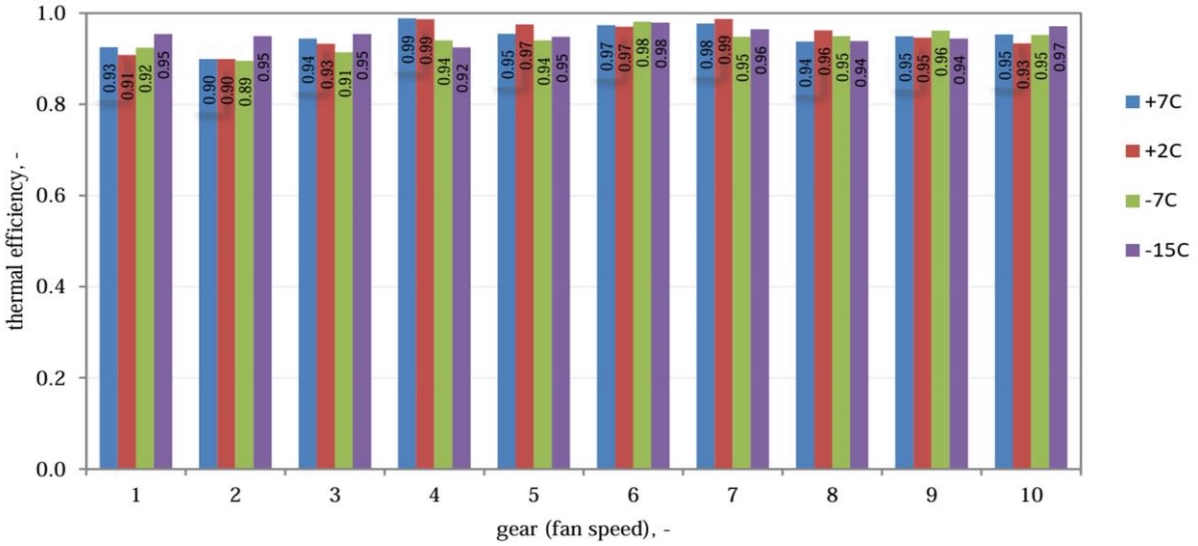


Fig. 7. Obtained ceramic regenerator's effectiveness.

In all analysed cases, the regenerator effectiveness exceeded 90%. The energy efficiency is influenced by the cycle duration and the length of the regenerator. In this article, only the results for the optimal cycle duration of 240 s and the optimal regenerator length are presented. Importantly, no water condensation occurred in the regenerator, which is a fundamental problem in the case of rotary and crossflow heat exchangers. In recuperators, electric preheaters are often used to preheat air to prevent condensation and water freezing. This solution significantly decreases heat recovery efficiency [16]. The absence of water vapour condensation in the ceramic regenerator can be attributed to two main factors. First, due to the short switching cycle in reversible operation mode, the ceramic mass is alternately heated and cooled at brief intervals, preventing its temperature from dropping to the dew point of the exhaust air. Second, the hygroscopic nature of the ceramic material allows moisture to be captured through adsorption rather than condensation, meaning that water vapour is retained within the material structure without forming a liquid phase.

2.2. Heat pump operation and performance

The heat supplied to the air stream was calculated from the difference in specific enthalpy between the supply and exhaust air. The specific enthalpy was calculated based on the temperature and relative humidity. The volumetric flow rate was measured using an ISA-standard nozzle equipped with pitot-tube measurements. The maximum supply air volumetric flow rate reached 1380 m³/h. The total heat supplied to the room during one cycle is given by:

$$Q_{cycle} = \int_{t=0}^{t=t_{half\ cycle}} \left[\dot{m}(t)\left(i_2(t) - i_3(t)\right)\right] dt,\ [\mathrm{J}], \quad (3)$$

where t = 0 [s] and $t_{half,cycle}$ [s] are, respectively, the time of beginning and ending of the half-cycle, $\dot{m}(t)$ [kg/s] is an air mass flow rate, $i_2(t)$ [kJ/kg] and $i_3(t)$ [kJ/kg] are, respectively, instantaneous specific enthalpies of the air supplied and removed.

The electrical energy supplied in one cycle consists of the energy used by the compressor, fan and automation system:

$$W_{cycle} = \int_{t=0}^{t=t_{cycle}} P_{el}\ (t)dt,\ [\mathrm{J}], \quad (4)$$

where t = 0 [s] and t_{cycle} [s] are, respectively, the beginning and ending times of the entire cycle, and $P_{el}(t)$ is the total electrical power supplied at a given moment.

This allows us to calculate the coefficient of performance (COP) during one cycle:

$$\mathrm{COP} = \frac{Q_{cycle}}{W_{cycle}}. \quad (5)$$

To determine the average heating capacity and electrical power, the total heat supplied and total electrical energy supplied were divided by the analysed time period:

$$\dot{Q}_{cycle} = \frac{Q_{cycle}}{\tau_1 - \tau_0},\ [\mathrm{W}], \quad (6)$$

$$P_{cycle} = \frac{W_{cycle}}{\tau_2 - \tau_0},\ [\mathrm{W}]. \quad (7)$$

3. Results and discussion

Studies of the vapour-compression heat pump with a regenerator were carried out for different outside temperatures in a range of 0.6°C to 8.6°C. The indoor air temperature was maintained approximately at 22°C. Each half-cycle of air supply and exhaust lasted 60 s, giving a full cycle duration of 120 s. Figure 8 shows the temperature changes over 30 full cycles (equivalent to 1 hour) at an outdoor temperature of 1.1°C. A close-up of tem-

perature changes during one cycle is shown in Fig. 9. The measured temperatures are: θ_I – indoor air temperature, [°C]; θ_{II} – condenser air-side temperature, [°C]; θ_{III} – outdoor air temperature, [°C]; θ_{IV} – evaporator air-side temperature, [°C].

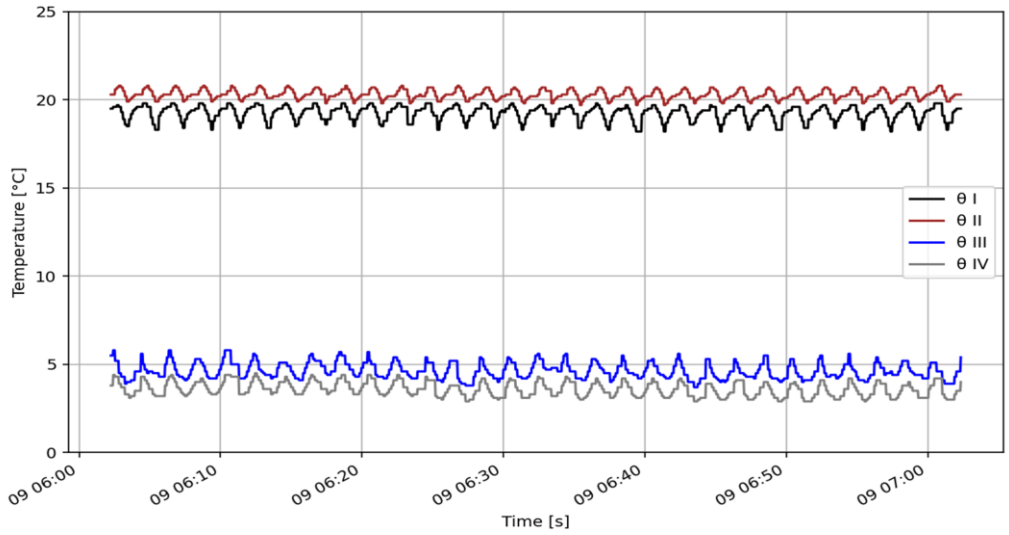


Fig. 8. Temperature changes during 30 full cycles.

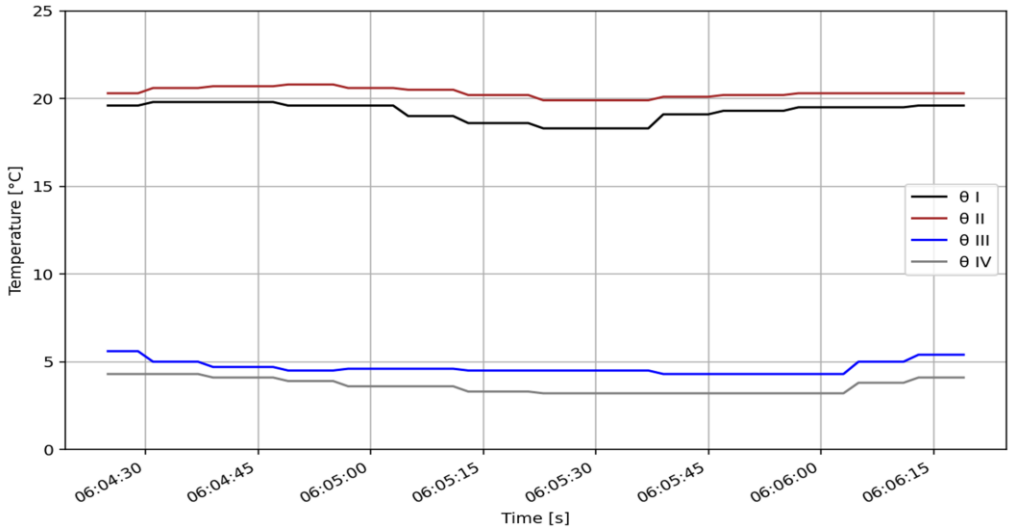


Fig. 9. Temperature changes during one full cycle.

Figure 10 presents changes in relative humidity during the same cycle as shown in Fig. 8. Measured relative humidities are: RH_I – indoor air relative humidity, [%]; RH_{II} – condenser air-side relative humidity, [%]; RH_{III} – outdoor air relative humidity, [%]; RH_{IV} – evaporator air-side relative humidity, [%]. The measuring points for temperature and relative humidity are shown in Fig. 3.

Figure 11 shows the changes in heating capacity and electrical power consumption during one full cycle for the outside temperature of 0.6°C. The electric power consumption varied only slightly, from 1150 W to 1220 W. The average heating capacity of this cycle was equal to 5306 W with a peak value exceeding 11 000 W, which is a result of accumulating heat in a ceramic regenerator. During the air exhaust phase, the heating capacity is equal to zero.

The experimental investigation of the device operating in heat pump mode was carried out under outdoor air temperature conditions ranging from 0.6°C to 8.6°C. The indoor temperature was equal to approximately 20°C, while the indoor relative humidity remained approximately 30% across all measurement series. The relatively low indoor relative humidity recorded throughout the experiments reflects the conditions of the laboratory facility in which the device was installed, rather than typical residential indoor climate conditions. The relative humidity of the outdoor air for the investigated measurement series as a function of outdoor temperature is presented in Fig. 12.

Refrigerant parameters remained stable across the tested outside temperature range. The system was operated to keep the discharge pressure at 15 bar. Refrigerant condensation and evaporation pressures are shown in Fig. 13. As the outdoor temperature increases, the evaporation pressure rises. This reduces the pressure difference between the suction and discharge sides of the compressor, resulting in lower power consumption and a higher COP.

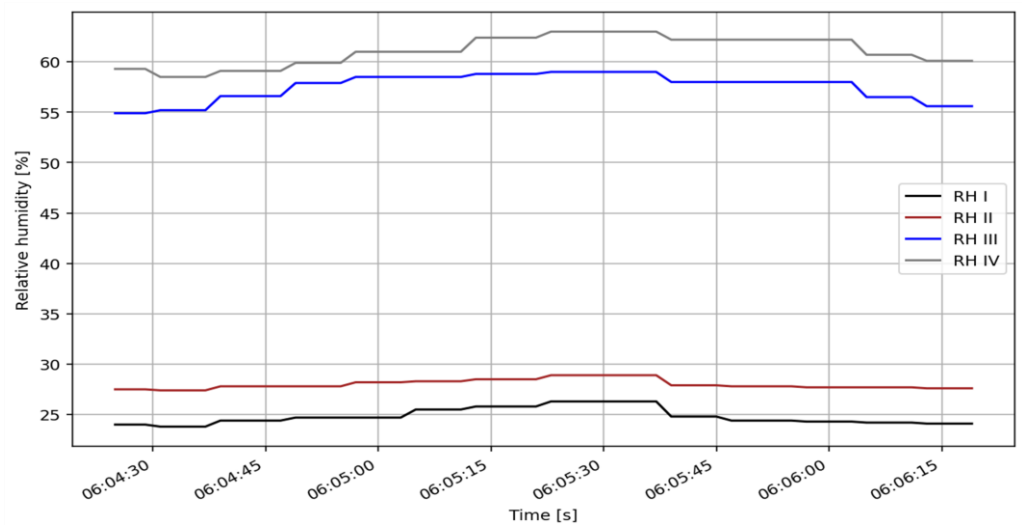


Fig. 10. Relative humidity changes during one full cycle.

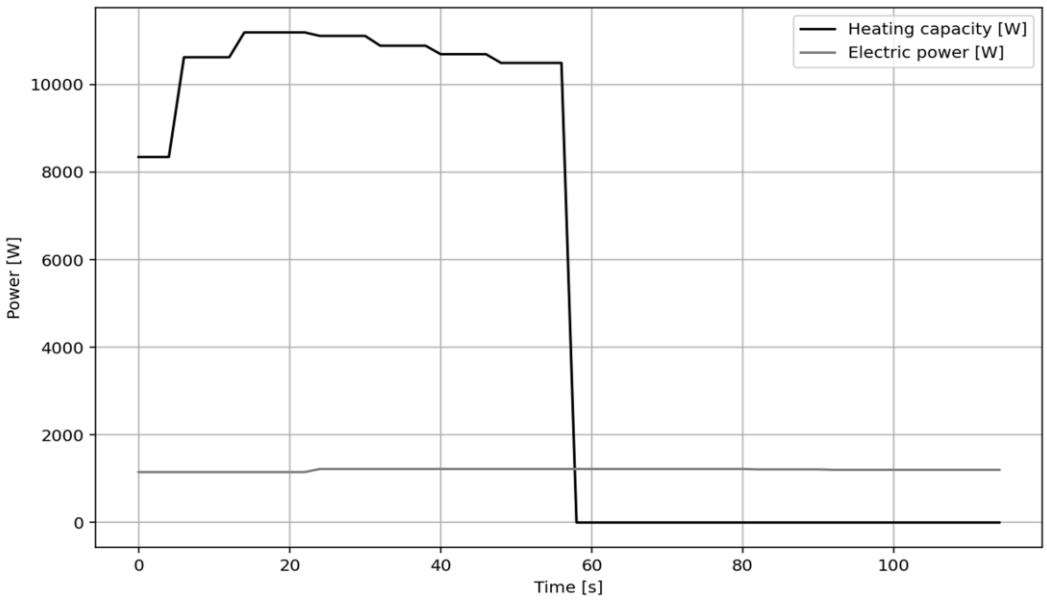


Fig. 11. Heating capacity and electrical power changes during one full cycle.

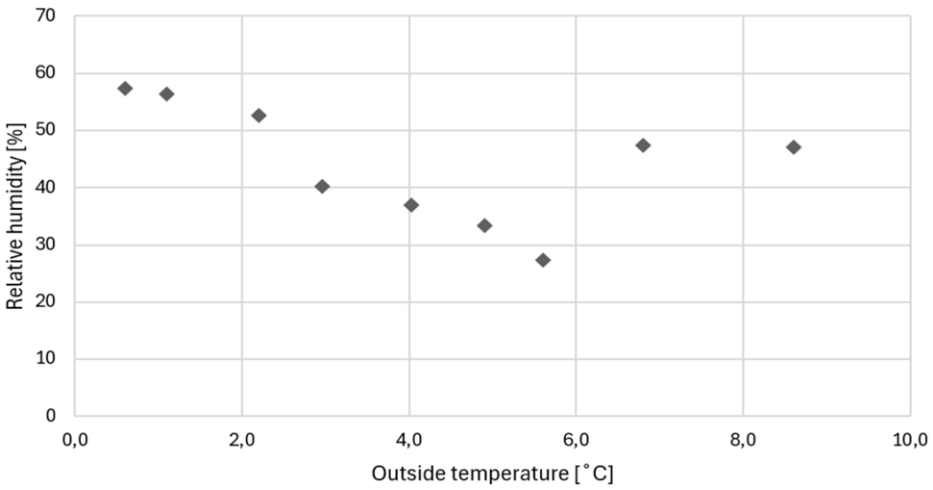


Fig. 12. Relative humidity vs. outside temperature.

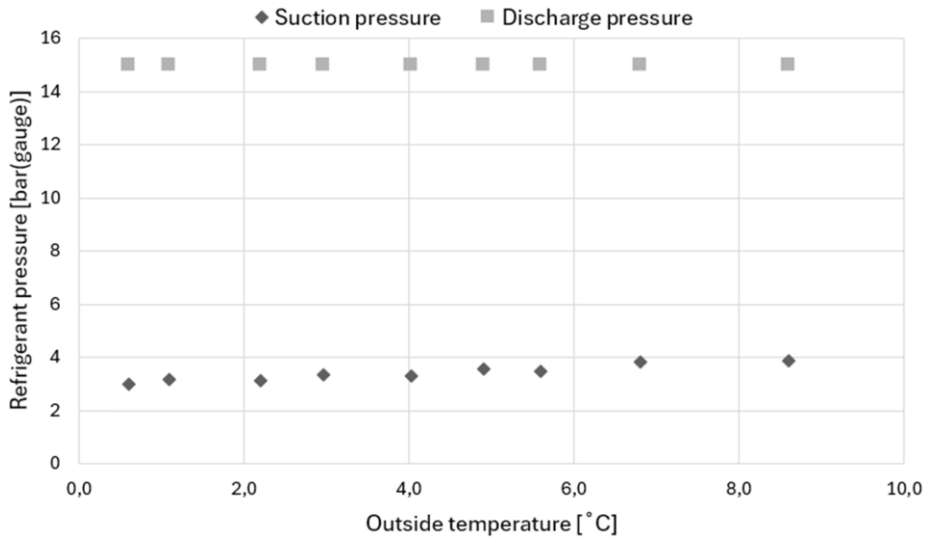


Fig. 13. Suction and discharge refrigerant gauge pressures vs. outside temperature.

The device's electrical power demand ranges from 1039 W to 1387 W. The electricity consumption of the rotary fan and automation system remained unchanged across the entire range of outside temperatures, amounting to 460 W. The heating capacity supplied to the room ranges from 4180 W to 5735 W. The uncertainty of the electrical power measurement is practically negligible, as it is equal to ±0.45%. The calculated expanded uncertainty of heating capacity, determined in accordance with the Guide to Uncertainty in Measurement (GUM) methodology [17], amounts to ±8.9% at a coverage factor of $k = 2$, corresponding to a confidence level of approximately 95%.

Heating capacity exhibited an increasing trend with decreasing outdoor air temperature. This phenomenon is a consequence of the decreasing temperature difference between the indoor and outdoor air as the outdoor temperature rises, which, at a constant mass flow rate and under maintained constant condensation pressure, results in a reduced heat flux delivered to the conditioned space. The electrical power consumption exhibits a slight decreasing trend with the increasing outdoor air temperature, driven by the gradual improvement in evaporator operating conditions: as the outdoor temperature rises, the evaporation temperature increases, reducing the pressure differential between the suction and discharge sides of the compressor, and thereby lowering the specific compression work.

Figure 14 shows the heating capacity of the device and its electrical power consumption at different outdoor temperatures.

Since both the heating capacity and the electrical power consumption decrease with increasing outdoor temperature at comparable rates, their ratio (COP) remains relatively stable across the investigated temperature range as shown in Fig 15. However, given the limited number of measurement series available, no statistically robust trend in COP as a function of outdoor temperature can be established from the present dataset, and this relationship warrants further investigation over a wider range of operating conditions. The COP of the heat pump with a ceramic regenerator was on average 3.70, and it reached the maximum value of 4.31 for the outside temperature of 1.1°C.

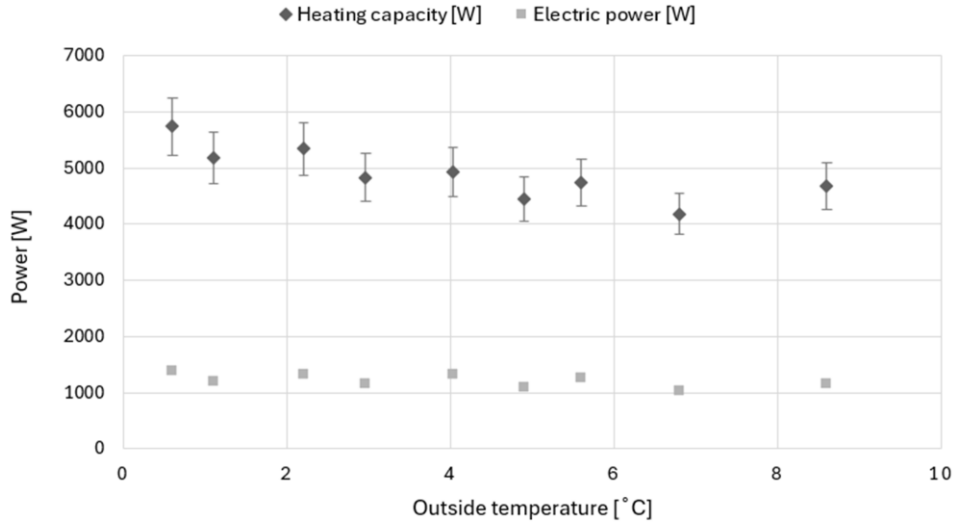


Fig. 14. Heating capacity and electric power vs. outside temperature.

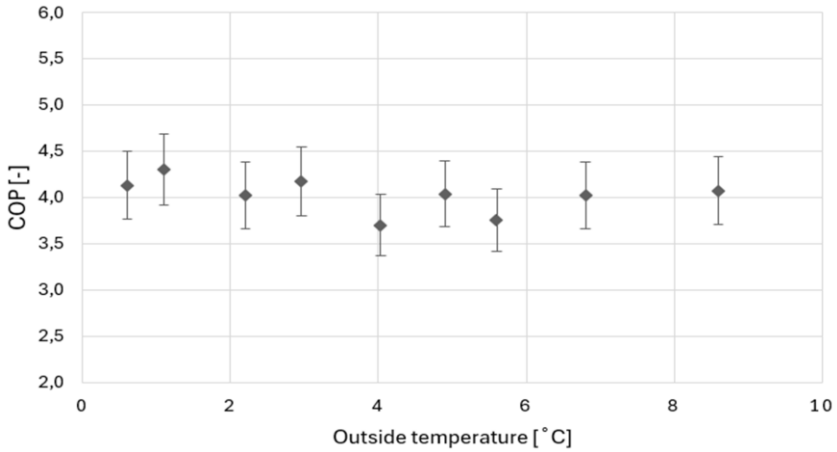


Fig. 15. COP vs. outside temperature.

4. Conclusions

This study experimentally characterised the performance of a compact reversible ventilation unit integrating a ceramic fixed-bed regenerator with an R290 vapour-compression heat pump. The following conclusions can be drawn from this study:

- Integration with an R290 vapour-compression heat pump enabled operation under the tested winter conditions without an auxiliary heat source. COP values of 3.70−4.31 were achieved at outdoor temperatures ranging from 0.6°C to 8.6°C, substantially exceeding 2.0−2.5 of conventional air-to-air heat pumps. The favourable evaporator conditions provided by warm exhaust air (~20°C) directly account for this elevated performance.
- Electrical power demand ranged from 1039 W to 1387 W, with the fan and automation contributing a constant 460 W. The average heating capacity ranged from 4180 to 5735 W, with characteristic double-capacity peaks during the supply phase from simultaneous regenerator and heat pump heat release.
- No water vapour condensation was observed in the ceramic matrix under any of the tested conditions, indicating that no electric pre-heating or defrosting was required during the experiments.
- The expanded COP uncertainty of ±8.9% (k = 2) is dominated by airflow (IRIS 250, ±5%) and humidity (SHT20, ±3% *RH*) measurements. Upgrading to a class 1 flowmeter and a ±1.5% *RH* sensor would reduce this to ~±4%. Future work should extend on testing below 0°C and investigating variable compressor speed effects on COP.

Acknowledgements

This study was conducted within the framework of a 501230104217 project conducted at the Institute of Heat Engineering of the Warsaw University of Technology and funded by Respireco sp. z o.o.

References

[1] Ministry of Infrastructure. (2022). *Regulation of the Minister of Infrastructure of 12 April 2002 on technical conditions to be met by buildings and their location* (consolidated text). Dz.U. 2022 item 1225 (in Polish)

[2] Rucinski, A., Grzebielec, A., Jaworski, M., Laskowski, R., Barylka, A., & Rusowicz, A. (2021). The problem of smog-particle removal in large cities – Experimental analysis of some filtration materials. *Energies*, 14(23), 8012. doi: 10.3390/en14238012

[3] Schumann, L., Hoerold, K.S., Tomaschewski, R.O., Cetin, Y.E., & Kriegel, M. (2026). Influence of a local ventilation system on patient and personnel protection in operating rooms. *Journal of Hazardous Materials*, 501, 140712. doi: 10.1016/j.jhazmat.2025.140712

[4] Dodoo, A., Gustavsson, L., & Sathre, R. (2011). Primary energy implications of ventilation heat recovery in residential buildings. *Energy and Buildings*, 43(7), 1566–1572. doi: 10.1016/j.enbuild.2011.02.019

[5] Niemierska, E., & Jadwiszczak, P. (2023). Experimental investigation of a ceramic heat regenerator for heat recovery in a decentralized reversible ventilation system. *International Communications in Heat and Mass Transfer*, 146, 106899. doi: 10.1016/j.icheatmasstransfer.2023.106899

[6] Aktershev, S.P., Mezentsev, I.V., & Mezentseva, N.N. (2022). Parametric study of a regenerative heat exchanger for ventilation with a periodic change in the air flow direction. *Applied Thermal Engineering*, 202, 117831. doi: 10.1016/j.applthermaleng.2021.117831

[7] Jedlikowski, A., Kanaś, P., & Anisimov, S. (2020). Heat and mass transfer inside the rotary heat exchanger operating under high speed rotor conditions. *International Journal of Heat and Mass Transfer*, 152, 119558. doi: 10.1016/j.ijheatmasstransfer.2020.119558

[8] Ventia Sp. z o.o. *Product catalog* [accessed 19 Feb. 2026]

[9] Kilkovský, B. (2020). Review of design and modeling of regenerative heat exchangers. *Energies*, 13(3), 759. doi: 10.3390/en13030759

[10] Liu, Z., Li, W., Chen, Y., Luo, Y., & Zhang, L. (2019). Review of energy conservation technologies for fresh air supply in zero energy buildings. *Applied Thermal Engineering*, 148, 544–566. doi: 10.1016/j.applthermaleng.2018.11.085

[11] Mikola, A., & Kõiv, T.-A. (2014). The efficiency analysis of the exhaust air heat pump system. *Engineering*, 6(13), 1037–1045. doi: 10.4236/eng.2014.613093

[12] Bani Issa, A.A., Liang, C., Groll, E.A., & Ziviani, D. (2025). Residential heat pump and air conditioning systems with propane (R290) refrigerant: Technology review and future perspectives. *Applied Thermal Engineering*, 266, 125560. doi: 10.1016/j.applthermaleng.2025.125560

[13] EN 378-1:2017-03. (2017). *Refrigerating systems and heat pumps—Safety and environmental requirements – Part 1: Basic requirements, definitions, classification and selection criteria*. European Committee for Standardization.

[14] International Electrotechnical Commission. (2022). *IEC 60539-1:2022 Directly heated negative temperature coefficient thermistors – Part 1: Generic specification*. Geneva, Switzerland.

[15] EN 308:2022. (2022). *Heat exchangers – Test procedures for establishing the performance of air-to-air heat recovery components*. Brussels, Belgium: European Committee for Standardization.

[16] Zawada, B. (2006). *Control systems in ventilation and air-conditioning systems*. Oficyna Wydawnicza Politechniki Warszawskiej (in Polish).

[17] Joint Committee for Guides in Metrology. (2008). *Evaluation of measurement data – Guide to the expression of uncertainty in measurement* (JCGM 100:2008). BIPM.

[18] Grzebielec, A. (2022). Investigation of a heat recuperator using ceramic inserts in winter and summer periods. *Szkło i Ceramika*, 2, 30–33 (in Polish).

[19] PN-EN 13141-8:2014-09. (2014). *Ventilation for buildings – Testing of performance of components/products for residential ventilation – Part 8: Performance testing of unducted mechanical supply and exhaust ventilation units (including heat recovery) for mechanical ventilation systems*. Polski Komitet Normalizacyjny, Warszawa, Poland (in Polish).

Co-published by
Institute of Fluid-Flow Machinery
Polish Academy of Sciences
Committee on Thermodynamics and Combustion
Polish Academy of Sciences

Copyright©2026 by the Authors under licence CC BY-NC-ND 4.0

http://www.imp.gda.pl/archives-of-thermodynamics/

Phase change material for thermal management of high-temperature proton exchange membrane fuel cells in electric vehicle

Nadiya Philip*, Prakash Chandra Ghosh

Indian Institute of Technology Bombay, Powai, Mumbai 400076, India
*Corresponding author email: nadiyaphilip.kulathunkal@gmail.com

Received: 13.01.2025; revised: 10.04.2026; accepted: 22.04.2026

Abstract

The current work examines the possibility of reducing the radiator size in high-temperature proton exchange membrane fuel cell vehicles by incorporating phase change material. Using pinch analysis optimisation, the research demonstrates that the radiator area in a Toyota Mirai car can be reduced by 4.7 times with the integration of D-mannitol (melting point 170°C) phase change material. The required quantity of D-mannitol accounts for only 0.62% of the vehicle's curb mass. Additionally, the work investigates the impact of operating temperature on radiator size, revealing that lower coolant inlet temperatures increase the minimum radiator area needed for sufficient heat dissipation. A 40°C increase in the inlet coolant temperature results in a 44% reduction in the radiator area. Consequently, a vehicle powered by low-temperature fuel cells (60−80°C) versus high-temperature fuel cells (120−180°C), under the same driving conditions, would require minimum radiator areas of 1.07 m^2 and 0.26 m^2, respectively. These results are expected to aid in the development of techno-economically feasible cooling systems in fuel cell vehicles.

Keywords: Thermal management; PEMFC; PCM; Radiator; Electric vehicle

Vol. 47(2026), No. 3, 25–30; doi: 10.24425/ather.2026.3651

Cite this manuscript as: Philip, N., & Ghosh, P.C. (2026). Phase change material for thermal management of high-temperature proton exchange membrane fuel cells in electric vehicle. *Archives of Thermodynamics*, 47(3), 25–30.

1. Introduction

Today, one of the main techniques for reducing carbon emissions in the transportation sector is automobile electrification [1]. To align with the International Energy Agency's agenda to limit the global temperature rise, it is required that the cumulative sale of electric vehicles (EVs) reach 1.8 billion by the year 2060 [2]. The escalating growth in the production and use of electrified vehicles is largely determined by energy storage technologies powering them like batteries and fuel cells. Compared to internal combustion engine (ICE) vehicles, which are characterised by low powertrain efficiency (with a maximum of 40% due to intermediate conversion into heat and associated thermodynamic losses) and significant emissions, fuel cell vehicles have superior efficiencies (with a minimum of 50% due to the direct conversion of chemical energy into electrical energy) and produce zero local emissions [3]. Fuel cell-based EVs also have the advantages of shorter refuelling time and longer driving ranges compared to battery EVs. However, currently, fuel cell vehicles require research efforts to develop less costly catalyst and electrode materials, better humidifiers, heat exchangers, etc., to improve the efficiency and durability of the system while reducing costs [4].

Nomenclature

a – acceleration, m/s^2
A – frontal area, m^2
C_d – drag coefficient
f_r – rolling friction
g – gravitational acceleration, m/s^2
m – vehicle curb mass, kg
v – vehicle speed, m/s

Greek symbols

α – road slope, °
ρ – air density, kg/m^3

Abbreviations and Acronyms

EV – electric vehicle
FCEV – fuel cell electric vehicle
ICE – internal combustion engine
PCM – phase change material
PEMFC– proton exchange membrane fuel cell
TDR – turn-down ratio
TMS – thermal management system

Effective thermal management of fuel cells in vehicles is important to operate the system at maximum efficiency. Literature reports that fuel cells generate a considerable amount of thermal energy, proportional to their electrical output. For example, a fuel cell with an efficiency of 50% and a capacity of 10 kW will produce 10 kW of electrical energy and 10 kW of thermal energy by electrochemical reactions [5]. This makes temperature regulation essential to prevent performance degradation in fuel cells that may happen due to the breakdown of the membrane and catalyst at elevated temperatures [6].

A proper thermal management system dissipates the generated heat and establishes a uniform temperature distribution across the fuel cell stack. Liquid cooling, typically with water and excess heat rejection via radiators, is the most widely adopted cooling strategy in fuel cell electric vehicles (FCEVs) [7,8]. However, compared to ICE vehicles for the same vehicle platform, fuel cell vehicles require a radiator with a 2−4 times larger frontal area [9,10]. A 60 kW Ford fuel cell vehicle powered by a proton exchange membrane fuel cell (PEMFC) is reported to require 1.5 times higher radiator area than a conventional vehicle to maintain the fuel cell within its optimum operating temperature range [11]. Similarly, Ahluwalia and group [12] reports the need for 125% higher frontal area in fuel cell vehicles as a result of their study on heat rejection from the vehicle with respect to stack temperature. The need for large radiators in fuel cell vehicles is primarily because of the minimal heat carried away by exhaust gases.

A large radiator necessitates a large frontal area, which increases the overall vehicle power demand. Various recent studies have researched improving the thermal management system compactness without compromising its efficiency. Prabakaran et al. [13,14], Su et al. [15] and Mohamed et al. [16] have proposed to improve the heat transfer via radiators by coupling spray cooling. Modifications in radiator design, such as improving the shape of the radiator intake grill and alternate fin structure have also been proposed by researchers [17,18]. However, the majority of these works report results of computational evaluations and require further optimisations and experiments before being commercialised.

Recent works have introduced the concept of phase change material (PCM) radiator thermal management system for fuel cell vehicles, where a PCM of suitable mass serves as a thermal reservoir, allowing for radiator size reduction [19,20]. PCMs can absorb and release large amounts of thermal energy (150−250 kJ/kg) during phase change. They are broadly categorised into three: organic PCMs, inorganic PCMs, and eutectic PCMs. Organic PCMs (e.g. paraffins, fatty acids) are biodegradable with low environmental impact, have good chemical stability as well as low toxicity, but exhibit low thermal conductivity (0.1−0.3 W/(m K)) and high flammability (limiting oxygen index ~ 17%). Meanwhile, inorganic PCMs (e.g. salt hydrates, metallic PCMs) have higher latent heat and thermal conductivity, non-flammability (limiting oxygen index ~60 %), and are 3−10 times cheaper compared to organic PCMs, but they show corrosiveness, supercooling issues, and potential environmental issues (harm soil/water if leaked, eutrophication risks). Eutectic PCMs are organic-organic, organic-inorganic, or inorganic-inorganic combinations that offer tailored melting points for specific applications [21,22].

The selection of PCMs for EV applications depends on key properties such as high latent heat, high thermal conductivity, high specific heat, melting point in the desired temperature range, minimum volume change during phase transition, stability, non-flammability, cost-effectiveness, etc. [13]. PCMs can easily integrate into existing vehicular thermal management systems (TMS) via encapsulation in polymer/aluminium modules, panels or shells with no major redesign. The high volumetric energy density of PCMs (180−300 MJ/m^3) allows compact placement in space constrained areas. Their near-isothermal operation allows rapid, effective buffering of transient heat loads, and their passive operation ensures minimal parasitic power requirement. The stored thermal energy has the potential to improve the energy efficiency of the system in scenarios such as cold start.

The current work investigates the potential for size reduction in radiators by implementing a PCM-based TMS in a high-temperature PEMFC-powered electric vehicle. High-temperature PEMFC vehicles are advantageous owing to enhanced electrochemical kinetics, higher carbon monoxide (CO) tolerance and simplified water management. Additionally, these systems also expel waste heat at a higher temperature, which can be recovered and utilised for direct heating [22,23].

In this study, the size optimisation of the PCM-radiator system components is carried out using pinch analysis. The key contributions of this research are: (i) determining the minimum radiator size for dissipating the heat from a high-temperature PEMFC stack, (ii) identifying appropriate commercial PCM and the mass necessary to compensate for the reduced radiator area,

(iii) defining a design space of feasible radiator sizes and corresponding PCM masses, allowing users to select the most suitable combination based on specific requirements, and (iv) analysing the effect of operating temperature on the TMS size.

2. Materials and methods

The study considers a light-duty 5-seater vehicle (Toyota Mirai) operated by a high-temperature PEMFC. For this work, it is assumed that PEMFC is the only power source in the vehicle. The vehicle specifications are given in Table 1. The vehicle follows a standard driving cycle (worldwide harmonised light duty test cycle − WLTC), so the analysis's results would also apply to real-world driving conditions. The power demanded by the light-duty vehicle can be estimated using the following formula [24]:

$$P_v = (0.5\rho C_d A v^2 + f_r m\cos\alpha + ma + mg\sin\alpha)v, \quad (1)$$

where: A – frontal area, a – acceleration, C_d – drag coefficient, f_r – rolling friction, g – gravitational acceleration, m – vehicle curb mass, v – vehicle speed, α – road slope, ρ – air density. To calculate the load demand by the vehicle, a road slope of zero is assumed.

Table 1. Specifications of system.

Parameter	Value
Mass of vehicle (kg)	1930
Frontal area of vehicle (m^2)	2.35
Coefficient of drag	0.29
Rolling friction coefficient	0.01
Coolant temperature at the inlet of fuel cell (°C)	170
Maximum rate of flow of a coolant (kg/s)	0.20
Specific heat of a coolant (kJ/(kg °C))	4.20
Environmental temperature (°C)	50
Allowed temperature rise in the stack (°C)	10
Overall heat transfer coefficient for radiator (kW/(m^2°C))	0.30
Fuel cell TDR (%)	20

Estimation of the power demand by the automobile gives an insight into the thermal energy generated by the fuel cell. The proposed thermal management system primarily consists of the PEMFC, coolant, radiator and heat exchanger containing PCM. The coolant exiting the PEMFC stack passes into a radiator and then through the PCM system to dissipate the thermal energy generated in the PEMFC stack. This ensures a uniform temperature for the coolant entering back into the stack. The drive cycle considered in this work and a schematic of the TMS are depicted in Fig. 1.

The pinch analysis technique adopted in this study is an algebraic optimisation method, by which the thermal management needs of the vehicle can be met with minimum resources. For this, the thermal energy generation by the PEMFC stack is compared with the heat rejected by the radiator size of the user's choice, to obtain the minimum PCM mass required for satisfactory thermal management. By using PCM, the excess thermal energy can be stored and reused at later periods to ensure the

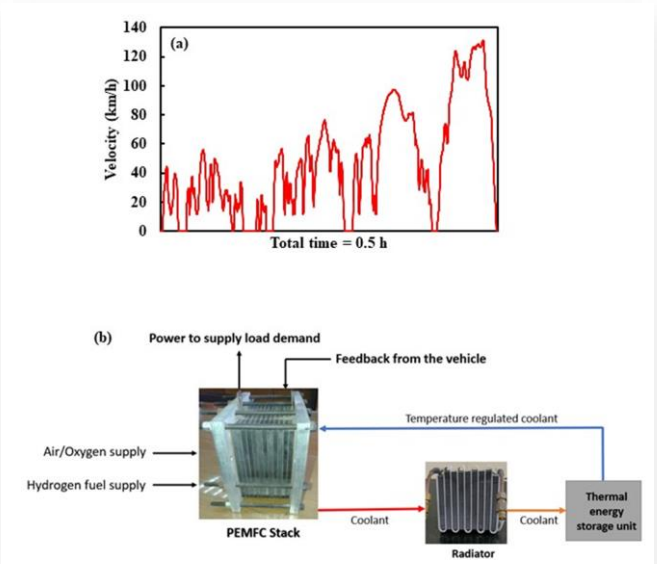


Fig. 1. (a) Worldwide harmonised light duty test cycle, (b) Illustration of the thermal management system.

thermal regulation of the coolant. This maintains the coolant temperature entering the PEMFC stack in the range of the desired operating temperature of the fuel cell. The PCM considered for this study is D-mannitol, which has a melting point of 170°C and a latent heat capacity of 297 kJ/kg [25].

The optimisation is subject to the constraints listed below:

1) The energy in the PCM unit at the start and finish of the driving cycle should be the same.
2) The minimum state of charge in the PCM unit at any given time should not be less than 0.
3) The overall heat transfer coefficient of the radiator unit lies between a lower limit (influenced by radiator turn-down ratio) and an upper limit.

The implementation of pinch analysis involves three major steps: calculation of thermal energy generated by the PEMFC stack, calculation of the cooling capacity of the radiator, and calculation of PCM mass. The parameters to be calculated in each step are summarised in Fig. 2 [19]. The software used for optimisation was the GRG Non-Linear Engine in Microsoft Excel.

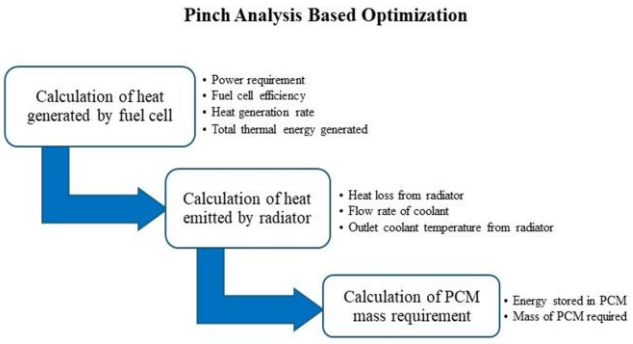


Fig. 2. Component-wise parameters to be evaluated for optimisation.

3. Results and discussion

The present study uses a PCM-based TMS to reduce the radiator size in fuel cell-powered vehicles. For this, a pinch analysis-based optimisation algorithm was adopted and applied to a standard drive cycle to study the effectiveness of the PCM system when used in a FCEV. A 1980 kg light-duty vehicle that follows a WLTC class-3 drive cycle (duration: 0.5 h) is considered here.

3.1. Sizing curve for the thermal management system

Sizing curves that depict the radiator area and corresponding PCM requirement are plotted to illustrate the feasible and infeasible operating regions. Each point on the sizing curve (Fig. 3) is the result of pinch analysis optimisation performed for a particular value of minimum radiator area. In each case, the mismatch between the cumulative thermal energy generated and the cumulative thermal energy dissipation by the chosen radiator size represents the cumulative thermal energy to be stored in the PCM unit. The points on the sizing curve and the region above it represent the feasible region. However, the region on the left and lower part of the sizing curve represents infeasible combinations of the radiator area and PCM mass either because of insufficient radiator size or due to limited PCM mass. It is seen that with respect to the constraints considered in this study, to ensure adequate heat dissipation through the radiator-PCM system, the radiator area should not be less than 0.26 m^2. Hence, the results show the possibility of decreasing the radiator area in a high-temperature powered PEMFC by 4.7 times when complemented with a suitable thermal energy storage system.

Pinch analysis results show that to dissipate the thermal energy generated by the stack with a radiator of area 0.26 m^2, 11.97 kg of D-mannitol PCM is essential. The required PCM mass corresponds to only about 0.62% of the vehicle's curb mass. The higher the radiator area, the lower the thermal energy to be stored and hence, the lower the PCM mass required. On investigating the sizing graphs for various radiator turn-down ratios (TDR), it is also evident that after a local minimum, there is a need for higher PCM mass despite the high radiator areas. The TDR constraint necessitates using additional PCM to store additional heat and ensure appropriate temperature regulation of the coolant.

3.2. Effect of operating temperature on the size of thermal management system

To understand the influence of the operating temperature of the fuel cell on the TMS size of the vehicle, it is required to perform a pinch analysis with different coolant temperatures. The TMS sizing is studied for cases of different inlet coolant temperatures entering the fuel cell unit. The analysis shows that the lower the inlet coolant temperature, the higher the minimum required radiator area for adequate heat dissipation. Furthermore, an increase in the inlet coolant temperature from 120°C to 180°C produces a drastic drop in the minimum required radiator area by 44.18%, while the required PCM mass declines by about 2%. Figure 4 shows the sizing curve for the radiator-PCM system for

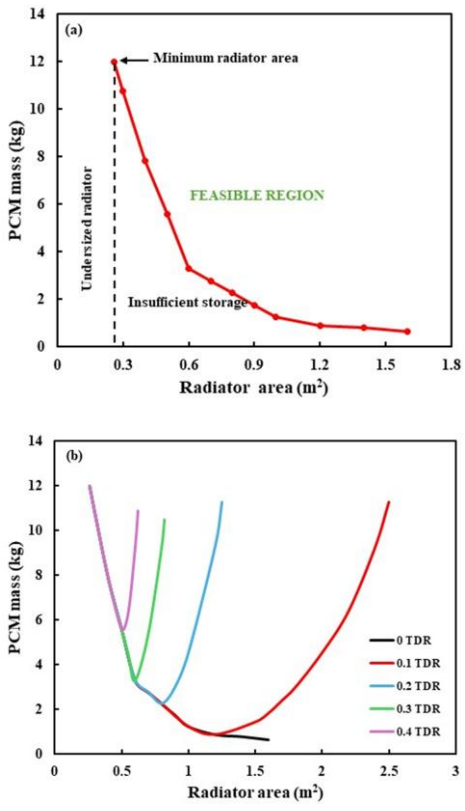


Fig. 3. (a) Sizing curve; (b) Sizing curves for various radiator turn-down ratios.

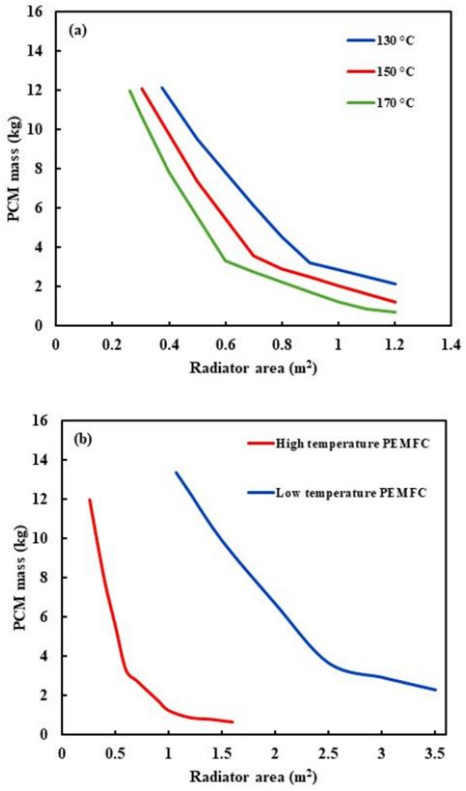


Fig. 4. Sizing curves for TMS in (a) high temperature PEMFC at various inlet coolant temperatures, (b) in high and low temperature PEMFCs.

the inlet coolant temperatures of 130°C, 150°C and 170°C. An increase in the coolant temperature by 40°C decreases the required radiator area by 0.12 m^2. This is because a greater temperature difference between the coolant and ambient air allows the same heat rejection with a smaller radiator area. Also, for a constant radiator area, PCM requirement increases with a reduction in the inlet coolant temperature. For instance, if we consider the TMS with the radiator areas of 0.5 m^2 and 1.0 m^2, it is evident that PCM requirement increases by ~2.0 kg (for 0.5 m^2) and ~0.80 kg (for 1.0 m^2) for every 20°C reduction in inlet coolant temperature.

In the same context, a comparison between the TMS (radiator-PCM) sizes for proton exchange membrane fuel cells, which work at low temperatures (60°C to 80°C) and high temperatures (120°C to 180°C) is also presented (Fig 4b). Due to the low difference between fuel cell operating temperature and ambient temperature, low-temperature PEMFCs require higher radiator areas when compared to high-temperature PEMFCs. To reduce the radiator size in these systems, paraffin wax and D-mannitol PCMs were selected for the low-temperature and high-temperature systems, respectively. The temperatures of the coolant entering the fuel cell were taken as 70°C (low-temperature PEMFC) and 170°C (high-temperature PEMFC). Pinch analysis optimisation was performed for the two systems for the same vehicle and driving conditions and the results are shown in Fig. 4b. From the figure, it is seen that while the minimum area requirement for the radiator in a high-temperature PEMFC system is 0.26 m^2, the low-temperature PEMFC system requires a radiator with at least 4.12 times larger area (1.07 m^2), even with the usage of maximum PCM. However, the mass of PCM required for the low-temperature PEMFC is only 11.70% higher than the mass of PCM required for the high-temperature PEMFC. Hence, irrespective of the type of PEMFC chosen for the FCEV, the mass of PCM required for maximum radiator area reduction does not exceed 0.70% of the vehicular curb mass.

4. Conclusions

The study explores the potential for reducing the size of the radiator in Toyota Mirai cars powered by a high-temperature proton exchange membrane fuel cell by incorporating a phase-change material into its thermal management system. This research makes a key contribution by using pinch analysis to determine the minimum size of radiator required to dissipate heat from a high-temperature PEMFC stack and defining a design space comprising radiator sizes and the corresponding masses of phase change material. The results show that by integrating 11.97 kg of D-mannitol PCM, the radiator area in the high-temperature fuel cell-powered vehicle can be reduced by 4.7 times. Additionally, the impact of fuel cell operating temperature on the vehicle's TMS size was also assessed. The analysis reveals that lower inlet coolant temperatures necessitate a larger minimum radiator area for effective heat dissipation. For instance, on increasing the inlet coolant temperature from 120°C to 180°C, there is a 44% reduction in the radiator area and a 2% decrease in the required PCM mass. Furthermore, if we analyse the same vehicle powered by a low-temperature fuel cell, the thermal management system would need a radiator with an area 4.12 times larger at minimum and a PCM mass 11.70% greater for appropriate heat dissipation.

The present study assesses the advantage of adding a PCM-based thermal energy storage unit in the TMS of a fuel cell vehicle. In addition to eliminating the disadvantages of using large radiators such as larger frontal area and increased fuel consumption, the usage of PCM can also improve the energy efficiency of the system through the utilisation of stored heat. The findings of this study are expected to contribute to the development of techno-economically feasible cooling systems for fuel cell vehicles, enabling more efficient and compact thermal management solutions.

References

[1] Adams, J.A., Yang, W.-C., Oglesby, K.A., & Osborne, K.D. (2000). The development of Ford's P2000 fuel cell vehicle. *SAE 2000 World Congress*, 6 March, Detroit, United States. doi: 10.4271/2000-01-1061

[2] Ahluwalia, R.K., Wang, X., Kwon, J., Rousseau, A., Kalinoski, J., James, B., & Marcinkoski, J. (2011). Performance and cost of automotive fuel cell systems with ultra-low platinum loadings. *Journal of Power Sources*, 196(10), 4619–4630. doi: 10.1016/j.jpowsour.2011.01.059

[3] Bargal, M.H.S., Souby, M.M., Abdelkareem, M.A.A., Sayed, M., Tao, Q., Chen, M., & Wang, Y. (2021). Experimental investigation of the thermal performance of a radiator using various nanofluids for automotive PEMFC applications. *International Journal of Energy Research*, 45(5), 6831–6849. doi: 10.1002/er.6274

[4] Bethoux, O. (2020). Hydrogen fuel cell road vehicles: State of the art and perspectives. *Energies*, 13(21), 5843. doi: 10.3390/en13215843

[5] Chen, Q., Zhang, G., Zhang, X., Sun, C., Jiao, K., & Wang, Y. (2021). Thermal management of polymer electrolyte membrane fuel cells : A review of cooling methods, material properties, and durability. *Applied Energy*, 286, 116496. doi: 10.1016/j.apenergy.2021.116496

[6] Forrest, K., Mac Kinnon, M.M., Tarroja, B., & Samuelsen, S. (2020). Estimating the technical feasibility of fuel cell and battery electric vehicles for the medium and heavy duty sectors in California. *Applied Energy*, 276, 115439. doi: 10.1016/j.apenergy.2020.115439

[7] Gong, C., Shen, J., Yu, Y., Wang, K., & Tu, Z. (2020). A novel radiator structure for enhanced heat transfer used in PEM fuel cell vehicle. *International Journal of Heat and Mass Transfer*, 157, 119926. doi: 10.1016/j.ijheatmasstransfer.2020.119926

[8] Gong, C., Shen, J., Yu, Y., Wang, K., & Tu, Z. (2020). Heat dissipation characteristic in the intake grille and radiator of a fuel cell vehicle. *International Journal of Green Energy*, 17(10), 591–601. doi: 10.1080/15435075.2020.1779078

[9] Haider, R., Wen, Y., Ma, Z.-F., Wilkinson, D.P., Zhang, L., Yuan, X., Song, S., & Zhang, J. (2021). High temperature proton exchange membrane fuel cells: progress in advanced materials and key technologies. *Chemical Society Reviews*, 50(2), 1138–1187. doi: 10.1039/d0cs00296h

[10] IEA (2023). Global EV Outlook 2023 – Analysis - IEA. *International Energy Agency*. https://www.iea.org/reports/global-ev-outlook-2023 [accessed 26 Apr. 2025]

[11] Jaguemont, J., Omar, N., Van den Bossche, P., & Mierlo, J. (2018). Phase-change materials (PCM) for automotive applications: A review. *Applied Thermal Engineering*, 132, 308–320. doi: 10.1016/j.applthermaleng.2017.12.097

[12] Li, G., Kujawski, W., & Rynkowska, E. (2022). Advancements in proton exchange membranes for high-performance high-temperature proton exchange membrane fuel cells (HT-PEMFC).

Reviews in Chemical Engineering, 38(3), 327–346. doi: 10.1515/revce-2019-0079

[13] Souby, M.M., Prabakaran, R., Liu, J., & Kim, S.C. (2024). Heat transfer and power consumption of an optimized low-pressure compact drizzling cooling module integrated PEMFC stack radiator. *International Communications in Heat and Mass Transfer*, 159(A), 108046. doi: 10.1016/j.icheatmasstransfer.2024.108046

[14] Mehling, H. (2024). Review of classification of PCMs, with a focus on the search for new, suitable PCM candidates. *Energies*, 17(17), 4455. doi: 10.3390/en17174455

[15] Mojiri, A., Grbac, N., Bourke, B., & Rosengarten, G. (2018). D-mannitol for medium temperature thermal energy storage. *Solar Energy Materials and Solar Cells*, 176, 150–156. doi: 10.1016/j.solmat.2017.11.028

[16] Philip, N., & Ghosh, P.C. (2022). A generic sizing methodology for thermal management system in fuel cell vehicles using pinch analysis. *Energy Conversion and Management*, 269, 116172. doi: 10.1016/j.enconman.2022.116172

[17] Philip, N., & Ghosh, P.C. (2023). Application of pinch analysis for optimal sizing of thermal management system in fuel cell powered heavy-duty trucks. *2023 IEEE IAS Global Conference on Renewable Energy and Hydrogen Technologies*, 11-12 March, Male, Maldives. doi: 10.1109/GlobConHT56829.2023.10087819

[18] Philip, N., & Ghosh, P.C. (2024). Optimal sizing of electrical and thermal energy storage systems for application in fuel cell based electric vehicles. *Journal of Energy Storage*, 83, 110753. doi: 10.1016/j.est.2024.110753

[19] Philip, N., Pradeep, N., Ghosh, P.C., & Reddy, K.S. (2024). Influence of heat transfer fluid on the thermodynamic performance of PCM-based thermal management system in fuel cell vehicle. *2024 International Conference on Electrical, Computer, and Energy Technologies*, 25 July, Sydney, Australia. doi: 10.1109/ICECET61485.2024.10698630

[20] Prabakaran, R., Souby, M.M., Liu, J., & Kim, S.C. (2024). Thermal performance of a stack cooling radiator coupled with spray cooling for the future fuel cell electric vehicles. *Applied Thermal Engineering*, 246, 122975. doi: 10.1016/j.applthermaleng.2024.122975

[21] Prabakaran, R., Souby, M.M., Liu, J., & Kim, S.C. (2024). Dynamic performance of a fuel cell stack radiator coupled with low pressure drizzling cooling and intermittent flow strategies. *International Journal of Heat and Mass Transfer*, 235, 126161. doi: 10.1016/j.ijheatmasstransfer.2024.126161

[22] Su, C.-Q., Wang, S., Liu, X., Tao, Q., & Wang, Y.-P. (2022). Experimental and numerical investigation on spray cooling of radiator in fuel cell vehicle. *Energy Reports*, 8, 1283–1294. doi: 10.1016/j.egyr.2021.11.174

[23] Wang, Y., Li, J., Tao, Q., Bargal, M.H.S., Yu, M., Yuan, X., & Su, C. (2020). Thermal management system modeling and simulation of a full-powered fuel cell vehicle. *Journal of Energy Resources Technology, Transactions of the ASME*, 142(6), 061304. doi: 10.1115/1.4045479

[24] Williamson, S.S., & Emadi, A. (2005). Comparative assessment of hybrid electric and fuel cell vehicles based on comprehensive well-to-wheels efficiency analysis. *IEEE Transactions on Vehicular Technology*, 54(3), 856–862. doi: 10.1109/TVT.2005.847444

[25] Xu, J., Zhang, C., Wan, Z., Chen, X., Chan, S.H., & Tu, Z. (2022). Progress and perspectives of integrated thermal management systems in PEM fuel cell vehicles: A review. *Renewable and Sustainable Energy Reviews*, 155, 111908. doi: 10.1016/j.rser.2021.111908

Co-published by
Institute of Fluid-Flow Machinery
Polish Academy of Sciences
Committee on Thermodynamics and Combustion
Polish Academy of Sciences

Copyright©2026 by the Authors under licence CC BY-NC-ND 4.0

http://www.imp.gda.pl/archives-of-thermodynamics/

Comparative experimental studies of the specific heat of Fe and Ni using scanning calorimetry methods

Robert Szczepaniak[a], Andrzej J. Panas[b*], Łukasz Omen[c], Maciej Starczewski[b], Maciej Kowalski[c]

[a]Polish Air Force University, Faculty of Aeronautics, 35 Dywizjonu 303 Str., 08-521 Dęblin, Poland
[b]Air Force Institute of Technology, 6 Księcia Bolesława Str., 01-494 Warsaw, Poland,
[c]Military University of Technology, Faculty of Mechatronics, Armament and Aerospace, 2 Gen. S. Kaliskiego Str., 00-908 Warsaw, Poland
*Corresponding author email: andrzej.panas@itwl.pl; andrzej.panas@wat.edu.pl

Received: 09.01.2026; revised: 18.05.2026; accepted: 29.05.2026

Abstract

This study presents comparative experimental investigations of the specific heat of materials undergoing phase transitions, with the aim of assessing the capabilities and metrological limitations of differential scanning calorimetry methods and instrumentation. Nickel and iron were selected as reference materials due to the availability of reliable literature data for verification. Two approaches to determining heat flux density in differential scanning calorimetry were compared using three calorimeters: Pyris 1 (PerkinElmer), DSC 3 (Mettler Toledo), and DSC 404 F1 Pegasus (Netzsch). Measurements were conducted in a protective atmosphere over a temperature range up to 600°C on samples that had been thermally stabilised prior to testing. For the Pyris 1 calorimeter, a proprietary measurement procedure based on heating and cooling cycles with isothermal holds was applied, enabling reliable determination of specific heat during heating and cooling. In contrast, for the DSC 3 and DSC 404 F1 instruments, the analysis was primarily based on heating data. The obtained results allowed analysis of the second-order phase transition in nickel, including determination of the transition end temperature and the temperature corresponding to the maximum differential scanning calorimetry peak. The phase transition in iron was characterised solely using data from the DSC 404 F1 instrument, due to measurement limitations of the remaining equipment. Additionally, three independent temperature-dependent specific heat characteristics were compared, obtained using a relative method with identical reference standards and standard differential scanning calorimetry signal conversion procedures. The results contribute to improved understanding of calorimetry methodology and measurement uncertainty in materials undergoing phase transitions.

Keywords: Specific heat capacity; Ferromagnetic phase transition; Heat-flow calorimetry; Power-compensation calorimetry

Vol. 47(2026), No. 3, 31–39; doi: 10.24425/ather.2026.3652

Cite this manuscript as: Szczepaniak, R., Panas, A.J., Omen, Ł., Starczewski, M., & Kowalski, M. (2026). Comparative experimental studies of the specific heat of Fe and Ni using scanning calorimetry methods. *Archives of Thermodynamics*, 47(3), 31−39.

1. Introduction

The specific heat of materials is one of the basic thermo-physical properties, important both from the point of view of scientific research and engineering applications [1,2]. Accurate knowledge of this quantity allows for effective modelling of thermal processes, optimisation of technological parameters, and design of materials and devices operating in variable temperature conditions. In the case of metals undergoing phase transitions, such as iron (Fe) and nickel (Ni), it is particularly important to take into account changes in specific heat as a function of temperature and the characteristics of these transitions, and research has been conducted for almost 100 years [3,4].

Differential scanning calorimetry (DSC) is one of the most commonly used methods for testing specific heat [5−9]. It is characterised by high sensitivity, the ability to perform measurements over a wide temperature range, and relatively simple laboratory procedures with an error of less than 3% [8,10]. Despite the popularity of this method, the results obtained may vary depending on the apparatus used, the measurement methodology

Nomenclature

c_p – specific heat capacity, J/(kg·K)
f – thermogram data
m – mass, kg
t – time, s
T – temperature, °C

Subscripts and Superscripts
base – baseline date
C – Curie
ref – reference
sp – specimen

Abbreviations and Acronyms
DSC − differential scanning calorimetry

and the method of data processing, in this case, thermograms. It is therefore advisable to conduct comparative studies to assess the consistency and precision of specific heat measurements performed with different devices and techniques within the DSC method.

This article presents the results of comparative experimental studies of the specific heat of iron and nickel, conducted using three different scanning calorimeters: PerkinElmer Pyris 1, Mettler Toledo DSC 3 and Netzsch DSC 404 F1 Pegasus. Iron and nickel were selected due to their ferromagnetic properties at room temperature and their loss in the second type of phase transition after exceeding the characteristic Curie temperature. Iron is additionally characterised by the occurrence of a first-order transition. These phenomena make it possible to use the characteristic temperature as an additional metrological parameter. The analysis examined the impact of measurement conditions and declared temperature change programmes, in particular the use of isothermal stops, on the measurement results. In addition to mutual comparison, the consistency of the obtained results with the literature data was also checked. Particular attention was paid to the characteristics of second-order phase transitions and the assessment of the metrological capabilities and limitations of individual devices.

Regardless of the specific objectives mentioned above, the research project is based on general methodological principles that focus on key issues across the entire field of modern thermal analysis. Very often, the measurement accuracy reported by authors is simply a repetition of data provided by manufacturers. The problem is that this information mainly concerns the repeatability of measurements and compliance with reference data obtained under specific experimental conditions. Not all of these conditions can be maintained during routine experiments. The results of the round-robin tests described in this article are intended to indicate the reliability of measurement results obtained under typical conditions, in terms of both qualitative and quantitative data.

2. Research equipment and subject of study

Although one might initially think that the research issue described above is limited solely to the problem of equipment, it should be noted at the outset that the measuring equipment was selected in such a way as to represent three different types of methods for implementing the idea of scanning calorimetry [11]. The Pyris 1 calorimeter from PerkinElmer is an example of the use of the heat flux compensation method (power compensated). The other two, Mettler Toledo DSC 3 and Netzsch DSC 404 F1 Pegasus, are heat flux calorimeters with different heat flux measurement methods. On the one hand, the design differences affect the diversity of measurement procedures, but on the other hand, they create the possibility of highlighting a different parameter or property determined in the measurements.

In this case, a comparison was made of the capabilities of three selected scanning calorimeters in terms of their suitability for testing the specific heat of metals undergoing second-order phase transitions. The analysis covered the effectiveness and limitations of individual devices in determining the thermal characteristics of nickel (Ni) and iron (Fe), with particular emphasis on the temperature range, DSC signal resolution and repeatability of results.

2.1. PerkinElmer Pyris 1 power compensated DSC

PerkinElmer Pyris 1 DSC is a power compensated differential scanning calorimeter designed for thermal analyses and precise determination of the thermal properties of materials, in particular specific heat (c_p), in a temperature range up to 710°C. This limitation results from the use of resistive temperature sensors and compensating resistance heaters in the measuring head to implement the idea of power compensation. The apparatus enables quantitative determination of specific heat based on the analysis of the heat flow signal recorded during controlled heating of the sample relative to a reference material with known thermal parameters according to a so-called three-curve method [12]. This method involves using data from three test series – a baseline series, a series using a standard, and a series using the test sample – to determine the specific heat based on the equation:

$$c_{p,\mathrm{sp}}(T) = c_{p,\mathrm{ref}}(T)\,\frac{m_{\mathrm{ref}}}{m}\,\frac{f_{\mathrm{sp}}(T)-f_{\mathrm{base}}(T)}{f_{\mathrm{ref}}(T)-f_{\mathrm{base}}(T)}, \qquad (1)$$

where: sp − indicates a specimen, ref – reference, and base – baseline data.

The function f represents thermograms signal data that could be recorded in mW in the case of an enthalpy calibrated instrument or in arbitrary units in the case of an only temperature calibrated apparatus. Typical measurements are performed on samples weighing from 5 mg to 100 mg, placed in standard aluminium encapsulated crucibles with lids. A single crystal of sapphire (Al_2O_3), characterised by a well-defined c_p value, is usually used as a reference standard. The mass of both the test sample and the standard is determined with a resolution of 0.01 mg and recorded in the Pyris software.

The measurement is carried out in a protective atmosphere, most often purified nitrogen, with a controlled carrier gas flow

in the range of 20–50 ml/min. The standard heating rate is 5–20 K/min, but it is possible to use non-standard temperature profiles, including procedures with isothermal stops, which allow the elimination of dynamic effects such as the thermal inertia of the system.

The calorimeter's measuring range covers temperatures from room temperature to approximately 600°C, depending on the configuration of the apparatus and the crucibles used. As part of extended testing procedures, it is possible to use a cyclic heating and cooling regime with short isotherms between temperature steps. This approach allows for:

- improved accuracy of the determined c_p values,
- reduction of the impact of irreversible phenomena and thermal instabilities,
- independent analysis of the DSC signal in heating and cooling cycles, which increases the reliability and repeatability of the results.

The specific heat values are calculated using dedicated Pyris software. The programme compares the heat flow signals from the sample and the standard, taking into account their masses, and allows direct determination of c_p as a function of temperature. The data obtained are presented in the form of graphs and tabular summaries of $c_p(T)$ values, which can be exported for further analysis.

Baseline correction and signal smoothing functions are available as part of the data analysis. In the case of materials undergoing phase transitions, it is also possible to determine the characteristic transition temperatures and calculate the enthalpy of heat transitions.

2.2. Mettler Toledo DSC 3

The Mettler Toledo DSC 3 differential calorimeter is an advanced heat-flux DSC device used, among other things, for the precise determination of the thermal properties of materials, in particular specific heat capacity (c_p) as a function of temperature. The measurement is based on the analysis of the difference in heat flow signals recorded during the controlled heating of the sample and a reference standard with known thermal properties. The samples for analysis usually weigh from a few to several milligrams and are placed in standard aluminium crucibles, usually with a lid, without a seal. A sapphire disc (Al_2O_3) is usually used as a reference standard, as its thermal properties are well known and documented. Both the sample and the standard are weighed accurately (with a resolution of 0.01 mg and an accuracy depending on the type of balance) and then placed in two identical measuring chambers of the calorimeter. The test procedure data are as follows:

- the measurement is carried out in a controlled protective atmosphere, usually in a stream of nitrogen or argon, with a fixed gas flow,
- the standard heating rate is 10 K/min, although it can be adjusted to the specific characteristics of the material being tested,
- the measurement range covers temperatures from room temperature to approximately 600–700°C, depending on the configuration of the apparatus and the crucibles used.

The device determines the difference in heat flow between the sample and the reference standard as a function of temperature. Based on this data, the dedicated STARe software calculates the direct value of the sample's specific heat, taking into account the previously performed calorimetric calibrations. The results are presented in the form of a $c_p(T)$ graph and in tabular form, taking into account measurement uncertainty. The software allows baseline correction to be applied to compensate for any DSC signal drift. The results obtained can be compared with literature data or used for further analysis, such as calculating the enthalpy of phase transitions, analysing the thermal properties of composites, or modelling thermal processes in engineering systems.

2.3. Netzsch DSC 404 F1 Pegasus

The Netzsch DSC 404 F1 Pegasus differential scanning calorimeter is a high-temperature heat-flux DSC device designed for precise study of the thermal properties of substances, including specific heat capacity (c_p) determination, in a wide temperature range – up to 1600°C. The apparatus allows the use of the three-run method (the three-curve method presented in paragraph 2.1 [12]), which is the standard procedure for determining c_p in relation to a sapphire standard.

The analysis is carried out on samples weighing typically from a few to several milligrams, placed in cylindrical crucibles made of a suitable material. Platinum-rhodium (Pt/Rh), aluminium oxide (Al_2O_3) or graphite crucibles are used for specific heat measurements, depending on the expected temperature range and chemical properties of the sample material. A certified sapphire disc (Al_2O_3) with a well-defined specific heat, supplied by the manufacturer (Netzsch), is used as a standard. The mass of all measuring elements is determined with a resolution of 0.01 mg and entered into the Proteus® Thermal Analysis software.

Determination of specific heat using the three-measurement method involves the following steps:

- baseline measurement – recording the thermal background of the system with empty crucibles in the sample (S) and reference (R) positions,
- standard test – recording the reference thermogram for the standard material sample, most often sapphire – crystalline aluminium trioxide, in crucible S and reference crucible R,
- sample testing – measurement with the tested material in crucible S and the reference crucible in position R, which allows the recording of a thermogram that forms the basis for determining the specific heat capacity of the tested material.

All three measurements must be carried out under identical conditions, which means:

- using the same measuring vessels – crucibles,
- maintaining the same heating rate (e.g., 10 K/min),
- ensuring an identical protective atmosphere (usually nitrogen or argon) and the same volume flow rate, typically 50−70 ml/min,

- application of the same temperature change programme typically defined in the range from −170°C or 20°C to 1000°C or 1600°C, depending on the system equipment.

Specific heat calculations are performed by Proteus® Thermal Analysis software, which uses signal differences obtained from three measurements (baseline, reference, sample) applying appropriate calorimetric relationships. The results are presented in the form of $c_p(T)$ graphs and tables, with the possibility of further data processing: smoothing, mathematical model fitting and export to external analytical formats. The software enables the assessment of the repeatability and precision of measurements, as well as advanced thermal analysis of materials undergoing phase transitions, including the determination of transition enthalpy and characteristic temperatures.

The system is particularly suitable for testing construction materials, ceramics, metal alloys and functional materials used at elevated temperatures.

2.4. Subject of research

Given the methodological objective of the study, it was decided to attempt to determine the specific heat of pure elements for which reliable literature data on specific heat are available – samples of pure metals: nickel (Ni) and iron (Fe) [13]. These materials were selected not only due to their well-documented thermo-physical properties, including specific heat, but also with regard to a second-order phase transition within the temperature range available in standard DSC calorimetry. This allows for the comparison of experimental results with literature data and the assessment of the accuracy and sensitivity of the measurement methods used. The following metals were therefore selected for the study:

- Nickel (Ni) – the material used had a purity of ≥ 99.9%. Nickel is a metal undergoing a second-order phase transition – ferromagnetic-paramagnetic ordering – at a Curie temperature ranging from approximately 355°C (628 K) [14], through 357°C (630 K) [15], 358°C (631 K) [16,17] to 360°C (633 K) [13] (Fig. 1). Due to its relatively sharp peak, this transition is particularly useful as a reference signal in DSC measurements. The presented reference positions of the Curie point (T_C) of nickel, both in terms of the abscissa, i.e. the temperature T_C, as shown – both along the x-axis (i.e., the temperature) and the y-axis (i.e., the corresponding specific heat value) – define the range to which the position of this point, as determined in these experiments, should be referenced. In fact, almost all T_C position test results fall within the range of 355°C ≤ T_C ≤ 360°C.
- Iron (Fe): the iron used was also characterised by high purity (≥ 99.5%). In the analysed temperature range, Fe undergoes a ferromagnetic-paramagnetic phase transition with a Curie temperature close to 770°C (1043 K) [13,18]. Due to the temperature limitations of some devices, full parameterisation of this transformation was only possible using the Netzsch DSC 404 F1 Pegasus high-temperature device. However, the measurement range of the tests performed with this device also covered the first order $\alpha-\gamma$ phase transformation.

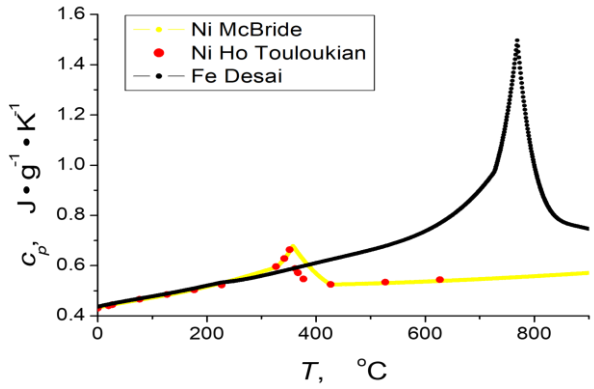


Fig. 1. Dependence of specific heat on temperature, showing the position of the Curie point as the peak of the second-order phase transition – measurements of specific heat for Ni [13,17] and Fe [18].

The nickel and iron samples were taken from a larger sample used for precise measurements of thermal expansion as a material with established thermal properties [19]. They were designed to ensure that the largest possible surface area of the bottom makes good contact with the bottom of the sample crucibles. The sample weights were selected to ensure compliance with the instruments' sensitivity requirements. All samples used in comparative tests are shown in Fig. 2.



Fig. 2. View of the samples used in the comparative tests.

Prior to measurement, the materials were subjected to thermal stabilisation (preliminary annealing) in a protective atmosphere in order to remove residual moisture and surface contaminants and to reduce the effects of history (e.g. stresses or oxidation). The temperature change programmes used are presented later in this paper.

3. Experimental research

3.1. Research methodology

The experiments using the three different differential calorimeters mentioned above were conducted using two temperature-change programs, which were compared in this study. The first program, developed for the PerkinElmer Pyris 1 DSC, utilised heating and cooling rate of 20 K/min applied in the temperature range from –40°C to 570°C in the range of 570−600°C, the rate was changed to 10 K/min in order to ensure stable conditions of

transition between the heating and cooling phases, in accordance with the dynamic characteristics of the apparatus (Fig. 3).

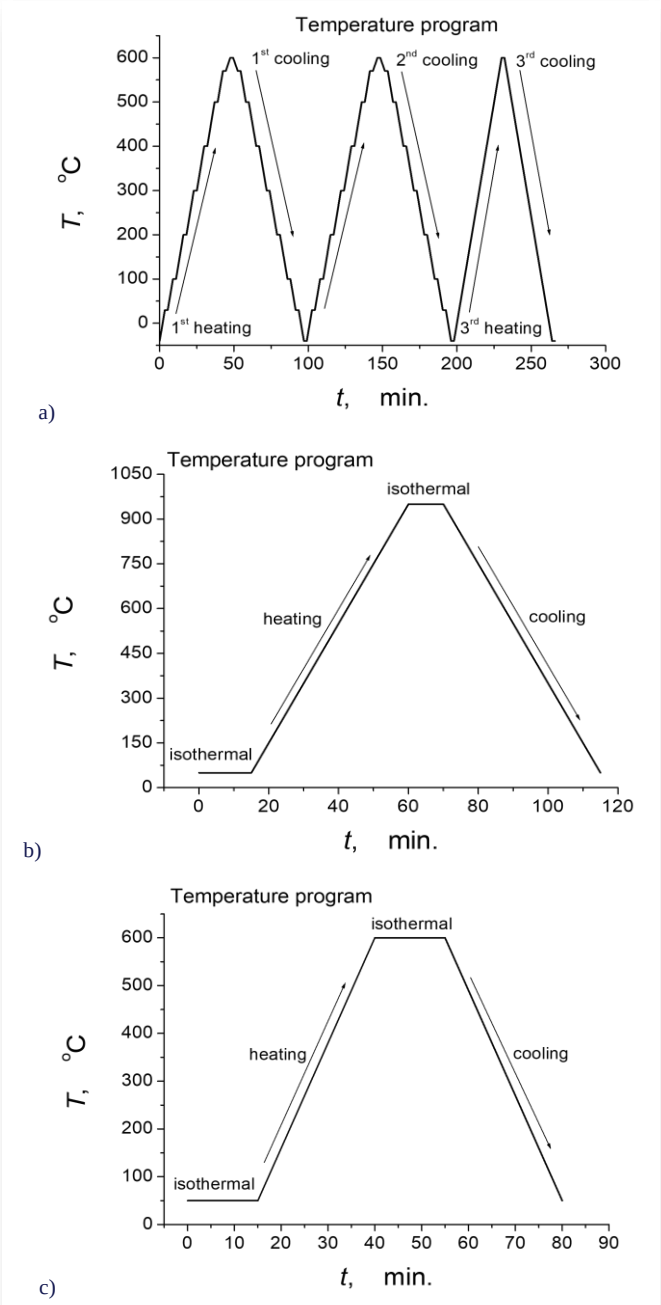


Fig. 3. Sample temperature programme for testing Ni (a, b) and Fe (c) materials on individual devices.

The temperature programme included two minutes of isotherm at the end of each heating and cooling stage in order to stabilise the temperature conditions and limit the impact of instrument equilibration time. The use of isotherms is an author's modification of the measurement procedure, aimed at improving the accuracy of determining the specific heat at constant pressure c_p [20,21]. The same program was used to conduct part of the research using the DSC 3 Mettler Toledo instrument. The measurements were carried out in a protective argon atmosphere at a constant flow rate of 20 ml/min (PerkinElmer) and in a protective nitrogen atmosphere at a constant flow rate of 150 ml/min (DSC 3 Mettler Toledo). The study also employed a standard heating and cooling program with a single ramp of linear temperature changes at a rate of 20 K/min in the range from room temperature to 600 °C (Ni: DSC F1 Pegasus 404 Netzsch and DSC 3 Mettler Toledo) or to 950°C (Fe: DSC F1 Pegasus 404 Netzsch; Fig. 3). When taking measurements with the Pegasus instrument, an argon flow rate was set to 70 ml/min. Data analysis was based on a standard calibration procedure using the so-called three-curve method and, additionally, the direct method (Mettler Toledo) including measurements for the reference system (empty aluminium vessels), reference material (sapphire) and the tested Ni and Fe samples. In accordance with the adopted methodology, the final results were obtained on the basis of DSC signals from the second or third heating and cooling cycle, i.e. after reaching a steady state in the sample-vessel-atmosphere system, as well as for the entire temperature range in order to present the discrepancies between individual temperature cycles.

3.2. Specific heat determination results

For calorimetric tests using DSC aimed at determining specific heat at constant pressure, two samples of Fe: with a mass of 230.72 mg in the shape of a cylinder with a diameter of approximately 4 mm (DSC 3 Mettler-Toledo tests), and an irregular in shape of 56.48 mg (PerkinElmer Pyris 1 and Netzsch DSC 4 F1 Pegasus studies) were applied. Two studied Ni samples were irregular in shape. The masses were equal to 63.90 mg (DSC 3) and 53.77 mg (Pyris 1 and DSC 4 F1 Pegasus). In both material cases, the investigated specimens were separated from a larger fragment of iron and nickel samples, respectively. It should be mentioned that the use of irregularly shaped samples is acceptable in DSC analysis, provided that the influence of the shape on the measurement uncertainty is taken into account and remains within the acceptable range of this uncertainty [22]. In the case of investigation of bulk metallic samples, these effects are negligible.

First, the temperature-dependent specific heat of the Fe sample, as determined in the experiments, will be analysed. The results are shown in Fig. 4.

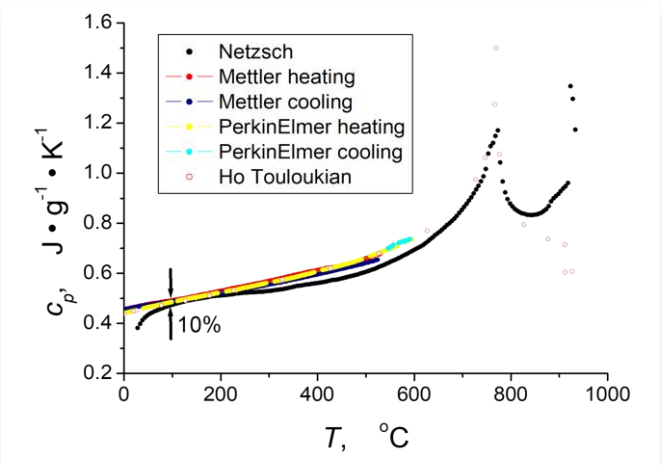


Fig. 4. Temperature characteristics of the specific heat of iron (Fe) determined using three different calorimeters, compared with reference data [13].

In addition to the measurement data collected within a temperature range limited to 600°C, the figure shows the results of measurements conducted using a DSC F1 Pegasus 404 calorimeter at temperatures up to about 950°C. When analysing these data, it is worth noting the significant deviation of the c_p values from those reported in the literature at temperatures above 850°C, which may indicate equipment limitations in this temperature range. In the ferromagnetic-paramagnetic transition region (T_C = 770°C [13]), the data consistency is more than satisfactory. Only this device made it possible to obtain data within the temperature range in discussion. For comparison, the results obtained using other calorimeters (Pyris 1, DSC 3) in the range up to 600°C are also presented, which show good agreement with the reference values.

For a more detailed analysis of the measurement results, Fig. 5 shows the variation of specific heat as a function of temperature over a narrower temperature range. The graph shows a high degree of consistency between the results obtained using Pyris 1 and DSC 3 calorimeters and the reference data. The data obtained using the F1 Pegasus 404 apparatus show a systematic underestimation of values compared to the other measurements. The results presented come from the third heating and cooling cycle, i.e. after the measurement conditions in the sample-vessel-atmosphere system had stabilised.

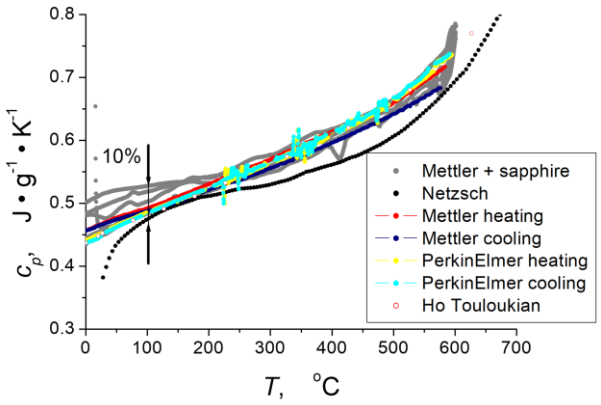


Fig. 5. The temperature characteristics of the specific heat of iron (Fe), determined using three different calorimeters, compared with reference data available in the literature [13].

The results of comparative studies on the specific heat of nickel as a function of temperature are shown in Fig. 6. The graph shows the results of measurements taken using three different calorimeters in the temperature range up to 600°C. It is important to note the significant deviation of the c_p value from the literature data in the case of measurements obtained using the DSC 3 calorimeter with the direct calculation method. The reason for this effect is difficult to identify, but the result itself illustrates the scale of problems that can be encountered in experimental studies of specific heat even for such well-defined materials as metallic elements.

Greater consistency between our test results and the data in the literature was achieved by using the three-curve procedure, referred to in the instrument's user manual as the "sapphire reference". This is illustrated by the comparison of the results of both types of measurements shown in Fig. 7. It should be noted

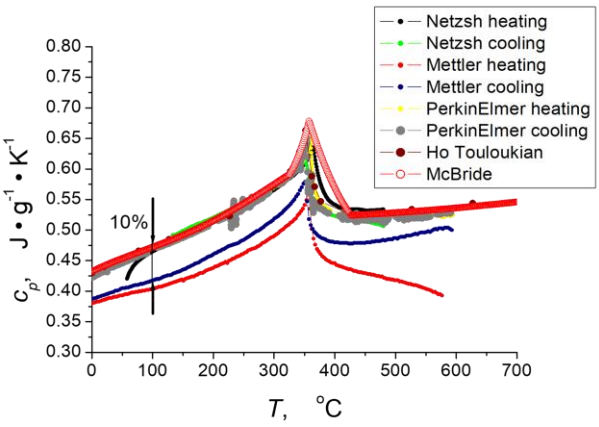


Fig. 6. The temperature characteristics of the specific heat of nickel (Ni), determined using three different calorimeters, compared with reference data available in the literature [13].

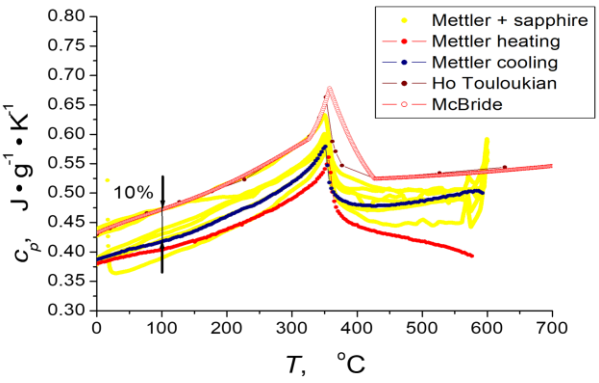


Fig. 7. Temperature characteristics of the specific heat of nickel (Ni) determined using a DSC 3 Mettler Toledo calorimeter by the three-curve method in comparison with reference data [13,18].

that the graph presents raw experimental data, which exhibit an artefact caused by irregular heating regime heat transfer in the form of apparent peaks at the extremes of the temperature range.

Based on the results of the specific heat measurements of nickel, the Curie temperature can be determined (T_C = 352°C [13]). The ferromagnetic transition is manifested by a characteristic lambda-shaped peak. The results of determining the position of the maximum of the temperature dependence of specific heat for the test results obtained using Pyris 1 and F1 Pegasus 404 devices are shown in Fig. 8a, and for the DSC 3 device in Fig. 8b.

The raw test results were further processed using a special computational procedure for approximation with B-spline curves [23] for cases where the range of the approximated data contained discontinuities in the first derivative of the temperature characteristic c_p. The test data for iron up to 600°C were approximated using a third-degree polynomial. This allowed us to determine representative specific heat characteristics as a function of temperature for each individual measurement. At the same time, the characteristic features of the peaks of the ferromagnetic phase transition were preserved. The results of the approximation, providing a summary illustration of the presented results in the context of their possible discrepancies, are shown in Fig. 9.

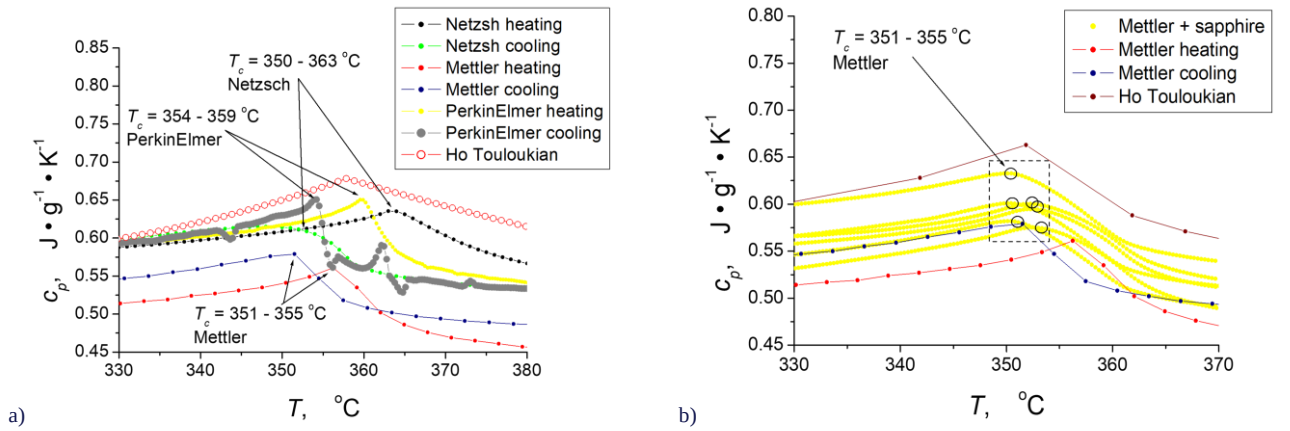


Fig. 8. Determination of the Curie temperature T_C for nickel: a) from measurements taken with Pyris 1 and DSC 404 F1 Pegasus devices, b) from calorimetric tests performed with a Mettler Toledo DSC 3 calorimeter.

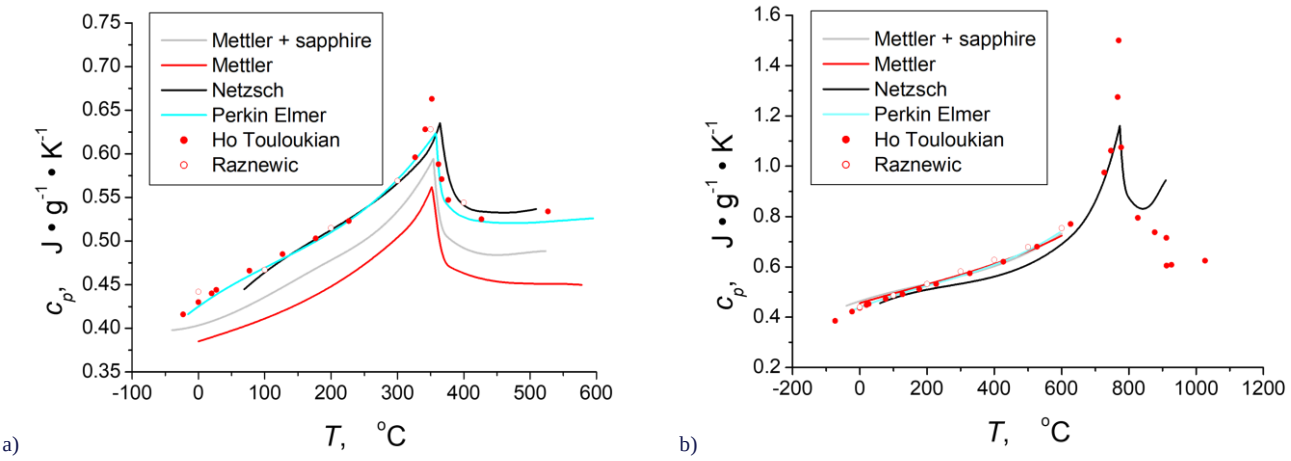


Fig. 9. Temperature-dependent specific heat at constant pressure characteristics for nickel (a) and iron (b) – B-spline [23] approximation results.

At the same time, these data provide an indirect answer to the question of measurement uncertainty. In thermal analysis studies, the emphasis is placed on the reproducibility of results and, where applicable, on agreement with data from reference materials [11]. It is possible to achieve better agreement than that shown in the data presented here. The results discussed above were obtained using standard procedures. Repeating measurements multiple times, using several samples, statistical averaging, and other such measures will yield a more satisfactory final result. However, this requires more effort and time. Therefore, the actual needs should be taken into account in each individual case.

It is also possible to estimate measurement uncertainty more accurately without resorting to interlaboratory comparisons. The problem, however, is that the necessary calculations must be performed for each individual case. And this time, it is not about, for example, the individual data of the tested samples, but rather about a set of data hidden within the calibration parameters. And when, for example, temperature calibration is involved, accounting for drift would require checking the calibration data each time. A case where temperature calibration data is critical is that of high-temperature-resolution measurements in the vicinity of phase transitions, as characterised in the monograph [20] and publication [24].

4. Conclusions

The aim of the study was to compare the metrological capabilities of selected methods and devices for determining the specific heat of materials undergoing second-order phase transitions, with particular emphasis on nickel and iron. The data obtained using three different differential scanning calorimeters (DSC), using both standard procedures and proprietary measurement methods, were analysed. In the course of the experiments, the influence of the test procedures used and the declared temperature change programmes on the specific heat values obtained and the results of the Curie point location identification were assessed. Particular attention was paid to comparing the results with available literature data and analysing the course of phase transitions. Based on the results obtained, the following conclusions were drawn:

- The tests showed that it is possible to obtain reliable specific heat measurements using the DSC method, even with irregularly shaped samples, provided that the measurement

conditions and uncertainty analysis are repeated. This is important from the point of view of industrial applications, where it is not always possible to prepare samples that comply with standard requirements.

- A comparison of three independent calorimeters (PerkinElmer Pyris 1, Mettler Toledo DSC 3 and Netzsch DSC 404 F1 Pegasus) allowed for an assessment of their metrological capabilities and the impact of device design and conversion algorithms on data quality. The Pyris 1 device ensures the highest repeatability and accuracy of results; the DSC 404 F1 Pegasus device allows satisfactory measurement results to be obtained in the high temperature range, while the DSC 3 device, despite the observed differences in results compared to the literature data, proved to be a device ensuring repeatable results of Curie point identification.
- The introduction of a proprietary measurement procedure with isothermal stops in the Pyris 1 apparatus made it possible to obtain consistent results in both heating and cooling regimes. This procedure can be a useful tool in further studies of phase transition materials, increasing the amount of available reference data.
- Analysis of the $c_p(T)$ data allowed the determination of characteristic parameters of the second type of phase transition for nickel. The convergence of the peak maximum temperature and the end of the transition in various measurements confirms the correctness of the methods used. This, of course, applies to the repeatability and accuracy of the measurement results that can be obtained.
- For iron, reliable mapping of the phase transition curve was only possible when using the DSC 404 F1 Pegasus apparatus. Slightly larger deviations in the low-temperature test results obtained with this device confirm the need for complementary tests.
- The specific heat values obtained were in satisfactory agreement with the literature data in the range up to 600°C. The test results obtained with the DSC 404 F1 Pegasus device show large differences from the reference data in the range above 850°C. Considering the difficulties in accurately determining the temperature characteristics of all thermo-physical quantities in the vicinity of phase transitions, especially of the first kind [19−21], this effect cannot be treated as a basis for questioning the correctness of the apparatus or the correctness of the measurement procedures. On the contrary, it is necessary to consider continuing this type of research using comprehensive complementary testing procedures. This will allow data to be obtained in the form of temperature dependencies of other thermophysical quantities [24], which will enable accurate identification of the issue and determination of reliable reference data.

The results of this research contribute to the methodology of calorimetry, providing both comparative data and practical guidelines for interpreting and verifying measurement results for metallic materials undergoing phase transitions. The results of the single-sample tests presented in this study provide detailed information regarding the selection of measurement procedures. This applies to the measurement procedure and the selection of the method for determining specific heat. Indirectly, they also provide guidance on the possible need to expand the project – by including a larger number of samples and cycles – in order to achieve statistical representativeness.

Acknowledgements

The work has been accomplished under the research project No. UGB 531-00050-W200-22 financed by the Military University of Technology.

References

[1] Drozdová, L., Smetana, B., Machů, M., Novák, V., Vontorová, J., Zlá, S., Kawuloková, M., Řeháčková, L., & Sorokina, S. (2022). Impact of Ni on the thermophysical and thermodynamic properties of Fe–C–Ni based alloys. *Journal of Materials Research and Technology*, 20, 4318–4332. doi: 10.1016/j.jmrt.2022.08.159

[2] Gerion, D., Hirt, A., Billas, I.M.L., Châtelain, A., & de Heer, W.A. (2000). Experimental specific heat of iron, cobalt, and nickel clusters studied in a molecular beam. *Physical Review B*, 62, 7491. doi: 10.1103/PhysRevB.62.7491

[3] Sykes, C., & Wilkinson, H. (1938). The specific heat of nickel from 100°C to 600°C. *Proceedings of the Physical Society*, 50, 834. doi: 10.1088/0959-5309/50/5/319

[4] Atapek, Ş.H., Erişir, E. & Gümüş, S. (2013). Modeling and thermal analysis of solidification in a low alloyed steel. *Journal of Thermal Analysis and Calorimetry*, 114(1), 179–183. doi: 10.1007/s10973-012-2930-1

[5] Perring, L., Kuntz, J.J., Bussy, F., & Gachon, J.C. (2001). Heat capacity measurements by differential scanning calorimetry in the Pd–Pb, Pd–Sn and Pd–In systems. *Thermochimica Acta*, 366(1), 31−36. doi: 10.1016/S0040-6031(00)00731-0

[6] Gałek, R., & Wilk, J. (2024). Investigations of the specific heat capacity of selected heterogeneous materials. *Archives of Thermodynamics*, 45(2), 91−98. doi: 10.24425/ather.2024.150855

[7] McHugh, J., Fideu, P., Herrmann, A., & Stark, W. (2010). Determination and review of specific heat capacity measurements during isothermal cure of an epoxy using TM-DSC and standard DSC techniques. *Polymer Testing*, 29(6), 759–765. doi: 10.1016/j.polymertesting.2010.04.004

[8] Bernardes, C.E.S., Joseph, A., & Minas da Piedade, M.E. (2020). Some practical aspects of heat capacity determination by differential scanning calorimetry. *Thermochimica Acta*, 687, 178574. doi: 10.1016/j.tca.2020.178574

[9] Jiao, Y., Liu, C.F., Cui, X.P., Zhang, J., Huang, L.J., & Geng, L. (2022). A new approach for measurement of the low-temperature specific heat capacity. *Measurement*, 203, 111892. doi: 10.1016/j.measurement.2022.111892

[10] Rudtsch, S. (2002). Uncertainty of heat capacity measurements with differential scanning calorimeters, *Thermochimica Acta*, 382(1−2),17−25. doi: 10.1016/S0040-6031(01)00730-4

[11] Wendlandt, W.W. (1986). *Thermal Analysis*. New York, John Wiley & Sons.

[12] McNaughton, J.L, & Mortimer, C.T. (1975). Differential Scanning Calorimetry. *IRS, Physical Chemistry Series 2*, Vol. 10, London, Butterworths (Norwalk: reprinted by Perkin-Elmer Corp.).

[13] Touloukian, Y.S., & Ho, C.Y. (1981). *Properties of selected ferrous alloying elements*. McGraw-Hill/CINDAS Data Series on

Material Properties, Vol. III-1 (pp. 196–198). McGraw-Hill Book Company, New York.

[14] Jin, K., Mu, S., An, K., Porter, W.D., Samolyuk, G.D., Stocks, G.M. & Bei, H. (2017). Thermophysical properties of Ni-containing single-phase concentrated solid solution alloys, *Materials & Design*, 117, 185–192, doi: 10.1016/j.matdes.2016.12.079

[15] Lang, X.Y., Zheng, W.T., & Jiang, Q. (2006). Size and interface effects on ferromagnetic and antiferromagnetic transition temperatures, *Physical Review B*, 73, 224444, doi: 10.1103/PhysRevB.73.224444

[16] Connelly, D.L., Loomis, J.S., & Mapother, D.E. (1971). Specific heat of nickel near the Curie temperature. *Physical Review B*, 3, 924. doi: 10.1103/PhysRevB.3.924

[17] McBride, B.J., Gordon, S., & Reno, M.A. (1993). Thermodynamic Data for Fifty Reference Elements. *NASA Technical Paper*, 3287/REV1.

[18] Desai, P.D. (1986). Thermodynamic Properties of Iron and Silicon, *Journal of Physical and Chemical Reference Data*, 15(3), 967, https://srd.nist.gov/JPCRD/jpcrd298.pdf

[19] Panas, A.J. (1998). *High temperature resolution investigation of linear thermal expansion – dilatometric thermal analysis*. WAT, Warszawa (in Polish).

[20] Panas, A.J. (2004). Comparative dilatometric and calorimetric studies of a-b phase transitions. In *Proceedings of the 26th International Thermal Conductivity Conference and the 14th International Thermal Expansion Symposium*, (Eds.) R.B. Dinwiddie, R. Mannello (pp. 530-539), August 6-8, 2001, Cambridge, Ma, DEStech Publications, Inc.

[21] Panas, A.J., & Panas, D. (2009). DSC investigation of binary iron-nickel alloys. *High Temperature – High Pressures*, 38, 63–78.

[22] Kalyanavalli, V., Ramadhas, T.K.A.,& Sastikumar, D. (2019). Determination of thermal diffusivity of Basalt fiber reinforced epoxy composite using infrared thermography. *Measurement*, 134, 673–678. doi: 10.1016/j.measurement.2018.11.004

[23] Panas, A.J. (2003). B-spline approximation of DSC data of specific heat of NiAl and NiCr alloys. *Archives of Thermodynamics*, 24(4), 47−65.

[24] Panas, A.J. (2010). Comparative-Complementary Investigations of Thermophysical Properties – High Thermal Resolution Procedures in Practice. In *Proceedings of Thermophysics 2010* (pp. 218−235), 3−5 November, Valtice, Czech Republic.

Co-published by
Institute of Fluid-Flow Machinery
Polish Academy of Sciences
Committee on Thermodynamics and Combustion
Polish Academy of Sciences

Copyright©2026 by the Authors under licence CC BY-NC-ND 4.0

http://www.imp.gda.pl/archives-of-thermodynamics/

Rheological and porous effects on mixed convection: Power-law fluid flow in a finned annular configuration

Youcef Lakahal*, Houssem Laidoudi

Faculty of Mechanical Engineering, University of Science and Technology of Oran Mohamed-Boudiaf, BP 1505, El -Menaouer, Bir El Djir 31000, Algeria
*Corresponding author email: youcef.lakahal@univ-usto.dz

Received: 07.06.2025; revised: 02.02.2026; accepted: 22.04.2026

Abstract

This study numerically investigates mixed-convection heat transfer of non-Newtonian power-law fluids in the annular space between a rotating outer cylinder and a stationary finned inner cylinder filled with a porous medium. The outer cylinder rotates at constant angular velocity and is maintained at a temperature lower than the finned inner cylinder, producing combined forced and buoyancy-driven flow. The governing equations were solved using the finite volume method implemented in Ansys CFX, with the fluid's rheology modelled by the Ostwald's law model. Parametric ranges include: Reynolds numbers from 5 to 35, Richardson numbers from 0 to 3, Darcy numbers from 10^{-5} to 10^{-2}, and power-law indices of 0.6, 1.0 and 1.6. The results show a transitional behaviour at a Richardson number of approximately 2.6 (for a Darcy number of 10^{-2}), beyond which the average Nusselt number becomes almost independent of the power-law index. Increasing rotational forcing enhances circulation and heat transfer, and under strong buoyancy the shear-thinning fluid (power-law index 0.6) yields up to 15–20% higher average heat transfer compared with the Newtonian case. The novelty of this work lies in the joint investigation of internal fins, outer-wall rotation and porous resistance in non-Newtonian media, which produces distinct flow regimes and offers practical guidance for porous heat exchanger and rotating-machine cooling designs.

Keywords: Complex fluid; Mixed convection; Porous media; Numerical investigation; Nusselt number; CFD

Vol. 47(2026), No. 3, 41–55; doi: 10.24425/ather.2026.3653

Cite this manuscript as: Lakahal, Y., & Laidoudi, H. (2026). Rheological and porous effects on mixed convection: Power-law fluid flow in a finned annular configuration. *Archives of Thermodynamics*, 47(3), 41–55.

1. Introduction

In recent years, the study of mixed convection in non-Newtonian or rheologically complex fluids has attracted considerable attention due to its importance in numerous engineering and industrial applications, including metal casting, enhanced oil recovery, glass manufacturing, biomedical devices and food processing. While many investigations have concentrated on forced convection in power-law fluids where flow is predominantly driven by external forces, researchers have also examined their thermal and flow behaviour around confined geometries, such as cylinders and ducts with different cross-sectional shapes. These studies often incorporate enclosures with adiabatic walls, structured inlets and outlets, or partially porous regions to better mimic real systems [1–3].

Complementary work has been devoted to natural convection, which arises solely from buoyancy forces induced by temperature gradients. Such investigations have considered power-law fluids within trapezoidal or wavy enclosures, typically featuring heated bases and either cooled or insulated boundaries [4,5].

Other studies have focused on rectangular and shallow cavities to evaluate how non-Newtonian rheology affects the onset of flow, velocity distribution, temperature fields and overall heat transfer efficiency under various thermal conditions [6,7].

Nomenclature

A – surface area of the inner cylinder, m^2
C_p – heat capacity of fluid, J/(kg K)
d – diameter of the inner cylinder, m
Gr – Grashof number
g – gravitational acceleration, m/s
I_2 – second invariant function of strain rate tensor
K – permeability, m^2
m – consistency index, Pa s^n
n – power-law index
Nu – Nusselt number (average value)
Nu_L – Nusselt number (local value)
p – pressure, Pa
Pr – Prandtl number
Re – Reynolds number
Ri – Richardson number
T – temperature, K
u, v – velocity components along x- and y-directions, m/s
x, y – Cartesian coordinates, m

Greek symbols

β_T – coefficient of volume expansion
η – dynamic viscosity, Pa s
ρ – density of fluid, kg/m^3
τ – stress tensor, Pa
Ω – rotation speed, 1/s

Subscripts and Superscripts

c – cold
h – hot
$*$ – dimensionless quantity

Abbreviations and Acronyms

ANN – artificial neural network
CFD – computational fluid dynamics

The interplay between forced and natural convection, known as mixed convection in power-law fluids, has also been widely analysed using numerical simulations. These studies emphasise the key influence of dimensionless parameters, such as the Reynolds number (Re), Richardson number (Ri) and power-law index (n) on both flow structures and heat transfer mechanisms. Investigations have been carried out in different geometries, including lid-driven and wall-driven cavities with isothermal, adiabatic or combined boundary conditions [8–13]. Configurations featuring internally heated blocks or asymmetric heating have revealed how geometric and thermal non-uniformities can modify flow circulation and enhance heat transfer [14–21].

Another aspect of growing interest is internal rotation within non-Newtonian domains. The presence of rotating components, such as cylinders, significantly affects streamlines, isotherms and the overall heat transfer rate, often characterised through the Nusselt number [22–27]. Further complexity has been introduced in studies involving triangular or inclined cavities filled with power-law nanofluids subjected to magnetic fields, where changes in parameters, such as Re, Ri, n and magnetic inclination, were found to strongly influence both heat and mass transport [28,29].

Recent numerical and experimental works have also explored complex geometries and non-uniform heating conditions, such as lid-driven cavities with embedded obstacles [30], compound cavity–channel systems incorporating multiple heat sources [31,32], and enclosures containing hemispherical heaters [33]. Investigations on micropolar and magnetised fluids have further demonstrated that localised magnetic effects can generate secondary vortices, enhancing flow mixing and thermal regulation [34]. Moreover, studies of double-lid cubic enclosures with distributed heat sources have highlighted the sensitivity of heat transfer and flow structures to variations in Re, Ri and nanoparticle concentration [35].

Recent developments in reliability engineering have emphasised the integration of machine learning with statistical modelling to improve predictive accuracy and system assessment. In [36,37], reliability analyses were conducted for the generalised exponential and generalised Rayleigh distributions, respectively, by incorporating the inverse power-law model within an artificial neural network (ANN) framework using Bayesian regularisation. These studies demonstrated that the combination of ANN-based learning and Bayesian regularisation significantly enhances the reliability prediction capability by minimising overfitting and improving model generalisation. The results confirmed that this hybrid approach provides more accurate lifetime estimation and better captures the complex reliability behaviour of engineering systems. Overall, [36,37] illustrate the growing potential of intelligent computational methods for advancing reliability modelling and analysis in modern industrial applications.

Despite this extensive literature, there remains a notable research gap concerning mixed convection in configurations that integrate rotating enclosures, internal fins and porous media. Most previous studies have addressed simpler geometries or neglected the presence of internal fins, even though fins play a vital role in modifying thermal performance by increasing the heat transfer surface area and disrupting flow symmetry. In addition, the effects of porous media on convective transport in non-Newtonian fluids have often been overlooked, limiting the practical relevance of existing models.

To address these gaps, the present study investigates mixed convection of power-law fluids in a complex annular configuration consisting of a rotating outer cylinder and a stationary finned inner cylinder embedded in a porous medium. This configuration is of particular interest for applications, such as rotating machinery, advanced cooling systems and compact heat exchangers. By systematically varying the Reynolds, Richardson, and Darcy numbers, as well as the power-law index, this work aims to clarify the coupled effects of rotation, non-Newtonian rheology, and porous resistance on fluid flow and heat transfer characteristics.

Numerical simulations are conducted using the finite volume method, providing detailed insights into the thermo-fluid dynamics within the enclosure. The results presented herein aim to

extend existing knowledge and offer a comprehensive framework for analysing non-Newtonian mixed convection in geometrically and physically complex systems relevant to modern thermal engineering applications.

2. Physical problem and mathematical formulations

Figure 1 presents the physical and computational configuration of the problem, consisting of a horizontal finned inner cylinder enclosed within a concentric outer cylinder. The inner cylinder, featuring uniformly distributed radial fins, is maintained at a higher temperature (T_h), while the outer boundary is held at a lower temperature (T_c), ensuring a consistent thermal gradient ($T_h > T_c$). The outer cylinder rotates counterclockwise with a constant angular velocity (Ω). The space between the two cylinders is filled with a porous medium saturated with a non-Newtonian power-law fluid. Three distinct power-law indices (n = 0.6, 1.0, and 1.6) are investigated to represent shear-thinning, Newtonian and shear-thickening behaviours, respectively.

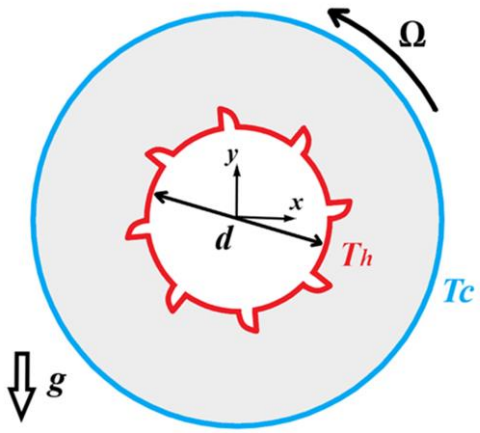


Fig. 1. Diagrammatic representation of the problem.

Mixed convection arises when both natural and forced convection mechanisms contribute to heat transfer. In this study, forced convection is induced by the rotation of the outer cylinder, while natural convection is driven by the temperature difference between the surfaces of the two cylinders. The Reynolds number determines the cylinder's rotational velocity value, while the Richardson number quantifies the balance between forced and natural convection effects. Four Richardson numbers are analysed: 0, 1, 2 and 3. The medium's permeability, represented by the Darcy number (Da), is investigated within the range of 10^{-5} to 10^{-2}.

The assumptions of laminar and non-Newtonian flow, steady state, mixed convection and constant fluid properties are adopted in this study. The equations of continuity, momentum and energy, subject to the Boussinesq approximation and the effect of negligible dissipation, are written in their dimensionless form as follows:

– the equation of continuity:

$$\frac{\partial u^*}{\partial x^*} + \frac{\partial v^*}{\partial y^*} = 0, \tag{1}$$

– the equation of momentum along the x-direction:

$$u^*\left(\frac{\partial u^*}{\partial x^*}\right) + v^*\left(\frac{\partial v^*}{\partial y^*}\right) = -\frac{\partial p^*}{\partial x^*} + \frac{1}{\mathrm{Re}}\left(\frac{\partial \tau^*_{xx}}{\partial x^*} + \frac{\partial \tau^*_{yx}}{\partial y^*}\right), \tag{2}$$

– the equation of momentum along the y-direction:

$$u^*\left(\frac{\partial v^*}{\partial x^*}\right) + v^*\left(\frac{\partial v^*}{\partial y^*}\right) = -\frac{\partial p^*}{\partial y^*} + \frac{1}{\mathrm{Re}}\left(\frac{\partial \tau^*_{xy}}{\partial x^*} + \frac{\partial \tau^*_{yy}}{\partial y^*}\right) + \mathrm{Ri}\, T^*, \tag{3}$$

– the equation of energy:

$$u^*\left(\frac{\partial T^*}{\partial x^*}\right) + v^*\left(\frac{\partial T^*}{\partial y^*}\right) = \frac{1}{\mathrm{Pe}}\left(\frac{\partial^2 T^*}{\partial x^{*2}} + \frac{\partial^2 T^*}{\partial y^{*2}}\right), \tag{4}$$

where Re and Pe are the Reynolds and Peclet numbers, Ri is the Richardson number, u^* and v^* are the fluid dimensionless velocities in the x^*- and y^*-directions, and dimensionless pressure and temperature are represented by p^* and T^*, respectively. The following represent the dimensionless variables:

$$x^* = \frac{x}{d}, \quad y^* = \frac{y}{d}, \tag{5}$$

$$u^* = \frac{u}{\Omega d}, \quad v^* = \frac{v}{\Omega d}, \tag{6}$$

$$p^* = \frac{p}{\rho(\Omega d)^2}, \quad T^* = \frac{T - T_c}{T_h - T_c}, \tag{7}$$

$$\mathrm{Pe} = \mathrm{RePr}. \tag{8}$$

where Pr is the Prandtl number and d is the inner cylinder's diameter.

The following equation represents the power-law fluid's behaviour:

$$\tau_{ij} = 2\eta\varepsilon_{ij}, \tag{9}$$

where the viscous stress tensors and the rate of deformation are represented, respectively, by ε_{ij} and τ_{ij}. ($i, j = x, y$). Furthermore, for power-law fluids, the fluid viscosity, denoted by η, is defined (in dimensional form) as follows:

$$\eta = m\left(\frac{I_2}{2}\right)^{\left(\frac{n-1}{2}\right)}, \tag{10}$$

where I_2 is the second invariant of the rate of deformation tensor, m is the consistency index, and n is the power-law index. A fluid that is shear-thinning is represented by $n < 1$, a Newtonian limit by a value of $n = 1$, and a shear-thickening fluid by $n > 1$. The following equation gives I_2 in Cartesian coordinates:

$$\left(\frac{I_2}{2}\right) = 2\left(\frac{\partial u}{\partial x}\right)^2 + 2\left(\frac{\partial v}{\partial y}\right)^2 + \left[\left(\frac{\partial u}{\partial y}\right) + \left(\frac{\partial v}{\partial x}\right)\right]^2. \tag{11}$$

Generally, Grashof number, Richardson number and Darcy number for power-law fluids are computed as follows:

$$\mathrm{Gr} = g\beta_T \Delta T d^3 \left(\frac{\rho}{m}\Omega^{1-n}\right)^2, \tag{12}$$

$$\mathrm{Ri} = \frac{g\beta_T \Delta T d^3}{(\Omega d)^2} = \frac{\mathrm{Gr}}{\mathrm{Re}^2}, \tag{13}$$

$$\mathrm{Da} = \frac{K}{d^2}, \tag{14}$$

where ρ, g, β_T, and K are the density of the fluid, the gravitational acceleration, volumetric expansion coefficient and permeability, respectively.

The Nusselt number, or average Nusselt number, is calculated by integrating local values along the inner cylinder's surface. The following are the local and average values of Nu, respectively:

$$\mathrm{Nu}_L = \left(\frac{\partial T^*}{\partial n}\right)_{wall}, \quad \mathrm{Nu} = \frac{1}{A}\int_S \mathrm{Nu}_L dA, \tag{15}$$

where $\boldsymbol{n}$ is the normal vector to the wall and S represents the surface of the heated inner cylinder.

3. Numerical procedure

The numerical simulations in this study were carried out using Ansys-CFX, a commercial computational fluid dynamics (CFD) tool that transforms the governing equations of fluid flow and heat transfer into algebraic form. These equations were discretised using the finite volume method, with boundary conditions applied throughout the computational domain. To ensure high solution accuracy, a convergence criterion of 10^{-6} was adopted for both the momentum and energy equations. The high-resolution scheme was utilised to accurately capture convection effects, while the SIMPLEC (semi-implicit method for pressure linked equations-consistent) algorithm was implemented to efficiently couple pressure and velocity fields, offering enhanced stability for steady-state analyses.

To validate the accuracy of the numerical results, a grid independence study was conducted, acknowledging the significant influence of mesh resolution on simulation precision. The computational domain was discretised using a hybrid mesh structure with refined quadrilateral elements in the vicinity of the inner and outer walls to better resolve boundary layer gradients. As illustrated in Fig. 2 and detailed in Table 1, three progressively refined mesh configurations were examined: M1 (coarse), M2 (medium) and M3 (fine). The average Nusselt number along the heated cylindrical surface was calculated

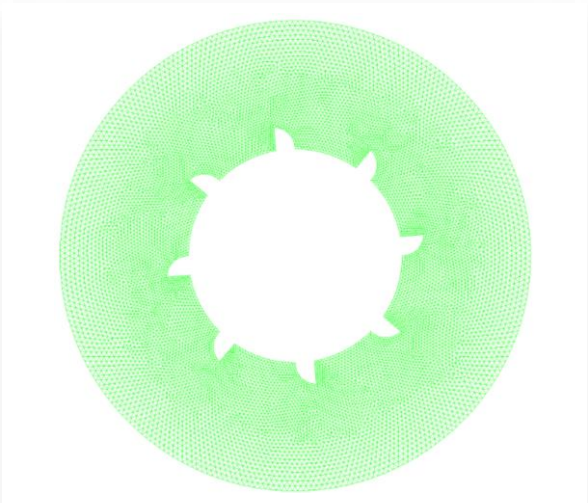


Fig. 2. The structure of the grid used for the calculations.

Table 1. Grid independency test for n = 1.6, Re = 25, Ri = 3 and Da = 10^{-3}.

Mesh	Elements	Nusselt number	Difference, %
M1	122 000	1.50581	1.53
M2	244 000	1.48278	0.0112
M3	488 000	1.48294	–

under representative conditions: n = 1.6, Re = 25, Ri = 3 and Da = 10^{-3}. The comparison showed that the medium-resolution mesh (M2) produced results nearly identical to those of the finest mesh (M3), confirming that M2 offers an optimal compromise between computational efficiency and solution accuracy. Hence, M2 was selected for all subsequent simulations, balancing computational cost and numerical precision.

The accuracy and robustness of the present numerical model were verified through comparisons with established benchmark studies. The first validation involved comparing results with the classical work of Kuehn and Goldstein [38] and the study by Matin and Khan [39], both of which examined buoyancy-driven flow in annular enclosures. For this case, the working fluid was considered Newtonian (n = 1) with properties of air (Pr = 0.71), and the Rayleigh number was varied from 10^3 to 10^6. As shown in Fig. 3A, the predicted variation of the average Nusselt number with Rayleigh number (Ra = Pr Gr) for Pr = 0.71 and n = 1 closely matches the reference data, confirming the model's ability to capture natural convection phenomena accurately.

A second comparison assessed the model's capability to represent non-Newtonian fluid behaviour, focusing on the influence of the power-law index. Results were compared to those reported by Matin et al. [40] under conditions of Pr = 100 and a blockage ratio of 0.25. The present model reproduced the same trend of heat transfer enhancement for shear-thinning fluids (n < 1) and suppression for shear-thickening fluids (n > 1), consistent with theoretical expectations. Figure 3B illustrates strong agreement in the Nusselt number variation with respect to n, validating the model's treatment of fluid rheology and ensuring accurate representation of non-linear viscosity effects.

Lastly, validation was extended to the study by Sheikholeslami [41], which investigated natural convection between concentric cylinders filled with a porous medium and subjected to a temperature difference between the inner and outer walls. The comparison was made at Da = 10^{-3} and Ra = 10^5. As seen in Fig. 3C, the present results show excellent consistency with the benchmark, further supporting the reliability of the adopted numerical approach. The close match across multiple validation cases confirms that the current CFD model is robust and capable of accurately resolving complex coupled effects of buoyancy, rotation and non-Newtonian fluid rheology in porous media.

4. Results and discussion

This study investigates the heat transfer and flow behaviour of a power-law fluid in a porous medium confined between a stationary finned inner cylinder and a rotating outer cylinder. The analysis focuses on the influence of key parameters: the Reynolds number (Re = 5, 15, 25 and 35), Richardson number (Ri = 0, 1, 2

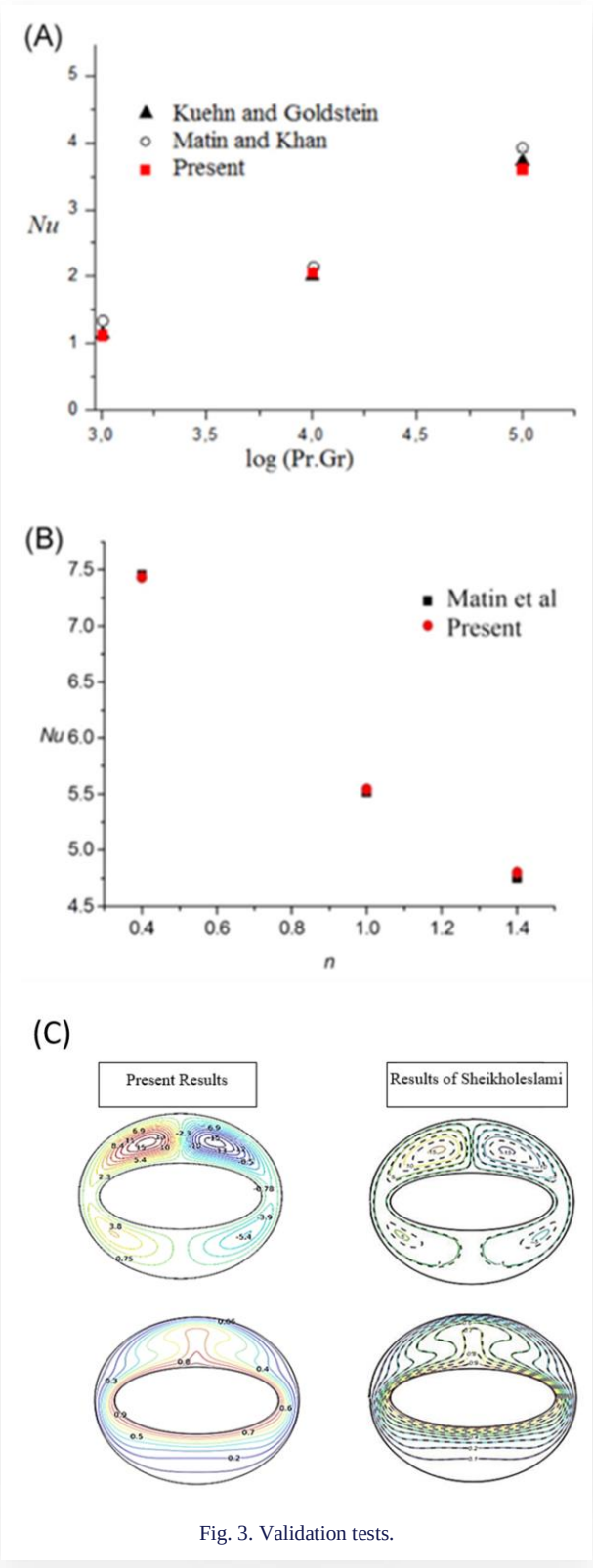


Fig. 3. Validation tests.

and 3), Darcy number (Da = 10^{-5} to 10^{-2}) and power-law index (n = 0.6, 1 and 1.6), with a fixed Prandtl number (Pr = 50). Flow dynamics and thermal performance are explored using streamlines, isotherms and the Nusselt number. Some parameter values are selected based on a previous study [42].

Mixed convection arises when both forced and natural convection mechanisms coexist. In this study, natural convection is driven by the temperature difference between the two cylinders, while forced convection results from the rotation of the outer cylinder. When Ri = 0, the flow is purely governed by forced convection. As Ri increases, buoyancy forces (representing natural convection) gradually become more significant. Simultaneously, the rotational speed of the outer cylinder, which governs the magnitude of forced convection, increases with Reynolds number.

Figure 4 illustrates the flow patterns represented by streamlines for various Reynolds numbers and power-law indices. At low Re, viscous forces dominate, resulting in smooth, symmetric streamlines around the finned inner cylinder. The flow remains relatively weak, with minimal recirculation. As Re increases, inertial effects become more pronounced, leading to the formation of a closed counter-rotating vortex on the left side of the domain. The streamlines extend further outward and form larger vortices, reflecting intensified flow activity around the fins.

At higher Re, the centrifugal force generated by the rotating outer cylinder significantly enhances momentum transfer, resulting in asymmetric vortical structures that extend toward the upper region of the enclosure. The secondary vortices near the fin tips indicate localised shear-layer separations, which enhance local mixing and amplify heat exchange along the finned surfaces.

For shear-thinning fluids (n = 0.6), the apparent viscosity decreases with increasing shear rate, which enhances fluid motion and results in more elongated and active recirculation zones, especially at higher Re. In contrast, as the power-law index increases (n = 1.6, shear-thickening behaviour), viscosity increases with shear rate, damping the fluid motion. This suppresses vortex formation, leading to smaller and less intense recirculation zones compared to the shear-thinning case.

Figure 5 displays the thermal fields (isotherms) under the same parameter conditions. The temperature distribution closely mirrors the fluid flow patterns. At low Re, nearly concentric isotherms are observed around the heated inner cylinder, indicating weak convective effects and localised thermal gradients. As Re increases, convection dominates, distorting the isotherms and pushing them outward due to intensified fluid motion.

This outward displacement signifies a transition from conduction-controlled to convection-dominated transport. The stretching of isotherms in the direction of rotation reflects enhanced azimuthal heat transport, while compression near stagnation zones reveals localised temperature build-up due to limited mixing.

The rotational direction of the outer cylinder enhances the effect of buoyancy on the right side of the domain, promoting heat transfer. On the upper part of the inner cylinder, the isotherms are further stretched and distorted, indicating stronger convective mixing. On the left side, however, the presence of recirculating flow thickens the isotherms and reduces thermal transport efficiency. A more detailed observation shows that the region downstream of the fin tip experiences a local thermal wake, where thermal diffusion dominates due to reduced local velocity magnitude. A notable feature is the tongue-like structure in the thermal boundary layer at the top of the inner cylinder. This structure reflects reduced fluid mixing, which limits

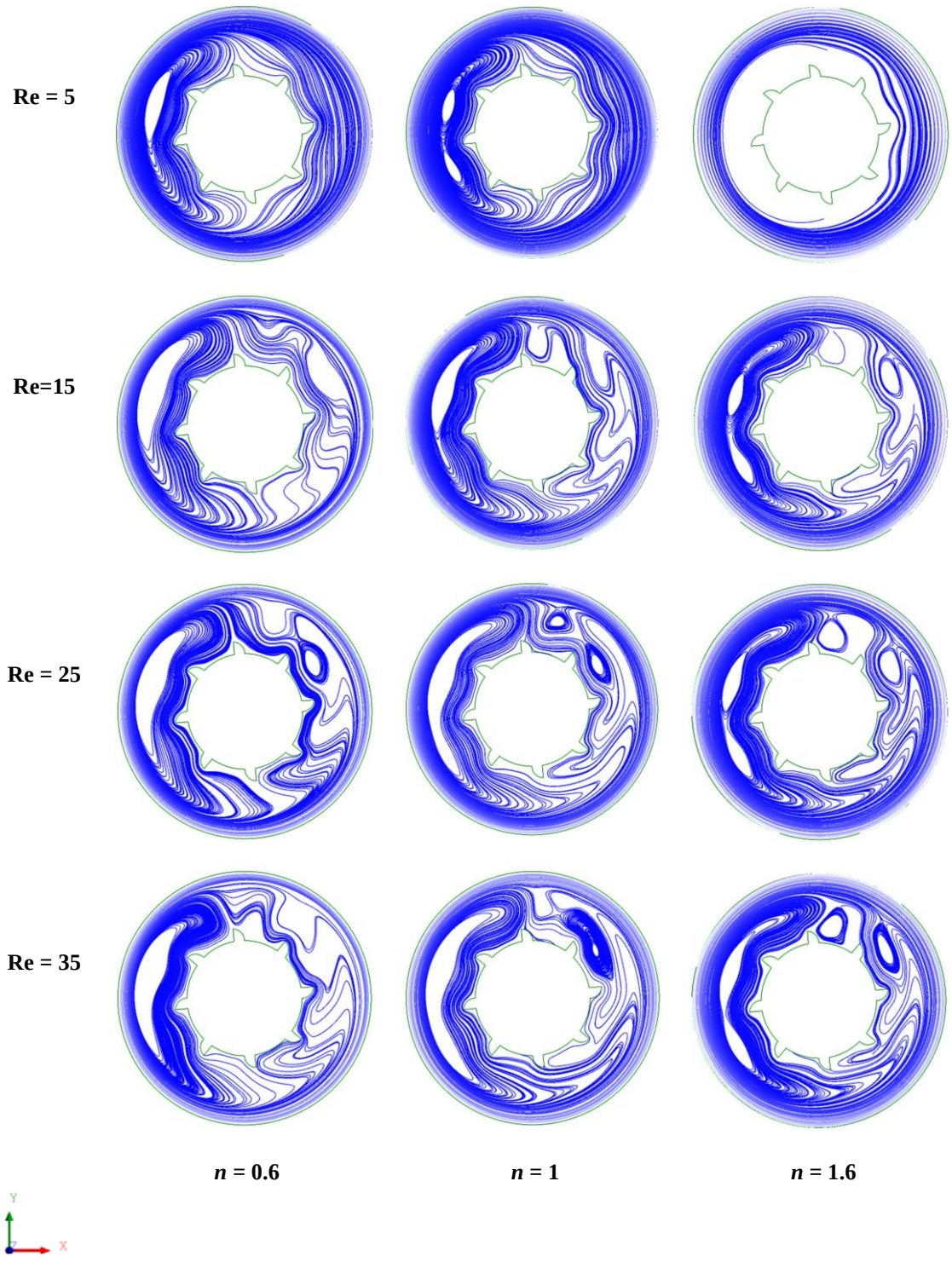


Fig. 4. Streamlines for various values of Re and n at Da = 10^{-2} and Ri = 3.

convective heat dispersion. As n increases, this tongue splits into two branches due to altered flow patterns. This bifurcation represents a competition between viscous damping (which stabilises the thermal layer) and centrifugal enhancement (which destabilises it). The higher viscosity of shear-thickening fluids suppresses upward motion above the finned cylinder, leading to localised heat accumulation and bifurcated thermal zones around the fins.

Figure 6 illustrates the flow patterns represented by streamlines for various Richardson numbers and power-law indices, at fixed values of Reynolds number (Re = 25) and Darcy number (Da = 10^{-2}). When Ri is low, forced convection is dominant, resulting in a stable rotational flow between the cylinders. As Ri increases, buoyancy forces become more significant, giving rise to vertically oriented flow structures and the development of counter-rotating vortices. At intermediate Ri (= 1–2), the flow field exhibits mixed characteristics; the

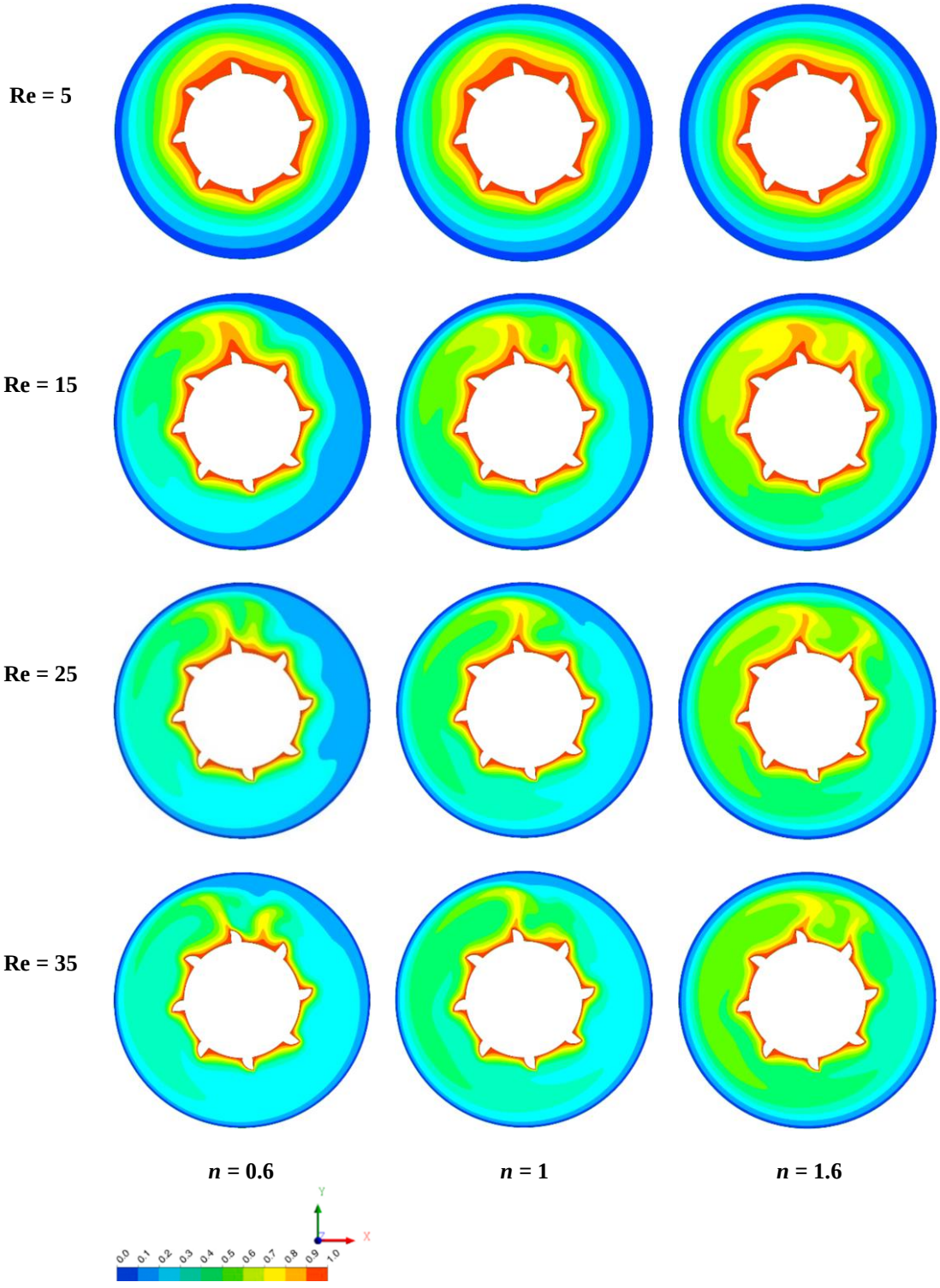


Fig. 5. Isotherms for various values of Re and n at Da = 10^{-2} and Ri = 3.

upper vortex strengthens as buoyancy lifts hot fluid upward, while the lower region remains rotation-driven. This dual mechanism introduces asymmetry in the streamline topology, redistributing shear stresses along the finned surface.

For the shear-thinning fluid (n = 0.6), the enhanced flow mobility leads to more elongated and active recirculation zones. In contrast, increasing n suppresses these features: the shear-thickening fluid (n = 1.6) exhibits higher apparent viscosity, which dampens the flow and yields smaller, weaker vortices. This demonstrates that buoyancy–viscosity coupling is nonlinear: buoyancy-induced motion is amplified in low-viscosity regions (shear-thinning), but strongly suppressed in high-viscosity zones (shear-thickening), leading to distinct thermal stratifications.

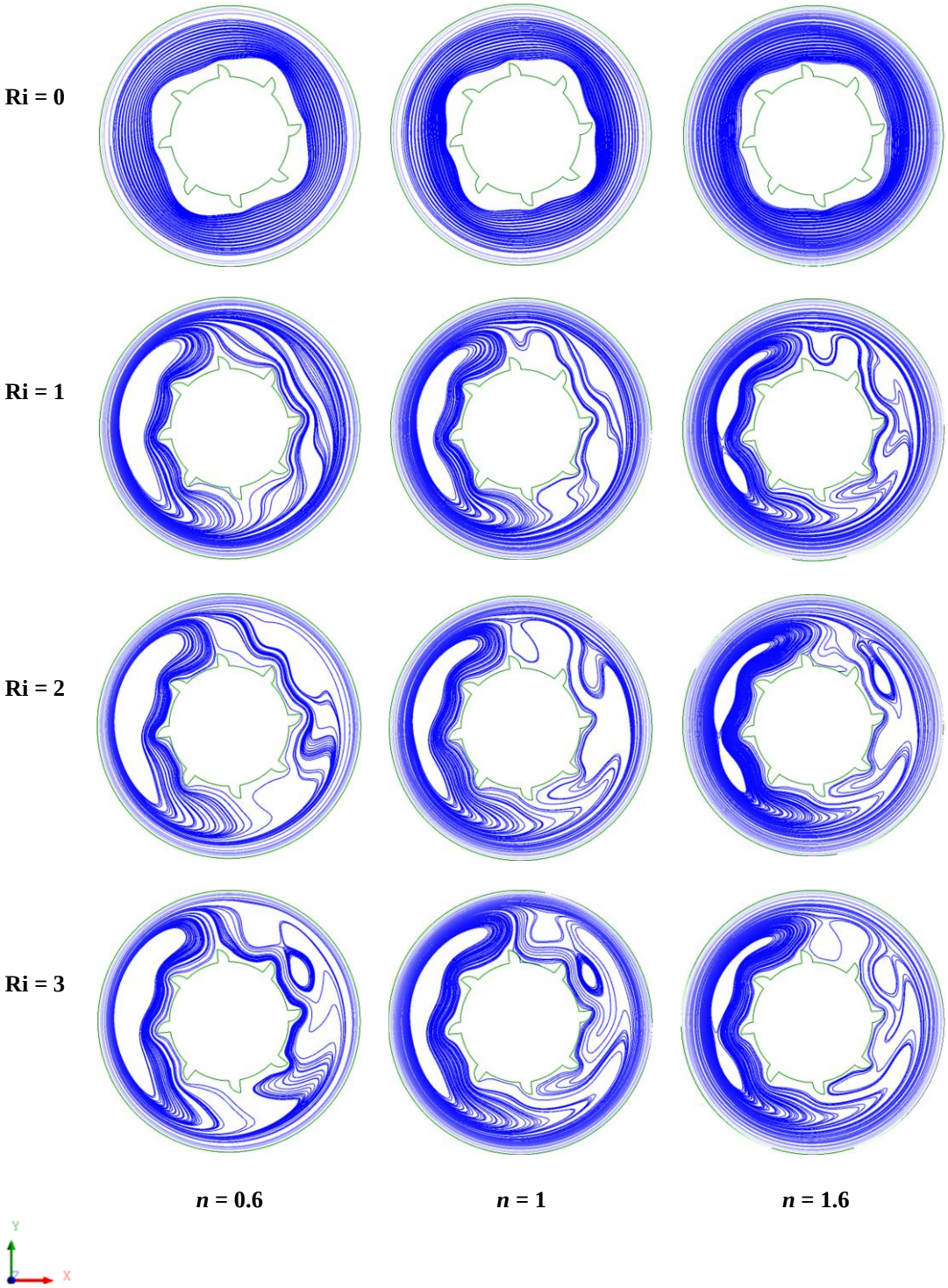


Fig. 6. Streamlines for various values of Ri and *n* at Da = 10^{-2} and Re = 25.

Figure 7 presents the corresponding isotherms under the same conditions. At Ri = 0, the isotherms remain nearly parallel, showing that forced convection dominates. As Ri increases, the isotherms distort vertically, indicating a growing influence of buoyancy-driven flow. The upward migration of isotherms at higher Ri indicates the formation of a thermal plume above the inner cylinder, characteristic of buoyancy-dominated convection. The left–right asymmetry intensifies with Ri increase, showing that buoyancy breaks rotational symmetry and creates preferential heat pathways along the upward direction.

For n = 0.6, the higher mobility produces thinner thermal boundary layers and more dispersed temperature fields. In contrast, for n = 1.6, reduced motion thickens the thermal layers, limiting heat diffusion and causing localised heat build-up near the inner cylinder. This inverse relationship between viscosity

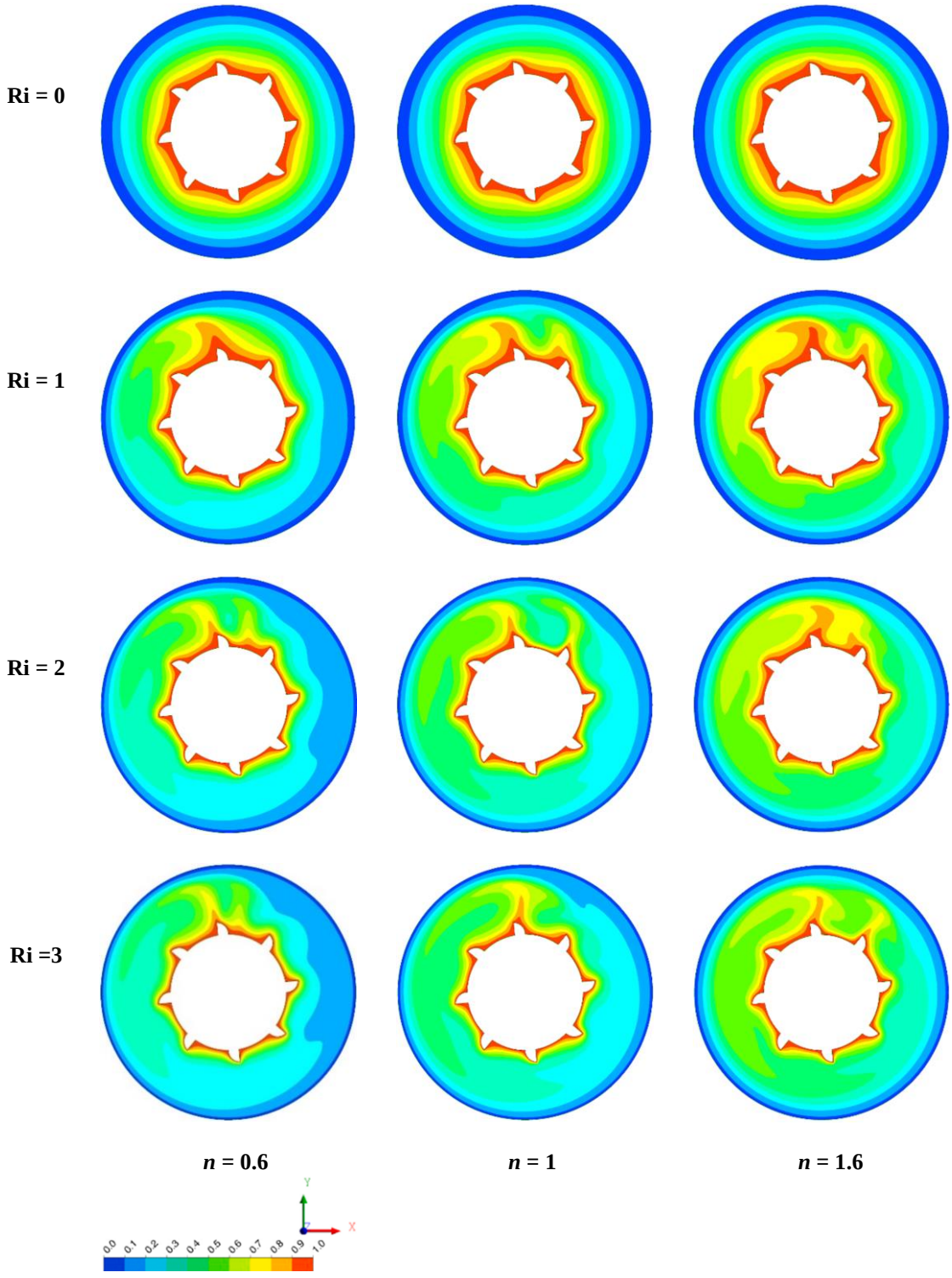


Fig. 7. Isotherms for various values of Ri and n at Da = 10^{-2} and Re = 25.

and boundary-layer thickness confirms that rheological properties govern not only momentum diffusion, but also the thermal resistance adjacent to the heated surfaces.

Figure 8 shows the streamline patterns for various Darcy numbers and power-law indices, at fixed Re = 25 and Ri = 3. At low Da, the porous matrix restricts fluid motion, resulting in weak, localised recirculation around the finned cylinder. As Da increases, permeability improves, allowing stronger motion and larger vortices to form. At intermediate Da values (10^{-4}–10^{-3}), the competition between viscous drag and porous resistance yields a partially developed circulation where flow leakage through the porous matrix modifies vortex symmetry. This interplay introduces a mixed conduction–convection regime that is highly sensitive to n.

For n = 0.6, shear-thinning behaviour intensifies recirculation, especially at higher Da, while for n = 1.6, higher viscosity inhibits

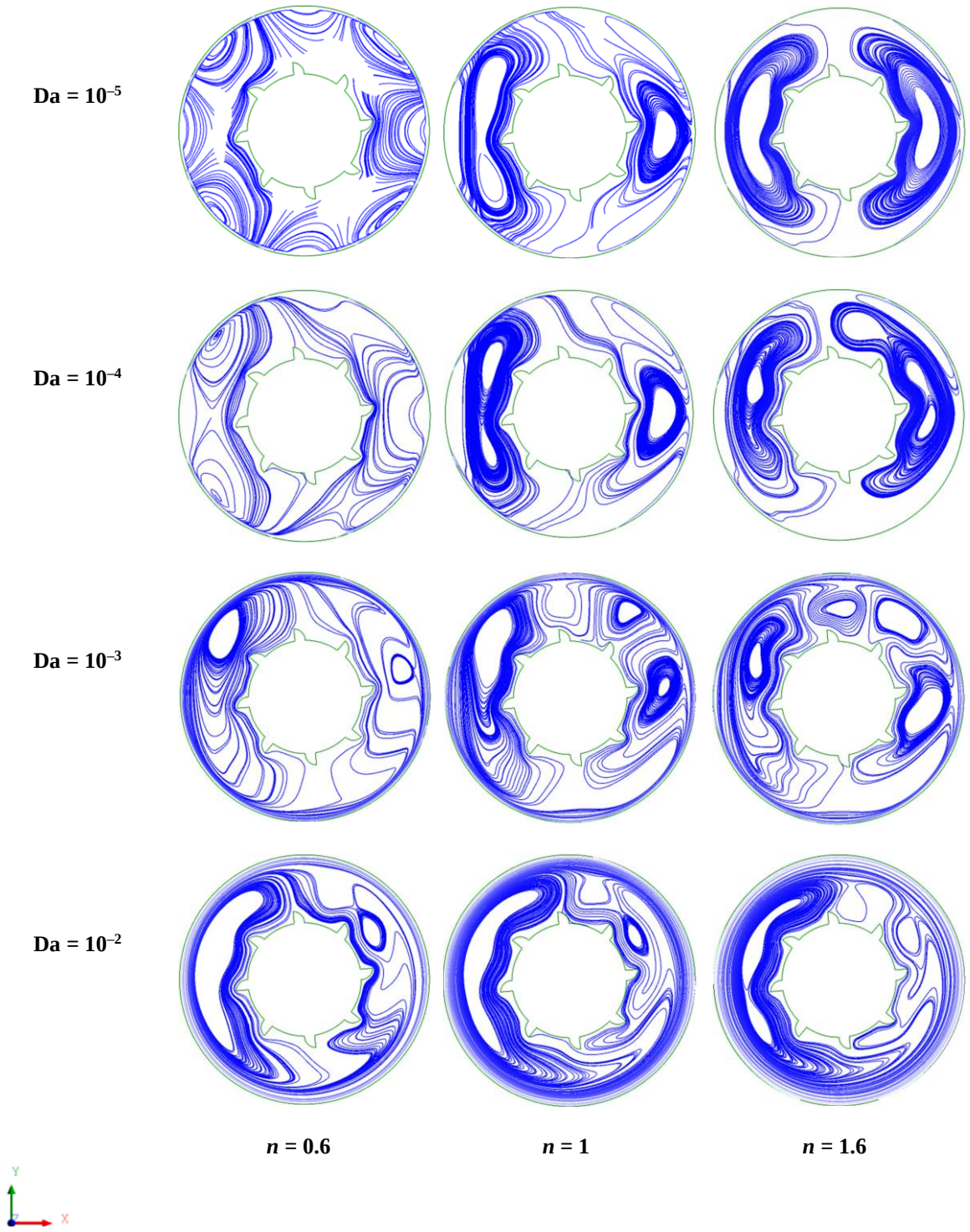


Fig. 8. Streamlines for various values of Da and *n* at Re = 25 and Ri = 3.

vortex development, producing smaller and weaker zones. This behaviour underscores that the porous structure modulates the influence of non-Newtonian viscosity; permeability enhancement magnifies rheological effects, whereas low Da dampens them.

Figure 9 displays the associated isotherms for the same Da, Re and Ri conditions. At low Da, limited flow mobility yields nearly concentric isotherms, reflecting conduction-dominated heat transfer. As Da increases, enhanced convection stretches and distorts the isotherms outward, especially for $n = 0.6$, which exhibits thinner boundary layers and better heat dispersion. The deformation of isotherms indicates a transition from localised conduction to bulk convection. At high Da, the temperature contours align with the dominant flow direction, confirming that fluid advection becomes the main heat transport mechanism.

For $n = 1.6$, high viscosity reduces fluid motion, producing thicker isotherms and localised thermal accumulation near the heated surface. These results emphasise the complex interaction between fluid rheology and porous-medium permeability in

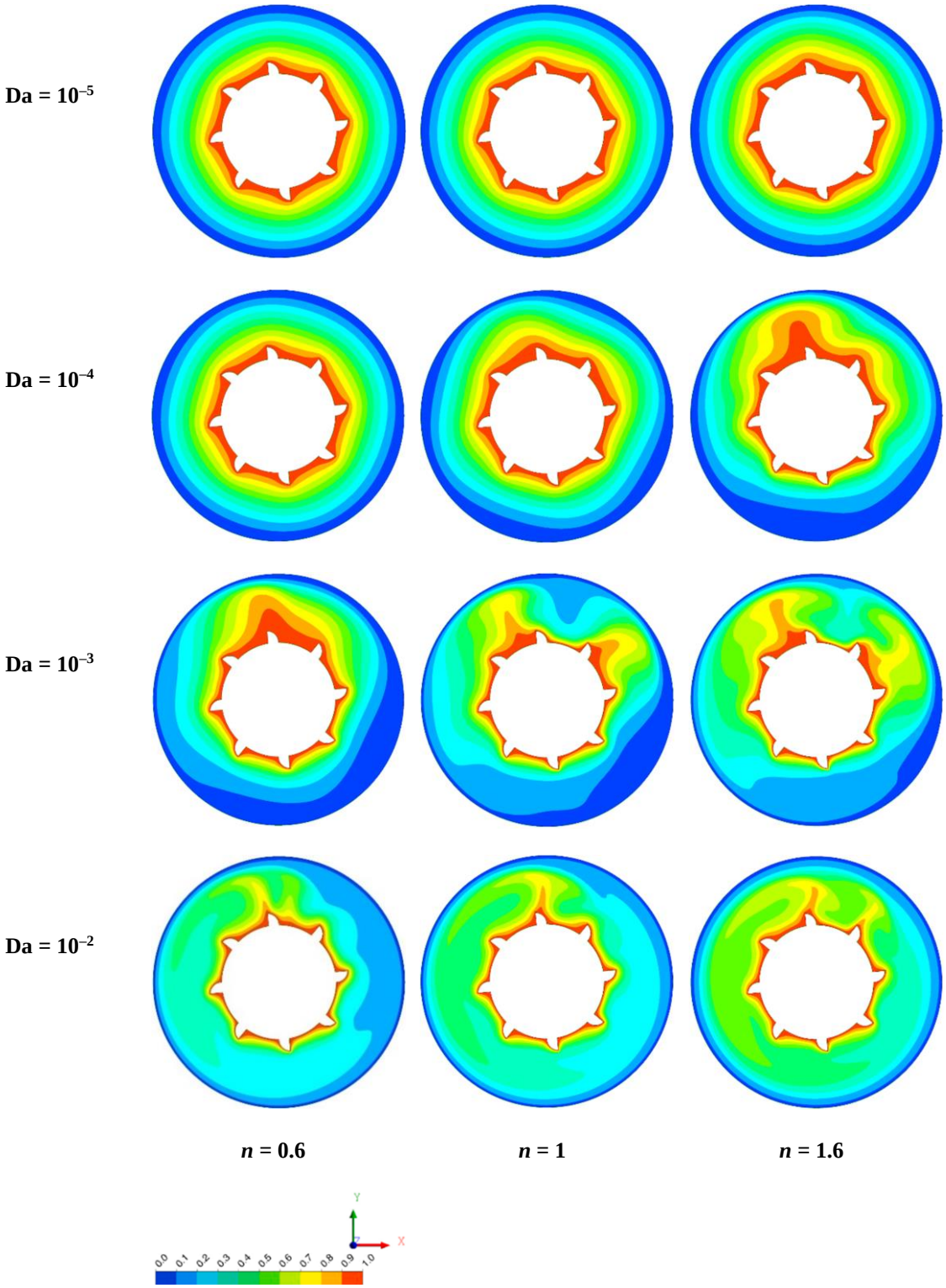


Fig. 9. Isotherms for various values of Da and *n* at Re = 25 and Ri = 3.

governing thermal transport. From a design standpoint, increasing Da enhances heat transfer up to a threshold, beyond which excessive permeability may shorten fluid residence time and slightly diminish local heat exchange.

Figure 10 illustrates how the average Nusselt number varies with Richardson number, power-law index and Reynolds number, at a fixed Darcy number ($Da = 10^{-2}$). At Re = 5, Nu remains nearly constant across Ri values, indicating that viscous effects dominate and suppress convective mixing. In this low-Re regime, heat transfer occurs mainly through conduction-like mechanisms, with negligible contributions from buoyancy forces.

As Re increases to 15 and 25, Nu rises more noticeably with Ri, reflecting the strengthening interaction between forced and natural convection. In these regimes, forced convection provides the baseline flow, while buoyancy-driven motion enhances mixing and promotes more effective thermal transport. The highest

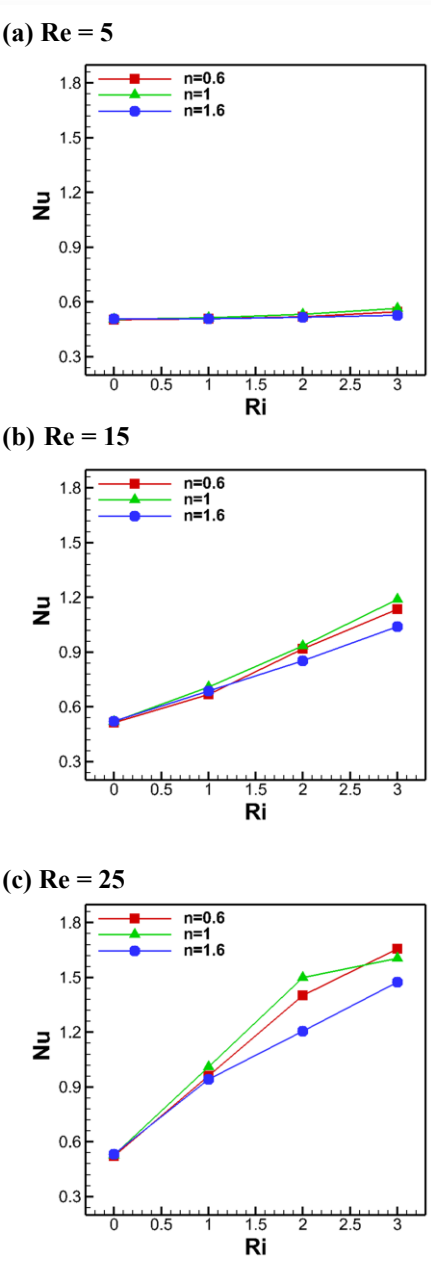


Fig. 10. Values of Nu vs. Ri and n at Da = 10^{-2} for: (a) Re = 5, (b) Re = 15 and (c) Re = 25.

Nu values are typically observed for n = 1 (Newtonian fluid), which balances fluid mobility and thermal diffusion most effectively.

For n = 0.6 (shear-thinning fluid), Nu values are generally lower than those for Newtonian fluids under most conditions, particularly at lower Re or Ri. Although reduced viscosity promotes flow mobility, it may reduce thermal gradients and limit effective mixing. However, at higher Re and Ri (where inertial and buoyancy effects dominate) this enhanced mobility can improve thermal performance. For example, at Re = 25 and Ri = 3, Nu for n = 0.6 surpasses that of n = 1. On the other hand, for n = 1.6 (shear-thickening fluid), increased viscosity restricts motion and leads to the lowest Nu values across all conditions examined.

Figure 11 presents the variation of Nu with Ri, n and Da, at fixed Re = 25. The influence of Da is strongly dependent on fluid rheology, indicating nonlinear interactions between permeability, viscosity behaviour and thermal gradients. At Da = 10^{-5}, the porous medium resists flow significantly, resulting in conduction-dominated heat transfer, where Nu remains low and nearly constant across all values of n and Ri. As Da increases to 10^{-4}

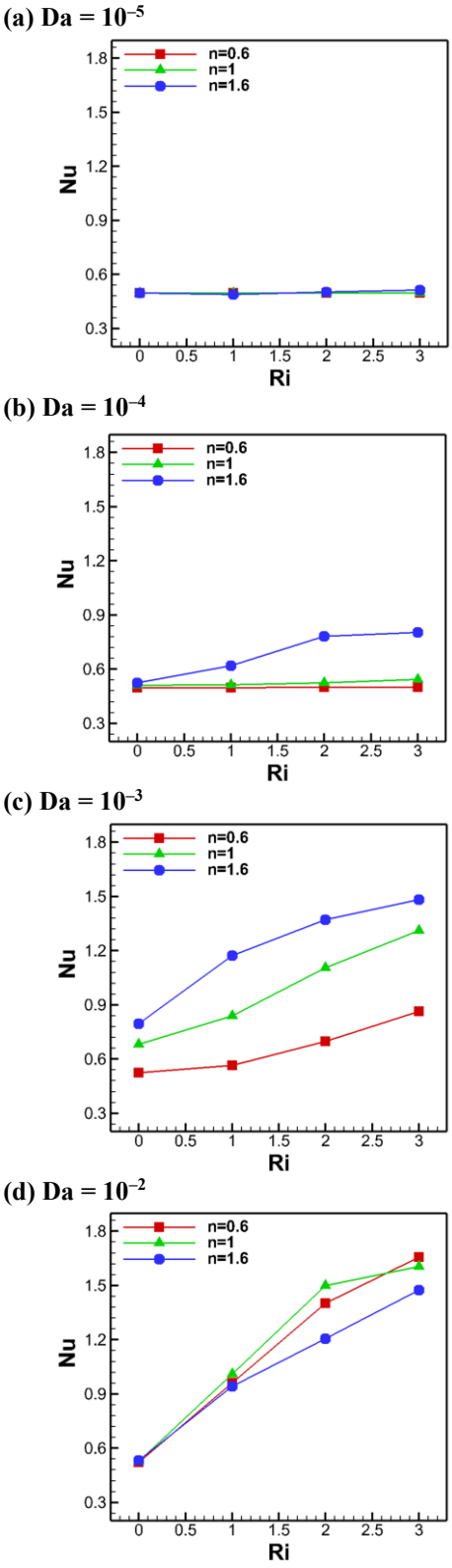


Fig. 11. Values of Nu vs. Ri and n at Re = 25 for: (a) Da = 10^{-5}, (b Da = 10^{-4}, (c) Da = 10^{-3} and (d) Da = 10^{-2}.

and 10^{-3}, permeability improves, allowing more vigorous convection and higher Nu values. Interestingly, the highest Nu values at these intermediate Da levels are observed for $n = 1.6$ (shear-thickening fluid). This suggests that, under moderate resistance, the increased shear-dependent viscosity promotes stronger temperature gradients and localised heat transfer enhancement.

At Da = 10^{-2}, the porous medium offers minimal resistance to flow, leading to robust convective heat transfer. Under these conditions, Newtonian fluids ($n = 1$) exhibit the highest Nu, benefiting from an optimal trade-off between flow and heat dispersion. Shear-thickening fluids ($n = 1.6$) underperform in this regime due to their higher viscosity, which limits motion and thermal mixing. Although shear-thinning fluids ($n = 0.6$) benefit from enhanced flow mobility, they do not achieve the highest Nu under any condition shown. This indicates that, despite faster flow, their reduced viscosity may hinder the development of strong thermal gradients, which are essential for efficient heat transfer.

A particularly noteworthy observation in Fig. 11 (for Da = 10^{-2}) is the critical Richardson number around Ri = 2.6, where the Nu values for the shear-thinning fluid ($n = 0.6$) and the Newtonian fluid ($n = 1$) intersect. This intersection marks a shift in the dominant heat transfer mechanism. For Ri < 2.6, Newtonian fluids outperform due to their balanced viscosity, which supports both momentum and thermal diffusion in mixed convection. As Ri increases and buoyancy dominates, the low viscosity of shear-thinning fluid allows for stronger buoyancy-driven flows and more effective convective mixing. Beyond Ri = 2.6, Nu for $n = 0.6$ exceeds that for $n = 1$, indicating better thermal performance in natural convection regimes. This finding highlights the nonlinear interaction between rheological properties and buoyancy forces, with important implications for optimising thermal systems involving non-Newtonian fluids in porous enclosures.

5. Conclusions

This study presented a numerical investigation of mixed convection heat transfer in a porous annulus formed by a stationary finned inner cylinder and a rotating outer cylinder, filled with a non-Newtonian power-law fluid. The governing equations were solved using the finite-volume method implemented in Ansys-CFX, with the fluid's rheology represented by the Ostwald's law model. The analysis systematically examined the combined influence of four key dimensionless parameters − the Reynolds number (Re), the Richardson number (Ri), the power-law index (n) and the Darcy number (Da) − on flow behaviour and heat transfer performance. The main conclusions are summarised as follows:

1) Increasing the Reynolds number from 5 to 25 enhances the flow circulation and convective strength, leading to a nearly 300% rise in the average Nusselt number at Ri = 3.
2) Shear-thinning fluids promote more vigorous recirculation and outperform Newtonian fluids ($n = 1.0$) under buoyancy-dominated conditions (Ri ≥ 2), while shear-thickening fluids ($n = 1.6$) suppress motion and reduce thermal transport due to their elevated apparent viscosity.
3) A transitional Richardson number of about Ri = 2.6 (for Da = 10^{-2}) marks the point where the Nusselt number becomes nearly independent of the power-law index. Beyond this value, shear-thinning fluids achieve 15–20% higher heat transfer than Newtonian fluids due to stronger buoyancy-driven circulation.
4) Porous permeability (Da) strongly affects the convection regime. Low Da values produce conduction-dominated flow, while higher Da ($\geq 10^{-3}$) enhances convective mixing and results in substantially larger Nusselt numbers through the combined effect of rotation and buoyancy.
5) Flow and thermal structures demonstrate nonlinear coupling among rheology, porous resistance and rotation, which controls the balance between forced and natural convection and defines the system's overall heat transfer efficiency.

These findings provide practical design insights for engineers developing compact thermal systems, including porous heat exchangers, geothermal units and rotating machinery cooling devices. The results enable the optimised selection of working fluids and operating parameters to achieve efficient performance under different flow and thermal conditions. Moreover, the integration of machine learning and optimisation techniques offers promising opportunities for the next generation of energy and cooling systems, particularly in applications where the interaction between non-Newtonian fluids and porous media plays a crucial role in determining system efficiency and reliability.

References

[1] Helmaoui, M., Laidoudi, H., Belbachir, A., Ayad, A., & Ghaniam, A. (2020). Forced convection heat transfer from a pair of circular cylinders confined in ventilated enclosure. *Diffusion Foundations*, 26, 104–111. doi: 10.4028/www.scientific.net/DF.26.104

[2] Mishra, L., Baranwal, A., & Chhabra, R. (2017). Laminar forced convection in power-law fluids from two heated cylinders in a square duct. *International Journal of Heat and Mass Transfer*, 113, 589–612. doi: 10.1016/j.ijheatmasstransfer.2017.05.117

[3] Mohebbi, R., Delouei, A.A., Jamali, A., Izadi, M., & Mohamad, A.A. (2019). Pore-scale simulation of non-Newtonian power-law fluid flow and forced convection in partially porous media: Thermal lattice Boltzmann method. *Physica A*, 525, 642–656. doi: 10.1016/j.physa.2019.03.039

[4] Malkeson, S.P., Alshaaili, S., & Chakraborty, N. (2023). Numerical investigation of steady state laminar natural convection of power-law fluids in side-cooled trapezoidal enclosures heated from the bottom. *Numerical Heat Transfer, Part A: Applications*, 83(7), 770–789. doi: 10.1080/10407782.2022.2157353

[5] Rashid, U., Shahzad, H., Lu, D., Wang, X., & Majeed, A.H. (2023). Non-Newtonian MHD double diffusive natural convection flow and heat transfer in a crown enclosure. *Case Studies in Thermal Engineering*, 41, 102541. doi: 10.1016/j.csite.2022.102541

[6] Lamsaadi, M., Naïmi, M., & Hasnaoui, M. (2005). Natural convection of non-Newtonian power law fluids in a shallow horizontal rectangular cavity uniformly heated from below. *Heat and Mass Transfer*, 41, 239–249. doi: 10.1007/s00231-004-0530-8

[7] Lamsaadi, M., Naïmi, M., Hasnaoui, M., & Mamou, M. (2006). Natural convection in a vertical rectangular cavity filled with a non-Newtonian power-law fluid and subjected to a horizontal temperature gradient. *Numerical Heat Transfer, Part A*, 49(10), 969–990. doi: 10.1080/10407780500324988

[8] Mahmood, F.T, Chowdhury, T.S., & Hasan, M.N. (2024). Fluid-structure interaction induced mixed convection characteristics in a lid-driven square cavity with non-Newtonian power-law fluids. *International Journal of Thermofluids*, 22, 100687. doi: 10.1016/ j.ijft.2024.100687

[9] Bilal, S., Khan, N.Z., Fatima, I., Riaz, A., Ansari, G.J., Alhazmi, S.E., & Tag El-Din, E.M. (2022). Mixed convective heat transfer in a power-law fluid in a square enclosure: Higher order finite element solutions. *Frontiers in Physics*, 10, 1079641. doi: 10.3389/ fphy.2022.1079641

[10] Lakahal, Y., & Laidoudi, H. (2025). Unraveling flow and thermal behavior of non-Newtonian fluids in triangular chambers: A computational study. *Heat Transfer*, 54(6), 4139–4152. doi: 10.1002/htj.23404

[11] Sharma, D.K., & Rana, B.K. (2025). Role of power-law fluids on mixed convection flows around revolving sphere. *Sādhanā*, 50(4), 257. doi: 10.1007/s12046-025-02896-7

[12] Thohura, S., Molla, M., Sarker, Md.M., Sarker, M.M.A., & Paul, M.C. (2021). Study of mixed convection flow of power-law fluids in a skewed lid-driven cavity. *Heat Transfer*, 50(6), 6328–6357. doi: 10.1002/htj.22174

[13] Hussain, S., Jamal, M., & Geridonmez, B.P. (2021). Impact of power law fluid and magnetic field on double diffusive mixed convection in staggered porous cavity considering Dufour and Soret effects. *International Communications in Heat and Mass Transfer*, 121, 105075. doi: 10.1016/j.icheatmasstransfer.2020. 105075

[14] Çolak, E., Ekici, Ö., & Öztop, H.F. (2021). Mixed convection in a lid-driven cavity with partially heated porous block. *International Communications in Heat and Mass Transfer*, 126, 105450. doi: 10.1016/j.icheatmasstransfer.2021.105450

[15] Kumar, S., Gangawane, K.M., & Oztop, H.F. (2021). A numerical study of mixed convection in a two-sided lid-driven tall cavity containing a heated triangular block for non-Newtonian power-law fluids. *Heat Transfer*, 50(5), 4806–4829. doi: 10.1002/htj. 22103

[16] Gangawane, K.M., & Oztop, H.F. (2020). Mixed convection in the semi-circular lid-driven cavity with heated curved wall subjugated to constant heat flux for non-Newtonian power-law fluids. *International Communications in Heat and Mass Transfer*, 114, 104563. doi: 10.1016/j.icheatmasstransfer.2020.104563

[17] Laidoudi, H. (2025). The effects of geometric shape and power-law index on the thermal activity and dynamic behavior of a complex fluid. *Emirates Journal for Engineering Research*, 30(1), 1. https://scholarworks.uaeu.ac.ae/ejer/vol30/iss1/1

[18] Vijayan, A., & Gangawane, K.M. (2021). Mixed convection in a tall lid-driven cavity with a triangular heat source for non-Newtonian power-law fluids. *Journal of Thermal Analysis and Calorimetry*, 146, 937–954. doi: 10.1007/s10973-020-10028-y

[19] Manchanda, M., & Gangawane, K.M. (2018). Mixed convection in a two-sided lid-driven cavity containing heated triangular block for non-Newtonian power-law fluids. *International Journal of Mechanical Sciences*, 144, 235–248. doi: 10.1016/j. ijmecsci.2018.06.005

[20] Gangawane, K.M., & Gupta, S. (2018). Mixed convection characteristics in rectangular enclosure containing heated elliptical block: Effect of direction of moving wall. *International Journal of Thermal Sciences*, 130, 100–115. doi: 10.1016/j.ijthermalsci. 2018.04.010

[21] Lakahal, Y., & Laidoudi, H. (2024). Flow and heat transfer of non-Newtonian fluids in confined triangular geometries: A computational approach. *Journal of the Serbian Society for Computational Mechanics*, 18(2), 110–127. doi: 10.24874/jsscm. 2024.18.02.07

[22] Aboud, E., Rashid, H., Jassim, H., Ahmed, S., Khafaji, S., Hamzah, H., & Ali, F. (2020). MHD effect on mixed convection of annulus circular enclosure filled with non-Newtonian nanofluid. *Heliyon*, 6(4), e03773. doi: 10.1016/j.heliyon.2020.e03773

[23] Bihiche, K., Lamsaadi, M., El hadoui, B., & Tizakast, Y. (2026). Double-diffusive natural convection of power-law fluids in an inclined square cavity with Soret effect. *Numerical Heat Transfer, Part A: Applications*, 87(1). doi: 10.1080/10407782.2025.2520816

[24] Barnoon, P., Toghraie, D., Dehkordi, R.B., & Abed, H. (2019). MHD mixed convection and entropy generation in a lid-driven cavity with rotating cylinders filled by a nanofluid using two-phase mixture model. *Journal of Magnetism and Magnetic Materials*, 483, 224–248. doi: 10.1016/j.jmmm.2019.03.108

[25] Selimefendigil, F., & Öztop, H.F. (2018). Mixed convection of nanofluids in a three-dimensional cavity with two adiabatic inner rotating cylinders. *International Journal of Heat and Mass Transfer*, 117, 331–343. doi: 10.1016/j.ijheatmasstransfer.2017.09.116

[26] Garmroodi, M.R.D., Ahmadpour, A., & Talati, F. (2019). MHD mixed convection of nanofluids in the presence of multiple rotating cylinders in different configurations: A two-phase numerical study. *International Journal of Mechanical Sciences*, 150, 247–264. doi: 10.1016/j.ijmecsci.2018.10.037

[27] Lakahal, Y., & Laidoudi, H. (2025). Buoyancy-driven flow and forced flow of complex fluid within a triangular chamber with a rotating body. *Acta Mechanica et Automatica*, 19(2), 224–240. doi: 10.2478/ama-2025-0027

[28] Hussain, S., & Öztop, H.F. (2021). Impact of inclined magnetic field and power-law fluid on double diffusive mixed convection in lid-driven curvilinear cavity. *International Communications in Heat and Mass Transfer*, 127, 105549. doi: 10.1016/j.icheatmasstransfer.2021.105549

[29] Nagarajan, S., & Ramachandran, S. (2025). Analysis of mixed convective-radiative heat transfer in a porous square cavity filled with various nanofluids. *Numerical Heat Transfer, Part A: Applications*, 86(1), 18–49. doi: 10.1080/10407782.2023.2257384

[30] Khalaf, A.F., Rashid, F.L., Basem, A., & Abbas, M.H. (2022). Numerical analysis in a lid-driven square cavity with hemispherical obstacle in the bottom. *Mathematical Modelling of Engineering Problems*, 9(6), 1639–1647. doi: 10.18280/mmep. 090625

[31] Rashid, F.L., Al-Gaheeshi, A.M.R., Alhwayzee, M., Ali, B., Shah, N.A., & Chung, J.D. (2023). Mixed convection in a horizontal channel–cavity arrangement with different heat source locations. *Mathematics*, 11(6), 1428. doi: 10.3390/ math11061428

[32] Rashid, F.L., Al-Gaheeshi, A.M.R., Rahman, M.H., & Basem, A. (2023). Mixed convection heat transfer in a channel-open cavity with two heat sources. *International Journal of Heat and Technology*, 41(1), 1–13. doi: 10.18280/ijht.410101

[33] Al-Gaheeshi, A.M.R., Rashid, F.L., Eleiwi, M.A., & Basem, A. (2023). Thermo-hydraulic analysis of mixed convection in a channel-square enclosure assembly with hemisphere source at the bottom. *International Journal of Heat and Technology*, 41(3), 551–562. doi: 10.18280/ijht.410307

[34] Ahmad, S., Ali, K., Sajid, T., Bashir, U., Rashid, F.L., Kumar, R., Ali, M.R., Hendy, A.S., & Darvesh, A. (2024). A novel vortex dynamics for micropolar fluid flow in a lid-driven cavity with magnetic field localization – A computational approach. *Ain Shams Engineering Journal*, 15(2), 102448. doi: 10.1016/j.asej.2023.102448

[35] Zhou, W., Yan, Y., Liu, X., Chen, H., & Liu, B. (2018). Lattice Boltzmann simulation of mixed convection of nanofluid with different heat sources in a double lid-driven cavity. *International Communications in Heat and Mass Transfer*, 97, 39–46. doi: 10.1016/j.icheatmasstransfer.2018.07.008

[36] Sindhu, T.N., Çolak, A.B., Lone, S.A., & Shafiq, A. (2023). Reliability study of generalized exponential distribution based on inverse power law using artificial neural network with Bayesian

regularization. *Quality and Reliability Engineering International*, 39(6), 2398–2421. doi: 10.1002/qre.3352

[37] Çolak, A.B., Sindhu, T.N., Lone, S.A., Shafiq, A., & Abushal, T.A. (2023). Reliability study of generalized Rayleigh distribution based on inverse power law using artificial neural network with Bayesian regularization. *Tribology International*, 185, 108544. doi: 10.1016/j.triboint.2023.108544

[38] Kuehn, T.H., & Goldstein, R.J. (1976). An experimental and theoretical study of natural convection in the annulus between horizontal concentric cylinders. *Journal of Fluid Mechanics*, 74(4), 695–719. doi: 10.1017/S0022112076002012

[39] Matin, M.H., & Khan, W.A. (2013). Laminar natural convection of non-Newtonian power-law fluids between concentric circular cylinders. *International Communications in Heat and Mass Transfer*, 43, 112–121. doi: 10.1016/j.icheatmasstransfer.2013.02. 006

[40] Matin, M.H., Pop, I., & Khanchezar, S. (2013). Natural convection of power-law fluid between two-square eccentric duct annuli. *Journal of Non-Newtonian Fluid Mechanics*, 197, 11–23. doi: 10.1016/j.jnnfm.2013.02.002

[41] Sheikholeslami, M. (2017). CuO–water nanofluid free convection in a porous cavity considering Darcy law. *The European Physical Journal Plus*, 132, 55. doi: 10.1140/epjp/i2017-11330-3

[42] Laidoudi, H., & Ameur, H. (2020). Investigation of the mixed convection of power-law fluids between two horizontal concentric cylinders: Effect of various operating conditions. *Thermal Science and Engineering Progress*, 20, 100731. doi: 10.1016/j.tsep.2020.100731

Co-published by
Institute of Fluid-Flow Machinery
Polish Academy of Sciences
Committee on Thermodynamics and Combustion
Polish Academy of Sciences

Copyright©2026 by the Authors under licence CC BY-NC-ND 4.0

http://www.imp.gda.pl/archives-of-thermodynamics/

A method for determining the current-carrying capacity and durability of power cables based on variable ambient temperature and solar radiation

Seweryn Szultka[a], Stanislaw Czapp[a*], Adam Tomaszewski[b], Marian Czapp[c]

[a]Gdańsk University of Technology, Narutowicza 11/12, Gdańsk 80-233, Poland
[b]Institute of Fluid-Flow Machinery, Polish Academy of Sciences, Fiszera 14, Gdańsk 80-231, Poland
[c]Koszalin University of Technology, Śniadeckich 2, Koszalin 75-453, Poland
*Corresponding author email: stanislaw.czapp@pg.edu.pl

Received: 30.01.2026; revised: 08.04.2026; accepted: 09.04.2026

Abstract

Modern power networks contain a large number of distributed energy sources, particularly photovoltaics. In the case of photovoltaic sources, the associated electrical installation components, including cables installed in free air, are exposed to solar radiation and significant ambient temperature variability. In the classical approach to calculating the current-carrying capacity of power cables in free air, a constant ambient temperature is assumed and the direct influence of solar radiation is usually not considered. Such an approach, under certain conditions for a given country, may lead to an underestimation of this capacity (a cold region of the country) or an overestimation (an exceptionally warm region of the country). This paper proposes an alternative approach for determining the current-carrying capacity of power cables. The concept takes into account daily and annual fluctuations in ambient temperature. This is based on actual data obtained from measurements with a measurement step of one hour. As a case study, the results of calculations for sample weather scenarios for northern Poland are shown. The analysis indicates that under certain real-world conditions, cables may be overheated, which reduces the durability of their insulation. For the case of non-rated ageing of cable insulation due to high temperature, a current-carrying capacity correction factor was determined. This approach, different from the normative scheme, allows for determining the thermal exposure of cables that is close to the real one. The analysis results can be useful in designing electrical installations, particularly when components are located on the building facade or roof.

Keywords: Electrical installations; Heat transfer; Power cables; Solar radiation

Vol. 47(2026), No. 3, 57–67; doi: 10.24425/ather.2026.3654

Cite this manuscript as: Szultka, S., Czapp, S., Tomaszewski, A., & Czapp, M. (2026). A method for determining the current-carrying capacity and durability of power cables based on variable ambient temperature and solar radiation. *Archives of Thermodynamics*, 47(3), 57–67.

1. Introduction

Determining the thermal parameters of electrical installations, including cable ratings, aroused the interest of researchers already at the end of the 19th century [1]. Currently, the main attention is paid to the continuous current-carrying capacity of power cables/wires, which depends on many factors, as stated in [2]. A general overview of the basic heat transfer concepts for cable systems and associated current-carrying capacity is given in [3]. There are different methods for determining this capacity. As presented by the authors of the paper [4], these include mainly the finite element method (FEM), which is extensively analysed in [5] with respect to buried power cables in contact with native soil or thermal backfill, as well as the IEC 60287 method [6,7], but the latter is usually used in practice. Standard IEC 60287-1-1 [6], along with the second part IEC 60287-2-1 [7], provides relationships that precisely indicate what the current-carrying capacity depends on. In the con-

Nomenclature

I_{dd} – current-carrying capacity of the cable, A
$I_{dd\text{-}cor}$ – current-carrying capacity of the cable with the effect of solar radiation, A
L_n – rated insulation durability at temperature τ_{dd}, year
L_x – insulation durability at temperature τ_x, year
L_{xi} – insulation durability corresponding to a given temperature in a time interval t_i, year
L_{tot} – resultant durability of insulation, year
R_e – electrical resistance of the core of a power cable, Ω
R_c – thermal resistance related to the heat emitted by the cable, K/W
t_i – relative partial interval of insulation operating time at a specific temperature

Greek symbols

$\Delta\Theta_{dd}$ – highest permissible temperature rise of the power cable, K
$\Delta\Theta_{dd\text{-}cor}$ – corrected permissible temperature rise of the power cable, K
$\Delta\Theta_s$ – temp. rise of the power cable caused by solar radiation, K
$\Delta\tau$ – change in temperature which causes a twofold change in the durability of the insulation, K
τ_{dd} – highest permissible long-term temperature of the power cable, °C
τ_o – ambient temperature, °C
τ_x – temperature other than the highest permissible long-term temperature, °C

Abbreviations and Acronyms

FEM – finite element method
IMGW-PIB – Institute of Meteorology and Water Management – National Research Institute
PV – photovoltaic
PVC – polyvinyl chloride

text of the relationships indicated there, many publications analyse the detailed impact of various factors on cables.

Paper [8] indicates that underground cables are affected by the temperature distribution around the cables, the burial depth of the cables, distances between the cables, the thermal resistivity of the soil, as well as the material for cable backfilling. The influence of soil parameters and soil structure on cable current-carrying capacity is also analysed in [9,10]. These papers emphasise the accuracy of the capacity calculations when cables are laid in multi-layered soils or within stabilised/thermal backfill. Good modelling results for such systems have been achieved in these papers. Paper [11] considers the temperature distribution of cables arranged in layers in cable channels. The layered arrangement affects the uneven temperature distribution of the cable layers, which can lead to local overheating of the cable's insulation. As shown in [12], for high-voltage cables, the bonding method of the metal sheaths is also crucial. Currents circulating in the metal sheaths may significantly heat the cables, reducing their current-carrying capacity. The authors of the paper [13] draw attention to the specific heat transfer characteristics when cables are placed in ducts. Previous standard-compliant approaches may lead to unacceptable inaccuracies, so their paper proposes a more precise approach that is simple enough to implement in computer calculations. The permissible load of underground cables is also associated with the phenomenon of local drying out of the soil (due to heat emission from the cables or the influence of local heat sources). This issue is discussed in detail in [14]. In [15], the phenomenon of drying out of the soil is also considered, but in a different scheme – it is assumed that the top layer of soil near the ground surface dries out, while the layer of soil under the cables does not dry out. This is related to some extent to the effect of solar radiation on the ground surface. An important factor determining the current-carrying capacity is the ambient temperature [16] – as the authors note, it has been changing around the world in recent years and even in one country it may result in different permissible loads for the same cable systems. Very high air temperatures in summer may affect the drying out of the soil around the cables and, consequently, the deterioration of the current-carrying capacity of the cables, as discussed in [17]. The authors point out that in some regions the temperatures may exceed 50°C. High summer temperatures and solar radiation may result (following strong heating of the ground surface) in a significant increase in the temperature of the soil surrounding the cable – it affects the permissible current of this cable, which is also raised in [18]. In some cases, a forced cooling system is used to improve the thermal conditions of buried power cables [19]. In advanced analysis using the FEM-based Arrhenius thermal aging model included in [20], the authors draw attention to the unfavourable thermal conditions of the cable environment as well. They point out possible solar irradiance and high ambient temperature levels, which should be taken into account when determining the current-carrying capacity of cables. In [21], the FEM-based Arrhenius approach is applied again; here, to assess the durability of cable lines exposed to thermal effects of a heating pipeline and several different types of pavements (for different levels of thermal conductivity, emissivity and solar absorptivity). Power cables may be laid in free air for some sections and exposed to direct solar radiation. This radiation is the source of the temperature increase of the cable insulation [22], even if cables are laid in protective pipes [23]. Particularly strong exposure of electrical installation elements, including cables, to high temperatures occurs in the case of photovoltaic (PV) systems, which are numerically demonstrated in [24] and measured in [25]. Paper [26] notes that PV cable systems are exposed to harsh operating conditions, among others, ultraviolet radiation and thermal stress. As a result, the cable insulation degrades, both in terms of electrical and mechanical properties. To decrease the temperature of the PV modules, cooling systems are applied [27,28] – this may beneficially reduce the temperature of the cable connectors in these modules.

A review of the literature and international standards allows us to draw the following conclusions:

- analyses of the current-carrying capacity of power cables usually concern the case when these cables are laid in the ground;
- previous studies have considered the direct impact of solar radiation on outdoor cables to a limited extent, but with the increasingly widespread use of PV systems, this issue has become highly relevant and large-scale;

- ambient temperature of cables (initial temperature before current loading) for a given region of the world is usually assumed to be constant throughout the year, as specified in the standard [29], however, in real conditions for electrical devices placed in the air, the ambient temperature can vary significantly throughout the day and throughout the year.

In the context of the above-mentioned observations, a research gap can be identified regarding a more detailed analysis of the thermal conditions of cables laid in the air – it is mainly about the direct impact of solar radiation and the daily-annual variability of ambient temperature. The exposure of cables to direct solar radiation, as well as the actual ambient temperature, is strongly related to the durability of cable insulation. It should be remembered that unexpected rapid ageing of this insulation reduces its insulating properties and may be the cause of fire and electric shock.

Therefore, this paper, being a modified and extended version of the conference paper [30], presents the results of measurements of daily-annual variability of ambient temperature for a selected region of Poland and the results of numerical calculations of the solar radiation effect. Based on this, sample scenarios of cable temperature changes throughout the day for different seasons are presented, enabling the assessment of the actual thermal exposure of cables in sunny locations. Having the expected temperatures of cable insulation throughout the year, their thermal durability is calculated. A correction factor for the current-carrying capacity of power cables is also determined to achieve insulation ageing at the rated level.

The concept proposed by the authors, based on numerical modelling of solar radiation and taking into account daily and annual ambient temperature variations, is an alternative approach to the design of cable systems. This concept can be used when designing power systems located outdoors and exposed to solar radiation.

2. Current-carrying capacity of cables and numerical calculations of the solar radiation effect

2.1. Current-carrying capacity of power cables according to the standards

The current-carrying capacity I_{dd} of power cables/wires for low-voltage systems can be determined based on the standards [6,7] and presented in the following simplified form [30]:

$$I_{dd} = \sqrt{\frac{\Delta\Theta_{dd}}{R_e R_c}} = \sqrt{\frac{\tau_{dd}-\tau_o}{R_e R_c}}, \tag{1}$$

where: $\Delta\Theta_{dd}$ – the highest permissible temperature rise of the power cable, τ_{dd} – the highest permissible long-term temperature of the power cable, τ_o – ambient temperature, R_e – electrical resistance of the core of a power cable, R_c – thermal resistance related to the heat emitted by the cable to the environment.

For further considerations, the key parameters in Eq. (1) are temperatures τ_{dd} and τ_o. The temperature τ_{dd} is related to the insulation material, and for polyvinyl chloride (PVC) insulated cables commonly used in electrical installations, it is τ_{dd} = 70°C. For design purposes, the ambient temperature in Poland is assumed to be τ_o = 25°C [29], and it is stated that the analysed element of the electrical installation is not exposed to solar radiation. Under such conditions, the maximum permissible temperature rise is $\Delta\Theta_{dd}$ = 45 K (70°C – 25°C). In the case of solar radiation, the current-carrying capacity I_{dd} should be corrected, taking into account the temperature rise of the conductor caused by this radiation. This is presented in the following relation:

$$I_{dd\text{-}cor} = \sqrt{\frac{\Delta\Theta_{dd\text{-}cor}}{R_e R_c}} = \sqrt{\frac{(\tau_{dd}-\tau_o)-\Delta\Theta_s}{R_e R_c}}, \tag{2}$$

where: $I_{dd\text{-}cor}$ – current-carrying capacity of the cable with the effect of solar radiation, $\Delta\Theta_{dd\text{-}cor}$ – corrected permissible temperature rise of the power cable, $\Delta\Theta_s$ – temperature rise of the power cable caused by solar radiation.

The main difficulty in determining the current-carrying capacity according to Eq. (2) is calculating the temperature rise caused by solar radiation. This rise depends, among other things, on solar irradiance, which in turn depends on latitude, season and time of the day. The temperature rise of the conductors caused by solar radiation has been estimated based on the developed numerical model.

2.2. Numerical calculations of the effect of solar radiation on cables

Numerical calculations were performed for a sample single-core low-voltage cable having a cross-sectional area of the core equal to 35 mm^2 (a cable with copper conductors, insulation and a PVC sheath, 2 m long), which is buried for half its length and arranged in free air for the remaining half (Fig. 1).

Since the ground surface is not perfectly smooth, a small obstacle (0.1 m high) is modelled in front of the cable. Computer simulations are intended to show, among other things, the cable's most vulnerable areas to overheating. The calculations

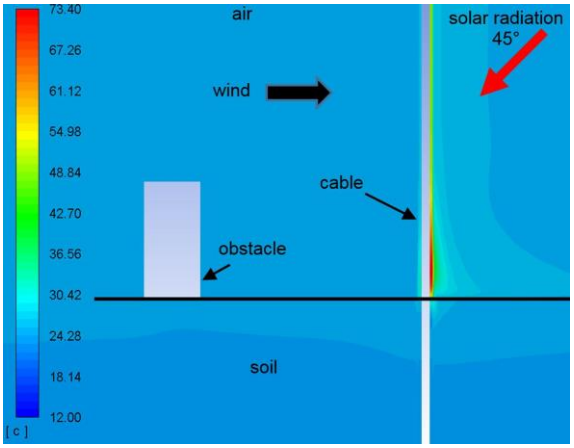


Fig. 1. Temperature distribution around a vertically placed cable exposed to solar radiation. The cable is not loaded with current. Maximum temperature: 73.40°C [30].

were performed for atmospheric conditions that often occur during summer in Poland or at similar latitudes. The air temperature was assumed to be 25°C, and the soil temperature at a depth of 1.2 m was taken as 12°C (consistent with geological data [31]). The calculations were performed for a wind speed of 1 m/s. The thermal conductivity of the soil was assumed to be 0.4 W/(m·K), which corresponds to a thermal resistivity of 2.5 (m·K)/W. It is considered to be quite unfavourable from the point of view of determining the continuous current-carrying capacity of power cables/wires [32,33]. The numerical model assumed solar radiation with an intensity of 1000 W/m^2 incident at an angle of 45° on the vertical cable – this angle reflects average summer conditions. The absorption coefficient of solar radiation for the cable insulation surface was set at 0.9. It was also assumed that the cable is not loaded with current. In this way, the effect of solar radiation alone on the cable temperature rise can be determined.

Stationary calculations were performed in Ansys Fluent, taking into account the effect of gravity. The *k-ε* standard turbulence model was used with the 'enhanced wall treatment' function activated, and 'full buoyancy effects' were enabled in the additional options to correctly model the effect of buoyancy during free convection modelling. The energy equation was activated to model thermal phenomena and obtain the temperature distribution in the computational domain. Air density varied with temperature according to the ideal gas equation of state. The airflow velocity was specified at the inlet, and the 'pressure outlet' boundary condition was applied at the outlet.

The temperature of the warmest points of the cable is as high as 73.40°C (Fig. 1), even though the cable is not loaded with current. The highest temperature area occurs just above the ground (the area above the ground is shielded from the wind by the aforementioned 0.1 m obstacle) on the side facing the incident sun.

Analysing the cable cross-section and the surrounding area at a height of 0.5 m above the ground, the simulation data shows that it is slightly over 51°C, which is significantly lower than for the section just above the ground, because air movement caused by the wind (cable cooling) is important. The exact temperature distribution in the cross-section at a height of 0.5 m is shown in Fig. 2.

Numerical analyses indicate that solar radiation can cause a cable temperature rise of:

- almost 50 K (73.40°C – 25°C) under very unfavourable conditions (intense sunlight, cable surrounded by still air, e.g. in a roof recess),
- 26 K (51°C – 25°C) under more favourable conditions (intense sunlight, but cable is cooled by wind).

The results of numerical analyses of the temperature increase of cable insulation caused by solar radiation were used to calculate the expected temperatures of this insulation for a selected region of Poland and assumed weather scenarios. The expected temperatures of the cables at specific times of day and year were used to determine the expected durability of the insulation.

3. Annual ambient temperature variation and cable thermal rating

Design calculations for cable current-carrying capacity and insulation durability usually refer to standard temperature conditions, which are generally considered to be the highest possible (most unfavourable) during the considered period of operation of the electrical installation. Design assumptions are generally known and available, but actual temperature conditions can vary significantly depending on the time of day and season. To provide a realistic estimate of the assumed ambient temperature variability for power cables installed outdoors, the authors of the study compiled daily temperatures for 2024, considering three weather scenarios:

- Scenario 1 (the most restrictive) – the highest temperature was assumed for each day considered;
- Scenario 2 – the average temperature was assumed for each day considered;
- Scenario 3 – the lowest temperature was assumed for each day considered.

The data regarding ambient temperature comes from the Gdańsk Świbno weather station, in northern Poland, and was provided by the Institute of Meteorology and Water Management – National Research Institute (Instytut Meteorologii i Gospodarki Wodnej – Państwowy Instytut Badawczy, IMGW-PIB).

As a result of the analysis of the distribution of the highest temperatures throughout the year (Scenario 1 – the most restrictive of those considered, Fig. 3), one warmest day was identified in each quarter of the year. The selected days and their temperature distributions are presented in Fig. 4 (bars 'A'). It was then assumed that electric current flowing through the power cables is equal to the current-carrying capacity, resulting in a 45 K increase in the cable insulation temperature (bars 'B' in Fig. 4).

Furthermore, it was assumed that for half of each quarter, solar radiation affects the power cables and causes a specific increase in insulation temperature – elevated 'C' columns relative to 'B' columns at selected times of the day. Table 1 provides, for example, a detailed summary of temperatures on a given/selected warmest day in the third quarter of 2024 – this is a numerical representation of the data from Fig. 4c. Column 2 in Table 1 contains a summary of the maximum hourly ambient temperatures based on meteorological data. Column 3 contains the cable insulation temperatures, assuming that the current flowing through the cable is equal to the current-carrying capacity – then the cable insulation

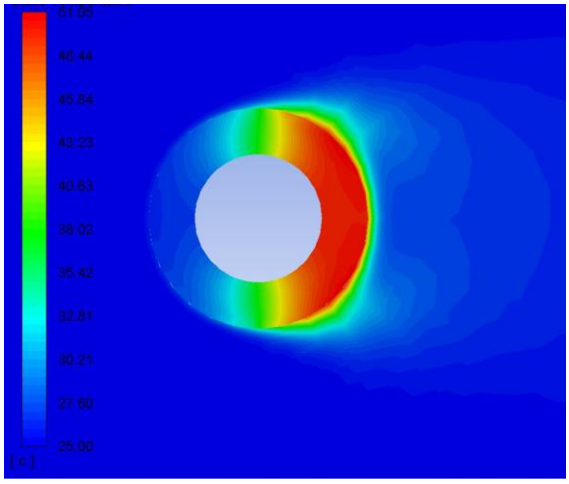


Fig. 2. Temperature fields in the cable cross-section at a height of 0.5 m above the ground. The arrangement is as in Fig. 1. The cable is not subjected to any current. The maximum temperature in the analysed cross-section is 51.05°C.

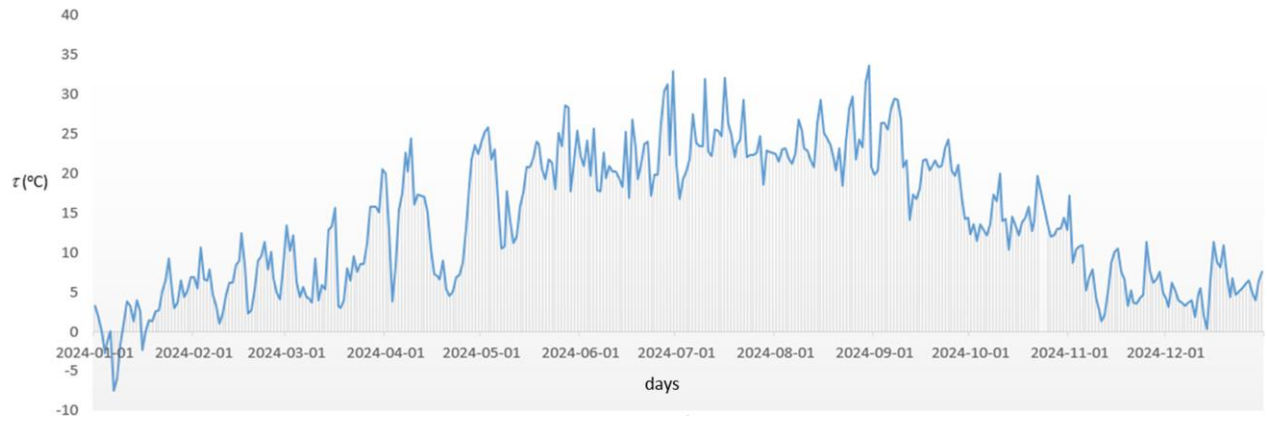


Fig. 3. The highest temperature for each day in 2024. Data from the IMGW-PIB Gdańsk Świbno station.
Own elaboration based on data from IMGW-PIB [30].

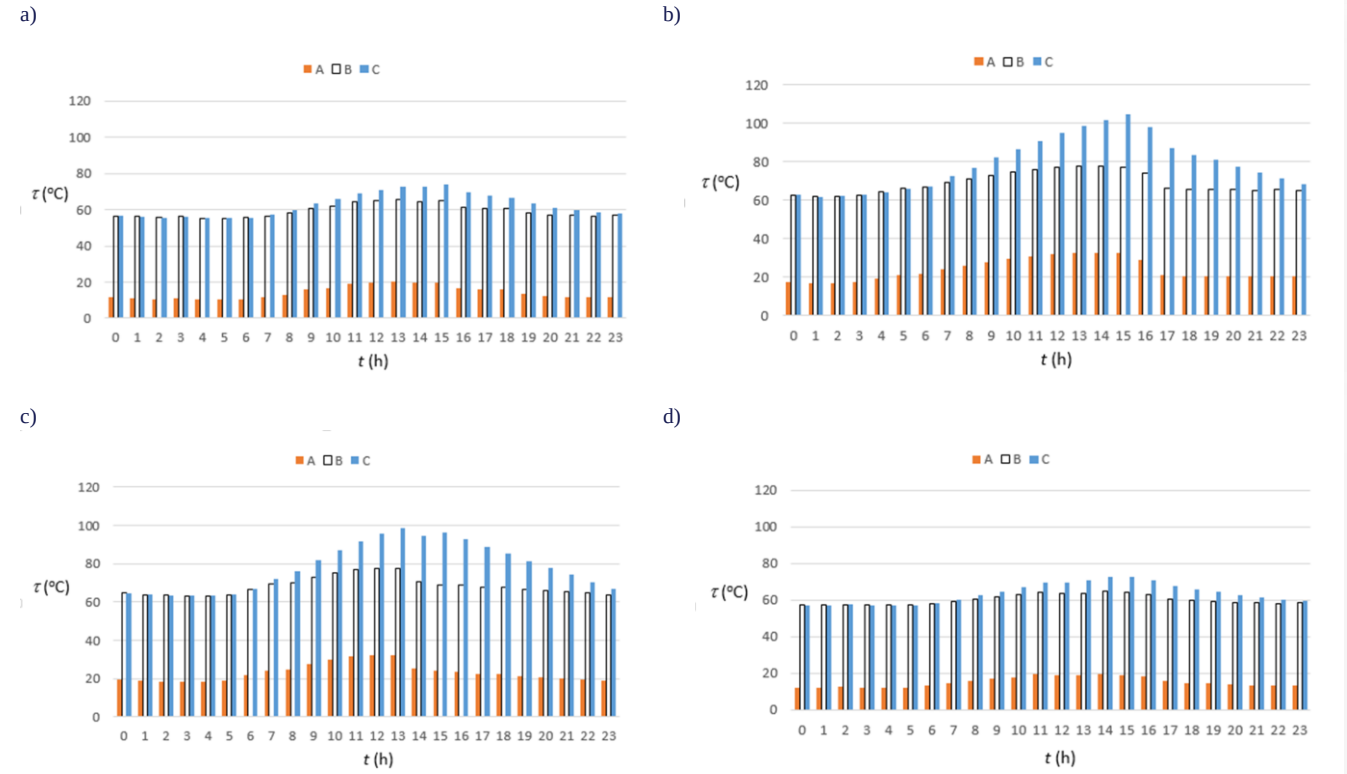


Fig. 4. Daily variation of air and cable insulation temperatures for selected days of 2024 in each quarter (Scenario 1): a) March 31 b) June 30, c) August 30, d) October 10. Bars: A – air temperature (IMGW-PIB data from the Gdańsk Świbno measuring station); B – calculated temperature of cable insulation in places shielded from direct solar radiation, cable loaded with current (I_{dd}); C – calculated temperature of cable insulation in places exposed to direct solar radiation, cable loaded with current (I_{dd}) [30].

temperature increase is 45 K. This corresponds to conditions without solar radiation lasting half of the quarter (assumed to be 45 days). In the case of solar radiation (the remainder of the quarter – also assumed to be 45 days), a further increase in insulation temperature is assumed at individual hours (column 4 in Table 1; Note: there is no column 4 for days without solar radiation). The resulting temperature values are shown in column 5. Similar calculations as in Table 1 were made for the remaining quarters of 2024.

The rated durability of the insulation (L_n) is assumed to be 25 years. The long-term permissible temperature τ_{dd} for PVC insulation is 70°C. The temperature τ_x was determined for each hour of the day (Fig. 4 and sample detailed data in Table 1), with 45 days without solar radiation and 45 days with radiation at specific times assumed for each quarter.

Based on the assumptions made above, the durability of the insulation at temperature τ_x was calculated according to the following relationship:

$$L_x = L_n 2^{\frac{\tau_{dd}-\tau_x}{\Delta\tau}}, \quad (3)$$

where L_n is the rated insulation durability at temperature τ_{dd}, τ_{dd} – the highest permissible long-term temperature of the power cable, τ_x – temperature other than the highest permissible long-

Table 1. Hourly temperature distribution (°C) for the warmest day in the third quarter of 2024 (Scenario 1) – representative day 2024-08-30 (data from IMGW-PIB). Bars 'A', 'B', and 'C' from Fig. 4.

Time of the day, h	Ambient temp. (bars 'A'), °C	Temperature of the cable loaded with current (I_{dd}), in places not exposed to solar radiation (bars 'B'), °C	Assumed increase in cable temperature due to solar radiation, °C	Temperature of the cable loaded with current (I_{dd}), in places exposed to solar radiation (bars 'C'), °C
0:00	19.5	64.5	0	64.5
1:00	18.9	63.9	0	63.9
2:00	18.4	63.4	0	63.4
3:00	18.3	63.3	0	63.3
4:00	18.2	63.2	0	63.2
5:00	18.8	63.8	0	63.8
6:00	21.7	66.7	0	66.7
7:00	24.1	69.1	3	72.1
8:00	25.0	70.0	6	76.0
9:00	27.7	72.7	9	81.7
10:00	29.9	74.9	12	86.9
11:00	31.8	76.8	15	91.8
12:00	32.5	77.5	18	95.5
13:00	32.2	77.2	21	98.2
14:00	25.3	70.3	24	94.3
15:00	24.0	69.0	27	96.0
16:00	23.8	68.8	24	92.8
17:00	22.7	67.7	21	88.7
18:00	22.4	67.4	18	85.4
19:00	21.4	66.4	15	81.4
20:00	20.7	65.7	12	77.7
21:00	20.2	65.2	9	74.2
22:00	19.5	64.5	6	70.5
23:00	18.9	63.9	3	66.9

term temperature, $\Delta\tau$ – a change in temperature which causes a twofold change in the durability of the insulation (assumed 8 K). Sample calculation results based on Eq. (3) are included in Table 2.

Due to the estimated variation of the cable insulation temperature over time, it is necessary to use the relationship for the resultant insulation durability:

$$L_{tot} = \frac{1}{\sum_{i=1}^{N}\left(\frac{t_i}{L_{xi}}\right)}, \tag{4}$$

where L_{xi} – insulation durability corresponding to a given temperature in the considered partial time interval t_i, t_i – relative partial interval of insulation operating time at a specific temperature.

Table 2. Example calculation results based on Eq. (3); Scenario 1.

Parameter	Value	L_x, year	Comments
τ_o, °C	29.9	–	–
τ_{dd}, °C	70	–	–
$\Delta\tau$, K	8	–	–
$\Delta\tau_{dd}$, K	45	–	–
τ_{x1},°C	74.9	16.35	places not exposed to solar radiation
$\Delta\Theta_s$, K	12	–	–
τ_{x2}, °C	86.9	5.78	places exposed to solar radiation

By applying Eq. (4), using the data presented in Fig. 4 and other assumptions, it was calculated that the insulation durability for the analysed conditions is 17.1 years. The calculations show that the expected actual insulation durability is significantly lower than the rated durability (25 years). Therefore, to maintain the rated insulation durability, the load should be reduced by 5.3% compared to the standard current-carrying capacity of power cables in the analysed case. Table 3 presents the results of the current-carrying capacity correction, for example, PVC-insulated cables with data included in the standard [33]. This correction allows for reducing the temperature rise of the cables caused by the flowing current from 45 K to approximately 40 K, which is sufficient to achieve an insulation durability of 25 years.

Table 3. Correction of the current-carrying capacity of PVC-insulated cables to achieve the rated insulation durability (25 years). Cables installed in locations exposed to solar radiation. Scenario 1.

Cross-section of conductor, mm²	2.5	2.5	4	4	6	6
Number of loaded conductors	2	3	2	3	2	3
Current-carrying capacity without correction, A (according to [33])	23	19.5	31	26	39	33
Correction factor	1×0.947					
Current-carrying capacity after correction, A	21.8	18.5	29.4	24.6	36.9	31.3

For a different weather scenario, the correction factor will have a different value and can be estimated based on temperature data for the analysed region of the country/world using the methodology presented in this study.

In order to better illustrate the usefulness of the indicated calculation method for determining the correction factor, two further scenarios were used, based on the actual average temperatures (Scenario 2) and lowest temperatures (Scenario 3) from the Gdańsk Świbno station, and based on operating time at a specific temperature in the year 2024.

Scenario 2 focuses on the use of average temperatures throughout each analysed day. The annual distribution of average (median) temperatures throughout the year is shown in Fig. 5. Similarly to Scenario 1, in Scenario 2, each representative day in each quarter was selected. The selection was based on the temperature in each quarter, as shown in Fig. 6.

Bars 'A', 'B' and 'C' presented in Fig. 6 were determined similarly to Scenario 1. Based on the assumptions made in Scenario 1, the insulation durability at a given temperature was calculated. Example results are provided in Table 4. By applying Eq. (4) and the assumptions previously described, the resulting insulation durability is 35.31 years. The calculated durability is therefore significantly higher than the assumed rated durability of 25 years of the insulation.

To fully utilise the technically assumed durability of cables, it is possible to increase the current-carrying capacity of power cables. For the assumed weather Scenario 2, the current-carrying

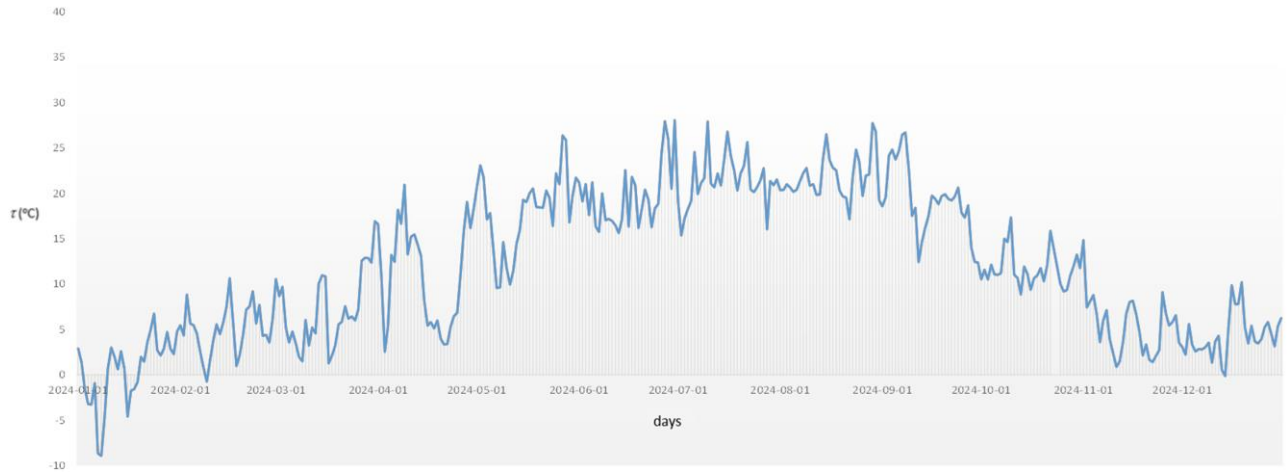


Fig. 5. The average temperature for each day in 2024. Data from the IMGW-PIB Gdańsk Świbno station. Own elaboration based on data from IMGW-PIB.

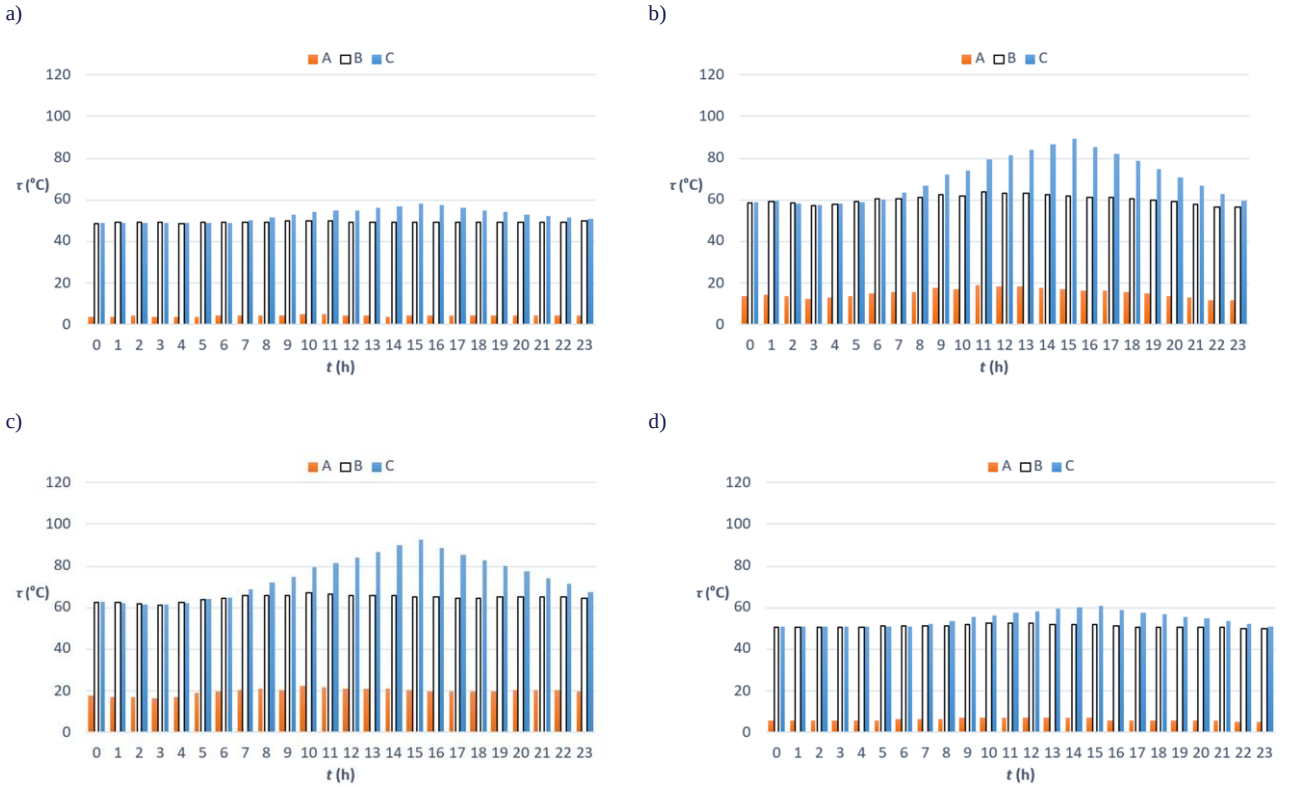


Fig. 6. Daily variation of air and cable insulation temperatures for selected days of 2024 in each quarter (Scenario 2): a) February 20, b) June 9, c) July 12, d) November 17. Bars: A – air temperature (IMGW-PIB data from the Gdańsk Świbno measuring station); B – calculated temperature of cable insulation in places shielded from direct solar radiation, cable loaded with current I_{dd}; C – calculated temperature of cable insulation in places exposed to direct solar radiation, cable loaded with current I_{dd}.

Table 4. Example calculation results based on Eq. (3); Scenario 2.

Parameter	Value	L_x (y)	Comments
τ_o, °C	22.1	–	–
τ_{dd}, °C	70	–	–
$\Delta\tau$, K	8	–	–
$\Delta\Theta_{dd}$, K	45	–	–
τ_{x1}, °C	67.1	32.14	places not exposed to solar radiation
$\Delta\Theta_s$, K	12	–	–
τ_{x2}, °C	79.1	11.36	places exposed to solar radiation

capacity of power cables can be adjusted/increased by 4.1%. Example values of the current-carrying capacity of power cables before and after applying the correction factor are given in Table 5.

The next scenario, i.e. Scenario 3, is based on the use of the lowest temperatures throughout each considered day. It is the most optimistic and somewhat risky scenario. The annual distribution of the lowest temperatures throughout the year is shown in Fig. 7. Similar to the previous two scenarios, each representative day in each quarter was selected.

Table 5. Correction of the current-carrying capacity of PVC-insulated cables to achieve the rated insulation durability (25 years). Cables installed in locations exposed to solar radiation. Scenario 2.

Cross-section of conductor, mm²	2.5	2.5	4	4	6	6
Number of loaded conductors	2	3	2	3	2	3
Current-carrying capacity without correction, A (according to [33])	23	19.5	31	26	39	33
Correction factor	1×1.041					
Current-carrying capacity after correction, A	23.9	20.3	32.3	27.1	40.6	34.4

The selection was based on the coldest day in each quarter, as shown in Fig. 8. Bars 'A', 'B' and 'C' presented in Fig. 8 were determined similarly to Scenario 1 and Scenario 2. Based on the assumptions made in the example presented, the insulation durability at a given temperature was calculated. The results of a sample calculation are provided in Table 6. The resultant durability of insulation was obtained as 81.23 years. Similarly to Scenario 2, the resulting durability of insulation is higher than the rated durability of 25 years. Hence, it is possible to increase the current-carrying capacity of power cables by as much as 12.4%. Further, theoretically, it is possible to introduce a correction (in this case a significant increase) of the current-carrying capacity (Table 7).

It is obvious that for scenarios 2 and 3 there is no need to correct/increase the current-carrying capacity – it can remain at the normative level (to maintain a high margin of safety).

The presented results should be interpreted with consideration of the uncertainty associated with the adopted input data and modelling assumptions. First, the numerical analysis was performed for a selected set of environmental conditions, including air temperature of 25°C, soil temperature of 12°C, wind speed of 1 m/s, solar irradiance of 1000 W/m^2, solar incidence angle of 45°, soil thermal conductivity of 0.4 W/(m·K), and solar absorptivity of the cable surface equal to 0.9. Therefore, the obtained temperature rises should be treated as representative for the assumed scenario and may vary under different local operating conditions.

Table 6. Example calculation results based on Eq. (3); Scenario 3.

Parameter	Value	L_x, year	Comments
τ_o, °C	9.9	–	–
τ_{dd}, °C	70	–	–
$\Delta\tau$, K	8	–	–
$\Delta\Theta_{dd}$, K	45	–	–
τ_{x1}, °C	54.9	16.35	places not exposed to solar radiation
$\Delta\Theta_s$, K	6	–	–
τ_{x2}, °C	60.9	54.99	places exposed to solar radiation

An additional source of uncertainty results from the simplifications adopted in the numerical model. The calculations were carried out as steady-state simulations using the standard k-ε turbulence model with enhanced wall treatment and full buoyancy effects. In real outdoor conditions, however, airflow and solar exposure reveal transient behaviour and may change over short periods. Consequently, the model should be regarded as an engineering approximation of the thermal effect rather than reproducing every instantaneous operating condition exactly. The uncertainty of the cable's durability calculations is also related to the adopted

Table 7. Correction of the current-carrying capacity of PVC-insulated cables to achieve the rated insulation durability (25 years). Cables installed in locations exposed to solar radiation. Scenario 3.

Cross section of conductor, mm²	2.5	2.5	4	4	6	6
Number of loaded conductors	2	3	2	3	2	3
Current-carrying capacity without correction, A (according to [33])	23	19.5	31	26	39	33
Correction factor	1×1.124					
Current-carrying capacity after correction, A	25.9	21.9	34.8	29.2	43.8	37.1

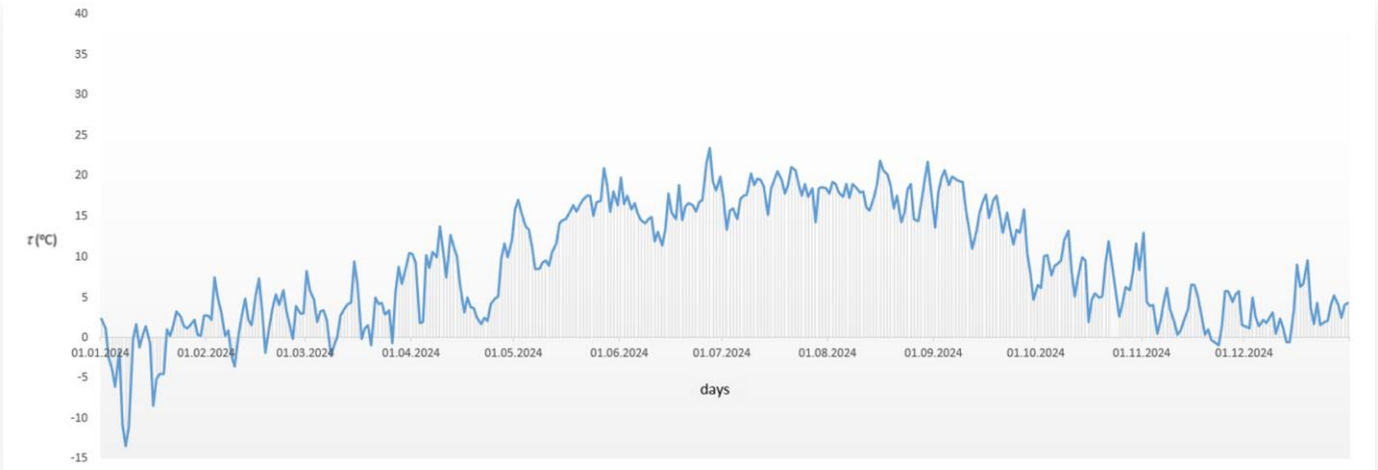


Fig. 7. The lowest temperature for each day in 2024. Data from the IMGW-PIB Gdańsk Świbno station. Own elaboration based on data from IMGW-PIB.

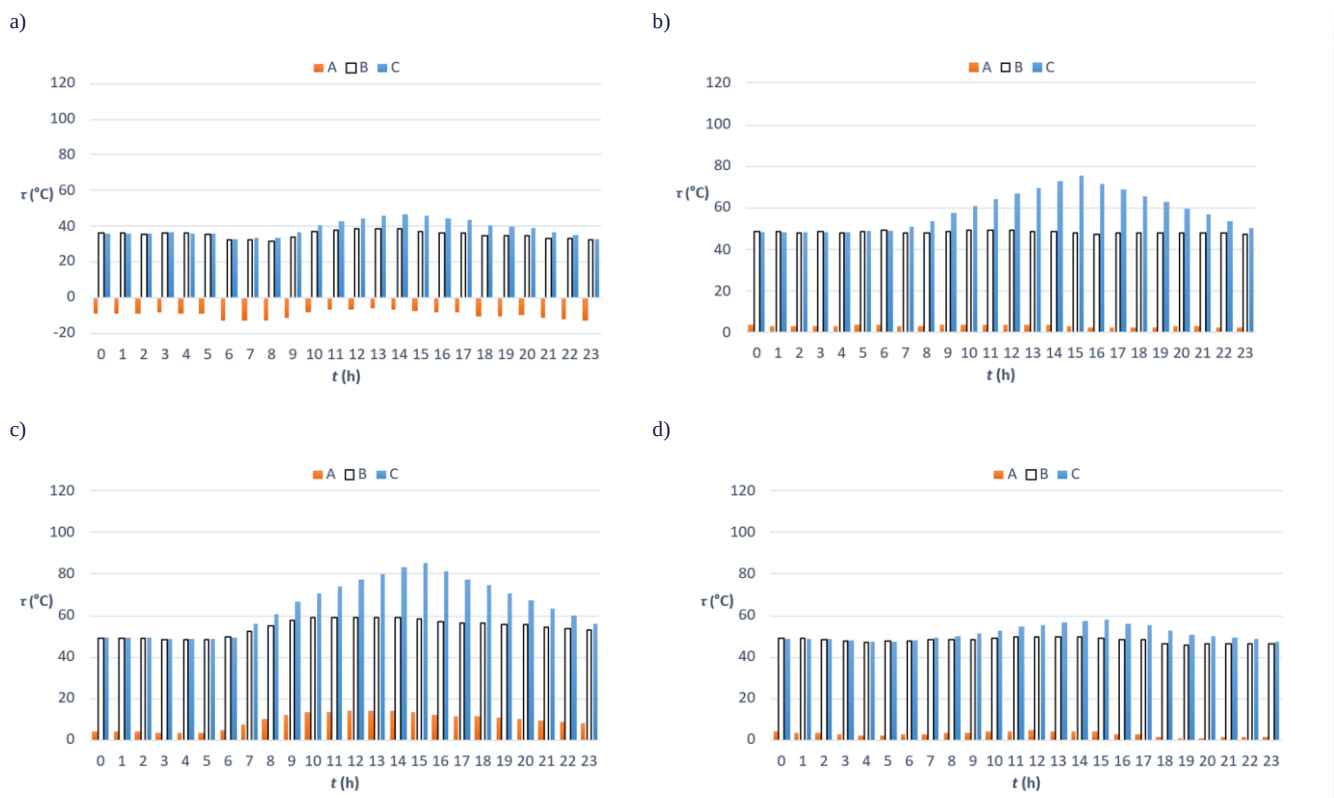


Fig. 8. Daily variation of air and cable insulation temperatures for selected days of 2024 in each quarter (Scenario 3): a) January 8, b) April 21, c) September 30, d) November 23. Bars: A – air temperature (IMGW-PIB data from the Gdańsk Świbno measuring station); B – calculated temperature of cable insulation in places shielded from direct solar radiation, cable loaded with current I_{dd}; C – calculated temperature of cable insulation in places exposed to direct solar radiation, cable loaded with current I_{dd}.

thermal-ageing model. In particular, the insulation lifetime was estimated using the assumed temperature interval causing a two-fold change in durability, equal to 8 K, and by applying representative daily temperature profiles for selected quarters of the year. Thus, the calculated insulation lifetime/durability should be interpreted as an estimate of expected long-term thermal exposure under the assumed scenarios, rather than as an exact prediction for every installation site. Despite these limitations, the proposed methodology remains useful for engineering analysis because it captures the dominant factors affecting free-air cable thermal loading, namely solar radiation and time-varying ambient temperature. The results are therefore suitable for comparative assessments, conservative design studies, and the determination of practical correction factors for cable current-carrying capacity.

4. Conclusions

The standard and practical determination of the current-carrying capacity of power cables assumes a constant design ambient temperature throughout the year. The authors of this paper, however, have proposed an alternative approach based on daily-annual variability of ambient temperature with a step of one hour, and accounting for the direct solar radiation.

The presented method for determining the expected cable temperature and associated insulation durability can be applied to electrical installations located in selected regions of the country or world, knowing, among other things, the local daily and annual ambient temperature variability. Taking into account local weather conditions, including expected solar radiation, allows for an estimate of cable insulation durability that is close to this realistic one. The approach proposed is particularly suitable for electrical installations placed on the facade or roof of a building.

The results obtained clearly demonstrate that solar radiation may significantly affect the thermal conditions of power cables installed in free air, which is consistent with previous findings reported in the literature. According to the obtained numerical modelling results, the authors' study indicates that under unfavourable local conditions (e.g. limited airflow), the temperature rise may reach values of up to 50 K above the ambient, which is comparable to or even exceeds typical design assumptions used in standard approaches.

In comparison with studies focusing on underground cables, where the thermal behaviour is strongly governed by soil properties and relatively stable boundary conditions, cables installed in free air are subject to much higher variability of environmental parameters. This variability is particularly related to insolation level, as well as daily and seasonal changes in ambient temperature, which are usually not taken into account in standard-based calculations (e.g., IEC 60287), where constant ambient temperature is assumed.

The results obtained in this paper are also consistent with other studies analysing the effect of ambient temperature profiles on cable current-carrying capacity, which indicate that the

use of constant design temperature may lead to inaccurate estimation of permissible current. However, the present study extends this approach by combining real hourly temperature data with the effect of solar radiation and linking these thermal conditions directly with insulation ageing.

The contribution of this work is the analytical evaluation of insulation durability under realistic operating conditions. While previous studies have mainly focused on temperature distribution or current-carrying capacity calculations, the present approach demonstrates that neglecting natural environmental variability may lead to a substantial reduction of insulation lifetime/durability (e.g. from 25 years to 17.1 years in the most restrictive scenario). This finding highlights the importance of considering both solar radiation and time-dependent ambient temperature in the design of outdoor electrical installations.

Furthermore, the proposed methodology allows for the determination of current-carrying capacity correction factor levels based on actual climatic data. This represents an advancement over standard approaches, which typically do not provide tools for such adjustments under variable environmental conditions. The obtained correction values (from approximately −5.3% to +12.4%, depending on the scenario) indicate that both conservative and optimised design strategies can be developed using the presented method.

Among the presented scenarios/assumptions for calculating the resultant durability of insulation of power cables, the measurement data leading to the determination of the lowest durability should be selected. Regarding the data analysed by the authors, it is suggested to adopt Scenario 1 (the most restrictive, but the safest) as a representative scenario for determining the current-carrying capacity of cables. If the cable system is critical, one may consider analysing historical temperature data from the last few years and taking the least favourable year.

References

[1] Holyk, C., & Anders, G.J. (2015). Power cable rating calculations – a historical perspective [History]. *IEEE Industry Applications Magazine*, 21(4), 6–64. doi: 10.1109/MIAS.2015.2417094

[2] de Leon, F. (2006). Major factors affecting cable ampacity. 2006 *IEEE Power Engineering Society General Meeting*, 18-22 June, Montreal, QC, Canada. doi: 10.1109/PES.2006.1708875

[3] Enescu, D., Colella, P., & Russo, A. (2020). Thermal assessment of power cables and impacts on cable current rating: An overview. *Energies*, 13(20), 5319. doi: 10.3390/en13205319

[4] Papadopoulos, T.A., Chrysochos, A.I., & Fotos, M. (2023). Comparison of power cables current rating calculation methods. *58th International Universities Power Engineering Conference (UPEC)*, 30 August – 01 September, Dublin, Ireland. doi: 10.1109/UPEC57427.2023.10294353

[5] Rerak, M., & Ocłoń, P. (2017). Thermal analysis of underground power cable system. *Journal of Thermal Science*, 26(5), 465–471, doi: 10.1007/s11630-017-0963-2

[6] IEC 60287-1-1 (2023). *Electric cables – Calculation of the current rating – Part 1-1: Current rating equations (100% load factor) and calculation of losses – General*.

[7] IEC 60287-2-1 (2023). *Electric cables – Calculation of the current rating – Part 2-1: Thermal resistance – Calculation*.

[8] Al-Dulaimi, A.A., Güneşer, M.T., & Hameed, A.A. (2021). Investigation of thermal modeling for underground cable ampacity under different conditions of distances and depths. *5th International Symposium on Multidisciplinary Studies and Innovative Technologies (ISMSIT)*, 21-23 Oct., Ankara, Turkey, 654–659. doi: 10.1109/ISMSIT52890.2021.9604732

[9] Ocłoń, P. (2021). The effect of soil thermal conductivity and cable ampacity on the thermal performance and material costs of underground transmission line. *Energy*, 231, 120803. doi: 10.1016/j.energy.2021.120803

[10] Ocłoń, P., Cisek, P., Pilarczyk, M., & Taler, D. (2015). Numerical simulation of heat dissipation processes in underground power cable system situated in thermal backfill and buried in a multi-layered soil. *Energy Conversion and Management*, 95, 352–370. doi: 10.1016/j.enconman.2015.01.092

[11] Xiong, L., Chen, Y., Jiao, Y., Wang, J., & Hu, X. (2019). Study on the effect of cable group laying mode on temperature field distribution and cable ampacity. *Energies*, 12(17), 3397. doi: 10.3390/en12173397.

[12] Yu, J., Gu, S., Xu, G., & Zhu, G. (2024). Calculation of metal sheath circulating currents in multi-circuit power cables laid in tunnels. *Ain Shams Engineering Journal*, 16(7), 103408. doi: 10.1016/j.asej.2025.103408

[13] Sedaghat, A., Lu, H., Bokhari, A., & de Leon, F. (2018). Enhanced thermal model of power cables installed in ducts for ampacity calculations. *IEEE Transactions on Power Delivery*, 33(5), 2404–2411. doi: 10.1109/TPWRD.2018.2841054

[14] Mróz M., Anders, G., Gulski, E. (2022). Soil dryout in the vicinity of cables with cyclic load installed in a backfill. *IEEE Transactions on Power Delivery*, 38(2), 1267–1276, doi: 10.1109/TPWRD.2022.3211851.

[15] Klimenta, D., Šućurović, M., & Tasić, D. (2026). Thermal modeling of the ground surface for the purpose of calculating the current-carrying capacity of underground cable lines using the FEM. *ICCK Transactions on Electric Power Networks and Systems*, 2(1), 47–57. doi: 10.62762/TEPNS.2026.891956

[16] Zain, W.A.B.W.M., Ali, N.H., Hamdan, M., Azis, N., Johari, D., & Rameli, N. (2022). The effect of the ambient temperature profile in the determination of power cable ratings. 2022 *IEEE International Conference on Power Systems Technology (POWERCON)*, 12–14 September, Malaysia. doi: 10.1109/POWERCON53406.2022.9929652

[17] Alwan, S., Jasim, A., & Hasan, Y. (2023). Derating factors for underground power cables ampacity in extreme environmental conditions: A comparative study. *International Journal of Heat and Technology*, 41(3), 709–715. doi: 10.18280/ijht.410325

[18] Klimenta, D., Perović, B., Klimenta, J., Jevtić, M., Milovanović, M., & Krstić, I. (2018). Modelling the thermal effect of solar radiation on the ampacity of a low voltage underground cable. *International Journal of Thermal Sciences*, 134, 507–516, doi: 10.1016/j.ijthermalsci.2018.08.012

[19] Brakelmann, H., & Anders, G.J. (2022). Analysis of the three-dimensional temperature distribution of forced cooled power cables. *IEEE Transactions on Power Delivery*, 37(2), 736–744. doi: 10.1109/TPWRD.2021.3069760

[20] Stojanović, M., Klimenta, J., Panić, M., Klimenta, D., Tasić, D., Milovanović, M., & Perović, B. (2023). Thermal aging management of underground power cables in electricity distribution networks: A FEM-based Arrhenius analysis of the hot spot effect. *Electrical Engineering*, 105, 647–662. doi: 10.1007/s00202-022-01689-z

[21] Klimenta, D., Panić, M., Klimenta, J., & Stojanović M. (2022). FEM-based Arrhenius modeling of the thermal effects of a heating pipeline and pavements on underground power cables. *Energy Reports*, 8 (Suppl. 13), 183–191. doi: 10.1016/j.egyr.2022.08.053

[22] Czapp, S., Szultka, S., Ratkowski, F., & Tomaszewski, A. (2020). Risk of power cables insulation failure due to the thermal effect of solar radiation. *Eksploatacja i Niezawodność – Maintenance and Reliability*, 22(2), 232–240. doi: 10.17531/ein.2020.2.6

[23] Brender, D., & Lindsey, T. (2008). Effect of rooftop exposure in direct sunlight on conduit ambient temperatures. *IEEE Transactions on Industry Applications*, 44(6), 1872–1878. doi: 10.1109/TIA.2008.2006301

[24] Czapp, S., Szultka, S., Tomaszewski, A., & Khan, L. (2025). The effect of PV modules on temperature conditions of nearby power cables. *Frontiers in Energy Research*, 13, 1499171. doi: 10.3389/fenrg.2025.1499171

[25] Perovic, B., Klimenta, D., Jevtic, M., & Milovanovic, M. (2019). A transient thermal model for flat-plate photovoltaic systems and its experimental validation. *Elektronika ir Elektrotechnika*, 25(2), 40–46. doi: 10.5755/j01.eie.25.2.23203

[26] Afia, R.S.A., Mustafa, E., & Tamus, Z.Á. (2021). Thermal-mechanical accelerated aging tests of XLPO insulation based photovoltaic cables: Inverse aging behavior. *International Conference and Workshop in Óbuda on Electrical and Power Engineering (CANDO-EPE 2021)*, 17–18 November, Budapest, Hungary. doi: 10.1109/CANDO-EPE54223.2021.9667894

[27] Abdulghafor, A.I., & Mnati, M.J. (2022). Design of thermoelectric radiant cooling – photovoltaic panels system in the building. *Archives of Thermodynamics*, 43(4), 85–108, doi: 10.24425/ather.2022.144407

[28] Ibrahim, O.A.A.M., Kadhim, S.A., & Al-Ghezi, M.K.S. (2023). Photovoltaic panels cooling technologies: Comprehensive review. *Archives of Thermodynamics*, 44(4) 581–617, doi: 10.24425/ather.2023.149720

[29] IEC 60287-3-1 (1999). *Electric cables – Calculation of the current rating – Part 3-1: Section on operating conditions – Reference operating conditions an selection of cable type*.

[30] Szultka, S., Czapp, S., Tomaszewski, A., & Czapp, M. (2025). Analysis of the temperature and durability of power cables exposed to solar radiation. *XVII Sympozjum Wymiany Ciepła i Masy*, 8-10 September, Kielce, Poland, 818–829 (in Polish).

[31] Jakusik, E., & Owczarek, M. (2008). Variability of ground temperature on the Polish coast. *Acta Agrophysica*, 12(2), 367–380 (in Polish).

[32] Musiał, E. (2008). Thermal load capacity and overcurrent protection of wires and cables. *Miesięcznik SEP, INPE: Informacje o Normach i Przepisach Elektrycznych*, 107, 3–41.

[33] IEC 60364-5-52 (2009). *Low-voltage electrical installations – Part 5-52: Selection and erection of electrical equipment – Wiring systems*.

Co-published by
Institute of Fluid-Flow Machinery
Polish Academy of Sciences
Committee on Thermodynamics and Combustion
Polish Academy of Sciences

Copyright©2026 by the Authors under licence CC BY-NC-ND 4.0

http://www.imp.gda.pl/archives-of-thermodynamics/

A novel passive solar energy space heating design of an emergency tent

Aed Ibrahim Owaid*, Sabah M. Hadi, Husam Sabeeh Al-Arab

Scientific Research Commission, Baghdad, Iraq
*Corresponding author email: aedaltaher@gmail.com

Received: 26.02.2026; revised: 09.07.2026; accepted: 21.07.2026

Abstract

The adjustable tent is utilised in construction sites, military camps, tourist locations, disaster relief efforts, rescue operations, nomadic living, and other situations. Current methods offer thermal comfort in tents but may elevate weight, expense and complexity. This study introduces a design for a passive solar heating tent that controls internal temperatures using renewable solar energy. This tent was designed using SolidWorks, featuring a Nylon 6.6 cover and a metal frame. The study's results indicate that the aperture area of the sun's trajectory is essential for the tent's energy harvesting capability. The design's principal characteristic is the rectangular prism-shaped air containers, comprising three passive solar containers (PSAC) and two insulation containers (ISC). These containers (PSAC and ISC) can be utilised during the winter and stored during the summer. To determine the minimum necessary aperture area, we computed the tent's maximum thermal losses, representing the required space heating load of 1000 W. We formulated an equation to determine the aperture area of the three-sided tent on the sun-exposed sides based on the azimuth and elevation angles that affect the solar collectors. The integration of the five containers (PSAC and ISC) with the tent enhances thermal insulation by reducing the heat transfer coefficient from 6.5 W/(m^2·K) to 0.168 W/(m^2·K).

Keywords: Passive solar heating; Rectangular prism-shaped air containers; Air containers; Emergency tent; SolidWorks.

Vol. 47(2026), No. 3, 69–77; doi: 10.24425/ather.2026.3655

Cite this manuscript as: Owaid, A.I., Hadi, S.M., & Al-Arab, H.S. (2026). A novel passive solar energy space heating design of an emergency tent. *Archives of Thermodynamics*, 47(3), 69−77.

1. Introduction

Since the dawn of civilisation, humans have created and employed tents constructed from natural materials. These tents function as a critical form of emergency shelter [1]. The International Federation of Red Cross and Red Crescent Societies (IFRC) continuously invests in upgrading tents [2], pointing out the significance of tents as essential tools in the initial phases of humanitarian assistance. Temporary shelters must be used when calamities strike, and there are not enough facilities to house the displaced. Shelter is a human right and a necessity for the population's physical and mental well-being [3].

The unstable global situation, changing weather and climate conditions, medical risks, and natural disasters have necessitated the need for temporary housing alternatives for the affected population. In addition, well over 42 million individuals have been forcibly displaced due to conflicts over the past decade, while 2.9 billion people have been affected by natural disasters in the first twelve years of this century [4−6]. Relief organisations, as international aid is estimated in 2019, offer emergency shelter to numerous affected individuals [7,8].

Thermal comfort refers to being content with ambient temperatures. The absence of adverse sensations associated with heat impacts is also assessed. Thermal comfort necessitates a ba-

Nomenclature

A – area, m^2
EoT– equation of time
F – factor
h – convection heat transfer coefficient, $W/(m^2 \cdot K)$
H – heat gain, W
I – rate of solar radiation, W/m^2
K – thermal conductivity, $W/(m \cdot K)$
l – window length, m
L – tent length, m
Lat – latitude, °
Lon– longitude, °
LT – local time, s
n – number of the day within the year
N – number of persons
Q – power, W
$\dot{Q}$ – heat flow rate, W
R – thermal resistance, $(m^2 \cdot K)/W$
ST – solar time
STM– standard time meridian, °
th – time hour angle, °
T – temperature, °C
U – overall heat transfer coefficient, $W/(m^2 \cdot K)$
$\dot{V}$ – volumetric air flow rate, m^3/s
w – window height, m
W – tent height, m
Z – azimuth angle, °

Greek symbols

α – elevation angle, °
δ – declination, °
η – conversion efficiency of the black paint

Subscripts and Superscripts

a – aperture
am – ambient
c – cross section
e – equipment
ex – external
$gain$– gain
h – harvested energy
hg – heat gain
i – internal static air
in – internal
inf – infiltration
l – latent
$loss$ – heat losses
o – outer moving air
P – persons
r – required power
S – sensible
sp – space
t – total
u – usage

Abbreviations and Acronyms

CLF – cooling load factor
CPVC– chlorinated polyvinyl chloride
IAC – insulation air containers
PMV – predicted mean vote
PPD – predicted percentage of dissatisfied
PSAC– passive solar air containers

lance between body heat production and loss [9–11]. The predicted mean vote (PMV) and predicted percentage of dissatisfied (PPD) indices are frequently employed to assess thermal comfort; however, some studies [12,13] suggest that the PPD index may not adequately represent individual perceptions in hot and humid environments, and PMV-PPD models exhibit certain limitations. Yang et al. [14] performed a supplementary study in Tianjin to corroborate this assertion. Environmental elements and tent attributes, such as materials, heating systems, location, and ventilation options, affect thermal comfort [15].

Conventional solar and non-solar air-conditioning tents combine renewable energy with temporary shelter, enhancing outdoor comfort. Air conditioning units in these tents maintain a stable temperature. Efficient air circulation, which means airflow that quickly distributes cooled or heated air, is key to energy savings and user comfort. High-quality thermal insulation materials that slow heat loss or gain, and advanced solar panel technology that uses solar cells to convert sunlight into usable electricity, are essential. Furthermore, materials that retain heat (store warmth for later use), resist fire (are non-flammable), and provide waterproofing (prevent water entry) further ensure safety and comfort [19]. Solar panels exchange sunlight for electrical energy, which powers air conditioning. Other tents use air-supply pipes (ducts that guide air) and ventilation fans (devices that move air) to boost airflow [20].

Although these approaches promise the thermal comfort of conventional solar and non-solar air-conditioning tents, they may also increase the tent's weight, cost, electrical consumption and complexity. This study presents a novel theoretical approach to design a passive solar heating tent that utilises free and renewable solar energy to maintain interior temperatures effectively. Using SolidWorks, we were able to design and simulate this tent, which has a metal base and a Nylon 6.6 cover. Additionally, the tent employs a sustainable passive solar system, making it environmentally friendly. Furthermore, this study highlights the vital effect of the varying aperture area resulting from the sun's trajectory on the energy harvested by the tent.

2. Materials and methods

We designed a four-person tent featuring a passive solar heating system utilising the SolidWorks software. The structure consists of a metal frame; it also features an outer layer made of nylon 6.6 fabric, known for its distinctive properties [21] and commonly utilised in parachutes because of its excellent air insulation. The design comprises a rectangular prism consisting of five containers – passive solar air containers and insulation air containers (PSAC and IAC) that can be assembled in the winter and disassembled in the summer: three coated passive solar air canisters (PSAC) for the walls and two insulating air containers (IAC) for the doorway and roof. PSACs are covered with black

nitrocellulose paint on one external side of each PSAC to improve solar radiation absorption efficiency.

The uncoated sides of these PSACs, on the other hand, feature openings at the top and bottom. The openings at the top and bottom of the tent match with the openings on either side of the containers. All containers are secured to the tent with adhesive tapes bonded to both the tent and the containers. When installed within the tent, each painted side of the containers is oriented towards the east, south and west, respectively, to optimise solar energy collection on their surfaces. Figure 1 (a and b) displays the setting.

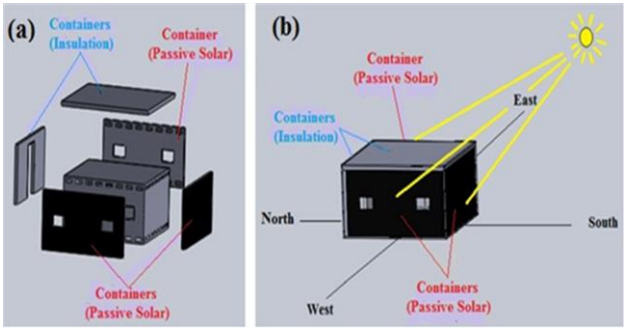


Fig. 1. (a) PSAC and IAC elements, and
(b) PSAC and IAC assembled in the tent.

The tent's entrance is located on the northern side, which is the fourth side. The variation in density will result in the energy absorbed from solar radiation heating the air within the PSAC, causing it to ascend to the top, where it will enter the tent through the upper openings, while cooler air will enter the container through the lower openings. The air circulation system elevates the tent's temperature during the day by employing the thermosiphon principle. This study aims to propose a theoretical design for an emergency tent with a novel solar heating system. This design is ready to be installed at any time, and all necessary mathematical calculations to validate it will be presented.

2.1. Space heating load and harvested energy

The required heating load is calculated by subtracting the heat obtained from occupants and objects within the tent while considering the heat losses through the tent's walls, ceiling and floor, with an internal temperature set at 22°C and an outside temperature of 0°C. The heat losses depend on the air properties, and the thermal resistances (R_t) are displayed in Fig. 2.

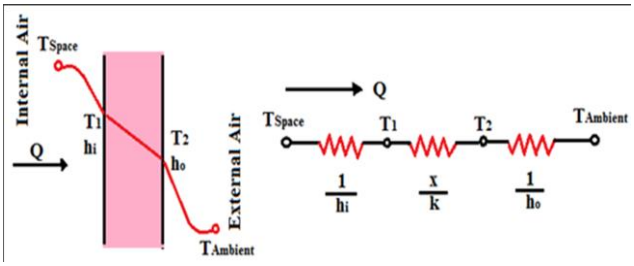


Fig. 2. Thermal resistances across the wall [23].

While the thermal conductivity (k) of the concrete floor equals 1.35 W/(m·K) [22], simultaneously, presuming the soil temperature to be between 10ºC and 14ºC. This study highlights two layers in the ground: the concrete layer (first) and the underlying soil layer (second). It is worth mentioning that this tent can also be set up directly on the ground without the use of a concrete layer.

2.1.1. Total amount of required power (Q_r)

The variation between heat losses (Q_{loss}) and heat gains (Q_{gain}) specifies the quantity of heat that must be supplied to the tent for the heating load (Q_r), which is:

$$Q_r = Q_{loss} - Q_{gain}, \quad (1)$$

where Q_r is the total amount of the required power in W.

- **Energy losses (Q_{loss})**

Load estimation is predicated on the assumption that the energy losses (Q_{loss}) of a tent are directly proportional to the temperature variation between its interior and exterior. In addition, the tent's wall cross sections that face the sun are involved in the calculations; despite the heat gain from the three PSAC, the calculations were based on the maximum thermal losses from the tent's walls, ceiling and floor:

$$Q_{loss} = UA_c(T_{sp} - T_{am}), \quad (2)$$

where A_c denotes the cross-sectional area of each layer. The overall heat transfer coefficient (U) for each element of the outer casing is obtained by the thermal resistance method, which accounts for the resistance of the convectional heat transfer on the inner and outer surfaces and the thermal conductivity resistance of all the layers of the material.

The overall heat transfer coefficient is given by [23]:

$$U = \frac{1}{R_t} = \frac{1}{\frac{1}{h_i} + \sum\frac{x}{k} + \frac{1}{h_o}}, \quad (3)$$

where X is the nylon 6.6 fabric thickness (0.8 mm); the thermal conductivity (k) of nylon used in the walls and roof is 0.25 W/(m·K), whereas the thermal conductivity of air is 0.0257 W/(m·K), the containers' thickness is 15 cm. The floor thickness is specified as 10 cm for concrete and 1 m for soil.

The convection heat transfer coefficient for internal static air is 8.29 W/(m^2·K), while the coefficient for moving air in winter is 34.1 W/(m^2·K) [22].

The total losses can be calculated as:

$$Q_{loss} = Q_1 + Q_2 + Q_3 + Q_4 + Q_5 + Q_6 + Q_7 + Q_{inf}, \quad (4)$$

Taking into account thermal losses: through the tent walls (Q_1, Q_2, Q_3), windows (Q_4), door (Q_5), ceiling (Q_6), floor (Q_7), and through infiltration (Q_{inf}). The notations (1−7) correspond to the values of A_c listed in Table 1.

- **Energy gain (Q_{gain})**

Persons residing in air-conditioned environments experience a loss of sensible heat that fluctuates according to their condi-

tion. This occurs because their bodies release heat when exposed to the tent's inner air, which is at 37°C. Furthermore, latent heat is generated from sweat on the body's surface and the evaporation of water in the lungs, which contributes thermal energy and decreases the heating load, along with the heat gain from electrical equipment:

$$Q_{gain} = Q_P + Q_e. \quad (5)$$

The sensible heat gained by individuals (Q_S) can be calculated using the equation [22]:

$$Q_S = N_P H_S CLF. \quad (6)$$

In refrigeration calculations, *CLF* denotes the cooling load factor, but in this context, it refers to the heat gain load factor per person. The value of H_s is dependent upon the person's activities within the tent and its magnitude. The latent heat gain from occupants (Q_l) in a space is expressed by the subsequent equation:

$$Q_l = N_P H_l . \quad (7)$$

H_l denotes the latent heat rate for an individual within the space, with its value dependent upon the nature of the person's activity.

The total heat gain due to the presence of people inside the tent (Q_p) was calculated from the following equation:

$$Q_P = Q_S + Q_l, \quad (8)$$

When calculating the heat gain load from equipment in the tent, references equate this gain to the power consumption of the devices, taking into account usage factors, and calculate the heat gains as follows [22]:

$$Q_e = P_e F_u F_{hg}, \quad (9)$$

where Q_e is the heat gain from equipment (W), P_e is the equipment power (W), F_u is the usage factor

$$F_u = \frac{Actual\ operating\ time}{Design\ period}; \quad (10)$$

F_{hg} is the heat gain factor, and the design period is 10 hours.

2.2. The main components of the tent and solar heating system

2.2.1. The main metal structure assembly

Figure 3 illustrates a primary metal framework of the tent (of size 4 m × 4 m × 2 m) designed for fast assembly and disassembly, which utilises metal assemblies secured at each of its eight corners with screws and nuts. The subsequent assemblies are as follows: for each tent, two symmetrical side metal components, fabricated from 40 mm × 40 mm × 1.25 mm square hollow section tubes, are employed. The symmetrical complexes on the right and left are interconnected at the top by ribs made of a square hollow section, with bond plates at the ends that attach the components affixed to the aforementioned complexes.

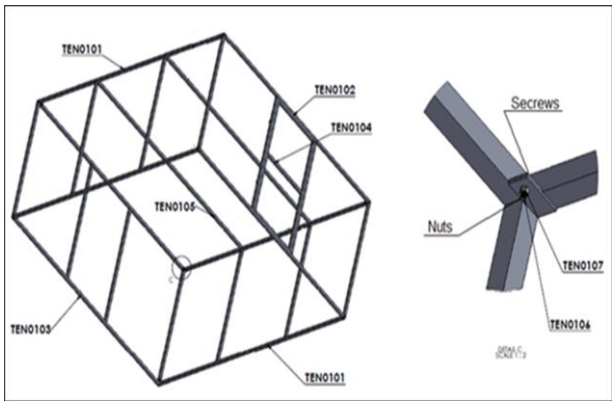


Fig. 3. The tent metal assemblies and their connections.

The next phase includes affixing the door frame to the primary construction of the tent utilising a door hinge. Subsequently, a body constructed from nylon 6.6 fabric is sewn and positioned over the framework in accordance with Fig. 4.

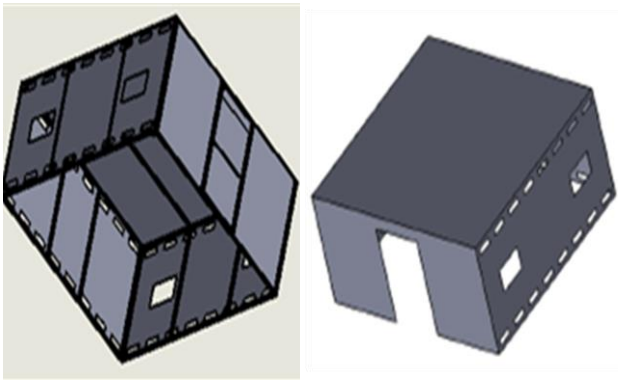


Fig. 4. The fabric framework of the tent.

Finally, the door fabric is attached to the door structure and metal frame using connecting belts and a fabric label. This connection allows air to pass between the frame and the fabric, effectively eliminating the effect of heat conduction between them.

2.3. PSAC and IAC

During this step, we have connected PSAC, specifically the left, right and rear, along with IAC for the door and roof. This procedure is illustrated in Fig. 5, which depicts the connections using belts and fabric sticker labels around the windows and their edges. PSAC and IAC are equipped with valves for the primary purpose of air filling. In order to take the form of a parallel rectangular shape, it employs an assembly of plastic tubes (2" C.P.V.C SCH 80) as illustrated in Fig. 6 to maintain their shapes by linking them at the outer corners and ends of the containers (PSAC and IAC), as depicted in Fig. 5.

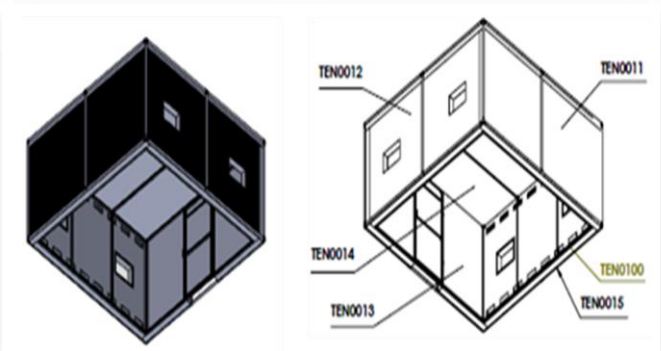


Fig. 5. Tent structure incorporating PSAC and IAC with CPVC tubing assembly.

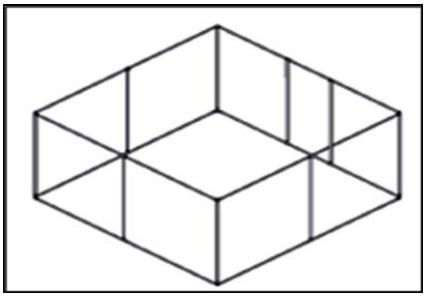


Fig. 6. Outer support tube assembly.

2.4. Sun trajectory calculations

Static solar containers (PSACs) capture solar radiation through their variable aperture area, defined as the section of PSAC oriented toward the sun that receives incident solar radiation. This mechanism controls the amount of solar energy harvested. The aperture area of PSAC varies from sunrise to sunset as the solar angles (azimuth and elevation) change. To compute the changing aperture of three PSACs facing the sun as a function of elevation and azimuth solar angles, the following mathematical relation was developed, Eq. (11):

$$A_a\,(z,\alpha) = L\cos(90+Z)\,2\cos(90-\alpha) + \\ +W\cos(Z)\,2\cos(\alpha). \quad (11a)$$

When subtracting the area of the tent windows, the equation becomes as follows:

$$A_a\,(z,\alpha) = L\cos(90+Z)\,2\cos(90-\alpha) + \\ -2l\cos(90+Z)\,w\cos(90-\alpha) + \\ +W\cos(Z)\,2\cos(\alpha). \quad (11b)$$

where Z denotes the azimuth angle, α represents the elevation angle. L and W indicate the length and height of PSAC, while l and w identify the length and height of the windows. The elevation angle (α) is determined according to [24]:

$$\alpha = sin^{-1}(\cos(Lat)\cos(\delta)\cos(th) + \sin(Lat)\sin(\delta)), \quad (12)$$

where th is the time hour angle, Lat is the position's latitude (33.27°), and δ is the declination. These parameters can be determined as [24–27]:

$$\delta = 23.45\sin\left(\frac{360}{365}(284+n)\right), \quad (13)$$

where n represents the number of the day within the year, and

$$th = 15(ST-12). \quad (14)$$

The solar time (ST) can be determined from [19]:

$$ST = LT + 4(Lon - STM) + EoT, \quad (15)$$

where LT is the local time, Lon is the local longitude (44.4°E), STM is the standard time meridian (45°E), EoT is the equation of time, which reads as [28]:

$$EoT = 9.87\sin(2\beta) - 7.53\cos(\beta) - 1.5\sin(\beta), \quad (16)$$

$$\beta = \frac{360}{364}(n-81), \quad (17)$$

$$Z = \arcsin(\sec(\alpha)\cos(\delta)\ \sin(th)). \quad (18)$$

3. Results and discussion

3.1. Energy losses and energy gain

- **Energy losses (Q_{loss})**

First, we have to set the values for the overall heat transfer coefficients using Eq. (3): U_1 = 0.168 W/(m²·K) for the right, left and rear walls and also for the door wall and ceiling, U_2 = 6.5 W/(m²·K) for the door, U_3 = 6.27 W/(m²·K) for the windows, U_4 = 5.14 W/(m²·K) for the floor.

Using Eq. (2) to calculate the heat losses yields the results presented in Table 1 for the floor concrete thickness of 10 cm and for dry soil of thickness 1 m (effective depth).

Table 1. Details of heat losses calculations.

Heat losses	Cross section area, m²	Values, W	Details
Q_1	7.52	55.58	right and left tent walls
Q_2	8	29.6	rear wall
Q_3	6.2	22.9	door wall
Q_4	0.96	132.4	windows
Q_5	1.8	257.4	door
Q_6	16	59.1	ceiling
Q_7	16 16	822.4 80	floor (concrete) floor (dry soil)

Note that the air infiltration ($\dot{Q}_{inf}$) is a contributing factor to heat loss and can be calculated using the method [22]:

$$\dot{Q}_{inf} = 1.22\,\dot{V}(T_{sp} - T_{am}), \quad (19)$$

where $\dot{V}$ represents the volumetric rate of air exchange, determined as:

$$\dot{V} = \frac{V\,n}{3600}. \quad (20)$$

The value *n* indicates the quantity of air changes. Assuming one-time air change (1), *V* represents the volume of a tent covering 32 m³. Applying the preceding formula, we derive:

$$\dot{V} = 0.00889 \text{ m}^3/\text{s}.$$

By substituting values of T_{sp} = 22°C and T_{am} = 0°C into Eq. (19), we obtain:

$$\dot{Q}_{inf} = 238.8 \text{ W}.$$

Placing the data from Table 1 and $\dot{Q}_{inf}$ into Eq. (4) gives:

$$Q_{loss} = 1618 \text{ W}.$$

- **Energy gain (Q_{gain})**

In the context of minor activities such as sitting or light work, the *CLF* value is 0.65, while the *CLF* value varies according to the duration of an individual's presence, with a range of 0.5−0.79 for a 4-hour presence [22]. Inputting the values of H_S, *CLF* and the number of individuals, *NP*, into the aforementioned Eq. (6) yields:

$$Q_s = 182 \text{ W}.$$

In addition, for sitting or light work, H_l is measured at 55 W [22]. Substituting values of H_l and the number of individuals into Eq. (7) yields:

$$Q_l = 220 \text{ W}.$$

Finally, substituting the values of Q_S and Q_l into Eq. (8) results in:

$$Q_P = 402 \text{ W}.$$

Assuming that the devices operate at completely full power, the heat gain factor is equal to 1, and the usage factor is based on actual operating time of the equipment. The calculations of the heat gain by the equipment using Eq. 9 are detailed in Table 2. The total heat gain by the equipment is 216 W.

Table 2. Details of the heat gain load for the equipment.

Equipment	Device number	Total Power, W	Actual operating time, h	Usage factor	Heat gain, W
Laptop and charger	2	130	4	0.4	52
Mobile charger	4	40	0.5	0.05	2
Kettle	1	2000	0.5	0.05	100
Monitor LED	1	70	6	0.6	42
Lighting LED	2	20	10	1	20

By substituting values of Q_p = 402 W and Q_d = 216 W in Eq. (5), we obtained the following:

$$Q_{gain} = 618 \text{ W}.$$

3.2. Total amount of required power (Q_r)

From Eq. (1): Q_r = 1000 W. Now the total energy (Q_t) required to heat the tent for a duration of 10 hours is as follows:

$$Q_t = Q_r \times \textit{used hours of day}, \quad (21)$$

$$Q_t = 1000 \times 10 \text{ hours} \times 3600 = 36000 \text{ kJ} = 10 \text{ kWh}.$$

3.3. Harvested energy and optical calculations

The energy collected from the sun via the PSAC is called harvested energy (Q_h). This energy can be expressed as:

$$Q_h = I\, A_a\, \eta. \quad (22)$$

To find the minimum aperture area (A_a) of the passive solar energy collector that must be exposed to solar radiation to meet the required load (as much as possible), we must assume that the calculated total energy (36000 kJ) is equal to the harvested energy (Q_h). Now:

$$A_a = \frac{Q_t}{I\eta}. \quad (23)$$

Between October and March, the average solar radiation for the winter, over a six-month duration of 10 hours daily, is 3.868 kWh/m² [29]. The absorptance of the black paint (cellulose nitrate) is 0.78, representing η [30]. Consequently, the required aperture area for the passive solar collector is:

$$A_a = \frac{10 \text{ kWh}}{3.868 \text{ kWh/m}^2 \text{ x } 0.78} = 3.31 \text{ m}^2.$$

Applying a cumulative method with spatial adjustments based on the sun's trajectory (azimuth and elevation) as detailed in Eqs. (11)−(18), Table 3 presents the amount of harvested energy obtainable over a nine-hour period. Measurements were recorded every ten minutes (see the appendix); however, for simplicity, the data presented in Table 3 represents hourly averages throughout the day. The coordinates for Baghdad, Iraq (33.27°N, 44.38°E) were employed in the calculations.

Table 3. The detailed data of harvested energy and actual aperture area with corresponding azimuth and elevation angles for every hour.

Time, hh:mm	Azimuth, deg.	Elevation, deg.	Aperture area, m²	Solar radiation, W/m²	Energy, kJ
07:30 a.m.	−58.16	4.42	4.71	19	-
08:30 a.m.	−48.64	14.49	6.54	169	1508.3
09:30 a.m.	−37.24	23.05	7.65	300	4727.8
10:30 a.m.	−23.62	29.42	7.87	400	7832.4
11:30 a.m.	−8.04	32.85	7.23	454	9167.5
12:30 p.m.	8.35	32.82	7.23	454	9015.0
01:30 p.m.	23.90	29.32	7.87	403	9239.6
02:30 p.m.	37.48	22.90	7.65	311	7949.3
03:30 p.m.	48.84	14.31	6.54	174	4981.7
04:30 p.m.	58.33	4.22	4.71	21	1497.2

Since the outside air temperature was assumed to be 0°C and the inside tent temperature was 22°C, we could calculate the required heating load by calculating the tent's thermal losses. According to Eq. (21), the calculations produced a heating energy load of 36 000 kJ. If the indoor temperature rises above 22°C, the windows can be opened to maintain the desired value.

On December 21, the shortest day of the year, which produces the least amount of energy during the winter, the accumulation approach can be used to measure the outcome at 10-minute intervals [31].

Figure 7 depicts the variation in the aperture area (Col. Area) as it correlates with changes in azimuth (Azm.) and elevation (Elev.) throughout the day.

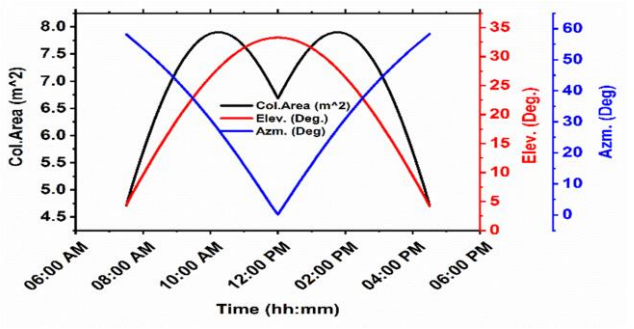


Fig. 7. The correlation involving aperture area, elevation and azimuth.

Figure 7 demonstrates that while elevation and azimuth varies throughout the day, the actual aperture area consistently exceeds its minimum calculated value of 3.31 m^2, indicating that the energy collected would be greater than the requirements for space heating.

Figure 8 illustrates the variation in aperture area in connection with variations in azimuth and elevation over a half-day period (from 7:30 a.m. to 12:00 p.m.). The identical occurrence is expected to take place throughout the forthcoming half-day (from 12:00 p.m. to 4:30 p.m.). The changing aperture area and the intensity of solar radiation will influence the efficiency of energy harvested from PSAC. The section of the aperture area curve depicted in Fig. 8 aligns with the Gaussian model, as illustrated within the figure.

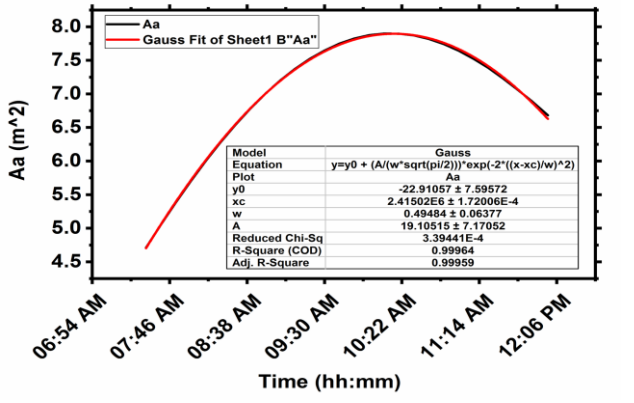


Fig. 8. Behaviour of aperture area variation with Gauss model fitting.

By employing Eq. (22), we can compute how much energy the PSAC captured from the sun's rays for the entire shortest winter day, as illustrated in Fig. 9. The result was 55 919.04 kJ. The solar radiation data for December 21 demonstrate the effect of changes in the aperture area (A_a) and solar radiation (S. Rad.) values on the quantity of harvested energy produced, as shown in Fig. 9.

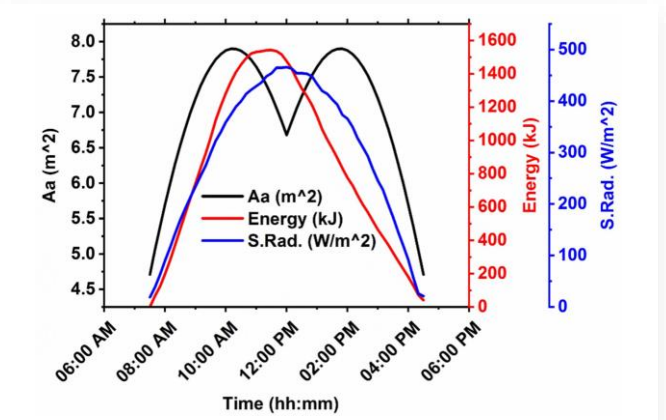


Fig. 9. The influence of aperture area and solar radiation on the energy harvested.

At 10:10 a.m., the maximum aperture area was measured as 7.898 m^2, with solar radiation recorded at 374 W/m^2, resulting in an energy gain of 1352.7 kJ. The highest recorded energy was 1542.44 kJ at 11:30 a.m. The aperture area measured 7.23 m^2 under solar radiation of 454 W/m^2. This variation arises from the simultaneous influence of aperture areas and solar radiation values on the energy obtained.

6. Conclusions

The project aimed to develop an innovative technique for designing an emergency passive solar heating tent that utilises renewable and cost-free solar energy to maintain appropriate internal temperatures.

The research demonstrates that a tent measuring 4 m × 4 m × 2 m can accommodate up to four people while providing the necessary space-heating load and usable solar energy. Another advantage of the tent is the simplicity of assembly and disassembly. The aperture area of PSAC, which varies throughout the day as the sun traverses the sky, determines the amount of energy that may be harvested.

This design simulation focuses only on the volumetric rate of air exchange and assumes one-time air change for simplicity.

Additional practical parameters, such as wind speed, pressure differences, air temperature differences and minimum ventilation, could influence the calculation of the heat losses. All these parameters will be taken into account in our future work.

References

[1] Davis, I. (1978). *Shelter after disaster*. UNESDOC Digital Library, Oxford Polytechnic Press.

[2] Poschl, R.A. (2017). *Modelling the thermal comfort performance of tents used in humanitarian relief*. Ph.D. dissertation, Loughborough University.

[3] Banks, B. A. (2024). *Write to Return: Huguenot Refugees on the Frontiers of the French Enlightenment*. McGill-Queen's Refugee and Forced Migration Studies, Vol. 14.

[4] Hantscher, S. (2019). The UNHCR and Environmentally Displaced Persons. In *The UNHCR and Disaster Displacement in the 21st Century: An Organizational Analysis* (pp. 119–192). Springer. doi: 10.1007/978-3-030-19689-9_5

[5] Murray, L. (2015). Sheltering from disaster. *Engineering & Technology*, 10(1), 58−61. doi: 10.1049/et.2015.0107

[6] Gentile, V., Nigra, M., Simonetti, M., & Perino, M. (2025). Design and testing of an emergency humanitarian tent for airborne risk mitigation with natural ventilation. *E3S Web of Conferences*, 672, 01006. doi: 10.1051/e3sconf/202567201006

[7] Cao, K., Lan, M., Wang, H., Li, Y., & Liu, X. (2023). The thermal environment and thermal comfort of disaster relief tents in high-temperature composite environment. *Case Studies in Thermal Engineering*, 50, 103453. doi: 10.1016/j.csite.2023.103453

[8] Ullal, A., Aguacil, S., Vannucci, R., Yang, S., Pernot, J.G., Licina, D., & Tombesi, P. (2022). Comparing thermal performance of standard humanitarian tents. *Energy and Buildings*, 264, 112035. doi: 10.1016/j.enbuild.2022.112035

[9] Matusiak, M. (2010). Thermal comfort index as a method of assessing the thermal comfort of textile materials. *Fibres & Textiles in Eastern Europe*, 18(2), 45–50.

[10] Rupp, R.F., Vásquez, N.G., & Lamberts, R. (2015). A review of human thermal comfort in the built environment. *Energy and Buildings*, 105, 178–205. doi: 10.1016/j.enbuild.2015.07.047

[11] De Dear, R.J., Akimoto, T., Arens, E.A., Brager, G., Candido, C., Cheong, K.W.D., & Zhu, Y. (2013). Progress in thermal comfort research over the last twenty years. *Indoor air*, 23(6), 442–461. doi: 10.1111/ina.12046

[12] Susanti, L. (2015). Thermal comfort evaluation of emergency tent using PMV and PPD model. In *Proceedings of the International Multi Conference of Engineers and Computer Scientists* (pp. 958−963), March 18–20, Hong Kong.

[13] Nicol, F., Humphreys, M., & Roaf, S. (2012). *Adaptive thermal comfort: principles and practice* (1st ed.). Routledge, London. doi: 10.4324/9780203123010

[14] Yang, H., Jiang, Y., Liu, J., & Gong, Z. (2016). The field investigation on thermal comfort of tent in early autumn of Tianjin. *MATEC Web of Conferences*, 61, 01001. doi: 10.1051/matecconf/20166101001

[15] Potangaroa, R., & Hynds, M. (2008). Thermal comfort tools for emergency shelter in major disasters. *Proceedings from CIB International Conference on Building Education and Research, School of the Built Environment* (pp. 1457–1472), 11–15 February 2008, Heritance Kandalama, Sri Lanka.

[16] Zemitis, J., Borodinecs, A., Bogdanovics, R., & Geikins, A. (2021). A case study of thermal comfort in a temporary shelter. *Journal of Sustainable Architecture and Civil Engineering*, 29(2), 139–149. doi: 10.5755/j01.sace.29.2.29240

[17] Yousef, M. (2023). More humane engineering ideas for the design of shelter units (camps) Renewable Energy Produced Tent Idea (weaving a home). *International Journal of Advanced Engineering and Business Sciences*, 4(3). doi: 10.21608/ijaebs.2023.210485.1083

[18] Butcher, K., & Craig, B. (Eds.). (2015). *Guide A Environmental design* (8th ed.). Chartered Institution of Building Services Engineers, London.

[19] Guangliang, H. (2012). *Solar air-conditioning tent*. China Patent CN 102400589 A, 04 April. https://lens.org/001-926-548-381-407 [accessed 22 Feb. 2026].

[20] Dai, M. (2014). *Solar ventilation-type tent*. China Patent CN 203394150 U, 15 January. https://lens.org/117-693-182-419-301 [accessed 22 Feb. 2026].

[21] King, J.A., Tucker, K.W., Vogt, B.D., Weber, E.H., & Quan, C. (1999). Electrically and thermally conductive nylon 6.6. *Polymer Composites*, 20(5), 643–654, doi: 10.1002/pc.10387

[22] Owen, M.S. (Ed.). (2009). *The 2009 ASHRAE Handbook: Fundamentals*. American Society of Heating. American Society of Heating, Refrigerating and Air-Conditioning Engineers

[23] Holman, J.P. (2010). *Heat transfer*. 10th ed. McGraw-Hill Series in Mechanical Engineering, Boston.

[24] Chen, X.M., Li, Y., Zhao, Z.G., Ma, T., & Wang, R.Z. (2018). General method to obtain recommended tilt and azimuth angles for photovoltaic systems worldwide. *Solar Energy*, 172, 46–57. doi: 10.1016/j.solener.2018.06.045

[25] Shivalingaswamy, T., & Kagali, B.A. (2012). Determination of the Declination of the Sun on a Given Day. *European Journal of Physics Education*, 3(1), 17−22.

[26] Abdurrahman, M., Gambo, J., Shitu, I.G., Yusuf, Y.A., Dahiru, Z., Idris, A.M., & Isah, A.A. (2019). Solar elevation angle and solar culmination determination using celestial observation; a case study of hadejia jigawa state, Nigeria. *International Journal of Advances in Scientific Research and Engineering*, 5(9), 8−17. doi: 10.31695/IJASRE.2019.33482

[27] Sproul, A. B. (2007). Derivation of the solar geometric relationships using vector analysis. *Renewable Energy*, 32(7), 1187−1205, doi: 10.1016 /j.renene. 2006. 05.001

[28] Duffie, J.A., Beckman, W.A., & Blair, N. (2020). *Solar engineering of thermal processes, photovoltaics and wind*. John Wiley & Sons.

[29] Ahmed, B.K., Younis, G.G., & Abdalwahid, Z. (2021). Estimation and Analysis of Solar Radiation on Horizontal and Inclined Surface for Baghdad City. *Iraqi Journal of Science*, 62(11), 4249–4259. doi: 10.24996/ijs.2021.62.11(SI).5

[30] Mutlak, F. (2011). *Design and fabrication of parabolic trough solar collector for thermal energy applications*. Ph.D. Thesis, University of Baghdad.

[31] Abdulla, F.M. (2019). Calculating the variations of sunrise, sunset and day length times for Baghdad city with comparison to different regions of the world in year 2019. *Iraqi Journal of Science*, 62(12), 2732–2741. doi: 10.24996/ijs.2019.60.12.24

Appendix

Table 4 presents the results of calculations of the harvested energy every ten minutes, along with the effects of azimuth and elevation on the aperture area and amount of energy harvested.

Table 4. The detailed data of harvested energy and actual aperture area every ten minutes with corresponding azimuth and elevation angles.

Time, hh:mm	Azimuth, deg.	Elevation, deg.	Aperture area, m²	Solar radiation, W/m²	Energy, kJ
07:30 AM	−58.16	4.42	4.71	19	-
07:40 AM	−56.68	6.19	5.05	38	65.11
07:50 AM	−55.17	7.91	5.38	63	123.34
08:00 AM	−53.60	9.61	5.70	90	198.38
08:10 AM	−51.10	11.28	5.10	116	281.88
08:20 AM	−50.35	12.90	6.27	143	371.90
08:30 AM	−48.64	14.49	6.54	169	467.74
08:40 AM	−46.88	16.04	6.78	192	562.44
08:50 AM	−45.08	17.54	6.10	213	652.80
09:00 AM	−43.20	18.10	7.19	234	742.30
09:10 AM	−41.28	20.40	7.37	254	831.67
09:20 AM	−39.29	21.75	7.52	274	919.93
09:30 AM	−37.24	23.05	7.65	300	1018.70
09:40 AM	−35.12	24.28	7.75	323	1122.28
09:50 AM	−32.96	25.45	7.82	340	1208.05
10:00 AM	−30.71	26.55	7.87	359	1283.91
10:10 AM	−28.41	27.58	7.898	374	1352.70
10:20 AM	−26.05	28.54	7.896	389	1410.05
10:30 AM	−23.62	29.42	7.87	400	1455.43
10:40 AM	−21.14	30.21	7.82	414	1494.01
10:50 AM	−18.62	30.92	7.74	422	1521.93
11:00 AM	−16.03	31.55	7.64	429	1531.93
11:10 AM	−13.40	32.08	7.52	436	1535.09
11:20 AM	−10.74	32.51	7.38	448	1542.14
11:30 AM	−8.04	32.85	7.23	454	1542.44
11:40 AM	−5.31	33.10	7.06	465	1536.25
11:50 AM	−2.59	33.24	6.87	465	1516.05
12:00 PM	0.16	33.29	6.68	466	1476.56
12:10 PM	2.90	33.23	6.875	463	1473.39
12:20 PM	5.63	33.08	7.06	454	1494.86
12:30 PM	8.35	32.82	7.23	454	1517.87
12:40 PM	11.05	32.47	7.38	453	1550.10
12:50 PM	13.70	32.02	7.52	448	1571.80
01:00 PM	16.33	31.48	7.64	433	1563.48
01:10 PM	18.90	30.85	7.74	420	1535.53
01:20 PM	21.43	30.13	7.82	414	1518.29
01:30 PM	23.90	29.32	7.87	403	1499.52
01:40 PM	26.33	28.43	7.90	393	1468.34
01:50 PM	28.67	27.47	7.90	373	1415.60
02:00 PM	30.97	26.43	7.87	366	1363.77
02:10 PM	33.20	25.32	7.82	350	1315.13
02:20 PM	35.37	24.15	7.75	328	1235.38
02:30 PM	37.48	22.90	7.65	311	1151.10
02:40 PM	39.52	21.60	7.52	293	1071.94
02:50 PM	41.50	20.25	7.37	268	977.43
03:00 PM	43.42	18.83	7.19	245	874.27
03:10 PM	45.28	17.37	6.10	228	785.47
03:20 PM	47.08	15.87	6.78	200	689.87
03:30 PM	48.84	14.31	6.54	174	582.69
03:40 PM	50.54	12.72	6.30	146	479.73
03:50 PM	52.18	11.09	5.10	119	380.51
04:00 PM	53.78	9.42	5.70	92	288.72
04:10 PM	55.34	7.72	5.38	57	193.19
04:20 PM	56.85	5.99	5.05	26	101.36
04:30 PM	58.33	4.22	4.71	21	53.69

Co-published by
Institute of Fluid-Flow Machinery
Polish Academy of Sciences
Committee on Thermodynamics and Combustion
Polish Academy of Sciences

Copyright©2026 by the Authors under licence CC BY-NC-ND 4.0

http://www.imp.gda.pl/archives-of-thermodynamics/

Dual-use PV canopies for public gardens: Performance, techno-economic feasibility and CO_2 mitigation of an 84.5 kWp grid-tied system in Baghdad, Iraq

Emad Jaleel Mahdi, Hussein Fawzi Hussein*, Ali Isam Ata

Scientific Research Commission, P.O. Box 10070, Al-Jadriya, Baghdad, Iraq
*Corresponding author email: husseinalaubi@live.co.uk

Received: 18.02.2026; revised: 13.05.2026; accepted: 30.06.2026

Abstract

This study presents a comprehensive energy, techno-economic and environmental assessment of a dual-use grid-connected photovoltaic canopy system implemented in a public urban garden in Baghdad, Iraq, under hot-arid climatic conditions. The photovoltaic system, designed as shading canopies integrated within recreational areas, has a total installed capacity of 84.5 kWp and operates under a net-metering configuration without battery storage. The system performance was evaluated using PVsyst simulation and independently cross-checked through a simplified analytical model developed in a spreadsheet-based framework using monthly solar-resource inputs and aggregate loss assumptions. The analytical model reproduced the same seasonal behaviour as the PVsyst simulation, with an annual deviation of only 1.51%. The results indicate an annual electricity generation of 133 189 kWh, corresponding to a specific yield of 1 577 kWh/kWp per year and a performance ratio of 79.6%, demonstrating reliable operation despite high ambient temperatures, dust exposure and other site-related losses. The irrigation demand of the public garden is supplied by a 4-hp electric pump requiring approximately 2 200 kWh per year, which represents only about 1.6% of the total annual photovoltaic production. Consequently, more than 130 MWh per year of surplus electricity is available for export to the national grid. The economic analysis revealed a levelised cost of electricity of approximately 44 IQD/kWh (≈ 0.034 USD/kWh), substantially lower than the prevailing commercial electricity tariff of about 120 IQD/kWh (≈ 0.092 USD/kWh), with a simple payback period of about 6 years and an internal rate of return of approximately 18%. Environmentally, replacing the previous diesel-based irrigation supply with the photovoltaic-supported electric system leads to an estimated annual reduction of approximately 113 tonnes of CO_2 emissions. Overall, the findings demonstrate that photovoltaic canopy systems provide a technically reliable, economically attractive and environmentally effective solution for urban irrigation while simultaneously delivering shading benefits, supporting grid interaction and improving the sustainability of public green spaces in hot-arid regions.

Keywords: Photovoltaic canopy; Urban solar irrigation; Grid-connected photovoltaic system; Techno-economic assessment; CO_2 mitigation; Hot-arid climate

Vol. 47(2026), No. 3, 79–88; doi: 10.24425/ather.2026.3657

Cite this manuscript as: Mahdi, E.J., Hussein, H.F., & Ata, A.I. (2026). Dual-use PV canopies for public gardens: Performance, techno-economic feasibility and CO_2 mitigation of an 84.5 kWp grid-tied system in Baghdad, Iraq. *Archives of Thermodynamics*, 47(3), 79−88.

1. Introduction

Urban green spaces such as public gardens and parks play a critical role in improving environmental quality, mitigating urban heat island effects and enhancing social well-being, particularly in densely populated cities located in hot-arid regions. However, maintaining these green infrastructures requires reliable and continuous irrigation, which in many developing countries still depends heavily on diesel-powered pumping systems. These systems are associated with high operational costs, fuel supply vulnerability, noise and significant greenhouse gas emissions [1–3]. As cities expand and climate conditions deteriorate,

Nomenclature

$E_{analytical}$ – energy estimated by the simplified analytical model, kWh
E_m – monthly electrical energy output, kWh
E_{PVsyst} – monthly or annual energy yield predicted by PVsyst, kWh
H_m – monthly in-plane solar irradiation, h
P_r – rated PV system capacity, kWp
PR_m – monthly effective performance ratio

Abbreviations and Acronyms

AC – alternating current
DC – direct current
IQD – Iraqi dinar
IRR – internal rate of return
LCOE – levelised cost of electricity
PV – photovoltaic
STC – standard test conditions

the energy–water nexus in urban irrigation has become an increasingly important challenge.

Photovoltaic (PV) energy has emerged as one of the most promising solutions for sustainable irrigation due to its modularity, declining costs, and suitability for regions with high solar irradiance [4–6]. In arid and semi-arid climates, solar energy availability often coincides with peak irrigation demand, making PV-powered irrigation systems particularly attractive. Nevertheless, most existing studies have focused on rural or agricultural irrigation schemes, frequently relying on off-grid configurations with battery storage, which increases system complexity, cost, and long-term maintenance requirements [7,8]. In contrast, grid-connected PV systems without storage, operating under net-metering schemes, remain underexplored for urban irrigation applications.

Recent research has emphasised the importance of system performance, degradation behaviour, and thermal effects on PV installations operating in harsh climates. Long-term exposure to high ambient temperatures, dust accumulation and thermal cycling can significantly affect PV efficiency and reliability [9–11]. Detailed performance assessment and loss analysis are therefore essential to ensure realistic energy yield predictions. Previous investigations have demonstrated that careful system design and monitoring can maintain high performance ratios even under challenging environmental conditions [12]. These aspects are particularly relevant for urban installations, where shading, architectural constraints and multifunctional land use must be considered.

An emerging concept in urban solar integration is the use of dual-use PV canopies, where PV modules are installed as shading structures over public spaces. Such systems offer multiple benefits: electricity generation, thermal comfort for users, reduced surface temperatures and improved land-use efficiency [13–15]. When applied to public gardens, PV canopies can simultaneously support irrigation energy demand and provide shaded recreational areas, contributing to both environmental sustainability and social value. Despite these advantages, quantitative assessments of PV canopy systems for urban irrigation, especially in hot-arid cities, remain limited in the literature.

In parallel, techno-economic analyses have become a cornerstone of evaluating renewable energy projects, particularly in regions where fossil-fuel-based solutions are still economically dominant. Studies conducted under Iraqi climatic conditions have demonstrated the critical role of thermal behaviour, material performance and system aging in determining the long-term viability of solar energy systems [16–18]. Moreover, replacing diesel-driven systems with electrically powered alternatives supplied by PV energy can yield substantial reductions in operating costs and carbon emissions, provided that system sizing and grid interaction are properly optimised [19].

Against this background, the present study addresses a clear research gap by providing a comprehensive energy, techno-economic and environmental assessment of a grid-connected PV canopy system used for urban irrigation in a hot-arid climate. The study is based on a real public garden located in Baghdad, Iraq, where a dual-use PV canopy system with an installed capacity of 84.5 kWp supplies a relatively small irrigation load while exporting most of the generated electricity to the national grid. Using PVsyst-based simulation, an independent simplified analytical model, realistic load profiles and detailed economic and emissions analysis, this work aims to:

(i) quantify the energy performance of the PV canopy system under local climatic conditions,
(ii) evaluate its economic feasibility in comparison with conventional diesel-based irrigation,
(iii) assess its contribution to CO_2 emission mitigation.

In addition to detailed software-based simulation, the study introduces an independent engineering cross-check model to enhance methodological transparency and improve the reproducibility of PV canopy performance estimation under hot-arid operating conditions. The analytical cross-check showed an annual deviation of only 1.51% relative to the PVsyst prediction, confirming acceptable agreement between the two approaches. The results provide practical insights for municipalities and decision-makers seeking scalable, multifunctional solar solutions for sustainable urban green infrastructure.

2. System description and methodology

2.1. Site description and climatic conditions

The investigated system is installed in a public urban garden located in Al-Ghazālīyah district, Baghdad, Iraq, at geographic coordinates of 33.33°N latitude and 44.27°E longitude, with an average altitude of approximately 28 m above sea level. The site lies within a hot-arid climatic zone, characterised by long, dry summers, high solar irradiance and elevated ambient temperatures during the irrigation season.

Baghdad receives high annual solar potential, with average global horizontal irradiation exceeding 1 800 kWh/m² per year, making it highly suitable for photovoltaic energy deployment. However, the same climatic conditions impose challenges related to thermal losses, dust accumulation and long-term system performance, which necessitate realistic modelling and conservative performance assumptions [9,11]. The geographical location of the public garden, the spatial arrangement of the PV canopy system, and the near-shading environment are illustrated in Fig. 1.

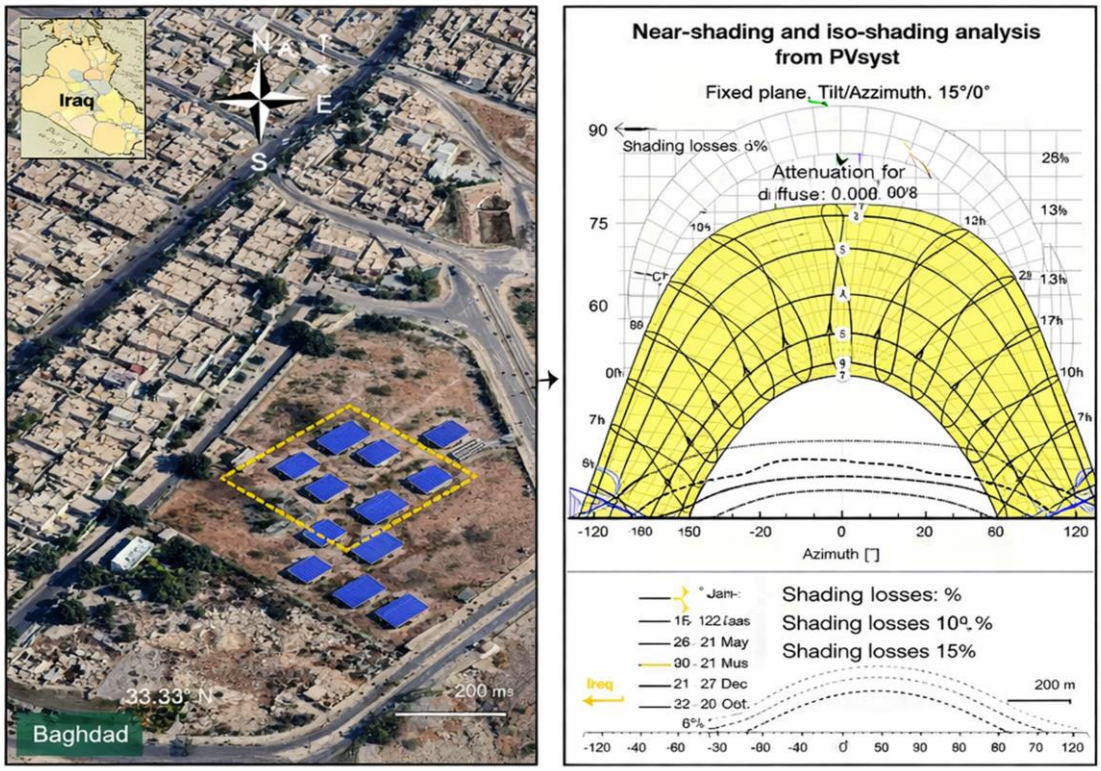


Fig. 1. Geographical location of the investigated public garden in Al-Ghazālīyah district, Baghdad, Iraq, showing the spatial layout of the PV canopy system and the corresponding near-shading and iso-shading analysis obtained from PVsyst.

2.2. Description of the PV canopy system

The photovoltaic installation is designed as a dual-use PV canopy system, where PV modules are mounted on shading structures integrated within the garden area. These canopies simultaneously provide electrical energy generation and shaded spaces for park users, thereby improving land-use efficiency and thermal comfort.

The total installed PV capacity of the system is 84.5 kWp, consisting of 128 monocrystalline PV modules, each rated at 660 Wp under standard test conditions (STC). The modules are arranged in eight strings of sixteen modules, mounted at a fixed tilt angle of 15° and an azimuth of 0°, optimised for annual energy production under local conditions. The total active module area is approximately 398 m². The structural configuration of the dual-use photovoltaic canopy system and its integration within the public garden are illustrated in Fig. 2.

Power conversion is achieved using two grid-connected inverters, each rated at 40 kWac, resulting in a direct current to alternating current (DC-to-AC) power ratio of approximately 1.06, which is consistent with best practices for minimising inverter clipping while enhancing energy yield. The system operates without battery storage and is directly connected to the national grid under a net-metering configuration.

The site characteristics and main technical specifications of the investigated grid-connected PV canopy system, including installed capacity, array configuration and inverter characteristics, are summarised in Table 1.

2.3. Irrigation load characterisation

The irrigation demand of the public garden is supplied by a single electric water pump rated at 4 horsepower (≈2.98 kW). Field inspection and operational assessment indicated that the garden requires approximately 10 000 litres of water per day, which can be delivered by operating the pump for two hours daily.

Under these operating conditions, the annual electricity consumption of the irrigation pump is approximately 2 200 kWh per year. Compared with the annual PV electricity



Fig. 2. Schematic configuration of the dual-use photovoltaic canopy system integrated within the public garden, showing the PV module arrangement, supporting structures, and the associated electrical components supplying irrigation and exporting surplus electricity to the grid.

Table 1. Site characteristics and technical specifications of the investigated grid-connected PV canopy system.

Parameter	Value	Unit
Location	Al-Ghazālīyah, Baghdad, Iraq	–
Latitude / Longitude	33.33° N / 44.27° E	–
Altitude	28	m
Climate zone	Hot-arid	–
PV system type	Grid-connected PV canopy (no storage)	–
Total installed capacity	84.5	kWp
Number of PV modules	128	units
Nominal power per module	660	Wp
PV module technology	Monocrystalline silicon	–
PV array configuration	8 strings × 16 modules	–
Tilt angle / azimuth	15° / 0°	–
Total module area	398	m^2
Number of inverters	2	units
Inverter rated power	40	kWac
Total inverter capacity	80	kWac
DC/AC ratio	1.06	–
Grid interaction	Net metering	–

production of the system, the irrigation load represents only about 1.6% of the total generated energy, allowing the majority of the PV output to be exported to the grid. This low load-to-generation ratio highlights the suitability of grid-connected operation and the economic importance of surplus energy export.

2.4. Performance modelling and simulation approach

The energy performance of the PV canopy system was evaluated using PVsyst (version 7.4.8), a widely validated simulation tool for photovoltaic system analysis. The model incorporates site-specific meteorological data derived from the Meteonorm database, including solar irradiance, ambient temperature and seasonal variability. The simulation accounts for the principal system losses, including soiling losses, thermal losses due to elevated module operating temperatures, light-induced degradation, module mismatch losses, ohmic losses in DC wiring, inverter conversion losses, and system unavailability. Near-shading effects caused by the canopy configuration were modelled using the linear shading approach implemented in PVsyst. The overall system performance was quantified using standard indicators, including annual energy yield, specific yield and performance ratio (PR).

2.5. Simplified analytical model and cross-validation approach

To complement the PVsyst-based simulation and improve methodological transparency, a simplified analytical model was developed to independently estimate the annual and monthly energy output of the PV canopy system. The analytical approach was based on the installed PV capacity, monthly solar resource and aggregate performance losses under local operating conditions.

The monthly electrical energy yield of the PV canopy system was estimated using the following simplified relationship:

$$E_m = P_r \times H_m \times PR_m, \quad (1)$$

where E_m is the monthly electrical energy output (kWh), P_r is the rated PV system capacity (kWp), H_m is the monthly in-plane solar irradiation expressed in equivalent peak-sun-hours, and PR_m is the monthly effective performance ratio. The term PR_m incorporates the main loss mechanisms affecting system operation, including thermal losses, soiling losses, mismatch losses, DC wiring losses, inverter losses and minor near-shading effects.

The simplified analytical model was implemented in a spreadsheet-based framework to provide an independent engineering cross-check of the simulation outputs. The purpose of this model is not to replace detailed photovoltaic simulation software, but rather to provide a transparent and reproducible validation tool for assessing the physical consistency of the predicted energy yield. The outputs of the analytical model were therefore compared with the PVsyst results at both monthly and annual scales in order to evaluate the agreement between the two approaches and strengthen confidence in the reported performance indicators.

To quantify the agreement between the analytical model and the PVsyst simulation, the relative deviation was calculated as follows:

$$Relative\ deviation\ (\%) = \\ = \left|E_{PVsyst} - E_{analytical}\right| / E_{PVsyst} \times 100, \quad (2)$$

where E_{PVsyst} is the monthly or annual energy yield predicted by PVsyst and $E_{analytical}$ is the corresponding value estimated by the simplified analytical model. This comparison was used to evaluate the consistency of the two approaches at both monthly and annual scales.

At the annual scale, the simplified analytical model showed a deviation of 1.51% relative to the PVsyst prediction, which indicates acceptable agreement for validation purposes under the adopted assumptions.

2.6. Techno-economic and environmental assessment methodology

The techno-economic and environmental evaluation was conducted after confirming the consistency of the PV energy output using both PVsyst simulation and the independent simplified analytical model. The economic assessment was performed using a life-cycle cost approach, considering capital investment, operation and maintenance costs, energy savings from diesel displacement and revenue from surplus electricity exported to the grid. The primary economic indicators used in this study include the levelised cost of electricity (LCOE), simple payback period, and internal rate of return (IRR). The environmental assessment focused on the reduction of greenhouse gas emissions achieved by replacing the diesel-powered irrigation system with an electrically driven pump supplied by photovoltaic energy. Carbon dioxide emission reductions were estimated using standard

emission factors associated with diesel fuel consumption and grid electricity generation [9].

2.7. Data reliability and assumptions

All system parameters, load profiles, and economic inputs were selected to reflect realistic operating conditions based on field observations, local climatic conditions and representative cost structures. Conservative assumptions were adopted where uncertainty existed in order to avoid overestimation of system performance or financial benefits. In addition, the simplified analytical model was intentionally formulated as an independent cross-check tool rather than a substitute for detailed PV simulation. This approach improves methodological transparency while maintaining consistency with the technical assumptions used in the PVsyst-based analysis.

3. Energy performance results and loss analysis

3.1. Annual energy yield and system productivity

The PV canopy system exhibits a high annual energy yield despite operating under hot-arid climatic conditions. The simulated annual electricity production reaches 133 189 kWh, corresponding to a specific yield of 1 577 kWh/kWp per year. This value is notably high for an urban installation and reflects the favourable solar resource of Baghdad combined with appropriate system sizing and orientation. The calculated performance ratio (PR) of 79.6% indicates efficient conversion of available solar irradiation into usable electrical energy, even when accounting for thermal losses, soiling and inverter inefficiencies. Such a PR value is comparable to, and in some cases higher than, those reported for PV systems operating in temperate climates, confirming the technical viability of PV installations in hot-arid urban environments when proper design practices are applied.

3.2. Monthly energy production profile

Monthly energy generation follows the expected seasonal solar irradiation pattern. Peak electricity production occurs between May and August, coinciding with maximum global horizontal irradiation and extended daylight hours. During this period, monthly energy output exceeds 13 MWh, with the highest contribution recorded in June and July. Lower production values are observed during winter months, particularly in December and January, due to reduced solar irradiance and shorter daylight duration. Nevertheless, even during these months, the system maintains stable operation and sufficient energy availability to fully cover the irrigation load. The consistency of the monthly production profile demonstrates the robustness of the canopy-mounted configuration against seasonal variability. A detailed month-by-month and annual energy balance of the investigated PV canopy system, including irrigation demand and surplus electricity exported to the grid, is presented in Table 2. A comparison between the monthly photovoltaic electricity generation and the irrigation energy demand is presented in Fig. 3, clearly showing that the irrigation load represents only a small fraction of the total PV production throughout the year.

Table 2. Monthly and annual energy balance of the investigated PV canopy system, irrigation demand, and surplus electricity exported to the grid.

Month	PV energy production, kWh	Irrigation energy demand, kWh	Energy exported to grid, kWh
January	9 139	187	8 952
February	9 209	169	9 040
March	11 725	187	11 538
April	13 224	181	13 043
May	13 831	187	13 644
June	14 648	181	14 467
July	14 322	187	14 135
August	13 246	187	13 059
September	12 522	181	12 341
October	10 324	187	10 137
November	8 772	181	8 591
December	8 138	187	7 951
Total (annual)	**133 189**	**2 200**	**130 989**

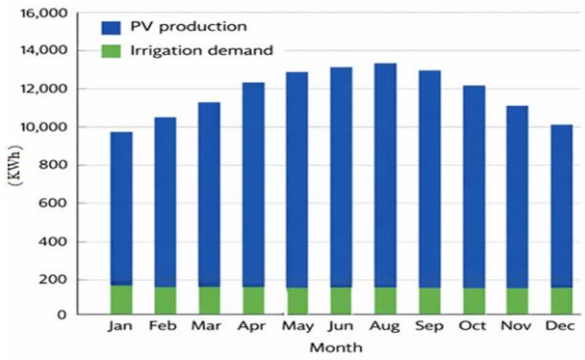


Fig. 3. Monthly photovoltaic electricity generation and irrigation energy demand of the investigated public garden, illustrating the large surplus electricity available for grid export throughout the year.

3.3. Load coverage and surplus energy export

The annual electricity demand of the irrigation system, estimated at 2 200 kWh, represents only approximately 1.6% of the total PV production. As a result, the system operates predominantly as an electricity-exporting installation, with more than 130 MWh per year of surplus energy injected into the national grid.

This pronounced mismatch between generation capacity and irrigation demand is intentional and reflects the dual-function design philosophy of the system. Rather than sizing the PV system solely to match the irrigation load, the canopy installation is optimised to maximise land-use efficiency and grid support while still fully satisfying local energy needs. From an operational standpoint, the irrigation load is entirely supplied by solar-generated electricity during daytime hours, while grid interaction ensures uninterrupted operation under all conditions.

3.4. Loss analysis and performance breakdown

A detailed loss analysis reveals the dominant mechanisms affecting system performance. Thermal losses constitute the larg-

est contribution, accounting for approximately 8.4% of the total energy reduction, which is consistent with the high ambient temperatures characteristic of Baghdad's climate. Soiling losses are estimated at 3%, reflecting conservative assumptions for dust accumulation under regular maintenance conditions.

Additional losses include light-induced degradation (approximately 2%), module mismatch losses (2%) and ohmic losses in DC cabling (approximately 1%). Inverter-related losses remain limited to around 2%, highlighting the suitability of the selected inverter configuration and DC-to-AC sizing ratio. Near-shading losses associated with the canopy geometry are negligible, contributing less than 0.3% to the overall energy reduction.

The cumulative impact of these losses results in an effective energy output that remains high relative to the available solar resource, confirming that no single loss mechanism critically undermines system performance. The key energy performance indicators and principal loss contributions affecting the investigated PV canopy system are summarised in Table 3.

Table 3. Key energy performance indicators and principal loss contributions of the investigated PV canopy system.

Indicator	Value	Unit
Annual energy production	133 189	kWh per year
Specific yield	1 577	kWh/kWp per year
Performance ratio (PR)	79.6	%
Global horizontal irradiation	1 818	kWh/m² per year
Effective irradiation on collectors	1 876	kWh/m² per year
Near-shading losses	0.26	%
Soiling losses	3.0	%
Thermal losses	8.36	%
Inverter losses	2.01	%
System availability	97.8	%

The contribution of the main loss mechanisms affecting the annual energy yield of the PV canopy system is summarised in the loss diagram presented in Fig. 4.

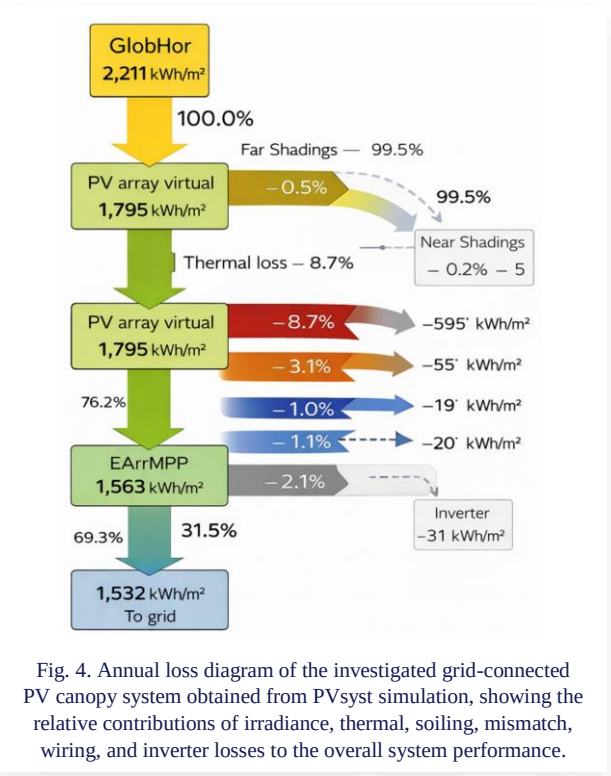


Fig. 4. Annual loss diagram of the investigated grid-connected PV canopy system obtained from PVsyst simulation, showing the relative contributions of irradiance, thermal, soiling, mismatch, wiring, and inverter losses to the overall system performance.

3.5. Cross-validation of PVsyst results using the simplified analytical model

To assess the robustness of the simulation results, the annual and monthly PV energy outputs predicted by PVsyst were independently cross-checked using the simplified analytical model described in Section 2.5. The analytical model reproduced the same seasonal production trend observed in the software simulation, with peak generation during late spring and summer and lower output during winter months.

At the annual scale, the analytical estimation showed acceptable agreement with the PVsyst result, with a total annual deviation of 1.51%. This indicates that the predicted energy yield is physically reasonable for the installed capacity, local solar resource and assumed loss conditions of the Baghdad site. Minor monthly deviations between the two approaches are expected because PVsyst incorporates more detailed sub-models related to thermal behaviour, incidence-angle effects and inverter operation, whereas the simplified analytical model applies aggregate monthly correction factors.

Overall, the comparison demonstrates that the reported performance indicators are not solely dependent on commercial software output, but are also supported by an independent engineering calculation framework. The simplified analytical model reproduced the same overall seasonal behaviour and annual performance trend obtained from PVsyst, and the annual deviation between the two approaches was limited to 1.51%, confirming the physical consistency of the predicted system output under the adopted operating assumptions. A detailed month-by-month comparison between the PVsyst predictions and the simplified analytical model estimates is presented in Table 4.

Note: The simplified analytical estimates were derived using monthly solar-resource inputs and aggregate loss assumptions to provide an independent engineering cross-check of the PVsyst results. The analytical model is intended for validation and transparency purposes rather than as an exact replacement for the detailed PVsyst simulation.

3.6. Reliability under hot-arid operating conditions

Operating in a hot-arid urban environment imposes challenges related to elevated module temperatures, dust exposure and prolonged summer operation. Despite these constraints, the system demonstrates stable performance indicators across the annual cycle. The acceptable agreement between PVsyst and the simplified analytical model, with an annual deviation of only 1.51%, further strengthens confidence in the reliability of the reported performance indicators under hot-arid operating conditions. The absence of battery storage also enhances system reliability by eliminating one of the most failure-prone components

in photovoltaic systems. The results indicate that grid-connected PV canopy systems can achieve high energy productivity and operational stability in extreme climates, provided that appropriate assumptions regarding losses and maintenance are incorporated into the design stage.

Table 4. Month-by-month comparison between PVsyst predictions and simplified analytical model estimates for the investigated PV canopy system.

Month	PVsyst energy, kWh	Analytical model energy, kWh	Absolute deviation, kWh	Relative deviation, %
January	9 139	8 152	987	10.80
February	9 209	8 643	566	6.14
March	11 725	10 883	842	7.18
April	13 224	12 524	700	5.29
May	13 831	13 372	459	3.32
June	14 648	13 614	1 034	7.06
July	14 322	13 654	668	4.66
August	13 246	13 304	58	0.44
September	12 522	12 417	105	0.84
October	10 324	9 639	685	6.64
November	8 772	8 024	748	8.52
December	8 138	6 948	1 190	14.62
Annual total	**133 189**	**131 174**	**2 015**	**1.51**

3.7. Summary of performance findings

Overall, the combined PVsyst simulation and independent analytical cross-validation confirm that the investigated PV canopy system not only satisfies the local irrigation demand with a large safety margin, but also functions as a significant distributed generation asset. The analytical model reproduced the seasonal and annual performance trends obtained from PVsyst, with an annual deviation of only 1.51%, supporting the physical consistency of the reported energy yield. The combination of high specific yield, favourable performance ratio and substantial surplus electricity export establishes the system as an effective model for integrating renewable energy into urban green infrastructure under hot-arid climatic conditions.

4. Techno-economic assessment

4.1. Economic framework and assumptions

The techno-economic evaluation of the proposed PV canopy system was conducted using a life-cycle cost approach that reflects realistic operating conditions and local market parameters. Capital expenditure includes PV modules, inverters, mounting structures, electrical accessories, and installation costs, while operational expenditure accounts primarily for routine maintenance and system supervision. In line with common practice for grid-connected PV systems without storage, annual operation and maintenance costs were assumed to be modest due to the absence of batteries and rotating mechanical components. All economic calculations were performed using conservative assumptions to avoid overestimation of financial benefits. Electricity tariffs, fuel prices and emission factors were selected based on prevailing local values and recent studies conducted under Iraqi climatic and economic conditions [9,11,16]. For clarity and international readability, selected monetary values originally expressed in Iraqi dinars (IQD) are also reported in equivalent U.S. dollars (USD) using a consistent representative exchange rate. An exchange rate of 1 USD = 1300 IQD was adopted for indicative currency conversion throughout the analysis.

4.2. Cost of electricity and competitiveness

The levelised cost of electricity (LCOE) produced by the PV canopy system was estimated at approximately 44 IQD/kWh (≈ 0.034 USD/kWh), considering the total life-cycle cost over an assumed system lifetime of 25 years. This value is significantly lower than the prevailing commercial electricity tariff of approximately 120 IQD/kWh (≈ 0.092 USD/kWh), indicating a cost reduction of nearly 63% per unit of delivered electricity.

This substantial difference highlights the economic advantage of photovoltaic energy in high-irradiance regions, particularly when systems are designed to operate without storage and are allowed to export surplus electricity to the grid. From a municipal perspective, such a reduction directly translates into long-term budgetary relief and improved energy cost predictability.

4.3. Diesel displacement and operating cost savings

Prior to PV system implementation, irrigation was supplied by a diesel-powered pump, characterised by high fuel consumption, frequent maintenance requirements, and sensitivity to fuel price fluctuations. Replacing this system with an electrically driven pump powered by solar-generated electricity results in immediate and sustained operating cost savings.

For the investigated case, the annual irrigation energy demand of 2 200 kWh is fully covered by PV generation, effectively eliminating diesel fuel consumption for irrigation purposes. The avoided cost of diesel fuel constitutes a significant portion of the annual savings, particularly when accounting for indirect costs associated with fuel transport, storage, and engine maintenance. These findings are consistent with previous studies demonstrating the economic vulnerability of diesel-based irrigation systems in comparison with solar-powered alternatives [6,7].

4.4. Revenue from surplus electricity export

A defining feature of the investigated system is the large surplus of electricity available for export to the national grid. Because the irrigation demand accounts for only a small fraction of the annual PV output, more than 130 MWh per year of electricity can be delivered to the grid under the adopted grid-connected operating scheme. This exported energy represents an important economic advantage of the system, as it improves overall electricity utilisation and enhances the financial value of the installation beyond its direct irrigation function. Unlike stand-alone systems, where excess generation may remain underutilised, the

grid-connected configuration enables productive use of the surplus electricity and strengthens the economic case for dual-use PV canopy deployment in urban public spaces.

4.5. Payback period and investment attractiveness

Based on the combined effects of reduced diesel dependence, lower electricity costs, and the economic value of surplus electricity export, the investigated PV canopy system achieves a simple payback period of approximately 6 years. This value falls within a practically acceptable range for municipal renewable energy investments and leaves a substantial portion of the system lifetime available for net economic benefit. The calculated internal rate of return (IRR) of approximately 18% further confirms the financial attractiveness of the project. These indicators show that the proposed system is not only environmentally beneficial, but also economically competitive as a long-term urban infrastructure investment.

4.6. Economic robustness and long-term perspective

One of the principal strengths of the investigated PV canopy system is its resilience to future economic uncertainty. In contrast to diesel-based irrigation systems, which remain highly sensitive to fuel price volatility and recurrent operating costs, the photovoltaic system is characterised by comparatively stable long-term operating expenses. This economic robustness becomes more pronounced when surplus electricity can be productively exported to the grid under a grid-connected operating scheme. In addition, the dual-use canopy configuration provides non-energy benefits, including shading and improved usability of public space, which further strengthen the overall value proposition of the system from a municipal planning perspective.

4.7. Summary of techno-economic findings

The techno-economic assessment confirms that the investigated PV canopy system represents a financially viable solution for urban irrigation in hot-arid regions. The combination of low electricity cost, productive utilisation of surplus generation through grid export, acceptable payback period, and favourable internal rate of return demonstrates that the system can deliver long-term economic value in addition to its environmental and functional benefits. The main techno-economic and environmental indicators of the investigated PV canopy system are summarised in Table 5.

Table 5. Main techno-economic and environmental indicators of the investigated PV canopy system.

Parameter	Value	Unit
System lifetime	25	years
Levelised cost of electricity (LCOE)	44 (≈ 0.034)	IQD/kWh (USD/kWh)
Commercial electricity tariff	120 (≈ 0.092)	IQD/kWh (USD/kWh)
Cost reduction compared to grid	63	%
Simple payback period	≈ 6	years
Internal rate of return (IRR)	≈ 18	%
Annual diesel fuel displacement	Fully eliminated	–
Annual CO_2 emission reduction	113	tonnes
Annual surplus energy exported	≈ 131	MWh

5. Environmental impact and CO_2 mitigation

5.1. Emission reduction through diesel replacement

The environmental benefits of the PV canopy system are primarily associated with replacing the previous diesel-powered irrigation supply with an electrically driven pump supported by photovoltaic energy. Diesel-based irrigation systems are a notable source of greenhouse gas emissions due to continuous fuel combustion and relatively low overall efficiency. In the investigated case, the transition to photovoltaic energy effectively eliminates diesel use for irrigation purposes.

Based on the adopted diesel displacement and grid-related emission assumptions, the avoided diesel fuel consumption corresponds to an estimated annual reduction of approximately 113 tonnes of CO_2. This reduction is achieved without compromising irrigation reliability or water delivery, highlighting the effectiveness of photovoltaic systems as a direct decarbonisation measure for urban service infrastructure. The environmental benefit of replacing diesel-powered irrigation with photovoltaic-powered irrigation is illustrated in Fig. 5, showing a substantial reduction in annual CO_2 emissions.

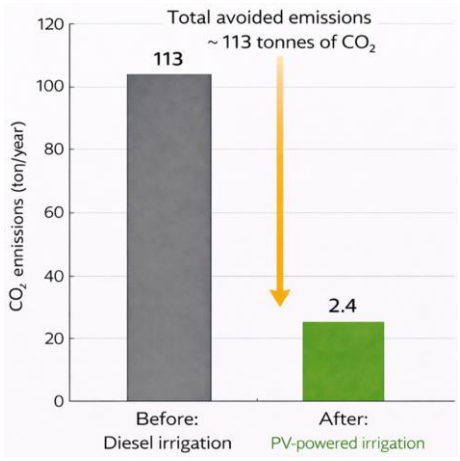


Fig. 5. Comparison of annual CO_2 emissions associated with diesel-based irrigation and photovoltaic-supported electric irrigation for the investigated public garden.

5.2. Contribution to grid decarbonisation

In addition to reducing local emissions through diesel displacement, the investigated PV canopy system contributes to grid decarbonisation by exporting more than 130 MWh per year of surplus solar electricity under the adopted grid-connected operating scheme. This exported electricity can offset part of the fossil-fuel-based generation that would otherwise be required to meet daytime demand. Although the carbon intensity of the national

grid may vary over time, the cumulative contribution of distributed photovoltaic generation remains environmentally significant, particularly in high-irradiance regions where daytime solar production is substantial. Accordingly, the environmental value of the system extends beyond the boundaries of the public garden itself and supports broader urban decarbonisation efforts.

5.3. Water–energy–climate co-benefits

The PV canopy configuration provides additional co-benefits that extend beyond direct electricity generation and carbon emission reduction. By functioning as shading structures within the public garden, the canopies can help reduce surface temperatures and limit direct solar exposure of soil and vegetation during peak summer conditions. This shading function may contribute to reduced evapotranspiration and improved local water-use efficiency, although these effects were not quantified in the present study. In addition, the integration of renewable energy generation into urban green spaces can support climate adaptation strategies by improving thermal comfort for users and enhancing the multifunctional value of public infrastructure.

5.4. Environmental significance at an urban scale

Although the present analysis focuses on a single public garden, the broader environmental implications become more significant when similar PV canopy systems are deployed across multiple urban parks and green spaces. Replication of this concept at the city scale could lead to cumulative reductions in diesel use, lower dependence on fossil-fuel-based electricity, and measurable decreases in urban carbon emissions. In addition to these direct energy-related benefits, wider deployment of PV canopies could support more climate-responsive urban infrastructure by combining renewable electricity generation with shading and improved public-space functionality. These considerations indicate that the environmental significance of the proposed system extends beyond the individual case study and may inform sustainable urban planning strategies in hot-arid cities.

6. Discussion

6.1. Comparison with existing studies

The performance indicators obtained in this study, particularly the specific yield of 1 577 kWh/kWp per year and the performance ratio of 79.6%, are consistent with, and in some cases superior to, values reported for PV systems operating in comparable hot-arid regions. Unlike many previous studies that focused mainly on ground-mounted or rooftop PV systems, the present work demonstrates that canopy-mounted configurations integrated into public urban spaces can achieve high productivity despite structural and near-shading constraints. In addition, the present study does not rely solely on commercial software output, as the PVsyst results were independently cross-checked using a simplified analytical model. This additional validation step improves the methodological transparency of the analysis and strengthens confidence in the reported energy performance trends. In particular, the annual deviation between the PVsyst output and the simplified analytical model was limited to 1.51%, indicating acceptable agreement between the two approaches for engineering validation purposes. From an economic standpoint, the reported LCOE of 44 IQD/kWh (≈ 0.034 USD/kWh) and payback period of approximately 6 years compare favourably with other solar irrigation solutions, particularly off-grid systems that rely on battery storage. The absence of storage not only reduces costs but also improves long-term reliability, which is a critical consideration for municipal infrastructure.

6.2. Design philosophy and system sizing

A key design insight emerging from this study is the deliberate oversizing of the PV canopy system relative to the direct irrigation load. Rather than minimising the installed PV capacity to match only the local pumping demand, the system was configured to maximise the functional value of the available urban space through simultaneous electricity generation, shading provision and grid interaction. This design philosophy differs from conventional solar irrigation configurations, which are typically sized to satisfy a specific agricultural or pumping load with limited consideration of broader urban functionality. In the investigated case, the relatively small irrigation demand enables most of the generated electricity to be exported to the grid, thereby improving the economic value of the installation while preserving its primary service role within the public garden. This multi-objective sizing strategy demonstrates that PV canopy systems can be planned not only as energy supply units, but also as integrated urban infrastructure assets.

6.3. Practical implications for municipalities

For municipalities in hot-arid regions, the results highlight a practical pathway for reducing dependence on diesel-based irrigation without introducing significant operational complexity. Grid-connected PV canopy systems offer predictable energy costs, minimal maintenance requirements and measurable environmental benefits while simultaneously improving the functional quality of public spaces through shading. In addition to supplying local irrigation demand, such systems can contribute surplus electricity to the grid, thereby enhancing the economic value of municipal solar investments. Importantly, the dual-use nature of the canopy installation may improve public acceptance by combining visible social benefits with clean energy generation. These features make PV canopy systems a promising option for sustainable urban green infrastructure planning in cities with high solar potential.

6.4. Limitations and future research

While the present study provides a comprehensive assessment based on detailed simulation and realistic operational assumptions, future work could extend the analysis through long-term monitoring of actual system performance under field conditions. Further research may also quantify microclimatic effects, water-saving potential and user comfort improvements associated with canopy shading, thereby strengthening the interdisciplinary value of such systems. Another limitation is that the independent analytical model was intentionally formulated as a simplified cross-check tool for validation purposes rather than as a repla-

cement for detailed dynamic PV simulation software. Nevertheless, its agreement with the PVsyst results, reflected by an annual deviation of only 1.51%, improves confidence in the physical consistency of the reported energy performance indicators.

7. Conclusions

This study evaluated the energy performance, techno-economic feasibility, and environmental impact of a grid-connected photovoltaic canopy system implemented for urban irrigation in a hot-arid climate using both detailed PVsyst simulation and an independent simplified analytical cross-check model. Based on a real public garden case in Baghdad, the system demonstrates high annual energy productivity, with 133 189 kWh per year of electricity generation, a specific yield of 1 577 kWh/kWp per year, and a performance ratio of 79.6%.

The irrigation load, accounting for only 1.6% of total PV production, is fully supplied by solar electricity, while the majority of generated energy is exported to the national grid. Economic analysis confirms the competitiveness of the system, with a levelised cost of electricity of 44 IQD/kWh (≈ 0.034 USD/kWh), a payback period of approximately 6 years, and an internal rate of return of about 18%. Environmentally, the system achieves an estimated annual reduction of approximately 113 tonnes of CO_2, primarily through diesel fuel displacement and grid support.

The close agreement between the software-based simulation and the independent analytical estimation enhances confidence in the reported results and improves the methodological transparency of the study. In particular, the annual deviation between the PVsyst prediction and the simplified analytical model was limited to 1.51%, confirming acceptable agreement between the two approaches for validation purposes. Overall, the findings demonstrate that PV canopy systems represent a technically reliable, economically viable, and environmentally effective solution for integrating renewable energy into urban green infrastructure. Beyond irrigation, such systems provide a scalable model for multifunctional solar deployment in hot-arid cities, supporting sustainable urban development and long-term decarbonisation strategies.

References

[1] International Energy Agency. (2023). *World energy outlook, 2023*. IEA Reports.

[2] Food and Agriculture Organization of the United Nations. (2011). *Energy-smart food for people and climate*. FAO.

[3] United Nations. (2022). *The sustainable development goals report 2022*. Department of Economic and Social Affairs, United Nations.

[4] Mekhilef, S., Saidur, R., & Safari, A. (2011). A review on solar energy use in industries. *Renewable and Sustainable Energy Reviews*, 15(4), 1777–1790. doi: 10.1016/j.rser.2010.12.018

[5] Burney, J., Woltering, L., Burke, M., Naylor, R., & Pasternak, D. (2010). Solar-powered drip irrigation enhances food security in the Sudano–Sahel. *Proceedings of the National Academy of Sciences of the United States of America*, 107(5), 1848–1853. doi: 10.1073/pnas.0909678107

[6] Closas, A., & Rap, E. (2017). Solar-based groundwater pumping for irrigation: Sustainability, policies, and limitations. *Energy Policy*, 104, 33–37. doi: 10.1016/j.enpol.2017.01.05.

[7] Chandel, S.S., Naik, M.N., & Chandel, R. (2015). Review of solar photovoltaic water pumping system technology for irrigation and community drinking water supplies. *Renewable and Sustainable Energy Reviews*, 49, 1084–1099. doi: 10.1016/j.rser.2015.04.083

[8] El-houari, H., Allouhi, A., Rehman, S., Buker, M.S., Kousksou, T., Jamil, A., & El Amrani, B. (2019). Design, simulation, and economic optimization of an off-grid photovoltaic system for rural electrification. *Energies*, 12(24), 4735. doi: 10.3390/en12244735

[9] Obaid, A.H., Mahdi, E.J., Hassoon, I.A., Hussein, F.H., Jasim, A.A.A.-S., Jafar, A.N., & Abdulghani, A.S. (2024). Evaluation of degradation factor effect on solar panels performance after eight years of life operation. *Archives of Thermodynamics*, 45(3), 221–226. doi: 10.24425/ather.2024.151708

[10] Jordan, D.C., & Kurtz, S.R. (2013). Photovoltaic degradation rates—An analytical review. Progress in Photovoltaics: *Research and Applications*, 21(1), 12–29. doi: 10.1002/pip.1182

[11] Mahdi, E.J., Hussein, H.F., Hassoon, I.A., & Jasim, A.A.-A. (2025). Analysis of solar panel surface thermal distribution using thermal imaging. *Journal of Renewable Energy and Environment*, 12(4), 74–80. doi: 10.30501/jree.2025.495645.2207

[12] Hasoon, I.A., Inad, K.I., Mahdi, E.J., & Hussein, H.F. (2025). Design and performance evaluation of an off-grid photovoltaic system for metallurgical laboratories. *Journal of the Minerals, Metals & Materials Society*, 77(12), 10158− 10164. doi: 10.1007/s11837-025-07867-1

[13] Barron-Gafford, G.A., Pavao-Zuckerman, M.A., Minor, R.L., Sutter, L.F., Barnett-Moreno, I., Blackett, D.T., Thompson, M., Dimond, K., Gerlak, A.K., Nabhan, G.P., & Macknick, J.E. (2019). Agrivoltaics provide mutual benefits across the food–energy–water nexus in drylands. *Nature Sustainability*, 2(9), 848–855. doi: 10.1038/s41893-019-0364-5

[14] Malu, P.R., Sharma, U.S., & Pearce, J.M. (2017). Agrivoltaic potential on grape farms in India. *Sustainable Energy Technologies and Assessments*, 23, 104–110. doi: 10.1016/j.seta.2017.08.004

[15] Dinesh, H., & Pearce, J.M. (2016). The potential of agrivoltaic systems. *Renewable and Sustainable Energy Reviews*, 54, 299−308. doi: 10.1016/j.rser.2015.10.024

[16] Hussein, H.F., Druga, L., Cojocaru, M., Dumitru, C., & Ghinea, A. (2018). Predicting and monitoring eutectic carbides proportion in cast austenitic Cr–Ni stainless steels. *UPB Scientific Bulletin, Series B*, 80(4), 169–180.

[17] Hussein, H.F., Druga, L., Cojocaru, M., Dumitru, C., & Ghinea, A. (2020). The structural evolution of refractory steel spare parts during the successive carburizing. *UPB Scientific Bulletin, Series B*, 82(1), 247–257.

[18] Mahdi, E.J., Hussein, H.F., & Saeed, F.R. (2025). Thermal performance comparison of aluminum and iron alloys in heat exchangers for solar water heating systems. *Next Materials*, 8, 100935. doi: 10.1016/j.nxmate.2025.100935

[19] Saeed, F., Abdulkader, J. & Hussein, H. (2025). Advance analysis of aluminum alloy welded joints microstructure. *Discover Materials*, 6, 27. doi: 10.1007/s43939-025-00491-5

Co-published by
Institute of Fluid-Flow Machinery
Polish Academy of Sciences
Committee on Thermodynamics and Combustion
Polish Academy of Sciences

Copyright©2026 by the Authors under licence CC BY-NC-ND 4.0

http://www.imp.gda.pl/archives-of-thermodynamics/

Numerical investigation of heat transfer in a partially porous-filled channel with core and wall configurations

Tuba Fatima[a], Saurabh Patel[b*]

[a]Indian Institute of Technology Mandi, Kamand, Mandi 175075, India
[b]Indian Institute of Technology Bombay, Powai, Mumbai 400076, India
*Corresponding author email: saurabhpatel015@gmail.com

Received: 30.05.2025; revised: 29.06.2025; accepted: 30.06.2026

Abstract

The numerical simulations are carried out for analysis of heat transfer enhancement in the partially filled channel with the horizontal porous layer, considering two different configurations: at the core and at the walls of the channel. The Darcy-Brinkman-Forchheimer equation is used to model flow through the porous medium, and the governing equations are solved using a finite volume method. The study investigates the effect of the porous layer thickness, thermal conductivity and Darcy number on heat transfer performance and pressure drop. The detailed parametric analysis quantifies variations in the Nusselt number and pressure drop for both configurations. The study reveals that the pressure drop is consistently lower for porous layers located at the channel walls compared to the core for all Darcy numbers. The Nusselt number increases by up to 88% as the porous layer thickness ratio rises to 0.8, then decreases by approximately 19.5% at a lower thermal conductivity ratio of 2.5, but continues to rise at a higher ratio of 25. Increasing the thermal conductivity ratio to 25 improves the Nusselt number by up to 80.5% compared to a ratio of 2.5. Additionally, for lower Darcy numbers (up to 10^{-4}), the higher Nusselt number is achieved when the porous layer is located at the core. However, for higher Darcy numbers (above 10^{-3}), the Nusselt number is higher when the porous layer is at the walls. The results reveal that the position of the porous layer within the channel significantly affects its thermal and hydrodynamic performance.

Keywords: Channel flow; Darcy number; Heat transfer; Porous media; Pressure drop

Vol. 47(2026), No. 3, 89–98; doi: 10.24425/ather.2026.3658

Cite this manuscript as: Fatima, T., & Patel, S. (2026). Numerical investigation of heat transfer in a partially porous-filled channel with core and wall configurations. *Archives of Thermodynamics*, 47(3), 89–98.

1. Introduction

Heat management in electronic components has become challenging due to technological advancement and miniaturisation. As conventional cooling methods are becoming obsolete, researchers are exploring alternative cooling technologies. The integration of porous materials into channels has shown great potential for enhancing heat transfer rates, with significant applications in electronic thermal management. The insertion of porous media in fluid channels modify the flow dynamics, resulting in reduced boundary layer thickness and enhanced heat transfer. Therefore, a detailed investigation of the heat transfer analysis is required for the optimal design of a channel containing porous inserts.

Heat transfer enhancement is crucial for improving the thermal performance of various industrial systems, including heat exchangers, cooling systems and electronic devices. The heat enhancement techniques are vital for sustainability and are categorised as either passive technique (e.g. porous inserts, nanofluids, turbulators), which require no extra energy, or active technique (e.g. magnetic fields, external pumps). Passive techniques are typically preferred for their low energy demands, offering a more sustainable alternative for improving heat transfer and flow without consuming large amounts of energy, which is increasingly important for energy-conscious industries.

Nomenclature

C – inertial coefficient
C_p – specific heat, J/(kg K)
Da – Darcy number
F – Forchheimer coefficient
g – gravitational acceleration, m/s^2
H – channel height, m
k – thermal conductivity, W/(m K)
k_r – thermal conductivity ratio
K – permeability, m^2
Nu – Nusselt number
p – pressure, Pa
Pr – Prandtl number
q'' – heat flux, W/m^2
r – porous layer thickness, m
r_p – porous layer thickness ratio
Re – Reynolds number
T – temperature, K
u – velocity in x-direction, m/s
$\vec{v}$ – velocity vector, m/s
x, y – Cartesian coordinates, m

Greek symbols

ε – porosity
θ – non-dimensional temperature
μ – dynamic viscosity, Pa·s
ρ – density, kg/m^3

Subscripts and Superscripts

c – core
e – effective
in – inlet
m – bulk mean
w – wall

The use of nanofluids, turbulators and porous inserts has been extensively studied in the literature as effective methods for enhancing heat transfer in various cooling systems. The details of these techniques, along with their performance metrics, working conditions and applications, are summarised in Table 1. Said et al. [1] presented a comprehensive review of passive heat transfer enhancement techniques employing nanofluids and turbulators. Alenezi et al. [2] experimentally investigated the effect of ultrasonic waves on heat transfer enhancement using the propylene glycol/water nanofluid in the minichannel. Their results showed that ultrasound at 27.8 kHz improved heat transfer, achieving a maximum Nusselt number increase of 11.3% for deionised water at the lowest flow rate (0.2 l/min). Although the study demonstrates the potential of active methods, the energy demand limits their applicability in low-power systems. The use of porous media is a well-established method for heat transfer enhancement, primarily due to its high surface area-to-volume ratio and ability to promote flow mixing. Hadim and Bethancourt [3] identified that full porous fills lead to prohibitive pressure drops, suggesting partial filling as a solution. Subsequent studies, such as Baig et al. [4], have continued this approach, often combining porous inserts with other methods like nanofluids. While the nanofluids and turbulators have been widely investigated, porous inserts have also shown more effective heat transfer enhancement while maintaining relatively low pressure drops and requiring no additional energy input. Owing to these advantages, porous materials represent an efficient and practical passive technique, motivating the present study to focus specifically on porous inserts for further investigation.

The study of heat transfer in porous channels or pipes, particularly under conditions such as constant wall temperature, constant heat flux and discrete heat sources, has received significant attention in recent research in the literature [3–9]. Several investigations have focused on understanding how these thermal boundary conditions influence flow behaviour and heat transfer in porous media. Hadim and Bethancourt [3] also investigated the parametric variation of heat source width in a channel and revealed that when the width of the heat source decreases, a significant increase in the heat transfer occurs and reduces the pressure drop. Hadim et al. [9] investigated the effect of discrete heat sources on the bottom wall of the porous channel using two different cases: full and partial porous channels. The results show the same heat transfer in both cases at low Darcy number and higher pressure drop in fully porous channels. Jen and Yan [10] proposed a 3D model to investigate the flow patterns in partially filled porous media. They revealed that strong counter rotating vortices are present in the channel because of the blowing effect of the porous layer. Hadim and North [11] investigated the effect of multiple inlet and outlet in a porous channel with a constant heat flux condition at the bottom wall. They observed that the pressure drop is minimised when the channel height equals the inlet width, while maintaining the same level of heat transfer enhancement. They also proposed the length-averaged correlation for the Nusselt number.

The use of porous materials in channels has been widely analysed with respect to its effects on flow behaviour, temperature change and pressure drop. Rachedi and Chikh [12] examined mixed convection heat transfer between a channel and an electronic component, inserting a porous material between the two. They demonstrated that at lower thermal conductivity ratios (up to 2), the effect on temperature drop is minimal. However, at higher thermal conductivity ratios (from 2 to 10), a temperature drop of 15% can be achieved. Yucel and Guven [13] studied forced convection heat transfer in parallel plates with multiple heat sources. They observed a significant rise in pressure drop with increasing Reynolds numbers in the presence of a porous layer. Huang et al. [14] investigated the effect of a porous cover on heat transfer enhancement in a channel using multiple heat sources. They revealed that the presence of a porous cover significantly enhances heat transfer compared to a setup without it. Da Silva Miranda and Anand [15] explored the role of porous baffles in enhancing convective heat transfer within channels. They found that a smaller spacing between the baffles results in better heat transfer performance, and that an increase in the

Table 1: Summary of important studies in heat transfer enhancement for channel/internal flows.

Authors	Geometry	Working fluid	Applications	Key findings
Alenezi et al. [2]	Minichannel	Propylene glycol/ water mixtures	Minichannel heat sinks, electronics cooling	1. Ultrasound (27.8 kHz) enhanced heat transfer, with a maximum Nusselt number increase of 11.3% for deionised water at the lowest flow rate (0.2 l/min).
Hadim and Bethancourt [3]	Porous channel	Dielectric fluid	Electronic cooling	1. A partially porous channel (porous layers only above heaters) achieves comparable heat transfer to a fully porous channel but with a much lower pressure drop. 2. Decreasing heat source width moderately improves heat transfer while significantly reducing pressure drop.
Baig et al. [4]	Microchannel	Al_2O_3-water nanofluid	Microchannel cooling, electronics thermal management	1. Finned cooking vessels significantly improve thermal performance and cooking rate compared to an unfinned vessel. 2. Hexagonal fins performed best, reducing boiling time by 13.63% and increasing maximum energy efficiency to 64.46%. 3. An economic analysis showed the hexagonal fin-based cooker could save up to 1495 MJ of fuel equivalent per year.
Promvonge [5]	Square duct with combined 30° V-fins and quadruple counter-twisted tapes	Air	Heat exchangers	1. The combined V-finned twisted tapes provide higher heat transfer and thermal performance than twisted tapes alone. 2. Heat transfer and friction factor increase with relative fin height but decrease with relative fin pitch.
Kalidasan et al. [6]	Solar box cooker with different fin configurations (pin, cross, hexagonal) on the cooking vessel	Water	Solar cooking	1. The fully wavy wall microchannel significantly enhances heat transfer, with a Nusselt number up to 3.87 times higher and thermal resistance only 0.41 times that of a smooth microchannel. 2. The flow becomes chaotic, intensifying fluid mixing and heat transfer with a relatively small pressure drop penalty.
Zhong et al. [7]	Square cross-section microchannel with fully wavy walls (all four sides)	Deionised water	Microchannel heat sinks for electronic cooling	1. The fully wavy wall microchannel significantly enhances heat trans-fer, with a Nusselt number up to 3.87 times higher and thermal resistance only 0.41 times that of a smooth microchannel. 2. The flow becomes chaotic, intensifying fluid mixing and heat transfer with a relatively small pressure drop penalty.
Mohammed et al. [8]	2D rib-groove channel (9 combinations of rectangular, triangular, trapezoidal ribs and grooves)	Nanofluids (Al_2O_3, CuO,SiO_2, ZnO with water, glycerin, engine oil)	Heat exchangers, turbine cooling, solar heaters	1. Rectangular rib-triangular groove provided the highest Nusselt number and best thermal enhancement factor. 2. SiO_2 nanofluid showed the highest heat transfer performance, despite its moderate conductivity, due to favourable thermophysical properties.

thermal conductivity ratio enhances heat transfer. Ko and Anand [16] also examined the effect of porous baffles on convective heat transfer in a channel, with the baffles installed alternately at the top and bottom walls. They revealed a 300% enhancement in heat transfer with baffles compared to the channel without them. Additionally, they developed a correlation between the ratio of heat transfer enhancement and the Reynolds number. Kim et al. [17] investigated the effect of porous material in a channel. They developed a correlation for the Nusselt number, specifically for Reynolds numbers in the range of 1000 to 3000.

The influence of temperature-dependent thermophysical properties on heat transfer enhancement in fully or partially porous channels has been examined in several studies. Dehghan et al. [18,19] examined the effect of thermal conductivity in porous channels. They proposed a correlation for the Nusselt number based on thermal conductivity and the shape of the channel. Mehata et al. [20] examined forced convection heat transfer in a wavy solar plant using porous blocks. They found that the average Nusselt number increased by 83.95% with the use of porous blocks compared to without them. Kaur et al. [21] investigated the effect of circular and semicircular heat sources in porous media and found that the lowest heat transfer occurred in the circular channel. Li et al. [22] examined the effect of multilayer porous inserts in a channel under non-equilibrium thermal conditions. The results showed that the pressure drop is directly proportional to the number of porous layers.

Due to their ability to enhance heat dissipation while maintaining a compact system design, channels partially filled with porous media have attracted considerable research attention. The temperature profile and Nusselt number used to quantify the heat transfer characteristics in such microchannels have been presented in previous studies [19,23]. Mahmoudi [24] developed analytical expressions for both the temperature field and Nusselt number in a microchannel. Dehghan [25] performed an

analytical study on the thermal behaviour of a channel partially filled with porous media. The addition of a porous material to a fluid undergoing convection results in a more uniform temperature distribution, which reduces thermal resistance and enhances heat transfer. The study also found that as the thickness of the porous material increases, the proportion of heat transferred by the porous medium relative to that transferred by the clear fluid flow increases. Dehghan et al. [26] developed analytical expressions for the local Nusselt number and the dimensionless temperature difference between the solid and fluid phases in a porous material placed inside a channel within the thermally developing region. Bibin et al. [27] numerically examined heat transfer in a partially filled porous channel using OpenFOAM. Their study reported that introducing a porous medium can enhance the heat transfer rate by 10.4 times compared to a channel without porous filling. They also found that this enhancement is most pronounced when the porous layer thickness ratio lies between 0.7 and 0.9. Kumar et al. [28] analysed heat transfer in sinusoidal, triangular, and trapezoidal channels containing porous media at their core. Their findings indicate that the trapezoidal channel achieves the highest thermal performance, with a maximum enhancement of 90%. Alkhamis [29] investigated heat transfer in a channel partially filled with porous material and equipped with solid turbulators. Their results indicate that the use of metal foam along with turbulator enhances both heat transfer and the friction factor. The combined effect of the metal foam and turbulators led to a fivefold improvement in thermal performance. Duan et al. [30] performed a numerical investigation of heat transfer in a wavy metal-foam sandwich configuration. Their analysis demonstrated that, under laminar flow conditions, the Nusselt number can increase by up to 118%.

Although many investigations have been conducted on heat transfer enhancement using porous layers in channels, a critical research gap remains. While the beneficial effects of partial porous layers are well recognised, a systematic numerical investigation into the influence of porous layer location and thickness ratio within a channel remains largely unexplored, particularly under constant heat flux boundary conditions. Addressing this gap, the present study focuses on analysing the effects of location of porous layer and thickness ratio on thermal and hydrodynamic performance to identify configurations that maximise heat transfer while minimising pressure losses. This study investigates convection heat transfer in a channel containing the porous layer with two different configurations: one near the walls and the other at the core of the channel. Partially filling the channel with the porous layer offers two primary benefits: it improves heat transfer performance and results in less pressure drop compared to a fully porous-filled channel. This work can be beneficial in industrial applications, such as heat exchangers, solar energy storage and electronic cooling. A uniform heat flux condition is applied at the channel wall. The effects of the thickness of the porous insert, thermal conductivity ratio and Darcy number on heat transfer enhancement are examined. Additionally, the velocity profile and pressure drop at different Darcy numbers are analysed to determine the optimal design of the channel.

2. Materials and methods

2.1 Governing equations

The governing equation for mass and momentum conservation for the fluid and porous region is explained in this section. The problem is simplified by assuming that the flow is 2D, steady and laminar. The Darcy-Brinkman-Forchheimer model [31] is employed to address the inertial effects in porous material.

The governing equations for mass and momentum conservation in the fluid region are as follows:

$$\nabla \cdot \vec{v} = 0, \tag{1}$$

$$\rho(\vec{v} \cdot \nabla)\vec{v} = -\nabla p + \mu \nabla^2 \vec{v}, \tag{2}$$

where $\vec{v}$ represents the velocity vector, μ denotes the dynamic viscosity, ρ is the density and p is the pressure.

The momentum equation, which incorporates the resistance of the porous medium using the Darcy-Forchheimer model [33], is given by [32]:

$$\frac{\rho}{\varepsilon}(\vec{v} \cdot \nabla)\vec{v} = -\nabla p + \frac{\mu}{\varepsilon}\nabla^2 \vec{v} - \frac{\mu}{K}\vec{v} - \frac{\rho F \varepsilon}{\sqrt{K}}|\vec{v}|\vec{v}, \tag{3}$$

where K represents the permeability, ε denotes the porosity, and F is the Forchheimer coefficient, which is a function of the porous geometry. Local thermal equilibrium is considered to be valid at the interface of the fluid and solid within the porous region.

The energy equation for fluid and porous region are written as [32]:

fluid region:

$$(\vec{v} \cdot \nabla)T = \frac{k}{\rho C_p}\nabla^2 T, \tag{4}$$

porous region:

$$(\vec{v} \cdot \nabla)T = \frac{k_e}{\rho C_p}\nabla^2 T, \tag{5}$$

where k is the thermal conductivity, C_p is the specific heat and T is temperature of the fluid, and k_e represents the effective thermal conductivity, which is influenced by the thermal conductivity of the solid phase.

To derive the non-dimensional form of the governing equations, scaling is applied to the velocity components, temperature and length, using the characteristic reference quantities: inlet velocity, heat flux and channel height, respectively. The dimensionless parameters are defined as follows:

$$X = \frac{x}{H}, \quad Y = \frac{y}{H}, \quad \vec{V} = \frac{\vec{v}}{u_{in}}, \quad P = \frac{p}{\rho u_{in}^2},$$
$$\mathrm{Re} = \frac{\rho u_0 H}{\mu}, \quad \mathrm{Da} = \frac{K}{H^2}, \quad \mathrm{Pr} = \frac{\mu C_p}{k}, \quad \theta = \frac{T - T_{in}}{q''(H/k)},$$
$$C = F\varepsilon, \quad r_p = \frac{r}{H}, \quad k_r = \frac{k_e}{k},$$

where H is the channel height, u_{in} is the inlet velocity in x-direction, u_0 is the average velocity in x-direction, q'' is the heat flux at the wall, θ is the non-dimensional temperature, r is the porous layer thickness, r_p is the porous layer thickness ratio, k_r is the thermal conductivity ratio, Pr is the Prandtl number and Re is the Reynolds number.

The non-dimensional form of the governing equations for mass and momentum conservation is written as:

$$\nabla \cdot \vec{V} = 0, \tag{6}$$

$$\frac{1}{\varepsilon}(\vec{V} \cdot \nabla)\vec{V} = -\nabla P + \frac{1}{\varepsilon\,\mathrm{Re}}\nabla^2\vec{V} - \frac{1}{\mathrm{Da\,Re}}\vec{V} - \frac{C}{\sqrt{\mathrm{Da}}}|\vec{V}|\vec{V}. \tag{7}$$

The energy equation in non-dimensional form is written as

$$(\vec{V} \cdot \nabla)\theta = \frac{k_r}{\mathrm{Re\,Pr}}\nabla^2\theta. \tag{8}$$

For flow in a channel, the Nusselt number for constant heat flux is calculated as [3]

$$\mathrm{Nu} = \frac{q''H}{k\,(T_w - T_m)} = \frac{1}{\theta_w - \theta_m}. \tag{9}$$

2.2 Problem statement and validation

Figure 1 illustrates the schematic of the computational domain. In one case, the porous layer is placed on the channel walls, and in the other case, the same porous material is located at the core of the channel. Geometric configurations partially or fully filled with a porous material are subjected to a constant and uniform heat flux. The flow enters the domain at a constant velocity and temperature. The thermophysical properties of the air are assumed to remain constant throughout the simulations. The model is based on assumptions that the porous region is uniform, isotropic, and filled with a single-phase fluid. The analysis spans a range of Darcy numbers (Da) from 10^{-6} to 1 and porous layer thickness ratio (r_p) from 0.2 to 1.

To mitigate the influence of grid-related effects on the simulation results, a grid independence study is conducted. The study examines the dimensionless axial velocity (u/u_{in}) profile in a partially filled channel with porous media. Three different mesh resolutions are tested, corresponding to 7500, 30 000 and 46 875 elements. The resulting axial velocity profiles are presented in Fig. 2. The variation in axial velocity for the 30 000 and 46 875 element cases is minimal, indicating grid independence. Based on these findings, a grid resolution of 30 000 elements is selected for further analysis to reduce computational cost.

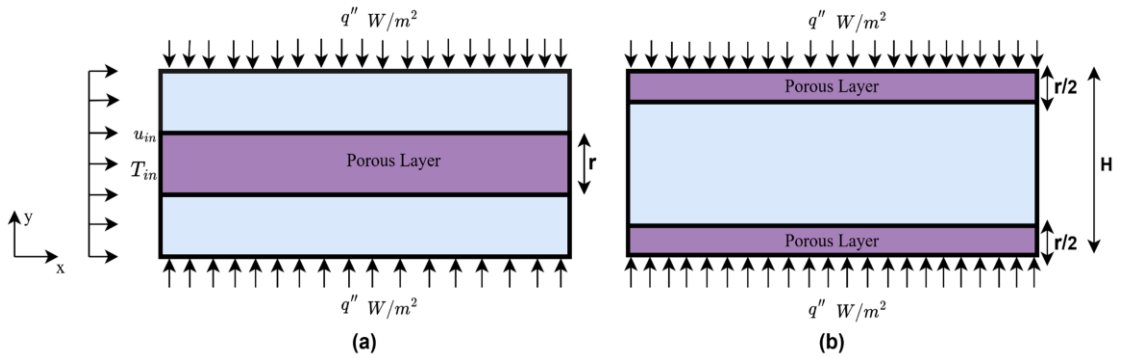


Fig. 1. The schematic representation of a partially filled channel used in the present study with two different configurations: (a) porous layer in the core of the channel, (b) porous layer at the walls of the channel.

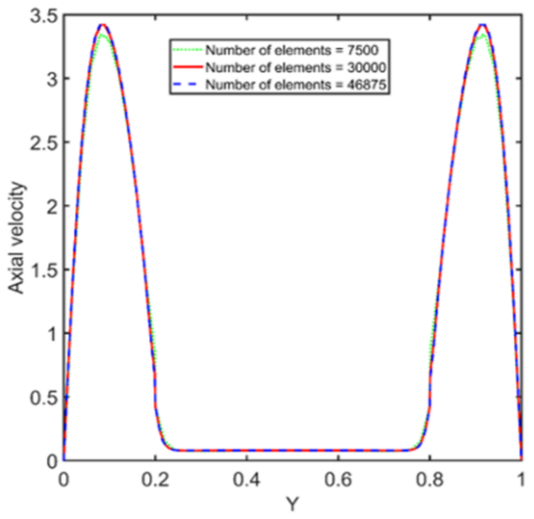


Fig. 2. Non-dimensional axial velocity variation for different grid resolutions at r_p = 0.6 and Da = 10^{-4}.

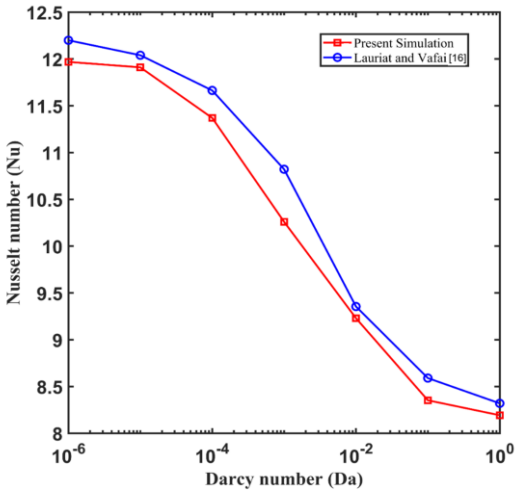


Fig. 3. Validation of the numerical model by comparing the Nusselt number variation with the Darcy number against benchmark results [17] for a fully porous channel.

To validate the numerical model, its results were compared with data reported in the literature. Specifically, the Nusselt number for flow through a fully porous channel with constant heat flux applied to the walls was compared to the findings of Lauriat and Vafai [34]. This comparison is presented in Fig. 3, where the agreement between the two sets of results demonstrates the accuracy of the developed numerical model in capturing the thermal performance of the porous medium.

To further establish the accuracy and reliability of the present numerical model, an additional validation is performed for a channel partially filled with porous media. The channel is partially porous, with porous layers placed directly above the heat sources, while the remaining regions of the channel are nonporous. The schematic representation of the validation geometry is shown in Fig. 4. The porous medium is modelled as homogeneous and isotropic and is saturated with a single-phase fluid that remains in thermal equilibrium with the solid matrix. The porosity and permeability are assumed to remain essentially uniform throughout the entire domain, including regions close to the channel walls.

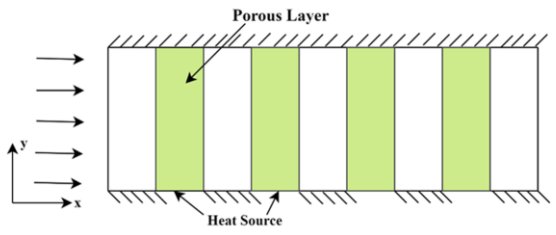


Fig. 4. Schematic diagram of a partially filled porous channel.

Additionally, the length-averaged Nusselt number is calculated at different Reynolds numbers and Darcy numbers for a partially filled porous channel. The obtained results (Fig. 5) exhibit good agreement with those reported in the previous study [9], further validating the numerical model used in the present work.

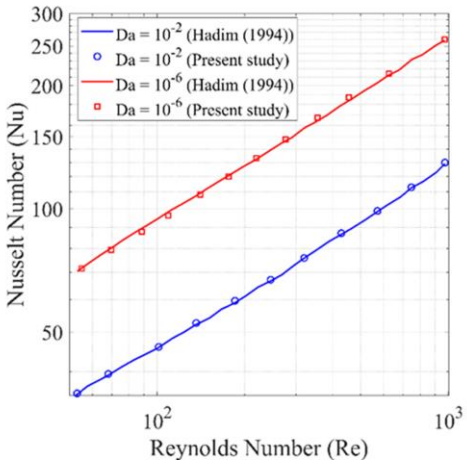


Fig. 5. Variation of the Nusselt number with the Reynolds number in a partially filled porous channel.

3. Results and discussion

The present study investigates the influence of a porous layer on heat transfer in a channel with two different configurations: one near the walls and the other in the core of the channel. The effects of the thickness ratio of the porous layer, the thermal conductivity ratio (k_r) and the Darcy number on heat transfer enhancement are examined. Additionally, the study examines the dimensionless axial velocity and pressure drop to optimise the balance between heat transfer enhancement and pumping power requirements.

3.1. Hydrodynamic characteristics

Figure 6 presents the axial velocity profiles for different values of porous layer thickness ratio (r_p). As the thickness ratio r_p increases, the fluid exhibits a channelling phenomenon, in which the flow is preferentially directed through the clear-fluid region between the porous layer and the channel wall. This results in

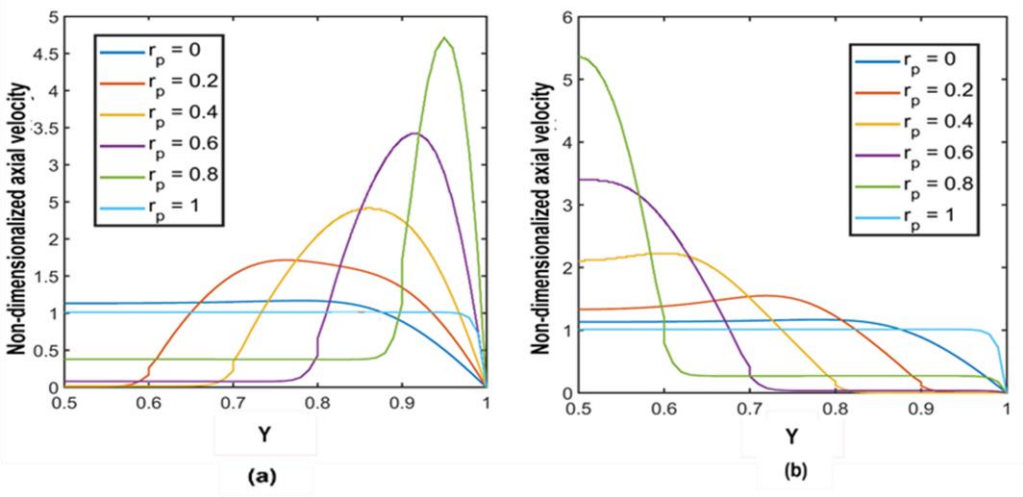


Fig. 6. The non-dimensional axial velocity profile for different porous layer thickness ratio (r_p) for both configurations: (a) porous layer embedded within the core of the channel, (b) porous layer at the walls of the channel.

a non-uniform distribution of flow, with fluid concentration occurring in localised regions around the porous layer, rather than maintaining a uniform flow across the entire cross-sectional area. For the case with a porous layer at the core (Fig. 6a), the maximum velocity of the fluid within the channel tends to increase and shift closer to the pipe surface as the thickness ratio increases, reaching a peak at r_p = 0.8. This increase in velocity is primarily attributed to the decrease in the cross-sectional area available for flow, which forces the fluid to accelerate to maintain the same flow rate. The peak velocity at r_p = 0.8 indicates an optimal configuration where the balance between the porous material's presence and the flow area is most favourable for fluid motion. For the configuration with the porous layer near the wall (Fig. 6b), the maximum fluid velocity increases and shifts toward the centre of the channel as the thickness ratio increases, reaching a peak at r_p = 0.8. This behaviour highlights the significant influence of the porous layer configuration on fluid dynamics, suggesting that careful design of these configurations can enhance thermal performance in applications, such as heat exchangers.

3.2. Pressure drop

The pressure drop in a channel is related to energy consumption. Reduced pressure losses allow for efficient fluid flow and enhance thermal performance. The pressure drop variation with different porous layer thickness ratios for the geometric configuration at different Darcy numbers is shown in Fig. 7. In this figure, subscript *c* represents the configuration when the porous layer is embedded within the core of the channel, and *w* represents the configuration when the porous layer is present at the wall of the channel. As the thickness of the porous layer increases, the resistance to fluid flow also rises, leading to higher pressure losses in both configurations of the channel, as depicted in Fig. 6. Similar pressure drop behaviour has been reported in previous studies [35,36]. This is primarily due to the increased surface area for frictional interactions and the longer path the fluid must traverse, which amplifies the energy required to maintain flow. Conversely, Darcy number is a measure of the porous medium's permeability relative to the fluid's viscosity, plays a crucial role in determining how easily fluid can flow through the material.

A higher Darcy number indicates greater permeability, which typically results in lower pressure losses for a given inlet velocity. It is interesting to note that there is a lower pressure drop when the porous layer is located near the wall than at the core of the channel. This trend becomes more pronounced as the thickness of the porous insert increases. This is because the porous layer on the walls allows for a more streamlined flow path, reducing turbulence and frictional losses. In contrast, a porous insert in the core can disrupt the flow more significantly, leading to increased resistance and higher pressure drop. For a fully porous channel, the pressure loss values are the same for both configurations.

3.3. Heat transfer characteristics

Figure 8 depicts the relationship between the Nusselt number (Nu) and the porous layer thickness ratio for a porous layer present in the channel core, under different Darcy numbers, at a lower thermal conductivity ratio. For a Darcy number of 10^{-2}, the thermal performance improves with increasing porous layer thickness, peaking at a porous layer thickness ratio of 0.6. However, as the porous layer thickness ratio is further increased to 0.8 and then to 1.0, the Nusselt number begins to decrease. In contrast, when the Darcy number is reduced to a value ranging between 10^{-3} and 10^{-6}, the trend changes. In these cases, the heat transfer performance continues to improve with increasing r_p up to 0.8, which results in significant enhancement of thermal performance compared to other cases. Similar to the previous case, a further increase in r_p from 0.8 to 1.0 results in a decrease in thermal performance. This is due to the channelling effect occurring for porous layer thickness ratio, r_p > 0.8. As the porous layer thickness increases beyond this point, the clear fluid gap becomes smaller, resulting in increased flow resistance. Consequently, the flow loses a distinct preferential path, leading to

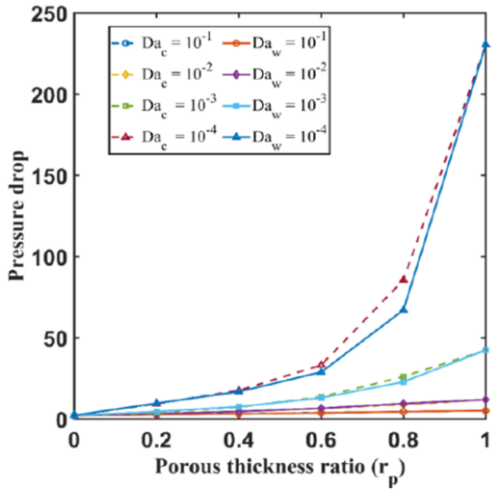


Fig. 7. Pressure drop with porous layer thickness ratio (r_p) at different Darcy numbers for both geometric configurations.

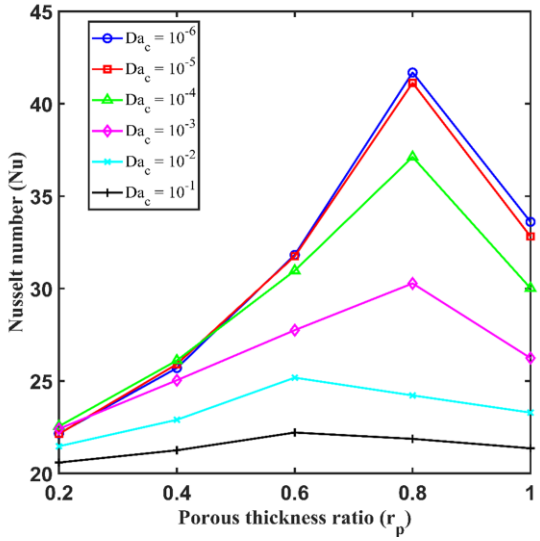


Fig. 8. Variation of the Nusselt number with the porous layer thickness ratio (r_p) at a thermal conductivity ratio (k_r) of 2.5 and different Darcy number (Da) values, when a porous layer is at the channel core.

a reduction in heat transfer performance, and resulting in a decrease in the Nusselt number. A similar variation in the Nusselt number has been reported in previous studies [36].

Figure 9 demonstrates the relationship between the Nusselt number (Nu), the porous layer thickness ratio (r_p) and the Darcy number (Da) for a higher thermal conductivity ratio. The results indicate that an increase in the thermal conductivity of the solid matrix improves the heat transfer rate. As the thermal conductivity ratio (k_r) increases, the porous material's ability to conduct heat also improves, resulting in higher Nusselt numbers. Notably, the impact of increasing thermal conductivity ratio becomes significant at higher porous layer thickness ratios. This is because as the porous layer thickness ratio (r_p) increases, the flow through the porous medium becomes less efficient, making the thermal conductivity of the solid matrix more important for heat transfer. Furthermore, when the porous material completely fills the channel (r_p = 1.0), the increase in thermal conductivity of the solid matrix results in the most substantial enhancement in heat transfer rates. In this fully filled configuration, the solid matrix can effectively conduct heat, maximising the thermal performance of the system. These findings emphasise that both the porous layer thickness ratio and the thermal conductivity of the solid matrix play a crucial role in heat transfer rates, with the extent of their impact being influenced by Darcy numbers.

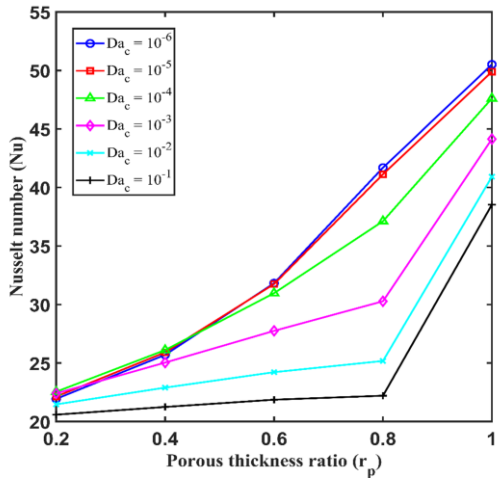


Fig. 9. Variation of the Nusselt number with the porous layer thickness ratio (r_p) at a thermal conductivity ratio (k_r) of 25 and for different Darcy number (Da) values, when a porous layer is at the channel core.

Figure 10 further demonstrates the influence of a higher thermal conductivity ratio on thermal performance across various configurations, comparing the porous layer placed at the core versus at the walls, for different Darcy numbers. Figures 10a and

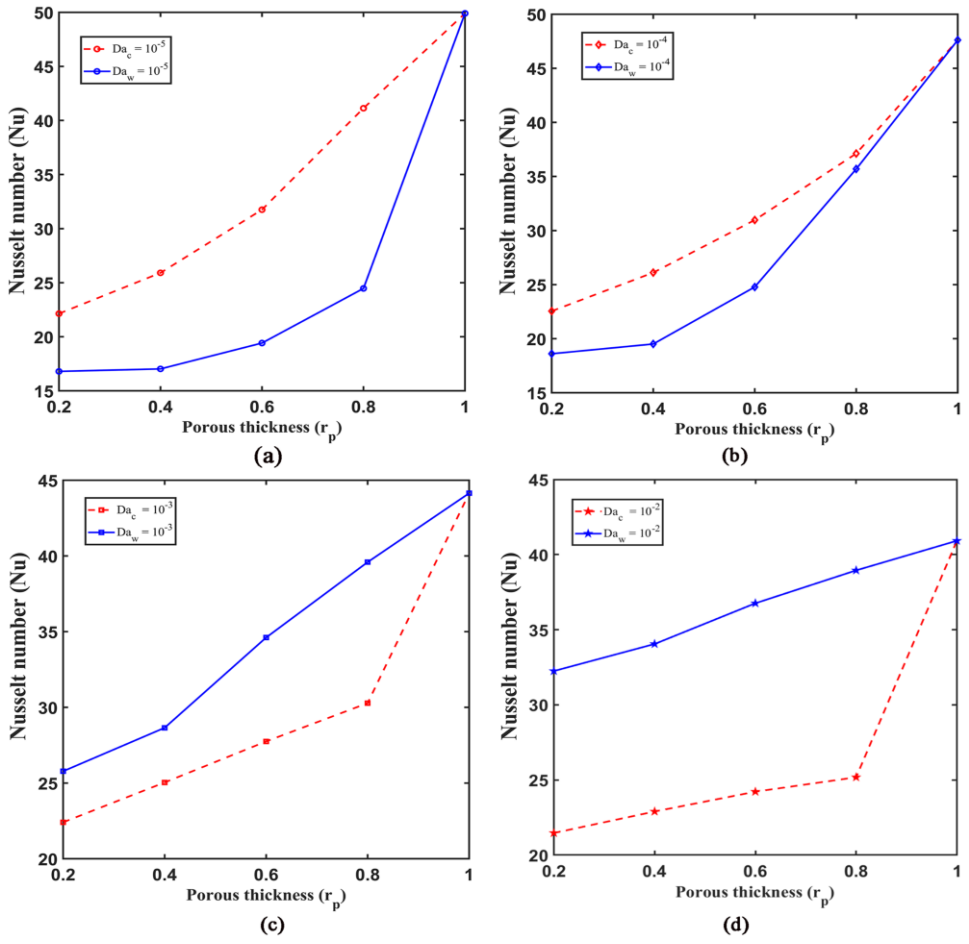


Fig. 10. Variation of the Nusselt number with respect to the porous layer thickness ratio (r_p) for two configurations: a porous layer in the core and a porous layer at the walls, for different Darcy numbers.

10b, corresponding to Darcy numbers of 10^{-5} and 10^{-4}, respectively, show that for less permeable porous media, positioning the porous layer in the channel core results in higher Nusselt numbers. However, this configuration also leads to higher pressure losses compared to the configuration with the porous layer adjacent to the walls, especially at lower Darcy numbers. In contrast, Figs. 10c and 10d, corresponding to Darcy numbers of 10^{-3} and 10^{-2}, respectively, reveal that higher permeability yields better thermal performance when the porous layer is located near the walls. This configuration achieves higher Nusselt numbers with lower pressure drops. The improved thermal performance in this case is due to higher permeability, which enhances fluid-wall interaction when the porous medium is adjacent to the walls, allowing the fluid to flow more freely and improving contact with the wall surface. This, in turn, increases convective heat transfer, resulting in a higher Nusselt number. Nusselt number as a function of the Darcy number for both cases for a porous layer thickness ratio of 0.8 is depicted in Fig. 11. The same value of the Nusselt number is observed for both configurations when the Darcy number is between 10^{-4} to 10^{-3}. The same transition of the Nusselt number with the Darcy number is seen for all porous layer thickness in this study. The thickness ratio of $r_p = 0.8$ is selected as it represents the optimal configuration that yields the maximum heat transfer enhancement among all thickness ratios investigated in the present study.

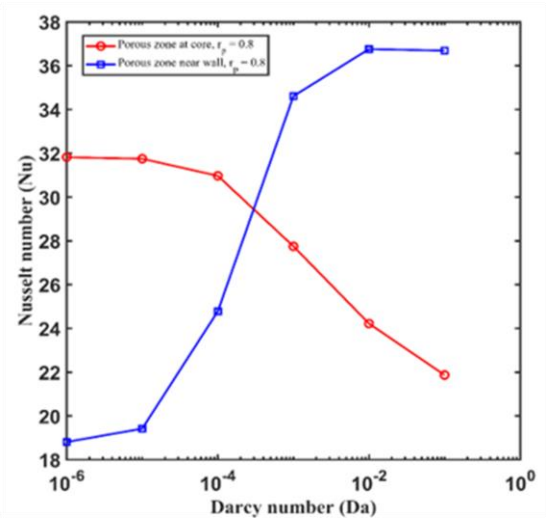


Fig. 11. Variation of the Nusselt number with the Darcy number at $r_p = 0.8$ for both configurations.

6. Conclusions

The present study numerically investigates the heat transfer enhancement in the channel using two different configurations: a porous layer in the channel core and a porous layer located near the channel wall. The effects of Darcy number ($0.000001 < Da < 0.01$), the ratio of porous layer thickness ($0.2 < r_p < 1$) and the thermal conductivity ratio are studied to understand how porous medium properties govern flow resistance and thermal performance. The main outcome of the study is summarised below:

1. The highest fluid velocity is observed when the porous layer thickness ratio is 0.8 in both geometric configurations. This indicates the optimal configuration for enhancing convective heat transfer between the fluid and the channel wall.
2. Pressure-drop analysis indicates that positioning the porous layer at the walls consistently results in lower pressure losses for all Darcy numbers, whereas placing the porous layer at the core introduces a stronger flow obstruction and therefore higher-pressure penalties. The pressure drop increases as the porous layer thickness ratio increases.
3. The results show that the porous layer thickness ratio plays a dominant role in flow-thermal behaviour. The maximum improvement in heat transfer is achieved at a thickness ratio of 0.8, where the Nusselt number increases by about 88% compared to the baseline. For the low thermal conductivity ratio of 2.5, increasing thickness beyond this point leads to a 19.5% reduction in the Nusselt number due to increased thermal resistance. In contrast, for a high conductivity ratio of 25, the heat transfer rate continues to rise with thickness, yielding as much as 80.5% improvement relative to the low-conductivity case.
4. At lower Darcy numbers, the Nusselt number is higher when the porous layer is located at the core of the channel, irrespective of the porous layer thickness ratio. In contrast, at higher Darcy numbers, the Nusselt number is higher when the porous layer is positioned near the walls, especially for high thermal conductivity ratios and for all porous layer thickness ratios.

References

[1] Said, Z., Mwesigye, A., Syam Sundar, L., Tiwari, A.K., Balasubramanian, K., Ali, H.M., Bellos, E., Gim, C., Ahmed, M.S. & Hwang, J.Y. (2025). Sustainable thermal solutions: Enhancing heat transfer with turbulators and nanofluids. *Advanced Energy and Sustainability Research*, 6(5), 2400335. doi: 10.1002/aesr.202400335

[2] Alenezi, A., Ali, H.M., & Phelan, P.E. (2025). Experimental investigation of the effect of ultrasonic waves on heat transfer enhancement and pressure drop for propylene glycol/water mixtures in a rectangular minichannel heat sink. *Applied Thermal Engineering*, 267, 125717. doi: 10.1016/j.applthermaleng.2025.125717

[3] Hadim, H.A., & Bethancourt, A. (1995). Numerical study of forced convection in a partially porous channel with discrete heat sources. *ASME Journal of Electronic Packaging*, 117(1), 46–51. doi: 10.1115/1.2792062

[4] Baig, M.F., Chen, G.M., & Tso, C.P. (2022). The thermal performance analysis of an Al_2O-water nanofluid flow in a composite microchannel. *Nanomaterials*, 12(21), 3821. doi: 10.3390/nano12213821

[5] Promvonge, P. (2015). Thermal performance in square-duct heat exchanger with quadruple V-finned twisted tapes. *Applied Thermal Engineering*, 91, 298–307. doi: 10.1016/j.applthermaleng.2015.08.047

[6] Kalidasan, B., Chinnasamy, S., Pandey, A.K., Hassan, M.A., & Sharma, K. (2023). Thermal performance analysis of solar box cookers using different fin configurations: An experimental investigation. *Journal of Thermal Analysis and Calorimetry*, 148(14), 7421–7440. doi:10.1007/s10973-023-12236-8

[7] Zhong, S., Zhang, C., & Fan, A. (2025). Numerical study on heat transfer enhancement of laminar flow in fully wavy wall microchannels. *Applied Thermal Engineering*, 266, 125782. doi: 10.1016/j.applthermaleng.2025.125782

[8] Mohammed, H.A., Al-Shamani, A.N., & Sheriff, J.M. (2012). Thermal and hydraulic characteristics of turbulent nanofluids flow in a rib-groove channel. *International Communications in Heat and Mass Transfer*, 39(10), 1584–1594. doi: 10.1016/j.icheatmasstransfer.2012.10.020

[9] Hadim, A. (1994). Forced convection in a porous channel with localized heat sources. *Journal of Heat Transfer*, 116(2), 465–472. doi: 10.1115/1.2911419

[10] Jen, T.-C., & Yan, T.Z. (2005). Developing fluid flow and heat transfer in a channel partially filled with porous medium. *International Journal of Heat and Mass Transfer*, 48(19–20), 3995–4009. doi: 10.1016/j.ijheatmasstransfer.2005.04.021

[11] Hadim, H., & North, M. (2005). Forced convection in a sintered porous channel with inlet and outlet slots. *International Journal of Thermal Sciences*, 44(1), 33–42. doi: 10.1016/j.ijthermalsci.2004.04.016

[12] Rachedi, R., & Chikh, S. (2001). Enhancement of electronic cooling by insertion of foam materials. *Heat and Mass Transfer*, 37, 371–378. doi: 10.1007/s002310100192

[13] Yucel, N., & Guven, R.T. (2007). Forced convection cooling enhancement of heated elements in parallel plate channels by using porous insert. *Numerical Heat Transfer, Part A: Applications*, 51(3), 293–312. doi:10.1080/10407780600762533

[14] Huang, P.C., Yang, C.F., Hwang, J.J., & Chiu, M.T. (2005). Enhancement of forced-convection cooling of multiple heated blocks in a channel using porous covers. *International Journal of Heat and Mass Transfer*, 48(3–4), 647–664. doi:10.1016/j.ijheatmasstransfer.2004.07.041

[15] Da Silva Miranda, B.M., & Anand, N.K. (2004). Convective heat transfer in a channel with porous baffles. *Numerical Heat Transfer, Part A: Applications*, 46(5), 425–452. doi: 10.1080/10407780490478515

[16] Ko, K.H., & Anand, N.K. (2003). Use of porous baffles to enhance heat transfer in a rectangular channel. *International Journal of Heat and Mass Transfer*, 46(22), 4191–4199. doi: 10.1016/S0017-9310(03)00251-5

[17] Kim, S.Y., Kang, B.H., & Kim, J.-H. (2001). Forced convection from aluminum foam materials in an asymmetrically heated channel. *International Journal of Heat and Mass Transfer*, 44(7), 1451–1454. doi: 10.1016/S0017-9310(00)00187-3

[18] Dehghan, M., Valipour, M.S., & Saedodin, S. (2015). Temperature-dependent conductivity in forced convection of heat exchangers filled with porous media: A perturbation solution. *Energy Conversion and Management*, 91, 259–266. doi: 10.1016/j.enconman.2014.12.011

[19] Dehghan, M., Rahmani, Y., Ganji, D.D., Saedodin, S., Valipour, M.S., & Rashidi, S. (2015). Convection-radiation heat transfer in solar heat exchangers filled with a porous medium: Homotopy perturbation method versus numerical analysis. *Renewable Energy*, 74, 448–455. doi: 10.1016/j.renene.2014.08.044

[20] Kaur, R., Sharma, S., & Chandra, A. (2024). Forced convection heat transfer from confined circular/semi-circular heaters and coolers with various orientations. *The Canadian Journal of Chemical Engineering*, 102(11), 3756–3775. doi: 10.1002/cjce.25439

[21] Mehta, S.K., Kumar, D., Mondal, P.K., & Wongwises, S. (2024). Characterisation of conjugate forced convection in a wavy solar power plant: The role of porous metallic blocks. *Chemical Engineering and Processing - Process Intensification*, 196, 109615. doi: 10.1016/j.cep.2023.109615

[22] Li, Q., Wang, Z., & Hu, P. (2024). Convective heat transfer in porous channel with multi-layer fractures under local thermal non-equilibrium condition. *International Journal of Heat and Mass Transfer*, 235, 126194. doi:10.1016/j.ijheatmasstransfer.2024.126194

[23] Dehghan, M., Mahmoudi, Y., Valipour, M.S., & Saedodin, S. (2015). Combined conduction–convection–radiation heat transfer of slip flow inside a micro-channel filled with a porous material. *Transport in Porous Media*, 108, 413–436. doi: 10.1007/s11242-015-0483-z

[24] Mahmoudi, Y. (2015). Constant wall heat flux boundary condition in micro-channels filled with a porous medium with internal heat generation under local thermal non-equilibrium condition. *International Journal of Heat and Mass Transfer*, 85, 524–542. doi: 10.1016/j.ijheatmasstransfer.2015.01.134

[25] Dehghan, M. (2015). Effects of heat generations on the thermal response of channels partially filled with non-Darcian porous materials. *Transport in Porous Media*, 110(3), 461–482. doi: 10.1007/s11242-015-0567-9

[26] Dehghan, M., Valipour, M.S., Keshmiri, A., Saedodin, S., & Shokri, N. (2016). On the thermally developing forced convection through a porous material under the local thermal non-equilibrium condition: An analytical study. *International Journal of Heat and Mass Transfer*, 92, 815–823. doi: 10.1016/j.ijheatmasstransfer.2015.08.091

[27] Bibin, K.S., Raj, S., Jayakumar, J.S., & Roy, K.K.E.B.R. (2024). OpenFOAM modelling of single-phase and two-phase heat transfer in square ducts partially filled with porous medium. *Experimental and Computational Multiphase Flow*, 6(4), 408–427. doi: 10.1007/s42757-024-0189-y

[28] Kumar, P., Dwivedi, R., & Pandey, K.M. (2024). Hybrid-nanofluid flow through partially porous wavy channels: Thermo-hydraulic performance and entropy analysis. *Heat Transfer Engineering*, 45(3), 211–232. doi: 10.1080/01457632.2023.2185487

[29] Alkhamis, N. (2025). Heat transfer enhancement for fluid flow inside a channel by using metal foam. *International Communications in Heat and Mass Transfer*, 162, 108574. doi: 10.1016/j.icheatmasstransfer.2024.108574

[30] Duan, X., Liu, X., Huang, X., Wang, Y., & Ding, C. (2025). A novel design for performance enhancement in sandwich heat transfer unit with partially filled metal foam. *International Communications in Heat and Mass Transfer*, 165(A), 109086. doi: 10.1016/j.icheatmasstransfer.2025.109086

[31] Nield, D.A., & Bejan, A. (2006). *Convection in Porous Media* (4th ed.). Springer. doi: 10.1007/978-1-4614-5541-7

[32] Chikh, S., Boumedien, A., Bouhadef, K., & Lauriat, G. (1998). Analysis of fluid flow and heat transfer in a channel with intermittent heated porous blocks. *Heat and Mass Transfer*, 33(5), 405–413. doi: 10.1007/S002310050208

[33] Whitaker, S. (1996). The Forchheimer equation: A theoretical development. *Transport in Porous Media*, 25(1), 27–61. doi: 10.1007/BF00141261

[34] Lauriat, G., & Vafai, K. (1991). Forced convective flow and heat transfer through a porous medium exposed to a flat plate or a channel. In *Convective Heat and Mass Transfer in Porous Media*. NATO Advanced Study Institute Series, 196, 289–327. Springer. doi: 10.1007/978-94-011-3220-6_9

[35] Bovand, M., Rashidi, S., & Esfahani, J.A. (2016). Heat transfer enhancement and pressure drop penalty in porous solar heaters: Numerical simulations. *Solar Energy*, 123, 145–159. doi: 10.1016/j.solener.2015.10.054

[36] Mahmoudi, Y., Karimi, N., & Mazaheri, K. (2014). Analytical investigation of heat transfer enhancement in a channel partially filled with a porous material under local thermal non-equilibrium condition: Effects of different thermal boundary conditions at the porous-fluid interface. *International Journal of Heat and Mass Transfer*, 70, 875–891. doi: 10.1016/j.ijheatmasstransfer.2013.11.048

Co-published by
Institute of Fluid-Flow Machinery
Polish Academy of Sciences
Committee on Thermodynamics and Combustion
Polish Academy of Sciences

Copyright©2026 by the Authors under licence CC BY-NC-ND 4.0

http://www.imp.gda.pl/archives-of-thermodynamics/

Mixed convective chemically reacted hybrid nanofluid flowing over a non-isothermal/non-isosolutal cone/wedge with heat generation/absorption: A numerical study

Chegu Ramprasad[a], Chundru Maheswari[a*], Bhavanam Naga Lakshmi[b], Tadavarthi Madhu Mohan[c], Ravuri Mohana Ramana[d]

[a]Department of Mathematics, Vasireddy Venkatadri International Technological University, Nambur-522508, Andhra Pradesh, India
[b]Department of Mathematics, Vignan Nirula Institute of Technology for Women, Guntur-522009, Andhra Pradesh, India
[c]Department of Physics, Vasireddy Venkatadri International Technological University, Nambur-522508, Andhra Pradesh, India
[d]Department of Mathematics, Narasaraopeta Engineering College (Autonomous), Narasaraopet-522601, Andhra Pradesh, India
*Corresponding author email: cmaheswari2014@gmail.com

Received: 26.09.2025; revised: 08.07.2026; accepted: 21.07.2026

Abstract

The current study explores a numerical investigation of steady-state, two-dimensional, incompressible, laminar mixed convective flow of a chemically reactive hybrid nanofluid composed of $Al_2O_3 - H_2O$ over a vertical non- isothermal/isosolutal wedge and cone configurations, taking into account the impact of a heat absorption or generation parameter. Utilising similarity transformations, the set of governing equations was reduced to a set of ordinary differential equations. This model incorporates the conservation equations for energy, mass and momentum, which are solved numerically by using the BVP-5C method and the Runge-Kutta shooting technique in MATLAB. The influences of key factors on the flow fields, as well as on the mass and heat transmission rates, are analysed and presented through graphical and tabular formats. The outcome reveals that both solutal and thermal Grashof numbers display a comparable influence on the flow behaviour. As these parameters increase, an enhancement in the velocity profile is observed, whereas concentration and temperature distributions tend to decline. Additionally, an increase in the heat generation and thermal radiation parameters results in elevated temperature distributions for both wedge and cone geometries. In contrast, the chemical reaction factor contributes to a decrease in concentration distribution. The influence is more prominent in the wedge configuration than in the cone, where the profile exhibits an increasing behaviour, while the cone shows a stronger response in scenarios where the profile decreases. The mass and heat transmission rates corresponding to the key parameters are presented in tabulated form. The proposed model has been rigorously verified against previously reported data and demonstrates excellent agreement.

Keywords: Wedge/cone; Thermal/mass Grashof numbers; Heat generation/absorption parameter; Chemical reaction

Vol. 47(2026), No. 3, 99–110; doi: 10.24425/ather.2026.3659

Cite this manuscript as: Ramprasad, C., Maheswari, C., Naga Lakshmi, B., Mohan, T.M., & Ramana, R.M. (2026). Mixed convective chemically reacted hybrid nanofluid flowing over a non-isothermal/non-isosolutal cone/wedge with heat generation/absorption: A numerical study. *Archives of Thermodynamics*, 47(3), 99−110.

1. Introduction

Hybrid nanofluids are engineered by suspending a combination of two or more different nanoparticles within a conventional heat transmission medium such as water (H_2O), motor oil, organic solvents or biological fluids. When these nanoparticles are uniformly dispersed, the resulting fluid exhibits significantly improved thermal conductivity and superior heat transfer features. As an innovative class of working liquids, hybrid nanofluids have shown great promise in various engineering and scien-

Nomenclature

a, b – constants
Bi – Biot number
C – concentration, kg/m^3
C_f – skin friction coefficient
C_w – concentration at wall, kg/m^3
C_∞ – ambient concentration (kg/m^3)
D_{hnf} – diffusion coefficient, m^2/s
g – acceleration due to gravity, m/s^2
Gc – mass Grashof number
Gr – thermal Grashof number
h_f – convective heat transfer coefficient, W/(m^2 K)
k_{hnf} – thermal conductivity of hybrid nanofluid, W/(m K)
k^* – mean absorption coefficient, m^{-1}
l – characteristic length of cone/wedge, m
n – power index
Nu$_x$ – Nusselt number
Pr – Prandtl number
Q – heat generation/absorption parameter
q_r – heat flux, W/m^2
r – radius of the cone, m
Rc – chemical reaction parameter
Rd – thermal radiation
Re$_x$ – local Reynolds number
s_1 – wall temperature parameter
s_2 – wall concentration parameter
S – suction parameter
Sc – Schmidt number
Sh$_x$ – Sherwood number
T – temperature, K
T_w – temperature at wall, K
T_∞ – ambient temperature, K
u, v – velocity components along the x– and y–axis, m/s
u_w – stretching velocity, m/s

Greek symbols

α – half-angle
β_C – solutal expansion coefficient, K^{-1}
β_T – thermal expansion coefficient, K^{-1}
μ_{hnf} – dynamic viscosity of hybrid nanofluid, kg/(m s)
ρ_{hnf} – density of hybrid nanofluid, kg/m^3
$(\rho C_p)_{hnf}$ – heat capacity of hybrid nanofluids, J/(kg K)
σ^* – Stefan-Boltzmann constant, W/(m^2 K^4)
ϕ_1, ϕ_2 – Cu and Al_2O_3 nano particles volume fraction

Subscripts and Superscripts

∞ – free stream
f – fluid
hnf – hybrid nanofluids
w – at the wall/surface

Abbreviations and Acronyms

EG – ethylene glycol
MHD – magnetohydrodynamics
ODEs – ordinary differential equations

tific domains, including microfluidic systems, transportation technologies, biomedical applications, defence mechanisms, naval architecture and acoustic devices. Due to its extensive spectrum of applications in engineering and science, the investigation of fluid flow over different geometrical shapes such as vertical cones and wedges has attracted considerable interest from researchers. These flow configurations are crucial in various industrial and technological operations, including fibre production, advanced thermal aerodynamics, cooling of nuclear systems, surface modification, spray deposition techniques, and polymer fabrication. Consequently, a substantial amount of analytical and computational investigations have led to explore the flow behaviour of Newtonian as well as non-Newtonian fluids across such geometrical domains.

Dawar et al. [1] analysed the convective transport of Williamson's nanoliquid through wedge and cone geometries by employing convective boundary conditions. The flow was studied under varying thermal and solutal conditions that were not uniform across the surface. Kumar et al. [2] explored the laminar flow of a Newtonian composite nanofluid containing various nanoparticles embedded in a basic fluid, considering both temperature-dependent and exponentially changing spatial heat generation over an isothermal wedge. Yahaya et al. [3] examined steady-state hybrid nanoliquid flowing over a penetrable, non-isothermal wedge and cone, incorporating the influence of radiation and convective boundary conditions in their heat transmission analysis. Sushila et al. [4] analysed the heat transmission behaviour of TiO_2 – CuO/water hybrid nanoliquid flowing over both static and moving wedges, taking into account the effects of thermal radiation and magnetic field within a porous medium.

Mixed convection represents fluid flow in which both forced convection, caused by external pressure gradients, and free convection, resulting from buoyancy forces, act simultaneously. This type of flow plays a substantial role in an extensive array of applications, like low-speed heat exchangers, cooling of electronic components, crystal formation, underground cable networks, chemical manufacturing, lubrication systems, boilers, emergency cooling in nuclear reactors, solar thermal systems, defrosting mechanisms, atmospheric circulation, vehicle windshield demisters, and ocean currents. Ramzan et al. [5] inspected mixed convection flow of a ternary hybrid nanoliquid over wedge and cone geometries characterised by non-isothermal and non-isosolutal distributions. Reddy et al. [6] investigated mixed convective magnetohydrodynamics (MHD) radiative flow of a Williamson's nanoliquid over a wedge, including the influence of inner heat generation and binary chemical reactions. The mixed convective heat and mass transfer behaviour of a magneto-nanofluid over a moving vertical plate, including thermal radiation, was examined by Chandra Reddy et al. [7]. The influence of time-dependent MHD mixed convection on hybrid nanofluid flow past a nonlinearly stretching surface in a porous medium was investigated by Mathews and Hymavathi [8].

The study of fluid flow involving chemical reactions is vital due to its substantial influence on both environmental and industrial operations. Such reactions play a crucial role in a widespread range of applications, such as nuclear reactor systems,

atomic energy generation, plastic fabrication, cable insulation processes, and many other industrial sectors. Amit and Shalini [9] conducted a numerical study on the influence of a nonlinear chemically reacting MHD convective flow of Maxwell liquid over penetrable surfaces, including a vertical cone/wedge/plate. AL Garalleh [10] investigated the mixed convection flow of a ternary hybrid nanoliquid composed of TiO_2, Al_2O_3 and SiO_2 over a stretched/shrunk wedge, considering the combined influences of chemical reaction and activation energy. Arabi et al. [11] explored the convection behaviour of a Williamson hybrid nanoliquid flowing over wedge and cone geometries within a porous surface, considering various nanoparticle shapes and the effect of a chemical response.

The study of temperature distribution influenced by heat generation (absorption) in moving fluids plays a crucial role in numerous physical contexts, including chemical reaction processes and the behaviour of dissociating fluids. Numerous investigations in the literature focus on heat transmission in the laminar flow of viscous liquids. In some works, heat generation is modelled either as a constant or as a function of spatial coordinates, while others have incorporated the effects of frictional heating and fluid expansion. Vajravelu and Nayfeh [12] investigated MHD convection along cone and wedge surfaces, considering variable surface temperatures and the presence of inner heat absorption/generation. Rekha et al. [13] studied the influence of a uniform heat sink/source on the flow of an incompressible nanofluid over cone and wedge geometries within a permeable medium. The influence of heat generation and thermal radiation under exponentially varying temperature and concentration conditions was investigated by Chandra Reddy et al. [14]. The same authors, in [15], carried out a numerical investigation of free convection heat and mass transfer characteristics in a heat-producing magneto-nanofluid past a vertically moving plate. Mathews and Hymavathi [16] explored the effects of a magnetic field, viscous dissipation, thermal radiation and internal heat generation/absorption on flows involving metallic and oxide nanoparticles over a permeable stretching sheet.

By applying the MATLAB BVP4C boundary-value problem solver, Ali et al. [17,18] numerically explored the influence of various nanoparticle shape factors, including blade, brick, cylindrical, platelet, and spherical forms, on nanofluid flow characteristics, considering unsteady $SiO_2 – H_2O$ motion along a stretchable cylinder and steady EG–Cu flow over a fixed stretching surface under Joule heating effects. Shahzad et al. [19] examined the characteristics of axisymmetric liquid film flow and the associated heat transfer over a time-dependent radially stretching surface, accounting for the influence of an applied transverse magnetic field. Zaman et al. [20] explored the thermal behaviour of Williamson nanofluids incorporating upward-moving motile thermophilic microorganisms along wedge and cone surfaces and further enhanced their study by employing an artificial neural network to support the numerical findings. Ahmed et al. [21] investigated the effects of thermal radiation on chemically reactive MHD hybrid nanofluid flow over elastically deformable wedge, plate, and cone configurations, while also accounting for surface tension gradients, Joule heating, and permeability of the medium. Sadiya et al. [22] analysed the simultaneous effects of these parameters on the flow behaviour of a ternary nanofluid moving through a porous medium over a rotating and stretching surface. Qureshi et al. [23] conducted a machine-learning-based analysis of MHD radiative ternary hybrid nanofluid flow, comprising multi-walled carbon nanotubes (MWCNTs) and Au/Ag nanoparticles suspended in blood, over a porous stretching sheet.

A thorough examination of existing literature demonstrates that the mixed convection flow of a chemically reactive $Al_2O_3 – Cu/H_2O$ hybrid nanofluid over wedge and cone geometries, considering the simultaneous influence of heat generation (absorption) and chemical reaction effects, remains uninvestigated. Aiming to address this gap, the present analysis explores the governing factors of heat and mass transfer in the flow system and builds upon the study of Yahaya et al. [3] by introducing heat generation within the boundary layer. The novelty of this study lies in its numerical assessment of how thermal and solutal Grashof numbers, together with heat generation (absorption) and chemical reaction factors, affect the behaviour of the hybrid nanoliquid over non-isothermal and non-isosolutal wedge and cone surfaces. A comparative evaluation between the two geometries is carried out to highlight the influence of the selected physical elements. This problem is tackled using the BVP5C numerical solver. Graphical representations are used to illustrate the influence of key variables, and tables are provided to report skin friction, mass and heat transmission rates for chosen parameter values. The results show strong consistency and offer valuable insights into the transport phenomena involved.

2. Mathematical modelling

This research presents a numerical exploration of steady-state, laminar, 2D incompressible mixed convective flow of a chemically reactive hybrid nanofluid composed of $Al_2O_3 – Cu/H_2O$ over vertical non-isothermal and non-isosolutal cone and wedge configurations, accounting for the impact of heat generation or absorption. Initially, a nanofluid is prepared by scattering copper (Cu) nanoparticles into water (H_2O), the basic fluid, with the volume fraction represented by ϕ_1. This $Cu – H_2O$ nanofluid is then further modified into a hybrid nanofluid, $Al_2O_3 – Cu/H_2O$, by incorporating aluminium oxide (Al_2O_3) nanoparticles, known for their superior thermal conductivity at a designated volume fraction ϕ_2. This study assumes that the nanoparticles are uniformly shaped and sized and that thermal equilibrium exists between the basic liquids and the suspended nanoparticles.

Figure 1 demonstrates the configuration and co-ordinate system for the 2D flow scenario, here the x–axis runs along the surface area of the cone or wedge and the y–axis is oriented perpendicular to it. The stretched velocity of the surface is defined as $u_w = v_f x/l^2$, and the liquid occupies the area $y \geq 0$. The surface temperature distribution is modelled as $T_w(x) = T_\infty + ax^{s_1}$, while the nanoparticle concentration at the surface is given by $C_w(x) = C_\infty + bx^{s_2}$, with the exponents s_1 and s_2 governing the spatial variation of temperature and concentration, respectively. A value of $s_1 = 0$ represents a surface with constant temperature (isothermal), and $s_2 = 0$ indicates a surface with uniform nanoparticle concentration (isosolutal). The cone or wedge is characterised by a half-angle α, with its radius defined as $r = x \sin\alpha$.

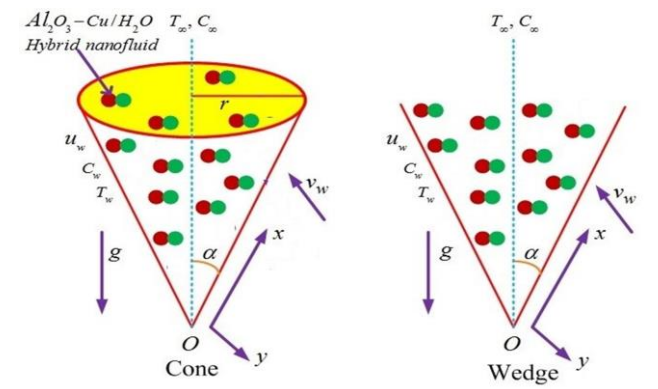


Fig. 1. Flow configuration schematic representation.

The two geometric configurations, cone and wedge, are distinguished using the following criteria:

i) for $\alpha \neq 0$ and $n = 0$, the structure corresponds to a wedge,

ii) for $\alpha \neq 0$ and $n = 1$, the configuration represents a cone.

Taking into account the aforementioned suppositions, the equations that govern this flow problem are established as follows [1,3,5,24]:

$$\frac{\partial}{\partial x}(r^n u) + \frac{\partial}{\partial y}(r^n v) = 0, \tag{1}$$

$$u\frac{\partial u}{\partial x} + v\frac{\partial u}{\partial y} = \frac{\mu_{hnf}}{\rho_{hnf}}\frac{\partial^2 u}{\partial y^2} + g\,[\beta_T(T - T_\infty) + \beta_c(C - C_\infty)]\cos\alpha, \tag{2}$$

$$u\frac{\partial T}{\partial x} + v\frac{\partial T}{\partial y} = \frac{k_{hnf}}{(\rho\, C_p)_{hnf}}\frac{\partial^2 T}{\partial y^2} - \frac{1}{(\rho\, C_p)_{hnf}}\frac{\partial q_r}{\partial y} + \frac{Q^*}{(\rho\, C_p)_{hnf}}(T - T_\infty), \tag{3}$$

$$u\frac{\partial C}{\partial x} + v\frac{\partial C}{\partial y} = D_{hnf}\frac{\partial^2 C}{\partial y^2} - K^*(C - C_\infty). \tag{4}$$

The corresponding boundary constraints [3,5] are:

at $y = 0$:

$$u = u_w,\ v = v_w,\ -k_{hnf}\frac{\partial T}{\partial y} = h_f(T_w - T),\ C = C_w, \tag{5a}$$

as $y \longrightarrow \infty$

$$u \longrightarrow 0, \quad T \longrightarrow T_\infty, \quad C \longrightarrow C_\infty. \tag{5b}$$

To simplify the analysis, the following similarity transformations are introduced [1,3]:

$$\eta = \frac{y}{l}, \quad u = \left(\frac{\nu_f x}{l^2}\right) f'(\eta),$$

$$v = -\left(\frac{\nu_f}{l}\right)(1+n) f(\eta), \quad \theta(\eta) = \frac{T - T_\infty}{T_w - T_\infty}, \tag{6}$$

$$\phi(\eta) = \frac{C - C_\infty}{C_w - C_\infty}.$$

Upon applying the similarity parameters defined by Eq. (6) to the governing Eqs. (1) to (4), it is observed that Eq. (1) is naturally satisfied, while Eqs. (2)–(4) are simplified to the non-linear ODEs shown below:

$$R_1 f''' + R_2(1+n) f f'' - R_2 f'^2 + R_2(\mathrm{Gr}\theta + \mathrm{Gc}\phi)\cos\alpha = 0, \tag{7}$$

$$\left(R_4 + \frac{4}{3}Rd\right)\theta'' + \mathrm{Pr}\,Q\,\theta + \mathrm{Pr}R_3(1+n) f\theta' - s_1 \mathrm{Pr} R_3 f'\theta = 0, \tag{8}$$

$$\phi'' + \frac{\mathrm{Sc}}{R_5}[(1+n) f\phi' - s_2 f'\phi - Rc\phi] = 0. \tag{9}$$

Here:

$$R_1 = \frac{\mu_{hnf}}{\mu_f},\ R_2 = \frac{\rho_{hnf}}{\rho_f},\ R_3 = \frac{(\rho C_p)_{hnf}}{(\rho C_p)_f},\ R_4 = \frac{k_{hnf}}{k_f},\ R_5 = \frac{D_{hnf}}{D_f}.$$

The corresponding boundary constraints are transformed to:

$$f'(0) = \phi(0) = 1, \quad f(0) = S\frac{1}{1+n}, \quad \theta'(0) = -\mathrm{Bi}\frac{(1-\theta(0))}{R_4},$$

$$f'(\infty) = \phi(\infty) = \theta(\infty) = 0. \tag{10}$$

Dimensionless quantities utilised in the governing equations are defined as follows [1,3,5,25]:

- thermal Grashof number: $\mathrm{Gr} = \frac{l^2 g \beta_T (T_w - T_\infty)}{\nu_f u_w}$,
- mass Grashof number: $\mathrm{Gc} = \frac{l^2 g \beta_C (C_w - C_\infty)}{\nu_f u_w}$,
- heat generation/absorption: $S = -\frac{l v_w}{\nu_f}$ ($S > 0$ indicating suction and $S < 0$ indicating injection),
- Biot number: $\mathrm{Bi} = \frac{h_f l}{k_f}$,
- Schmidt number: $\mathrm{Sc} = \frac{\nu_f}{D_f}$,
- chemical reaction parameter: $Rc = \frac{K^* l^2}{\nu_f}$.

As per Rosseland's [26] diffusion estimate, the radiative heat flux q_r is formulated in the following manner, as outlined in references [27–29]:

$$q_r = -\frac{4}{3}\frac{\sigma^*}{k^*}\frac{\partial T^4}{\partial y}.$$

The factors k^* and σ^* designate the mean absorption coefficient and Stefan–Boltzmann constant respectively. By applying a Taylor's series extension to T^4 around the ambient temperature T_∞ and avoiding higher order terms, the expression streamlines to: $T^4 \approx 4\,T_\infty{}^3 T - 3\,T_\infty{}^4$.

Physical and thermal characterisations of the basic liquid H_2O and nanoparticles Al_2O_3, Cu, along with those of the hybrid nanofluid Al_2O_3 – Cu/H_2O, are presented in Tables 1 and 2 given below.

Table 1. Al_2O_3, Cu and H_2O thermo-physical properties [33,34].

Properties	Cu	Al_2O_3	H_2O
C_p, J/(kg K)	385	765	4179
ρ, kg/m³	8933	3970	997.1
k, W/(m K)	400	40	0.613
Pr			6.2

Table 2. Al_2O_3 – Cu/H_2O hybrid nanoliquid thermo-physical properties [1,5,30–32].

Properties	Al_2O_3 – Cu/H_2O hybrid nanoliquid
Viscosity (μ)	$\mu_{hnf} = \frac{\mu_f}{(1-\phi_1-\phi_2)^{2.5}}$
Density (ρ)	$\rho_{hnf} = \phi_2\rho_2 + \phi_1\rho_1 + (1-\phi_1-\phi_2)\rho_f$
Heat capacity (ρC_p)	$(\rho C_p)_{hnf} = \phi_2(\rho C_p)_2 + \phi_1(\rho C_p)_1 + (1-\phi_1-\phi_2)(\rho C_p)_f$
Thermal conductivity (k)	$\frac{k_{hnf}}{k_f} = \frac{\frac{\phi_2 k_2+\phi_1 k_1}{\phi_2+\phi_1} + 2k_f + 2(\phi_2 k_2+\phi_1 k_1) - 2(\phi_2+\phi_1)k_f}{\frac{\phi_2 k_2+\phi_1 k_1}{\phi_2+\phi_1} + 2k_f - (\phi_2 k_2+\phi_1 k_1) + (\phi_2+\phi_1)k_f}$
Diffusion coefficient (D)	$D_{hnf} = (1-\phi_1-\phi_2)D_f$

The key physical quantities appropriate to the current problem are discussed as follows:

$$C_f = \frac{\mu_{hnf}}{\rho_f u_w^2}\left(\frac{\partial u}{\partial y}\right)_{y=0}, \tag{11a}$$

$$\mathrm{Nu}_x = \frac{-x}{k_f(T_w-T_\infty)}\left[\left(k_{hnf}\frac{\partial T}{\partial y}\right)_{y=0} - (q_r)_{y=0}\right], \tag{11b}$$

$$\mathrm{Sh}_x = \frac{-x}{D_B(C_w-C_\infty)}\left(\frac{\partial C}{\partial y}\right)_{y=0}. \tag{11c}$$

Substituting the similarity variables defined in Eq. (6) into Eq. (11) yields the non-dimensional forms of the physical quantities, as presented below:

$$\mathrm{Re}_x^{1/2} C_f = R_1 f''(0), \tag{12a}$$

$$\mathrm{Re}_x^{-1/2}\mathrm{Nu}_x = -\left(R_4 + \frac{4}{3}Rd\right)\theta'(0), \tag{12b}$$

$$\mathrm{Re}_x^{-1/2}\mathrm{Sh}_x = -\phi'(0). \tag{12c}$$

3. Method of solution

The system of Eqs. (7) to (9), along with the corresponding boundary constraints, is solved numerically by utilising the BVP5C solver available in MATLAB. To implement this method, all higher-order differential equations (DEs) are first reduced to a set of first-order equations. The formulation of the problem and procedural flow of the BVP5C technique are illustrated in Fig. 2.

Let:

$$f = y_1,\quad \frac{df}{d\eta} = \frac{dy_1}{d\eta} = y_2,\quad \frac{d^2f}{d\eta^2} = \frac{dy_2}{d\eta} = y_3,\quad \frac{d^3f}{d\eta^3} = \frac{dy_3}{d\eta}, \tag{13}$$

$$\theta = y_4,\quad \frac{d\theta}{d\eta} = \frac{dy_4}{d\eta} = y_5,\quad \frac{d^2\theta}{d\eta^2} = \frac{dy_5}{d\eta}, \tag{14}$$

$$\phi = y_6,\quad \frac{d\phi}{d\eta} = \frac{dy_6}{d\eta} = y_7,\quad \frac{d^2\phi}{d\eta^2} = \frac{dy_7}{d\eta}. \tag{15}$$

Substitution of Eqs. (13)–(15) into Eqs. (7)–(9) yields the transformed equations given below:

$$R_1\frac{dy_3}{d\eta} + R_2(1+n)y_1y_3 - R_2{y_2}^2 + \\ +R_2(\mathrm{Gr}\,y_4 + \mathrm{Gc}\,y_6)\cos\alpha = 0, \tag{16}$$

$$\left(R_4 + \frac{4}{3}Rd\right)\frac{dy_5}{d\eta} + \\ +\mathrm{Pr}(Q\,y_4 + R_3(1+n)y_1y_5 - s_1R_3y_2y_4) = 0, \tag{17}$$

$$\frac{dy_7}{d\eta} + \frac{\mathrm{Sc}}{R_5}[(1+n)y_1y_7 - s_2y_2y_6 - Rc\,y_6] = 0, \tag{18}$$

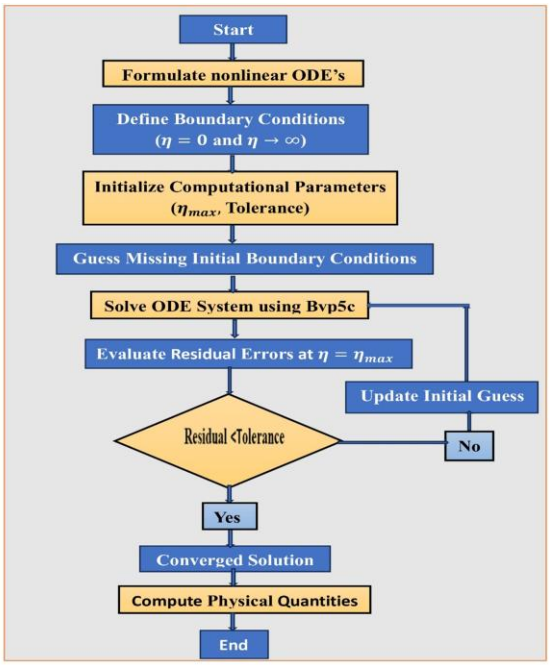


Fig. 2. Iterative BVP5C solution flowchart.

along with the boundary constraints:

$$y_1(0) = \frac{S}{1+n},\quad y_2(0) = y_6(0) = 1,$$

$$y_5(0) = -\frac{\mathrm{Bi}(1-y_4(0))}{R_4}, \tag{19}$$

$$y_2(\infty) = y_4(\infty) = y_6(\infty) = 0, \tag{20}$$

$$\frac{dy_3}{d\eta} = \frac{-R_2(1+n)y_1y_3 + R_2{y_2}^2 - R_2(\mathrm{Gr}\,y_4 + \mathrm{Gc}\,y_6)\cos\alpha}{R_1}, \tag{21}$$

$$\frac{dy_5}{d\eta} = \frac{-\mathrm{Pr}(Qy_4 + R_3(1+n)y_1y_5 - s_1R_3y_2y_4)}{\left(R_4 + \frac{4}{3}Rd\right)}, \tag{22}$$

$$\frac{dy_7}{d\eta} = -\frac{\mathrm{Sc}}{R_5}[(1+n)y_1y_7 - s_2y_2y_6 - Rc\,y_6]. \tag{23}$$

The BVP5C solver generates a solution that is continuous and possesses a continuous first-order derivative over the interval [0, ∞]. Equations (19)–(23) are programmed in MATLAB, and their solutions are obtained using the BVP5C routine. This approach ensures that the convergence criteria are adequately met 10^{-6}.

4. Results and discussion

This section presents graphical illustrations of the temperature $\theta(\eta)$, velocity $f'(\eta)$ and concentration $\phi(\eta)$ distributions for the

hybrid nanofluid Al_2O_3 – Cu/H_2O flowing over a vertical, non-isothermal and non-isosolutal, penetrable wedge and cone. A comparative assessment of the cone and wedge geometries is carried out to evaluate how the leading governing factors impact the flow, temperature and concentration characteristics. The influence of various factors, such as thermal Grashof number Gr, mass Grashof number Gc, heat absorption or generation parameter Q, radiation parameter Rd, Schmidt number Sc, chemical reaction parameter Rc, Biot number Bi, and suction parameter S, on these distributions is analysed and discussed. To explore the physical performance of the structure, the boundary value problem stated in Eqs. (16)–(20) is solved utilising MATLAB's BVP5C solver. The results are provided in both graphical and tabular representations to provide a comprehensive understanding of the underlying physical mechanism. A detailed investigation has been conducted on the skin friction coefficient, Sherwood number and Nusselt number with respect to the major influencing parameters.

The effect of thermal Grashof number, ranging between $1 \le \mathrm{Gr} \le 8$, on $f'(\eta)$, $\theta(\eta)$ and $\phi(\eta)$ distributions of Al_2O_3 – Cu/H_2O hybrid nanoliquid flowing over a wedge and cone is presented in Figs. 3 to 5.

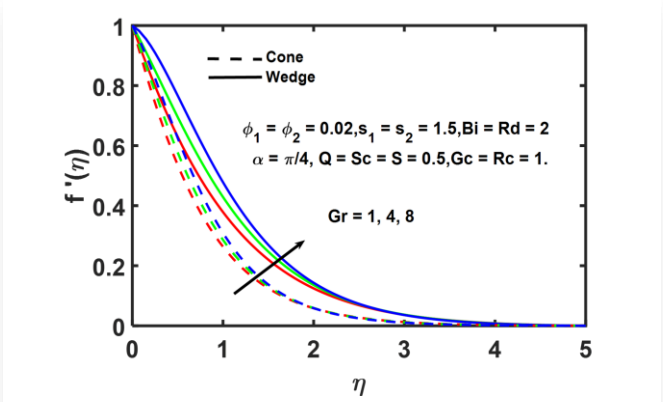


Fig. 3. Thermal Grashof number's effect on velocity profile.

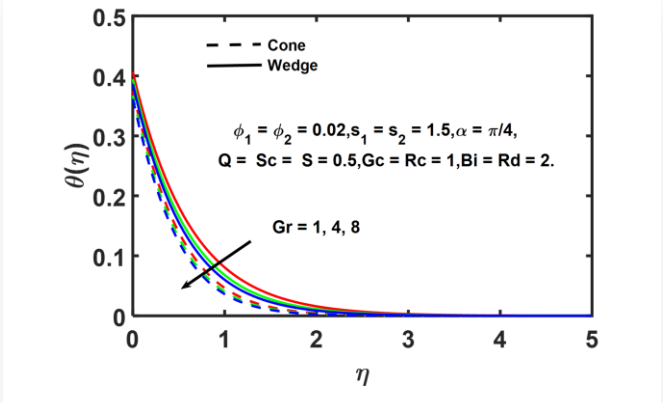


Fig. 4. Thermal Grashof number's effect on temperature profile.

As the values of Gr increase, the velocity distribution rises, while the temperature and concentration distributions exhibit a decreasing tendency. An increase in Gr reduces the boundary layer thickness due to stronger buoyancy forces generated by temperature transformations. This enhances the liquid motion and raises the velocity distribution. This increased acceleration promotes more effective mixing and advection, resulting in a dilution phenomenon that reduces solute concentration. As a result, the concentration boundary layer becomes thinner, further diminishing the concentration distribution. In addition, larger temperature gradients produce stronger buoyant forces, which enhance convective heat transfer. This intensified convection helps dissipate heat more efficiently, thereby reducing the liquid's temperature. The impact is more pronounced for the wedge compared to the cone.

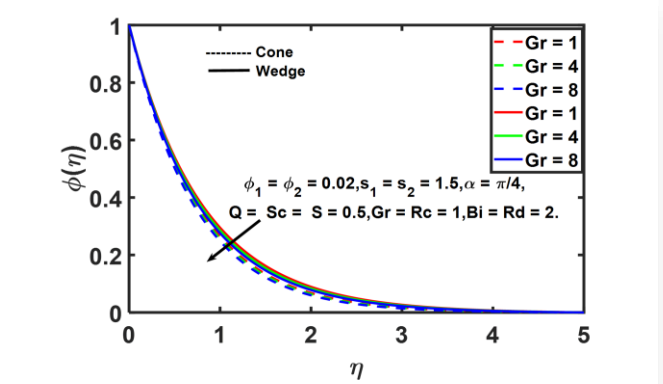


Fig. 5.Thermal Grashof number's effect on concentration profile.

Figures 6 to 8 depict the influence of the mass Grashof number, ranging between $0.1 \le \mathrm{Gc} \le 0.9$, on $f'(\eta)$, $\theta(\eta)$ and $\phi(\eta)$ profiles for both wedge and cone configurations. In a manner similar to Gr, increasing Gc enhances the $f'(\eta)$ profile, whereas $\theta(\eta)$ and $\phi(\eta)$ profiles show a decreasing trend.

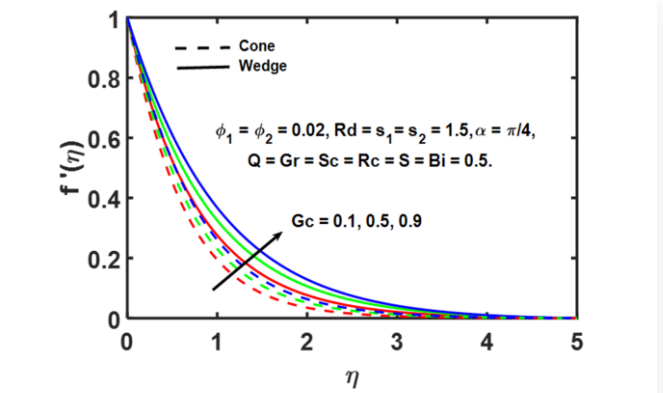


Fig. 6. Mass Grashof number's effect on velocity profile.

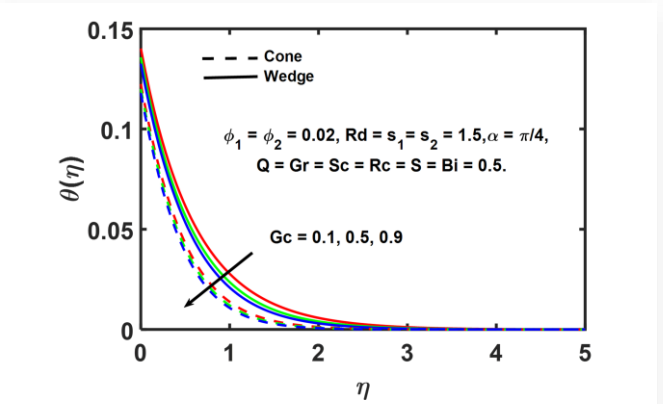


Fig. 7. Mass Grashof number's effect on temperature profile.

This phenomenon arises because the mass Grashof number is directly associated with buoyancy forces; as Gc rises, buoyancy effects become more significant, thereby accelerating the fluid flow. It is also witnessed that the impact of Gc is more pronounced for the wedge compared to the cone in all three profiles.

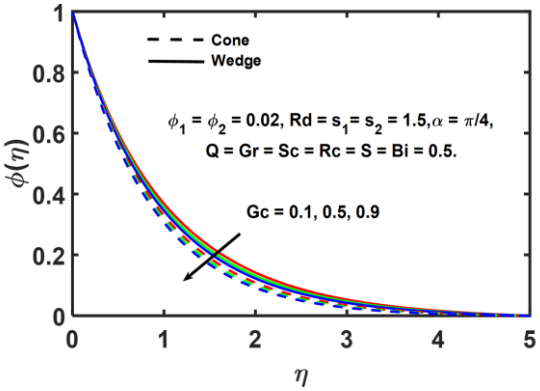


Fig. 8. Mass Grashof number's effect on concentration profile.

Figure 9 illustrates the variation in the $\theta(\eta)$ profile with cumulative values of the radiation parameter, within the range $1 \le Rd \le 2$, for both the wedge and cone. It is noted that as Rd increases, the temperature distribution in the $Al_2O_3 - Cu/H_2O$ hybrid nanofluid rises for both geometries. This occurs because a higher Rd indicates greater thermal radiation, which contributes additional energy to the fluid. Accordingly, more heat is absorbed by the hybrid nanofluid particles, leading to a thicker thermal boundary layer and an elevated temperature profile.

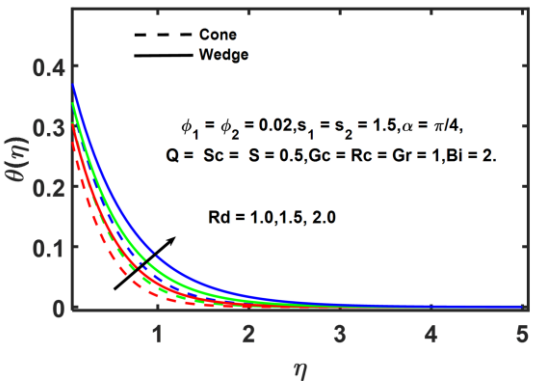


Fig. 9. Thermal radiation parameter's influence on temperature profile.

Figure 10 illustrates the effect of increasing the heat generation parameter, within the range $1.1 \le Q \le 1.3$, on the $\theta(\eta)$ profile for both the wedge and cone geometries. As Q increases, more thermal energy is transferred to the hybrid nanofluid, leading to a rise in stored internal energy within the liquid particles. This results in a thicker boundary layer and a corresponding rise in the temperature profile.

Figure 11 presents the variation of the temperature profile $\theta(\eta)$ of the hybrid nanoliquid with respect to changes in the wall temperature parameter $1 \le s_1 \le 2$, for both wedge and cone geometries. It is evident that $\theta(\eta)$ reduces with the increasing s_1 value. This reduction is due to the strong influence of higher s_1 values on the thermal boundary layer, which becomes thinner, resulting in a lower temperature distribution. Among these three parameters, their effects on $\theta(\eta)$ are found to be more important in the case of the wedge compared to that of the cone.

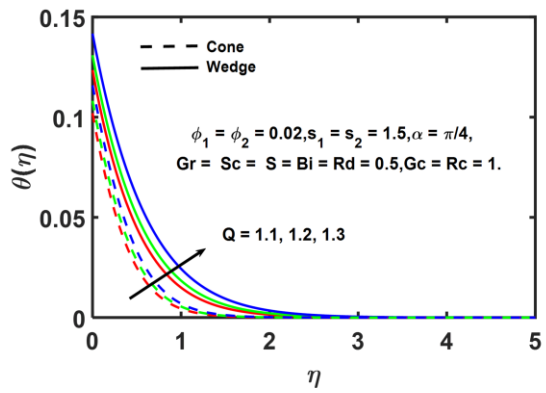


Fig. 10. Heat source factor's influence on temperature profile.

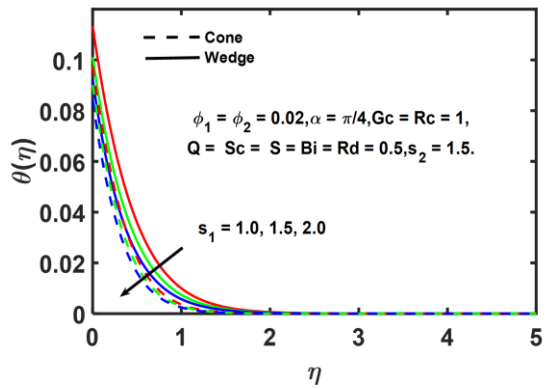


Fig. 11. Wall temperature parameter's influence on temperature profile.

Figures 12 to 14 demonstrate the influence of the chemical reaction factor ($1 \le c \le 3$), Schmidt number ($2 \le Sc \le 4$), and wall concentration parameter ($1 \le s_2 \le 3$) on the $\phi(\eta)$ profile for both the wedge and cone. The plots reveal a consistent decline in $\phi(\eta)$ with the increasing values of Rc, Sc and s_2. This behaviour is attributed to the inverse relationship between viscosity and the chemical reaction rate; an increase in Rc results in a reduction of both viscosity and concentration distribution. Similarly, a rise in Sc implies a decrease in the molecular diffusivity of the liquid, which in turn diminishes the concentration levels within the boundary layer. Regarding the wall concentration factor, as s_2 upsurges, the boundary layer becomes thinner, leading to a decrease in the concentration profile. In all these three cases, the decrease in $\phi(\eta)$ is more pronounced for the cone configuration than for the wedge.

Figures 15 to 17 present the impact of the suction factor within the range $1 \le S \le 2$ on $f'(\eta)$, $\theta(\eta)$ and $\phi(\eta)$ profiles for both cone and wedge. As S increases, all three profiles exhibit a downward trend. This behaviour is attributed to the stronger suction drawing liquid toward the surface, which modifies the boundary layer and reduces the fluid velocity. The inward pull of the fluid lessens surface friction, thereby increasing the rate of heat transfer and resulting in a decreased $\theta(\eta)$ distribution. Suction also eliminates low-energy fluid near the surface, effect-

tively drawing the hybrid nanoliquid closer to the wedge or cone surfaces. The decline in $f'(\eta)$, $\theta(\eta)$ and $\phi(\eta)$ is more significant in the case of the cone than in the wedge.

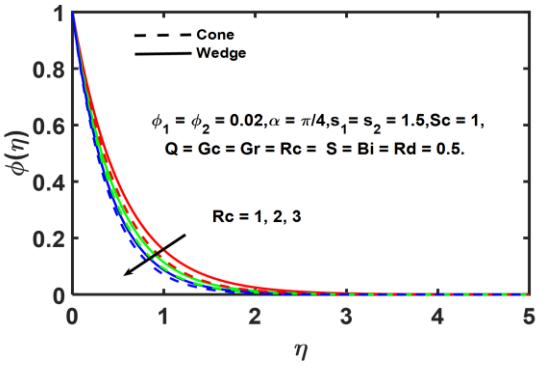


Fig. 12. Chemical reaction parameter's effect on concentration profile.

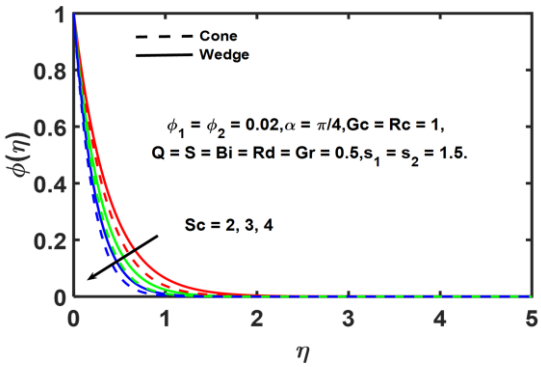


Fig. 13. Schmidt quantity's effect on concentration profile.

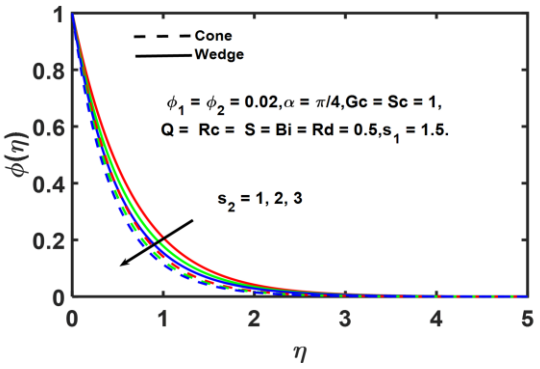


Fig. 14. Wall concentration parameter's effect on concentration profile.

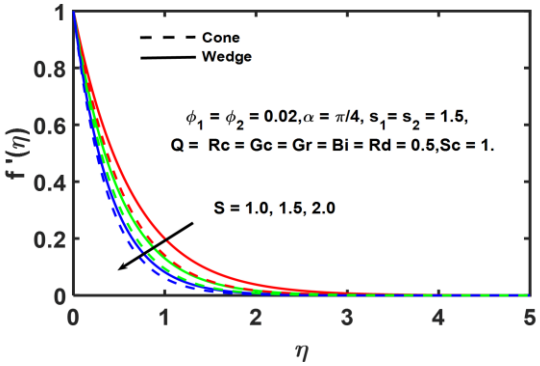


Fig. 15. Suction factor's influence on velocity profile.

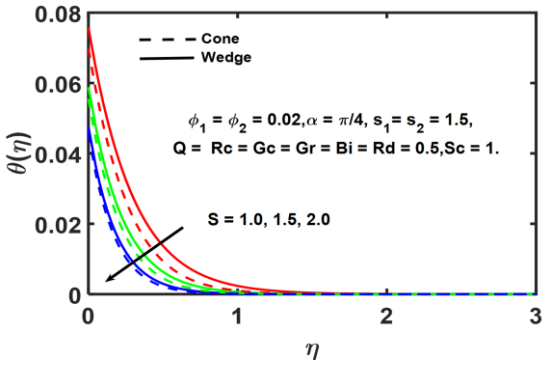


Fig. 16. Suction factor's influence on temperature profile.

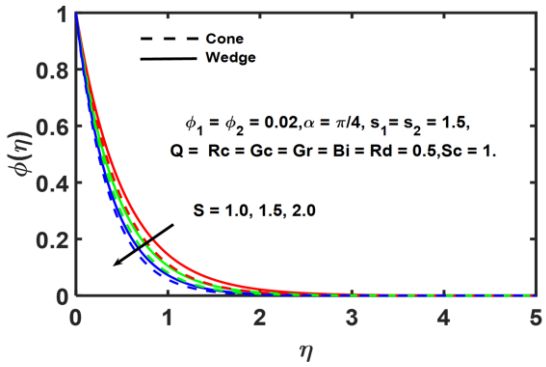


Fig. 17. Suction factor's influence on concentration profile.

Figure 18 illustrates the effect of Biot number, ranging between $1 \leq \mathrm{Bi} \leq 2$, on the $\theta(\eta)$ profile for both the cone and wedge. Bi represents the ratio of convective heat transfer at the surface to conductive heat transfer within the surface. An increase in Bi indicates stronger convective heat exchange between the cone and wedge surface and the neighbouring hybrid nanofluid. As a result, $\theta(\eta)$ increases, leading to a thicker thermal boundary layer. This influence is more important in the wedge configuration than in the case of the cone.

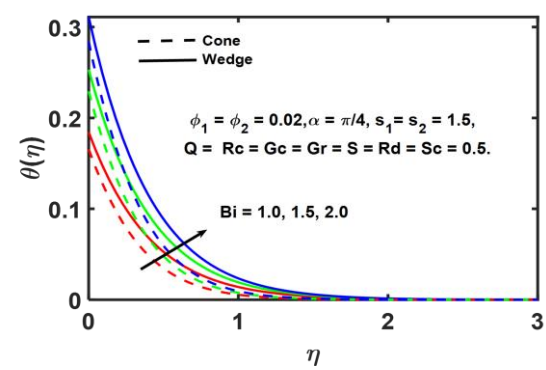


Fig. 18. Biot number's influence on the temperature profile.

Tables 3 and 4 demonstrate the effects of Gr, Gc, *Rd*, *Q*, Sc and *Rc* on the skin friction coefficient C_f, Nusselt number Nu_x and Sherwood number Sh_x for the hybrid nanofluid $Al_2O_3 - Cu/H_2O$ over both cone and wedge geometries. The computations are carried out with fixed values: $\phi_1 = \phi_2 = 0.02$, $\alpha = \pi/4$, $s_1 = s_2 = 1$, Sc = 0.2, *Rd* = *Q* = Gr = Gc = *Rc* = *S* =

Table 3.Influences of Gr, Gc, *Rd*, *Q*, Sc and *Rc* on C_f and Nu_x for both the cone and wedge.

Gr	Gc	*Rd*	*Q*	Sc	*Rc*	C_f		Nu_x	
						Cone	Wedge	Cone	Wedge
0.1						−1.411734	−1.176412	0.616064	0.605640
0.2						−1.409805	−1.173662	0.616071	0.605653
0.3						−1.407876	−1.170915	0.616077	0.605667
0.4						−1.405948	−1.168170	0.616083	0.605681
	0.1					−1.642275	−1.420108	0.614557	0.603147
	0.4					−1.460673	−1.226097	0.615756	0.605161
	0.7					−1.294884	−1.048459	0.616690	0.606633
	1.0					−1.139337	−0.881631	0.617470	0.607814
		1.0				−1.400719	−1.160468	0.765981	0.749786
		1.5				−1.397266	−1.155199	0.911128	0.887971
		2.0				−1.393672	−1.149638	1.051824	1.020541
		2.5				−1.389945	−1.143819	1.188288	1.147751
			0.1			−1.405233	−1.167917	0.621241	0.614034
			0.2			−1.404964	−1.167401	0.620081	0.612257
			0.3			−1.404675	−1.166823	0.618843	0.610299
			0.4			−1.404361	−1.166172	0.617516	0.608127
				0.2		−1.404021	−1.165427	0.616090	0.605693
				0.3		−1.441769	−1.199960	0.615791	0.605267
				0.4		−1.470497	−1.227122	0.615558	0.604919
				0.5		−1.492936	−1.249013	0.615375	0.604632
					0.5	−1.404021	−1.165427	0.616090	0.605693
					0.6	−1.408361	−1.170228	0.616056	0.605635
					0.7	−1.412498	−1.174799	0.616024	0.605580
					0.8	−1.416448	−1.179155	0.615993	0.605527

Table 4. Influences of Gr, Gc, *Rd*, *Q*, Sc and *Rc* on Sh_x for both the cone and wedge.

Gr	Gc	*Rd*	*Q*	Sc	*Rc*	Sh_x	
						Cone	Wedge
0.1						0.606284	0.571215
0.2						0.606336	0.571292
0.3						0.606387	0.571368
0.4						0.606439	0.571445
	0.1					0.582707	0.550370
	0.4					0.601217	0.566799
	0.7					0.616125	0.580182
	1.0					0.628864	0.591689
		1.0				0.606641	0.571756
		1.5				0.606824	0.572047
		2.0				0.607042	0.572397
		2.5				0.607293	0.572802
			0.1			0.606447	0.571426
			0.2			0.606456	0.571445
			0.3			0.606467	0.571467
			0.4			0.606478	0.571492
				0.2		0.606491	0.571521
				0.3		0.773045	0.721728
				0.4		0.925505	0.858809
				0.5		1.067523	0.986330
					0.5	0.606491	0.571521
					0.6	0.625225	0.590917
					0.7	0.643397	0.609699
					0.8	0.661046	0.627916

Bi = 0.5. Note that when evaluating the impact of a specific parameter, all other parameters are kept constant to isolate its effect on C_f, Nu_x and Sh_x.

Tables 3 and 4 indicate that an increase in Gr from 0.1 to 0.4 leads to a slight rise in C_f, Nu_x and Sh_x for both cone and wedge configurations. For the cone, these values are increased by approximately 0.4%, 0.003% and 0.03%, respectively, while for the wedge, the corresponding increases are about 0.7%, 0.006% and 0.04%. When Gc is increased from 0.1 to 1.0, noticeable enhancements are observed. For the cone, C_f, Nu_x and Sh_x increase by approximately 31%, 0.5% and 8%, respectively, while for the wedge, the corresponding increases are about 38%, 0.8% and 8%. As *Rd* increases from 1.0 to 2.5, the cone configuration shows increases of approximately 0.8% in C_f, 55% in Nu_x and 0.1% in Sh_x. For the wedge, the corresponding increases are about 1.4%, 53% and 0.2%, respectively. As *Q* increases from 0.1 to 0.4, both C_f and Sh_x exhibit slight increases by 0.06% and 0.01%, respectively, for the cone and by 0.15% and 0.01% for the wedge. In contrast, Nu_x decreases by 0.6% for the cone and 1% for the wedge. As $0.2 \leq Sc \leq 0.5$, both C_f and Nu_x decrease by 6% and 0.1% for the cone and by 7% and 0.2% for the wedge, respectively. In contrast, Sh_x shows a substantial increase of 76% for the cone and 73% for the wedge. Lastly, increasing *Rc* from 0.5 to 0.8 results in slight reductions in C_f and Nu_x by 0.9% and 0.02% for the cone, and by 1.18% and 0.03% for the wedge. Meanwhile, Sh_x increases by 9% for the cone and 10% for the wedge.

To ensure the validity of the present model, Tables 5 and 6, along with the bar diagrams shown in Figs. 19 and 20, present the computed values of $-f''(0)$ and $-\theta'(0)$ for the specific case when $\phi_1 = 0.00001$ and all other parameters ϕ_2, *Rd*, s_2, *Q*, Gr, Gc, Sc and *Rc* are set to zero, with $Bi = 10^6$. The outcomes demonstrate strong agreement with the existing results reported

in [3,35,36] for the cone configuration, thereby supporting the accuracy of the present formulation.

Table 5.Validation of $-f''(0)$ against existing results for a wedge.

Pr	α	s_1	S	$-f''(0)$		
				Hassanien et al. [35]	Yahaya et al. [3]	Present results
6.2	1	1	1	1.618034	1.61803	1.618281
			0.5	1.280777	1.28078	1.281515
			−0.5	0.780781	0.78078	0.782412
			0	1.00000	1.00001	1.001396

Table 6.Validation of $-\theta'(0)$ against existing results for a wedge.

Pr	α	s_1	S	$-\theta'(0)$		
				Waini et al. [36]	Yahaya et al. [3]	Present results
1	0	0	0	0.5820	0.58201	0.582013
		1		1.0000	1.00001	1.000011
		2		1.3333	1.33333	1.333333
0.72		1		0.8086	0.80864	0.808645

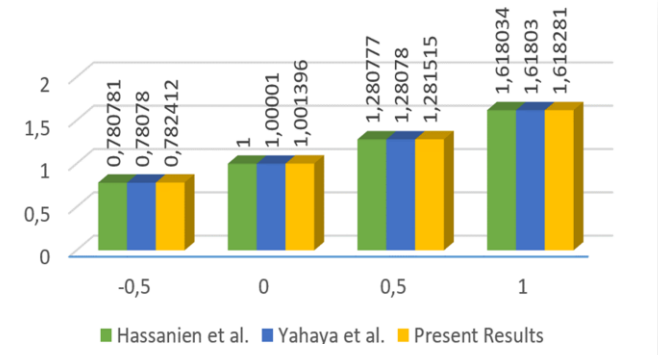


Fig. 19. Comparison of $-f''(0)$ for different values of S.

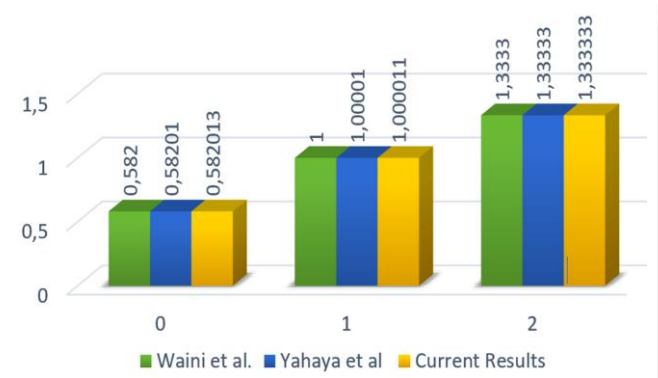


Fig. 20. Comparison of $-\theta'(0)$ for different values of s_1.

5. Conclusions

This work presents a mathematical model for analysing the steady, laminar, two-dimensional mixed convective flow of a chemically reactive hybrid nanoliquid consisting of $Al_2O_3 - Cu/H_2O$ over vertical non-isothermal/non-isosolutal wedge and cone surfaces, incorporating the influence of the heat generation factor. The nonlinear ODE system is numerically solved using MATLAB's BVP-5C solver. The key findings derived from this analysis are outlined below:

- As the values of Gr increase, an enhancement in the velocity profile is observed, whereas both concentration and temperature profiles tend to decline. A similar performance is noted for Gc as well.
- Rising values of Rd, Q and Bi leads to a rise in the temperature distribution of the hybrid nanoliquid for both geometries, whereas an opposite behaviour is noticed with the rise in s_1.
- A consistent decline in $\phi(\eta)$ is observed with increasing values of *Rc*, Sc and s_2. With an increase in S, all three profiles $f'(\eta)$, $\theta(\eta)$ and $\phi(\eta)$ show a decreasing trend.
- An increase in Gr, Gc, *Rd* and Q leads to a rise in the skin friction coefficient, whereas *Rc* produces a contrasting effect. The rate of heat transfer, represented by the Nusselt number, improves with higher Gr, Gc and *Rd* but declines as Q and *Rc* increase. Moreover, the Sherwood number is observed to increase with growing values of Gr, Gc, *Rd*, Q and *Rc* for cone and wedge geometries.

References

[1] Dawar, A., Shah, Z., Tassaddiq, A., Kumam, P., Islam, S., & Khan, W. (2021). A convective flow of Williamson nanofluid through cone and wedge with non-isothermal and non-isosolutal conditions: a revised Buongiorno model. *Case Studies in Thermal Engineering*, 24, 100689. doi: 10.1016/j.csite.2021.100869

[2] Kumar, A., Ray, A.K., Saha, S., Tanwar, D.V., Kumar, B., & Sheremet, M.A. (2023) Flow of hybrid nanomaterial over a wedge: shape factor of nanoparticles impact. *The European Physical Journal Plus*, 138, 901. doi: 10.1140/epjp/s13360-023-04535-8

[3] Yahaya, R.I., Arifin, N.Md., Mustafa, M.S., Pop, I., Ali, F.M., & Mohamed Isa, S.S.P. (2025). Mixed convection hybrid nanofluid flow past a non-isothermal cone and wedge with radiation and convective boundary condition: Heat transfer optimization. *Case Studies in Thermal Engineering*, 66, 105768. doi: 10.1016/j.csite.2025.105768

[4] Sushila, C., Jarwal, V.K., Prasun, C., Loganathan, K., & Pattanaik B. (2024). Mass-Based Hybrid Nanofluid Model for Thermal Radiation Analysis of MHD Flow over a Wedge Embedded in Porous Medium. *Journal of Engineering*, 18, 9528362. doi: 10.1155/2024/9528362

[5] Ramzan, M., Kumam, P., Lone, S.A., Seangwattana, T., Saeed, A., & Galal, A.M. (2023). A theoretical analysis of the ternary hybrid nanofluid flows over a non-isothermal and non-isosolutal multiple geometries. *Heliyon*, 9(4), e14875. doi: 10.1016/j.heliyon.2023.e14875

[6] Reddy, M.V., Ajithkumar, M., Lone, S.A., Ali, F., Lakshminarayana, P., & Saeed, A. (2024). Magneto-Williamson nanofluid flow past a wedge with activation energy: Buongiorno model. *Advances in Mechanical Engineering*, 16(1). doi: 10.1177/16878132231223027

[7] Chandra Reddy, P., Raju, M.C., Raju, G.S.S., & Varma, S.V.K. (2016). Free convective magneto-nanofluid flow past a moving vertical plate in the presence of radiation and thermal diffusion.

Frontiers in Heat and Mass Transfer, 7, 28. doi: 10.5098/hmt.7.28

[8] Mathews, J., & Talla, H. (2024). Unsteady magnetohydrodynamic free convection and heat transfer flow of Al_2O_3 – Cu/water nanofluid over a non-linear stretching sheet in a porous medium. *Archives of Thermodynamics*, 45(1), 165–173. doi: 10.24425/ather.2024.150449

[9] Amit, P., & Shalini, J. (2019). Influence of non-linear chemical reaction on MHD convective flow for maxwell fluid over three different permeable vertical surfaces. *Journal of Nanofluids*, 8, 671–682. doi:10.1166/jon.2019.1639

[10] AL Garalleh, H. (2024). Numerical simulation of heat transport mechanism in chemically influenced ternary hybrid nanofluid flow over a wedge geometry. *Discover Applied Sciences*, 6, 449. doi: 10.1007/s42452-024-06141-4

[11] AI-Arabi, T.H., Mahdy, A., Rashad, A.M., Saad, W., & Nabwey, H.A. (2022). Convective flow of a Williamson hybrid nanofluid in a porous medium through a cone and wedge with the effect of the shape of nanoparticles. *Heat Transfer*, 51(8), 7009−7029. doi: 10.1002/htj.22634

[12] Vajravelu, K., & Nayfeh, J. (1992). Hydromagnetic convection at a cone and a wedge. *International Communications in Heat and Mass Transfer*, 19(5), 701–710. doi: 10.1016/0735-1933(92)90052-J

[13] Rekha, M.B., Sarris, I.E., Madhukesh, J.K., Raghunatha, K.R., & Prasannakumara, B.C. (2022). Activation energy impact on flow of AA7072-AA7075/water based hybrid nanofluid through a cone, wedge and plate. *Micromachines*, 13(2), 302. doi: 10.3390/mi13020302

[14] Chandra Reddy, P., Umamheswar, M., Harinath Reddy, S., Raju, A.B.M., & Raju, M.C. (2022). Numerical study on the parabolic flow of MHD fluid past a vertical plate in a porous medium. *Heat Transfer*, 51(4), 3418−3430. doi: 10.1002/htj.22457

[15] Chandra Reddy, P., Raju, M.C., & Raju, G.C. (2016). Free convective heat and mass transfer flow of heat-generating nanofluid past a vertical moving porous plate in a conducting field. *Special Topics & Reviews in Porous Media: An International Journal*, 7(2), 161−180. doi: 10.1615/SpecialTopicsRevPorousMedia.2016016973

[16] Mathews, J., & Talla, H. (2025). Unsteady magnetohydrodynamic free convection flow of Al_2O_3 – Cu/water nanofluid over a permeable linear stretching sheet through a porous medium with viscous dissipation and heat source/sink. *Journal of Thermal Engineering*, 11(2), 344–356. doi: 10. 14744/thermal.0000919

[17] Ali, R., Iqbal, A., Abbass, T., Arshad, T., & Shahzad, A. (2024). Unsteady flow of silica nanofluid over a stretching cylinder with effects of different shapes of nanoparticles and Joule heating. *Archives of Thermodynamics*, 45(3), 115–126. doi: 10.24425/ather.2024.151222

[18] Ali, R., Mitalipova, A., Ul Hussan, S.W., Kurbanaliev, A., Shahzad, A., & Abduzhabbarov, M. (2025). Shape effects on steady flow and heat transfer of Cu-nanofluid over a nonlinear stretching surface with Joule heating. *Archives of Thermodynamics*, 46(3), 89–104. doi: 10.24425/ather.2025.156581

[19] Shahzad, A., Gulistan, U., Ali, R., Iqbal, I., Benim, A.C., Kamran, M., Ud-Din Khan, S., Ud-Din Khan, S., & Farooq, A. (2020). Numerical study of axisymmetric flow and heat transfer in a liquid film over an unsteady radially stretching surface. *Mathematical Problems in Engineering*, 2020, 1−9. doi: 10.1155/2020/6737243

[20] Zaman, M., Jahan, S., Sohail, M., Farman, M., Nisar., K.S. (2025). Thermal analysis of Williamson nanofluid in cone and wedge geometries: an ANN optimization. *Journal of Thermal Analysis and Calorimetry*, 150, 17413–17435. doi: 10.1007/s10973-025-14658-y

[21] Galal, A.M., Abbas, M., Rajab, A.B., Alsaydi, H.A., Abdallah, S.A.O., Abd EL-Gawaad, N.S., Akgül, A., & Shafique, M. (2022). Simulation of thermally radiative flow of hybrid nanofluid over wedge, plate and cone with elastic-deformation and surface tension gradient. *Journal of Radiation Research and Applied Sciences*, 18(2), 1275−1281, 101396. doi: 10.1016/j.jrras.2025.101396

[22] Sadiya, A.B., & Sucharitha, G. (2025). Computational analysis of MHD ternary hybrid nanofluid flow with thermochemical reactions through a porous medium on a rotating stretching sheet. *Discover Nano*, 20, 168. doi: 10.1186/s11671-025-04353-0

[23] Qureshi, H., Zubair, M., & Altmeyer, S.A. (2025). Machine learning investigation of ternary-hybrid radiative nanofluid over stretching and porous sheet. *Nanomaterials*, 15(19), 1525. doi: 10.3390/nano15191525

[24] Ramana, R.M., Maheswari, Ch., Mohiddin Shaw, S., Dharmaiah, G., Fernandez-Gamiz, U., & Noeiaghdam, S. (2024). Numerical investigation of 3-D rotating hybrid nanofluid Forchheimer flow with radiation absorption over a stretching sheet. *Results in Engineering*, 22, 102019. doi: 10.1016/j.rineng.2024.102019

[25] Raju, K.V., Maheswari, Ch., Ramana, R.M., Varma. S.V., & Raju, M.C. (2026). Comparative numerical study between MHD Forchheimer nano and hybrid nanofluid flows over stretching sheet under aligned magnetic field in the presence of radiation absorption. *International Journal of Modelling and Simulation*, 46(4), 1450–1467. doi: 10.1080/02286203.2024.2393306

[26] Rosseland, S. (1931). *Astrophysik Auf Atomtheoretischer Grundlage*, Springer Berlin Heidelberg. doi: 10.1007/978-3-662-26679-3

[27] Ishak, A. (2010). Thermal boundary layer flow over a stretching sheet in a micropolar fluid with radiation effect. *Meccanica*, 45(3), 367−373. doi: 10.1007/s11012-009-9257-4

[28] Magyari, E., & Pantokratoras, A. (2011). Note on the effect of thermal radiation in the linearized Rosseland approximation on the heat transfer characteristics of various boundary layer flows. *International Communication in Heat and Mass Transfer*, 38(5), 554−556. doi: 10.1016/j.icheatmasstransfer.2011.03.006

[29] Bataller, R.C. (2008). Radiation effects for the Blasius and Sakiadis flows with a convective surface boundary condition. *Applied Mathematics and Computation*, 206(2), 832−840. doi: 10.1016/j.amc.2008.10.001

[30] Sheremet, M., Oztop, H.F., Pop, I., & Al-Salem, K. (2016). MHD free convection in a wavy open porous tall cavity filled with nanofluids under an effect of corner heater. *International Journal of Heat and Mass Transfer*, 103, 955–964. doi: 10.1016/j.ijheatmasstransfer.2016.08.006

[31] Merkin, J.H., Pop, I., Lok, Y.Y., & Grosan, T. (2021). *Similarity Solutions for the Boundary Layer Flow and Heat Transfer of Viscous Fluids, Nanofluids, Porous Media, and Micropolar Fluids*. Elsevier Academic Press. doi: 10.1016/C2019-0-01299-X

[32] Nazir, U., Sohail, M., Hafeez, M.B., & Krawczuk, M. (2021). Significant production of thermal energy in partially ionized hyperbolic tangent material based on ternary hybrid nanomaterials. *Energies*, 14(21), 6911. doi: 10.3390/en14216911

[33] Khashi'ie, N.S., Waini, I., Mukhtar, M.F., Zainal, N.A., Bin Hamzah, K., Arifin, N.M. & Pop, I. (2022). Response surface methodology (RSM) on the hybrid nanofluid flow subject to a vertical and permeable wedge. *Nanomaterials*, 12(22), 4016. doi: 10.3390/nano12224016

[34] Oztop, H.F., & Abu-Nada, E. (2008). Numerical study of natural convection in partially heated rectangular enclosures filled with

nanofluids. *International Journal of Heat Fluid Flow*, 29(5), 1326–1336. doi: 10.1016/j.ijheatfluidflow.2008.04.009

[35] Hassanien, I.A., Abdullah, A.A., & Gorla, R.S.R. (1998). Flow and heat transfer in a power-law fluid over a nonisothermal stretching sheet. *Mathematical and Computer Modeling*, 28(9), 105–116. doi: 10.1016/S0895-7177(98)00148-4

[36] Waini, I., Ishak, A., & Pop, L. (2021). Hybrid nanofluid flow over a permeable non-isothermal shrinking surface. *Mathematics*, 9(5), 538. doi: 10.3390/math9050538

Co-published by
Institute of Fluid-Flow Machinery
Polish Academy of Sciences
Committee on Thermodynamics and Combustion
Polish Academy of Sciences

Copyright©2026 by the Authors under licence CC BY-NC-ND 4.0

http://www.imp.gda.pl/archives-of-thermodynamics/

Physics-Informed Deep Learning Optimisation for Heat Transfer Analysis of Non-Similar Flow over Porous Moving Surface

Syed Shahzad Ali[a], Muhammad Imran Khan[a,b*], Mohammed Almakki[b], Ahmed Zeeshan[a,c]

[a]Department of Mathematics and Statistics, International Islamic University Islamabad, 44000, Pakistan
[b]School of Engineering, Architecture and Interior Design, Amity University Dubai, P.O. Box 345019, Dubai International Academic City, United Arab Emirates
[c]Department of Mathematics, College of Science, Korea University, 145 Aman-ro, Seongbuk-gu, Seoul 02841 Republic of Korea
[*]Corresponding author email: muhammad.phdma132@iiu.edu.pk

Received: 20.12.2025; revised: 21.06.2026; accepted: 30.06.2026

Abstract

The investigation of fluid flow and thermal behaviour near continuous moving surfaces is an active and important area of research with direct applications across numerous engineering processes. Physics-informed neural networks gain a significant role in fluid dynamics and engineering applications due to their ability to integrate physical laws directly into the learning process of neural networks. This work expands the use of physics-informed neural networks to address thermal and momentum boundary layer issues of non-Newtonian fluid. The primary concern is to investigate momentum and thermal boundary layer under tangent hyperbolic non-Newtonian fluid flow circumstances. Due to the shear thinning and shear thickening behaviour of the non-Newtonian fluid, it has wide application in various domains. The physical constraints of the governing equations are solved using physics-informed neural networks. The models are constructed and trained using TensorFlow, and the predictions produced by this method are contrasted with those derived using Richardson extrapolation and adaptive moment estimation optimisation. The adaptive moment estimation optimiser is a well-known gradient-based optimisation technique that is frequently used in fluid dynamics, particularly when governing equations are solved using machine learning, deep learning, or physics-informed neural networks. The impact of various parameters has been analysed and shown graphically. The Lorentz force opposes fluid motion, producing a retarding effect that decreases velocity. The Darcy and Forchheimer drag forces increase with decreasing porosity, resulting in substantial momentum suppression and less convective heat evacuation, which raises the local temperature.

Keywords: Physics-informed neural networks; Python programming; Non-Newtonian fluid; Inclined magnetic field; Mixed convection

Vol. 47(2026), No. 3, 111–123; doi: 10.24425/ather.2026.7508

Cite this manuscript as: Ali, S.S., Khan, M.I., Almakki, M., & Zeeshan, A. (2026). Physics-Informed Deep Learning Optimisation for Heat Transfer Analysis of Non-Similar Flow over Porous Moving Surface. *Archives od Thermodynamics*, 47(3), 111−123.

1. Introduction

Artificial intelligence is the domain of emerging computers and robots that are capable of behaving in ways that both mimic and go beyond human capabilities. Programs having artificial intelligence (AI) capabilities can interpret and analyse data to provide information or initiate activities automatically without human intervention. Machine learning is a branch of artificial intelligence that employs algorithms to automatically extract knowledge and identify trends from data, then use that knowledge to make ever-better decisions. Machine learning has a broad range of applications, including prognostication, design and speech recognition, optimisation and image processing [1−3]. A neural network is an artificial intelligence based model

Nomenclature

a – radius of the cylinder, m
b_i – bias term of network
B_0 – magnetic field strength, Wb/m^2
C_p – specific heat capacity, J/(kg K)
C_f – skin friction, Pa
Da – Darcy parameter
Ec – Eckert number
g – gravitational acceleration, m/s^2
Gr – Grashof number
k_f – fluid thermal conductivity, W/(m K)
K – permeability, m^2
L^2 – error
L_{data}, $L_{physics}$, L_{BC} – data loss, physics loss, boundary condition loss
M – magnetic parameter
Nu – Nusselt number
p – pressure, Pa
Pr – Prandtl number
q_w – wall heat flux, W/m^2
Q – heat generation and absorption parameter
Rd – thermal radiation parameter
Re – Reynolds number, Re $= Dv\rho\ /\mu$
R_f, R_θ, R_{BC} – residuals of momentum equation, energy equation and boundary condition
t – time, s
T – temperature, K
T_w – surface temperature, K
T_∞ – ambient temperature, K
u, v – velocity components, m/s
U_∞ – ambient velocity, m/s
w – weight of the network
We – Weissenberg number
x, y – horizontal and vertical coordinate axes, m

Greek symbols

α – thermal diffusivity, m^2/s
ϵ – required tolerance
μ – dynamic viscosity, Pa/s
ν – kinematic viscosity, m^2/s
ξ, η – dimensionless variables
ρ – density, kg/m^3
σ – electrical conductivity, S/m
τ_w – wall shear stress, Pa
θ – dimensionless temperature
φ – magnetic inclination angle, deg

Abbreviations and Acronyms

ADAM – adaptive moment estimation
AI – artificial intelligence
FCN – fully connected network
ML – machine learning
MSE – mean squared error
ODEs – ordinary differential equations
PDEs – partial differential equations
PINN – physics-informed neural network

that is inspired by the brain's structure and operation. It possesses enormous applications in many sectors, such as computational materials and chemical sciences [4,5], pharmaceutical sector [6], biomedical sciences [7], climate forecasting [8], robotics [9], and aerospace and mechanical engineering [10,11]. The neural network is motivated by the universal approximation theorem, which asserts that a feedforward neural network with at least one hidden layer may approximate any continuous function within some level of accuracy, especially for simple functions [12]. A neural network is one of the main supervised machine learning models, wherein input data is transformed into associated outputs. Training is performed using a given dataset of input-output pairs to modify the network parameters such that the difference between estimated and actual values is minimised. The method of convergence is through the optimisation of a loss function, usually quantified by mean squared error (MSE). This optimisation process relies on gradient-based algorithms with automatic differentiation for the efficient backpropagation of errors and the tuning of the network's performance, Baydin et al. [13].

Figure 1 shows that the artificial intelligence is a broader concept, however, machine learning is a subset of AI. Supervised learning may also be used to solve differential equations. To solve a differential equation means that one is seeking a mapping of input physical variables provided to corresponding unknown physical values, which are the estimated solution. A neural network is learned to approximate this solution in a non-linear way so that it can estimate the solution of the equation at any input point. Two major drawbacks are, however, present: first, the network has difficulty extrapolating solutions for input variables outside the range of training data. Second, the training procedure can converge failing when dealing with a large dataset.

Physics-informed neural network (PINN**)** is a machine learning framework that incorporates the laws of physics into the training section of a neural network. PINNs are designed by incorporating governing physical equations into the loss function as constraints, which helps to ensure precise output predictions even in areas with limited or no data. This section presents various strategies to apply PINNs to complex systems and problems. PINN involves minimising the residual of the governing differential equation evaluated at various points within the domain. Boundary conditions are incorporated either by announcing soft constraints with corresponding boundary data values in the minimisation process or by strictly enforcing the solution with hard constraints. To get over this restriction, more physics-based data are integrated into the classical neural network. In simulating physical and engineering problems represented by

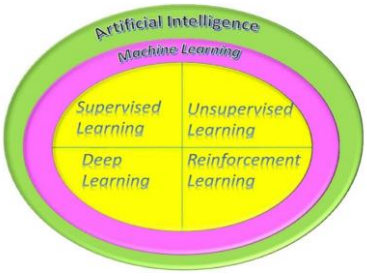


Fig. 1. Flow chart representation of artificial intelligence and machine learning.

differential equations, these methods are commonly referred to as physics-informed neural networks (PINNs). In these methods, the given set of data points, which are called collocation points, is utilised so that the learned solution obeys the governing differential equations. A new loss function, called physics loss, is added to the original loss function of the learning system. This second constraint punishes the training process, making the solution both partly driven by the initial data and partly by the physics underlying it, thus considerably limiting the solution space. With partial differential equations, little known data is needed. Therefore, PINN methods are regarded as more physics-informed than data-driven methods. Cuomo et al. [14] investigated the use of PINNs to approximate solutions to initial value problems. Bararnia and Esmaeilpour [15] examined thermal analysis of boundary layer flow with PINNs. They concluded that Pr in a heat equation is a crucial variable whose value significantly alters the number of artificial neurons and layers needed to produce the intended effects. Due to the fascinating phenomena and applications of neural networks and PINNs in the fluid mechanics domain, there are many researchers who pay attention to scrutinising an approximate solution of a fluid problem [16−21].

Non-Newtonian fluids are important in engineering and manufacturing industries because of their special physical properties, especially their viscosity, which is dependent on applied forces. These fluids find their application in manufacturing protective gear like body armour and safety helmets. Visco-plastic fluids possess dual characteristics – behaving like solids when subject to high stress and as fluids when subject to moderate stress. For instance, they minimise boundary layer thickness of airfoils, turbine blades and ship hulls for lower drag force, resulting in considerable savings in fuel consumption and improved efficiency. The first approximation theory was developed by Prandtl [22], who described a mathematical basis flow with a high Reynolds number and derived equations for a two-dimensional boundary layer. Finding a closed-form solution for a governing equation and dealing with boundary layer theory has never been a simple task. These governing equations are numerically solved using a variety of techniques, such as the shooting method, homotopy analysis methodology and finite difference method. Non-Newtonian fluids play a significant role in engineering and manufacturing industries owing to their unique physical properties. Numerous items, including safety gear and body armour, are manufactured using non-Newtonian fluids. Peng et al. [23] have discussed the use of non-Newtonian fluids. The topics of [24,25] include fluid flow and heat transfer enhancement of non-Newtonian fluid flow problems. Numerous research that uses different geometrical structures and computational methods to examine the non-Newtonian fluid model can be identified in [26−30]. Numerical investigation of heat transfer and boundary layer flow of a semi-infinite vertical plate with slip condition was made to evaluate rheological characteristics of Casson fluid [31]. Ramachandra Prasad et al. [32] examined non-Newtonian flow and heat transfer over a partial slip horizontal cylinder using an implicit finite difference method. For more interesting and advanced literature, we can view references [33−37].

In the domains of fluid dynamics, PINNs are used to solve Navier-Stokes equations, boundary layer flows, and to simulate complex phenomena like turbulence and multiphase flows. In the field of heat and mass transfer, PINNs are applied to solve problems involving conduction, convection, radiation and phase-change processes. PINNs are used in aerodynamics to forecast lift, drag, and pressure distributions with lower computing costs in airfoil and wing simulations. In order to build structures that maximise aerodynamic performance while minimising resistance, they are frequently employed in shape optimisation jobs. In aerodynamics, cylinder structure is applied to make design of aircraft and rockets.

Therefore, the main objective of this research work is to implement physics-informed neural networks (PINNs) to study non-similar boundary layer flow of tangent hyperbolic fluid over a cylinder with buoyancy effects. The author applied the adaptive moment estimation (ADAM) optimiser to evaluate an approximate solution of non-similar tangent hyperbolic fluid over a cylinder. The Python platform is implemented for programming purposes.

2. Mathematics-based system modelling

In this investigation, we considered steady, two-dimensional flow and heat transfer behaviour of a non-Newtonian tangent hyperbolic fluid along a horizontal cylinder with thermal radiation and Joule heating effects. The fluid is presumed to be incompressible and subjected to the tangent hyperbolic model, taking into consideration shear-thinning characteristics. Figure 2, shows the flow problem. Here, a represents the cylinder radius. Since ($0 \le \phi \le \pi$), $\phi = x/a$ is a y-axis angle. Also, a constant magnetic field with strength B_0 is imposed in the radial direction of the cylinder. The symbol g represents gravity, and T_w is a constant temperature.

With the above assumptions, the governing equations are as follows [31−35]:

$$\frac{\partial u}{\partial x} + \frac{\partial v}{\partial y} = 0, \tag{1}$$

$$u\frac{\partial u}{\partial x} + v\frac{\partial u}{\partial y} = \nu\left[(1-n)\left(\frac{\partial^2 u}{\partial y^2}\right) + \sqrt{2}\,n\left(\frac{\partial u}{\partial y}\right)\left(\frac{\partial^2 u}{\partial y^2}\right)\right] + -\frac{\nu}{k}u + Cu^2 + g\beta sin\left(\frac{x}{a}\right)(T - T_\infty) - \frac{\alpha B_0^2}{\rho}\sin^2\varphi\, u, \tag{2}$$

$$u\frac{\partial T}{\partial x} + v\frac{\partial T}{\partial y} = \alpha\frac{\partial^2 T}{\partial y^2} - \frac{1}{\rho C_p}\frac{\partial q_x}{\partial y} + \frac{\sigma}{\rho C_p}\sin^2\varphi\, B_0^2 u^2 + + \frac{\mu}{\rho C_p}\left(\frac{\partial u}{\partial y}\right)^2 + \frac{Q_0}{\rho C_p}(T - T_\infty). \tag{3}$$

Boundary conditions to solve Eqs. (1)−(3) are defined as:

$$y = 0: \qquad u = 0, \quad v = 0, \quad T = T_w, \tag{4a}$$

$$y = \infty: \qquad u \to 0, \quad v \to 0, \quad T = T_\infty. \tag{4b}$$

Non-similarity transformations are given below:

$$\xi = \frac{x}{a}, \qquad \eta = \frac{y}{a}\sqrt[4]{\mathrm{Gr}}, \qquad f(\xi,\eta) = \frac{\psi}{\nu_f \xi \sqrt[4]{\mathrm{Gr}}},$$

$$\theta(\xi,\eta) = \frac{T - T_\infty}{T_w - T_\infty}, \qquad \mathrm{Gr} = \frac{g\beta_f (T_w - T_\infty)a^3}{{\nu_f}^2}. \tag{5}$$

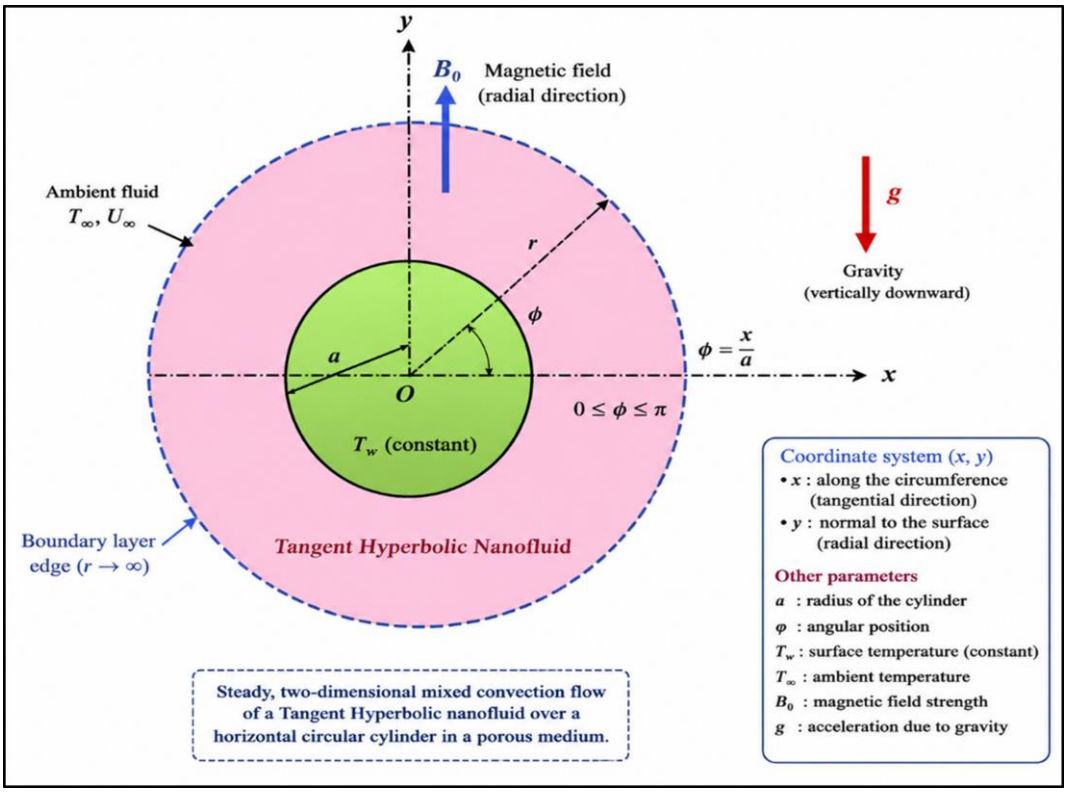


Fig. 2. Schematic flow diagram of tangent hyperbolic flow over a horizontal cylinder.

While applying the non-similarity transformation on the governing equations, the continuity equation is inherently satisfied, whereas the remaining Eqs. (2)–(3) are obtained as:

$$(1-n)f''' + n\mathrm{We}ff'' - (1+\xi\Lambda)f'^2 + \\ -\left(M\sin^2\varphi + \frac{1}{\mathrm{Da}}\right)f' + \frac{\sin\xi}{\xi}\theta = \xi\left(f'\frac{\partial f'}{\partial\xi} - f''\frac{\partial f}{\partial\xi}\right), \quad (6)$$

$$\frac{1}{\mathrm{Pr}}\left[1+\frac{4}{3}Rd\right]\theta'' + f\theta' + \sin^2\varphi J\xi^2 f'^2 + \\ + \mathrm{Ec}\xi^2 f''^2 + Q\theta = \xi\left(f'\frac{\partial\theta}{\partial\xi} - \theta'\frac{\partial f}{\partial\xi}\right). \quad (7)$$

The boundary conditions are transformed as follows:

$$\eta = 0: \qquad f' = 0, \quad f = 0, \quad \theta = 1, \quad (8a)$$

$$\eta \to \infty: \qquad f' = 0, \quad \theta = 0. \quad (8b)$$

The flow input parameters are $M = \frac{\sigma_f {B_0}^2 a^2}{\rho_f \nu_f \sqrt{\mathrm{Gr}}}$, represents magnetic field intensity, the Prandtl number is defined as $\mathrm{Pr} = \frac{\nu_f}{\alpha_f}$, $\mathrm{Da} = \frac{K\sqrt{\mathrm{Gr}}}{a^2}$ is the Darcy parameter, lambda (Λ) is equal to Ca, the radiation parameter $Rd = \frac{4\sigma^* {T_\infty}^3}{k^* k_f}$, $Q = \frac{Q_0 a^2}{(\rho C_p)_f \nu_f \mathrm{Re}}$ is the heat generation and absorption parameter, the Eckert number $\mathrm{Ec} = \frac{\mu {\nu_f}^2 \mathrm{Gr}}{a^2 C_p (T_w - T_\infty)}$, and the Weissenberg number is denoted by $\mathrm{We} = \frac{\sqrt{2}\nu\Lambda x \mathrm{Gr}^{3/4}}{a^3}$.

Now we establish two significant flow output responses in fluid and heat transfer analysis, i.e. C_f and Nu. Skin friction is the resistance offered by a fluid due to viscosity when it flows over a surface. The Nusselt number (Nu) indicates the effectiveness of convective heat transfer relative to conduction. Both parameters are vital in the optimisation of designs for fluid flow and heat exchange systems, and they are defined as:

$$C_f = \frac{2\tau_w}{\rho_f u_\infty^2}, \qquad \mathrm{Nu}_x = \frac{x q_w}{k_f (T_w - T_\infty)}, \quad (9)$$

where τ_w and q_w are:

$$\tau_w = \left[\mu\left(\frac{\partial u}{\partial y}\right) + \frac{1}{\beta c}\left(\frac{\partial u}{\partial y}\right) - \frac{1}{6\beta c^3}\left(\frac{\partial u}{\partial y}\right)^3\right]_{y=o}, \quad (10)$$

$$q_w = -k_f\left[1 + \frac{16\sigma^* T_\infty^3}{3k^* k_f}\right]\left(\frac{\partial T}{\partial y}\right)_{y=0}. \quad (11)$$

By simplifying, Eq. (9) becomes:

$$C_f \mathrm{Gr}^{-\frac{3}{4}} = (1-n)\xi f''(\xi,0) - \frac{n}{2}\mathrm{We}\xi\left(f''(\xi,0)\right)^2, \quad (12)$$

$$\frac{\mathrm{Nu}}{\sqrt[4]{\mathrm{Gr}}} = -\theta'(\xi,0). \quad (13)$$

3. Local non-similarity method

In dealing with non-similarity boundary layers, a widely used concept is the idea of local similarity. Within this concept, the right-hand sides of Eqs. (6) and (7) are presumed to be sufficiently small, essentially replacing them with approximations to zero. This keeps the computational exercise simple, generating a system of ordinary differential equations. As such, the local similarity solution, or the first level of truncation, has computa-

tional attractiveness but may provide numerical answers of questionable accuracy. The ambiguity stems from the question of whether to ignore the right-hand side of the equations when ξ is not small. To alleviate this shortcoming, Minkowycz and Sparrow [38], Sparrow and Yu [39] proposed a local non-similarity technique for finding solutions to non-similar boundary layer equations. For obtaining the local non-similarity solution of Eqs. (9)–(16), we introduce new dependent variables as addressed in [38,39].

3.1. First level of truncation

Assuming that ξ is very small ($\xi \ll 1$), derivatives of ξ are ignored, and Eqs. (6)–(8) are transformed into:

$$(1+n)f''' - (1+\xi\Lambda)f'^2 + n\mathrm{We}f''f''' + \\ -\left(M\sin^2\varphi + \frac{1}{\mathrm{Da}}\right)f' + \frac{\sin\xi}{\xi}\theta = 0, \quad (14)$$

$$\frac{1}{\mathrm{Pr}}\left[1+\frac{4}{3}Rd\right]\theta'' + f\theta' + J\sin^2\varphi\,\xi^2 f'^2 + \\ + \mathrm{Ec}\xi^2 f''^2 + Q\theta = 0, \quad (15)$$

$$\eta = 0: \quad f'(\xi,0) = f(\xi,0) = 0, \quad \theta(\xi,0) = 0, \quad (16a)$$

$$\eta \to \infty: \quad f'(\xi,\infty) = 0, \quad \theta(\xi,\infty) = 0. \quad (16b)$$

3.2. Second level of truncation

At the second level truncation, we introduce new functions:

$$g = \partial f/\partial\xi,\ h = \partial g/\partial\xi,\ \phi = \partial\theta/\partial\xi,\ \varphi = \partial\phi/\partial\xi.$$

We differentiate Eqs. (14)–(16) with respect to ξ and obtain the following system of ODEs:

$$(1+n)f''' + n\mathrm{We}f''f''' - (1+\xi\Lambda)f'^2 + \\ -\left(M\sin^2\varphi + \frac{1}{\mathrm{Da}}\right)f' + \frac{sin\xi}{\xi}\theta = \xi(f'g' - f''g), \quad (17)$$

$$\frac{1}{\mathrm{Pr}}\left[1+\frac{4}{3}Rd\right]\theta'' + f\theta' + J\sin^2\varphi\,\xi^2 f'^2 + \\ + \mathrm{Ec}\xi^2 f''^2 + Q\theta = \xi(f'\phi - \theta' g), \quad (18)$$

$$(1+n)g''' + n\mathrm{We}(fg'' + f''g) - f'g' + f''g + \\ -g'^2 - \xi\Lambda g'^2 - \Lambda f'^2 - \left(M\sin^2\varphi + \frac{1}{\mathrm{Da}}\right)g' + \\ + \frac{\sin\xi}{\xi}\phi + \theta\left(\frac{\xi\cos\xi - \sin\xi}{\xi^2}\right) = \xi(g'g' - g''g), \quad (19)$$

$$\frac{1}{\mathrm{Pr}}\left[1+\frac{4}{3}Rd\right]\phi'' + f\phi' + 2\theta' g + \mathrm{Ec}\left(\xi^2 g'^2 + 2f'^2\xi\right) + \\ + J\sin^2\varphi\left(\xi^2 g'^2 + 2f'^2\xi\right) - f'\phi + Q\phi = \xi(\phi g - g\phi'), \quad (20)$$

$$\eta = 0: \quad g'(\xi,0) = g(\xi,0) = 0, \quad \phi(\xi,0) = 1, \quad (21a)$$

$$\eta \to \infty: \quad g'(\xi,\infty) = 0, \quad \phi(\xi,\infty) = 0. \quad (21b)$$

4. Physics-informed neural network

Three parallel layers occur in an architecture of PINNs, i.e. the input layer, hidden and output layer. The intention of a fully connected network (FCN) is to collect data, process them and produce an output. We initialise the basic stages of PINN implementation by dividing a one-dimensional domain in η discrete points, or nodes, in a bid to find non-similar partial differential equations (PDEs). These nodes illustrate independent variable's oscillation between 0 and η_∞. A flow chart representation of PINN is illustrated in Fig. 3, where red nodes represent the collocated nodes and blue nodes represent the boundary nodes. The only boundary conditions needed to assemble an approximate solution are the Dirichlet and Neumann boundary conditions. The η-axis is partitioned into m equal segments and contains m+1 nodes, where η_0 is set as the first node, and η_m is a last/final node. ODEs need to be satisfied at the intermediate nodes between η_0 and η_m, which are the considered collocated nodes scattered along the η-axis.

The initial or input layer holds data (η_i) as shown in Fig. 3. We define an output function as $\hat{y}_i = [f_i(\eta), \theta_i(\eta)]$.

In this analysis, weight and bias are two learning parameters that are incorporated in the function $\hat{y}_i = F(x_i, w, b)$. In order to achieve a sufficient approximation function, such learning parameters need to be advanced in a way that $\hat{y}_i$ appropriately anticipates the desired value y_i (sample output data). The loss function determines the deviation of (y_i) and $(\hat{y}_i)$. One such method to calculate the loss function is by means of the mean

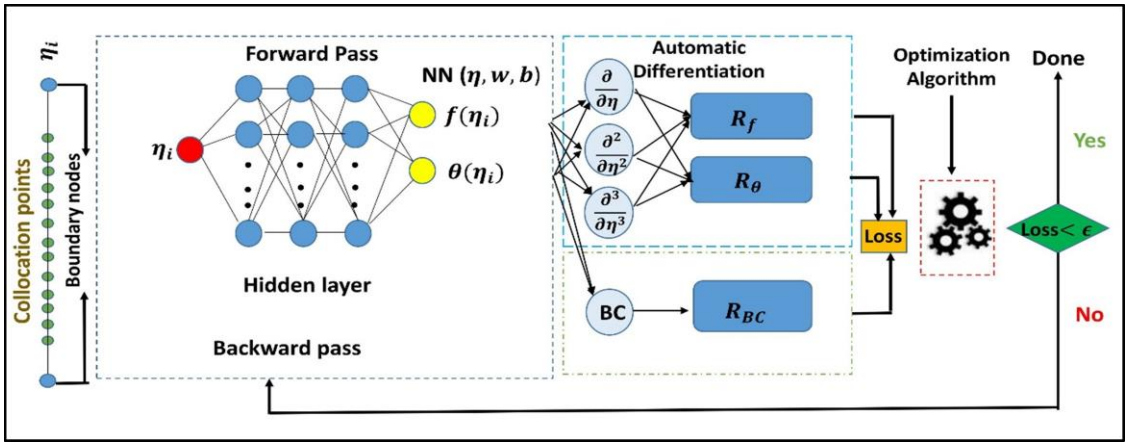


Fig. 3. Schematic flow chart of PINNs.

squared error format given by:

$$\text{Loss} = \frac{\left[\sum_{i=0}^{i=m}(y_i - \widehat{y_i})^2\right]}{m}. \quad (22)$$

The input data η_i are entered into the network as illustrated in Fig. 3. One neuron exists in the input or starting layer, which holds the given data. Following that, there are three hidden layers with an arbitrary number of neurons, and the output layer, depicted in Fig. 3, which consists of two neurons. In the architecture discussed above, each neuron is fully connected through linkages enabling information to pass between the neurons. Every link has a weight $w_{i,j}^k$, which decreases or increases the quantity of data that flows from the source node to destination nodes. Weight is utilised to calculate the contribution of every node to output outcomes, and a weighted sum of inputs is considered. A bias term is added to calculate the involvement of all nodes on predicted nodes:

$$z_i = b_i + \left(\sum_{j=1}^{j=n} a_j w_{i,j}^k\right). \quad (23)$$

The bias term (b_i) is assigned to input and hidden layers, with a value of unity. The regression analysis is employed using function $f(x) = \alpha x + \beta$, where α and β signify the weight and neural network simulation biases, respectively. An activation function is applied, which computes the output within a determined range. The tangent hyperbolic function is utilised in the present study, and the obtained z_i is forwarded through the given activation function:

$$\text{Output}(i) = \tanh(z_i). \quad (24)$$

For computation of the output z_i, data flows forward from one neuron to another. Before computing the estimated value $\widehat{y_i}$, the procedure is done layer by layer. As the procedure starts with the weight and biases being predicted, it is assumed that there will be a considerable difference between $\widehat{y_i}$ and y_i. It is required to adjust weight and bias parameters in a way that reduces the calculated loss function. Finding a variable weight and bias value that gives a minimised loss function is referred to as optimisation. We used an adaptive moment estimation (ADAM) to optimise the loss function by tuning the weights and biases. The iterative procedure proceeds until the loss function meets specified convergence criteria. Loss functions of the ordinary differential equation (ODE) type were addressed by Raissi et al. [40–42]. The total loss function is divided into three types: data loss, physics loss and boundary condition loss. For the physics loss, we define residual functions as [43–45]:

$$L_{data} = \frac{1}{N}\sum_{i=1}^{N}(\widehat{y_i} - y_i)^2. \quad (25)$$

The momentum boundary layer residuals are defined as:

$$R_f = (1+n)f''' - (1+\xi\Lambda)f'^{\mathbf{2}} + na\text{We}f''f''' + -\left(\frac{1}{\text{Da}}\right)f' + \frac{\sin\xi}{\xi}\theta. \quad (26)$$

Residuals in the thermal boundary layer are as follows:

$$R_\theta = \frac{1}{\text{Pr}}\left[1 + \frac{4}{3}Rd\right]\theta'' + f\theta' + \text{Ec}M\xi^2 f'^{\mathbf{2}} + \text{Ec}\xi^2 f''^2. \quad (27)$$

The physics loss function is given by:

$$L_{physics} = \frac{1}{N}\sum_{i=1}^{N}(R_f^2 + R_\theta^2). \quad (28)$$

The loss due to the boundary condition is:

$$L_{BC} = \frac{1}{N}\sum_{i=1}^{N}[f'(0)^2 + f(0)^2 + (\theta(0)-1)^2 + + f'(\infty)^2 + \theta(\infty)^2]. \quad (29)$$

The total loss can be calculated as:

$$Total\ loss = L_{data} + L_{physics} + L_{BC}. \quad (30)$$

5. Outcome evaluation and discussion

The solution of the problem under consideration has non-similar PDEs – Eqs. (6)–(8), which are solved through the well-known non-similarity method. The derived non-similar PDEs are reduced to ODEs as specified in Eqs. (14)–(16) through application of the first and second level of truncation. The derived system of ODEs is solved through the physics informed neural network method. We assumed 15 hidden layers and 84 neurons in a neural network architecture. The PINN prediction is evaluated at a fixed convergence tolerance 10^{-3}. An L^2-error is computed throughout the training process to assess the accuracy and validity of the PINN scheme. The comparison between PINN predictions and the numerical solution (obtained using bvp4c) is presented in Figs. 4–5. As seen in Fig. 4, there are notable differences between the numerical and PINN-projected solutions for temperature and velocity at lower iteration levels. The PINN solution for $f(\xi,\eta)$, $f'(\xi,\eta)$, $f"(\xi,\eta)$ and $\theta(\xi,\eta)$, $\theta'(\xi,\eta)$ differs significantly from the numerical solution at the start of training due to the random initialisation of the trainable parameters. This random initialisation of the trainable parameters does not satisfy the governing equations and boundary conditions; as a result, the PINN prediction deviates from the numerical solution at lower iteration levels.

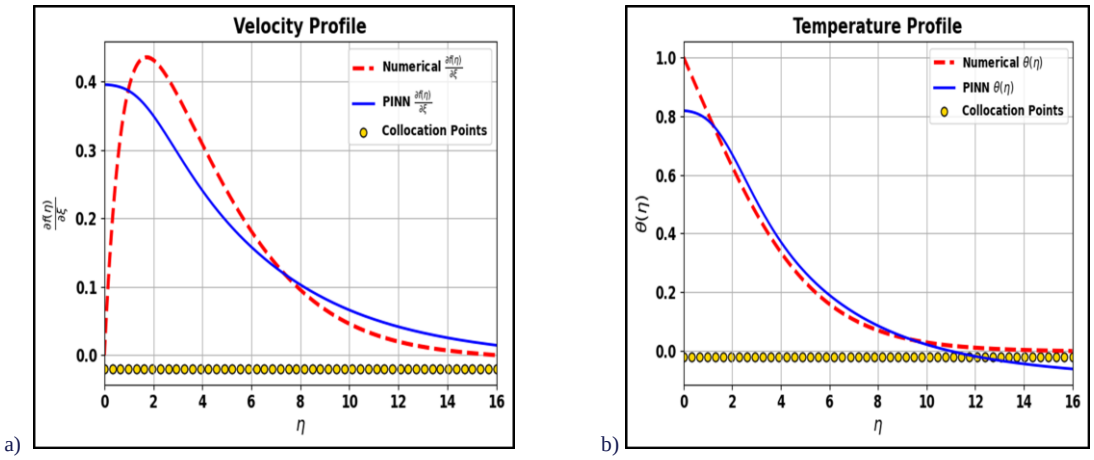
Nevertheless, an L^2-error decreases when the increased number of iterations, as depicted in Table 1.To illustrate the accuracy and stability of the solution, we increased the number of iterations to four thousand and eight hundred, as well as the number of hidden layers and neurons, as shown in Fig. 5. The comparison suggests that PINN outcome and numerical solution (achieved using bvp4c) are matched perfectly, thus demonstrating the credibility and consistency of the developed PINN approach to solve non-similar boundary layer flow of non-Newtonian fluid [46–51].

The physics loss and total loss function of the computed solution are shown in Fig. 6(a–b). The difference between the numerical results and PINN-predicted results is characterised by the L^2-error estimate. Table 1 illustrates L^2-error of the developed problem under consideration for various iteration numbers and learning rates. It is observed that when the number of iterations is increased, then the computation cost increases, but the accuracy and the precision of predicted solution increases. The accuracy of the model can also be enhanced by increasing the number of neurons while keeping a fixed number of hidden layers [52–58]. Increasing the number of neurons, L^2-error estimate

reduces, which indicates the solution reliability, as shown in Table 2. It is clear that when the loss function reduces, the network can infer the expected patterns with low accuracy. In Table 2, we consider the mesh size of 0.05. Similarly, Table 3 presents an L^2-error estimate for the mesh size of 0.02. The solution is observed to be convergent and reliable.

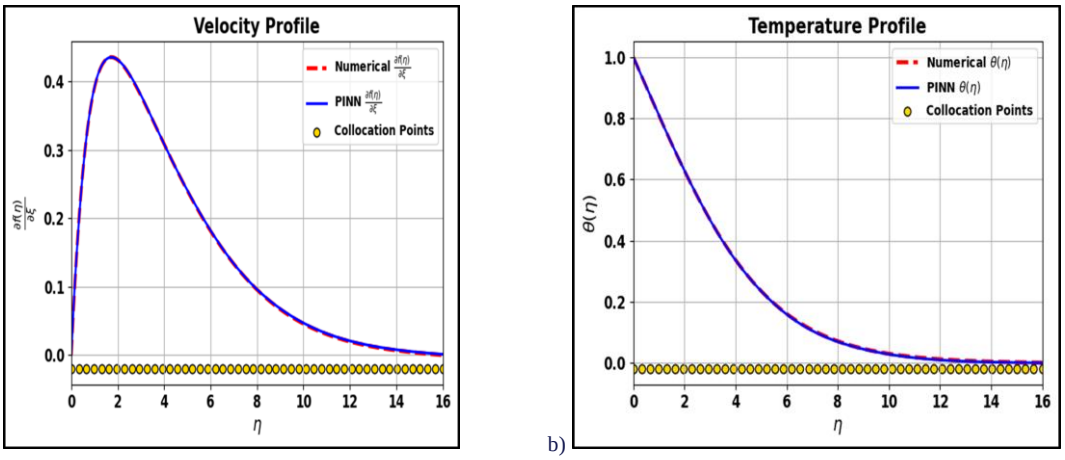
Table 4 shows L^2-error estimates for the flow response outputs, i.e. $\frac{\partial f}{\partial \eta}(\xi,\eta)$ and $\theta(\xi,\eta)$, for various values of magnetic parameter M. As evident in Table 4, the minimum errors are obtained for $M = 5$, reflecting the best accuracy of the PINN model.

Figure 7 displays the influence of magnetic field intensity M, on flow response outputs, i.e. $\theta(\xi,\eta)$ and $\frac{\partial f}{\partial \eta}(\xi,\eta)$. Figure 7a shows the effect of M on the velocity gradient, and it is noted that the velocity decreases with the increasing value of M.



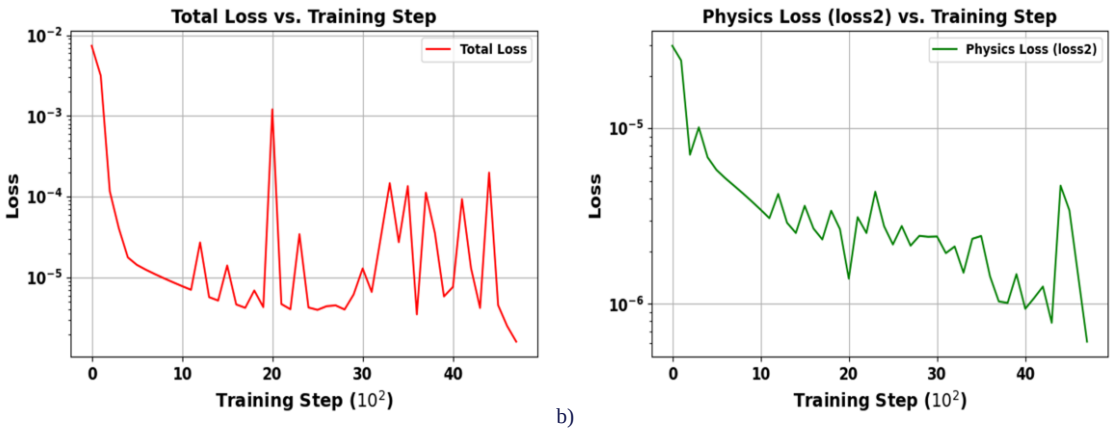
a) b)

Fig. 4. The comparison of numerical and PINN predicted solutions for velocity and temperature (low iteration number).



a) b)

Fig. 5. The comparison of numerical and PINN predicted solutions for velocity and temperature (large iteration number).



a) b)

Fig. 6. Loss function for flow response outputs.

Table 1. L^2-error between the predicted and numerical solution for different numbers of iterations and training steps.

Iteration	Training steps	L^2-error
100	10 000	0.061065
400	40 000	0.013647
800	80 000	0.007030
1200	120 000	0.004858
1600	160 000	0.006481
2000	200 000	0.004257
2400	240 000	0.009814
2800	280 000	0.003473
3200	320 000	0.003778
3600	360 000	0.008236
4000	400 000	0.004909
4400	440 000	0.002409
4800	480 000	0.001560

Table 2. L^2-error flow outputs response, i.e. (ξ,η), $\frac{\partial f}{\partial \xi}(\xi,\eta)$, $\frac{\partial^2 f}{\partial \xi^2}(\xi,\eta)$ and $\theta(\xi,\eta)$, $\frac{\partial \theta}{\partial \xi}(\xi,\eta)$ for various neuron numbers at $\eta_\infty = 5$, $\Delta = 0.05$.

Index	Hidden layers	Neurons	L^2-error of $f(\xi,\eta)$	L^2-error of $\frac{\partial f}{\partial \xi}(\xi,\eta)$	L^2-error of $\frac{\partial^2 f}{\partial \xi^2}(\xi,\eta)$	L^2-error of $\theta(\xi,\eta)$	L^2-error of $\frac{\partial \theta}{\partial \xi}(\xi,\eta)$
0	4	8	0.000866	0.001808	0.001555	0.000978	0.001327
1	4	16	0.001112	0.001209	0.000951	0.000952	0.000322
2	4	32	0.001169	0.001864	0.001947	0.001087	0.000323
3	4	64	0.000715	0.000993	0.000864	0.000563	0.000334

Table 3. L^2-error for flow outputs response, i.e. $f(\xi,\eta)$, $\frac{\partial f}{\partial \xi}(\xi,\eta)$, $\frac{\partial^2 f}{\partial \xi^2}(\xi,\eta)$ and $\theta(\xi,\eta)$, $\frac{\partial \theta}{\partial \xi}(\xi,\eta)$ for various neuron numbers at $\eta_\infty = 10$, $\Delta = 0.02$.

Index	Hidden layers	Neurons	L^2-error of $f(\xi,\eta)$	L^2-error of $\frac{\partial f}{\partial \xi}(\xi,\eta)$	L^2-error of $\frac{\partial^2 f}{\partial \xi^2}(\xi,\eta)$	L^2-error of $\theta(\xi,\eta)$	L^2-error of $\frac{\partial \theta}{\partial \xi}(\xi,\eta)$
0	4	8	0.002477	0.004453	0.003391	0.001578	0.001981
1	4	16	0.004044	0.004369	0.002940	0.001647	0.000128
2	4	32	0.011884	0.006617	0.004095	0.004044	0.001846
3	4	64	0.003274	0.002536	0.002067	0.001630	0.001027

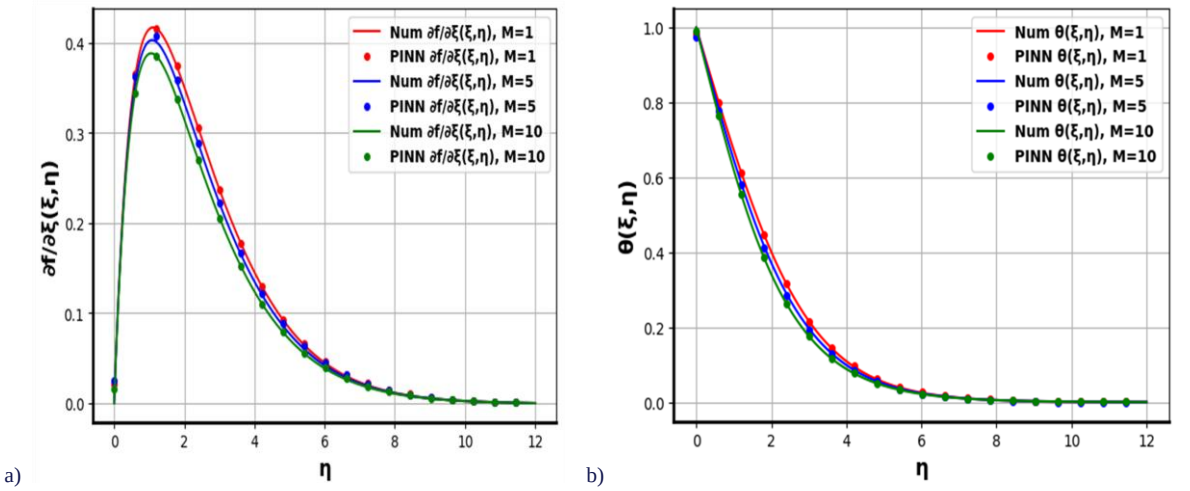
Table 4. L^2-error for flow outputs response, i.e. $\frac{\partial f}{\partial \xi}(\xi,\eta)$ and $\theta(\xi,\eta)$ for different values of M.

Index	M	L^2-error of $\frac{\partial f}{\partial \xi}(\xi,\eta)$	L^2-error of $\theta(\xi,\eta)$
0	1	0.031009	0.035468
1	5	0.006992	0.003424
2	10	0.040139	0.048676

Figure 7b indicates that the temperature profile drops more sharply as M is increased, which means that higher magnetic fields assist thermal diffusion and inhibit fluid motion. Such behaviour is representative of the traditional magnetohydrodynamic (MHD) phenomenon under which the Lorentz force acts to oppose fluid flow and alter heat transfer.

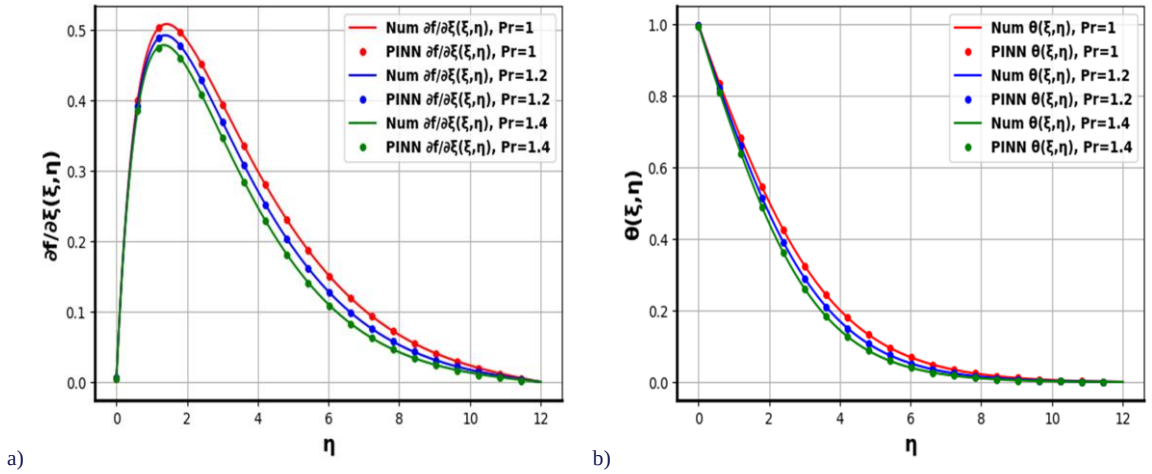
Table 5 displays the L^2-error estimates of the flow $f'(\xi,\eta)$ and $\theta(\xi,\eta)$ for various values of the Prandtl number Pr. It shows that prediction errors increase with the increasing value of Pr. Figure 8 plots the effect of Pr on both the velocity and temperature profiles. It is seen from Fig. 8a that the velocity profile diminishes with the increasing Pr, as would be expected because a greater Prandtl number represents a fluid of lower thermal diffusivity and thus a thinner velocity boundary layer is formed. Figure 8b shows that the temperature profile decays more precipitously with the greater Pr, representing a more intense thermal gradient and less heat diffusion. These trends match exactly the theoretical behaviour of boundary layer flows.

Table 6 shows L^2-errors of the velocity gradient $\frac{\partial f}{\partial \xi}(\xi,\eta)$ and $\theta(\xi,\eta)$ for various values of the radiation parameter Rd. The minimum L^2-errors for both fields occur at $Rd = 2$, which means that the PINN model is the best at higher radiation levels at $Rd = 2$. On the other hand, the maximum errors occur at $Rd = 1$, which shows a lower accuracy under a weaker radiative impact. Figure 9a shows that the velocity gradient $\frac{\partial f}{\partial \xi}(\xi,\eta)$ increases with the increase of Rd, which characterise greater fluid motion due to higher radiation of heating. Figure 9b illustrates that the temperature of fluid decreases with the increasing Rd values. All these findings provide evidence of strong effects of radiation on the flow velocity and temperature.



a) b)

Fig. 7. Flow field and temperature profile for various values of *M*.



a) b)

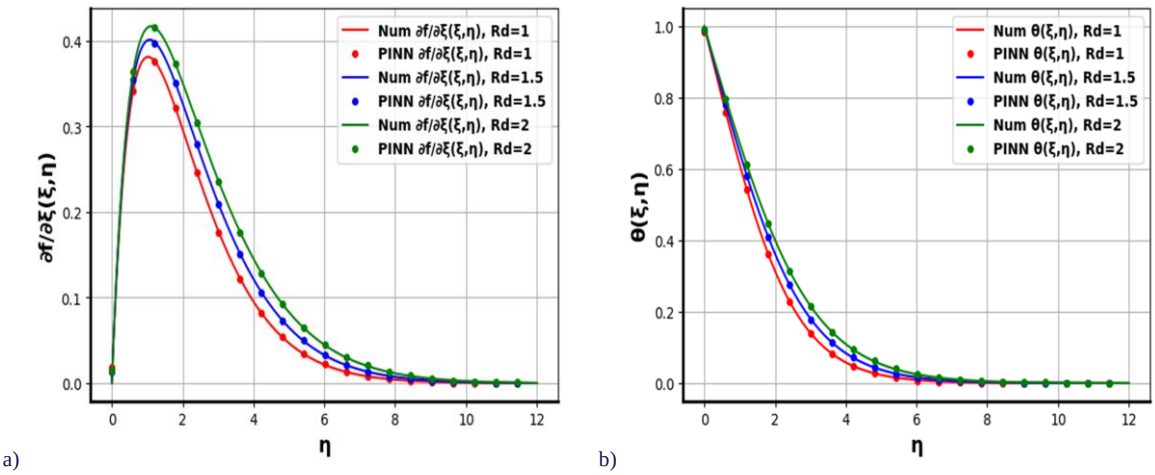
Fig. 8. Flow field and temperature profile for various values of Pr.

Table 5. L^2-error for different values of Pr.

Index	Pr	L^2-error of $\frac{\partial f}{\partial \xi}(\xi,\eta)$	L^2-error of $\theta(\xi,\eta)$
0	1.0	0.001743	0.000628
1	1.2	0.004053	0.002097
2	1.4	0.018577	0.013197

Table 6. L^2-error for different values of *Rd*.

Index	*Rd*	L^2-error of $\frac{\partial f}{\partial \xi}(\xi,\eta)$	L^2-error of $\theta(\xi,\eta)$
0	1	0.009623	0.004741
1	1.5	0.007378	0.002921
2	2.0	0.006445	0.003846



a) b)

Fig. 9. Flow field and temperature profile for various values of *Rd*.

Table 7 indicates the L^2-errors for the velocity gradient $f'(\xi,\eta)$ and temperature profile $\theta(\xi,\eta)$ for various values of parameter n. The lowest error appears at $n = 0.1$, which suggests a high accuracy of the PINN model for small values of n. Correspondingly, when the value of n increases up to 0.7, errors also increase, and it shows that the model becomes less accurate with the increased nonlinearity or complexity of flow. Figure 10a indicates that the velocity gradient increases with the increasing n; it shows the formation of a stronger momentum boundary layer. In Fig.10b, the temperature profile decreases more slowly with the increasing n, as a result of a thicker thermal boundary layer. This is in accordance with the increased convection and heat transfer due to increasing n.

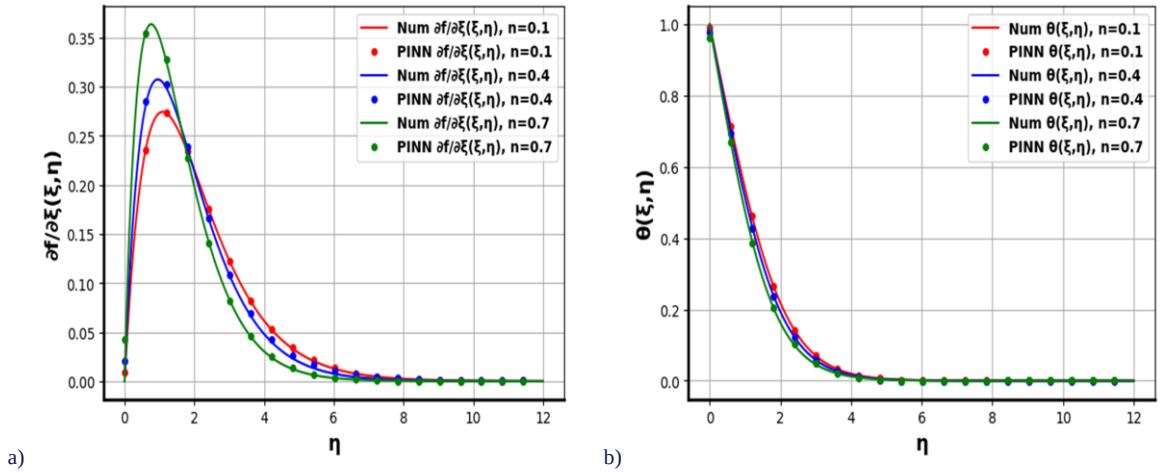
Table 8 presents L^2-errors for the velocity gradient $f'(\xi,\eta)$ and $\theta(\xi,\eta)$ for various values of Weissenberg number We in a tangent hyperbolic fluid. The largest errors are obtained at

Table 7. L^2-error for different values of n.

Index	n	L^2-error of $\frac{\partial f}{\partial \xi}(\xi,\eta)$	L^2-error of $\theta(\xi,\eta)$
0	0.1	0.007542	0.003344
1	0.4	0.008851	0.005889
2	0.7	0.026852	0.025722

Table 8. L^2-error for different values of We.

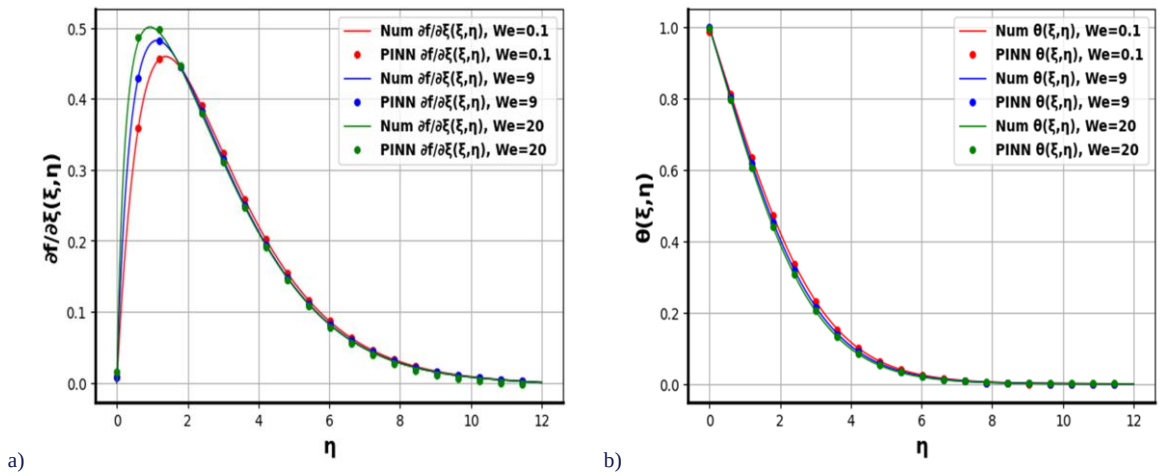
Index	We	L^2-error of $\frac{\partial f}{\partial \xi}(\xi,\eta)$	L^2-error of $\theta(\xi,\eta)$
0	0.1	0.030139	0.050238
1	9.0	0.003156	0.001225
2	20.0	0.005392	0.003613



a) b)

Fig. 10. Flow field and temperature profile for various values of n.

We = 0.1, which reflects the fact that the PINN model performs poorly under low elastic effects. With the increasing value of We, the errors decrease precipitously, reflecting a better performance of the model with moderate elasticity, while a minor error is observed at We = 20, perhaps due to higher flow complexity. Figure 11a indicates that the velocity gradient becomes stronger, developing earlier with We, which captures the fluid's increased elasticity and resistance to deformation. In Fig. 11b, the temperature profile is shown to decrease faster for large values of We. These trends verify that the tangent hyperbolic fluid is more responsive and thermally efficient with the growing We, and the PINN model well represents these variations.



a) b)

Fig. 11. Flow field and temperature profile for various values of We.

6. Conclusions

A benchmark simulation of non-similar boundary layer flow of non-Newtonian fluid with thermal radiation effects over a cylinder embedded in a porous medium is made in this study, using physics-informed neural networks. Training the networks with loss functions in charge of meeting the governing equations and boundary conditions served as the foundation for an approximate solution. It is discovered that the networks could accurately predict the solutions when their learning rate was less than 10^{-4}. L^2-error is investigated to show the accuracy and validity of the developed PINN methodology to solve non-similar boundary layer flow over a cylinder. The numerical and tabulated results are presented to ensure the accuracy of the proposed scheme. The primary considerations are as follows:

- The temperature distribution and convective flow field are significantly influenced by the buoyant force. The heat transfer and momentum boundary layer grow for increasing values of λ against a fixed value of $\eta = 12$.
- Momentum diffuses more quickly than heat at high Pr numbers, resulting in a narrower thermal boundary layer. By developing steeper temperature gradients close to heated surfaces, this accelerates the rate of heat transfer. Thus, with the improving values of Pr, the outputs $f'(\eta, \xi)$ and $\theta(\eta, \xi)$ raise.
- A high thermal radiation parameter indicates that surface convection outpaces internal conduction, leading to sharp temperature gradients within the solid and enhanced heat exchange at the surface.
- The accuracy was assessed using the L^2-error between the PINN and bvp4c solutions, which consistently decreased as the number of neurons and iterations increased. At 12 000 iterations, the L^2-error reached a minimum of $4.39 \cdot 10^{-3}$.
- At 1000 and 2000 training epochs, the PINN solution and the numerical solution were initially very different, but at 12 000 epochs, they demonstrated great agreement, signifying the importance of network size and training depth.

References

[1] Heaton, J. (2018). Review of book: Goodfellow I., Bengio Y. and Courville A.: Deep learning: MIT Press, 2016, ISBN: 0262035618. *Genetic Programming and Evolvable Machines*, 19(1), 305−307. doi: 10.1007/s10710-017-9314-z

[2] Lv, S.X., Peng, L., & Wang, L. (2018). Stacked autoencoder with echo-state regression for tourism demand forecasting using search query data. *Applied Soft Computing*, 73, 119−133. doi: 10.1016/j.asoc.2018.08.024

[3] Peng, L., Liu, S., Liu, R., & Wang, L. (2018). Effective long short-term memory with differential evolution algorithm for electricity price prediction. *Energy*, 162, 1301−1314. doi: 10.1016/j.energy.2018.05.052

[4] Agrawal, A., & Choudhary, A. (2019). Deep materials informatics: Applications of deep learning in materials science. *MRS Communications*, 9(3), 779−792. doi: 10.1557/mrc.2019.73

[5] Goh, G.B., Hodas, N.O., & Vishnu, A. (2017). Deep learning for computational chemistry. *Journal of Computational Chemistry*, 38(16), 1291−1307. doi: 10.1002/jcc.24764

[6] Chen, H., Engkvist, O., Wang, Y., Olivecrona, M., & Blaschke, T. (2018). The rise of deep learning in drug discovery. *Drug Discovery Today*, 23(6), 1241−1250. doi: 10.1016/j.drudis.2018.01.039

[7] Kelly, M.F., Parker, P.A., & Scott, R.N. (1990). The application of neural networks to myoelectric signal analysis: A preliminary study. *IEEE Transactions on Biomedical Engineering*, 37(3), 221−230. doi: 10.1109/10.52324

[8] Olaiya, F., & Adeyemo, A.B. (2012). Application of data mining techniques in weather prediction and climate change studies. *International Journal of Information Engineering and Electronic Business*, 4(1), 5–59. doi: 10.5815/ijieeb.2012.01.07

[9] Pierson, H.A., & Gashler, M.S. (2017). Deep learning in robotics: a review of recent research. *Advanced Robotics*, 31(16), 821−835. doi: 10.1080/01691864.2017.1365009

[10] Izzo, D., Märtens, M., & Pan, B. (2019). A survey on artificial intelligence trends in spacecraft guidance dynamics and control. *Astrodynamics*, 3(4), 287−299. doi: 10.1007/s42064-018-0053-6

[11] Cohen, N., Sharir, O., & Shashua, A. (2016). On the expressive power of deep learning: A tensor analysis. *Proceedings of Machine Learning Research*, 49, 698−728; *29th Annual Conference on Learning Theory*, June 23−26, New York, USA.

[12] Hornik, K., Stinchcombe, M., & White, H. (1989). Multilayer feedforward networks are universal approximators. *Neural Networks*, 2(5), 359−366.

[13] Baydin, A.G., Pearlmutter, B.A., Radul, A.A., & Siskind, J.M. (2018). Automatic differentiation in machine learning: a survey. *Journal of Machine Learning Research*, 18(153), 1−43.

[14] Cuomo, S., Di Cola, V.S., Giampaolo, F., Rozza, G., Raissi, M., & Piccialli, F. (2022). Scientific machine learning through physics–informed neural networks: Where we are and what's next. *Journal of Scientific Computing*, 92(3), 88. doi: 10.1007/s10915-022-01939-z

[15] Barania, H., & Esmaeilpour, M. (2022). On the application of physics informed neural networks (PINN) to solve boundary layer thermal-fluid problems. *International Communications in Heat and Mass Transfer*, 132, 105890. doi: 10.1016/j.icheatmasstransfer.2022.105890

[16] Shoaib, M., Kainat, S., Alabduljabbar, A.A., Nisar, K.S., & Zahoor Raja, M.A. (2025). Integrated intelligent neuro-evolutionary computing approach to study SEIRC model representing campylobacteriosis transmission dynamics. *Applied Mathematics in Science and Engineering*, 33(1), 2441257. doi: 10.1080/27690911.2024.2441257

[17] Mao, Z., Jagtap, A.D., & Karniadakis, G.E. (2020). Physics-informed neural networks for high-speed flows. *Computer Methods in Applied Mechanics and Engineering*, 360, 112789. doi: 10.1016/j.cma.2019.112789

[18] Alahmadi, H., Iqbal, J., & Abbasi, F.M. (2025). Artificial neural network aided computing for two dimensional magnetohydrodynamic peristaltic movement of nanofluid with heat and mass transfer. *Engineering Applications of Artificial Intelligence*, 154, 110990. doi: 10.1016/j.engappai.2025.110990

[19] Hanrahan, S., Kozul, M., & Sandberg, R.D. (2023). Studying turbulent flows with physics-informed neural networks and sparse data. *International Journal of Heat and Fluid Flow*, 104, 109232. doi: 10.1016/j.ijheatfluidflow.2023.109232

[20] Ali, I., Raja, M.A.Z., Chang, C.Y., Khan, M.P., Shoaib, M., & Shu, C.M. (2025). Novel Machine Predictive Exogenous Knowledge Driven Neuro-Structures for Unsteady Squeezing Nanofluidic Model with Rotating-Oscillating Disks. *International Journal of Thermophysics*, 46(12), 182. doi: 10.1007/s10765-025-03648-9

[21] Baty, H., & Baty, L. (2023). Solving differential equations using physics informed deep learning: a hand-on tutorial with benchmark tests. *arXiv*, 2302.12260. doi: 10.48550/arXiv.2302.12260

[22] Prandtl, L. (1905). Uber Flussigkeitsbewegung bei sehr kleiner Reibung. In: *Verhandlungen des III Internationalen Mathematiker Kongresses* (pp. 485–491), 8–13 August 1904, Heidelberg, B.G. Teubner, Leipzig (in German).

[23] Peng, Y., Lv, B.H., Yuan, J.L., Ji, H.B., Sun, L., & Dong, C.C. (2014). Application and prospect of the non-Newtonian fluid in industrial field. *Materials Science Forum*, 770, 396−401. doi: 10.4028/www.scientific.net/MSF.770.396

[24] Crespí-Llorens, D., Vicente, P., & Viedma, A. (2015). Generalized Reynolds number and viscosity definitions for non-Newtonian fluid flow in ducts of non-uniform cross-section. *Experimental Thermal and Fluid Science*, 64, 125−133. doi: 10.1016/j.expthermflusci.2015.02.005

[25] Hauswirth, S.C., Bowers, C.A., Fowler, C.P., Schultz, P.B., Hauswirth, A.D., Weigand, T., & Miller, C.T. (2020). Modeling cross model non-Newtonian fluid flow in porous media. *Journal of Contaminant Hydrology*, 235, 103708. doi: 10.1016/j.jconhyd.2020.103708

[26] Sohail, M., Nazir, U., Singh, A., Tulu, A., & Khan, M.J. (2024). Finite element analysis of cross fluid model over a vertical disk suspended to a tetra hybrid nanoparticles mixture. *Scientific Reports*, 14(1), 1520. doi: 10.1038/s41598-024-51262-w

[27] Awais, M., & Salahuddin, T. (2024). Radiative magnetodydrodynamic cross fluid thermophysical model passing on parabola surface with activation energy. *Ain Shams Engineering Journal*, 15(1), 102282. doi: 10.1016/j.asej.2023.102282

[28] Khan, M.I., Rauf, A., & Shah, A. (2021). Numerical investigation of viscous effects on the nonlinear Burgers equation. *Turkish Journal of Mathematics*, 45(1), 529–539. doi: 10.3906/mat-2001-7

[29] Khan, M.I., Zeeshan, A., Arain, M.B., Alqahtani, A.S., & Malik, M.Y. (2025). Temporal stability and non-unique solution of reacting Eyring Powell flows over shrinking wedges using neural networks. *Engineering Applications of Artificial Intelligence*, 141, 109828. doi: 10.1016/j.engappai.2024.109828

[30] Zeeshan, A., Khan, M. Z., Khan, I., & Pervaiz, Z. (2023). Sensitivity analysis and numerical investigation of hybrid nanofluid in contracting and expanding channel with MHD and thermal radiation effects. In *Nanomaterials and Nanoliquids: Applications in Energy and Environment* (pp. 281–310). Springer Nature Singapore.

[31] Subba Rao, A., Ramachandra Prasad, V., Bhaskar Reddy, N., & Anwar Bég, O. (2015). Heat transfer in a Casson rheological fluid from a semi-infinite vertical plate with partial slip. *Heat Transfer – Asian Research*, 44(3), 272−291. doi: 10.1002/htj.21115

[32] Ramachandra Prasad, V., Subba Rao, A., & Anwar Bég, O. (2013). Flow and heat transfer of Casson fluid from a horizontal circular cylinder with partial slip in non-Darcy porous medium. *Journal of Applied & Computational Mathematics*, 2(2), 1000127. doi: 10.4172/2168-9679.1000127

[33] Fatima, N., Ghodhbani, R., Khalid, N., Khan, M.I., Taha, T., Ijaz, N., & Saleem, N. (2025). Machine learning-based prediction of heat transfer enhancement in carreau fluids with impact of homogeneous and heterogeneous reactions. *Multiscale and Multidisciplinary Modeling, Experiments and Design*, 8(2), 145. doi: 10.1007/s41939-025-00734-1

[34] Shaheen, S., Mahmood, T., Raja, M.A.Z., Al-Yarimi, F.A., Arain, M.B., & Hu, J. (2025). Machine learning-based investigation of activation energy for bio-convective boundary layer flow inspired by challenges in aerospace heat transfer systems. *Engineering Applications of Artificial Intelligence*, 160, 111917. doi: 10.1016/j.engappai.2025.111917

[35] Ibrahim, W., & Gizewu, T. (2020). Nonlinear mixed convection flow of a tangent hyperbolic fluid with activation energy. *Heat Transfer*, 49(5), 2427−2448. doi: 10.1002/htj.21729

[36] Jan, A., Mushtaq, M., & Hussain, M. (2024). Heat transfer enhancement of forced convection magnetized cross model ternary hybrid nanofluid flow over a stretching cylinder: non-similar analysis. *International Journal of Heat and Fluid Flow*, 106, 109302. doi: 10.1016/j.ijheatfluidflow.2024.109302

[37] Shaheen, S., Huang, H., Arain, M.B., Al-Zubaidi, A., & Tageldin, E.M. (2023). Concentration and thermal analysis of immiscible tangent hyperbolic fluid with distinct viscosity through horizontal asymmetric channel: Theoretical and observational study. *Case Studies in Thermal Engineering*, 50, 103386. doi: 10.1016/j.csite.2023.103386

[38] Minkowycz, W.J., & Sparrow, E. (1978). Numerical solution scheme for local nonsimilarity boundary-layer analysis. *Numerical Heat Transfer, Part B: Fundamentals*, 1(1), 69−85. doi: 10.1080/10407797809412161

[39] Sparrow, E.M., & Yu, H.S. (1971). Local non-similarity thermal boundary-layer solutions. *Journal of Heat Transfer*, 93(4), 328−334. doi: 10.1115/1.3449827

[40] Raissi, M., Perdikaris, P., & Karniadakis, G.E. (2017). Physics informed deep learning (part I): Data-driven solutions of nonlinear partial differential equations. *arXiv*, 1711.10561. doi: 10.48550/arXiv.1711.10561

[41] Raissi, M., Perdikaris, P., & Karniadakis, G.E. (2019). Physics-informed neural networks: A deep learning framework for solving forward and inverse problems involving nonlinear partial differential equations. *Journal of Computational Physics*, 378, 686−707. doi: 10.1016/j.jcp.2018.10.045

[42] Raissi, M., Yazdani, A., & Karniadakis, G.E. (2020). Hidden fluid mechanics: Learning velocity and pressure fields from flow visualizations. *Science*, 367(6481), 1026−1030.

[43] Iqbal, J., Akbar, Y., & Alam, M.M. (2026). Thermal enhancement and energy minimization using Powell–Eyring nanofluid flow in PTSC for solar-powered aircraft: a combined RSM, ANN, and sensitivity analysis. *Journal of Thermal Analysis and Calorimetry*, 151(2), 1717−1741. doi: 10.1007/s10973-025-15104-9

[44] Rehman, A.U., & Khan, M.I. (2025). Advanced computational intelligence approach for heat transfer and entropy generation in non-Newtonian third grade magnetohydrodynamics peristaltic transport through asymmetric channels. *International Communications in Heat and Mass Transfer*, 169, 109947. doi: 10.1016/j.icheatmasstransfer.2025.109947

[45] Min, Z., Shaheen, S., Arain, M.B., & Al-Yarimi, F.A. (2026). Theoretical analysis of heat and mass transfer in a cilia-induced bi-layer Giesekus fluid flow under viscosity gradient. *International Communications in Heat and Mass Transfer*, 172, 110448. doi: 10.1016/j.icheatmasstransfer.2025.110448

[46] Khan, M.I., Asgher, Z., Zeeshan, A., & Xu, H. (2025). Integrating artificial intelligence for stability assessment in Casson hybrid nanofluid flow using LMS-BPNN. *Neural Computing and Applications*, 37(21), 16231−16252. doi: 10.1007/s00521-025-11320-4

[47] Min, Z., Shaheen, S., Arain, M.B., Zeeshan, A., & Hussein, H.S. (2026). AI-based analysis of heat transfer in Williamson nanofluids over a vertically stretching sheet. *International Journal of Hydrogen Energy*, 208, 153383. doi: 10.1016/j.ijhydene.2026.153383

[48] Akbar, Y., Li, K., Iqbal, J., Yang, X., & Mao, X. (2026). Thermodynamic analysis of nanofluid with aggregated and non-aggregated nanoparticles. *International Journal of Heat and Fluid Flow*, 118, 110205. doi: 10.1016/j.ijheatfluidflow.2025.110205

[49] Sokolov, A., Ali, R., & Turek, S. (2015). An AFC-stabilized implicit finite element method for partial differential equations on evolving-in-time surfaces. *Journal of Computational and Applied Mathematics*, 289, 101−115. doi: 10.1016/j.cam.2015.03.002

[50] Shoaib, M., & Javed, T. (2024). Sensitivity analysis of non-isothermal mixed convective heat and mass transfer in nanofluid flow over a horizontal circular cylinder with Brownian motion. *Numerical Heat Transfer, Part B: Fundamentals*, 85(8), 984−1008. doi: 10.1080/10407790.2023.2259088

[51] Aziz, T., Mahomed, F.M., Shahzad, A., & Ali, R. (2014). Travelling wave solutions for the unsteady flow of a third grade fluid induced due to impulsive motion of flat porous plate embedded in a porous medium. *Journal of Mechanics*, 30(5), 527−535. doi: 10.1017/jmech.2014.17

[52] Iqbal, J., & Akbar, Y. (2026). Sensitivity analysis of drag reduction and aerothermal heating in Hypersonic Glide Vehicles (HGVs) under magnetic fields and nanofluid coatings. *International Communications in Heat and Mass Transfer*, 171, 110032. doi: 10.1016/j.icheatmasstransfer.2025.110032

[53] Ali, R., Mitalipova, A., Hussan, S.W.U., Kurbanaliev, A., Shahzad, A., & Abduzhabbarov, M. (2025). Shape effects on steady flow and heat transfer of Cu-nanofluid over a nonlinear stretching surface with Joule heating. *Archives of Thermodynamics*, 46(3), 89−104. doi: 10.24425/ather.2025.156581

[54] Shoaib, M., Javed, T., & Iftikhar, B. (2026). Sensitivity analysis of MHD Casson hybrid nanofluid and heat transfer with Joule heating. *Multidiscipline Modeling in Materials and Structures*, 22(1), 192−217. doi: 10.1108/MMMS-02-2025-0053

[55] Akbar, Y., Iqbal, J., Turabi, Y.U.U.B., Anwar, T., & Alam, M.M. (2025). Magneto-radiative effects on thermal fields and irreversibility in a lid-driven wavy square enclosure with a central heater. *Journal of Thermal Analysis and Calorimetry*, 150(25), 21171−21184. doi: 10.1007/s10973-025-14973-4

[56] Ali, R., Iqbal, A., Abbass, T., Arshad, T., & Shahzad, A. (2024). Unsteady flow of silica nanofluid over a stretching cylinder with effects of different shapes of nanoparticles and Joule heating. *Archives of Thermodynamics*, 45(3), 115–126. doi: 10.24425/ather.2024.151222

[57] Alkinidri, M., Iqbal, J., & Abbasi, F.M. (2025). Thermal transport and irreversibility analysis for radially magnetized Carreau–Yasuda nanofluids flow over polished surfaces. *Modern Physics Letters B*, 39(29), 2550168. doi: 10.1142/S0217984925501684

[58] Iqbal, J., Abbasi, F.M., Alam, M.M., & Akbar, Y. (2025). Thermal and energy optimization of hybrid nanofluid flow in parabolic trough surface collectors (PTSCs) using statistical modeling, neural networks, and sensitivity analysis for solar-powered aircraft. *Physics of Fluids*, 37(8), 082065. doi: 10.1063/5.0279425

Co-published by
Institute of Fluid-Flow Machinery
Polish Academy of Sciences
Committee on Thermodynamics and Combustion
Polish Academy of Sciences

Copyright©2026 by the Authors under licence CC BY-NC-ND 4.0

http://www.imp.gda.pl/archives-of-thermodynamics/

Analysis of oscillatory flow and heat transfer of Maxwell fluid through a porous circular microchannel with Hall effects

Muhammad Yousuf Rafiq, Zaheer Abbas, Ayesha Naeem*

The Islamia University of Bahawalpur, Baghdad-ul-Jadeed Campus, Hasilpur Road, Bahawalpur 63100, Pakistan
*Corresponding author email: ayeshanaeem432@gmail.com

Received: 30.07.2025; revised: 13.03.2026; accepted: 30.03.2026

Abstract

The oscillatory flow and heat transfer of a viscoelastic Maxwell fluid through a porous, rough circular microchannel are investigated in the presence of magnetohydrodynamic and Hall effects, velocity slip, and internal heat generation or absorption. The governing continuity, momentum and energy equations, coupled with the Maxwell constitutive relation, are formulated in cylindrical coordinates and non-dimensionalised. An analytical solution is obtained using the regular perturbation technique by treating wall roughness as a small parameter. Closed-form expressions for velocity and temperature are derived in terms of modified Bessel functions, and the shear stress and Nusselt number are evaluated. The results show that the magnetic parameter suppresses the axial velocity due to the Lorentz force, whereas the Hall parameter and Darcy number enhance the flow by alleviating electromagnetic and porous resistance. Velocity slip increases the near-wall velocity, while wall roughness reduces the overall flow intensity. Thermal analysis indicates that the temperature and Nusselt number increase with the heat source parameter and the Peclet number.

Keywords: Oscillatory flow; Maxwell fluid; Porous microchannel; Hall effect; Heat sink/source

Vol. 47(2026), No. 3, 125–137; doi: 10.24425/ather.2026.7509

Cite this manuscript as: Rafiq, M.Y., Abbas, Z., & Naeem, A. (2026). Analysis of oscillatory flow and heat transfer of Maxwell fluid through a porous circular microchannel with Hall effects. *Archives of Thermodynamics*, 47(3), 125–137.

1. Introduction

Oscillatory flow refers to the back-and-forth motion of fluid particles under the influence of periodic driving forces, commonly encountered in microfluidic and biological systems. This flow behaviour becomes particularly significant in confined geometries like microchannels, where inertial and elastic effects interact. The study of oscillatory flow helps understand complex transport phenomena in non-Newtonian fluids. It is widely applied in lab-on-chip devices, biomedical diagnostics, oil recovery, drug delivery systems, inkjet printing, chemical mixing processes, energy harvesting devices and thermal control systems. Ray et al. [1] conducted both analytical and numerical investigations to determine the development length of sinusoidally oscillating laminar pipe flows in moderate to high Reynolds number regimes. Astakhov et al. [2] investigated the phase reduction of a pair of coupled van der Pol oscillators subjected to an external harmonic force, incorporating asymmetric repulsive coupling between them. Aygun and Aydin [3,4] examined the hydrodynamics of piston-driven laminar pulsating flow for five dissimilar values of frequencies and compared the numerical and analytical solutions. Sato et al. [5] experimentally investigated the forced synchronisation of both the quasiperiodic state and the internally locked state in a thermoacoustic oscillator system. Aslan et al. [6] demonstrated the oscillatory flow and thermal features under the steady-state condition within a corrugated wavy channel. Additionally, three turbulence models were employed to examine the flow behaviour. Wang et al. [7] explored

Nomenclature

b – slip parameter
$\boldsymbol{B}$ – magnetic flux density vector, T
B_0 – magnitude of the applied uniform magnetic flux density, T
C_p – specific heat, J/(kg K)
Da – Darcy number
I_0, K_0 – zero-order modified Bessel functions of the first and second kind, respectively
$\boldsymbol{J}$ – current density, A/m^2
k – corrugation's wave number
k_p – permeability of porous medium, m^2
K – thermal conductivity, W/(m K)
m – Hall parameter
M – magnetic parameter
p – pressure, Pa
$P(t)$ – time-dependent oscillatory pressure gradient, Pa/m
Pe – Peclet number
Pr – Prandtl number
Q_0 – heat generation, W/m^3
r, θ, x – cylindrical coordinates (radial distance, angular coordinate, height)
R – mean radius, m
Re – Reynolds number
S – source/sink parameter
t – time, s
T – temperature, K
u_x – velocity component in x-direction, m/s
U – velocity, m/s
U_0 – characteristic velocity scale, m/s
$\boldsymbol{V}$ – velocity vector, m/s
$\widetilde{(\cdot)}$ – complex amplitude of the harmonically oscillating variable

Greek symbols

α – complex radial parameter
λ – relaxation time (Maxwell fluid parameter)
μ – dynamic viscosity, Pa·s
ν – kinematic viscosity, m^2/s
ξ – perturbation parameter (ratio of the wall-corrugation amplitude to the mean radius of the microchannel)
ρ – density, kg/m^3
σ – electrical conductivity, S/m
$\boldsymbol{\tau}$ – stress tensor, Pa
φ – amplitude of the pressure gradient
χ – generic dependent variable in the perturbation expansion
ω – oscillation frequency, rad/s

Abbreviations and Acronyms

MHD– magnetohydrodynamics
EOF – electroosmotic

the impact of rib shapes on oscillating flow and heat transfer in heat exchangers by deriving the solution numerically. Then, Li et al. [8] employed the perturbation technique to obtain the closed-form solution for the oscillating flow of Jeffrey fluid in a rough circular microchannel under the slip condition. Huang et al. [9] scrutinised the axial change of flow behaviour in the 3D rectangular channel with a deformable upper wall and compared the results with the experimental outcomes. The comparative examination of two-phase oscillatory flow with the experimental results was analysed by Duraziński et al. [10]. Yu et al. [11] discussed the impact of varying injecting angles on the flow behaviour and thermal features of liquid flow in the piston's galleries. Manthani et al. [12] examined the flow characteristics of a water-vinyl acetate system in the millichannel and computed the results numerically.

The flow of non-Newtonian fluids induced by surface motion plays a crucial role in various industrial and manufacturing processes due to their broad range of applications. Examples include optical fibre production, polymer processing, cooling of metallic surfaces and drilling operations. Since no single model can capture all the complex behaviours of non-Newtonian fluids, researchers have developed various models to better understand their rheological characteristics. Non-Newtonian fluids are generally classified into differential, rate-type and integral-type models. One of the significant non-Newtonian fluids is the Maxwell fluid. The Maxwell fluid is a fundamental viscoelastic non-Newtonian model that describes materials exhibiting both fluid-like and solid-like behaviour. It combines the effects of viscosity and elasticity through a linear relationship between stress and strain rate with a characteristic relaxation time. The Maxwell model is particularly useful for simulating fluids that undergo stress relaxation over time, such as polymer melts and biological fluids. Its ability to capture memory effects makes it ideal for studying unsteady and oscillatory flows in microfluidic and electrokinetic systems. Jian et al. [13,14] extended the study of Maxwell fluid in microchannels featuring different shapes under various circumstances. Li et al. [15] obtained an analytical solution for the transient electroosmotic velocity of generalised Maxwell fluids in a microchannel and a microtube, employing the Laplace technique. The outcomes were obtained by the linearised Poisson-Boltzmann equation along with the Cauchy momentum equation and the generalised Maxwell constitutive relation. Escandon et al. [16,17] demonstrated the transient EOFs (electroosmotic flows) of viscoelastic Maxwell fluids in microchannels with complex geometries, both annular and slit types, considering multilayer configurations and asymmetric zeta potentials. By employing analytical and partial-analytical techniques, they highlighted how elastic properties, electrokinetic effects and boundary asymmetries influence the oscillatory behaviour, symmetry and time evolution of velocity profiles in microfluidic systems. The unsteady magnetised flow of Maxwell fluids in a circular microchannel was analysed by Shah et al. [18] under an electric field depending on temperature, using the Debye-Hückel estimation. They derived the solution analytically and expressed the outcomes graphically. Yang et al. [19] investigated the unsteady oscillatory EOF flow of Maxwell fluid within a microchannel featuring an isosceles right triangular cross section. Due to the complexity of the problem, a numerical solution was derived. Feng et al. [20] introduced a fractional continuity model to scrutinise the gyrating EOF slip flow of generalised Maxwell fluids under an alternating electric field. The model captures the extended memory effects of viscoelastic fluids and provides insight into flow behaviour influenced by fractional dynamics and electrokinetic parameters.

Chang et al. [21] explored the electroosmotic flow (EOF) of a viscoelastic Maxwell fluid in a microchannel with sinusoidal wall unevenness, driven by an alternating pressure gradient and electric field. The effects of fluid elasticity, wall geometry, and external forcing on velocity distribution and mean flow behaviour were analytically investigated by using the Debye-Hückel approximation and boundary perturbation method.

Magnetohydrodynamics (MHD) examines the behaviour of electrically conducting fluids in the manifestation of a magnetic field, playing a vibrant role in numerous engineering and geophysical applications. The inclusion of the Hall effect is significant when the magnetic field is strong or the density of the fluid is low, causing a decoupling of electron and ion motion. This generates a secondary electric field perpendicular to both the magnetic and electric fields, which alters the current distribution and flow behaviour. Incorporating Hall currents in MHD analysis enhances the accuracy of modelling plasma flows, semiconductor processing and astrophysical phenomena. Jha et al. [22−25] investigated an MHD natural convection flow in vertical microchannels, highlighting the influence of Hall effects and induced magnetic fields. Their studies provide valuable insight into electromagnetic effects on microchannel heat and fluid transport under various magnetic field configurations. Roja and Gireesha [26] numerically investigated the MHD flow of a couple-stress fluid through a vertical microchannel, incorporating Hall effects and internal heat generation. Their study highlighted the impact of electromagnetic and thermal forces on non-Newtonian fluid behaviour in microchannel environments. Sadiq Basha et al. [27] analysed the steady MHD free convective flow in a vertical microchannel filled with a porous medium, considering Hall and ion-slip effects. Their study emphasised the impact of electromagnetic parameters on velocity and temperature profiles in microscale transport systems. Kundu and Saha [28] provided a comprehensive review of electromagnetohydrodynamic flow and heat transfer in microchannels, highlighting the interplay of electric and magnetic fields on fluid behaviour. Their analysis offers valuable insights into optimising thermal and flow performance in microscale systems. Bilal et al. [29] explored the unsteady flow of a hybrid nanofluid driven by peristaltic pumping in a wavy microchannel, incorporating the effects of electric and magnetic fields. Their study emphasised the role of Hall currents and slip boundary conditions, offering insights relevant to microfluidic and biomedical applications. Goyal and Srinivas [30] analysed the magnetic effect and entropy generation for the pulsating flow of two immiscible fluids, taking into consideration Joule heating and a first-order chemical reaction. They adopted the 4th-order Runge-Kutta numerical technique to evaluate the solution. Roja et al. [31] explored the influence of Hall effects on non-Newtonian fluid flow past an inclined microchannel under slip and convective boundary conditions. Their study provides valuable insights into electromagnetic and boundary interactions in complex fluid systems. Padma et al. [32] explored the magnetised flow of pulsating Casson fluid by considering the vertical porous medium along with slip conditions. They also discussed thermal features, including the entropy generation for the considered problem. Bala and Srinivas [33] scrutinised the magnetised flow of two incompressible Newtonian fluids over an inclined channel with the permeable medium and examined the thermal features incorporating the effect of heat flux, Joule heating and entropy generation. Srinivas et al. [34] examined the periodic pressure gradient and thermal features of the pulsatile and peristaltic flow of a particle fluid. They observed that the variations in pressure enhanced the fluid mixing, improving the thermal characteristics within the medium.

The literature review reveals a lack of studies on Maxwell fluid in a rough circular channel. Therefore, the main motivation behind this work is to analyse the magnetised flow of a Maxwell fluid under the influence of the Hall effect within a porous, rough circular microchannel. Additionally, the thermal characteristics of the fluid are also scrutinised in the presence of the heat sink/source parameter. The analytical solution for velocity and temperature is derived by the perturbation technique. The inspiration for the current study is the practical application of non-Newtonian fluid flow in rough circular microchannels, e.g. in biomedical devices, such as lab-on-a-chip systems and targeted drug delivery, microelectronics, oil and gas industries, and in chemical microreactors, etc. The impact of key parameters on the velocity and temperature is discussed graphically, while the effects on shear stress and Nusselt number are described in tabular form.

2. Problem formulations

The current work explores the oscillatory flow of a magnetised Maxwell fluid within a rough circular porous microchannel under the influence of the Hall effect and slip boundary conditions. The thermal characteristics of the fluid are also examined with the effect of thermal radiation and a heat sink/source. A cylindrical polar coordinate system (r, θ, x) is used to indicate the radial direction, azimuthal direction and central axis, respectively, as demonstrated in Fig. 1. The flow occurs due to an oscillatory pressure gradient with the uniform magnetic field acting perpendicular to the axial direction. A sinusoidal wave of slight amplitude is assumed to represent the corrugation of wall roughness and can be stated as

$$r = R + R\xi \sin(k\theta), \tag{1}$$

where R signifies the mean radius, k is the corrugation's wave number, and ξ ($\xi \ll 1$) is the perturbation parameter defined as the ratio of the amplitude of wall corrugations to the mean radius of the microchannel.

The flow governing equations are given by:

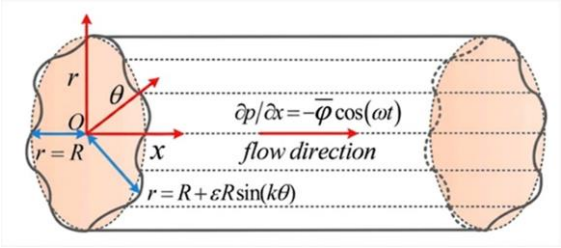


Fig. 1. Schematic diagram of the problem.

$$\nabla \cdot \boldsymbol{V} = 0, \tag{2}$$

$$\rho \frac{\partial \boldsymbol{V}}{\partial t} = -\nabla \cdot (p\mathbf{I} + \boldsymbol{\tau}) + \frac{\boldsymbol{J}\times\boldsymbol{B}}{1+m^2} + \frac{\mu}{k_p}, \tag{3}$$

$$\rho C_p \left(\frac{\partial T}{\partial t} + \boldsymbol{V} \cdot \nabla T\right) = K\nabla^2 T + Q_0, \tag{4}$$

where $\boldsymbol{V}$ is the velocity vector, $\boldsymbol{B}$ signifies magnetic field strength, $\boldsymbol{J}$ is the current density, $\mathbf{I}$ is the identity tensor, $\boldsymbol{\tau}$ is the stress tensor, m is the Hall parameter, ρ designates the density, K symbolises the thermal conductivity, C_p is the specific heat at constant pressure, T is the temperature, p indicates pressure, t is the time, Q_0 is the heat source/sink, and μ describes the dynamic viscosity. The stress tensor for an incompressible Maxwell fluid is given by

$$\boldsymbol{\tau} + \lambda \frac{D\boldsymbol{\tau}}{Dt} = 2\mu\mathbf{A}, \tag{5}$$

where λ is the relaxation time (a Maxwell fluid parameter), $\frac{D}{Dt}$ is the material derivative, and $\mathbf{A} = \frac{1}{2}(\nabla\boldsymbol{V} + \nabla\boldsymbol{V}^T)$ represents the rate-of-strain tensor. Under the assumed conditions, the stress tensor for the Maxwell fluid is simplified as

$$\left(1 + \lambda\frac{\partial}{\partial t}\right)\tau_{rx} = \mu\frac{\partial u_x}{\partial r}. \tag{6}$$

where τ_{rx} is the shear stress in the x-direction on a constant r-plane, and u_x denotes the velocity component in x-direction.

The time-dependent velocity field is taken as

$$\boldsymbol{V} = \big(0,0,u_x(r,\theta,t)\big). \tag{7}$$

The normal magnetic field is applied in the direction opposite to the direction of motion, which, according to Ohm's law, gives

$$\boldsymbol{J}\times\boldsymbol{B} = (0,0,-\sigma B_0^2 u_x), \tag{8}$$

where σ denotes electrical conductivity and B_0 is the magnitude of the applied magnetic flux density.

According to the above-mentioned assumptions, the governing equations are reduced to

$$\left(1 + \lambda\frac{\partial}{\partial t}\right)\left(\rho\frac{\partial u_x}{\partial t} + \frac{\partial p}{\partial x}\right) = \mu\left(\frac{\partial^2 u_x}{\partial r^2} + \frac{1}{r}\frac{\partial u_x}{\partial r} + \frac{1}{r^2}\frac{\partial^2 u_x}{\partial\theta^2}\right) + \\ -\frac{\mu}{k_p}u_x + \frac{-\sigma B_0^2 u_x}{1+m^2}, \tag{9}$$

$$\rho C_p\frac{\partial T}{\partial t} = K\left(\frac{\partial^2 T}{\partial r^2} + \frac{1}{r}\frac{\partial T}{\partial r} + \frac{1}{r^2}\frac{\partial^2 T}{\partial\theta^2}\right) + Q_0, \tag{10}$$

$$u_x|_{r=0} < \infty, \qquad T|_{r=0} < \infty,$$
$$\left(u_x + b\frac{\partial u_x}{\partial r}\right)\Big|_{r=R+\xi R\sin(k\theta)} = 0, \quad T|_{r=R+\xi R\sin(k\theta)} = 0, \tag{11}$$

where b is the slip parameter.

The expressions for pressure gradient, velocity and temperature in the x-direction for the oscillations in the form of a complex function are obtained as:

$$\frac{\partial p}{\partial x} = -P(t) = -\varphi\cos(\omega t) = -\varphi\Re\{e^{i\omega t}\}, \tag{12}$$

$$u_x(r,\theta,t) = \Re\{\tilde{u}(r,\theta)e^{i\omega t}\}, \tag{13}$$

$$T(r,\theta,t) = \Re\{\tilde{T}(r,\theta)e^{i\omega t}\}, \tag{14}$$

where $\Re\{\cdot\}$ shows the real part, ω is the angular frequency of oscillation, and φ represents the amplitude of a pressure gradient, $P(t)$ denotes the time-dependent oscillatory pressure gradient, and $\widetilde{(\cdot)}$ denotes the complex amplitude of the corresponding harmonically oscillating variable.

Inserting Eqs. (12)–(14) into Eqs. (9)–(11) yields:

$$i\omega\tilde{u}(r,\theta) = \left[\frac{\partial^2\tilde{u}(r,\theta)}{\partial r^2} + \frac{1}{r}\frac{\partial\tilde{u}(r,\theta)}{\partial r} + \frac{1}{r^2}\frac{\partial^2\tilde{u}(r,\theta)}{\partial\theta^2}\right]\left(\frac{\nu}{1+i\omega\boldsymbol{\lambda}}\right) + \\ + \frac{-\sigma B_0^2\tilde{u}}{1+m^2} - \frac{\mu}{k_p}\tilde{u} + \frac{\varphi}{\rho}, \tag{15}$$

$$\rho C_p i\omega\tilde{T}(r,\theta) = K\left[\frac{\partial^2\tilde{T}(r,\theta)}{\partial r^2} + \frac{1}{r}\frac{\partial\tilde{T}(r,\theta)}{\partial r} + \frac{1}{r^2}\frac{\partial^2\tilde{T}(r,\theta)}{\partial\theta^2}\right] + Q_0, \tag{16}$$

where $\nu = \mu/\rho$ is the kinematic viscosity.

The reduced boundary conditions are:

$$\tilde{u}|_{r=0} < \infty, \qquad \tilde{T}\big|_{r=0} < \infty,$$
$$\left(\tilde{u} + b\frac{\partial\tilde{u}}{\partial r}\right)\Big|_{r=R+\xi R\sin(k\theta)} = 0, \quad \tilde{T}\big|_{r=R+\xi R\sin(k\theta)} = 0. \tag{17}$$

The non-dimensional variables are defined as

$$r^* = \frac{r}{R}, \qquad t^* = \omega t, \qquad u^*(r^*,\theta) = \frac{\tilde{u}(r,\theta)}{U_0}, \\ b^* = \frac{b}{R}, \qquad \lambda^* = \omega\lambda, \qquad T^*(r^*,\theta) = \frac{\tilde{T}-T_0}{T_1-T_0}, \\ M = \sqrt{\frac{\sigma\omega}{\mu}}RB_0, \quad \mathrm{Da} = \frac{k_p}{r^2}, \qquad \mathrm{Re} = \frac{R^2\omega}{\nu}, \\ \mathrm{Pr} = \frac{C_p\mu}{K}, \qquad \mathrm{Pe} = \mathrm{Pr}R, \qquad S = \frac{R\omega Q_0}{T_1-T_0}, \tag{18}$$

where U_0 is the characteristic velocity scale, M is the magnetic parameter, Da denotes Darcy number, Pr – Prandtl number, Re – Reynolds number, Pe – Peclet number, S is the source parameter, T_0 and T_1 are the reference temperatures used for nondimensionalisation, and T_1–T_0 represents the characteristic temperature difference.

After removing the stearic signs for simplification, Eqs. (15) and (16) in non-dimensional form are reduced as

$$\frac{\partial^2 u}{\partial r^2} + \frac{1}{r}\frac{\partial u}{\partial r} + \frac{1}{r^2}\frac{\partial^2 u}{\partial\theta^2} - \left(i\mathrm{Re} + \frac{M^2}{1+m^2} + \frac{1}{\mathrm{Da}}\right)(1+i\lambda)u + \\ +(1+i\lambda)\varphi = 0, \tag{19}$$

$$\mathrm{Pe}\,T = \frac{\partial^2 T}{\partial r^2} + \frac{1}{r}\frac{\partial T}{\partial r} + \frac{1}{r^2}\frac{\partial^2 T}{\partial\theta^2} + S. \tag{20}$$

The dimensionless boundary conditions are defined as

$$u|_{r=0} < \infty, \qquad T|_{r=0} < \infty,$$
$$\left(u + b\frac{\partial u}{\partial r}\right)\Big|_{r=1+\xi\sin(k\theta)} = 0, \quad T|_{r=1+\xi\sin(k\theta)} = 0. \tag{21}$$

3. Analytic solution

As Eqs. (19) and (20) are the second-order partial differential equations (PDE's), the perturbation technique is employed to derive the solution by assuming the perturbation parameter $\xi \ll 1$

$$\chi(r,\theta) = \chi_0(r) + \xi\chi_1(r,\theta) + \xi^2\chi_2(r,\theta) + \cdots, \quad (22)$$

where the velocity and temperature are collectively represented by χ.

The zero, first, and second order equations in velocity and temperature are derived from Eqs. (19) and (20) as

$$\frac{d^2u_0}{dr^2} + \frac{1}{r}\frac{du_0}{dr} - \alpha^2 u_0 + \frac{1}{A}\alpha^2\chi = 0, \quad (23)$$

$$\mathrm{Pe}\, T_0 = \frac{d^2T_0}{dr^2} + \frac{1}{r}\frac{dT_0}{dr} + S, \quad (24)$$

$$\frac{\partial^2u_1}{\partial r^2} + \frac{1}{r}\frac{\partial u_1}{\partial r} + \frac{1}{r}\frac{\partial^2u_1}{\partial\theta^2} - \alpha^2 u_1 = 0, \quad (25)$$

$$\mathrm{Pe}\, T_1 = \frac{\partial^2T_1}{\partial r^2} + \frac{1}{r}\frac{\partial T_1}{\partial r} + \frac{1}{r}\frac{\partial^2T_1}{\partial\theta^2}, \quad (26)$$

$$\frac{\partial^2u_2}{\partial r^2} + \frac{1}{r}\frac{\partial u_2}{\partial r} + \frac{1}{r}\frac{\partial^2u_2}{\partial\theta^2} - \alpha^2 u_2 = 0, \quad (27)$$

$$\mathrm{Pe}\, T_2 = \frac{\partial^2T_2}{\partial r^2} + \frac{1}{r}\frac{\partial T_2}{\partial r} + \frac{1}{r}\frac{\partial^2T_2}{\partial\theta^2}, \quad (28)$$

where

$$\alpha^2 = (1+i\lambda)\left(i\mathrm{Re} + \frac{M^2}{1+m^2} + \frac{1}{\mathrm{Da}}\right)$$

and

$$A = i\mathrm{Re} + \frac{M^2}{1+m^2} + \frac{1}{\mathrm{Da}}.$$

By applying Taylor's series, the slip boundary condition along $r = 1$ is expanded as

$$0 = \left[u_0 + b\frac{du_0}{dr}\right]\Big|_{r=1} + \xi\left[u_1 + b\frac{\partial u_1}{\partial r} + \sin(k\theta)\left(\frac{du_0}{dr} + b\frac{d^2u_0}{dr^2}\right)\right]\Big|_{r=1} +$$

$$+\xi^2\left[u_2 + b\frac{\partial u_2}{\partial r} + \sin(k\theta)\left(\frac{\partial u_1}{\partial r} + b\frac{\partial^2u_2}{\partial r^2}\right) + \frac{\sin^2(k\theta)}{2}\left(\frac{d^2u_0}{dr^2} + b\frac{d^3u_0}{dr^3}\right)\right]\Big|_{r=1} + \mathrm{O}(\xi^3), \quad (29)$$

$$0 = T_0|_{r=1} + \xi\left[T_1 + \sin(k\theta)\frac{dT_0}{dr}\right]\Big|_{r=1} + \xi^2\left[T_2 + \sin(k\theta)\frac{\partial T_1}{\partial r} + \frac{\sin^2(k\theta)}{2}\frac{d^2T_0}{dr^2}\right]\Big|_{r=1} + \mathrm{O}(\xi^3). \quad (30)$$

The related boundary conditions are

$$\xi^0\begin{cases} u_0|_{r=1} = -b\frac{du_0}{dr}\Big|_{r=1}, & |u_0|_{r=0}| < \infty, \\ T_0|_{r=1} = 0, & |T_0|_{r=0}| < \infty, \end{cases} \quad (31)$$

$$\xi^1\begin{cases} u_1|_{r=1} = -\sin(k\theta)\left(\frac{du_0}{dr} + b\frac{d^2u_0}{dr^2}\right)\Big|_{r=1} - b\frac{\partial u_1}{\partial r}\Big|_{r=1}, & |u_1|_{r=0}| < \infty, \\ T_1|_{r=1} = -\sin(k\theta)\left(\frac{dT_0}{dr}\right)\Big|_{r=1}, & |T_1|_{r=0}| < \infty, \end{cases} \quad (32)$$

$$\xi^2\begin{cases} u_2|_{r=1} = -\sin(k\theta)\left(\frac{\partial u_1}{\partial r} + b\frac{\partial^2u_1}{\partial r^2}\right)\Big|_{r=1} - \frac{\sin^2(k\theta)}{2}\left(\frac{d^2u_0}{dr^2} + b\frac{d^3u_0}{dr^3}\right)\Big|_{r=1} - b\frac{\partial u_2}{\partial r}\Big|_{r=1}, & |u_2|_{r=0}| < \infty, \\ T_2|_{r=1} = -\sin(k\theta)\left(\frac{\partial T_1}{\partial r}\right)\Big|_{r=1} - \frac{\sin^2(k\theta)}{2}\left(\frac{d^2T_0}{dr^2}\right)\Big|_{r=1}, & |T_2|_{r=0}| < \infty. \end{cases} \quad (33)$$

3.1. Zero-order solution

The zero-order velocity and temperature equations, together with their corresponding boundary conditions, are obtained from Eqs. (23), (24) and (31) as follows

$$\begin{cases} \frac{d^2u_0}{dr^2} + \frac{1}{r}\frac{du_0}{dr} - \alpha^2 u_0 + \frac{1}{A}\alpha^2\chi = 0, \\ u_0|_{r=1} = -b\frac{du_0}{dr}\Big|_{r=1}, \quad |u_0|_{r=0}| < \infty, \end{cases} \quad (34)$$

$$\begin{cases} \mathrm{Pe}\, T_0 = \frac{d^2T_0}{dr^2} + \frac{1}{r}\frac{dT_0}{dr} + S, \\ T_0|_{r=1} = 0, \qquad |T_0|_{r=0}| < \infty. \end{cases} \quad (35)$$

The solution of Eqs. (34) and (35) is obtained in the form of a Bessel function with the imaginary argument as

$$u_0(r) = \frac{1}{A}\varphi + B_1 I_0(0, r\alpha) + B_2 K_0(0, r\alpha), \quad (36)$$

$$T_0(r) = \frac{S}{\mathrm{Pe}} + B_3 I_0\left(0, \sqrt{\mathrm{Pe}}\, r\right) + B_4 K_0\left(0, \sqrt{\mathrm{Pe}}\, r\right), \quad (37)$$

where I_0 and K_0 are the zero-order modified Bessel functions of the first and second kind, respectively.

Substituting the condition $|u_0|_{r=0}| < \infty$ and $|T_0|_{r=0}| < \infty$ in Eq. (36) and (37) gives $B_2 = 0$ and $B_4 = 0$. Further, applying the boundary conditions from Eqs. (34) and (35) gives

$$B_1 = -\frac{\varphi}{A[I_0(0,\alpha) + b\xi I_0[1,\alpha]]}, \quad (38)$$

$$B_3 = -\frac{S}{\mathrm{Pe}\, I_0\left(0, \sqrt{\mathrm{Pe}}\right)}. \quad (39)$$

and the zero-order velocity and temperature take the form:

$$u_0(r) = \frac{1}{A}\varphi + B_1 I_0(0, r\alpha) =$$

$$= \frac{1}{A}\varphi\left[1 - \frac{I_0(0,r\alpha)}{I_0(0,\alpha)+b\alpha I_0(1,\alpha)}\right], \quad (40)$$

$$T_0(r) = \frac{S}{\mathrm{Pe}}\left[1 - \frac{I_0[0,\sqrt{\mathrm{Pe}}\, r]}{I_0[0,\sqrt{\mathrm{Pe}}]}\right]. \quad (41)$$

3.2. First order solution

Similar to the zero-order formulation, the first-order velocity and temperature equations, along with boundary conditions, are:

$$\begin{cases} \frac{\partial^2 u_1}{\partial r^2} + \frac{1}{r}\frac{\partial u_1}{\partial r} + \frac{1}{r}\frac{\partial^2 u_1}{\partial \theta^2} - \alpha^2 u_1 = 0, \\ u_1|_{r=1} = \left[\sin(k\theta)\left(\frac{-du_0}{dr} - b\frac{d^2u_0}{dr^2}\right) - b\frac{\partial u_1}{\partial r}\right]\Big|_{r=1}, \\ |u_1|_{r=0}| < \infty, \end{cases} \quad (42)$$

$$\begin{cases} \mathrm{Pe}\, T_1 = \frac{\partial^2 T_1}{\partial r^2} + \frac{1}{r}\frac{\partial T_1}{\partial r} + \frac{1}{r}\frac{\partial^2 T_1}{\partial \theta^2}, \\ T_1|_{r=1} = -\sin(k\theta)\frac{dT_0}{dr}, \qquad |T_1|_{r=0}| < \infty. \end{cases} \quad (43)$$

The method of separation of variables derives the final expression for the first-order velocity and temperature as

$$u_1(r,\theta) = C_6 \sin(k\theta)\, I_0(k, r\alpha) =$$

$$-[b\alpha I_0(0,\alpha) - (-1+b)\, I_0(1,\alpha)] \times \frac{B_1\alpha \sin(k\theta) I_0(k,r\alpha)}{(1+kb)I_0(k,\alpha)+b\alpha I_0(k+1,\alpha)}, \quad (44)$$

$$T_1(r) = D_6 \sin(k\theta)\, I_0\left(k, \sqrt{\mathrm{Pe}}\, r\right) =$$

$$= -\frac{\sqrt{\mathrm{Pe}}\, I_0(1,\sqrt{\mathrm{Pe}}) B_3 \sin(k\theta) I_0(k,\sqrt{\mathrm{Pe}}\, r)}{I_0(k,\sqrt{\mathrm{Pe}})}, \quad (45)$$

where B_1 and B_3 are the zero-order integration constants defined in Eqs. (38) and (39), respectively, while C_6 and D_6 are the first-order constants determined by applying the boundary conditions in Eqs. (42) and (43).

3.3. Second order solution

The governing equations and boundary conditions for the second-order problem are:

$$\begin{cases} \frac{\partial^2 u_2}{\partial r^2} + \frac{1}{r}\frac{\partial u_2}{\partial r} + \frac{1}{r}\frac{\partial^2 u_2}{\partial \theta^2} - \alpha^2 u_2 = 0, \\ u_2|_{r=1} = -\sin(k\theta)\left(\frac{\partial u_1}{\partial r} + b\frac{\partial^2 u_1}{\partial r^2}\right)\Big|_{r=1} - \frac{\sin^2(k\theta)}{2}\left(\frac{d^2u_0}{dr^2} + b\frac{d^3u_0}{dr^3}\right)\Big|_{r=1} - b\frac{\partial u_2}{\partial r}\Big|_{r=1}, \qquad |u_2|_{r=0}| < \infty. \end{cases} \quad (46)$$

$$\begin{cases} \mathrm{Pe}\, T_2 = \frac{\partial^2 T_2}{\partial r^2} + \frac{1}{r}\frac{\partial T_2}{\partial r} + \frac{1}{r}\frac{\partial^2 T_2}{\partial \theta^2}, \\ T_2|_{r=1} = -\sin(k\theta)\left(\frac{\partial T_1}{\partial r}\right)\Big|_{r=1} - \frac{\sin^2(k\theta)}{2}\frac{d^2T_0}{dr^2}\Big|_{r=1}, \qquad |T_2|_{r=0}| < \infty. \end{cases} \quad (47)$$

Similarly to zero and first order solution, the second order solution is also finalised on the similar pattern as

$$u_2(r,\theta) = E_3 \cos(2k\theta)\, I_0(2k, r\alpha) + E_5 I_0(0, r\alpha) = \frac{2B_6D_1 + A_1D_2}{4}\left[\frac{I_0(2k,r\alpha)\cos(2k\theta)}{(1-2kb)I_0(2k,\alpha)+b\alpha I_0(1+2k,\alpha)} - \frac{I_0(0,r\alpha)}{I_0(0,\alpha)+b\alpha I_0(1,\alpha)}\right], \quad (48)$$

$$T_2(r,\theta) = F_3 \cos(2k\theta)\, I_0\left(2k, \sqrt{\mathrm{Pe}}\, r\right) + F_5 I_0\left(0, \sqrt{\mathrm{Pe}}\, r\right) = \frac{2C_6E_1 + A_3E_2}{4}\left[\frac{I_0\left(2k,\sqrt{\mathrm{Pe}}\, r\right)\cos(2k\theta)}{I_0\left(2k,\sqrt{\mathrm{Pe}}\right)} + \frac{I_0\left(0,\sqrt{\mathrm{Pe}}\, r\right)}{I_0\left(2k,\sqrt{\mathrm{Pe}}\right)+b\alpha I_0\left(0,\sqrt{\mathrm{Pe}}\right)}\right], \quad (49)$$

where A_1, A_3, B_6, C_6, D_1, D_2, E_1, E_2, E_3, E_5, F_3 and F_5 are auxiliary/integration constants arising from the perturbation solution and boundary condition algebra. C_6 is inherited from the first-order solution, while the remaining constants used at second order are fixed by the corresponding conditions in Eqs. (46) and (47).

3.4. Approximate analytical solution

The approximate analytic solution of velocity and temperature takes the form:

$$u(r,\theta) = A - \frac{AI_0(0,r\alpha)}{I_0(0,\alpha)+b\alpha I_0(1,\alpha)} - \xi I_0(k, r\alpha) B_1\alpha \sin(k\theta)\left[\frac{B_1\alpha \sin(k\theta) I_0(k,r\alpha)}{(1+kb)I_0(k,\alpha)+b\alpha I_0(k+1,\alpha)}\right] +$$

$$+ \frac{2B_6D_1 + A_1D_2}{4}\left[\frac{I_0(2k,r\alpha)\cos(2k\theta)}{(1-2kb)I_0(2k,\alpha)+b\alpha I_0(1+2k,\alpha)} - \frac{I_0(0,r\alpha)}{I_0(0,\alpha)+b\alpha I_0(1,\alpha)}\right], \quad (50)$$

$$T(r,\theta) = \frac{S}{\mathrm{Pe}} + \left[1 - \frac{I_0\left(0,\sqrt{\mathrm{Pe}}\, r\right)}{I_0\left(0,\sqrt{\mathrm{Pe}}\right)}\right] A_3 \sin(k\theta)\left[\frac{\xi I_0\left(1,\sqrt{\mathrm{Pe}}\right) I_0\left(k,\sqrt{\mathrm{Pe}}\, r\right)}{I_0\left(k,\sqrt{\mathrm{Pe}}\right)}\right] + \left(\frac{2D_6F_1 + B_3F_2}{4}\right)\xi^2\left[\frac{I_0\left(2k,\sqrt{\mathrm{Pe}}\, r\right)\cos(2k\theta)}{I_0\left(2k,\sqrt{\mathrm{Pe}}\, r\right)} + \frac{I_0\left(0,\sqrt{Pe}\, r\right)}{I_0\left(0,\sqrt{\mathrm{Pe}}\right)}\right]. \quad (51)$$

where ξ is the perturbation parameter representing the dimensionless wall roughness. It is substantial to mention that if the wall roughness is neglected, i.e. $\xi = 0$, then the problem is reduced from a rough circular channel to a smooth one.

4. Shear stress

The wall shear stress for unidirectional incompressible flow, where the tangential stress at the channel wall is proportional to

the radial gradient of the axial velocity, can be expressed mathematically as

$$\tau = \left.\frac{\partial u}{\partial r}\right|_{r=1}, \tag{52}$$

which can be obtained by differentiating the approximate velocity solution and evaluating it at $r = 1$.

5. Nusselt number

The dimensionless Nusselt number to determine the rate of heat transfer is obtained from the approximate temperature solution evaluated at the wall (Eq. (51)):

$$\mathrm{Nu}(r) = -\left.\frac{\partial T}{\partial r}\right|_{r=1}. \tag{53}$$

6. Observations and discussion

The current study presents the closed-form solution of magnetised flow of Maxwell fluid along with the Hall effect in a porous, rough circular microchannel with slip boundary conditions. The thermal characteristics of the flow in the presence of a heat source are analysed in detail. The perturbation technique is applied to derive the solution, which is found in the form of a Bessel function. The impact of controlling parameters on the fluid's velocity and temperature is given graphically. Additionally, the impact of the fluid parameter, Darcy number and Hall parameter, on shear stress and the influence of the source parameter and Peclet number on the Nusselt number are shown in tabular form. The characteristics of oscillatory flow are dominantly affected by the frequency parameter, which is represented by the angular Reynolds number. At low frequencies, the viscous forces are dominant, and the fluid is able to completely relax the oscillatory pressure gradient, resulting in a smooth velocity profile and an increased flow rate. However, at higher frequencies, the inertial forces become more pronounced, leading to a reduction in velocity magnitude due to the limited diffusion of momentum in the channel. Additionally, higher frequencies cause a phase lag between the velocity and the applied pressure gradient. In circular microchannels, this results in the development of annular velocity profiles and backflow regions. The slip at the wall becomes less effective with increasing frequency due to the dominance of oscillatory inertia. Wall roughness further disrupts the flow at higher frequencies, leading to an increase in near-wall fluctuations and a reduction in the overall transport. As a result, the flow rate decreases with increasing frequency.

The accuracy and reliability of the present work was validated through a comparison of the obtained velocity profiles with those of the previous study by Li et al. [8].

6.1. Velocity distribution

Figures 2–4 show the impact of different parameters on the velocity profile of a Maxwell fluid, while Figs. 5–7 depict the velocity contours for the variation of the relaxation time (λ), the Darcy number (Da) and the magnetic parameter (M), respectively. Figure 2a represents the effect of amplitude (φ) on velocity, showing that the velocity increases with increasing φ . This is because the oscillatory motion rises with the increment in amplitude, inducing an inclination in the fluid's motion. The influence of the slip parameter (b) on the velocity profile is portrayed in Fig. 2b. It is noted that velocity rises near the wall of the microchannel, and overall velocity also increases with increasing the slip parameter, as the upsurge in b induces a decline in the friction at the wall, causing an ease for the fluid flow due to the slip condition. Figure 3a explains the impact of the relaxation time (λ) on the velocity distribution. It is perceived that the velocity profile enhances significantly with the rise in λ. Physically, an increase in λ causes a strong elastic behaviour of the fluid and delayed relaxation, which aids the propagation of oscillatory flow, causing an increment in the liquid motion. As can be seen from Fig. 3b, as the perturbation parameter (ξ) increases, more energy is dissipated near the wall due to enhanced resistance or irregular surface interaction. This leads to increased friction and momentum loss in the fluid layers. As a consequence, the axial velocity decreases throughout the channel. Additionally, the disturbance disrupts the smooth flow pattern, further reducing the net flow efficiency. Therefore, a higher perturbation parameter suppresses velocity due to dominant damping and resistance effects.

Figure 4a illustrates the impact of magnetic parameter (M) on the fluid flow showing that velocity declines with an increase in the magnetic effect. It is because, this effect attributed towards Lorentz force acts as a resistive force to the flow, causing a dampness in the flow. Figure 4b implies that the velocity profile enhances with the rise in Hall effect. The increment in Hall

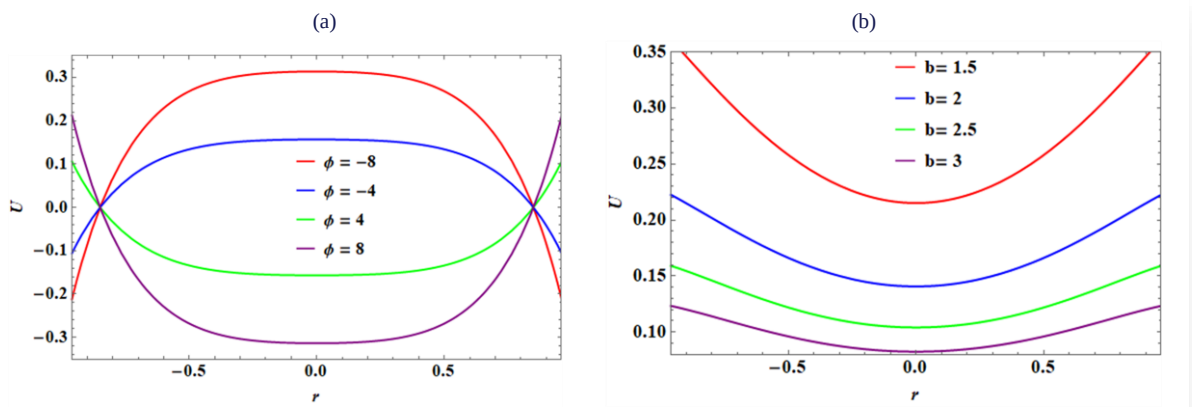


Fig. 2. Velocity profile change with amplitude (a) and slip parameter (b).

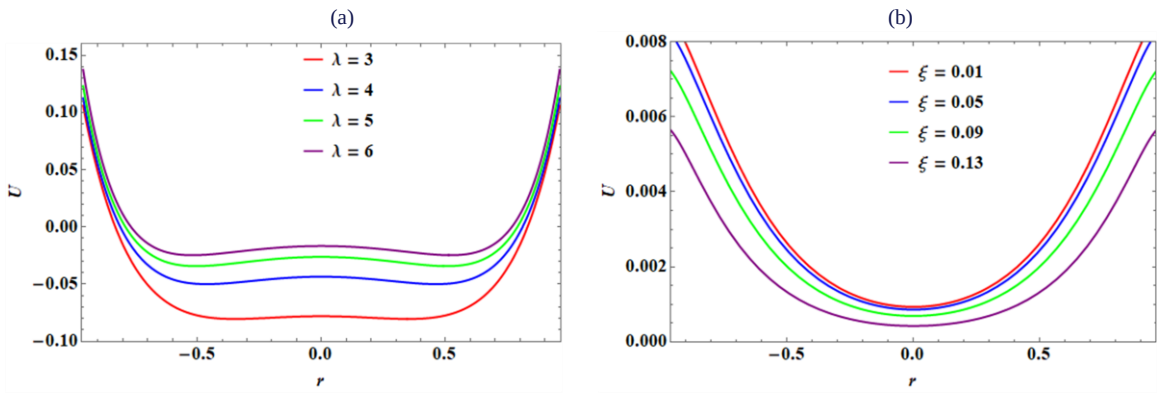


Fig. 3. Change of the velocity profile with the relaxation time (a) and perturbation parameter (b).

effect leads to the decline in electrical conductivity generation, which opposes the dampness caused by the magnetic field, resulting in the enhancement of the velocity. The impact of porosity on the fluid flow is depicted in Fig. 4c. The escalation in Darcy number (Da) causes an increment in the permeability of the medium which aids the fluid to flow, causing an upsurge in the fluid velocity. Figure 4d compares the present velocity profile with the results of Li et al. [8] under the corresponding limiting conditions. The close agreement between the two profiles validates the accuracy of the present analytical solution.

Figure 5 verifies the same behaviour as observed in Fig. 3a. Figure 6 presents velocity contours for increasing Darcy number and shows the enhancement of velocity due to reduced porous resistance, whereas Fig. 7 presents velocity contours for increasing magnetic parameter and confirms the suppressing effect of the Lorentz force. These contour trends are consistent with the corresponding velocity-profile results in Fig. 4.

6.2. Temperature distribution

Figures 8a and b show the impact of the source parameter (S) and Peclet number (Pe) on the temperature profile, respectively. The rise in temperature with the increase in S is due to the fact that the increment in the source parameter adds more energy to the fluid, inducing an upsurge in the fluid temperature. In microchannel flows, an increase in the Peclet number indicates stronger convective heat transfer relative to conductive heat transfer. As Pe increases, the fluid transports thermal energy more effectively along the flow direction. This causes heat to accumulate within the fluid bulk, raising the overall temperature.

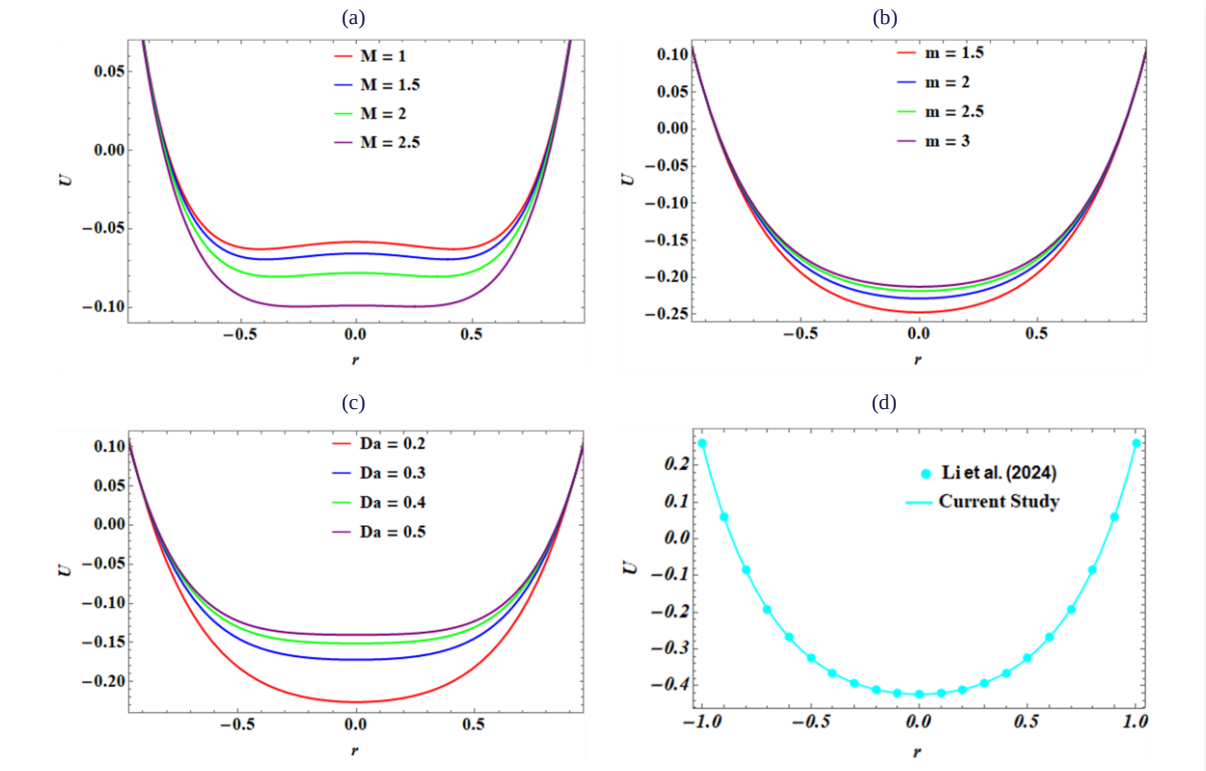


Fig. 4. Velocity profile change with magnetic parameter (a), Hall parameter (b), Darcy number (c), and the comparison with the previous study (d).

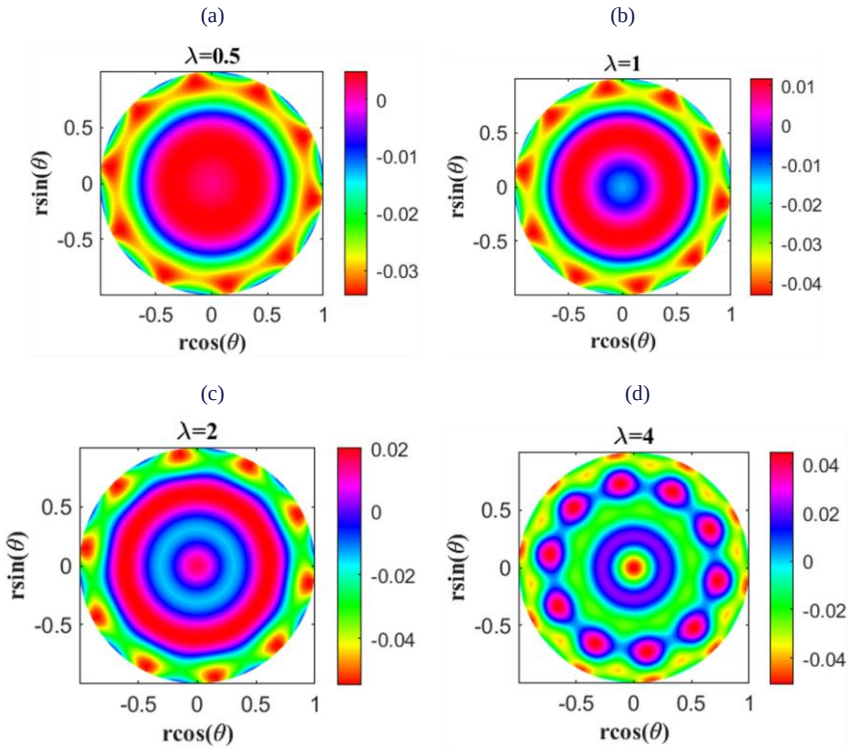


Fig. 5. Velocity contours for various values of relaxation time: (a) λ = 0.5, (b) λ = 1, (c) λ = 2, (d) λ = 4.

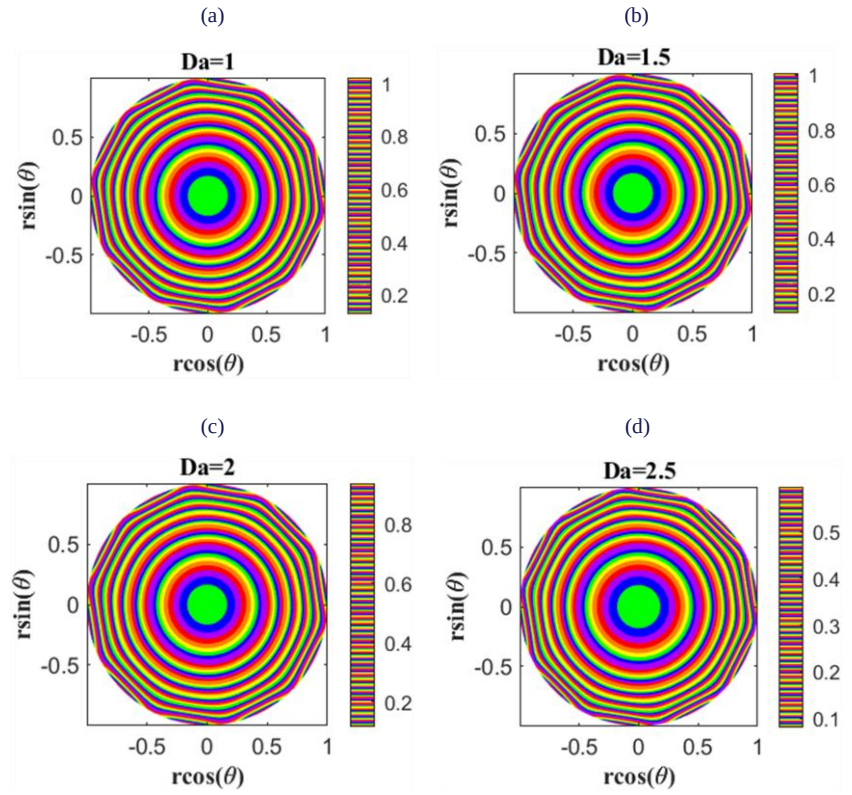


Fig. 6. Velocity contours for various values of Darcy number: (a) Da = 1, (b) Da = 1.5, (c) Da = 2, (d) Da = 2.5.

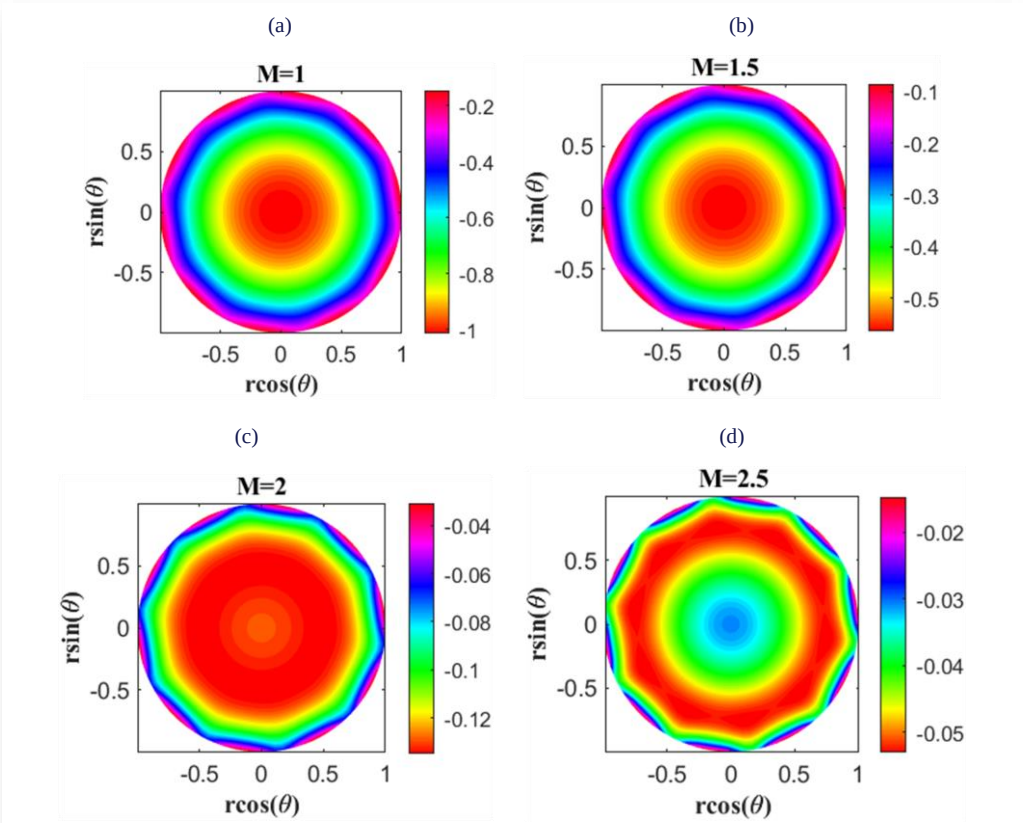


Fig. 7. Velocity contours for various values of magnetic parameter: (a) M = 1, (b) M = 1.5, (c) M = 2, and (d) M = 2.5.

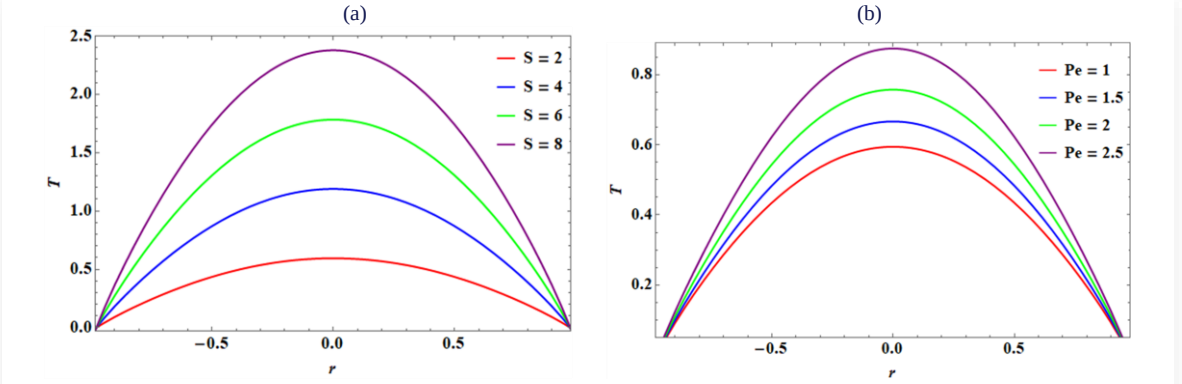


Fig. 8. Temperature profile change with source parameter (a) and Peclet number (b).

Figures 9 and 10 present the temperature contours for the variation in Peclet number and heat source parameter, respectively. It is observed that the temperature rises with the increment in both parameters, verifying the trend shown in Fig. 8. The increase in the source parameter adds significant energy to the fluid, causing an increase in the temperature, whereas the increment with increasing Peclet number shows that the fluid transmits the energy more efficiently.

Table 1 depicts the effect of the relaxation time, Darcy number and Hall parameter on the shear stress of the fluid. It is observed that shear stress rises with an increase in relaxation time, while it declines as the Darcy number and Hall parameter increase. Table 2 is produced to portray the influence of the source parameter and Peclet number on the Nusselt number. It is noted that the Nusselt number upsurges for both parameters, as the increase in the source parameter and Peclet number enhances the heat transfer, causing an increase in the Nusselt number.

7. Conclusions

In this study, the magnetised oscillatory flow of a Maxwell fluid through a porous circular microchannel with a rough wall, considering both no-slip and slip boundary conditions with the Hall effect, is analysed. In addition to examining the influence of slip length, wave number and wall roughness on the velocity and volumetric flow rate, we extended the analysis to include the effects of the magnetic parameter, Hall effect and Darcy number on the velocity profiles, as well as the Peclet number and heat

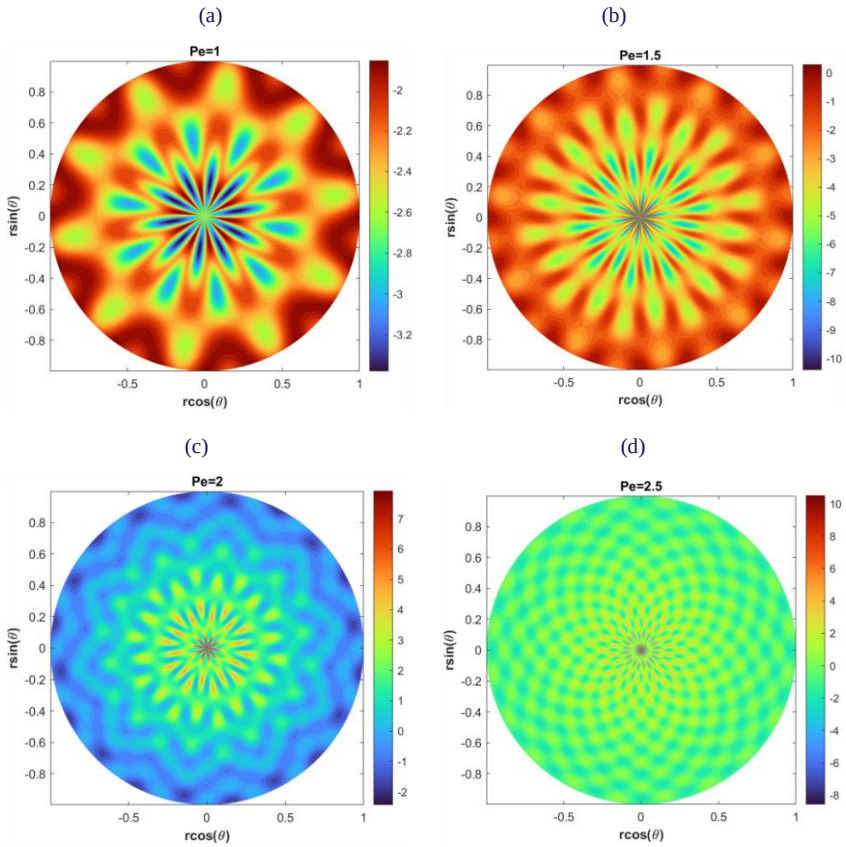


Fig. 9. Temperature contours for various Peclet numbers: (a) Pe = 1, (b) Pe = 1.5, (c) Pe = 2, and (d) Pe = 2.5.

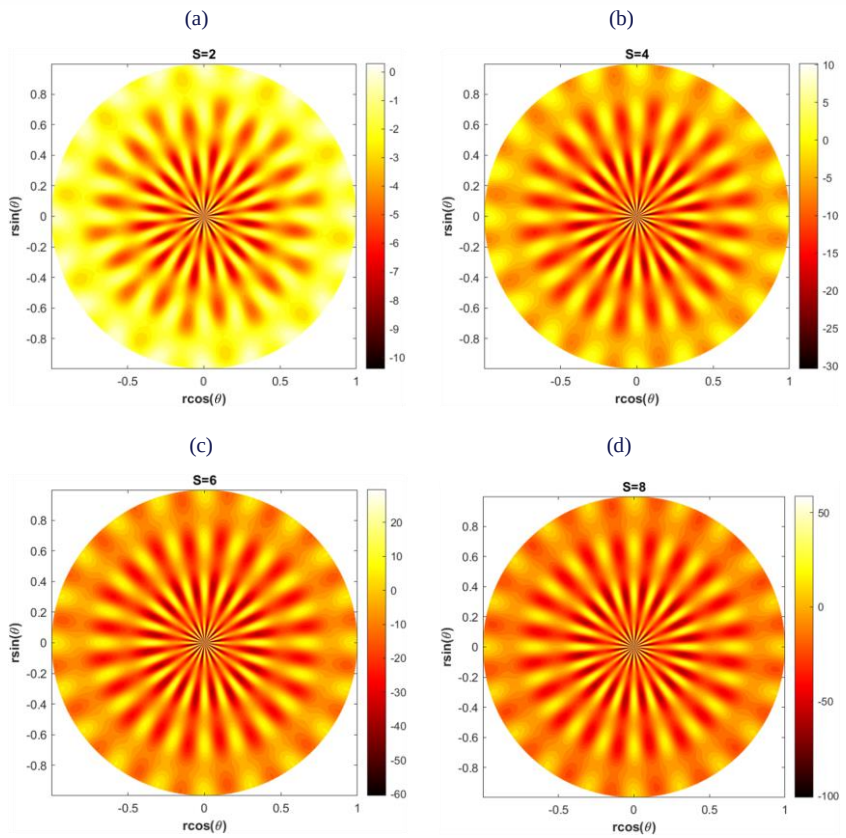


Fig. 10. Temperature contours for various values of heat source/sink parameter:
(a) S = 2, (b) S = 4, (c) S = 6, and (d) S = 8.

Table 1. The impact of relaxation time (λ), Darcy number (Da), and Hall parameter (m) on the shear stress (τ).

Parameters			Shear stress
Relaxation time	Darcy number	Hall parameter	
2	0.2	2.0	1.53776
3	0.2	2.0	1.45982
4	0.2	2.0	1.51182
5	0.2	2.0	1.63513
6	0.2	2.0	1.81535
2	0.2	1.5	1.55540
–	0.3	–	1.49933
–	0.4	–	1.48191
–	0.5	–	1.47420
–	0.6	–	1.47007
2	0.2	1.5	1.55540
–	–	2.0	1.53776
–	–	2.5	1.52867
–	–	3.0	1.52347
–	–	3.5	1.52025

Table 2. The impact of the source parameter (S) and Peclet number (Pe) on the Nusselt number.

Parameters		Nusselt number
Source parameter	Peclet number	
1.0	2.0	0.81177
1.5	–	1.32176
2.0	–	1.76234
2.5	–	2.20293
3.0	–	2.64325
3.5	–	3.0841
2.0	1.0	1.48937
–	1.5	1.61065
–	2.0	1.76234
–	2.5	1.95782
–	3.0	2.21966
–	3.5	2.58916

source/sink parameter on the thermal characteristics of the flow. The following are the key findings.

- Velocity increases with the slip length and wall roughness at a low Reynolds number.
- The magnetic field suppresses velocity due to the Lorentz force, while the Hall effect causes a rise in the fluid velocity.
- A heat source and a higher Peclet number lead to an increase in the temperature profile.
- The Nusselt number increases with an increase in the source parameter and the Peclet number.
- Shear stress increases for Maxwell's fluid parameter while it declines with an increase in porosity and Hall current.

References

[1] Ray, S., Ünsal, B., & Durst, F. (2012). Development length of sinusoidally pulsating laminar pipe flows in moderate and high Reynolds number regimes. *International Journal of Heat and Fluid Flow*, 37, 167–176. doi: 10.1016/j.ijheatfluidflow.2012.06.001

[2] Astakhov, S., Fujiwara, N., Gulay, A., Tsukamoto, N., & Kurths, J. (2013). Hopf bifurcation and multistability in a system of phase oscillators. *Physical Review E – Statistical, Nonlinear and Soft Matter Physics*, 88(3), 032908. doi: 10.1103/PhysRevE.88.032908

[3] Aygun, C., & Aydin, O. (2014). Hydrodynamics of piston-driven laminar pulsating flow: Part 1. Developing flow. *Nuclear Engineering and Design*, 274, 164–171. doi: 10.1016/j.nucengdes.2013.11.022

[4] Aygun, C., & Aydin, O. (2014). Hydrodynamics of piston-driven laminar pulsating flow: Part 2. Fully developed flow. *Nuclear Engineering and Design*, 274, 172–180. doi: 10.1016/j.nucengdes.2014.02.020

[5] Sato, M., Hyodo, H., Biwa, T., & Delage, R. (2020). Synchronization of thermoacoustic quasiperiodic oscillation by periodic external force. *Chaos: An Interdisciplinary Journal of Nonlinear Science*, 30(6), 063109. doi: 10.1063/5.0004381

[6] Aslan, E., Ozsaban, M., Ozcelik, G., & Guven, H.R. (2021). A numerical analysis of convection heat transfer and friction factor for oscillating corrugated channel flows. *Heat Transfer Engineering*, 42(3-4), 181–190. doi: 10.1080/01457632.2019.1699287

[7] Wang, J., Deng, X., Jia, D., Lei, J., & Xie, G. (2023). Numerical investigation on effects of rib shapes on oscillating flow and heat transfer in heat exchanger channels. *Thermal Science and Engineering Progress*, 42, 101919. doi: 10.1016/j.tsep.2023.101919

[8] Li, D., Li, H., Ma, L., & Lan, S. (2024). Oscillating flow of Jeffrey fluid in a rough circular microchannel with slip boundary condition. *Chinese Journal of Physics*, 91, 107–129. doi: 10.1016/j.cjph.2024.07.015

[9] Huang, A., Pande, S.D., Feng, J., & Christov, I.C. (2025). Oscillatory flows in three-dimensional deformable microchannels. *Journal of Fluid Mechanics*, 1022, A38. doi: 10.1017/jfm.2025.10771

[10] Duraziński, T., Nowak, A.I., Ishimoto, J., & Pietrowicz, S. (2025). Oscillatory two-phase flow dynamics in capillary tubes under microgravity conditions: Numerical modeling and qualitative analysis of the flow structures. *International Journal of Multiphase Flow*, 184, 105107. doi: 10.1016/j.ijmultiphaseflow.2024.105107

[11] Yu, B., Deng, X., Lei, J., Jia, D., He, S., & Zhang, Y. (2025). Numerical investigation on effects of oil jet angle on oscillating flow and heat transfer characteristics in a piston's dual-cooling galleries. *Applied Thermal Engineering*, 268, 125960. doi: 10.1016/j.applthermaleng.2025.125960

[12] Manthani, N., Nanavath, V.L., & Vedantam, S. (2025). Effect of superimposing oscillatory flow in a milli-channel with static internals – A numerical study. *The Canadian Journal of Chemical Engineering*, 103(2), 927–940. doi: 10.1002/cjce.25389

[13] Jian, Y.-J., Liu, Q.-S., & Yang, L.-G. (2011). AC electroosmotic flow of generalized Maxwell fluids in a rectangular microchannel. *Journal of Non-Newtonian Fluid Mechanics*, 166(21-22), 11581172 1304–1314. doi: 10.1016/j.jnnfm.2011.08.009

[14] Jian, Y., Su, J., Chang, L., Liu, Q., & He, G. (2014). Transient electroosmotic flow of general Maxwell fluids through a slit microchannel. *Zeitschrift für Angewandte Mathematik und Physik*, 65, 435–447. doi: 10.1007/s00033-013-0341-1

[15] Li, X.-X., Yin, Z., Jian, Y.-J., Chang, L., Su, J., & Liu, Q.-S. (2012). Transient electro-osmotic flow of generalized Maxwell fluids through a microchannel. *Journal of Non-Newtonian Fluid Mechanics*, 187-188, 43–47. doi: 10.1016/j.jnnfm.2012.09.005

[16] Escandón, J., Jiménez, E., Hernández, C., Bautista, O., & Méndez, F. (2015). Transient electroosmotic flow of Maxwell fluids in a slit microchannel with asymmetric zeta potentials. *European Journal of Mechanics – B/Fluids*, 53, 180–189. doi: 10.1016/j.euromechflu.2015.05.001

[17] Escandón, J.P., Torres, D.A., Hernández, C.G., Gómez, J.R., & Vargas, R.O. (2022). Transient analysis of the electro-osmotic flow of multilayer immiscible Maxwell fluids in an annular microchannel. *Colloids and Interfaces*, 6(4), 60. doi: 10.3390/colloids6040060

[18] Shah, N.A., Mahsud, Y., Aziz, M., & Tlili, I. (2020). Analytical solutions for unsteady electrohydrodynamics flows of Maxwell fluids in microchannels with circular cross section. *Physics of Fluids*, 32(1), 013107. doi: 10.1063/1.5128688

[19] Yang, X., Wang, S., Zhao, M., & Xiao, Y. (2021). Electroosmotic flow of Maxwell fluid in a microchannel of isosceles right triangular cross section. *Physics of Fluids*, 33(12), 123113. doi: 10.1063/5.0076425

[20] Feng, C., Si, X., Cao, L., & Zhu, B. (2021). The slip flow of generalized Maxwell fluids with time-distributed characteristics in a rotating microchannel. *Applied Mathematics Letters*, 120, 107260. doi: 10.1016/j.aml.2021.107260

[21] Chang, L., Zhao, G., Buren, M., Sun, Y., & Jian, Y. (2024). Alternating current electroosmotic flow of Maxwell fluid in a parallel plate microchannel with sinusoidal roughness. *Micromachines*, 15(1), 4. doi: 10.3390/mi15010004

[22] Jha, B.K., Malgwi, P.B., & Aina, B. (2018). Hall effects on MHD natural convection flow in a vertical microchannel. *Alexandria Engineering Journal*, 57(2), 983–993. doi: 10.1016/j.aej.2017.01.038.

[23] Jha, B.K., & Aina, B. (2018). Impact of induced magnetic field on magnetohydrodynamic (MHD) natural convection flow in a vertical annular micro-channel in the presence of radial magnetic field. *Propulsion and Power Research*, 7(2), 171–181. doi: 10.1016/j.jppr.2018.04.004

[24] Jha, B.K., & Malgwi, P.B. (2019). Hall current and ion-slip effects on free convection flow in a vertical microchannel with an induced magnetic field. *Heat Transfer – Asian Research*, 48(8), 3812–3830. doi: 10.1002/htj.21569

[25] Jha, B.K., & Malgwi, P.B. (2020). Hall and ion-slip effects on MHD mixed convection flow in a vertical microchannel with asymmetric wall heating. *Engineering Reports*, 2(9), e12241. doi: 10.1002/eng2.12241

[26] Roja, A., & Gireesha, B.J. (2020). Hall effects on MHD couple stress fluid flow through a vertical microchannel subjected to heat generation: A numerical study. *Heat Transfer*, 49(8), 4738–4758. doi: 10.1002/htj.21850

[27] Sadiq Basha, P.M., Veera Krishna, M., & Nagarathna, N. (2020). Hall and ion-slip effects on steady MHD free convective flow through a porous medium in a vertical microchannel. *Heat Transfer*, 49(8), 4264–4280. doi: 10.1002/htj.21826

[28] Kundu, B., & Saha, S. (2022). Review and analysis of electromagnetohydrodynamic flow and heat transport in microchannels. *Energies*, 15(19), 7017. doi: 10.3390/en15197017

[29] Bilal, M., Javid, K., & Ali, N. (2023). Unsteady flow of hybrid fluid via peristaltic pumping in wavy micro-channel under electric and magnetic field effects: An application of Hall device and slip boundary. *Proceedings of the Institution of Mechanical Engineers, Part E: Journal of Process Mechanical Engineering*, 237(6), 2157–2170. doi: 10.1177/09544089231157512

[30] Goyal, K., & Srinivas, S. (2023). Entropy generation analysis for hydromagnetic two-layered pulsatile immiscible flow with Joule heating and first-order chemical reaction. *Case Studies in Thermal Engineering*, 47, 103046. doi: 10.1016/j.csite.2023.103046

[31] Roja, A., Saadeh, R., Kumar, R., Qazza, A., Khan, U., Ishak, A., & Pop, I. (2024). Ramification of Hall effects in a non Newtonian model past an inclined microchannel with slip and convective boundary conditions. *Applied Rheology*, 34(1), 2450046. doi: 10.1515/arh-2024-0010

[32] Padma Devi, M., Srinivas, S., & Vajravelu, K. (2024). Entropy generation in two-immiscible MHD flow of pulsating Casson fluid in a vertical porous space with slip effects. *Journal of Thermal Analysis and Calorimetry*, 149, 7449–7468. doi: 10.1007/s10973-024-13337-8

[33] Bala Anasuya, J., & Srinivas, S. (2024). Heat transfer characteristics of magnetohydrodynamic two-fluid oscillatory flow in an inclined channel with saturated porous medium. *Proceedings of the Institution of Mechanical Engineers, Part E: Journal of Process Mechanical Engineering*, 238(1), 427–440. doi: 10.1177/09544089221146364

[34] Anasuya, J.B., Srinivas, S., & Merugu, V. (2025). Interaction of pulsatile and peristaltic flow of a particle-fluid suspension with thermal effects. *International Communications in Heat and Mass Transfer*, 163, 108728. doi: 10.1016/j.icheatmasstransfer.2025.108728

Co-published by
Institute of Fluid-Flow Machinery
Polish Academy of Sciences
Committee on Thermodynamics and Combustion
Polish Academy of Sciences

Copyright©2026 by the Authors under licence CC BY-NC-ND 4.0

http://www.imp.gda.pl/archives-of-thermodynamics/

Numerical investigation of a double twisted tube heat exchanger in different configurations

Ali K. Abdul Razzaq[a*], Khudheyer S. Mushatet[b], Riyam Ali Khaled[c]

[a]Iraq Ministry of Defense, Al-Nasiriyah 64001, Iraq
[b]University of Thi-Qar, Al-Nasiriyah 64001, Iraq
[c]Ministry of Oil, Thi-Qar Oil Company, Al-Nasiriyah 64001, Iraq
[*]Corresponding author email: aliengn717@gmail.com

Received: 05.09.2025; revised: 09.02.2026; accepted: 25.02.2026

Abstract

This study investigates the thermal and hydraulic performance of three configurations of double twisted tube heat exchangers (DTTHEs): circular (DCTTHE), elliptical (DETTHE) and square (DSTTHE) tubes, all with a twist ratio of 5. Numerical simulations were performed using Ansys Fluent with the *k*-*ε* turbulence model at Reynolds numbers ranging from 5000 to 25 000 to analyse heat transfer enhancement mechanisms. The working fluids were hot water and cold water, with varied inlet mass flow rates. Key performance parameters, such as the Nusselt number, overall heat transfer coefficient, pressure drop and effectiveness, were computed. Results demonstrate that DETTHE outperforms the other configurations, achieving superior heat transfer efficiency due to intensified secondary flows and vortices that enhance fluid mixing and disrupt thermal boundary layers. DETTHE exhibited the highest overall heat transfer coefficient, Nusselt number and effectiveness, with a maximum improvement in overall performance factor of approximately 74% and 300%, compared to DCTTHE and DSTTHE, respectively. However, this enhancement came at the cost of higher pressure drops. Temperature contours revealed uniform thermal distribution and improved heat exchange in DETTHE, particularly at the outlet region. Enhanced turbulence, secondary flow generation and stronger mixing near the tube walls contributed to these improvements. The study highlights the trade-off between thermal performance and hydraulic losses. The findings from this comparative analysis provide insights into the relative performance of different double twisted tube designs. Among the designs, DETTHE achieved the highest performance factor, making it a promising solution for compact and high-efficiency industrial heat exchangers.

Keywords: Twisted tube heat exchanger; Thermal-hydraulic performance; Double-tube heat exchanger; Heat transfer enhancement

Vol. 47(2026), No. 3, 139–146; doi: 10.24425/ather.2026.7512

Cite this manuscript as Razzaq, A.K.A., Mushatet, K.S., & Khaled, R.A. (2026). Numerical investigation of a different configurations double twisted tube heat exchanger. *Archives of Thermodynamics*, 47(3), 139–146.

1. Introduction

Heat exchangers play a vital role in numerous industrial and engineering applications, making their design a multifaceted and demanding discipline. Beyond financial and durability considerations, thorough hydraulic and thermal performance analysis is essential in their development [1]. Strategies to enhance thermal efficiency frequently involve a trade-off; for instance, design features that intensify heat transfer (e.g. fins, baffles, twist tape, twist tube or surface roughening) often simultaneously increase hydraulic resistance, leading to higher pressure drops and greater pumping power requirements.

Heat transfer enhancement techniques fall into two categories: active and passive. Among these, passive methods have attracted significant attention due to their cost efficiency and simplicity [2]. A common passive approach involves flow-modifying devices like twisted tape, which generates secondary flows alongside axial motion, intensifying turbulence. This enhanced

Nomenclature

A_s – heat transfer surface area, m^2
C – heat capacity rate, W/K
C_p – specific heat, J/(kg K)
d – inner tube diameter, m
D – outer tube diameter, m
D_h – hydraulic diameter, m
k – turbulent kinetic energy, J/kg
L – length, m
LMTD – logarithmic mean temperature difference, K
$\dot{m}$ – mass flow rate, kg/s
p – twist pitch, mm
P – pressure, Pa
ΔP_T – total pressure drop, Pa
Q_{avg} – average heat transfer rate, W
Re – Reynolds number, Re $= Du\rho/\mu$
t – time, s
T – temperature, K
Tr – twisted ratio
u, v, w – velocity components, m/s
U – overall heat transfer coefficient, W/(m^2 K)
x, y, z – Cartesian coordinates, m

Greek symbols

Γ – thermal conductivity, W/(m^2 K)
ε – turbulent energy dissipation, m^2/s^3
ϵ – heat exchanger effectiveness
η – overall performance index, 1/Pa
μ – dynamic viscosity, Pa s
ρ – density, kg/m^3

Subscripts and Superscripts

c – cold
eff – effective
h – hot
i – inlet
o – outlet
t – turbulent

Abbreviations and Acronyms

DCTTHE – double circular twisted tube heat exchanger
DETTHE – double elliptical twisted tube heat exchanger
DSTTHE – double square twisted tube heat exchanger

mixing reduces the boundary layer thickness within the heat exchanger tube [3].

A critical synthesis of the literature on heat transfer enhancement using twisted geometries reveals a complex landscape defined by significant advancements, yet marked by persistent methodological gaps and unresolved questions regarding optimal configuration and scalability. The existing body of work can be broadly categorised and critically evaluated along several thematic lines. A primary focus has been on the geometric evolution from simple inserts to complex channel shapes. Early investigations effectively established the foundational principle that swirl flow induces thinning of the thermal boundary layer and improves fluid mixing. Studies employing twisted tape inserts, such as those by Salam et al. [3] and Murali et al. [4], consistently demonstrate this, reporting Nusselt number enhancements of 2.3−2.9 times and 1.4−1.8 times higher friction factors compared to smooth tubes. However, a critical limitation of this approach is the inherent trade-off between heat transfer augmentation and pressure drop, as the solid tape core significantly obstructs flow. This limitation prompted a shift towards twisted tubes themselves (e.g. elliptical, oval), which generate swirl without a central obstruction. For instance, Wu et al. [5] and Cheng et al. [6] found that twisted elliptical and oval tubes improve the synergy between the velocity vector and the temperature gradient, achieving performance evaluation criteria (PEC) in the range of 1.6−1.7. This transition from inserts to integral twisted geometries represents a pivotal development, moving towards systems that enhance heat transfer more efficiently by working with the flow path rather than obstructing it.

Within the domain of twisted tubes, a critical analytical gap emerges concerning the comparative impact of different geometric parameters under consistent flow regimes. For instance, while Cheng et al. [6] and Luo et al. [7] both investigated twisted oval tubes, their studies were confined to laminar flow (Reynolds numbers less than 2000). Their findings on the optimal twist pitch are not directly transferable to the turbulent regime studied by Alempour et al. [8] (Reynolds numbers ranging from 4000 to 16 000). This creates a significant knowledge gap: the interaction between twist pitch, aspect ratio and flow regime is poorly understood, making it difficult to predict performance across different operational scales. Furthermore, the work of Kim et al. [9] added another layer of complexity, suggesting that for twisted elliptic tubes, the number of revolutions has a substantial impact on thermal performance, while the aspect ratio's variation is "negligible" – a conclusion that may be specific to their chosen geometric range and contradicts the importance placed on flattening ratios in other studies like Cheng et al. [6]. This apparent contradiction underscores the lack of a unified geometric optimisation framework.

The pursuit of further enhancement has led to hybrid systems, which combine twisted geometries with nanofluids. The research of Mushatet and Youssif [10,11], Alempour et al. [8], and others consistently show a synergistic effect. For example, Mushatet and Youssif [11] reported a remarkable 214% heat transfer enhancement using Al_2O_3/water nanofluid in a tube with a twin twisted tape insert. However, a critical analysis of these hybrid studies reveals a common, and potentially limiting, methodological trend: a heavy reliance on numerical simulations [8,10–12] or highly controlled experimental setups. While these approaches are invaluable for parametric analysis, they often fail to fully capture the long-term practical challenges, such as nanoparticle sedimentation, corrosion, and increased pumping power costs associated with the compounded pressure drops from both the twist and the nanofluid, as noted by Karimi et al. [13].

This synthesis exposes a critical and underexplored niche in the literature. First, there is a pronounced disconnect between studies focused on geometric optimisation and those investigating hybrid nanofluid applications; few works systematically dissect whether the performance gains from a hybrid system are

due to a truly optimal geometry or simply the additive effect of the nanofluid. Second, the literature is heavily fragmented according to flow regimes, with most studies operating exclusively in either laminar [5,7,8] or turbulent [4,11,12] conditions, with a notable scarcity of research that bridges this divide. Finally, there is an overreliance on numerical models that have not been extensively validated against experimental data for the specific combination of complex geometries and nanofluids.

This study explores the thermal performance of double-twisted-tube heat exchangers by analysing three geometric configurations: circular, elliptical and square. Using 3D computational modelling, the research assesses the flow behaviour, heat transfer efficiency and overall system effectiveness across different twisted tube designs. A mesh independence analysis was performed, with stringent checks on mesh quality (including orthogonal quality and aspect ratio) to ensure solution accuracy in Ansys Fluent. Furthermore, critical dimensionless parameters – such as Reynolds number, Nusselt number and overall performance metrics – were computed, alongside a detailed evaluation of average heat transfer rates and exchanger effectiveness.

2. Mathematical analysis

The study examines three configurations of twisted double-tube heat exchangers, each with a twist ratio (Tr = p/D, where p denotes the twist pitch and D denotes the outer tube diameter) of 5 and a uniform tube thickness of 4 mm. The first design illustrated in Fig. 1 (left side) features circular tubes, with an inner tube diameter (d_i) of 18 mm and an outer tube diameter (D_i) of 50 mm, spanning a length (L) of 1 m. In this counter-flow arrangement, hot water passes through the inner tube while cold water flows through the outer annular space, with varying mass flow rates tested for both fluids. The second configuration, illustrated in Fig. 1 (middle), employs elliptical twisted tubes with semi-major and semi-minor radii of 13 mm and 6.3 mm, respectively. The third design, depicted in Fig. 1 (right side), utilises square twisted tubes with side lengths of 15.9 mm (inner) and 44.3 mm (outer). All models are constructed from aluminium and share identical operational parameters for comparative analysis.

The dynamics of fluid flow are governed by fundamental conservation laws — mass, momentum, and energy —which form the basis for numerical simulations and analytical solutions in fluid mechanics. The continuity equation enforces the principle of mass conservation, ensuring that the combined mass flow rate at the inlets is equal to that at the outlets:

$$\frac{\partial(\rho u)}{\partial x}+\frac{\partial(\rho v)}{\partial y}+\frac{\partial(\rho w)}{\partial z}=0, \tag{1}$$

where u, v, and w are the velocity vector components, ρ is the density, and x, y and z are the Cartesian coordinates. Alongside the momentum and energy equations, this framework enables precise modelling and analysis of fluid behaviour under varying conditions [14].

Within this investigation, the Navier-Stokes equations govern momentum conservation, enabling precise evaluation of pressure and velocity profiles across the heat exchanger [15]:

$$\left(\frac{\partial u^2}{\partial x}+\frac{\partial uv}{\partial y}+\frac{\partial uw}{\partial z}\right)=-\frac{1}{\rho}\frac{\partial P}{\partial x}+\frac{\partial}{\partial x}\left(2\mu_{eff}\frac{\partial u}{\partial x}\right)+\frac{\partial}{\partial y}\left(\mu_{eff}\frac{\partial u}{\partial y}\right)+$$
$$+\frac{\partial}{\partial z}\left(\mu_{eff}\frac{\partial u}{\partial z}\right)+\frac{\partial}{\partial y}\left(\mu_{eff}\frac{\partial v}{\partial x}\right)+\frac{\partial}{\partial z}\left(\mu_{eff}\frac{\partial w}{\partial x}\right), \tag{2}$$

$$\left(\frac{\partial vu}{\partial x}+\frac{\partial v^2}{\partial y}+\frac{\partial vw}{\partial z}\right)=-\frac{1}{\rho}\frac{\partial P}{\partial x}+\frac{\partial}{\partial x}\left(\mu_{eff}\frac{\partial v}{\partial x}\right)+\frac{\partial}{\partial y}\left(2\mu_{eff}\frac{\partial v}{\partial y}\right)+$$
$$+\frac{\partial}{\partial z}\left(\mu_{eff}\frac{\partial v}{\partial z}\right)+\frac{\partial}{\partial x}\left(\mu_{eff}\frac{\partial u}{\partial y}\right)+\frac{\partial}{\partial z}\left(\mu_{eff}\frac{\partial w}{\partial y}\right), \tag{3}$$

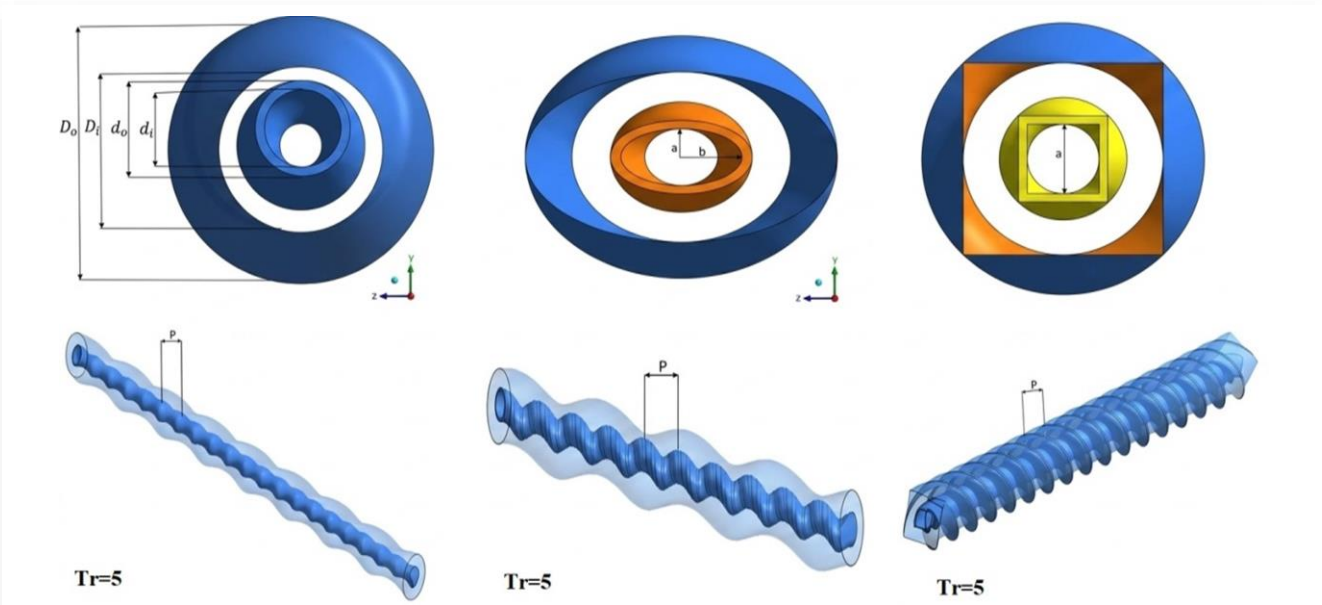


Fig. 1. A schematic illustration of a dual-loop heat exchanger configurations (circular tube, elliptical tube, square tube); cross-sections and 3D isometric views.

$$\left(\frac{\partial wu}{\partial x}+\frac{\partial wv}{\partial y}+\frac{\partial w^2}{\partial z}\right)=-\frac{1}{\rho}\frac{\partial P}{\partial x}+\frac{\partial}{\partial x}\left(\mu_{eff}\frac{\partial w}{\partial x}\right)+\frac{\partial}{\partial y}\left(\mu_{eff}\frac{\partial w}{\partial y}\right)+$$
$$+\frac{\partial}{\partial z}\left(2\mu_{eff}\frac{\partial w}{\partial z}\right)+\frac{\partial}{\partial x}\left(\mu_{eff}\frac{\partial u}{\partial z}\right)+\frac{\partial}{\partial y}\left(\mu_{eff}\frac{\partial v}{\partial z}\right). \quad (4)$$

where P is the pressure and μ_{eff} is the effective dynamic viscosity.

The energy conservation equation governs thermal energy transfer within fluid systems by accounting for heat exchange and mechanical work. In this analysis, it enables precise determination of temperature fields and heat flux across the heat exchanger's fluid and solid domains. The governing energy equation for fluid flow is expressed as [15]:

$$\frac{\partial uT}{\partial x}+\frac{\partial vT}{\partial y}+\frac{\partial wT}{\partial z}=\frac{\partial}{\partial x}\left(\Gamma_{eff}\frac{\partial T}{\partial x}\right)+\frac{\partial}{\partial y}\left(\Gamma_{eff}\frac{\partial T}{\partial y}\right)+$$
$$+\frac{\partial}{\partial z}\left(\Gamma_{eff}\frac{\partial T}{\partial z}\right), \quad (5)$$

where T is the temperature and Γ_{eff} represents the overall (effective) thermal conductivity.

In the above equations, effective parameters are described as follows [15]:

$$\mu_{eff}=\mu+\mu_t, \quad (6)$$

$$\Gamma_{eff}=\Gamma+\Gamma_t, \quad (7)$$

where μ and μ_t represent the viscosity as the baseline physical property and the turbulent dynamic viscosity, respectively. The latter becomes zero for laminar flow. Similarly, Γ and Γ_t denote the intrinsic/baseline and turbulent thermal conductivity, respectively.

The current investigation employs the k-ε turbulence model for analysing the outer boundary layer region. Selected for its computational efficiency and predictive reliability, this model demonstrates exceptional capability in resolving turbulent flow characteristics adjacent to solid boundaries while ensuring numerical stability in undisturbed flow regions. Particularly advantageous for complex flow geometries, the model accurately predicts separation phenomena and manages adverse pressure gradients. It was applied to account for the turbulent boundary-layer interactions that are central to the present study, as expressed by the governing equations below [15]:

$$\rho\left(\frac{\partial}{\partial x}(ku)+\frac{\partial}{\partial y}(kv)+\frac{\partial}{\partial z}(kw)\right)=\frac{\partial}{\partial x}\left(\frac{\mu_t}{\sigma_k}\frac{\partial k}{\partial x}\right)+\frac{\partial}{\partial y}\left(\frac{\mu_t}{\sigma_k}\frac{\partial k}{\partial y}\right)$$
$$+\frac{\partial}{\partial z}\left(\frac{\mu_t}{\sigma_k}\frac{\partial k}{\partial z}\right)+G-\rho\varepsilon, \quad (8)$$

$$\rho\left(\frac{\partial}{\partial x}(\varepsilon u)+\frac{\partial}{\partial y}(\varepsilon v)+\frac{\partial}{\partial z}(\varepsilon w)\right)=\frac{\partial}{\partial x}\left(\frac{\mu_t}{\sigma_\varepsilon}\frac{\partial \varepsilon}{\partial x}\right)+\frac{\partial}{\partial y}\left(\frac{\mu_t}{\sigma_\varepsilon}\frac{\partial \varepsilon}{\partial y}\right)$$
$$+\frac{\partial}{\partial z}\left(\frac{\mu_t}{\sigma_\varepsilon}\frac{\partial \varepsilon}{\partial z}\right)+C_{1\varepsilon}\rho\frac{\varepsilon}{k}G-C_{2\varepsilon}\rho\frac{\varepsilon^2}{k}, \quad (9)$$

where k is the turbulent kinetic energy, G represents the rate of its production per unit volume, ε is the turbulence dissipation rate, and $C_{1\varepsilon}$ = 1.44, $C_{2\varepsilon}$ = 1.92, σ_k = 1, σ_ε = 1.3.

The twisted tube configuration introduces a paradigm in double-tube heat exchanger design, demanding comprehensive characterisation of key thermal-hydraulic parameters. Critical numbers including Reynolds and Nusselt, along with friction factor, effectiveness and heat transfer coefficients, form the fundamental framework for performance prediction and optimisation. This investigation employs the following relations [16]:

$$\mathrm{Re}=\frac{\rho D_h u}{\mu}, \quad (10)$$

$$D_{h,i}=d_i, \quad (11)$$

$$D_{h,o}=D_i-d_o, \quad (12)$$

where $D_{h,i}$ and $D_{h,o}$ denote the hydraulic diameter of the inner and outer tube, respectively.

The logarithmic mean temperature difference is expressed by [16]

$$\mathrm{LMTD}=\frac{\Delta T_1-\Delta T_2}{\ln\left(\frac{\Delta T_1}{\Delta T_2}\right)}, \quad (13)$$

where

$$\Delta T_1=T_{hi}-T_{co}, \quad (14)$$

$$\Delta T_2=T_{ho}-T_{ci}. \quad (15)$$

In the above, subscripts h and c refer to hot and cold fluid, respectively, whereas subscripts i and o stand for inlet and outlet, respectively.

The effectiveness of a heat exchanger is defined as [16]

$$\epsilon=\frac{q_{act}}{q_{max}}, \quad (16)$$

where

$$q_{act}=C_c(T_{co}-T_{ci}), \quad (17)$$

$$q_{max}=C_{min}(T_{hi}-T_{ci}), \quad (18)$$

where C_{min} is the lower value of capacity rates C_h or C_c:

$$C_h=\dot{m}_h C_{ph}, \qquad C_c=\dot{m}_c C_{pc},$$

where C_p is the specific heat and $\dot{m}$ is the mass flow rate.

The Nusselt number and convective heat transfer coefficient are given as, respectively:

$$\mathrm{Nu}=\frac{h D_h}{K_f}, \quad (19)$$

$$h=\frac{\dot{m}_h C_{ph}(T_i-T_o)}{A_s(T_m-T_s)}, \quad (20)$$

where A_s is the heat transfer surface area, K_f is the thermal conductivity of the fluid, T_s is the wall temperature and T_m is bulk temperature of the fluid.

The overall performance index can be expressed as follows [17]:

$$\eta=\frac{\epsilon}{\Delta P_T}, \quad (21)$$

where ΔP_T is the total pressure drop.

3. Mesh modelling and mesh independence

The computational domain was created using Ansys Design Modeler (2023R1) and meshed within the Ansys Workbench environment. To accurately resolve the critical flow physics, a hybrid meshing strategy was employed. This involved the use of

Table 1. Meshing independence.

DETTHE			DCTTHE			DSTTHE		
No. of grid elements	*U*	*U*, deviation	No. of grid elements	*U*	*U*, deviation	No. of grid elements	*U*	*U*, deviation
1789045	1650	0.09	468384	569.19	0.0300	2321543	1350	0.07
2120000	1810	0.03	761362	585.12	0.0087	2865097	1450	0.03
2527348*	1879	0.01	1208000*	590.22	0.0055	3155185*	1495	0.02
2956732	1910	–	1782044	593.45	–	3754321	1533	–

*) mesh size selected for further analysis

tetrahedral elements in the core volume, coupled with disciplined inflation layers at the walls to capture near-wall gradients, and targeted local refinement in regions prone to high velocity gradients and flow separation, such as the lee of the helical twists.

A mesh independence study was conducted, monitoring key performance parameters (e.g. Nusselt number and pressure drop). As detailed in Table 1, the solution demonstrated stability for the selected mesh (marked with an asterisk), with variations in the overall heat transfer coefficient below a predefined threshold of, e.g., 1% upon further refinement. This confirms that the computational results are quantitatively independent of the mesh discretisation, providing confidence in the reliability of the subsequent simulation data.

4. Boundary conditions

The numerical simulations commenced upon implementing the prescribed boundary conditions. For the hot water stream, multiple mass flow rates were examined to investigate varying thermal-hydraulic conditions, while maintaining a constant flow rate for the cold water circuit. The study explored Reynolds numbers ranging from 5000 to 25 000, with fixed inlet temperatures of 25°C for the cold fluid and 70°C for the hot fluid. Adiabatic conditions were imposed on all external surfaces to ensure thermal isolation of the system.

5. Results and discussion

Figure 2 illustrates the variation in hot fluid outlet temperature for the DCTTHE, DETTHE and DSTTHE configurations as a function of Reynolds number at Tr = 5. The DETTHE configuration exhibits the lowest outlet temperature due to enhanced heat transfer from the cold fluid. In contrast, the DCTTHE shows a consistently higher outlet temperature compared to both DSTTHE and DETTHE across all Reynolds numbers, primarily because it generates less turbulence than the other configurations.

Figure 3 illustrates the variation of the cold fluid outlet temperature (T_{co}) with Reynolds number for the DCTTHE, DSTTHE and DETTHE configurations at a twist ratio (Tr = 5). DETTHE presents the highest outlet temperatures across all Reynolds values, followed by DSTTHE, while DCTTHE exhibits the lowest T_{co}. This behaviour can be attributed to the more pronounced swirl motion and stronger secondary vortices generated within DETTHE, which enhance mixing and intensify local convective heat transfer. In contrast, although DCTTHE

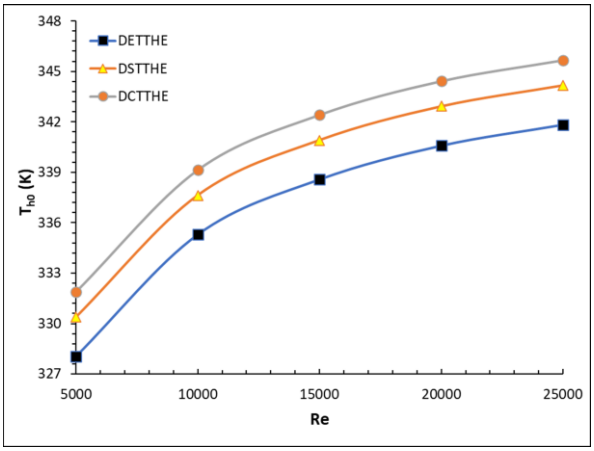


Fig. 2. Variation of the hot water outlet temperature with Reynolds number for DCTTHE, DSTTHE and DETTHE at Tr = 5.

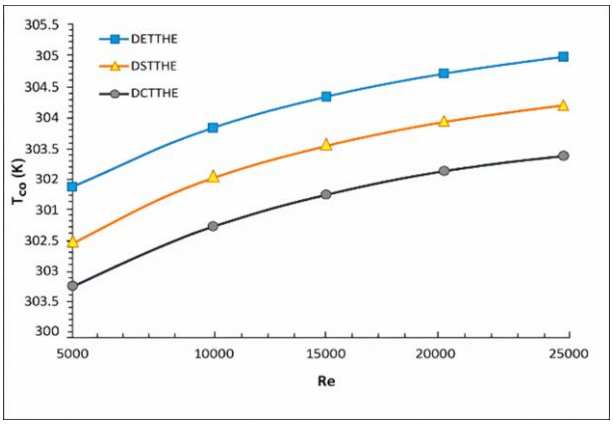


Fig. 3. Variation of the cold water outlet temperature with Reynolds number for DCTTHE, DSTTHE and DETTHE at Tr = 5.

contains internal twisting, its lower induced turbulence strength results in reduced thermal exchange, leading to lower outlet temperatures.

Figure 4 illustrates the temperature difference $T_h - T_c$ between hot and cold fluids for the three configurations at Tr = 5. The temperature difference decreases with the Reynolds number due to higher fluid velocity, with DCTTHE demonstrating the largest differential. This trend stems from the DETTHE's superior turbulence, which reduces T_{ho} by facilitating more efficient cold-fluid heat absorption.

The overall heat transfer coefficient (U) variation is depicted in Fig. 5. U rises with Reynolds number for all designs, driven

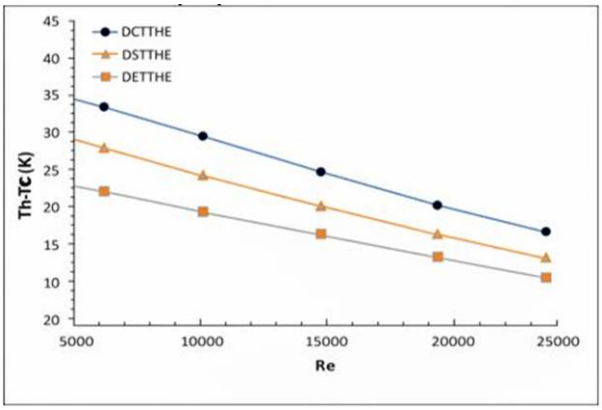


Fig. 4. Variation of the temperature difference between the hot and cold fluids with Reynolds number for DCTTHE, DETTHE and DSTTHE at Tr = 5.

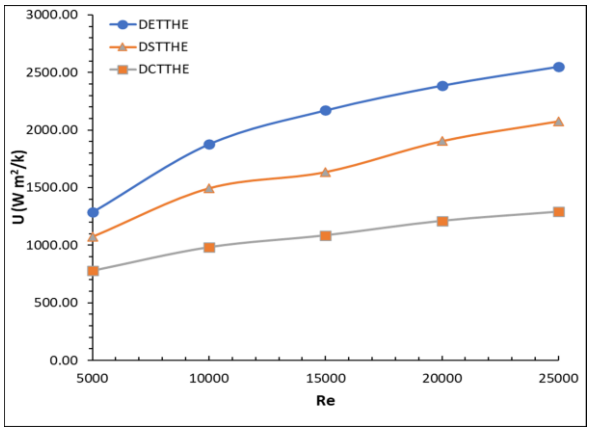


Fig. 5. Variation of the overall heat transfer coefficient with Reynold number for DCTTHE, DSTTHE and DETTHE at Tr = 5.

by greater thermal energy extraction from the hot fluid. DETTHE outperforms other designs due to vortices generated by its geometry, which amplify both heat transfer and pressure drop by disrupting the momentum boundary layer.

Figure 6 compares heat exchanger effectiveness (ϵ) across configurations. Effectiveness decreases at higher Re values due to a significant reduction in fluid residence time inside the tube.

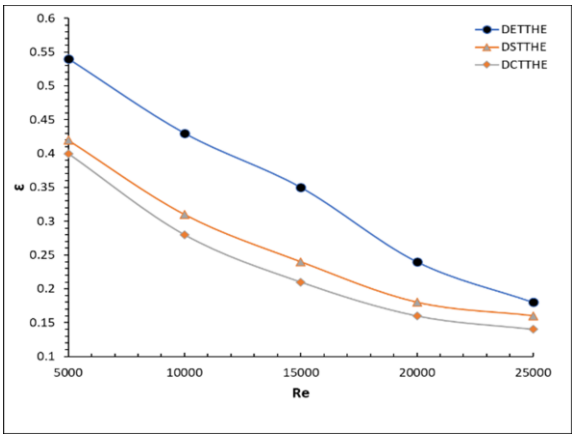


Fig. 6. Variation of the heat exchanger effectiveness with Reynolds number for DCTTHE, DETTHE and DSTTHE at Tr = 5.

At high flow velocities, the available time for heat exchange becomes insufficient to fully benefit from the increased heat transfer coefficient. Moreover, for the enhanced geometries (DETTH, DSTTHE and DCTTHE), the improvement in turbulence becomes less influential at high Reynolds numbers, while the associated pressure drop remains high, resulting in a relative decrease in effectiveness.

The Nusselt number trends are shown in Fig. 7. The Nu values increase with an increase in Reynolds number, as heightened turbulence thins the thermal boundary layer. For DETTHE, it surpasses those for other configurations due to its larger effective surface area and flow disruption.

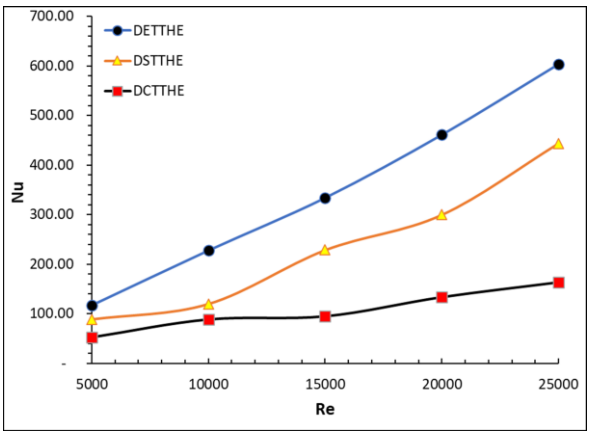


Fig. 7. Variation of the Nusselt number with Reynolds number for DCTTHE, DSTTHE and DETTHE at Tr = 5.

Pressure drop (ΔP_T) and average heat transfer rate (Q_{avg}) are analysed in Figs. 8 and 9, respectively. DETTHE incurs the highest ΔP_T due to intensified vortices, while also achieving the greatest Q_{avg} from enhanced fluid velocity and turbulence.

Finally, Fig. 10 evaluates the overall performance index (η). The value for DETTHE peaks at a lower Reynolds number (Re = 5000), exceeding the values for DCTTHE and DSTTHE by approximately 0.0025 and 0.0040, respectively. Performance declines across the Re range (Re = 5000–25 000) as pressure drop penalties outweigh thermal gains. Vortex generation, modulated by Tr = 5, critically influences this trade-off.

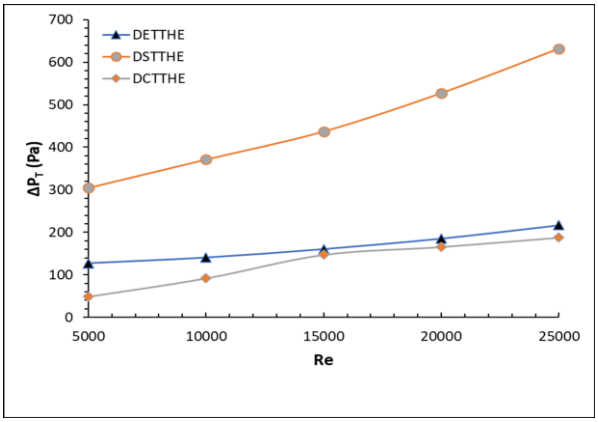


Fig. 8. Variation of the total pressure drop with Reynolds number for DCTTHE, DSTTHE and DETTHE at Tr = 5.

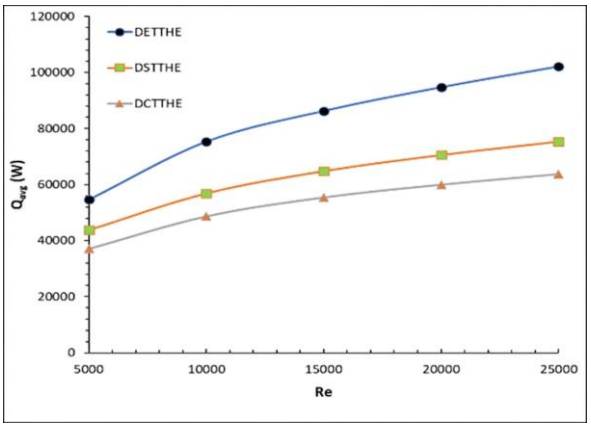


Fig. 9. Variation of average heat transfer rate with Reynolds number for DCTTHE, DSTTHE and DETTHE at Tr = 5.

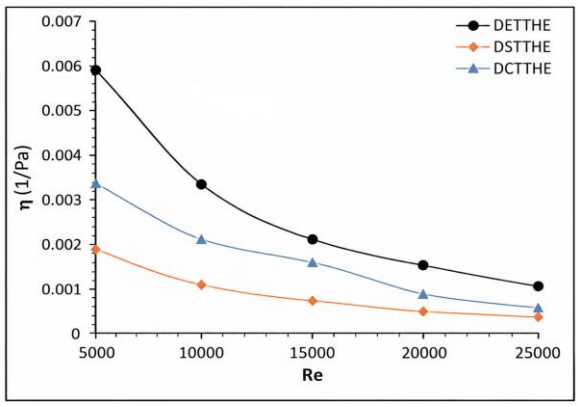
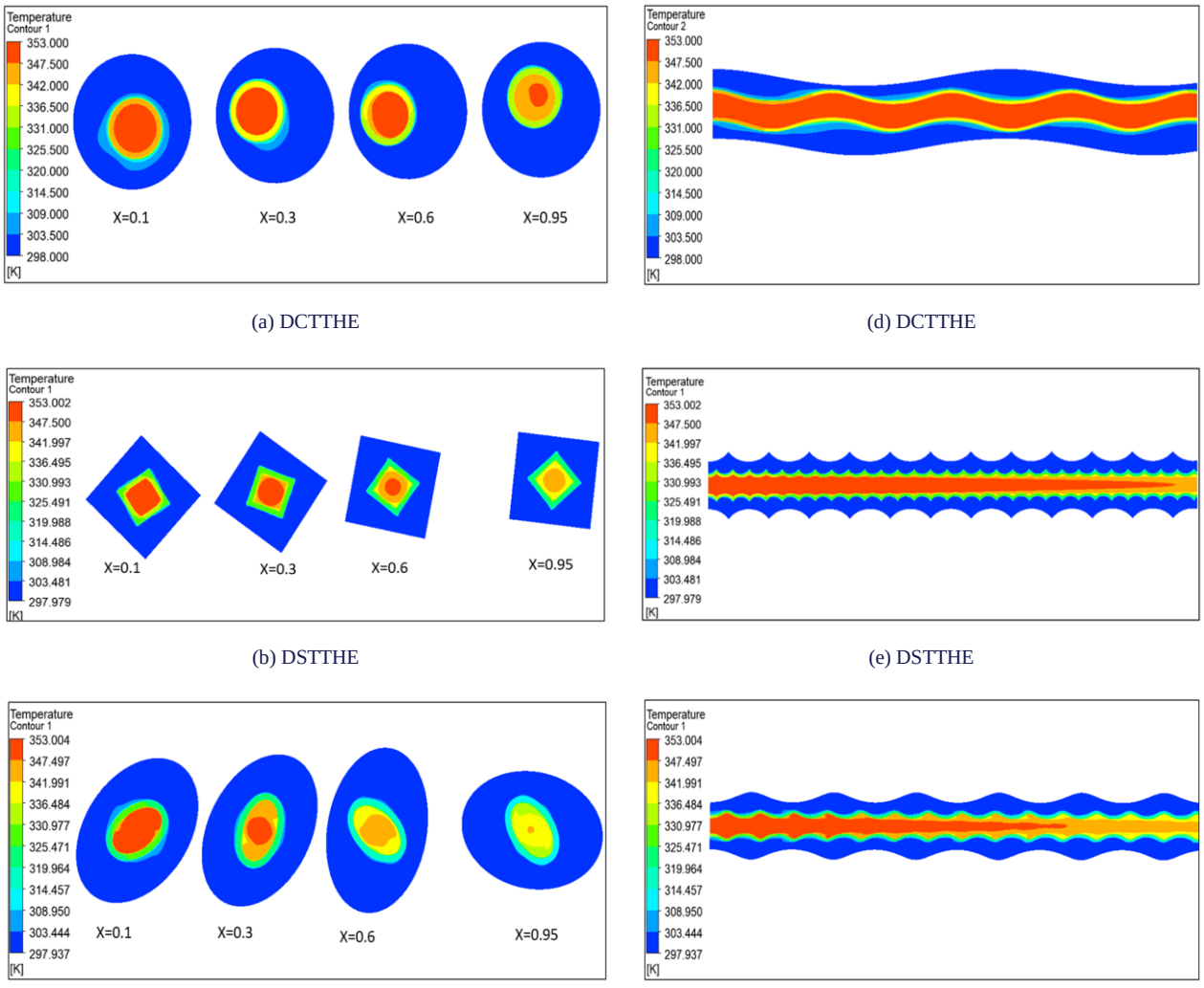


Fig. 10. Variation of the overall performance factor with Reynolds number for DCTTHE, DSTTHE and DETTHE at Tr = 5.

Figure 11 shows the temperature contours for various configurations of the double twisted tube heat exchanger – specifically DCTTHE, DSTTHE and DETTHE – at selected axial positions (0.1 m, 0.3 m, 0.6 m, and 0.95 m), under a Reynolds number of 25 000 and a twist ratio (Tr) of 5. At the inlet region, the temperature of the hot fluid is at its highest. As heat is transferred through the tube wall to the cold fluid, the temperature of the hot stream gradually decreases along the flow direction, reaching its



(a) DCTTHE

(d) DCTTHE

(b) DSTTHE

(e) DSTTHE

(c) DETTHE

(f) DETTHE

Fig. 11. Temperature distributions for DCTTHE, DSTTHE and DETTHE at Re = 25 000, Tr = 5.

lowest value near the outlet. The twisting in each configuration promotes thermal interaction between fluid layers, causing the bulk temperature at each cross-section to rise due to internal energy redistribution. This interlayer exchange enhances thermal equilibrium within the flow. The application of twisted geometries significantly improves temperature uniformity across circular, square and elliptical tube shapes. Notably, for all three designs, the highest temperature contours are observed near the outlet region (x = 0.95 m), indicating elevated thermal levels at the tube exit. At a twist ratio of 5, the inner wall's thermal boundary layer is disrupted by increased velocity and the development of secondary flows. The induced vortices intensify mixing within the fluid, leading to a progressive rise in temperature toward the outlet. The resulting temperature distribution around the inner tube surface exhibits a clear variation, emphasising the impact of twist-induced flow dynamics.

6. Conclusions

This study numerically evaluated the thermal and hydrodynamic performance of three twisted double tube heat exchanger configurations — circular (DCTTHE), square (DSTTHE) and elliptical (DETTHE) — under turbulent flow conditions with a fixed twist ratio of 5. The results demonstrated that the elliptical twisted tube (DETTHE) consistently outperformed the other geometries across all Reynolds numbers, exhibiting the highest Nusselt number, overall heat transfer coefficient and exchanger effectiveness. The enhanced performance is attributed to stronger secondary flows and turbulence generated by the elliptical twist, which improved fluid mixing and disrupted thermal boundary layers. DCTTHE exhibited the lowest thermal performance due to weaker turbulence generation, while DSTTHE showed intermediate results. Temperature distribution analysis confirmed more uniform heat transfer in DETTHE, particularly near the outlet. The study also found that performance gains were more pronounced at lower Reynolds numbers, with diminishing returns as flow velocity increased. While pressure drop increased with higher turbulence, DETTHE still achieved the best overall thermal-hydraulic performance. Temperature contour analysis further validated improved heat distribution and uniformity in the twisted configurations. These findings confirm that twisted elliptical designs significantly enhance heat transfer efficiency and are well-suited for industrial applications requiring compact and high-performance heat exchangers.

References

[1] Mushatet, K.S., Rishak, Q.A., & Fagr, M.H. (2020). Experimental and numerical investigation of swirling turbulent flow and heat transfer due to insertion of twisted tapes of new models in a heated tube. *Applied Thermal Engineering*, 171, 115070. doi: 10.1016/j.applthermaleng.2020.115070

[2] Razzaq, A.K.A., & Mushatet, K.S. (2023). A Review study for a twisted tube heat exchanger. *Journal of Nanofluid*s, 12(2), 299−317. doi: 10.1166/jon.2023.1926

[3] Salam, B., Biswas, S., Saha, S., & Bhuiya, M.M.K. (2013). Heat transfer enhancement in a tube using rectangular-cut twisted tape insert. *Procedia Engineering*, 56, 96−103. doi: 10.1016/j.proeng.2013.03.094

[4] Murali, G., Nagendra, B., & Jaya, J. (2020). CFD analysis on heat transfer and pressure drop characteristics of turbulent flow in a tube fitted with trapezoidal-cut twisted tape insert using Fe_3O_4 nano fluid. *Materials Today: Proceedings*, 21(1), 313−319. doi: 10.1016/j.matpr.2019.05.451

[5] Wu, C.C., Chen, C.C., Yang, Y.T., & Huang, K.H. (2018). Numerical simulation of turbulent flow forced convection in a twisted elliptical tube. *International Journal of Thermal Sciences*, 132, 199−208. doi: 10.1016/j.ijthermalsci.2018.05.028

[6] Cheng, J., Qian, Z., & Wang, Q. (2017). Analysis of heat transfer and flow resistance of twisted oval tube in low Reynolds number flow. *International Journal of Heat and Mass Transfer*, 109, 761−777. doi: 10.1016/j.ijheatmasstransfer.2017.02.061

[7] Luo, C., Song, K.W., & Tagawa, T. (2021). Heat transfer enhancement of a double pipe heat exchanger by co-twisting oval pipes with unequal twist pitches. *Case Studies in Thermal Engineering*, 28, 101411. doi: 10.1016/j.csite.2021.101411

[8] Alempour, S.M., Arani, A.A.A., & Najafizadeh, M.M. (2020). Numerical investigation of nanofluid flow characteristics and heat transfer inside a twisted tube with elliptic cross section. *Journal of Thermal Analysis and Calorimetry*, 140, 1237−1257. doi: 10.1007/s10973-020-09337-z

[9] Kim, H.R., Kim, S., Kim, M., Park, S.H., Min, J.K., & Ha, M.Y. (2016). Numerical study of fluid flow and convective heat transfer characteristics in a twisted elliptic tube. *Journal of Mechanical Science and Technology*, 30, 719−732. doi: 10.1007/s12206-016-0127-4

[10] Mushatet, K.S., & Youssif, F.K. (2018). Prediction the thermal and hydrodynamic performance of nano fluids flow in a tube coupled with double twisted tape. *ARPN Journal of Engineering and Applied Sciences*, 13(12), 4012−4021.

[11] Mushatet, K.S., & Youssif, F.K. (2018). Modeling whirling motion and heat transfer intensification in a heated tube with a twin twisted tape. *2018 International Conference on Advance of Sustainable Engineering and its Application ICASEA*, (pp. 215−220), 14–15 March, Wasit-Kut, Iraq. doi: 10.1109/ICASEA.2018.8370984

[12] Mashayekhi, R., Eisapour, A.H., Eisapour, M., Talebizadehsardari, P., Rahbari, A. (2022). Hydrothermal performance of twisted elliptical tube equipped with twisted tape insert. *International Journal of Thermal Sciences*, 172(A), 107233. doi: 10.1016/j.ijthermalsci.2021.107233

[13] Karimi, A., Al-Rashed, A.A., Afrand, M., Mahian, O., Wongwises, S., & Shahsavar, A. (2019). The effects of tape insert material on the flow and heat transfer in a nanofluid-based double tube heat exchanger: Two-phase mixture model. *International Journal of Mechanical Sciences*, 156, 397−409. doi: 10.1016/j.ijmecsci.2019.04.009

[14] Razzaq, A.K.A., & Mushatet, K.S. (2024). Influence of the twisting and nano fluids on performance of a triangular double tube heat exchanger. *Kerntechnik*, 89(3), 265−282. doi: 10.1515/kern-2023-0132

[15] Razzaq, A.K.A., & Mushatet, K.S. (2021). A numerical study for a double twisted tube heat exchanger. *International Journal of Heat & Technology*, 39(5), 1583−1589. doi: 10.18280/ijht.39052

[16] Razzaq, A.K.A., & Mushatet, K.S. (2024). Assessment the thermal performance of square twisted double tube heat exchanger with Al_2O_3 nanofluid. *Chemical Product and Process Modeling*, 19(4), 653−669. doi: 10.1515/cppm-2024-0047

[17] Razzaq, A.K.A., & Mushatet, K.S. (2021). Evaluation the performance of the double tube heat exchanger by using combined twisted tube and nano fluid. *International Journal of Mechanical Sciences*, 7(1), 6618−6628.

Co-published by
Institute of Fluid-Flow Machinery
Polish Academy of Sciences
Committee on Thermodynamics and Combustion
Polish Academy of Sciences

Copyright©2026 by the Authors under licence CC BY-NC-ND 4.0

http://www.imp.gda.pl/archives-of-thermodynamics/

Enhancing Solar Still Productivity through Fin, Solar Collector and Wick Modifications: A Comprehensive Review

Akashdeep Negi[1*], Lalit Ranakoti[2], Kapil Kumar Sharma[1], Adhirath Mandal[3], Mansi Sharma[4], Deepak Kumar[5], Jeetendra Mohan Khare[6], Shobhit Sharma[6], Prabhakar Bhandari[7], Sneha Singh[8]

[1]Department of Mechanical Engineering, Graphic Era Deemed to be University, Dehradun 248002, Uttarakhand, India
[2]Department of Mechanical Engineering, (Alliance School of Applied Engineering), Alliance University, Bengaluru 562106, Karnataka, India
[3]Department of Mechanical Engineering and Design, Jaypee Institute of Information Technology, Noida 201309, Uttar Pradesh, India
[4]Department of Computer Science Engineering, Jaypee Institute of Information Technology, Noida 201309, Uttar Pradesh, India
[5]Department of Mechanical Engineering, COER University, Roorkee 247667, Uttarakhand, India
[6]Department of Mechanical Engineering, SR Group of Institutions, Jhansi 284002, Uttar Pradesh, India
[7]Department of Mechanical Engineering, School of Engineering and Technology, K.R. Mangalam University, Gurugram 122103, Haryana, India
[8]Graphic Era School of Management, Graphic Era Deemed to be University, Dehradun 248002, Uttarakhand, India
[*]Corresponding author email: akashdeepnegi6@gmail.com

Received: 09.06.2025; revised: 23.04.2026; accepted: 10.08.2026

Abstract

Solar distillation has emerged as a vital technique for providing fresh water to communities at an economic level. Among various systems, the solar still has been recognised as a promising technology due to its simple design, low maintenance requirements and environmental benefits, particularly in reducing carbon footprint and supporting sustainable development goals. However, the yield of a solar still is highly dependent on solar intensity, which drops significantly at night, thereby limiting its overall efficiency. So, this review article explores a wide range of low-cost modifications for improving the evaporation rate and freshwater yield. The article covers the fabrication process of the solar still and discusses various design modifications. These modifications include the effects of fin geometry and placement. Furthermore, the article examines the integration of external attachments such as flat plate collectors (FPC) and evacuated tube collectors (ETC) to enhance heat transfer. The influence of wick materials, their types and placement within the solar still are also analysed. Lastly, the article provides a key recommendation highlighting the potential future research for the development of high-performance solar stills.

Keywords: Solar still; Yield improvement; Evaporation rate; Fins; Solar collector; Wicks

Vol. 47(2026), No. 3, 147–156; doi: 10.24425/ather.2026.7514

Cite this manuscript as: Negi, A., Ranakoti, L., Sharma, K.K., Mandal, A., Sharma, M., Kumar, D., Khare, J.M., Sharma, S., Bhandari, P., & Singh, S. (2026). Enhancing Solar Still Productivity through Fin, Solar Collector and Wick Modifications: A Comprehensive Review, *Archives of Thermodynamics*, 47(3), 147–156.

1. Introduction

Fresh water is a fundamental necessity for all living beings to sustain their day-to-day routines. This concept is undeniably acceptable around the globe, but the efforts to adequately address this challenge remain insufficient. Fresh water supply to every household is now become a challenge due to continuous increasing population and limited water resources. It was estimated that freshwater demand may rise by 55% by the end of 2050 [1]. This challenge intensifies further due to rapid industrialisation and its consequences, that is pollution of the available water resources. Therefore, exponential rise in freshwater demand has been observed in the last few decades. Considering developing countries, in particular arid and remote areas, there is a large shortage of electricity, and conventional methods to treat impure water

are not feasible for producing fresh water [2]. Major sources of fresh water in such regions are canals, groundwater, lakes, water streams, etc., which are either insufficient in amount or not adequately clean [3]. These concerns underscore the dire need for a sustainable technique for water treatment, which is efficient, reliable and pocket friendly.

It has been estimated that freshwater availability is limited (less than 3%) and distributed unevenly throughout the globe [4]. Despite that, saline water is plenty in nature and covers 97% area of the total water bodies [5]. However saline water cannot be considered for drinking due to the high content of total dissolved solids (TDS), salt, and bad pH [6]. Various water treatment methods can be employed to treat saline water efficiently, and later they can be employed for betterment of the society. These water filtration techniques include reverse osmosis (RO), electrodialysis (ED), multistage flash distillation (MFD), nanofiltration membrane (nFM), solar distillation using a solar still,

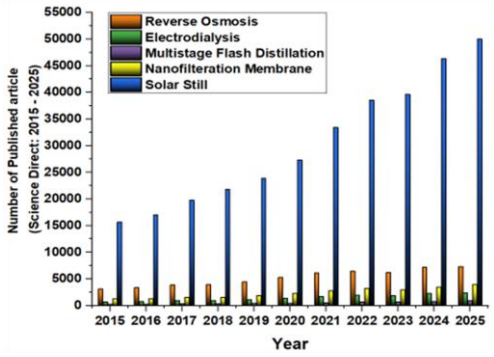


Fig. 1. Number of published articles in ScienceDirect from 2015 to 2025 (source: ScienceDirect).

and so on [7–11]. Nonetheless, the dilemma arises regarding which technique to use due to their respective advantages and disadvantages.

For instance, data collected (published articles) for five major water treatment techniques, that is reverse osmosis, electrodialysis, multistage flash distillation, nanofiltration membrane, and solar still taken from ScienceDirect for the years 2015 to 2025, as represented in Fig. 1, suggesting that research and development in the field of solar still is currently leading by a very big margin due to renewable energy input and ease of water purification. Data also signifies a steady rise in research publications for reverse osmosis but still trailing behind solar still by a huge margin. The lower number of publications in the field of electrodialysis, multistage flash distillation and nanofiltration membrane indicates the shift of research and development for water purifying techniques towards sustainable and low-cost freshwater production methods.

Several key components of the solar still and its working principles have been presented in Fig. 2. The solar still system is an airtight chamber, covered with a transparent sheet of glass at the top. The saline or contaminated water is poured through the inlet into the basin of the solar still. The solar radiation is incident through the glass and impinges on the system's basin [12]. The material used for the basin has high radiation absorptivity properties. These materials include different grades and gauges of steel, mild steel (MS), copper, stainless steel (SS), galvanised iron (GI), aluminium, and so on [13]. Good insulation materials, especially foam, thermocol, glass wool, rock wool, and so on, are used to reduce the losses from sides and bottom [14]. The thermal radiation impinges on the basin surface and enhances the temperature of the contaminated water, causing evaporation and leaving behind all the impurities in the basin.

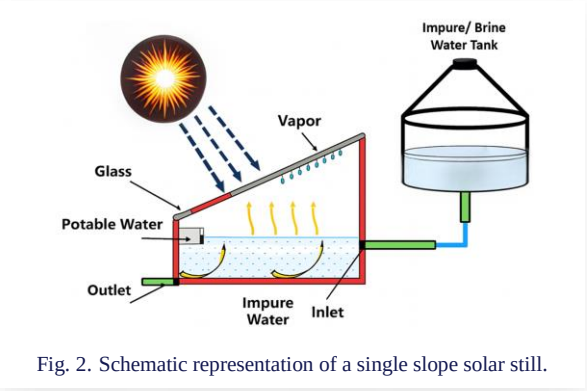


Fig. 2. Schematic representation of a single slope solar still.

The evaporated water gets condensed over the glass surface due to the temperature difference between the basin water and the glass surface. The condensed water droplets are collected in a separate clean container that can be used for domestic purposes [15].

Solar desalination has shown its prominence in getting attention from various scholars due to its ease of working principle, construction, manoeuvrability, maintenance, and so on [16]. Yet, along with several advantages, it has certain disadvantages such as low distillate yield, even zero at night due to the unavailability of solar energy. Earlier studies [17] reported an overall daily distillate yield of less than 3 kg/m^2 a day using a basic design of the solar still, which is quite low. Papers [18–19] have suggested that the yield of the solar still depends on the heat transfer rate (at evaporation and condensation) within the system. A higher evaporation rate results in more vapour generation, while condensation helps turn that vapour back into water droplets.

In addition, Fig. 3 presents a schematic classification of solar stills based on passive and active systems. Passive solar stills rely entirely on sunlight, making them simple, low-cost and suitable for small-scale use [20]. They include conventional designs such as basin-type stills, which vary in shape (single slope, double slope, pyramid) and number of basins, as well as models enhanced with reflectors or condensers [21]. To improve efficiency, modified designs introduce features like wick materials, rotating cylinders, or innovative shapes such as stepped, tubular, or concave forms, all aimed at increasing evaporation and condensation rates. Hybrid solar stills take this a step further by combining the still with technologies like photovoltaic panels, solar ponds, or waste heat sources to boost performance [22].

Active solar stills are designed for higher productivity by incorporating external energy support [23]. They are often integrated with solar collectors, such as flat plate or concentrating collectors, to preheat water, with circulation occurring naturally or through pumps [24]. More advanced systems use components like evacuated tubes, heat pipes, or parabolic collectors to achie-

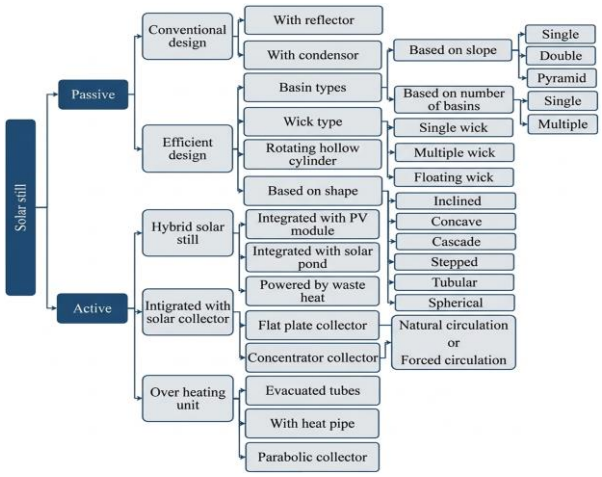


Fig. 3. Yield improvement techniques of the solar still.

ve higher temperatures and faster distillation. Overall, the classification shows how solar still technology evolves from simple, standalone units to more advanced and efficient systems capable of producing greater amounts of fresh water [25].

In addition, the efficiency of a solar still can be enhanced by minimising the losses occurring in a solar still. Major losses that occur in a solar still are due to radiation and convection. Proper care can prevent heat losses from the solar still by applying insulating materials [14]. Several types of insulations have been utilised in solar stills [15,26–28], such as foam, thermocol, saw dust and glass wool, focusing on specific insulating thickness. Without knowing about the thickness of insulation to be applied over the solar still, the effective output will not be achieved. For instance, the thickness of insulation of 60 mm for a single slope solar still (SSSS) operating at a water depth of 40 mm can produce a yield up to 80% as reported by Khalifa et al. [29]. Results have also been reported for insulating thickness of above 60 mm, which certainly performed better in terms of yield but only during the nocturnal period. It was observed that materials such as sawdust (of thermal conductivity 0.08 W/(m·K)), glass wool (0.04 W/(m·K)), and plywood (0.13 W/(m·K)) are commonly used as insulation in solar stills to minimise heat loss to the surroundings. A brief summary of the previously used insulation materials is given in Table 1.

More focus has been given to enhancing the yield of the solar still system during the nocturnal period, and to do so, various developments have been done in the past that could store energy during peak hours and can deliver back to the system during low sunshine hours, i.e. the nocturnal period. Enhancement of yield can also be achieved by modifying the solar still system in which utilisation of flat plate collector, application of tilted khes wicks and incorporation of absorbers are included [15]. The rate of evaporation which eventually determines the yield of the solar still can also be tailored by incorporating phase change materials in the water basin, using fins at the surface, and incorporating nanoparticles with the basin water [30,31]. These modifications in the solar still help in improving the overall surface area and lead to higher yields as compared to the yield of an unmodified solar still. The said modifications of the solar still are cheap and do not require any complex engagements and have proved to be highly promising in enhancing the solar still yield [32]. Therefore, this work primarily focuses on discussing various such modifications and techniques under practice for solar still yield enhancement at a very low cost.

2. Modifications in the solar still

2.1. Yield enhancement using fins

Integration of fins on the basin of the solar still can be seen in Fig. 4. It has been evident from the past literature that the integration of fins improves the heat transfer rate of the system. It increases the surface area, resulting in improved basin water temperature and distillate yield. Notable enhancement in the yield of the solar still of about 3.07 l/m^2 can be obtained by integrating fins at the surface, incorporating a phase change material, applying wicks and utilising a condenser. These changes applied all together in a single slope solar still (SSSS) were reported to have a yield 39.47% higher than that for a conventional conical solar still (CSS) without any modification [33]. The complete setup along with the yield obtained by the systems can be seen in Fig. 5.

Additionally, it has been concluded that the integration of fins increases the greenhouse effect within the solar still as reported by Rabhi et al. [34]. As per the study, apart from improving the heat transfer rate, fins are also used to evenly distribute water within the basin of the solar still [35]. The materials used to fabricate the fins are crucial, as the heat transfer properties of the system depend on them [36]. Contrary to this, Sebaii et al. [37] reported no significant improvement in varying fin materials. During the study, different fin materials such as aluminium, glass, stainless steel, brass, copper, iron and mica were used in solar stills. Figure 6 presents the complete 2D model of the setup along with the dimensions of the fins. As discussed previously, various factors such as the type of fins and geometry

Table 1. Summary of the relevant studies on insulation materials.

Publication	Insulation material	Thickness of insulation (mm)	Modifications	Enhancement (%)
Agarwal et al. [68]	rockwool	4	copper tubes and copper cylinders filled with PCM	92.02
Ramzy et al. [69]	steel wool pads	–	internal reflectors and woven wire mesh	22.1
Karthikeyen et al. [70]	thermocol	–	nanomaterial with colour die	66.7
Negi et al. [64]	foam	30	blackened inclined wick	14.9
Omara et al. [71]	saw dust	40	fins	40

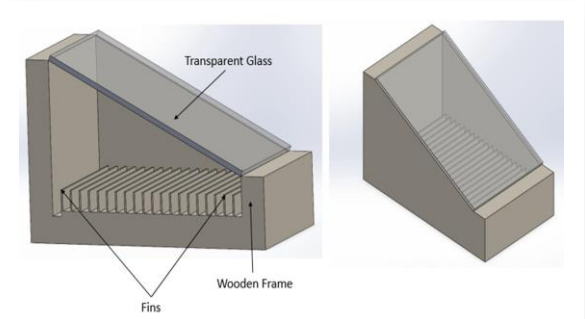


Fig. 4. Fins integrated solar still.

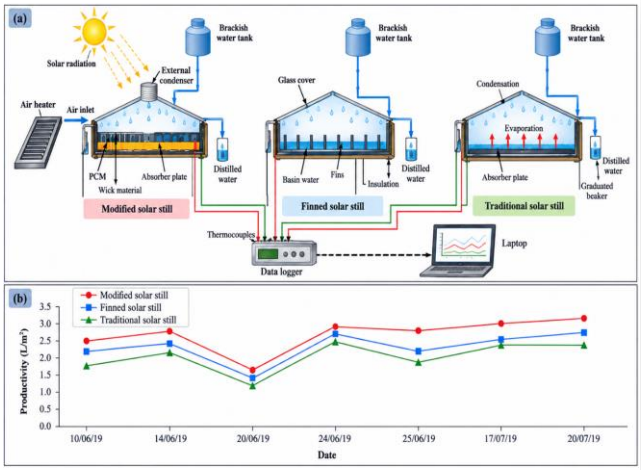


Fig. 5. Schematic diagram of the experimental setup (a), and yield obtained from the respective solar still (b) (drawn based on [33]).

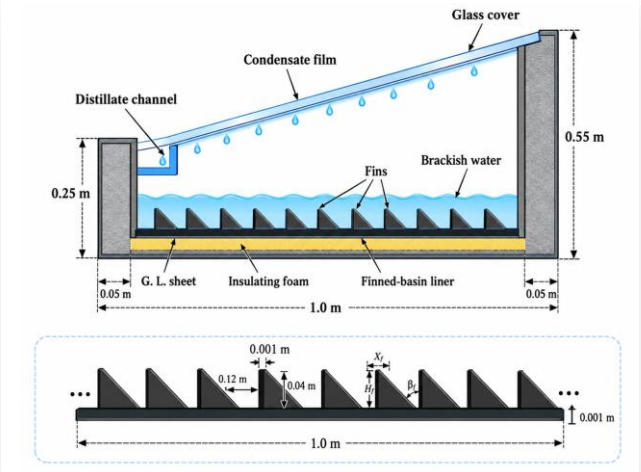


Fig. 6. Experimental setup modified with fins (drawn based on [37]).

are the influencing parameters that directly improve the efficacy of the solar still. In a recent study, Panchal et al. [38] experimented with vertical and inclined fins incorporated in a solar still. The inclined fins were tilted at a 30° angle. It was observed that the distillate yield of inclined fins was slightly higher compared to vertical fins. The yield was improved by 26.77 % and 24.19 % for an inclined and vertical fins-based solar still compared to CSS. Also, Rajaseenivasana et al. [39] tested circular and square-shaped fins with varying water depth (1–3 cm) in SSSS. It has been reported that square-shaped fins in a solar still have higher distillate yield compared to circular fins. Based on the study, it was concluded that increasing the fin's height has a great impact on the rate of heat transfer, as reported in the literature. Apart from this, it has been observed that increasing fin quantity and width can significantly reduce the overall distillate yield [40]. This was observed due to higher heat loss from the side and bottom of the still. To reduce these losses, an acrylic material-based casing was used with aluminium fins. These modifications decrease the heat losses and improve the overall temperature of the basin water and hence contribute to overall improved water yield [41]. Modi et al. [42] experimented on a solar still with and without hollow circular fins. It was reported that the evaporative area of the still was significantly improved compared to the still without fins. Furthermore, it has been observed that the number of fins also influences the distillate yield of the system. Islam et al. [43] reported significant improvement in the distillate yield using 14 fins and 4kg of fly ash. Apart from this, Panchal et al. [44] studied the effect of porosity on SSSS. The obtained results show a 42.3% improvement in distillate yield with porous fins compared to CSS.

Few studies have incorporated both fins and energy storage materials simultaneously with the solar distillation setup. Simultaneously using these modifications increases the yield of the modified system and significantly lowers the cost per litre of obtained water (CPL). In a similar fashion, Kumar et al. [45] modified a conventional solar still with aluminium, galvanised iron (GI) based fins and paraffin wax. Among fin materials, aluminium was superior due to its thermo-physical properties. The authors report a 36% improvement in the overall distillate yield for CSS, when compared to the conventional solar still. In another study, the authors studied the effect of fins above and beneath the absorber plate with paraffin wax. It has been evident from the study that the placement of the fins above the absorber plate increases the surface area of the system, while extending fins beneath the plate increases the heat storage capacity of the system. This modification increases the distillate yield of CSS by 55.59%. Also, these modifications lower CPL of the obtained distillate [46]. In another study, Abdullah et al. [47] modified the shape of the basin. Additionally, fins were covered with jute cloth to increase the capillary action. The CuO-based nPCM was used to store energy for improved distillate yield for a longer period. Apart from this, three heaters were provided to heat the basin water up to its evaporation temperature. These modifications improve the distillate yield by 196% as compared to a reference CSS, as reported by the author.

2.2. Yield enhancement using solar collectors

Solar collectors or solar water heating devices utilise solar energy to convert radiation into useful heat, particularly for water heating applications. These solar collectors are coupled with solar stills to enhance the overall efficiency of the system by improving the evaporation rate. The collectors enhance the inlet

basin water temperature, thereby reducing the amount of energy required for water evaporation. Various collector designs are capable of providing a wide range of operating temperatures. The classification of the solar water heating systems can be seen in Fig. 7. Among these, a flat plate collector (FPC) and an evacuated tube solar collector (ETSC) are frequently used in the solar still. Flat plate collectors (FPCs) typically operate within the range of 20–80°C, whereas evacuated tube solar collectors (ETSCs) operate effectively at higher temperatures, between 50–200°C [48].

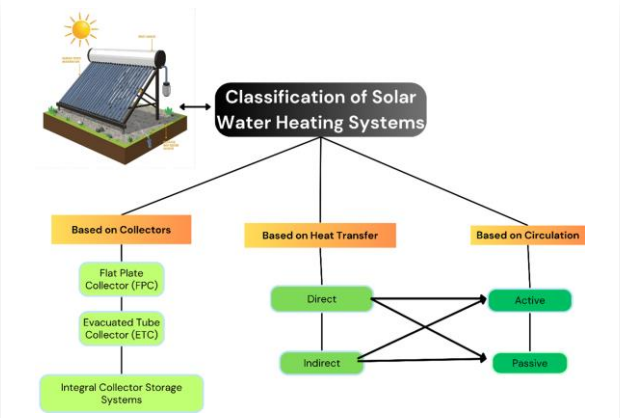


Fig. 7. Classification of solar water heating systems.

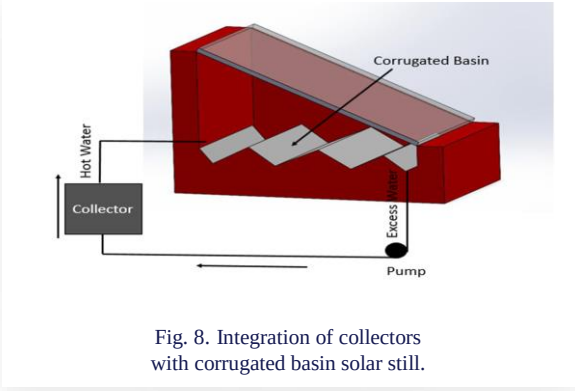


Fig. 8. Integration of collectors with corrugated basin solar still.

Among these, FPCs are the most commonly used due to their simple construction, low maintenance requirements and cost-effectiveness, yet they generally offer lower efficiency and outlet temperatures compared to other collector types. A scheme of utilisation of collectors in the solar still can be seen in Fig. 8.

The mass flow rate of the water, intensity of the solar radiation, and properties of the absorber material are the crucial factors that improve the brine water temperature. In this regard, Negi et al. [15] observed a maximum yield of 3.99 kg/m^2·a day from a tilted wick solar still fabricated from stainless steel material integrated with flat plate collectors at an optimal flow rate of 0.041 kg/s. Furthermore, Raju et al. [49] reported a 41% increase in distillate yield when a solar still was coupled with a single FPC compared to a conventional still. Furthermore, connecting three FPCs in series with the still enhanced the yield by up to 89%. Similarly, Badran et al. [50] demonstrated that integrating an FPC with a solar still increased its productivity by approximately 36% relative to CSS. Furthermore, according to Sabiha et al. [51], FPCs exhibit two major drawbacks, i.e. a significant convective heat loss through the glass cover from the absorber plate and the absence of a sun-tracking mechanism, which restricts their ability to consistently capture the maximum solar radiation throughout the day.

According to [52], evacuated tube solar collectors (ETSCs) exhibit significantly higher efficiencies than flat plate collectors (FPCs). ETSCs are capable of capturing both direct and diffuse solar radiation. In addition to their superior thermal performance, they offer advantages such as convenient installation and ease of transportation. Applications that demand higher operating temperatures, such as seawater desalination, air conditioning, space heating, refrigeration, and various industrial heating processes, benefit more from ETSCs than from FPCs [53]. Moreover, ETSCs are suitable for other high-temperature applications, including instantaneous gas heaters, boost element-integrated single solar tank systems, and boost tank-incorporated solar preheaters [54].

Mangal et al. [55] reported that FPCs achieve their peak energy output primarily at midday when the sun's rays are perpendicular to the collector surface. In contrast, the cylindrical design of ETSCs enables passive solar tracking throughout the day, allowing the incident sunlight to strike the tubes at an approximately 90° angle, thus maintaining continuous high absorption. Additionally, ETSCs are less affected by low ambient temperatures and wind, owing to the vacuum layer between the inner and outer tubes. This vacuum effectively minimises convective and conductive heat losses by eliminating air within the evacuated tube. Furthermore, Ayompe et al. [56] conducted an investigation to compare the performance of an FPC and a heat pipe evacuated tube solar collector (ETSC) for domestic water heating. Under similar climatic conditions, FPC and ETSC achieved 46.1% and 60.7% efficiencies, respectively, while the corresponding system efficiencies were 37.9% and 50.3%.

The integration of evacuated tube collectors with solar stills offers a highly effective method for improving heat transfer and increasing distillate yield. For instance, Panchal et al. [57] experimented by modifying a double slope solar still (DSSS) with fins and ETSC. Incorporating both fins and ETSC increases the system's yield by 25% when compared to DSSS with ETSC alone. In the other study, Mevada et al. [58] modified CSS with ETSC, zig-zag condensers and fins. The authors reported a 73.45% improvement in distillate yield with the above-mentioned modifications compared to CSS. Apart from this, carbon credit values of the modified solar still (MSS) and CSS were reported to be 5.8$ and 2.9$ per year, respectively. The complete pictorial view of the experimental setup modified with a zig-zag shaped condenser can be seen in Fig. 9.

2.3. Yield enhancement integrating wicks

Wicks such as jute, cotton, khes (porous cotton) cloth are being used to improve the efficacy of the system. Along with this, it has been reported that wicks are low-cost modifications that are used to improve the evaporation area and capillary action of the system. These modifications are simple in construction, and they are incorporated in the design of the still, as shown in Fig. 10.

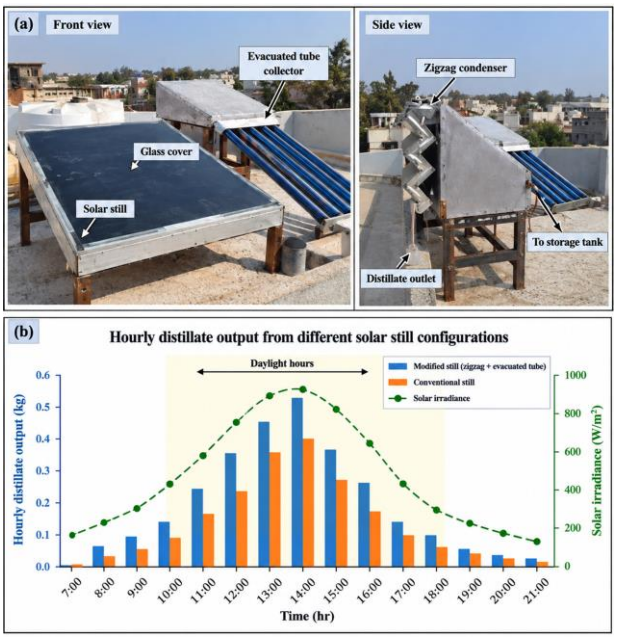


Fig. 9. Experimental setup of a solar still modified with a zigzag condenser and evacuated tube collector (a), and variation of hourly distillate output with time along with solar irradiance (b) (drawn based on [58]).



Fig. 10. Modified solar still with inclined wick.

Researchers have made significant efforts to enhance the productivity of solar stills through both experimental investigations and numerical simulations. For instance, Namshad et al. (2013) [59] examined the performance of flat and rippled wick inverted V-type solar stills (SS) operating under a drip regime in Kerala, considering various climatic conditions. Utilising wicks inside the solar still results in a higher increase in temperature, which in a higher distillate yield. Observations suggested that an increase in rippled angle may lead to a decrease in the productivity [60].

In a recent review, Jobrane et al. [61] analysed various internal and external enhancement techniques applied to wick-type solar stills designed for potable water production. Similarly, Manikandan et al. [62] reviewed the developments and performance improvements of several wick-type solar still configurations.

Furthermore, it was evident that integrating tilted wicks (khes material) inside the basin at the angle of 30º (as presented in Fig. 11) improves the distillate yield by 37.17% compared to CSS [63]. This enhancement in yield was obtained by the extra exposed area of the wick. Apart from this, it has been observed that incorporating these modifications can help mitigate the carbon footprint. With a similar objective, CSS was modified with a black painted basin and tilted wick at various inclinations. It has been reported that a blackened basin with a tilted wick mitigates 2.01 ton of CO_2 per year, which is higher compared to CSS [64]. Other wicks such as an inclined wick, a vertical rotating wick, a floating wick, multiple wicks, a moving wick, and black painted wick are also integrated with the system. For instance, integrating a movable wick can significantly improve the distillate yield of CSS, as reported by Lee et al. [65]. It has been reported that the yield obtained by the system increased by 7% compared to the reference solar still. Similarly, integrating a convex-shaped absorber and jute cloth as a wick, and nanocomposites can lead to an improvement in the distillate yield of a tubular solar still (TSS) by 114.2% [66]. Tanaka et al. [67] investigated and validated the result for improved yield using a tilted wick in a vertical multi-effect solar still. Few studies suggest that applying both wick and fins simultaneously leads to a significant improvement in distillate yield compared to CSS.

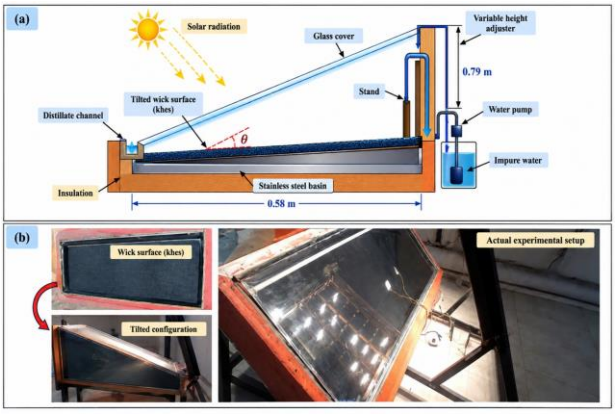


Fig. 11. Schematic diagram of the modified solar still (a), and photograph of the actual experimental setup (b) (drawn based on [64]).

3. Discussion and challenges

The importance of using solar stills can be observed in several arid and coastal areas where the intensity of the solar radiation is high and the quality of water to be purified is poor. Solar stills also hold an edge over other purifying techniques when the cost is considered a critical factor. On the contrary, solar stills exhibit low yield mostly due to the unavailability of sunlight and therefore remain non-operational during the night time.

Several design alterations have been proposed in the literature to enhance the evaporation rate and consequently its yield. These modifications include utilisation of nanofluids, thermal energy storage materials (sensible and latent), preheating the basin water and integration of external attachments, including FPCs and ETCs. Furthermore, the importance of insulation plays a crucial role in minimising heat loss from sides and bottoms. As far as the thickness of the insulating material is concerned, it has been found that 60 mm thickness of styrofoam material can significantly reduce heat losses. This ensures im-

proved basin water temperatures, leading to a higher rate of evaporation.

Furthermore, improving the surface area is highly recommended while enhancing the evaporation rate. This can be achieved by integrating the fins and wicks alone or simultaneously. The material that is utilised for the fabrication of fins and wicks should possess favourable thermo-physical properties, and also a high capillary action. The inclination at which the fins and wicks are placed inside should need a critical assessment. Fins improve the water distribution within the basin. Among various materials studied, aluminium fins exhibit a higher thermal conductivity and performance compared to glass, stainless steel or brass. Research further suggests that inclined fins (around 30°) and square geometries provide higher distillate yields than vertical or circular fins due to improved surface exposure. However, increasing the number or width of fins can lead to higher heat losses through the sidewalls, thereby reducing efficiency. The combination of fins with phase change materials such as paraffin wax or nanoparticle-enhanced PCMs has shown yield improvements ranging from 50% to 190%, while also significantly lowering the cost per litre of produced water.

The use of wick materials such as jute, cotton, and their fabric cloths has been proven to significantly enhance the evaporation rate and overall efficiency of solar stills. These low-cost, easily implemented modifications increase the effective surface area and promote capillary water movement. Among different configurations, tilted wicks (inclined according to the location latitude) have demonstrated yield improvements of up to 37% over conventional stills. Additional performance gains have been reported for blackened basins, movable wicks and multilayer wick systems, which also contribute to carbon footprint reduction. Furthermore, hybrid setups combining wicks with fins or nanoparticles suspended absorbers have achieved an improved yield exceeding 100%, highlighting the potential of wick-assisted hybrid stills as a sustainable and economical approach for freshwater production.

Additionally, the integration of evacuated tube collectors with the solar still enables operation of the system at higher temperatures, leading to better heat retention and greater overall productivity. Compared to flat plate collectors, which are inexpensive and easy to construct but limited by higher heat losses and lower temperature ranges (20–80°C), evacuated tube collectors operate efficiently at 50–200°C and benefit from passive solar tracking due to their cylindrical configuration. Studies report yield enhancements of 36–73% when evacuated tube collectors are combined with fins, condensers, or other hybrid design features.

4. Conclusions and recommendation

Solar stills are economical devices that can provide a fresh water supply to the backward arid areas. However, the low distillate yield of the solar still attracts researchers to seek for alternatives in order to improve the solar still yield. The following conclusions can be drawn based on the above discussion:

a) The low yield of conventional solar stills necessitates performance enhancement through effective modifications such as improved insulation, fins, wicks, and solar collector integration.
b) Integration of fins significantly improves heat transfer and evaporation by increasing the effective surface area, resulting in yield enhancement of up to 39.47%, compared to conventional solar stills.
c) Fin geometry and configuration play a critical role; incorporating inclined fins improved the yield of the solar still by approximately 26.66%, whereas vertical fins resulted in an improvement of about 24.19%, while square fins show better performance than circular ones.
d) Integration of solar collectors effectively increases basin water temperature, leading to productivity improvements of 36% to 89% with flat plate collectors (FPCs).
e) Evacuated tube collectors (ETSCs) demonstrate superior performance due to higher operating temperatures (50–200°C) and improved efficiency (up to ~60.7%), compared to FPCs.
f) Hybrid systems combining ETSCs with fins and condensers can enhance the yield by 25% to 73.45%, making them highly effective for large-scale applications.
g) Wick materials significantly enhance evaporation through capillary action, with tilted wick configurations improving the yield by up to 37.17%, compared to conventional systems.

Future research should focus on developing a road map for hybrid solar still systems by integrating multiple modification techniques such as fins, wicks, phase change materials and solar collectors. Furthermore, there is a strong scope for optimisation of key design and operating parameters, including fin geometry, wick inclination, insulation thickness (around 60 mm), and water depth, to achieve maximum efficiency under varying climatic conditions. Additionally, the use of advanced materials such as nanomaterials and nano-enhanced phase change materials can further improve heat transfer and energy storage capabilities. Also, future work should be concentrated on integrating yield improvements with detailed techno-economic analysis of various solar still modifications to identify the most efficient and cost-effective configurations.

References

[1] Proskuryakova, L.N., Saritas, O., & Sivaev, S. (2018). Global water trends and future scenarios for sustainable development: the case of Russia. *Journal of Cleaner Production*, 170, 867–879. doi: 10.1016/j.jclepro.2017.09.120

[2] Al-Karaghouli, A., & Kazmerski, L.L. (2013). Energy consumption and water production cost of conventional and renewable-energy-powered desalination processes. *Renewable and Sustainable Energy Reviews*, 24, 343–356. doi: 10.1016/j.rser.2012.12.064

[3] Loucks, D.P., & Van Beek, E. (2017). Water resources planning and management: An overview. In *Water Resource Systems Planning and Management: An Introduction to Methods, Models, and Applications* (pp. 1–49). Springer, Cham. doi: 10.1007/978-3-319-44234-1_1

[4] Sophocleous, M. (2004). Global and regional water availability and demand: prospects for the future. *Natural Resources Re-*

search, 13(2), 61–75. doi: 10.1023/B:NARR.0000032644.16734.f5

[5] Mishra, R.K. (2023). Fresh water availability and its global challenge. *British Journal of Multidisciplinary and Advanced Studies: Sustainability*, 4(3), 1–78. doi: 10.37745/bjmas.2022.0207

[6] Adjovu, G.E., Stephen, H., James, D., & Ahmad, S. (2023). Measurement of total dissolved solids and total suspended solids in water systems: A review of the issues, conventional, and remote sensing techniques. *Remote Sensing*, 15(14), 3534. doi: 10.3390/rs15143534

[7] Shon, H.K., Phuntsho, S., Chaudhary, D.S., Vigneswaran, S., & Cho, J.J.D.W.E. (2013). Nanofiltration for water and wastewater treatment–a mini review. *Drinking Water Engineering and Science*, 6(1), 47–53. doi: 10.5194/dwes-6-47-2013, 2013

[8] Ukiwe, L.N., Ibeneme, S.I., Duru, C.E., Okolue, B.N., Onyedika, G.O., & Nweze, C.A. (2013). Chemical and electro-coagulation techniques in coagulation-flocculation in water and wastewater treatment – A review. *Journal of Advances in Chemistry*, 9(3), 1988–1999. doi: 10.24297/jac.v9i3.1006

[9] Särkkä, H., Bhatnagar, A., & Sillanpää, M. (2015). Recent developments of electro-oxidation in water treatment – A review. *Journal of Electroanalytical Chemistry*, 754, 46–56. doi: 10.1016/j.jelechem.2015.06.016

[10] Malaeb, L., & Ayoub, G.M. (2011). Reverse osmosis technology for water treatment: State of the art review. *Desalination*, 267(1), 1–8. doi: 10.1016/j.desal.2010.09.001

[11] Tiwari, G.N., Singh, H.N., & Tripathi, R. (2003). Present status of solar distillation. *Solar Energy*, 75(5), 367–373. doi: 10.1016/j.solener.2003.07.005

[12] Muftah, A.F., Alghoul, M.A., Fudholi, A., Abdul-Majeed, M.M., & Sopian, K. (2014). Factors affecting basin type solar still productivity: A detailed review. *Renewable and Sustainable Energy Reviews*, 32, 430–447. doi: 10.1016/j.rser.2013.12.052

[13] Mohiuddin, S.A., Kaviti, A.K., Rao, T.S., & Sikarwar, V.S. (2022). Historic review and recent progress in internal design modification in solar stills. *Environmental Science and Pollution Research*, 29(26), 38825–38878. doi: 10.1007/s11356-022-19527-x

[14] Ali, A., Issa, A., & Elshaer, A. (2024). A comprehensive review and recent trends in thermal insulation materials for energy conservation in buildings. *Sustainability*, 16(20), 8782. doi: 10.3390/su16208782

[15] Negi, A., Dhindsa, G.S., & Sehgal, S.S. (2022). Experimental investigation on single basin tilted wick solar still integrated with flat plate collector. *Materials Today: Proceedings*, 48, 1439–1446. doi: 10.1016/j.matpr.2021.09.210

[16] Younis, O., Hussein, A.K., Attia, M.E.H., Aljibori, H.S.S., Kolsi, L., Togun, H., Ali, B., Abderrahmane, A., Subkrajang, K., & Jirawattanapanit, A. (2022). Comprehensive review on solar stills – latest developments and overview. *Sustainability*, 14(16), 10136. doi: 10.3390/su141610136

[17] Sahu, R., & Tiwari, A.C. (2023). Experimental investigation for performance enhancement of single slope solar still using nanofluids under winter conditions. *Desalination and Water Treatment*, 304, 1–11. doi: 10.5004/dwt.2023.29799

[18] Manokar, A.M., Murugavel, K.K., & Esakkimuthu, G. (2014). Different parameters affecting the rate of evaporation and condensation on passive solar still – A review. *Renewable and Sustainable Energy Reviews*, 38, 309–322. doi: 10.1016/j.rser.2014.05.092

[19] Muthu Manokar, A., Prince Winston, D., Kabeel, A.E., Ravishankar, S., & Arunkumar, T. (2018). Different parameter and technique affecting the rate of evaporation on active solar still – a review. *Heat and Mass Transfer*, 54(3), 593–630. doi: 10.1007/s00231-017-2170-9

[20] Chaurasiya, P.K., Rajak, U., Singh, S.K., Verma, T.N., Sharma, V.K., Kumar, A., & Shende, V. (2022). A review of techniques for increasing the productivity of passive solar stills. *Sustainable Energy Technologies and Assessments*, 52, 102033. doi: 10.1016/j.seta.2022.102033

[21] Yusof, M.F., Zainol, M.R.R.M.A., Sandu, A.V., Riahi, A., Zakaria, N.A., Shaharuddin, S., Aziz, M.S.A., Mohamed Noor, N., Vizureanu, P., Zawawi, M.H., & Ikhsan, J. (2022). Clean Water Production Enhancement through the Integration of Small-Scale Solar Stills with Solar Dish Concentrators (SDCs) – A Review. *Sustainability*, 2022, 14, 5442. doi: 10.3390/su14095442

[22] Al-Kayiem, H.H., Mohamed, M.M., & Gilani, S.I. (2023). State of the art of hybrid solar stills for desalination. Arabian *Journal for Science and Engineering*, 48(5), 5709–5755. doi: 10.1007/s13369-022-07516-8

[23] Chauhan, V.K., & Al-Hamadani, A.A. (2024). Passive and Active Exploitation of Renewable Energy. In *Thermal Evaluation of Indoor Climate and Energy Storage in Buildings* (pp. 219–248). CRC Press. doi: 10.1201/9781003415695-8

[24] Al-Obaidi, M.A., Alsadaie, S., Alsarayreh, A., Sowgath, M.T., & Mujtaba, I.M. (2024). Integration of renewable energy systems in desalination. *Processes*, 12(4), 770. doi: 10.3390/pr12040770

[25] Kapse, V.M., Rupesh Ratnakar, G., & Mohammad Jubin, S. (2026). Optimizing the Various Operating Parameters of Active Solar Still for Water Purification. *Heat Transfer*, 55(3), 2035–2053. doi: 10.1002/htj.70180

[26] Sahoo, B.B., Sahoo, N., Mahanta, P., Borbora, L., Kalita, P., & Saha, U.K. (2008). Performance assessment of a solar still using blackened surface and thermocol insulation. *Renewable Energy*, 33(7), 1703–1708. doi: 10.1016/j.renene.2007.09.009

[27] Asadabadi, M.J.R., & Sheikholeslami, M. (2022). Impact of utilizing hollow copper circular fins and glass wool insulation on the performance enhancement of pyramid solar still unit: an experimental approach. *Solar Energy*, 241, 564–575. doi: 10.1016/j.solener.2022.06.029

[28] Arunkumar, T., Kabeel, A.E., Raj, K., Denkenberger, D., Sathyamurthy, R., Ragupathy, P., & Velraj, R. (2018). Productivity enhancement of solar still by using porous absorber with bubble-wrap insulation. *Journal of Cleaner Production*, 195, 1149–1161. doi: 10.1016/j.jclepro.2018.05.199

[29] Khalifa, A.J.N., & Hamood, A.M. (2009). Effect of insulation thickness on the productivity of basin type solar stills: an experimental verification under local climate. *Energy Conversion and Management*, 50(9), 2457–2461. doi: 10.1016/j.enconman.2009.06.007

[30] Lipiński, W., Abbasi-Shavazi, E., Chen, J., Coventry, J., Hangi, M., Iyer, S., Kumar, A., Li, L.F., Li, S., Pye, J., Torres, J.F., Wang, B., Wang, Y., & Wheeler, V.M. (2021). Progress in heat transfer research for high-temperature solar thermal applications. *Applied Thermal Engineering*, 184, 116137. doi: 10.1016/j.applthermaleng.2020.116137

[31] Jani, H.K., & Modi, K.V. (2018). A review on numerous means of enhancing heat transfer rate in solar-thermal based desalination devices. *Renewable and Sustainable Energy Reviews*, 93, 302–317. doi: 10.1016/j.rser.2018.05.023

[32] Muftah, A.F., Alghoul, M.A., Fudholi, A., Abdul-Majeed, M.M., & Sopian, K. (2014). Factors affecting basin type solar still productivity: A detailed review. *Renewable and Sustainable Energy Reviews*, 32, 430–447. doi: 10.1016/j.rser.2013.12.052

[33] Tuly, S. S., Rahman, M. S., Sarker, M. R. I., & Beg, R. A. (2021). Combined influence of fin, phase change material, wick, and external condenser on the thermal performance of a double slope

solar still. *Journal of Cleaner Production*, 287, 125458. doi: 10.1016/j.jclepro.2020.125458

[34] Rabhi, K., Nciri, R., Nasri, F., Ali, C., & Bacha, H.B. (2017). Experimental performance analysis of a modified single-basin single-slope solar still with pin fins absorber and condenser. *Desalination*, 416, 86–93. doi: 10.1016/j.desal.2017.04.023

[35] Mohaisen, H.S., Esfahani, J.A., & Ayani, M.B. (2021). Improvement in the performance and cost of passive solar stills using a finned-wall/built-in condenser: An experimental study. Renewable Energy, 168, 170–180. doi: 10.1016/j.renene.2020.12.056

[36] Abdulateef, A.M., Mat, S., Abdulateef, J., Sopian, K., & Al-Abidi, A.A. (2018). Geometric and design parameters of fins employed for enhancing thermal energy storage systems: a review. *Renewable and Sustainable Energy Reviews*, 82, 1620–1635. doi: 10.1016/j.rser.2017.07.009

[37] El-Sebaii, A.A., & El-Naggar, M. (2017). Year round performance and cost analysis of a finned single basin solar still. *Applied Thermal Engineering*, 110, 787–794. doi: 10.1016/j.applthermaleng.2016.08.215

[38] Panchal, H., Mevada, D., Sadasivuni, K.K., Essa, F.A., Shanmugan, S., & Khalid, M. (2020). Experimental and water quality analysis of solar stills with vertical and inclined fins. *Groundwater for Sustainable Development*, 11, 100410. doi: 10.1016/j.gsd.2020.100410

[39] Rajaseenivasan, T., & Srithar, K. (2016). Performance investigation on solar still with circular and square fins in basin with CO_2 mitigation and economic analysis. *Desalination*, 380, 66–74. doi: 10.1016/j.desal.2015.11.025

[40] Panchal, H., & Mohan, I. (2017). Various methods applied to solar still for enhancement of distillate output. *Desalination*, 415, 76–89. doi: 10.1016/j.desal.2017.04.015

[41] Chauhan, V.K., Shukla, S.K., Tirkey, J.V., & Rathore, P.K.S. (2021). A comprehensive review of direct solar desalination techniques and its advancements. *Journal of Cleaner Production*, 284, 124719. doi: 10.1016/j.jclepro.2020.124719

[42] Modi, K., & Jani, H. (2021). Experimental and theoretical assessment of dual-slope single-basin solar still with the circular cross-sectional hollow-fins. *Cleaner Engineering and Technology*, 4, 100231. doi: 10.1016/j.clet.2021.100231

[43] Islam, A., Sharma, A., & Singh, P.K. (2021). Performance study on customized solar still by optimum fins for production of distilled water. *Materials Today: Proceedings*, 45, 3517–3520. doi: 10.1016/j.matpr.2020.12.960

[44] Panchal, H., & Sathyamurthy, R. (2020). Experimental analysis of single-basin solar still with porous fins. *International Journal of Ambient Energy*, 41(5), 563–569. doi: 10.1080/01430750.2017.1360206

[45] Sathish Kumar, T.R., Balaji, G., Deepak Kumar, A., Sivanath, K., & Thirumalai, S. (2021). Performance comparison of solar stills with different fin materials coupled with PCM energy storage. *Journal of Physics: Conference Series*, 2054, 012022, International Conference on Advances in Thermal Engineering and Applications, 19–20 March, Tamil Nadu, India. doi: 10.1088/1742-6596/2054/1/012022

[46] Sathish Kumar, T.R., & Jegadheeswaran, S. (2022). Experimental investigation on finned solar still with enhanced thermal energy storage. *Journal of Thermal Science and Engineering Applications*, 14(9), 091001. doi: 10.1115/1.4053228

[47] Abdullah, A.S., Omara, Z.M., Essa, F.A., Alqsair, U.F., Aljaghtham, M., Mansir, I.B., Shanmugan, S., & Alawee, W. H. (2022). Enhancing trays solar still performance using wick finned absorber, nano-enhanced PCM. *Alexandria Engineering Journal*, 61(12), 12417–12430. doi: 10.1016/j.aej.2022.06.033

[48] Tyagi, V.V., Kaushik, S.C., & Tyagi, S.K. (2012). Advancement in solar photovoltaic/thermal (PV/T) hybrid collector technology. *Renewable and Sustainable Energy Reviews*, 16(3), 1383–1398. doi: 10.1016/j.rser.2011.12.013

[49] Raju, V.R., & Narayana, R.L. (2018). Effect of flat plate collectors in series on performance of active solar still for Indian coastal climatic condition. *Journal of King Saud University – Engineering Sciences*, 30(1), 78–85. doi: 10.1016/j.jksues.2015.12.008

[50] Badran, O.O., & Al-Tahaineh, H.A. (2005). The effect of coupling a flat-plate collector on the solar still productivity. *Desalination*, 183(1–3), 137–142. doi: 10.1016/j.desal.2005.02.046

[51] Sabiha, M.A., Saidur, R., Mekhilef, S., & Mahian, O. (2015). Progress and latest developments of evacuated tube solar collectors. *Renewable and Sustainable Energy Reviews*, 51, 1038–1054. doi: 10.1016/j.rser.2015.07.016

[52] Zubriski, S.E., & Dick, K.J. (2012). Measurement of the efficiency of evacuated tube solar collectors under various operating conditions. *Journal of Green Building*, 7(3), 114–130. doi: 10.3992/jgb.7.3.114

[53] Budihardjo, I., Morrison, G.L., & Behnia, M. (2003). Development of TRNSYS models for predicting the performance of water-in-glass evacuated tube solar water heaters in Australia. In *Proceedings of ANSZES Annual Conference*, 256, Melbourne, Australia.

[54] Pei, G., Li, G., Zhou, X., Ji, J., & Su, Y. (2012). Comparative experimental analysis of the thermal performance of evacuated tube solar water heater systems with and without a mini-compound parabolic concentrating (CPC) reflector (C<1). *Energies*, 5(4), 911–924. doi: 10.3390/en5040911

[55] Mangal, D., Lamba, D.K., Gupta, T., & Jhamb, K. (2010). Acknowledgement of evacuated tube solar water heater over flat plate solar water heater. *International Journal of Engineering*, 4(4), 279–284.

[56] Ayompe, L.M., Duffy, A., Mc Keever, M., Conlon, M., & McCormack, S.J. (2011). Comparative field performance study of flat plate and heat pipe evacuated tube collectors (ETCs) for domestic water heating systems in a temperate climate. *Energy*, 36(5), 3370–3378. doi: 10.1016/j.energy.2011.03.034

[57] Panchal, H., Kumar Sadasivuni, K., Suresh, M., Yadav, S., & Brahmbhatt, S. (2020). Performance analysis of evacuated tubes coupled solar still with double basin solar still and solid fins. *International Journal of Ambient Energy*, 41(9), 1031–1037. doi: 10.1080/01430750.2018.1501745

[58] Mevada, D., Panchal, H., & Sadasivuni, K.K. (2021). Investigation on evacuated tubes coupled solar still with condenser and fins: Experimental, exergo-economic and exergo-environment analysis. *Case Studies in Thermal Engineering*, 27, 101217. doi: 10.1016/j.csite.2021.101217

[59] Namshad, T., Ayush, K.R., Salih, K.C., James, A., Ahammed, S., Vayalilakath, H., & Suneesh, P.U. (2013). Performance Analysis of Flat and Rippled Wick-Inverted V-Type Solar Still Integrated with Drip System in Kerala Climatic Conditions. *International Scholarly Research Notices*, 2013(1), 126234. doi: 10.1155/2013/126234

[60] Zhang, L., Li, X., Zhong, Y., Leroy, A., Xu, Z., Zhao, L., & Wang, E.N. (2022). Highly efficient and salt rejecting solar evaporation via a wick-free confined water layer. *Nature Communications*, 13(1), 849. doi: 10.1038/s41467-022-28457-8

[61] Jobrane, M., Kopmeier, A., Kahn, A., Cauchie, H.M., Kharroubi, A., & Penny, C. (2021). Internal and external improvements of wick type solar stills in different configurations for drinking water production – A review. *Groundwater for Sustainable Development*, 12, 100519. doi: 10.1016/j.gsd.2020.100519

[62] Manikandan, V., Shanmugasundaram, K., Shanmugan, S., Janarthanan, B., & Chandrasekaran, J. (2013). Wick type solar stills: a review. *Renewable and Sustainable Energy Reviews*, 20, 322–335. doi: 10.1016/j.rser.2012.11.046

[63] Fayaz, Z., Dhindsa, G.S., & Sokhal, G.S. (2022). Experimental study of solar still having variable slope tilted wick in the basin to enhance its daily yield. *Materials Today: Proceedings*, 48, 1421–1426. doi: 10.1016/j.matpr.2021.09.195

[64] Negi, A., Verma, R.P., Saxena, A., Ranakoti, L., Bhandari, P., Singh, T., & Tiwari, G.N. (2023). Design and performance of black painted Khes wick modified solar still: An experimental and 5E analysis. International Journal of Thermofluids, 20, 100491. doi: 10.1016/j.ijft.2023.100491

[65] Lee, G.R., Cho, S.H., Lim, B.J., Choi, S.M., & Park, C.D. (2021). Experimental study on a novel multi-effect diffusion solar distiller with wick-free plate. *Solar Energy*, 230, 250–259. doi: 10.1016/j.solener.2021.10.032

[66] Essa, F.A., Alawee, W.H., Mohammed, S.A., Dhahad, H.A., Abdullah, A.S., & Omara, Z.M. (2021). Experimental investigation of convex tubular solar still performance using wick and nanocomposites. *Case Studies in Thermal Engineering*, 27, 101368. doi: 10.1016/j.csite.2021.101368

[67] Tanaka, H. (2017). Parametric investigation of a vertical multiple-effect diffusion solar still coupled with a tilted wick still. *Desalination*, 408, 119–126. doi: 10.1016/j.desal.2017.01.019

[68] Agrawal, R., & Singh, K.D.P. (2021). Performance evaluation of double slope solar still augmented with binary eutectic phase change material and steel wool fibre. *Sustainable Energy Technologies and Assessments*, 48, 101597. doi: 10.1016/j.seta.2021.101597

[69] Ramzy, K., Abdelaziz, E.A., Alswat, M., Kabeel, A.E., Al-Nagdy, A.A., & Abdelgaleel, M. (2025). Evaluation of solar distiller performance using steel wool pads, internal reflectors, and woven wire mesh: economic, environmental, and sustainability analysis. *Journal of Thermal Analysis and Calorimetry*, 150(1), 723–742. doi: 10.1007/s10973-024-13742-z

[70] Karthikeyan, J., Selvaraj, P., & Nagaraj, G. (2020). Day and night yield performance analysis of solar still for saline water using energetic materials with thermocol insulation. *Materials Today: Proceedings*, 33, 4848–4851. doi: 10.1016/j.matpr.2020.08.395

[71] Omara, Z.M., Hamed, M.H., & Kabeel, A.E. (2011). Performance of finned and corrugated absorbers solar stills under Egyptian conditions. *Desalination*, 277(1-3), 281–287. doi: 10.1016/j.desal.2011.04.042

Co-published by
Institute of Fluid-Flow Machinery
Polish Academy of Sciences
Committee on Thermodynamics and Combustion
Polish Academy of Sciences

Copyright©2026 by the Authors under licence CC BY-NC-ND 4.0

http://www.imp.gda.pl/archives-of-thermodynamics/

Enhancement of buoyancy-driven flow in an annular system by using nano-encapsulated phase change material fluid

Asmaa Nadia Bouguesri[a*], Houssem Laidoudi[b], Abderrahmane Aissa[c]

[a]Faculty of Mechanical Engineering, University of Science and Technology of Oran – Mohamed Boudiaf (USTO-MB), BP 1505, El-Menaouer, Bir El Djir 31000, Oran, Algeria
[b]Department of Mechanical Engineering, Faculty of Sciences and Technology, University of Mohamed El Bachir El Ebrahimi, El-Anasser, Bourdj Bou Arreridj 34030, Algeria
[c]Laboratoire de Physique Quantique de la Matiére et Modélisation Mathématique (LPQ3M), University of Mascara, Mascara 29000, Algeria
[*]Corresponding author email: asmaanadia.bouguesri@univ-usto.dz

Received: 02.08.2025; revised: 22.04.2026; accepted: 10.08.2026

Abstract

This study examines natural convection heat transfer in a two-dimensional annular cavity, with the inner boundary stipulated by the orthogonal intersection of two ellipses. The geometric configuration is defined by the ratio of the radii of the heated inner surface to the cooled outer cylinder such as $RR = a/r = 0.4$. The enclosure is filled with a porous medium and exposed to a uniform magnetic field, while the working fluid comprises water combined with nano-encapsulated phase change material (NEPCM) particles. The governing equations that include buoyancy effects, magnetic forces, porous medium resistance and phase-change behaviour are resolved with the Galerkin weighted residual finite element method. The flow is presumed to be steady, laminar and incompressible. A comprehensive parametric study is conducted to investigate the impact of governing physical and geometrical factors, encompassing the Rayleigh number (10^3–10^6), Hartmann number (0–80), Darcy number (10^{-5}–10^{-2}), nano-encapsulated phase change material volume fraction (0–5%), and cavity inclination angle (0°–80°). The outcomes demonstrate the progression of the flow structure, thermal field, heat transfer rate and distribution of specific heat capacity ratio within the enclosure. The elevated Ra and Da amplify convective circulation, whereas the increased Ha inhibits fluid mobility. The incorporation of nano-encapsulated phase change material markedly enhances thermal storage and mitigates temperature differences. The findings underscore the promise of NEPCM-based fluids, in conjunction with tailored cavity geometries, particularly enhancing the cross-section angles of the heated obstacle for enhanced heat management and energy-efficient mechanical system applications.

Keywords: Annular space; Natural convection; Nano-encapsulated phase change material; Heat transfer rate; Galerkin weighted residual finite element method

Vol. 47(2026), No. 3, 157–172; doi: 10.24425/ather.2026.7515

Cite this manuscript as: Bouguesri, A.N., Laidoudi, H., & Aissa, A. (2026). Enhancement of buoyancy-driven flow in an annular system by using nano-encapsulated phase change material fluid. *Archives of Thermodynamics*, 47(3), 157–172.

1. Introduction

Natural convection heat transfer is a widespread research domain owing to its fundamental relevance in manufacturing processes, like in marine engineering [1], heat exchangers [2], solar collectors [3], electronic cooling devices [4] and refrigeration systems [5], and so on. Free convection is a fundamental heat transfer mechanism, which arises from thermal gradients that create changes in fluid density, leading to the ascent of the warmer, lighter fluid and the descent of the cooler, denser fluid. The annular space with diverse cross-sectional morphologies of an interior cylinder, including circular, elliptical, and square

Nomenclature

a – major elliptical radius, m
b – minor elliptical radius, m
B_0 – magnetic flux density, T
C_p – specific heat capacity, J/(kg K)
Cr – ratio of heat capacity
Da – Darcy number
f – non-dimensional form of phase change behaviour
g – gravitational acceleration, m/s^2
h_{sf} – latent heat of the core, kJ/kg
H – aspect ratio, $H = b/a$
Ha – Hartmann number
k – thermal conductivity, W/(m K)
K_0 – permeability, m^2
L – length of the annular space, $L = r - a$, m
n, s – normal direction
N_c – suspension conductivity enhancement factor
Nu_l – local Nusselt number
$\overline{\mathrm{Nu}}$ – average Nusselt number
N_v – suspension dynamic viscosity enhancement factor
p – pressure, Pa
P – dimensionless pressure
Pr – Prandtl number
r – radius of the outer cylinder, m
Ra – Rayleigh number
RR – radii ratio, $RR = a/r$
Ste – Stefan number
T_c, T_h – cold and hot temperatures, K
T_{fu} – fusion temperature, K
T_{Mr} – temperature melting interval, K
u, v – velocity along x, and y directions, m/s
U, V – dimensionless velocity components
x, y – Cartesian coordinates, m
X, Y – dimensionless coordinates

Greek symbols

α – thermal diffusivity, m^2/s
β – thermal expansion coefficient, 1/K
ε – porosity of the porous medium
θ – dimensionless temperature
λ – dimensionless heat capacity
ι – mass ratio of the shell and core of NEPCM
μ – dynamic viscosity, kg/(s m)
ρ – density, kg/m^3
ϕ – nanoparticle volume fraction, %

Subscripts and Superscripts

b – mixture
co – core of the NEPCM
f – host fluid
p – NEPCM particle
sh – NEPCM shell

Abbreviations and Acronyms

ANN – artificial neural network
GFEM – finite element method
MHD – magnetohydrodynamic
NEPCM – nano-encapsulated phase change material
PCM – phase change material

shapes, was the focus of scientific scrutiny owing to its potential of enhancing heat transfer efficiency. The research initiatives aim to contribute to the integration of these concepts into industrial frameworks.

A considerable number of numerical and experimental studies have significantly expanded our understanding of natural convection heat transfer in circular enclosures. For example, Kuehn and colleagues [6] conducted an experimental investigation to examine the effects of eccentricity and Rayleigh number on the thermal performance of horizontal cylindrical annuli. Similarly, Wang and co-workers [7] applied a computational method based on the central difference approach and validated their results using the Mach-Zehnder interferometer in an annular configuration. In a different series of studies, Laidoudi and colleagues [8–11] performed numerous numerical analyses in cold circular enclosures containing one or more hot concentric internal cylinders arranged in various configurations. Helmaoui et al. [12] investigated the effect of a pair of heated semi-circular tubes, while Khudhair et al. [13] demonstrated that vibration enhances heat transfer in annular spaces at low Rayleigh numbers, achieving improvements of up to 3.8 times when the inner cylinder is eccentrically positioned at the bottom. At higher Rayleigh numbers, natural convection dominates and vibration has minimal effect. Furthermore, Majdi et al. [14] examined natural convection in a horizontal concentric ring and concluded that the radius ratio and Rayleigh number strongly influence heat transfer, whereas the inclination angle has little impact.

Additional insight was provided by Horimek et al. [15], who performed computational studies of natural convection between two concentric ellipses under fifty configurations with two heating conditions. Their research highlighted the influence of Rayleigh number, aspect ratio and orientation on flow dynamics, temperature distributions and average Nusselt number, demonstrating that geometry substantially affects heat transfer and thermal uniformity. Moreover, Laidoudi et al. [16] and Mohammed [17] showed that varying the inclination angle of non-circular inner tubes, such as elliptical or triangular shapes, can also influence heat transfer efficiency.

In recent decades, numerous strategies have been proposed to improve heat transfer performance, particularly for natural convection systems. Effective approaches include the use of cavities filled with porous media, which alter fluid flow and thermal characteristics through their permeability and porosity, as well as the application of magnetic fields to control the flow. For instance, Abdullah et al. [18] analysed natural convection within a vertical porous annulus, while Azzouz et al. [19] studied the effect of magnetic forces on natural convection in a circular enclosure containing four internal cylinders, emphasising their relevance to thermal performance. Wang et al. [20] demonstrated that, in a radiative magnetohydrodynamic natural convection system within a horizontal annulus, the magnetic field suppresses fluid motion and heat transfer, whereas radiation and fluid optical properties modify flow patterns and reduce angular variations in heat transfer.

Nanofluids, with their superior thermal conductivity and favourable rheological properties, have emerged as promising fluids for enhancing heat transfer, improving both energy transport and flow characteristics compared with conventional fluids [21]. Abdullah et al. [22] conducted computational modelling of natural convection in an inclined annular enclosure filled with an aluminium oxide-water nanofluid using the stream function-vorticity method, showing that heat transfer is affected by the Rayleigh number, inclination angle and nanoparticle volume fraction. Joby et al. [23] reviewed the effects of internal object geometry and enclosure tilt on natural convection in rectangular enclosures, emphasising the roles of Rayleigh number, nanoparticles, and porous media while noting that most previous studies were numerical, laminar and simplified, limiting their practical applicability. Other relevant studies include Mahdy et al. [24], who investigated magneto-natural convection of a micropolar hybrid nanofluid over a vertical plate in a porous medium; Payam et al. [25], who examined the influence of heat source eccentricity on entropy generation and natural convection of a copper-water nanofluid within a porous annulus; and Allouche et al. [26], who used silver-magnesium oxide nanofluid in a ring-shaped cavity considering radiation and heat absorption/generation, employing the finite volume method with the Gauss-Seidel approach. Bouzerzour et al. [27] studied a confocal elliptical annulus filled with a silver-water nanofluid, while Ali et al. [28] investigated an egg-shaped porous copper nanofluid enclosure with an internal cylindrical object using the finite element method based on the Galerkin approach. Tayebi et al. [29] examined magnetohydrodynamic natural convection in a circular annulus filled with a carbon nanotube-based nanofluid containing a heat-generating solid cylinder.

Phase change materials are acknowledged for their ability to reduce energy consumption and improve thermal storage capabilities; however, their limited thermal conductivity constrains overall effectiveness. Nano-encapsulated phase change materials address this limitation by enhancing thermo-physical properties, expediting thermal responses and facilitating integration with cooling systems, photovoltaic modules and energy storage devices, as demonstrated by Mebarek-Oudina et al. [30]. Alomari et al. [31] demonstrated that the Rayleigh number, NEPCM concentration and the orientation of the magnetic field significantly affect heat transfer in cavities composed of oscillating fins. Conversely, the paper [32] indicated that magnetic fields may decrease heat transfer by as much as 25.9%, even in the presence of enhancements from nanoparticles and elevated Rayleigh numbers. Rashid et al. [33] conducted a review on heat transfer across different cavity geometries utilising phase change materials and non-equilibrium phase change materials. Additionally, Abderrahmane et al. [34] showed that an increase in Rayleigh and Darcy numbers within a porous, magnetised inverse T-shaped enclosure leads to a notable enhancement in the average Nusselt number. Mehryan et al. [35] observed that within eccentric annuli, a particle concentration of 5% optimises heat transfer, while variations in eccentricity or cylinder elevation lead to a decrease in efficiency. Ghalambaz et al. [36] investigated NEPCM suspensions within eccentric annular geometries, demonstrating improved thermal performance through mechanisms of absorption, storage and release, with optimal fusion temperatures varying according to the Rayleigh number. Furthermore, the paper [37] illustrated that NEPCM suspensions incorporating eccentric copper foam within shell-and-tube configurations enhance thermal storage efficiency.

The latest advances involve the studies of Hussain et al. [38], who investigated the phenomenon of magneto-bioconvection in non-Newtonian electro-rheological phase change materials within H-type cavities populated by oxytactic microorganisms. Their research elucidates the influence of various parameters, including cavity aspect ratio, Darcy and Hartmann numbers, as well as Rayleigh and bioconvection Rayleigh numbers, on the dynamics of flow and thermal characteristics. Their research demonstrated that an elevated cavity aspect ratio improves the performance, whereas higher Hartmann numbers diminish nanofluid velocity and the distribution of microorganisms, with artificial neural networks (ANNs) effectively forecasting critical parameters. El Shehabey et al. [39] utilised incompressible smoothed particle hydrodynamics to investigate thermosolutal convection of NEPCM suspensions within a Bezier annulus. Their findings indicate that the Frank-Kamenetskii number, Soret-Dufour effects, Rayleigh number and nanoparticle fraction have a substantial impact on the temperature, velocity and performance of NEPCM. Additionally, artificial neural networks (ANNs) demonstrated efficacy in predicting average Nusselt and Sherwood numbers. The findings from these studies indicate that NEPCMs, when integrated with sophisticated cavity geometries, magnetic fields, bioconvection effects and computational intelligence tools, present significant opportunities for enhancing heat transfer and thermal energy storage in intricate systems.

Considering the existing literature, ring-shaped cavities featuring diverse inner cylinder shapes (circular, triangular, square) have been thoroughly examined regarding their implications for natural convection heat transfer, particularly in relation to contemporary manufacturing systems. Despite the existence of various studies on this subject, there is a scarcity of comprehensive analysis regarding the mixtures of water-based nano-encapsulated phase change materials within an annular space that includes an internally shaped cylinder. This study seeks to address the existing gap by analysing enclosures featuring an elliptical inner cylinder positioned at various inclination angles with the intention of providing more guidance to industrial manufacturers in optimising configurations that improve heat transfer rates and minimise potential discrepancies in thermal performance. The present research examines the occurrence of laminar natural convection heat transfer taking place within an eccentric circular cavity, which is cooled at its outer boundary and contains a heated inner cylinder created by the orthogonal intersection of two similar elliptical cylinders. The annular space includes a porous medium and is subjected to a magnetic force. The host fluid is comprised of water and nano-encapsulated phase change material. This research investigates the influence of various parameters including the Rayleigh number (10^3–10^6), Hartmann number (0–80), Darcy number (10^{-5}–10^{-2}), nanoparticle volume fraction (0–5%), and inclination angle (0–80°). The analysis fo-

cuses on the average Nusselt number, flow structures, temperature distribution and heat capacity ratio.

2. Problem formulation

As shown in Fig. 1, the problem under study is a 2d ring-shaped hollow comprising two elliptical cylinders of identical size crossing perpendicularly to form a concentric inner cylinder. The outer space is a circular enclosure sustained at a cold temperature T_c, designated by its radius r, whereas the interior cylinder is regarded as warmer at a temperature T_h ($T_h > T_c$).

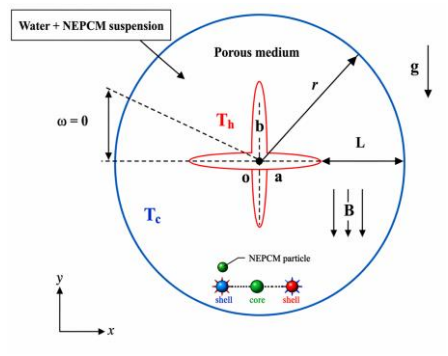


Fig. 1. Representation of the physical problem.

Table 1. Thermo-physical properties of the working fluid [35,40].

Material	P (kg/m³)	β (×10⁻⁵ K⁻¹)	C_p (kJ/(kg K))	K (W/(m K))
Water base: fluid	997.1	21	4.179	0.613
Nonadecane: core	721	–	2.037	–
Polyurethane: shell	786	17.28	1.3177	–

The elliptical section is geometrically represented by the aspect ratio, defined as the ratio of the semi-minor axis b to the semi-major axis a ($H = b/a = 0.1$). The radial gap between the exterior and interior cylinders is delineated by ($L = r - a$). The radii ratio, known as the ratio of the semi-major axis a to the radius r of the cold space, is defined as $RR = a/r = 0.4$. The annular space is occupied by a porous medium and is affected by a magnetic force. The elliptical cylinder is slanted at an angle ω that fluctuates between 0° to 80°. The injected fluid is a combination of pure water and nano-encapsulated PCM, regarded as an incompressible and Newtonian fluid. An NEPCM is formed of a PCM core, which is nonadecane and a polyurethane encapsulating shell developed from polymeric ingredients to guarantee thermal stability and prevent leakage.

The Boussinesq approximation is employed to deal with the thermal buoyancy force brought about by vertical temperature gradients. The analysis aims to assess the influence of several fundamental governing and geometrical parameters on the flow behaviour, thermal patterns, and heat capacity ratio. Namely, the inclination angle, Darcy number, Rayleigh number, Hartmann number, as well as the volume fraction ratio and the Nusselt number. Thermo-physical features of the working fluid are presented in Table 1.

3. The governing equations

This inquiry pertains to laminar and stationary flow. The fundamental equations of continuity, momentum, and energy are resolved in two dimensions within the framework of the Cartesian coordinate system. Consequently, the governing equations can be outlined as [34,35,37,38]:

$$\frac{\partial u}{\partial x} + \frac{\partial v}{\partial y} = 0, \tag{1}$$

$$\frac{\rho_b}{\varepsilon^2}\left(u\frac{\partial u}{\partial x} + v\frac{\partial u}{\partial y}\right) = -\frac{\partial p}{\partial x} + \frac{\mu_b}{\varepsilon}\nabla^2 \mathrm{u} - \frac{\mu_b}{K_0}u, \tag{2a}$$

$$\frac{\rho_b}{\varepsilon^2}\left(u\frac{\partial v}{\partial x} + v\frac{\partial v}{\partial y}\right) = -\frac{\partial p}{\partial y} + \frac{\mu_b}{\varepsilon}\nabla^2 \mathrm{v} + \beta_b \rho_b g(T - T_c) + -\frac{\mu_b}{K_0} - \frac{\sigma B_0^2}{\rho}v, \tag{2b}$$

$$\left(\rho C_p\right)_b\left(u\frac{\partial T}{\partial x} + v\frac{\partial T}{\partial y}\right) = k_b \nabla^2 T, \tag{3}$$

where u and v denote the velocity components in both x- and y-axes, respectively. P indicates the pressure, whereas T stands for the temperature.

Boundary conditions

The boundary conditions for heat transfer and fluid flow are defined in accordance with the schematic model laid out in Fig. 1:

at the cold boundary (cylinder):

$$u = v = 0 \text{ and } T = T_c, \tag{4a}$$

at the hot boundary:

$$u = v = 0 \text{ and } T = T_h. \tag{4b}$$

The suspension's bulk features:

The expression that follows provides the global density of the NEPCM mixture:

$$\rho_b = (1 - \phi)\rho_f + \phi\rho_p. \tag{5}$$

However, the density of the nanoparticles is:

$$\rho_b = \frac{(1+\iota)\rho_{co}\rho_{sh}}{\iota\rho_{co} + \rho_{sh}}. \tag{6}$$

The notations f, p, co, sh characterise the base fluid, added nanoparticles, the core and the shell, while ρ_f, ρ_p, ρ_{co}, ρ_{sh} and ι are the host fluid density, the additional nanoparticle density, the core and shell densities, and the mass ratio of the shell and core constituents, given by ι~0.447, respectively. In addition, ϕ denotes the concentration of the NEPCM particles [35,40].

Also, the density of the PCM core is found by averaging the densities of its liquid and solid forms. Upon incorporating the NEPCM into the water-based suspension, and based on the energy equation, the specific heat capacity of the suspension is ascertained as being:

$$C_{p,b} = \frac{(1-\phi)(\rho C_p)_f + \phi(\rho C_p)_p}{\rho_p}. \quad (7)$$

At the lack of phase change, the heat capacity of an encapsulated nanoparticle is expressed as:

$$C_{p,p} = \frac{(C_{p,co} + \iota C_{p,sh})\rho_{co}\rho_{sh}}{(\rho_{sh} + \iota\rho_{co})\rho_p}. \quad (8)$$

The internal material, often designated as the core, can be represented by calculating the average of the specific heat capacities of its solid and liquid states. This methodology elucidates the role of latent heat during phase transitions in influencing the effective heat capacity of the NEPCM, without considering the state of the nanoparticle core, whether it be solid or liquid. The latent heat associated with phase transitions can be integrated into the specific heat of the core by employing various profiles, including rectangular, triangular, or sinusoidal functions – Eqs. (9)–(11). The enhanced formulation for thermal capacity is presented as follows [40]:

$$C_{p,p} = vC_{p,co} + \frac{h_{sf}}{T_{Mr}}, \quad (9)$$

$$c_{p,p} = c_{p,co} + \left\{\frac{\pi}{2}\left(\frac{h_{sf}}{T_{Mr}} - C_{p,co}\right)\sin\left(\pi\frac{T - T_{fu} + (T_{Mr}/2)}{T_{Mr}}\right)\right\}, \quad (10)$$

$$C_{p,p} = C_{p,co} + 2\left(\frac{h_{sf}}{T_{Mr}^2} - \frac{C_{p,co}}{T_{Mr}}\right)(T - T_{fu}). \quad (11)$$

Most of researchers use a simplified method to deal with the problems, such as the linear interpolation. In this work, the sinusoidal function – Eq. (10) – is employed to maintain numerical convergence. T_{Mr} in this instance signifies the temperature band which involves the phase alteration. To prevent the energy equilibrium from becoming erratic, this discrepancy is intended. The aggregate specific heat capacity of the nanoparticle's core is determined by the function T_{Mr}, which entails both sensible and latent heat contributions. In this case, the phase transition occurs over a finite temperature range centred at the fusion temperature T_{fu} with a melting-range width of T_{Mr}.

$$uc_{p,p} = c_{p,co} + \left\{\frac{\pi}{2}\left(\frac{h_{sf}}{T_{Mr}} - c_{p,co}\right)\sin\left(\pi\frac{T - T_{fu} + (T_{Mr}/2)}{T_{Mr}}\right)\right\}\begin{Bmatrix} 0,\ T < T_{fu} - \frac{T_{Mr}}{2} \\ 1, T_{fu} - \frac{T_{Mr}}{2} < T < T_{fu} + \frac{T_{Mr}}{2} \\ 0,\ T > T_{fu} + \frac{T_{Mr}}{2} \end{Bmatrix}. \quad (12)$$

The volumetric thermal expansion of the mixture is estimated by the formula:

$$\beta_b = (1-\phi)\beta_f + \phi\beta_p. \quad (13)$$

Furthermore, the dynamic viscosity and thermal conductivity of a solution containing nano-encapsulated particles have been widely investigated by different scientists. As a result, these quantities are determined via linear expressions [40]:

$$\frac{k_b}{k_f} = 1 + \phi N_c, \quad (14)$$

$$\frac{\mu_b}{\mu_f} = 1 + \phi N_v. \quad (15)$$

The preceding formulas indicate that N_c and N_v stand for thermal conductivity and dynamic viscosity enhancement factors, respectively. In a mixture with nanoparticles, higher values of these parameters enhance the effective thermal conductivity and dynamic viscosity. In several types of nanofluids and hybrid nanofluids, Ghalambaz et al. [40] implemented set values for N_c and N_v that were compatible for $\phi < 5\%$, which is a specific nanoparticle volume fractional percentage [40]; the values taken in this study are $N_c = N_v = 3$ [40–43].

The governing equations in non-dimensional form:

The following variables are introduced to alter the governing equations and the boundary conditions into a non-dimensional form:

$$X = \frac{\bar{x}}{L},\ Y = \frac{\bar{y}}{L},\ RR = \frac{a}{r},\ P = \frac{\bar{p}L^2}{\rho_f\alpha_f^2},\ \theta = \frac{T - T_c}{\Delta T},$$

$$L = r - a,\ \alpha_f = \frac{k_f}{(\rho c_p)_f},\ U = \frac{\bar{u}L}{\alpha_f},\ V = \frac{\bar{v}L}{\alpha_f}. \quad (16)$$

where $\Delta T = T_h - T_c$.

The dimensionless key parameters that govern the natural convection heat transfer in a porous medium with a magnetic field are represented by the Rayleigh number 'Ra', Prandtl number 'Pr', Darcy number 'Da', and Hartmann number 'Ha' are also introduced:

$$\mathrm{Ha} = B_0 L\sqrt{\frac{\sigma_f}{\mu_f}}, \quad (17)$$

$$\mathrm{Ra} = \frac{g\rho_f\beta_f\Delta T L^3}{\alpha_f\mu_f}, \quad (18)$$

$$\mathrm{Pr} = \frac{\mu_f}{\alpha_f\rho_f}, \quad (19)$$

$$\mathrm{Da} = \frac{K_0}{L^2}. \quad (20)$$

The set of governing equations (1)–(3) can then be converted into the following set of non-dimensional equations:

$$\frac{\partial U}{\partial X} + \frac{\partial V}{\partial Y} = 0, \quad (21)$$

$$\varepsilon^{-2}\left(\frac{\rho_b}{\rho_f}\right)\left(U\frac{\partial U}{\partial X} + V\frac{\partial U}{\partial Y}\right) = -\frac{\partial P}{\partial X} + \mathrm{Pr}\,\varepsilon^{-1}\left(\frac{\mu_b}{\mu_f}\right)\nabla^2 U - \frac{\mathrm{Pr}}{\mathrm{Da}}\left(\frac{\mu_b}{\mu_f}\right)U, \quad (22a)$$

$$\varepsilon^{-2}\left(\frac{\rho_b}{\rho_f}\right)\left(U\frac{\partial V}{\partial X} + V\frac{\partial V}{\partial Y}\right) = -\frac{\partial P}{\partial Y} + \mathrm{Pr}\,\varepsilon^{-1}\left(\frac{\mu_b}{\mu_f}\right)\nabla^2 V + \left(\frac{\beta_b}{\beta_f}\right)\mathrm{Ra}\,\mathrm{Pr}\,\theta - \mathrm{Ha}^2\,V - \frac{\mathrm{Pr}}{\mathrm{Da}}\left(\frac{\mu_b}{\mu_f}\right)V, \quad (22b)$$

$$\frac{(\rho C_p)_b}{(\rho C_p)_f}\left(U\frac{\partial\theta}{\partial X}+V\frac{\partial\theta}{\partial Y}\right)=\left(\frac{k_b}{k_f}\right)\nabla^2\theta, \tag{23}$$

with

$$\left(\frac{\rho_b}{\rho_f}\right)=(1-\phi)+\phi\left(\frac{\rho_p}{\rho_f}\right), \tag{24}$$

$$\left(\frac{\beta_b}{\beta_f}\right)=(1-\phi)+\phi\left(\frac{\beta_p}{\beta_f}\right). \tag{25}$$

It is postulated that NEPCM particles expand in a manner that is identical to that of the host fluid, water, due to the absence of a slip mechanism between the base fluid and NEPCMs. Thus, the thermal expansion ratio is approximately $\beta_p/\beta_f \sim 1$.

The relative heat capacity of the basic fluid and the suspension Cr can be found via [40]:

$$\mathrm{Cr}=\frac{(\rho C_p)_b}{(\rho C_p)_f}=(1-\phi)+\phi\lambda+\frac{\phi}{\delta\mathrm{Ste}}f. \tag{26}$$

The sensible heat capacity ratio λ, Stefan number Ste, the dimensionless melting interval Θ, and fusion parameter f are established as [35,40]:

$$\lambda=\frac{(C_{p,co}+\iota C_{p,sh})\rho_{co}\rho_{sh}}{(\rho C_p)_f(\iota\rho_{co}+\rho_{sh})}, \tag{27}$$

$$\mathrm{Ste}=\frac{(\rho C_p)_f(T_h-T_c)(\iota\rho_{co}+\rho_{sh})}{\alpha_f(h_{sf}\,\rho_{co}\,\rho_{sh})}, \tag{28},$$

$$\Theta=\frac{T_{Mr}}{\Delta T}=\frac{T_{Mr}}{T_h-T_c}, \tag{29}$$

$$f=\frac{\pi}{2}\sin\left(\frac{\pi}{\theta}\left(\theta-\theta_{fu}+\frac{\Theta}{2}\right)\right)\begin{cases}0,\ \theta<\theta_{fu}-\frac{\Theta}{2}\\ 1,\theta_{fu}-\frac{\Theta}{2}<\ \theta<\theta_{fu}+\frac{\Theta}{2}\\ 0,\ \theta>\theta_{fu}+\frac{\Theta}{2}\end{cases} \tag{30}$$

This leads to the identification of the non-dimensional temperature of fusion θ_{fu} as:

$$\theta_{fu}=\frac{T_{fu}-T_c}{T_h-T_c}. \tag{31}$$

The final form of the derived governing equations is as follows:

$$\frac{\partial U}{\partial X}+\frac{\partial V}{\partial Y}=0, \tag{32}$$

$$\varepsilon^{-2}\left((1-\phi)+\phi\frac{\rho_b}{\rho_f}\right)\left(U\frac{\partial U}{\partial X}+V\frac{\partial U}{\partial Y}\right)=-\frac{\partial P}{\partial X}+\mathrm{Pr}\,\varepsilon^{-1}(1+\phi N_v)\nabla^2U-\frac{\mathrm{Pr}}{\mathrm{Da}}(1+\phi N_v)U, \tag{33a}$$

$$\varepsilon^{-2}\left((1-\phi)+\phi\frac{\rho_b}{\rho_f}\right)\left(U\frac{\partial V}{\partial X}+V\frac{\partial V}{\partial Y}\right)=-\frac{\partial P}{\partial Y}+\mathrm{Pr}\,\varepsilon^{-1}(1+\phi N_v)\nabla^2V+\left((1-\phi)+\phi\left(\frac{\beta_p}{\beta_f}\right)\right)\mathrm{Ra}\,\mathrm{Pr}\,\theta-\mathrm{Ha}^2V-\frac{\mathrm{Pr}}{\mathrm{Da}}(1+\phi N_v)V, \tag{33b}$$

$$\left((1-\phi)+\phi\lambda+\frac{\phi}{\delta\mathrm{Ste}}f\right)\left(U\frac{\partial\theta}{\partial X}+V\frac{\partial\theta}{\partial Y}\right)=(1+\phi N_c)\nabla^2\theta. \tag{34}$$

Boundary conditions in dimensionless form

The non-dimensional model of the boundary conditions can be formulated as:

at the cold wall (cylinder):

$$U=V \text{ and } \theta=0, \tag{35a}$$

at the hot cylinder:

$$U=V \text{ and } \theta=1. \tag{35b}$$

The foregoing equation describes the local heat transfer across the heated wall:

$$\mathrm{Nu}=-(1+\phi N_c)\frac{\partial\theta}{\partial Y}. \tag{36}$$

The overall heat transfer rate is determined from the integration of the earlier developed mathematical expressions:

$$\overline{\mathrm{Nu}}=\frac{1}{2\pi}\int_0^{2\pi}\mathrm{Nu}\,\mathrm{d}Y. \tag{37}$$

4. Computational procedure

The fundamental equations can be resolved using several approaches. In the investigated problem, the Galerkin weighted residual finite element method is employed to streamline the computing procedure.

This method converts the differential equations governing the heat transfer and fluids motion into algebraic formulas that can be numerically solved. For the discretisation of the non-dimensional governing equations, a non-uniform triangular mesh is employed. A damped Newton technique with a minimum damping factor of 10^{-6} is utilised to solve the coupled momentum and energy equations, and the Galerkin approach is applied for handling the residuals. The PARDISO direct solver is implemented to improve numerical stability during matrix factorisation by incorporating a pivot perturbation value of 10^{-8}. The convergence criterion for the modelling process is determined by the tolerances defined by the solver. The relative tolerance is fixed at 10^{-6}, ensuring that the solution was deemed converged when the relative change between successive iterations fell below 0.1%.

A grid resolution analysis was conducted to verify the mesh independence of the outcomes, utilising the average Nusselt number as the reference parameter. Table 2 presents a summary of the results corresponding to different mesh densities: fine, finer, extra fine and extremely fine. The distinction between the extra fine and extremely fine meshes is barely noticeable. ΔNu is approximately 0.0193, suggesting that the solution has effect-

Table 2. Discretisation sensitivity analysis for Ra = 10^5, Ha = 0, ω = 0, ϕ = 5%.

Mesh size	Number of elements	Average Nusselt number	CPU time (s)
Fine	9640	7.1929	14
Finer	18174	7.2786	37
Extra fine	32896	7.2950	58
Extremely fine	88746	7.3143	137

tively reached convergence. Despite the increased computational time associated with the extremely fine mesh, which is 137 s in contrast to 58 s for the extra fine mesh, it is selected for all subsequent simulations. This choice ensures mesh independency and highly accurate outcomes, capturing all flow, thermal gradients, along with fluctuations in the optimal heat capacity ratio.

The typical quantities of the non-dimensional variables are established as follows: Ste = 0.313, λ = 0.4, Pr = 6.2, ρ_p / ρ_f = 0.9, θ_{fu} = 0.3, T_{Mr} = 0.05, and $N_c = N_v$ =3.

The numerical model underwent additional validation through a comparative analysis with benchmark data provided by Ghalambaz et al. [40]. Average Nusselt numbers were computed for Rayleigh numbers with ϕ = 0 and Pr = 0.7, and the findings were compared with the reference values. The data presented in Table 3 indicate a high level of concordance with the benchmark, demonstrating a maximum relative error of 0.04% across all examined cases. The robust quantitative correlation validates the precision of the governing equations, the models of material properties, and the suitability of the existing computational framework for parametric analysis.

Finally, the precision and reliability of the proposed framework were verified by comparing the streamline, temperature and Cr ratio with those reported by Ghalambaz et al. [40], as illustrated in Fig. 2. The close agreement demonstrates the robustness of the numerical model and validates its use for the sensitivity and parametric studies.

Table 3. Comparison of the mean Nusselt number at the hot wall with values published in [40] under the conditions of ϕ = 0 and Pr = 0.7.

Ra	Nu average [40]	Nu average (Present study)	Relative error (%)
10^3	1.1174	1.1178	0.0358
10^4	2.2441	2.2443	0.0089
10^5	4.5174	4.5182	0.0177
10^6	8.8167	8.8188	0.0238

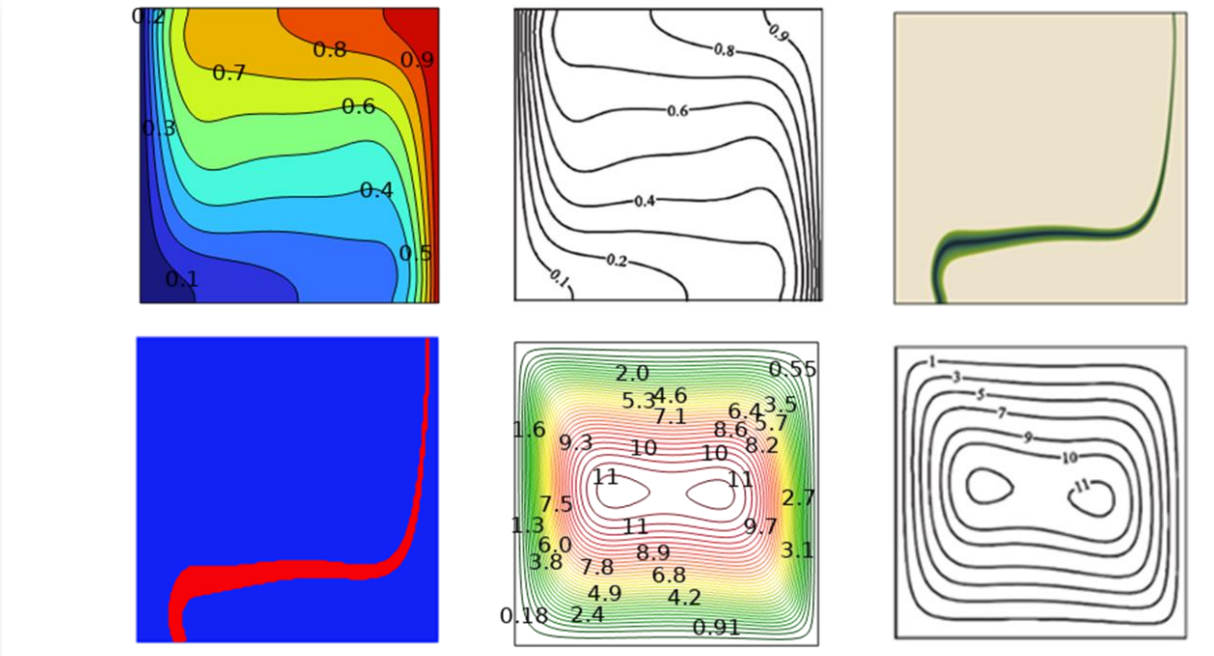


Fig. 2. Comparison of the present results (temperature, heat capacity and streamline contours, from left to right) with those of Ghalambaz et al. [40] placed on the right-side for Ra = 10^5, Ha = 0, Pr = 6.2, ω = 0°.

5. Results and discussion

In the first place, it is apparent that all contours (streamlines, isotherms and heat capacity ratio) exhibit an axisymmetric pattern along the *y*-axis for all the cases studied.

5.1. Effect of Rayleigh number for ω = 0°

Figure 3 demonstrates the significance of varied Rayleigh number values (Ra = 10^3–10^6) on streamline contours of fluid flow, thermal features and heat capacity ratio, considering Ha = 0, ϕ = 0.05, Pr = 6.2, and Da = 10^{-2} at a constant inclination angle of $\omega = 0^{\circ}$.

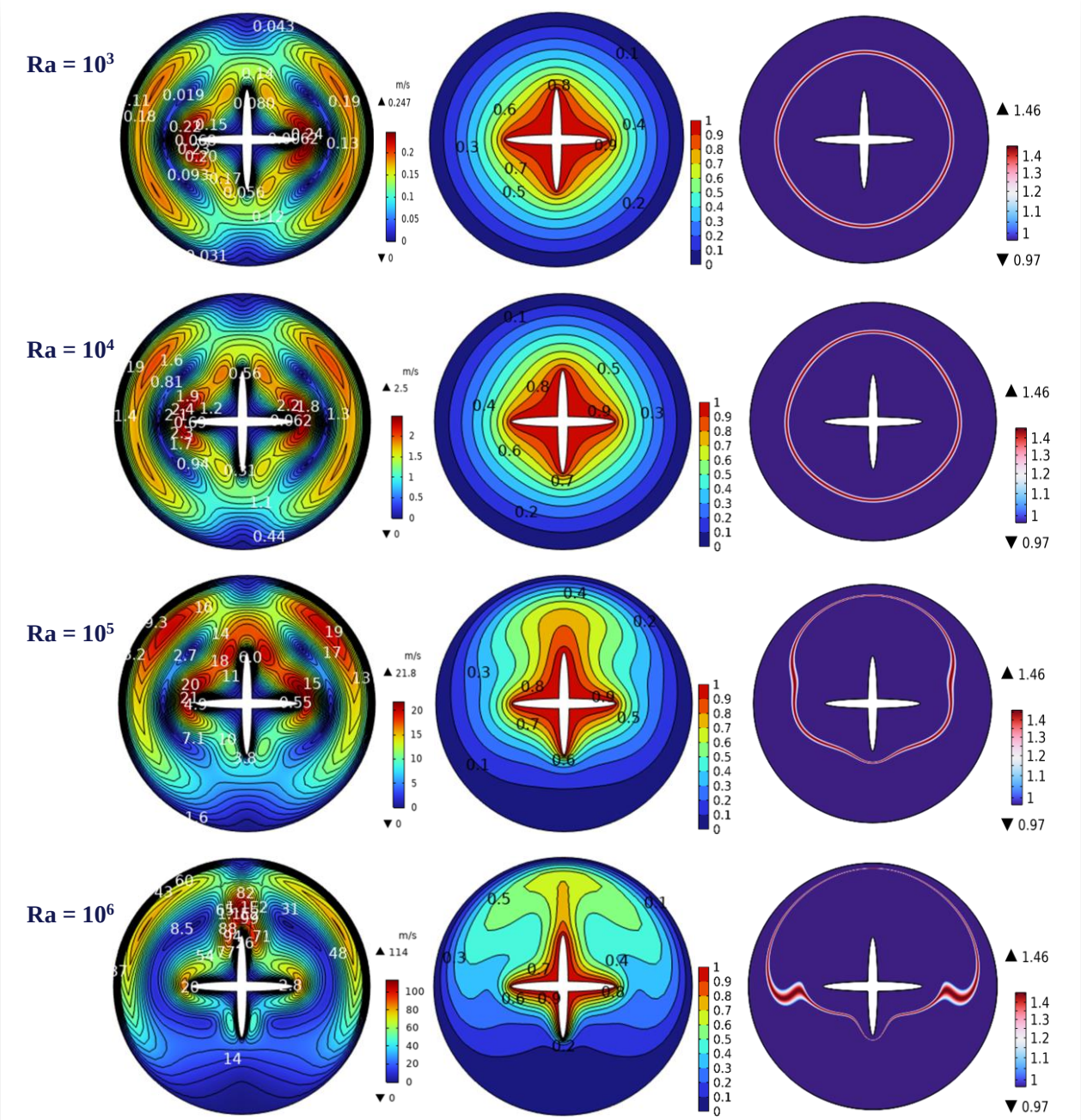


Fig. 3. Rayleigh number influence on streamline patterns (left), temperature (centre) and heat capacity ratio (right) for Ha = 0, ϕ = 0.05, Pr = 6.2 and Da = 10^{-2}. Streamlines show an increase in maximum velocity from 0.0247 m/s (Ra = 10^3) to 114 m/s (Ra = 10^6), while isotherms vary in the range 0–1.

The fluid flow profile exhibits a marked intensification of motion, especially in the regions adjacent to the hot and cold sides of the cylinders. As the Rayleigh number increases, the velocity within the annular space rises significantly, causing the flow to extend upward along the wall boundaries. Near the upper portion of the heated cylinder, the velocity reaches its maximum at Ra = 10^6 due to the dominance of convective heat transfer. The thermal distribution pattern shows a gradual temperature rise from the heated cylinder toward the cooler one. The increase in Ra further amplifies this effect, as the hot fluid migrates toward the cold region, leading the warmer, lighter fluid to ascend and the cooler, denser fluid to descend in response to the thermal gradient. At Ra = 10^6, the temperature field develops a characteristic mushroom-shaped layer that expands progressively. This behaviour reflects the mechanism of thermal buoyancy, wherein fluid near the hot surface becomes less dense and rises, while fluid near the cold surface gains density and sinks. The Cr ratio layer forms a closed circular contour around the heated cylinder, marking the region where the phase transition occurs within the cavity. Increasing the dimensionless parameter distorts this contour, causing it to widen along the lateral sides while narrowing near the cold wall and the lower section of the heated area. The resulting slender shape of the layer delineates the most favourable region for phase-change heat transfer to take place.

5.2. Effect of the Hartmann number for $\omega = 0°$

Figure 4 depicts the effect of increasing Hartmann number on the flow field, temperature distribution and heat capacity ratio for Ra = 10^6, $\phi = 0.05$, Pr = 6.2 and Da = 10^{-2} at a fixed inclination angle $\omega = 0^{\circ}$.

The streamline contours show that increasing the magnetic field intensity (Hartmann number) leads to a reduction in the overall flow rate due to the Lorentz force, which acts as a resistive mechanism opposing fluid motion. The isotherms indicate a more uniform temperature distribution under stronger magnetic effects. The heat capacity ratio contours exhibit a mushroom-shaped layer surrounding the heated cylinder, characterised by thicker lateral regions that narrow towards both the lower part of the hot boundary and the vicinity of the cold wall. As the non-dimensional parameter increases, this pattern shows no deformation.

5.3. Darcy number impact for $\omega = 0°$

Figure 5 presents the permeability influence in the porous medium cavity denoted by the Darcy number at Ra = 10^6, $\phi = 0.05$, Pr = 6.2, and Da = 10^{-2} at a fixed inclination angle $\omega = 0^{\circ}$.

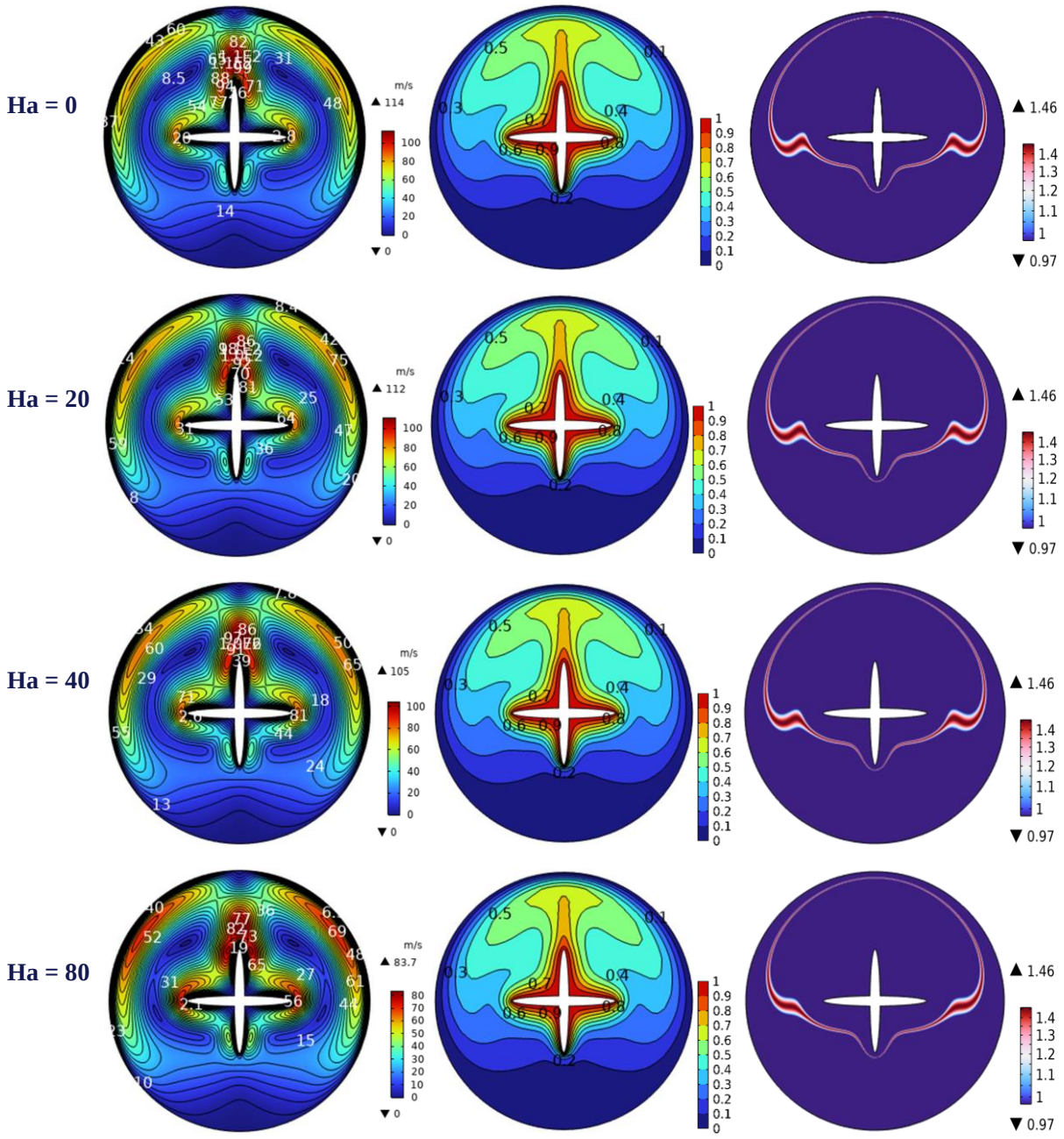


Fig. 4. Hartmann number influence on streamline patterns (left), temperature (centre) and heat capacity ratio (right) for Ra = 10^6, $\phi = 0.05$, Pr = 6.2 and Da = 10^{-2}. Streamlines show a decrease in maximum velocity from 114 m/s (Ha = 0) to 83.7 m/s (higher Ha), while isotherms vary in the range 0–1.

The velocity contours reveal that increasing the Darcy number promotes stronger fluid movement inside the enclosure, particularly around the extremities of the lateral edges of the heated cylinder, its upper section and along the cold boundary.

The thermal field displays an initially uniform distribution from the hot region to the cold region; as the Darcy number rises, this distribution expands outward and develops into a mushroom-shaped thermal layer.

The heat capacity ratio contours exhibit a curved boundary encircling the heated obstacle. As the dimensionless parameter increases, this boundary undergoes noticeable deformation: it becomes thinner near the cold wall and in the lower part of the hot boundary, while the lateral regions expand and become comparatively thicker.

5.4. The influence of inclination angle ω (10°, 30°, 60°, and 80°) on the streamlines, isotherms and Cr patterns

Figures 6, 7, and 8 designate the streamlines, isotherms and Cr contours, respectively, at multiple degrees of inclination angle and Ra number with Ha = 0, ϕ = 0.05, Pr = 6.2 and Da = 10^{-2}.

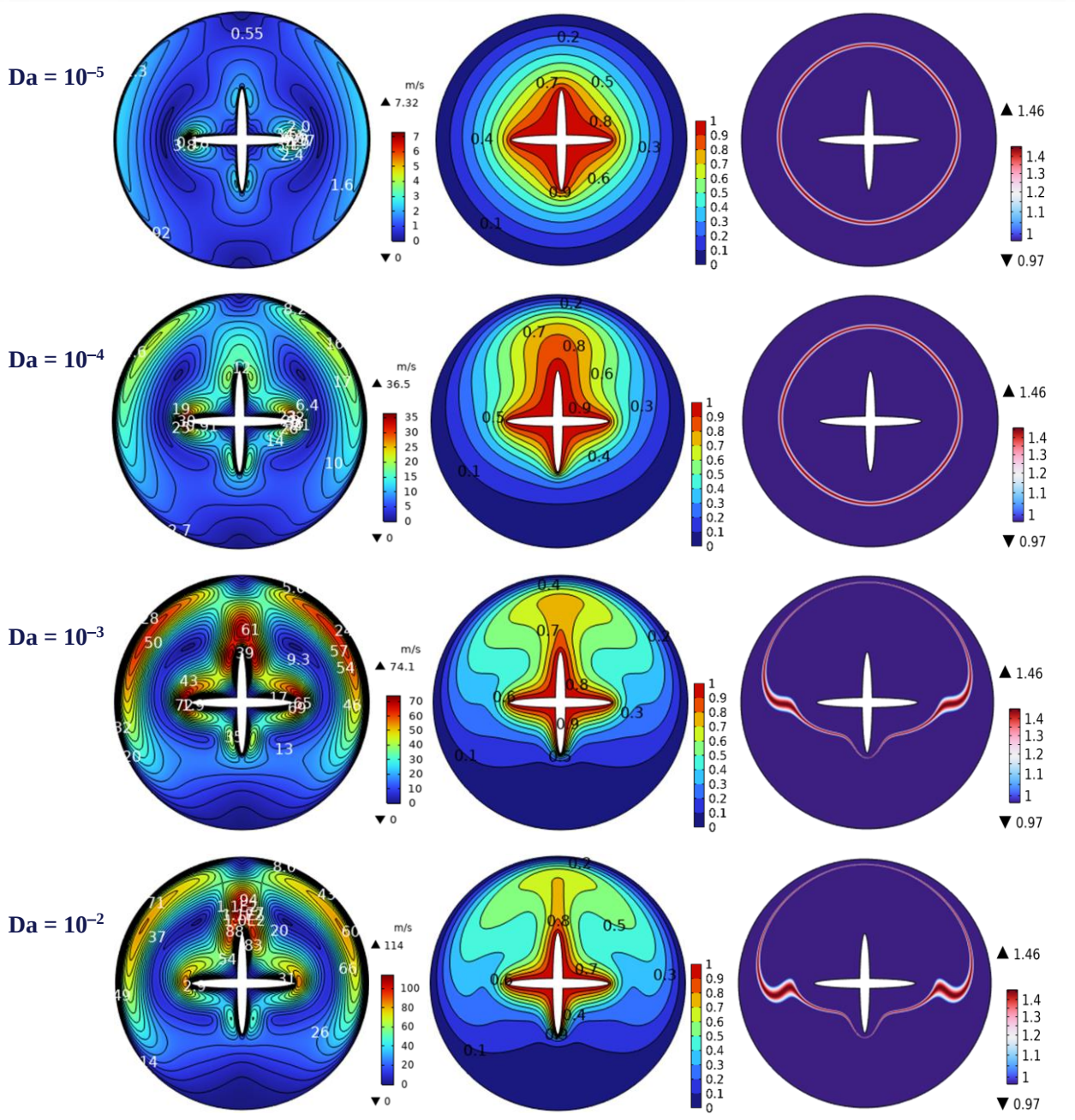


Fig. 5. Darcy number influence on velocity (left), temperature (centre) and heat capacity ratio (right) for Ha = 0, ϕ =0.05, Pr = 6.2 and Ra = 10^6. Streamlines show an increase in maximum velocity from 7.32 m/s (Da = 10^{-5}) to 114 m/s (Da = 10^{-2}), while isotherms vary in the range 0–1.

As observed, the inclination angle ω exerts a significant influence on the streamlines, isotherms and Cr ratio patterns. Notably, an inclination of 10° behaves as the angular counterpart of 80°, while 30° mirrors 60°.

The streamline patterns indicate that the velocity reaches its maximum near the corners of the inner cylinder and along the sidewalls of the outer enclosure, generating concentrated velocity zones on both the left and right sides. Increasing both the Rayleigh number and the inclination angle enhances the fluid motion, causing the flow to accelerate and extend upward across the upper region of the annular domain.

Figure 7 illustrates the thermal field, where the temperature is the highest near the heated surface and gradually diffuses towards the cooler region. The rise in Rayleigh number facilitates the upward migration of heat within the cavity, producing a mushroom-shaped isotherm pattern. As the inclination angle increases, the heat distribution expands, resulting in a more pronounced deformation of this mushroom-like structure.

Figure 8 displays the heat capacity ratio, characterised by a thick, curved boundary surrounding the heated cylinder. For inclination angles of 10° and 80°, increasing the Rayleigh number causes this boundary to bend outward, becoming broader along the lateral sides while narrowing near the upper region of the outer cylinder and the lower region adjacent to the heated surface at Ra = 10^6. Additionally, a semi-circular line emerges near the lower wing of the cavity. A similar behaviour is ob-

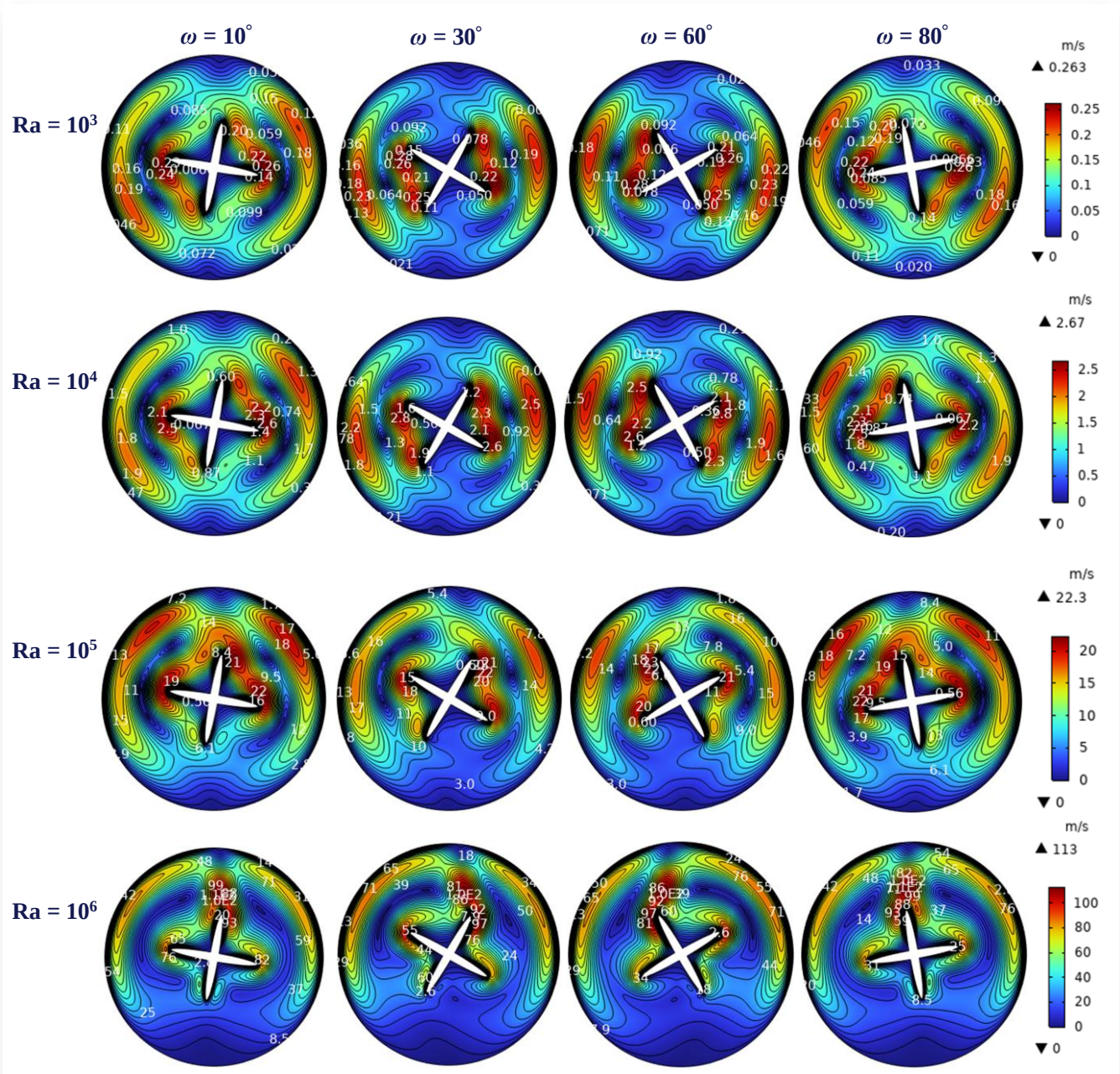


Fig. 6. Streamlines for various values of inclination angle (ω =10º, 30º, 60º, 80º, respectively) and Ra number for Ha = 0, ϕ =0.05, Pr = 6.2 and Da = 10^{-2}. The maximum velocity increases from 0.263 m/s (Ra = 10^3) to 113 m/s (Ra = 10^6).

served for inclination angles of 30° and 60°, although the pattern more closely resembles a mushroom-like contour enveloping the hot boundary.

5.5. Average Nusselt number influence

Figure 9 presents variations of the average Nusselt number with the Rayleigh number (10^3–10^6) for different Hartmann numbers (0–20), Darcy numbers (10^{-5}–10^{-2}), NEPCM volume fractions (0%–5 %), and inclination angles (10°–80°).

Figure 9a shows that the Nusselt number decreases as both the Hartmann and Rayleigh numbers increase. This reduction is attributed to the resistive action of the Lorentz force, which suppresses fluid motion and consequently slows the heat transfer rate within the cavity.

Figure 9a illustrates a direct correlation between the Darcy and Rayleigh numbers, demonstrating that an increase in the Rayleigh number leads to a corresponding rise in the Darcy number. As the Darcy number increases, the permeability of the porous medium improves, enhancing convective heat transfer and resulting in a higher Nusselt number.

Figure 9a demonstrates that the increasing NEPCM volume fraction (0–0.05) augments the thermal storage capacity of the suspension. This behaviour confirms a direct proportionality between the Rayleigh number and the NEPCM concentration, enabling more efficient heat transport and producing higher Nusselt number values.

Figure 9d highlights the influence of the inclination angle, showing that its increase leads to larger Rayleigh number values. Unlike the previous cases, increasing the inclination angle from 0° to 30° results in a reduction of the Nusselt number, indicating diminished heat transfer. In contrast, for inclination angles between 60° and 80°, the Nusselt number rises significantly, indicating an enhancement of heat transfer across the annular region.

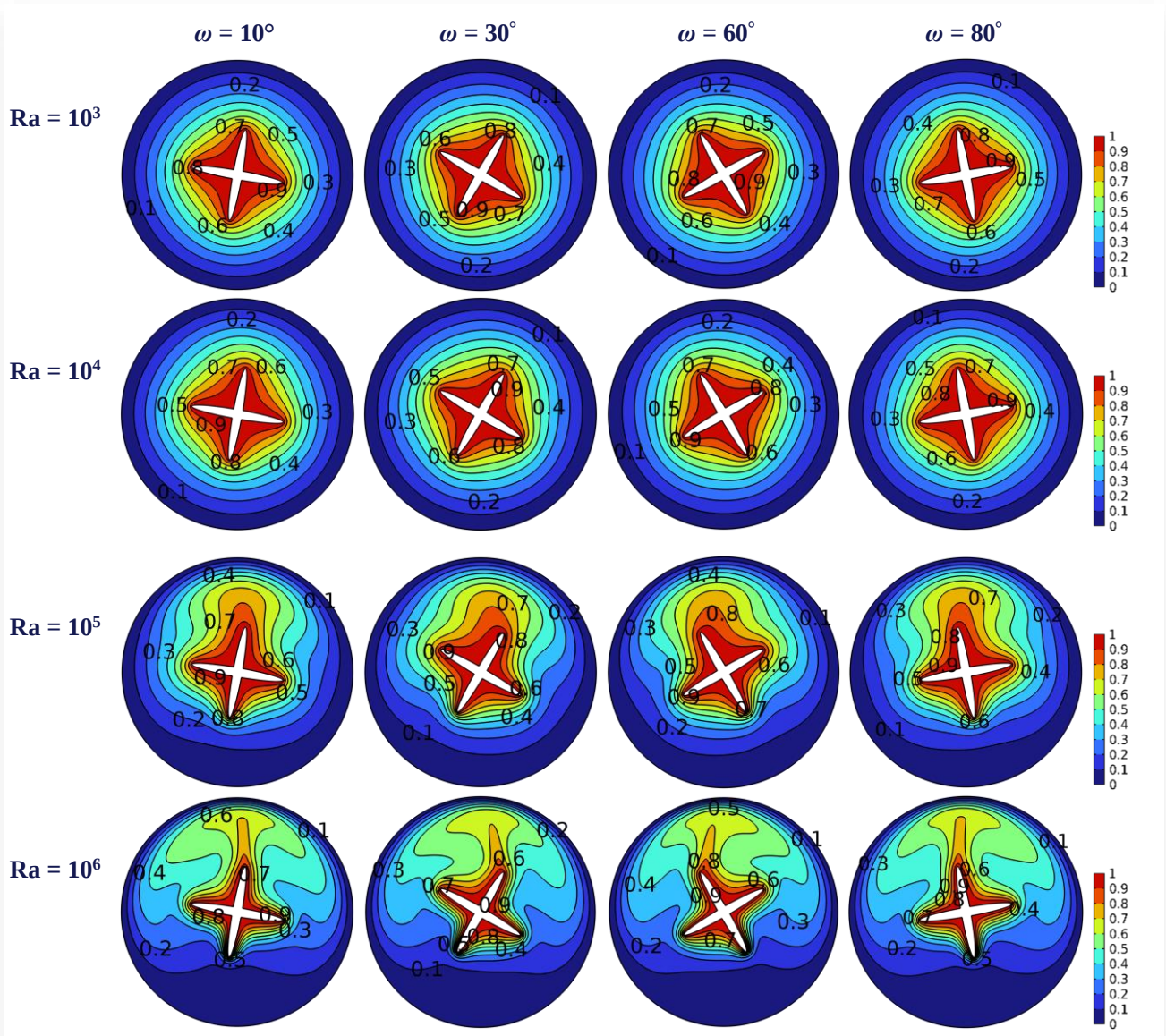


Fig. 7. Isotherms for various values of inclination angle (ω = 10°, 30°, 60°, 80°, respectively) and Ra number for Ha = 0, ϕ = 0.05, Pr = 6.2 and Da = 10^{-2}.

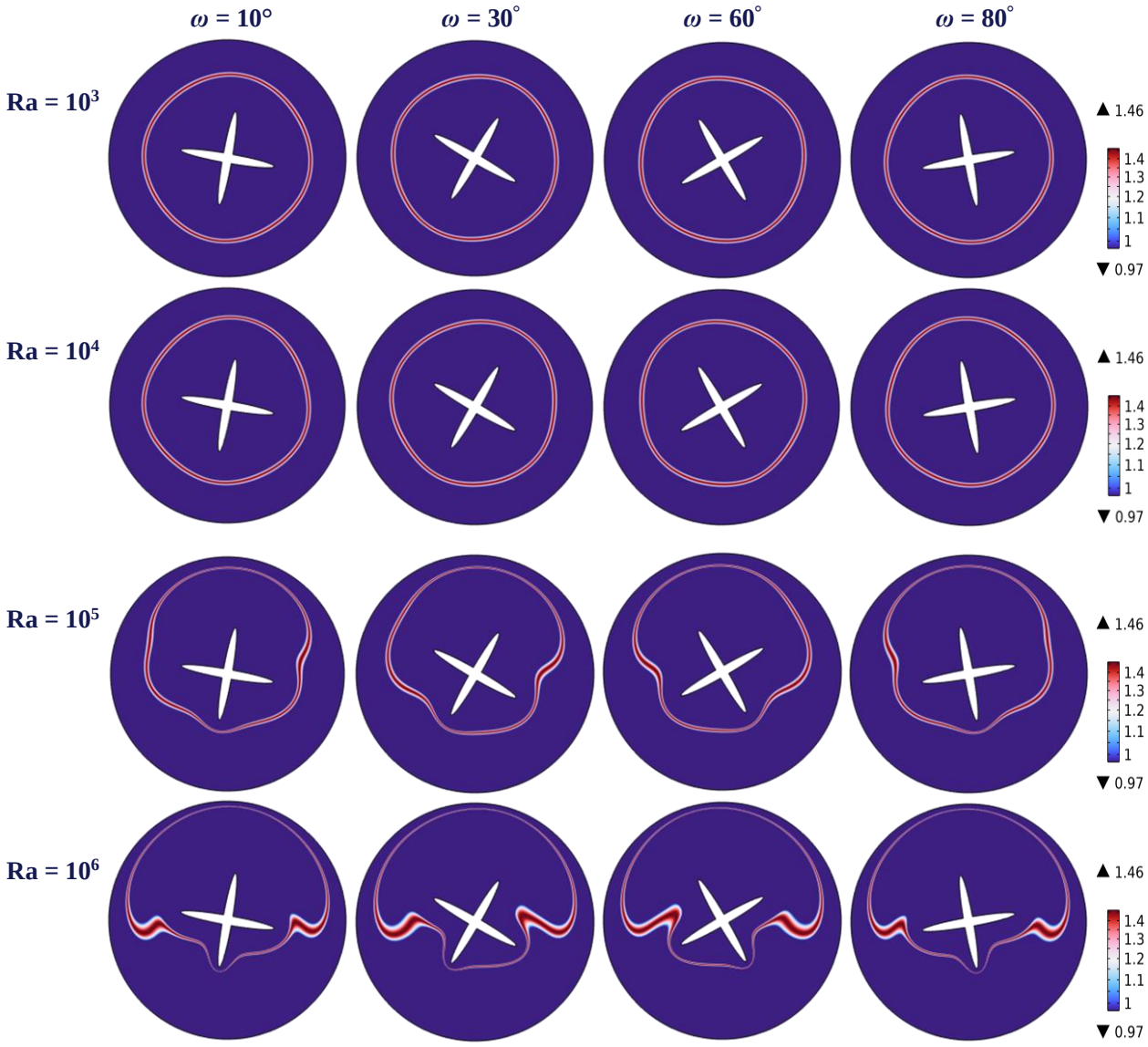


Fig. 8. Heat capacity ratio patterns for various values of inclination angle (ω = 10º, 30º, 60º, 80º) and Rayleigh number for Ha = 0, ϕ = 0.05, Pr = 6.2 and Da = 10^{-2}.

The Nusselt number trends indicate that configurations with inclination angles between 0° and 30° are better suited for thermal insulation applications, as they promote energy efficiency and help preserve temperature differences. Conversely, inclination angles ranging from 60° to 80° are more advantageous for processes requiring intensified heat transfer.

6. Conclusions

The presented work undertakes a numerical analysis of a two-dimensional annular space comprising a cold outer cylinder and a hot inner obstacle generated through the overlap of two congruent elliptical cylinders. The aspect ratio of the overlapping cylinders is 0.1, and the radii ratio between the annular spaces is 0.4.

The suspension incorporated is NEPCM, which is a composite nanofluid developed by suspending nano-encapsulated phase change materials in pure water. The enclosure is porous and subject to the influence of a magnetic field. This study investigates the effects of several dimensionless parameters on streamline patterns, isotherms and the heat capacity ratio (Cr). The parameters considered are the Rayleigh number (10^3–10^6), Darcy number (10^{-5}–10^{-2}) and Hartmann number (0–80), along with the inclination angle of the intersecting inner cylinders ω (0°–80°). The results also highlight the practical implementation of these geometries in contemporary applications.

At ω = 0°, the fields of velocity, temperature, and concentration ratio exhibit symmetry throughout the annular space. The flow velocity is particularly high along the lateral sides of the

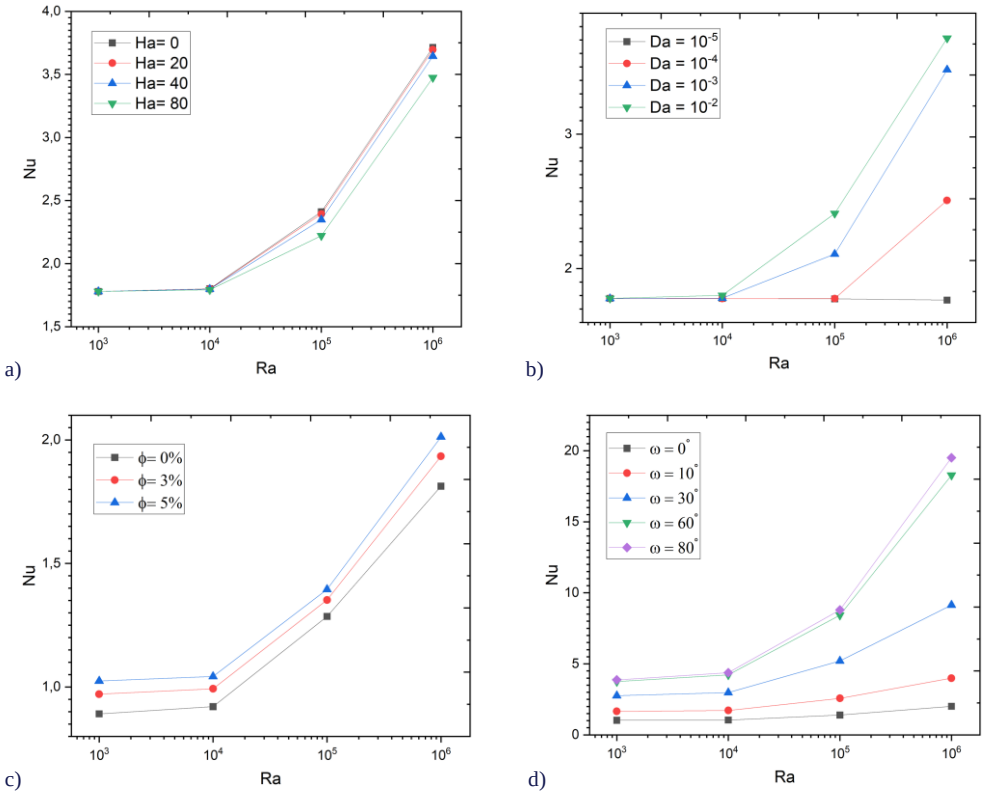


Fig. 9. Average Nusselt number as a function of Rayleigh number for different values of Hartmann number (a), Darcy number (b), NEPCM volume fraction (c), and inclination angle (d).

inner cylinder and near the sidewall of the outer enclosure. Increasing the Rayleigh and Darcy numbers strengthens the vortices and promotes stronger convective currents. This intensification enhances the temperature gradients, increases the heat transfer rate and modifies the spatial distribution of the NEPCM effective heat capacity, with higher values becoming concentrated near the boundary regions and extending along the sidewalls.

Additionally, the Lorentz forces generated by the magnetic field significantly affect the flow, reducing convective velocities as the Hartmann number increases. This leads to weakened vortices, a uniform nanoparticle distribution and a decrease in the average Nusselt number, reflecting a reduced heat transfer intensity, while the inclination angle ω directly influences the level of imbalance and asymmetry of the flow rate, thermal gradient and Cr patterns.

Lastly, the changes in the average Nusselt number with regard to Ra, Da, Ha, ϕ and ω are provided to shed light on their relevance in specific sectors of industry. For instance, inclination angles ranging from 0° to 30° signify that the configuration performs as an insulator due to slower heat transfer rates, in contrast to angles between 60° and 80°, which are more beneficial to heat transfer enhancement.

References

[1] Li, C., Zhao, Z., Liu, X., & Ding, J. (2023). Numerical study of the effect of natural convection on heat transfer in type B LNG cargo tank. *International Joint Conference on Civil and Marine Engineering* (pp. 499–502), 3–6 November, Dalian, China. doi: 10.1049/icp.2024.0263

[2] Dirkse, M.H., van Loon, W.K., van der Walle, T., Speetjens, S.L., & Bot, G.P. (2006). A computational fluid dynamics model for designing heat exchangers based on natural convection. *Biosystems Engineering*, 94(3), 443–452. doi: 10.1016/j.biosystemseng.2006.04.007

[3] Phiraphat, S., Prommas, R., & Puangsombut, W. (2017). Experimental study of natural convection in PV roof solar collector. *International Communications in Heat and Mass Transfer*, 89, 31–38. doi: 10.1016/j.icheatmasstransfer.2017.09.022

[4] Zhang, G., Jiang, S., Yao, W., & Liu, C. (2016). Enhancement of natural convection by carbon nanotube films covered microchannel-surface for passive electronic cooling devices. *ACS Applied Materials & Interfaces*, 8(45), 31202–31211. doi: 10.1021/acsami.6b08815

[5] Laguerre, O., & Flick, D. (2004). Heat transfer by natural convection in domestic refrigerators. *Journal of Food Engineering*, 62(1), 79–88. doi: 10.1016/S0260-8774(03)00173-0

[6] Kuehn, T.H., & Goldstein, R.J. (1978). An experimental study of natural convection heat transfer in concentric and eccentric horizontal cylindrical annuli. *ASME Journal of Heat and Mass Transfer*, 100(4), 635–640. doi: 10.1115/1.3450869

[7] Wang, S. (1995). An experimental and numerical study of natural convection heat transfer in horizontal annuli between eccentric cylinders. *Journal of Thermal Science*, 4(1), 38–43. doi: 10.1007/BF02653162

[8] Laidoudi, H. (2020). Natural convection from four circular cylinders in across arrangement within horizontal annular space. *Acta Mechanica et Automatica*, 14(2), 98–102. doi: 10.2478/ama-2020-0014

[9] Laidoudi, H. (2020). Buoyancy-driven flow in annular space from two circular cylinders in tandem arrangement. *Metallurgical and Materials Engineering*, 26(1), 87–102. doi: 10.30544/481

[10] Laidoudi, H., & Ameur, H. (2021). Investigation of the natural convection within a cold circular enclosure containing three equal-sized cylinders of hot surface. *Defect and Diffusion Forum*, 409, 49–57. doi: 10.4028/www.scientific.net/ddf.409.49

[11] Laidoudi, H., Ameur, H., Sahebi, S.A.R., & Hoseinzadeh, S. (2022). Thermal analysis of steady simulation of free convection from concentric elliptical annuli of a horizontal arrangement. *Arabian Journal for Science and Engineering*, 47(12), 15647–15660. doi: 10.1007/s13369-022-06717-5

[12] Helmaoui, M., Laidoudi, H., Ghenaim, A. (2021). Natural convection from two hot semi-circular cylinders confined in cold circular cylinder. *Defect and Diffusion Forum*, 409, 58–66. doi: 10.4028/www.scientific.net/ddf.409.58

[13] Khudhair, B.K., Saleh, A.M., & Ekaid, A.L. (2023). Influence of vertical vibration on natural heat convection coefficients. *Pertanika Journal of Science and Technology*, 31(3), 1555–1586. doi: 10.47836/pjst.31.3.24

[14] Majdi, H.S., Habeeb, L.J., Elmnifi, M., & Alderoubi, N. (2022). Transient free convection between two horizontal concentric cylinders. *International Journal of Mechanical Engineering*, 7(1), 596–609.

[15] Horimek, A., Abdelmoumene, F., & Ait Messaoudene, N. (2023). Numerical Study of Natural Convection between Two Concentric Ellipses with Different Shapes and Imposed Temperatures. *Mechanical Engineering Technologies and Applications*, 2, 105–128. doi: 10.2174/9789815124125123020l

[16] Laidoudi, H., Helmaoui, M., Bouzit, M., & Ghenaim, A. (2021). Natural convection of Newtonian fluids between two concentric cylinders of a special cross-sectional form. *Thermal Scienc*e, 25(5B), 3701–3714. doi: 10.2298/TSCI200201190L

[17] Mohammed, A.A. (2021). Natural convection heat transfer inside horizontal circular enclosure with triangular cylinder at different angles of inclination. *Journal of Thermal Engineering*, 7(1), 240–254. doi: 10.18186/thermal.849812

[18] Alguboori, A.R., Al-azzawi, M.M., Kalash, A.R., & Habeeb, L.J. (2020). Natural convection heat transfer in an inclined elliptic enclosure with circular heat source. *Journal of Mechanical Engineering Research and Developments*, 43(6), 207–222.

[19] Azzouz, R., & Hamida, M.B. (2023). Natural convection in a circular enclosure with four cylinders under magnetic field. *Processes*, 11(8), 2444. doi:10.3390/pr11082444

[20] Wang, W., Li, B.W., & Hu, Z.M. (2019). Magnetohydrodynamic natural convection in cylindrical annulus. *Journal of Heat Transfer*, 141(6), 062502. doi:10.1115/1.4042811

[21] Ali, A.R.I., & Salam, B. (2020). A review on nanofluid: preparation, stability, thermophysical properties, heat transfer characteristics and application. *SN Applied Sciences*, 2(10), 1636. doi: 10.1007/s42452-020-03427-1

[22] Mahmood, M.A., Mustafa, M.A., Al-Azzawi, M.M., & Abdullah, A.R. (2020). Natural convection heat transfer in a concentric annulus vertical cylinders embedded with porous media. *Journal of Advanced Research in Fluid Mechanics and Thermal Sciences*, 66(2), 65–83.

[23] Jobby, A., Khatamifar, M., & Lin, W. (2025). A comprehensive review on the natural convection heat transfer in horizontal and inclined closed rectangular enclosures with internal objects at various heating conditions. *Energies*, 18(4), 950. doi: 10.3390/en18040950

[24] Mahdy, A., El-Zahar, E.R., Rashad, A.M., Saad, W., & Al-Juaydi, H.S. (2021). The magneto-natural convection flow of a micropolar hybrid nanofluid over a vertical plate saturated in a porous medium. *Fluids*, 6(6), 202. doi: 10.3390/fluids6060202

[25] Gholamalipour, P., Siavashi, M., & Doranehgard, M.H. (2019). Eccentricity effects of heat source inside a porous annulus on the natural convection heat transfer and entropy generation of Cu-water nanofluid. *International Communications in Heat and Mass Transfer*, 109, 104367. doi: 10.1016/j.icheatmasstransfer.2019.104367

[26] Allouche, B., Djezzar, M., Allouche, S., & Tayebi, T. (2026). Natural convection heat transfer in an eccentric annulus filled with hybrid nanofluid under the influence of thermal radiation and heat generation/absorption. *Numerical Heat Transfer, Part A: Applications*, 87(1), 2386607. doi: 10.1080/10407782.2024.2386607

[27] Bouzerzour, A., Djezzar, M., Oztop, H.F., Tayebi, T., & Abu-Hamdeh, N. (2020). Natural convection in nanofluid filled and partially heated annulus: Effect of different arrangements of heaters. *Physica A: Statistical Mechanics and its Applications*, 538, 122479. doi: 10.1016/j.physa.2019.122479

[28] Ali, F.H., Almensoury, M.F., Hashim, A.S., Al-Amir, Q.R., Hamzah, H.K., & Hatami, M. (2024). Nanofluid natural convection of hot concentric cylinder in oval-shaped porous cavity at different eccentricity. *International Journal of Numerical Methods for Heat & Fluid Flow*, 34(5), 2146–2176. doi: 10.1108/HFF-08-2023-0494

[29] Tayebi, T., Öztop, H.F., & Chamkha, A.J. (2021). MHD natural convection of a CNT-based nanofluid-filled annular circular enclosure with inner heat-generating solid cylinder. *The European Physical Journal Plus*, 136(2), 150. doi: 10.1140/epjp/s13360-021-01106-7

[30] Mebarek-Oudina, F., & Chabani, I. (2023). Review on nano enhanced PCMs: insight on nePCM application in thermal management/storage systems. *Energies*, 16(3), 1066. doi: 10.3390/en16031066

[31] Alomari, M.A., Hassan, A.M., Alajmi, A., Sadeq, A.M., Alqurashi, F., & Flayyih, M.A. (2025). A comprehensive numerical analysis of heat transfer enhancement in NEPCM-water mixtures using oscillating fin and oriented magnetic fields. *International Communications in Heat and Mass Transfer*, 161, 108455. doi: 10.1016/j.icheatmasstransfer.2024.108455

[32] Alomari, M.A., Hassan, A.M., Sadeq, A.M., Alqurashi, F., & Flayyih, M.A. (2025). MHD Heat Transfer Enhancement in a Curvilinear Enclosure With Oscillating Wall and Nano-Encapsulated PCM: A Fluid-Structure Interaction Analysis. *Heat Transfer*, 54(6), 4049–4072. doi: 10.1002/htj.23399

[33] Rashid, F.L., Mohammed, H.I., Dulaimi, A., Al-Obaidi, M.A., Talebizadehsardari, P., Ahmad, S., & Ameen, A. (2023). Analysis of heat transfer in various cavity geometries with and without nano-enhanced phase change material: A review. *Energy Reports*, 10, 3757–3779. doi: 10.1016/j.egyr.2023.10.036

[34] Abderrahmane, A., Al-Khaleel, M., Mourad, A., Laidoudi, H., Driss, Z., Younis, O., Guedri, K., & Marzouki, R. (2022). Natural convection within inversed T-shaped enclosure filled by nano-enhanced phase change material: Numerical investigation. *Nanomaterials*, 12(17), 2917. doi: 10.3390/nano12172917

[35] Mehryan, S.A.M., Ghalambaz, M., Gargari, L.S., Hajjar, A., & Sheremet, M. (2020). Natural convection flow of a suspension containing nano-encapsulated phase change particles in an eccentric annulus. *Journal of Energy Storage*, 28, 101236. doi: 10.1016/j.est.2020.101236

[36] Ghalambaz, M., Mehryan, S.A.M., Ayoubloo, K.A., Hajjar, A., El Kadri, M., Younis, O., Pour, M.S., & Hulme-Smith, C. (2021). Thermal energy storage and heat transfer of nano-enhanced phase

change material (NePCM) in a shell and tube thermal energy storage (TES) unit with a partial layer of eccentric copper foam. *Molecules*, 26(5), 1491. doi: 10.3390/molecules26051491

[37] Ghalambaz, M., Mehryan, S.A.M., Mozaffari, M., Zadeh, S.M. H., & Pour, M.S. (2020). Study of thermal and hydrodynamic characteristics of water-nano-encapsulated phase change particles suspension in an annulus of a porous eccentric horizontal cylinder. *International Journal of Heat and Mass Transfer*, 156, 119792. doi: 10.1016/j.ijheatmasstransfer.2020.119792

[38] Hussain, S., Aly, A.M., Alsedias, N., & Çolak, A.B. (2024). Integrating artificial intelligence in investigating magneto-bioconvection flow of oxytactic microorganisms and nano-enhanced phase change material in H-type cavity. *Thermal Science and Engineering Progress*, 49, 102497. doi: 10.1016/J.TSEP.2024.102497

[39] Elshehabey, H.M., Aly, A.M., Lee, S.W., & Çolak, A.B. (2024). Integrating artificial intelligence with numerical simulations of Cattaneo-Christov heat flux on thermosolutal convection of nano-enhanced phase change materials in Bézier-annulus. *Journal of Energy Storage*, 82, 110496. doi: 10.1016/J.EST.2024.110496

[40] Ghalambaz, M., Chamkha, A.J., & Wen, D. (2019). Natural convective flow and heat transfer of nano-encapsulated phase change materials (NEPCMs) in a cavity. *International Journal of Heat and Mass Transfer*, 138, 738–749. doi: 10.1016/j.ijheatmasstransfer.2019.04.037

[41] Sheikholeslami, M., & Sadoughi, M.K. (2018). Simulation of CuO-water nanofluid heat transfer enhancement in presence of melting surface. *International Journal of Heat and Mass Transfer*, 116, 909–919. doi: 10.1016/j.ijheatmasstransfer.2017.09.086.

[42] Zaraki, A., Ghalambaz, M., Chamkha, A.J., Ghalambaz, M., & De Rossi, D. (2015). Theoretical analysis of natural convection boundary layer heat and mass transfer of nanofluids: effects of size, shape and type of nanoparticles, type of base fluid and working temperature. *Advanced Powder Technology*, 26(3), 935–946. doi : 10.1016/j.apt.2015.03.012

[43] Ghalambaz, M., Doostani, A., Izadpanahi, E., & Chamkha, A.J. (2017). Phase-change heat transfer in a cavity heated from below: the effect of utilizing single or hybrid nanoparticles as additives. *Journal of the Taiwan Institute of Chemical Engineers*, 72, 104–115. doi: 10.1016/j.jtice.2017.01.010

Co-published by
Institute of Fluid-Flow Machinery
Polish Academy of Sciences
Committee on Thermodynamics and Combustion
Polish Academy of Sciences

Copyright©2026 by the Authors under licence CC BY-NC-ND 4.0

http://www.imp.gda.pl/archives-of-thermodynamics/

Experimental validation of the CFD model of heat losses from the horizontal rectangular flue gas duct exposed to wind and solar radiation

Liliana Mirosz

Warsaw University of Technology, Department of District Heating and Gas Systems, Faculty of Environmental Engineering, Nowowiejska 20, Warsaw 00-653, Poland
Author email: liliana.mirosz@pw.edu.pl

Received: 29.09.2025; revised: 28.04.2026; accepted: 12.06.2026

Abstract

The article presents the experimental validation of a numerical model of heat losses from a horizontal rectangular flue gas duct situated outside a heating plant building. The duct is insulated with mineral wool mats and protected with galvanised sheet metal. The model was developed in ANSYS Fluent 2024 R2, incorporating the effects of wind velocity and solar radiation. The computational domain is defined as encompassing the duct and the surrounding airspace. A sensitivity analysis of the mesh on the simulation results was performed. The validation experiment was conducted at an operational coal-fired heating plant under various wind and sunlight conditions. The measurement of the heat flux density was conducted by means of heat flux sensors. The validation indicators, that is to say, the process validation metric and the relative root mean square error, confirm the consistency between the simulation results and the heat flux density measurements on the bottom and side walls. The numerical model that has been utilised is capable of being employed in analyses of flue gas duct modernisation, with the objective of reducing heat losses from flue gases flowing through the duct.

Keywords: Computational fluid dynamics; Heat losses; Rectangular flue gas duct; Solar radiation; Thermal insulation

Vol. 47(2026), No. 3, 173–186; doi: 10.24425/ather.2026.7516

Cite this manuscript as: Mirosz, L. (2026). Experimental validation of the CFD model of heat losses from the horizontal rectangular flue gas duct exposed to wind and solar radiation. *Archives of Thermodynamics*, 47(3), 173–186.

1. Introduction

Statistics Poland [1] have reported that in 2024, district heating was utilised for the heating of 45% of households in Poland. This share is so large that even a negligible enhancement in the energy efficiency of heat generation has the potential to markedly diminish the environmental impact of heat production in residential buildings. According to data from the Energy Regulatory Office [2], the average efficiency of licensed sources was 84% in 2024, representing a 5pp increase since 2002. The efficiency level is determined by the magnitude of various heat losses that occur in the process of heat production. For coal-fired heating plants, the following factors warrant consideration: exhaust heat loss carried by flue gases into the environment, incomplete combustion loss caused by the presence of combustible particles in fly ash and slag, heat losses to the environment through convection and radiation, physical heat contained in combustion residues (the so-called physical enthalpy of residues), and incomplete combustion loss resulting from the partial combustion of gaseous combustible components in flue gases. Figure 1 shows examples of the shares of these heat losses for a coal-fired water boiler.

Nomenclature

a_1 – model constant
CV(RMSE)– relative root mean square error coefficient, %
c_p – specific heat capacity at constant pressure, J/(kg K)
D – measured value
D_ω – cross-diffusion term, kg/(m^3 s^2)
d – hydraulic diameter, m
e – error, %
E – comparison error
F_1, F_2– first and second blending functions
G – energy production, kg/(m/s^3)
GCI – grid convergence index, %
Gr – Grashof number
g – gravitational force, m/s^2
h – characteristic cell size, m
H – height, m
I – turbulence intensity, %
k – kinetic energy of turbulence, m^2/s^2
Ma – Mach number
n – number of measurements in a series
N – number of grid cells
p – pressure, Pa
p_{conv} – order of convergence
Q – heat flux density, W/m^2
r – grid refinement ratio
Re – Reynolds number
RMSE– root mean square error
s – standard deviation
S – modulus of the mean rate-of-strain tensor, 1/s
S_{num} – numerical simulation value
t – temperature, ^{o}C
t_p – Student's t-distribution coefficient for confidence level p
T – absolute temperature, K
u_a – type A standard uncertainty
u_b – systematic standard uncertainty
u_c – combined standard uncertainty
U – uncertainty
U_V – process validation metric
V – computational domain volume, m^3
$\boldsymbol{w}$ – velocity vector, m/s
w_x – velocity component in the x-axis direction, m/s
x – segment length in x-axis direction, m
y^+ – dimensionless wall distance in turbulence models

Greek symbols

α^* – coefficient damping the turbulent viscosity
β^* – modified dissipation coefficient for k
β_i – blended dissipation coefficient for ω
γ_1 – production coefficient for ω
δ – thickness, m
λ – thermal conductivity, W/(m K)
μ – dynamic viscosity, $\mu = \rho k/\omega$, kg/(m s)
μ_t – turbulent viscosity, kg/(m s)
ν – kinematic viscosity, m^2/s
ν_{dof} – number of degrees of freedom
ρ – density, kg/m^3
σ – diffusion coefficient
ω – turbulence dissipation rate, 1/s

Subscripts and Superscripts

a – relative
c – total
D – experimental value
ext – extrapolated
i – measurement number in a series
k – turbulent kinetic energy
SN – numerical simulation value
SPD – due to input data
t – turbulent
x – coordinate direction
v – viscous sublayer
ω – turbulence dissipation rate
1 – for wall layers
2 – for the region far from the wall
‘ – fluctuation of a variable

Abbreviations and Acronyms

CFD – computational fluid dynamics
GCI – grid convergence index

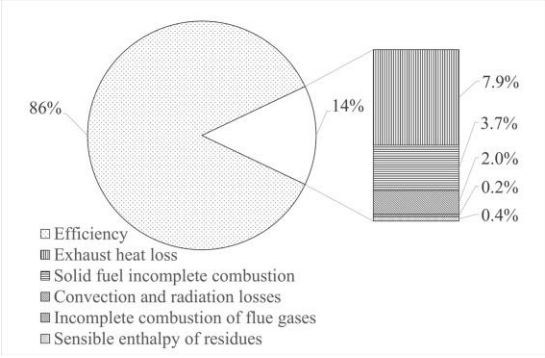


Fig. 1. Shares of heat losses for an example coal-fired water boiler (own study based on [3]).

In the case of a boiler that is operated in accordance with the established guidelines, exhaust loss constitutes the most significant element in its energy balance. As Zhang et al. [3] assert, this may account for as much as 8–9% in the case of coal-fired water boilers, a subject to be analysed later in this article. This phenomenon of heat losses can be mitigated through various means, including the reduction of flue gas temperature, with due consideration for the issue of sulphur corrosion on the walls of both horizontal and vertical flue gas ducts. The conditions for its occurrence are associated with the location of the ducts, which, in the context of heating plants, are partially situated outside the building. Subsequently, the flue gas is exposed to meteorological conditions, including wind and precipitation, which prompt a rapid cooling process. It is imperative to maintain the temperature of the flue gas above the so-called acid dew point, where the mixture of sulfuric acid and water vapour condenses, leading to the corrosion of ducts. Consequently, proper insulation of the flue gas discharge route, and even at the design stage, the optimal route for reducing heat loss, is a factor that significantly affects the efficiency of district heating production.

It is evident that a considerable number of heating plants and combined heat and power plants are currently in operation in Poland. It is important to note that many of these facilities were constructed several decades ago. The modernisation of existing flue gas ducts has been demonstrated to result in a substantial enhancement of the efficiency of district heating production. The magnitude of this increase can be estimated using numerical simulations, provided that the extent to which they reflect reality is known. The validation of numerical models of flue gas flows in heating plants by comparing simulation results with measurements on actual facilities is a subject that is rarely described in the literature. The primary rationale for this is the complexity inherent in such studies, which is compounded by the extensive scale of the model and frequently necessitates disruption to the existing installation.

A review of the extant literature reveals a paucity of research on the validation of numerical models for a horizontal rectangular section of flue gas ducts based on measured heat flux density. Nevertheless, there are a number of publications that address this topic in specific areas.

Matas et al. [4] and Chen et al. [5] described the issue of a rectangular horizontal section of a flue gas duct, focusing on flow velocities. Matas et al. [4] validated a numerical model of the flue gas system between the boiler and the fan by comparing the simulation results with measurement data obtained at a combined heat and power plant. The model under consideration incorporated short rectangular horizontal sections. It was determined that the correspondence between the simulation outcomes and the measurement data was deemed to be satisfactory, as evidenced by the findings concerning the flue gas flow rates and velocity distribution. Chen et al. [5] presented an analysis of the numerical simulation results for a rectangular flue gas duct, examining the conditions upstream and downstream of an electrostatic precipitator. The velocity distribution was also described. The publication did not include any validation.

Conversely, El-Shafie [6] utilised temperature measurements to validate a numerical model, albeit for a vertical circular flue gas duct discharging flue gas from a glass furnace. The demonstration revealed a substantial degree of concordance between the temperature distribution that was derived from the numerical simulation and the measurement results.

None of the above publications takes into account the current influence of wind. None of the numerical models presented cover the air around the flue gas duct. Nevertheless, this approach is frequently employed in numerical simulations of flows around buildings, as articulated by Huang et al. [7]. The literature provides comprehensive guidelines for the numerical simulation and validation of numerical models of buildings, with consideration for external air flow (see, for example, Franke et al. [8], Tominaga et al. [9]). Outside the boiler room building, the flue gas duct is significantly affected by the external air. Consequently, it appears that, in numerical simulations, it could be treated in the same way as a building.

It has been observed that the aforementioned publications neglect to consider the impact of solar radiation, a factor that is undoubtedly implicated in the intensity of heat exchange between the flue gases and the environment.

The present work serves to augment the extant body of knowledge concerning the impact of outside air and solar radiation on heat losses from flue gas ducts. The objective of this study is to utilise numerical simulations to formulate solutions that enhance the efficiency of district heating production by reducing heat losses from flue gas ducts.

2. Numerical model of heat losses from the flue gas duct of a heating plant

2.1. Fundamental equations of conservation

Computational fluid dynamics (CFD) is a technique for solving problems involving fluid flow and the accompanying heat exchange using numerical methods. It is imperative that these solutions adhere to the established laws of conservation in the physics of the phenomenon. It is imperative to acknowledge the fundamental principle of fluid mechanics: the conservation of mass. In accordance with Newton's second law of motion, the change in momentum of a fluid particle must be equal to the sum of the forces acting upon it. In accordance with Newton's first law of motion, the change in energy must be equal to the sum of the changes in heat transfer and the changes in work done on the fluid element.

The law of conservation of mass gives rise to the continuity equation described in Eq. (1), under the assumption that the phenomenon is steady-state. The numerical model investigated in this study involves two fluids: flue gas and air. Both are assumed to be incompressible with respect to pressure changes, as the Mach number remains below 0.3. While flue gas is also considered incompressible with respect to thermally induced density changes, due to the dominance of forced convection within the duct, air is treated as thermally compressible. This approach is necessary to model the mixed convection around the duct, which is key to capturing buoyancy effects caused by flow separation as the wind encounters the structure. Equation (1) represents the continuity equation for both fluids

$$\nabla \cdot (\rho \boldsymbol{w}) = 0, \tag{1}$$

where: ρ – density, $\boldsymbol{w}$ – velocity vector. In the case of flue gas, the density is assumed constant, whereas for air, it varies according to the thermal compressibility assumption.

The law of momentum change is described by the momentum conservation equation. This work presents its averaged version, i.e. the Reynolds equation described in Eq. (2). The velocity component in the *x*-axis direction is given. In addition to the aforementioned assumptions, the fluid flow is turbulent, and gravity is taken into account in the *x*-axis direction, with the opposite sign:

$$\nabla \cdot (\rho \boldsymbol{w} w_x) = -\frac{\partial p}{\partial x} + \nabla \cdot (\mu \nabla w_x) - \nabla \cdot \left(\rho \overline{w_x{}' \boldsymbol{w}'}\right) - \rho g, \tag{2}$$

where: w – velocity, p - pressure, x – segment length in the x-axis direction, μ – dynamic viscosity, g – gravitational acceleration, and other quantities as indicated in Eq. (1). The subscript x denotes the vector component in the x-axis direction, and ’ denotes fluctuations of variables. Analogous equations describe the conservation of momentum’ in the other directions.

In the analysed phenomenon of heat exchange between flue gas and air, the influence of gravity on the flow from the flue gas side is negligible. However, this is not the case on the air side. The phenomenon of mixed convection can be defined as a combination of free convection, which is influenced by temperature differences and affects density, and forced convection, which is driven by the action of wind. In order to estimate the influence of gravity, the ratio of the Grashof number to the square of the Reynolds number was calculated for the measurement from the experiment at the highest wind velocity. The result obtained was 0.04, which, according to Bejan [10], indicates a small but not negligible influence of buoyancy forces on air density. It is important to note that this effect will increase as the wind velocity decreases. It is therefore evident that all simulations were performed with due consideration for gravitational forces.

The governing law of energy changes is regulated by the energy conservation equation, as outlined in Eq. (3). Along with the previously stated assumptions, there are no internal heat sources, and energy dissipation due to working against viscous forces can be neglected:

$$\nabla \cdot \left(\rho c_p \boldsymbol{w} T\right) = \nabla \cdot (\lambda \nabla T) - \nabla \cdot \left(\rho c_p \overline{\boldsymbol{w}' T'}\right), \tag{3}$$

where: c_p – specific heat capacity at constant pressure, T – absolute temperature, λ – thermal conductivity.

2.2. Turbulence model

The phenomenon of heat exchange in the flue gas duct was modelled using the software programme ANSYS Fluent 2024 R2. It is widely used in numerical simulations of flows around buildings that take into account the influence of external air velocity, as described by Huang et al. [7].

In the analysed case, turbulent motion occurs on both the flue and air sides. In the proximity of the walls, the nature of the flow undergoes a transformation. In order to achieve a reliable representation of the flow field within a reasonable computational time, appropriate turbulence models are selected. It is posited that these models provide a reliable approximation of the effect of turbulence on the average velocity, pressure and temperature fields. This enables accurate and stable calculation results to be obtained with an acceptable computational effort.

In the aforementioned issue, the Reynolds-averaged Navier-Stokes (RANS) model was selected, in which all vortex scales are modelled, the so-called Shear-Stress Transport (SST k–ω). This model has been employed in analogous analyses within the extant literature (see, for example, Matas et al. [4]). The model demonstrates an effective solution to the equations in the wall layer at low speeds. In the fully turbulent area far from the wall, the k–ε model is employed. Hamisu et al. [11] posit that the recommended value of y^+ for the SST k–ω model is approximately 1, although values up to 5 are deemed acceptable.

The phenomenon of turbulence is taken into account in CFD in the k–ω SST model by solving the equations of kinetic energy transport of turbulence and turbulence dissipation rate, respectively:

$$\nabla \cdot (\rho k \boldsymbol{w}) = \nabla \cdot [(\mu + \mu_t \sigma_k) \nabla k] + G_k - \rho \beta^* \omega k, \tag{4}$$

$$\nabla \cdot (\rho \omega \boldsymbol{w}) = \nabla \cdot [(\mu + \mu_t \sigma_\omega) \nabla \omega] + \gamma_1 \frac{\omega}{k} G_k - \rho \beta_i \omega^2 + D_\omega. \tag{5}$$

The model also incorporates a specific formulation for turbulent viscosity, a blended dissipation coefficient and a cross-diffusion term, respectively:

$$\mu_t = \frac{\rho k}{\omega} \frac{1}{\max\left[\frac{1}{\alpha^*}, \frac{SF_2}{a_1 \omega}\right]}, \tag{6}$$

$$\beta_i = F_1 \beta_{i,1} + (1 - F_1) \beta_{i,2}, \tag{7}$$

$$D_\omega = 2(1 - F_1) \rho \sigma_{\omega,2} \frac{1}{\omega} \nabla k \cdot \nabla \omega, \tag{8}$$

where: k – turbulent kinetic energy, μ_t – turbulent viscosity, σ_k, σ_ω – diffusion coefficients both equal to 0.5 in wall layers, and equal to 1.0 and 0.856 ($\sigma_{\omega,2}$) far from the walls, respectively, G_k – production of turbulent kinetic energy, β^* – modified dissipation coefficient for k equal to 0.09, ω – specific dissipation rate, γ_1 – production coefficient for ω equal to 0.52 for high-Reynolds number flows, β_i – blended dissipation coefficient for ω, D_ω – cross-diffusion term, α^* – coefficient damping the turbulent viscosity equal to 1 for high-Reynolds number flows, S – modulus of the mean rate-of-strain tensor, F_1, F_2 – first and second blending functions, a_1 – model constant equal to 0.31, $\beta_{i,1}$, $\beta_{i,2}$ – dissipation coefficients for ω equal to 0.075 in wall layers and 0.0828 far from the walls, respectively.

The mathematical formulation follows the original notation proposed by Menter [12], while coefficients and model implementation are based on the ANSYS Fluent documentation [13]. It was assumed that the flue gas is incompressible with respect to both pressure and temperature changes. In contrast, air was modelled as incompressible regarding pressure but thermally compressible, as described in Subsection 2.1. The phenomenon is assumed to be steady-state, and no internal heat sources are present.

2.3. Solar radiation model

In order to account for the impact of solar radiation on the flue gas duct, the Solar Load Model in ANSYS Fluent 2024 R2 was utilised. In this model, the impact of solar radiation is determined on the basis of three factors. Firstly, data on the location of the actual installation must be taken into account. Secondly, the date of the measurement series must be considered. Thirdly, the solar radiation coefficient must be taken into account. The solar radiation coefficient was calculated on the basis of the air temperature measured in conditions of shade and in the sun during the measurement series in the validation experiment. For the measurement series for which a cloudless sky was observed, this coefficient was assumed to be equal to 1. This corresponds to the difference in air temperature between the measurement in the shade and in direct sunlight, as measured at that time. For the remaining measurement series, the insolation coefficient was calculated in relation to the above-mentioned measurement series, based on the current difference in air temperature measured in the shade and in direct sunlight.

The absorptivity of the duct walls, ground (predominantly grass) and building envelope was assumed to be 0.8, accounting for material properties, ageing, and coal dust deposition typical

of the coal-fired heating plant environment. Carvalho et al. [14] reported an albedo of 0.25 for grass corresponding to an absorption coefficient of 0.75. In this study, the absorption coefficient was increased to 0.8 to reflect the significant darkening of vegetation caused by coal dust accumulation. Similarly, the building envelope's absorptivity was based on Yu et al. [15], who identified a range of 0.65 – 0.85 for grey wall-facing materials. The value of 0.8 was selected due to long-term environmental exposure. For blue-painted steel ducts, the baseline from Liu et al. [16] (0.63–0.75 for grey coatings) was adjusted to 0.8. This adjustment accounts for the higher near-infrared absorption typical of standard blue pigments compared to grey ones, as well as the further increase in absorptivity caused by coal dust contamination.

While ANSYS Fluent also allows for radiation exchange calculations between surfaces and gases, the Radiation Model was not activated for two main reasons. First, at the investigated temperatures (below 400 K for flue gas, and below 300 K for air), gases are generally considered transparent [17]. Furthermore, since radiant energy emission is proportional to the fourth power of absolute temperature, its contribution at these moderate temperatures is negligible compared to convective fluxes observed in this study. Consequently, omitting the radiation model does not significantly impact the final results.

2.4. Geometry of the computational domain

The geometry of the model was created in ANSYS DesignModeler. The issue was regarded as a three-dimensional problem. The modelled geometry is shown in Fig. 2:

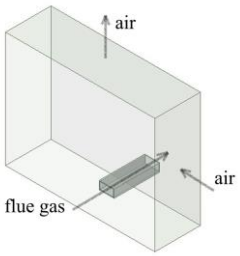


Fig. 2. Geometric model showing the direction of flue gas and air flows (ANSYS DesignModeler 2024 R2).

The duct in question was modelled with a thickness of 4 mm, with the material used being steel sheet. The duct insulation is composed of two mineral wool mats, each measuring 50 mm in thickness, which are sheathed in 0.5 mm-thick galvanised sheet metal. The duct exhibits a rectangular cross-section, with the following internal dimensions: width of 2.12 m, height of 1.06 m, length of 7.04 m. The geometry of the model is such that it takes into account the volume of the duct and the insulation. The sheets were modelled as surfaces with thicknesses assigned in ANSYS Fluent 2024 R2.

The direction of flow of flue gas and the direction of air inlet are perpendicular to each other. The location of the air outlet is above rather than behind the duct. This is due to the proximity of a building, which blocks the flow. The dimensions of the computational domain, in the absence of guidelines for flue ducts, were based on guidelines for modelling wind flow around buildings, presented by Franke et al. [8] and Tominaga et al. [9]. The domain extends 10H above the duct, while a distance of 5H was modelled between the wind inlet plane and the duct, where H is the height of the duct. The selection of these values was informed by a blockage ratio of 7%. This ratio is utilised to ascertain the distances between the wind inlet and outlet, and the object around which the wind flows. The ratio is defined as the cross-sectional area of the obstacle (in this case, the channel) divided by the cross-sectional area of the air domain in the direction of air inflow. The location of the installation was a determining factor in the dimensions of the air domain: 11.5H behind the channel (building boundary) and 4 m below the channel (ground level). The width of the computational domain was assumed to be equal to the length of the analysed section.

2.5. Discretisation of the computational domain

The spatial discretisation of the computational domain performed in ANSYS ICEM CFD 2024 R2 is presented in Fig. 3.

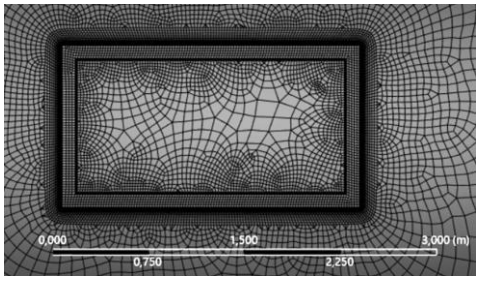


Fig. 3. Numerical mesh: view from the flue gas inlet toward the duct (ANSYS ICEM CFD 2024 R2).

The limit for the minimum cell size in the fully turbulent area on the air side was assumed based on the cube root of the duct volume, i.e. 0.27 m, in accordance with the guidelines for buildings provided by Franke et al. [8].

The mesh was refined near the duct walls in order to rectify the issue of heat transfer in the wall layers. These are the layers, in which the fluid's viscosity is a significant factor in determining its flow. For the purpose of this study, the thickness of the aforementioned zone was estimated for flue gases based on the formula for turbulent flow through a pipe, Eq. (9), as posited by Schlichting and Gersten [18]. Such flow is divided into a viscous sublayer and a turbulent core:

$$\delta_v = 122 \frac{\ln \mathrm{Re}}{\mathrm{Re}\, \mathrm{G}(\ln \mathrm{Re})} d, \tag{9}$$

where: δ_v – thickness of the viscous sublayer of flue gas, Re – Reynolds number, and function G(ln Re) is equal to 1.35 at $2300 < \mathrm{Re} < 10^7$, and d – hydraulic diameter.

However, the thickness of the wall layer was calculated according to the formula given by Schlichting and Gersten [18] for turbulent flow along a plate:

$$\delta_t = 0.14 \frac{\mathrm{Re}}{\ln \mathrm{Re}} \mathrm{G}(\ln \mathrm{Re}) \frac{\nu}{w}, \tag{10}$$

where δ_t is the thickness of the turbulent boundary layer of air,

v is the kinematic viscosity, and function G(ln Re) is equal to 15 at $10^5 < \mathrm{Re} < 10^6$.

According to Duan et al. [19], the Reynolds number on the flue gas side was determined using the square root of the channel cross-sectional area as the characteristic dimension. On the air side, the channel width was taken as the characteristic dimension for the flow along the plate.

The thicknesses at which mesh refinement is important were calculated for the data from each measurement series. The maximum values recorded were 0.004 m on the flue gas side and 0.04 m on the air side. On this basis, the grid refinement at the walls was modelled accordingly so that it covered at least the estimated thickness of the wall zone. The layer thickness growth rate was set at 1.2, at which the independence of the grid influence on the numerical simulation result, as determined by the grid convergence index (GCI), is less than 1%. In accordance with the recommendations set out by Franke et al. [8], the maximum value for numerical simulations of wind flow around buildings, it should not exceed 1.2. The thicknesses of the first layer in the wall zone are 0.0001 m on the flue gas side and 0.0003 m on the air side, respectively. In the context of these thicknesses, the maximum values of y^+ at the walls did not exceed 5, in accordance with the recommendations for the SST k–ω turbulence model.

The simulations were executed on a grid, the independence analysis of which is presented in the following chapter. The total number of mainly hexahedral volume elements was approximately 2 million. The quality of the mesh was verified to ensure numerical stability and accuracy. The skewness reached a maximum value of 0.8 (with an average of 0.2), and the minimum orthogonal quality was 0.2 (with an average of 0.9). Although a maximum aspect ratio reached 1005 (with an average of 86 for the entire domain), these peak values occurred exclusively within the wall layers. In the computational domain far from the walls, the maximum aspect ratio remained below 6.

2.6. Mesh independence analysis

The independence of the results from the mesh used was tested using GCI. This method is frequently employed to estimate discretisation error in numerical fluid dynamics analyses, as evidenced by the works of Franke et al. [8] and Celik et al. [20]. According to Roache [21], GCI is derived from the generalised Richardson extrapolation method, which determines the numerical uncertainty associated with spatial discretisation errors. The relative error of the test of independence of results from the mesh necessitates solutions for a minimum of three grids of varying refinement. A uniform refinement in all directions was assumed between successive meshes, and the layer growth rate was modified in the wall area (changes of approximately 25%). The number of layers at the walls was adjusted to cover the estimated total thickness of the near-wall layer. In all types of grids, meticulous attention was paid to ensure adequate quality. This was achieved by analysing the aspect ratio, orthogonality and skewness of its elements. If deemed necessary, the mesh division along the flue gas duct axis was corrected.

Celik et al. [20] proposed the following methodology for calculating GCI from Eq. (11) based on the results of numerical simulations on three distinct grids, designed as follows: fine – 1, medium – 2, and coarse – 3:

$$\mathrm{GCI}_1^{21} = \frac{1.25 e_a^{21}}{r_{21}^{p_{\mathrm{conv}}-1}}, \tag{11}$$

where: e_a – relative error between the results obtained from the two meshes, r – grid refinement ratio (recommended > 1.3), p_{conv} – order of convergence.

The relative error between the results from two meshes is calculated from:

$$e_a^{21} = \left| \frac{S_{\mathrm{num},1} - S_{\mathrm{num},2}}{S_{\mathrm{num},1}} \right|, \tag{12}$$

where S_{num} stands for the numerical simulation value.

The grid refinement ratio, expressed as

$$r_{21} = \frac{h_2}{h_1} \tag{13}$$

is determined based on the characteristic cell size using the equation:

$$h_1 = \left(\frac{V}{N_1} \right)^{1/3}, \tag{14}$$

where V is the computational domain volume and N is the number of grid cells.

The order of convergence of the numerical method is determined iteratively according to the equation:

$$p_{\mathrm{conv}} = \frac{1}{\ln(r_{21})} \left| \ln \left| \frac{S_{\mathrm{num},3} - S_{\mathrm{num},2}}{S_{\mathrm{num},2} - S_{\mathrm{num},1}} \right| + \right.$$

$$\left. + \ln \left(\frac{r_{21}^{p_{\mathrm{conv}}} - \mathrm{sgn}\left(\frac{S_{\mathrm{num},3} - S_{\mathrm{num},2}}{S_{\mathrm{num},2} - S_{\mathrm{num},1}} \right)}{r_{32}^{p_{\mathrm{conv}}} - \mathrm{sgn}\left(\frac{S_{\mathrm{num},3} - S_{\mathrm{num},2}}{S_{\mathrm{num},2} - S_{\mathrm{num},1}} \right)} \right) \right|, \tag{15}$$

for which the quantities are described in the preceding formulas.

The relative error extrapolated between the results obtained from the two grids is calculated from:

$$e_{\mathrm{ext}}^{21} = \left| \frac{S_{\mathrm{ext}}^{21} - S_{\mathrm{num},1}}{S_{\mathrm{ext}}^{21}} \right|, \tag{16}$$

where the extrapolated value is expressed as:

$$S_{\mathrm{ext}}^{21} = \frac{\left(r_{21}^{p_{\mathrm{conv}}} S_{\mathrm{num},1} - S_{\mathrm{num},2} \right)}{\left(r_{21}^{p_{\mathrm{conv}}} - 1 \right)}. \tag{17}$$

In Table 1, the GCI for the measurement with the highest wind velocity is presented, along with several additional values that were obtained through the utilisation of the aforementioned methodology. The GCI for the medium and fine grids was found to be below 1%. The solution was within the asymptotic range of convergence. Although the medium grid was sufficient, the fine grid was selected for the final simulations to ensure maximum numerical precision.

2.7. Material properties, boundary and initial conditions

As illustrated in Tables 2 and 3, the physical properties are assigned to individual surfaces and volumes. The material

Table 1. Results of the study on the independence of results from grid refinement.

Grid type	Fine	Medium	Coarse
Number of elements	1 985 410	829 650	312 240
Grid refinement ratio	1.34	1.39	–
Characteristic cell size, m	0.11	0.15	0.21
Maximum element, m	0.27	0.34	0.42
Layer thickness growth factor	1.2	1.5	1.9
Relative error, %	0.3	0.9	–
Extrapolated relative error, %	0.2	0.5	–
Grid convergence index, %	0.25	0.65	–

Table 2. Physical properties of materials.

	Mineral wool mat	Steel	Reference
Thermal conductivity, W/(m K)	0.0002t+0.033	50	[22]
Density, kg/m³	100	7 800	mat: [23] steel: [22]
Specific heat capacity, J/(kg K)	750	450	[23]

t – arithmetic mean of the flue gas and air temperatures

Table 3. Physical properties of gases – average values for all measurements.

	Flue gas [22]	Air [24,25]
Thermal conductivity, W/(m K)	0.0281	0.0250
Density, kg/m³	0.977	1.225 (at 288.15 K)
Dynamic viscosity, kg/(m s)	1.904×10^{-5}	1.778×10^{-5}
Specific heat capacity, J/(kg K)	1 026	1 041

properties were adopted in accordance with established standards. The properties of gases were obtained from established standards and authoritative publications on air and gas mixtures. Regarding density, different density models were applied to each fluid. Air was modelled as an incompressible ideal gas, where density varies with a local temperature. This approach accurately captures the buoyancy effects around the duct. In contrast, the flue gas was modelled with a constant density.

The initial conditions were established at the inlet to the flue gas duct and the air domain. These conditions included the velocity and temperature, as determined by the experimental study, as well as the turbulence intensity, which was calculated using the equation proposed by Russo and Basse [26]:

$$I = 0.14\mathrm{Re}^{-0.0790}, \tag{18}$$

where I denotes the turbulence intensity. The Reynolds number was determined for the square root of the channel cross-sectional area as a characteristic dimension, in accordance with the recommendation of Duan et al. [19].

Table 4. Inlet initial conditions for all measurement series.

Measurement series	Temperature, K		Velocity, m/s	
	Flue gas	Air	Flue gas	Air
1	363.8	282.0	6.7	2.7
2	365.2	282.2	6.8	3.7
3	366.1	282.3	6.9	3.2
4	362.1	282.5	8.5	2.5
5	364.3	284.5	6.3	2.7
6	364.8	284.3	6.3	3.0
7	364.8	284.1	6.4	1.9
8	364.9	286.0	6.4	1.9
9	364.7	286.4	6.3	3.2
10	363.4	286.3	6.2	4.1

The temperature and velocity values for all measurement series are presented in Table 4. The turbulence intensity for the flue gas is 5% in all cases, while for the air, it varies between 4% and 5%. The hydraulic diameter is 1.413 m for the flue gas and 10.1 m for the air.

The boundary conditions are described in Table 5. The steel duct walls were modelled on both sides of the insulation body using the Shell Conduction option, allowing for heat conduction within the plane of the metal sheets. A no-slip condition was set on the duct walls, as they are fluid-solid interfaces. An adiabatic condition was applied to the cross-sections of the duct walls (duct ends). A constant temperature equal to the air temperature was assumed on the ground and on the building side, while the other side walls of the wind domain were designated as symmetry boundaries.

The flue gas and air inlets were modelled as velocity-inlet, while the outlets were modelled as pressure-outlet. At the pressure-outlets, a zero-pressure gradient was assumed, with the backflow temperature and turbulence parameters set to values

Table 5. Summary of boundary conditions and numerical settings.

Boundary name	Type	Thermal conditions	Momentum conditions
Flue gas inlet	Velocity-inlet	Temperature (Tab. 4)	Velocity (Tab. 4) and turbulence parameters
Flue gas outlet	Pressure-outlet	Backflow: inlet value	Gauge pressure: 0, backflow: inlet value
Duct walls	Wall	Coupled (shell conduction)	No-slip
Duct ends	Wall	Adiabatic	–
Air inlet	Velocity-inlet	Temperature (Tab. 4)	Velocity (Tab. 4) and turbulence parameters
Air outlet	Pressure-outlet	Backflow: inlet value	Gauge pressure: 0, backflow: inlet value
Wind domain, side walls	Symmetry	–	–
Ground / building	Wall	Temperature: air inlet value	No-slip

corresponding to the respective inlet conditions. This was justified because the temperature drop of the flue gas along the investigated part of the insulated duct is minimal, and the ambient air outside maintains a nearly uniform temperature throughout the domain.

2.8. Basic assumptions in numerical modelling

The issue was modelled as a time-steady problem.

Both flue gas and air were treated as incompressible with respect to pressure changes, as the Mach number was below 0.3. Therefore, a pressure-based calculation module was selected.

The calculations were performed in double precision.

A coupled algorithm was used to solve the system of pressure and velocity equations. In order to solve the pressure equation, due to the presence of mixed convection, the PRESTO! (pressure staggering option) discretisation scheme was used, while second-order upwind schemes were used for the remaining equations.

Franke et al. [8] and Celik et al. [20] posit that the residual value resulting from solving the aforementioned equations should be a minimum of 1×10^{-4}, and that this should be reduced further for the purposes of validation. In accordance with the recommendation of Franke et al. [8], the parameter under investigation should be observed simultaneously. If it remains unchanged during successive iterations, the simulation can also be considered convergent. The convergence criterion was established at a residual value of 1×10^{-6}, with a simultaneous heat flux density variability of less than 0.01% in the final 100 iterations.

3. Experimental validation of the numerical model in a real heating plant

3.1. Test methodology

In order to analyse the phenomenon of heat losses from the horizontal flue gas duct of a heating boiler, an existing system located in a municipal heating plant was selected for the purpose of this study. The boiler operating parameters were meticulously monitored at the plant, which demonstrated that the flue gas losses during the experiment ranged from 4 to 5%. The heat source employed was a WR-25 water grate boiler, which was fuelled by hard coal with an average calorific value of 23 MJ/kg. The nominal parameters, in conjunction with the range of values obtained from measurements during the experiment, are presented in Table 6.

Table 6. Characteristics of the WR-25 water-grate boiler: nominal and experimentally obtained values.

	Nominal values	Values during the experiment
Thermal power, MW	32	19 – 24
Efficiency, %	82	73 – 81
Boiler feed water temperature, °C	70	65 – 72
Heating water temperature, °C	150	115 – 128
Flue gas volume downstream of the boiler, m³/h	53 000	23 000 – 47 000



Fig. 4. The examined section of the flue gas duct on a satellite map of the heating plant (own work, based on geoportal.gov.pl).

Figure 4 presents a satellite map of the analysed section of the flue gas duct located downstream of the dust extraction system. The system in question connects to the ducts from the other boilers operating within the plant just before entering the chimney.

In Figure 5, the measurement stations are indicated. The initial measurement station is situated 1.3 m posterior to the elbow. The measurement holes are located at an interval of 7.04 m. In the section of the duct that was analysed, there was an absence of fully developed flow in the cross-section, which can be attributed to the configuration of the duct. Bejan [27] asserts that fully developed turbulent flow occurs after approximately 10 equivalent diameters have passed behind the disturbance. In this case, such a section would have to start after approximately 14 m. The analysed flue gas duct did not contain any such section.

The measurements were taken a few days after the boiler was started up, when thermal equilibrium had been achieved.

Heat flux sensors were utilised to assess heat losses. The components were installed on the bottom and upper walls of the duct, and situated within the cross-section of the measuring opening, with an approximate distance of 60 cm from the duct axis. The installation of the components along the duct axis was rendered infeasible by the presence of metal sheet joints. The sensor was positioned on the side wall in a location exhibiting uniform insulation quality. This location was selected on the ba-

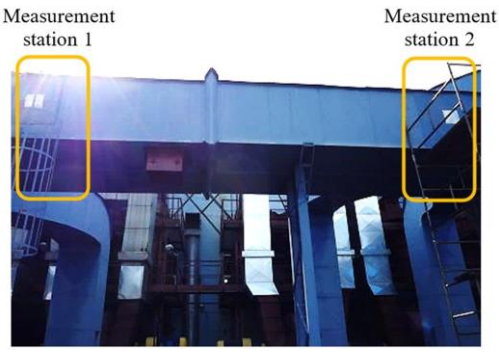


Fig. 5. Measurement stations on the tested section of the duct (own archive).

sis of thermal imaging tests, with the sensor placed at a distance of approximately 60 cm from the measuring station.

The flue gas temperature was measured using PT100 thermometric resistors. During the measurements, the surrounding air humidity was measured using a capacitive humidity probe, and the current weather conditions (cloud cover, precipitation) were recorded. The device was located at the duct support, which was positioned approximately in the middle of the duct section that had been selected for measurement. This section was situated in a location that was sheltered from wind and sun.

The calculations furthermore incorporated the readings of instruments that had been permanently installed in the heating plant, including the mass of coal fed to the boiler, the excess air coefficient, the CO_2 and O_2 content in the flue gas, the flue gas velocity, the wind azimuth and velocity, the ambient air temperature, as well as the air temperature in direct sunlight.

The measurement of air humidity and flue gas temperature was conducted at an interval of 10 s, while the electromotive force measurements from heat flux sensors were recorded at a frequency of 2 min. The readings from the heating plant instruments were recorded as 10-min. averages. The measurement data, which had been prepared for the purpose of validating the numerical model, were grouped into 10-min averages.

3.2. Experimental results and discussion

During the course of the measurements, considerable fluctuations in the heat flux sensor for the upper wall were observed. A rigorous examination of the relationship between the heat flux density on the subject wall and the ambient air temperature in direct sunlight revealed a discernible correlation. Subsequent analysis indicated that this correlation was attributed to the impact of solar radiation, which exhibited a marked intensity that was significantly higher than that observed in other areas. Pearson's correlation coefficient for the heat flux density of the upper wall with the air temperature in direct sunlight was 0.9. Consequently, the outcomes derived from the bottom and side walls (Pearson's coefficients of 0.6 and 0.1, respectively) were selected for validation.

The measurement series were analysed in terms of wind pressure on the duct. The location of the heating plant building is such that it is in close proximity to the duct. The building functions as a barrier to south and west winds. The wind velocity value was obtained from the heating plant's instruments; consequently, it was not measured exactly at the duct location. Following the consideration of wind azimuth readings, as determined by the data measured at the heating plant, the validation was conducted exclusively on those measurements during which the wind was not blowing from the direction of the building.

Figure 6 shows the results of the heat flux density measurements together with the total uncertainty bars. The graph also shows the values of ambient air temperature, air temperature in direct sunlight, wind velocity and the temperature difference between the flue gas and the air. The values are connected by lines to make the profiles of the variables easier to read. During measurements, the heat losses obtained from the bottom wall ranged from 28 to 37 W/m^2, and from 29 to 44 W/m^2 from the side wall. In each measurement series, the total uncertainty of the heat flux

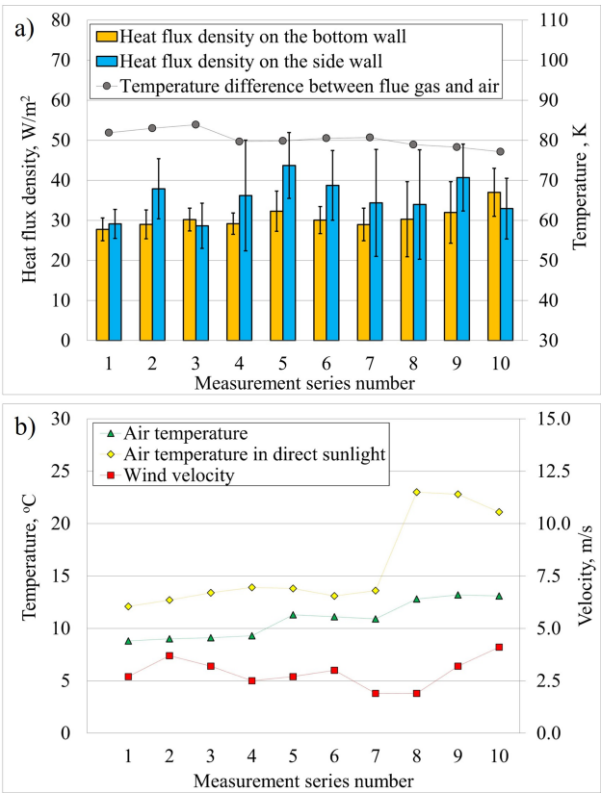


Fig. 6. Experimental results for heat flux density (a) and weather parameters (b).

density from the bottom wall was lower than that of the side wall. For the bottom wall, the total measurement uncertainty is clearly greater where solar radiation heats the flue gas duct walls intensively.

The obtained heat flux density profiles show a negative correlation with the temperature difference between the flue gases and the air. This is due to the simultaneous influence of weather phenomena, such as solar radiation and wind velocity, on the temperature of the duct wall (Pearson's coefficient is –0.7 for the bottom wall and –0.4 for the side wall). The measured electromotive force increases as the temperature of the duct wall increases. This temperature increase is due not only to the temperature difference between the media on both sides of the wall, but also to solar radiation and conduction of absorbed heat along the wall. The incorrect correlation is clearly visible in measurements 8–10. During these measurements, a significant rise in heat losses was observed despite a decrease in the temperature difference between the flue gas and the air. This decrease should result in decreased heat losses, yet a negative Pearson coefficient was obtained.

As shown above, measuring heat losses with heat flux sensors, which have the advantage of not requiring significant interference with the existing installation, is also subject to considerable uncertainty due to current weather conditions, particularly those resulting from the intensity of solar radiation and wind gusts. Nevertheless, bearing these limitations in mind and accounting for measurement uncertainty, the test results were used to validate the numerical model of heat exchange in the heating plant's flue gas duct.

4. Simulation results and model validation

All simulations were considered to have converged because the behaviour equations reached the assumed residual value, and the heat flux density stabilised below 0.01% in at least the last 100 iterations in all simulations.

Figure 7 shows the results of the numerical simulation compared with the results of the experimental study, together with the total uncertainty. In the case of the bottom wall, the measuring sensor was mounted approximately 60 cm from the duct axis in the windward direction, while the simulation result includes the average heat flux density across the entire surface.

The consistency of the numerical calculations with the experimental data was analysed using two methods. The first

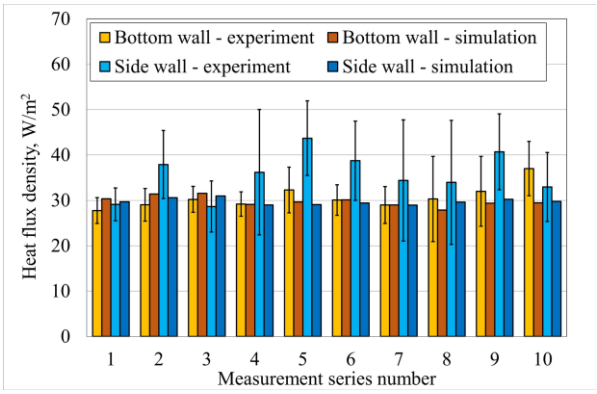


Fig. 7. Comparison of simulation and experimental results.

method leads to the determination of the key validation metric, U_V. This method was described by Stern et al. [22], for example. It takes into account errors and uncertainties in both data categories to assess the level of validation. The second method is used when there is insufficient data to calculate the aforementioned errors and uncertainties, and it calculates the relative coefficient of variation of the root mean square error CV(RMSE). This method was employed to compare the results with those in the literature, even though the data were available. No publications describing the validation of numerical models by an experiment conducted in the presence of variable weather conditions based on the first method were found. The second method, on the other hand, is used in publications concerning the validation of analyses of phenomena on external building elements.

In the method used to determine the validation metric U_V, the comparison error E should not exceed the metric itself, indicating good agreement between the results obtained in the numerical simulation and the experiment on the actual object:

$$E = |\bar{D} - S_{\text{num}}|, \tag{19}$$

$$U_V{}^2 = U_D{}^2 + U_{SPD}{}^2 + U_{SN}{}^2, \tag{20}$$

where: E – comparison error, $\bar{D}$ – mean measured value, U_V – process validation metric, U_D – uncertainty of experimental values, U_{SPD} – uncertainty due to input data (e.g. material data), U_{SN} – uncertainty of numerical simulation.

The uncertainty of the values obtained in the experiment (U_D) was taken as the expanded uncertainty according to Eqs. (21)–(25). The confidence level p was taken to be 95%, and the number of degrees of freedom was taken to be 4. Therefore, the Student's t-distribution critical value was 2.7765.

$$U_D = t_p(\nu_{\text{dof}})u_{c,i}, \tag{21}$$

$$\nu_{\text{dof}} = n - 1, \tag{22}$$

$$u_{c,i} = \sqrt{u_a^2 + u_b^2}, \tag{23}$$

$$u_a = \frac{s}{\sqrt{n}}, \tag{24}$$

$$s = \sqrt{\frac{1}{n-1}\sum_{i=1}^{n}[D_i - \bar{D}]^2}, \tag{25}$$

where: $t_p(\nu_{\text{dof}})$ – Student's t-distribution coefficient for confidence level p and degrees of freedom ν_{dof}, $u_{c,i}$ – combined standard uncertainty for measurement number i, n – number of measurements in a series, u_a – type A standard uncertainty, u_b – systematic standard uncertainty, s – standard deviation, D_i – i-th measured value.

Errors resulting from the use of the input data (U_{SPD}) were determined based on the assumption that heat losses mainly depend on the temperature difference between flue gas and air, as well as the insulation thickness and thermal conductivity coefficient. According to Żarnowski and Wiśniewski [29], the thermal conductivity coefficient of mineral wool insulation does not change significantly over time; therefore, this parameter was omitted in the analysis of uncertainties resulting from the use of input data. The heat flux density is directly proportional to the temperature difference between the flue gases and the air, and inversely proportional to the thickness of the insulation:

$$Q \sim \frac{\Delta T}{\delta}, \tag{26}$$

where: ΔT – temperature difference between flue gas and air, δ – insulation thickness.

The uncertainty in the insulation thickness was assumed to be 3%, due to settlement, in accordance with the results of the study by Nagy et al. [30]. In the absence of measurement uncertainty for the air temperature, which was measured by devices permanently installed in the heating plant, the total uncertainties of the temperature difference were determined only on the basis of the systematic and random errors of the flue gas temperature measurements. A value of approximately 1% was obtained for all measurements. The total uncertainty of the heat flux density resulting from the use of input data was determined in accordance with the law of uncertainty propagation, assuming a linear relationship between the temperature difference, insulation thickness and heat losses.

The GCI obtained in the grid independence analysis was adopted as the uncertainty of the numerical simulation (U_{SN}).

When analysing the compliance of the numerical simulation results with the measurement data, a second method was employed to determine CV(RMSE) according to the following equations:

$$\mathrm{CV(RMSE)} = \frac{\mathrm{RMSE}}{\bar{D}} 100, \tag{27}$$

$$\mathrm{RMSE} = \sqrt{\frac{1}{n}\sum_{i=1}^{n}(S_{\mathrm{num}} - D_i)^2}, \tag{28}$$

where: CV(RMSE) – relative root mean square error, RMSE – root mean square error, i – measurement number in a single measurement series, n – number of measurements in a single measurement series.

The validation results are presented in Fig. 8. With the exception of measurements 4 and 6 for the side wall, the comparison error E does not exceed the validation metric U_V, proving that the numerical simulation results are consistent with the measurements within the accepted uncertainty limits. CV(RMSE) ranged from 7% to 22% for the bottom wall and from 9% to 36% for the side wall. These high percentage values result from the low absolute value of the measured heat flux and the variability of weather conditions during the experiment, which were averaged for each 10-min measurement series. Similar levels can be found in the literature. For example, Demanega et al. [31] calculated CV(RMSE) for heat losses from a building's window surface. The measurements were taken on cloudless days using heat flux sensors. Depending on the numerical model selected, the relative root mean square error ranged from 16% to 38%.

Figure 9 shows the heat flux density distributions across the bottom and side walls of the duct. It should be noted that the extreme values observed during the experiment do not coincide with the numerical extremes (see Fig. 7). Therefore, Fig. 9 presents the simulation results for the bottom wall measurement series, corresponding to both the numerical and experimental extremes (the latter being intermediate in the simulation). For all illustrated series, heat flux density on the bottom wall on the windward side is significantly lower. Regarding the side wall, a single simulation result is presented (for the series with the highest experimental heat flux density), which is sufficient to demonstrate that the heat flux density is distributed more evenly along its surface. The characteristic profile shape on the bottom wall remains consistent regardless of the heat flux density magnitude (covering maximum, minimum and intermediate values). It confirms the robustness of the model in reproducibly capturing the heat transfer patterns across all measurement series.

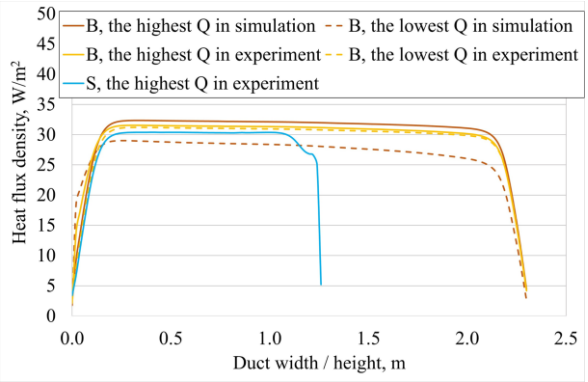


Fig. 9. Heat flux density (Q) across the bottom (B) and side (S) wall of the duct (wind reversal on the bottom wall opposite to the horizontal axis reversal).

The heat flux density distributions illustrate the result from the velocity field and wind streamlines shown in Fig. 10. After flowing into a channel-shaped obstacle, the air stream separates and changes direction, forming vortices that lead to a local decrease in convection intensity. In turn, the intensity of convection affects the air temperature around the duct, the field of which is presented in Fig. 11. Both figures refer to the series with the highest heat flux density, which was obtained in simulations on the bottom wall.

The nature of the wind flow described affects the variation in heat losses on the surface of individual walls and between them. Figure 12 illustrates the temperature field on the outer sur-

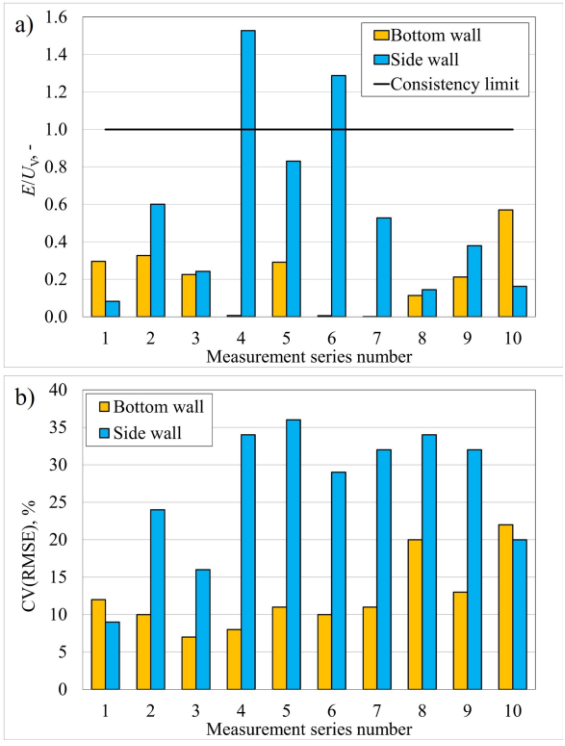


Fig. 8. Validation consistency: a) validation metric (E/U_v), and b) relative root mean square error (CV(RMSE)).

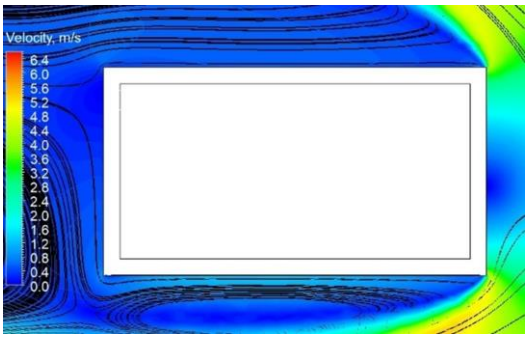


Fig. 10. Velocity field and air flow streamlines around the duct; right side of the illustration corresponds to the windward side (ANSYS CFD-Post 2024 R2).

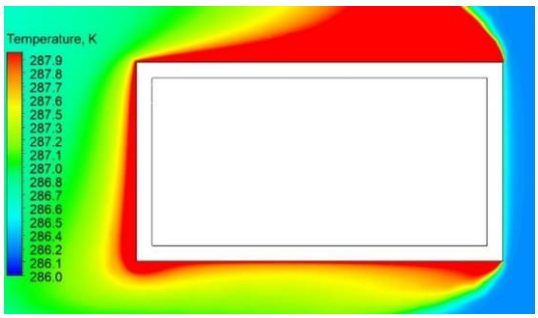


Fig. 11. Air temperature field around the duct; right side of the illustration corresponds to the windward side (ANSYS CFD-Post 2024 R2).

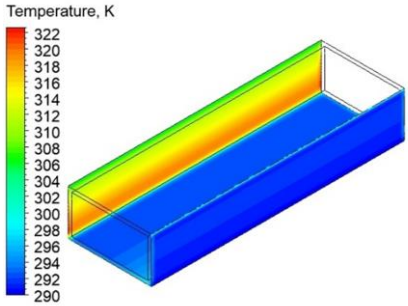


Fig. 12. Temperature field on the duct walls; right side of the illustration corresponds to the windward side (ANSYS CFD-Post 2024 R2).

faces of the bottom and side walls. As can be seen from the difference in surface temperature, heat losses on the leeward side of the side walls are lower than on the windward side. The side walls follow the typical trend of lower temperatures on the windward side. For the bottom wall, the temperature is higher on the windward side than on the leeward side. This phenomenon is attributed to the separation of the air stream at the leading edge and the formation of local flow disturbances, which reduce local heat transfer efficiency despite the windward orientation.

Figure 13 shows the temperature field in the flue gas duct insulation. On the windward and bottom sides of the duct, the temperature of the insulation in contact with the outside air is significantly lower than on the top wall and leeward side.



Fig. 13. Temperature field in the duct insulation; right side of the illustration corresponds to the windward side (ANSYS CFD-Post 2024 R2).

5. Summary and conclusions

The article describes the process of validating a numerical model of the heat exchange between the flue gas flowing through the horizontal, rectangular duct of a heating plant and the surrounding air. The model considers the effects of wind and solar radiation. The computational domain includes both the duct and the surrounding airspace. This was defined based on guidelines for numerical simulations for buildings.

The validation experiment was conducted under variable weather conditions, including cloud cover, air temperature and wind velocity.

Validation was carried out for the bottom and side walls of the duct. This was analysed in two ways. The uncertainty-based method showed that, for almost all measurement series, the comparison error did not exceed the validation metric. In contrast, the second method, which did not take uncertainty into account, produced fairly high values of the relative mean square error coefficient: up to 22% for the bottom wall and 36% for the side wall. However, these values are comparable to those reported in the literature, describing the experimental validation of models of external building elements exposed to rapidly changing weather conditions. It should be noted that heat losses measured with heat flux sensors are subject to high error due to rapidly changing intensity of solar radiation, wind velocity and wind direction. Nevertheless, they are a research tool that interferes very little with the existing installation.

The results obtained indicate that the developed numerical model can be used to analyse flue gas duct modernisation in order to reduce heat losses from flue gases flowing through the duct in terms of the bottom and side walls. These analyses may include the actual sunlight conditions, as well as the wind velocity and temperatures at a given location.

To summarise, the following specific conclusions were drawn from the research:

– the upper wall was excluded from the validation process due to extreme heat flux fluctuations caused by direct solar exposure. A very high Pearson correlation coefficient (0.9) between the heat flux density and air temperature in direct sunlight confirmed that solar radiation dominated the thermal signal, making these measurements unsuitable for reliable numerical comparison;
– the validation showed a significantly higher discrepancy for the side walls compared to the bottom wall. This is attributed to the high sensitivity of heat flux sensors to rapid solar radiation changes, which introduces measurement uncertainty that affects the final validation results for those surfaces;
– the numerical model, utilising the k–ω SST turbulence model, correctly captured the well-known phenomenon of flow separation at the leading edge of the duct. The resulting vortices explain the specific heat flux density profile on the bottom wall observed in the simulations;
– the numerical model demonstrated robustness, as the characteristic shape of the heat flux density profile on the bottom wall remained consistent across measurement series,

regardless of the heat flux density magnitude. This confirms that the model reproducibly captures the underlying heat transfer patterns under boundary conditions observed during the experiment.

The study leads to the following general conclusions:

– the use of heat flux sensors, while subject to environmental interference, is a non-invasive diagnostic method for large-scale energy systems where operational continuity is required;
– the application of an uncertainty-based validation approach (based on the E/U_V ratio) is recommended for evaluating industrial models in uncontrolled environments (changing weather conditions), as it provides a more objective measure of accuracy than the standard error coefficient CV(RMSE), by accounting for experimental uncertainty;
– the developed numerical model offers an important step towards making thermal insulation of ducts in district heating infrastructure adaptable to individual location and environmental conditions.

References

[1] Statistics Poland. (2026). *Energy consumption in households in 2024*. Statistics Poland; Statistical Office in Rzeszów (in Polish).

[2] Department of Electricity and Heat Markets of the Energy Regulatory Office (ERO) in cooperation with the ERO Branch Offices. (2025). *Heat energy in figures – 2024*. Energy Regulatory Office (in Polish).

[3] Zhang, Q., Yi, H., Yu, Z., Gao, J., Wang, X., Linc, H., & Shen, B. (2018). Energy-exergy analysis and energy efficiency improvement of coal-fired industrial boilers based on thermal test data. *Applied Thermal Engineering*, 144, 614–627. doi: 10.1016/j.applthermaleng.2018.08.069

[4] Matas, R., Kňourek, J., & Novák, M. (2024). Analysis and validation of CFD simulations for flow in the large power station flue gas system. *EPJ Web of Conferences*, 299, 01025. doi: 10.1051/epjconf/202429901025

[5] Chen, G.Y., Yuan, G.D., Zheng, L.Y., Guo, X.K., Lv, A.L., Geng, Y., Cui, Z.Z., Long, H., Yan, B.B., Ni, Y., & Long, Z.W. (2013). Analysis of flow in power plant flue via Fluent simulations. *Advanced Materials Research*, 838–841, 2630–2633. doi: 10.4028/www.scientific.net/AMR.838-841. 2630

[6] El-Shafie, M. (2022). Theoretical and experimental analysis of temperature decay along an industrial chimney using analytical and k-ω turbulence models. *Case Studies in Chemical and Environmental Engineering*, 6, 100264. doi: 10.1016/j.cscee.2022.100264

[7] Huang, W., Xu, Q., Zhao, B., Lv, Q., & Wang, G. (2025). Urban multi-scale building energy modelling (BEM) and computational fluid dynamics (CFD) integration: Tools, strategies and accuracy for energy microclimate analysis. *Journal of Building Engineering*, 103, 112041. doi: 10.1016/j.jobe.2025.112041

[8] Franke, J., Hellsten, A., Schlünzen, H., & Carissimo, B. (2007). *Best practice guideline for the CFD simulation of flows in the urban environment*. COST Action 732: Quality Assurance and Improvement of Microscale Meteorological Models.

[9] Tominaga, Y., Mochida, A., Yoshie, R., Kataoka, H., Nozue, T., Yoshikawa, M., & Shirasawa, T. (2008). AIJ guidelines for practical applications of CFD to pedestrian wind environment around buildings. *Journal of Wind Engineering and Industrial Aerodynamics*, 96(10–11), 1749–1761. doi: 10.1016/j.jweia.2008.02.058

[10] Bejan, A. (2013). External natural convection. In *Convection heat transfer* (pp. 168–232). Wiley.

[11] Hamisu, M.T., Jamil, M.M., Umar, S.U., Sa'ad, A. (2019). Numerical study of flow in asymmetric 2D plane diffusers with different inlet channel lengths. *CFD Letters*, 11(5), 1–21.

[12] Menter, F.R. (1994). Two-equation eddy-viscosity turbulence models for engineering applications. *AIAA Journal*, 32(8), 1598–160521. doi: 10.2514/3.12149

[13] Ansys. (2024). *Ansys Fluent Theory Guide* (Release 2024 R2). Ansys, Inc.

[14] Carvalho, H.D.R., Chang, B., McInnes, K.J., Heilman, J.L., Wherley, B., & Aitkenhead-Peterson, J.A. (2021). Energy balance and temperature regime of different materials used in urban landscaping. *Urban Climate*, 37, 100854. doi: 10.1016/j.uclim.2021.100854

[15] Yu, B., Chen, Z., Shang, P. & Yang, J. (2008). Study on the influence of albedo on building heat environment in a year-round. *Energy and Buildings*, 40(5), 945–951. doi: 10.1016/j.enbuild.2007.07.009

[16] Liu, H., Chen, Z., Chen, B., Xiao, X. & Wang, X. (2014). Studies on the temperature distribution of steel plates with different paints under solar radiation. *Applied Thermal Engineering*, 71(1), 342–354. doi: 10.1016/j.applthermaleng.2014.06.031

[17] Bergman, T.L. & Lavine, A.S. (2017). *Fundamentals of Heat and Mass Transfer* (8th ed.). Wiley.

[18] Schlichting, H., & Gersten, K. (2017). Fundamentals of boundary–layer theory. In *Boundary-Layer Theory* (pp. 29–49). Springer. doi: 10.1007/978-3-662-52919-5

[19] Duan, Z., Yovanovich, M.M., & Muzychka, Y.S. (2012). Pressure drop for fully developed turbulent flow in circular and noncircular ducts. *Journal of Fluids Engineering*, 134(6), 061201. doi: 10.1115/1.4006861

[20] Celik, I.B., Ghia, U., Roache, P.J., Freitas, C.J., Coleman, H., & Raad, P.E. (2008). Procedure for estimating and reporting uncertainty in s due to discretisation in CFD applications. *Journal of Fluids Engineering*, 130(7), 078001. doi: 10.1115/1.2960953

[21] Roache, P.J. (1994). Perspective: A method for uniform reporting of grid refinement studies. *Journal of Fluids Engineering*, 116(3), 405–413. doi: 10.1115/1.2910291

[22] Polski Komitet Normalizacyjny. (2019). *PN-EN 13384-1+A1: 2019-07. Chimneys – Methods for thermal and flow calculations – Part 1: Chimneys connected to a single heating appliance*. PKN (in Polish).

[23] Polski Komitet Normalizacyjny. (2004). *PN-EN 13384-1:2004. Chimneys – Methods of thermal and flow calculations – Part 1: Chimneys connected to a single furnace*. PKN (in Polish).

[24] Kruczek, S. (2001). *Boilers. Designs and calculations*. Oficyna Wydawnicza Politechniki Wrocławskiej (in Polish).

[25] Oleśkowicz-Popiel, C., & Wojtkowiak, J. (1997). Formulas approximating the physical properties of air. *Ciepłownictwo, Ogrzewnictwo, Wentylacja*, 28(3), 324 (in Polish).

[26] Russo, F., & Basse, N.T. (2016). Scaling of turbulence intensity for low-speed flow in smooth pipes. *Flow Measurement and Instrumentation*, 52, 101–114. doi: 10.1016/j.flowmeasinst.2016.09.012

[27] Bejan, A. (2013). Turbulent duct flow. In *Convection heat transfer* (pp. 369–397). Wiley.

[28] Stern, F., Wilson, V.R., Coleman, W.H., & Paterson, G.E. (2001). Comprehensive approach to verification and validation of CFD simulations—Part 1: Methodology and procedures. *Journal of Fluids Engineering*, 123(4), 792–802. doi: 10.1115/1.1412235

[29] Żarnowski, T., & Wiśniewski, T. (2014). Ageing of fibrous insulation used in heating and power engineering. *Instal*, 12, 21–27 (in Polish).

[30] Nagy, B., Nemes, R., & Simon, T. (2020). Effect of built-in mineral wool insulation durability on its thermal and mechanical performance. *Journal of Thermal Analysis and Calorimetry,* 139, 169–181. doi: 10.1007/s10973-019-08384-5

[31] Demanega, I., De Michele, G., Pernigotto, G., Gasparella, A., & Avesani, S. (2023). Development and experimental validation of a CFD model for the thermal behaviour assessment of complex fenestration systems. *Journal of Building Engineering,* 68, 106150. doi: 10.1016/j.jobe.2023.106150

Co-published by
Institute of Fluid-Flow Machinery
Polish Academy of Sciences
Committee on Thermodynamics and Combustion
Polish Academy of Sciences

Copyright©2026 by the Authors under licence CC BY-NC-ND 4.0

http://www.imp.gda.pl/archives-of-thermodynamics/

Experimental investigation of flow boiling heat transfer in a minichannel heat exchanger with countercurrent hot and cold fluid circuits

Kinga Strąk[a*], Dariusz Strąk[b]

[a]Kielce University of Technology, al. Tysiąclecia Państwa Polskiego 7, Kielce 25-314, Poland
[b]Independent Researcher, ul. Zagórska 72/1, Kielce 25-362, Poland
[*]Corresponding author email: kzietala@tu.kielce.pl

Received: 01.03.2026; revised: 12.06.2026; accepted: 30.06.2026

Abstract

This study presents a novel experimental investigation of flow boiling heat transfer in a minichannel module with simultaneous hot and cold fluid circuits. The novelty of the work lies in the analysis of a multilayer minichannel configuration with interacting hot and cold working fluids, enabling detailed evaluation of interfacial heat transfer mechanisms. Experiments were conducted in two groups of six parallel minichannels with rectangular cross-sections (1.5 mm depth, 20 mm width, and 140 mm length, hydraulic diameter 2.77 mm), heated by a 1000 W halogen lamp. The system was tested under steady laminar countercurrent flow conditions at a heat flux of 6000 W/m^2, with FC-72 fluid and distilled water mass flow rates of 0.006 kg/s and 0.0087 kg/s, respectively, and an inclination angle of 165°. The temperature of the outer copper plate surface was measured using an infrared camera. Local heat transfer coefficients were calculated using a one-dimensional computational approach at the heated plate – FC-72, FC-72 – central plate, central plate – water and water – closing plate interfaces. The results show the distributions of temperature and heat transfer coefficients along the channel length. An increase in the heat transfer coefficient was observed at the heated plate – FC-72 interface, whereas decreasing values were found at the remaining interfaces. The one-dimensional approach was validated using computational fluid dynamics simulations, showing a maximum discrepancy of 26.6% at the heated plate – FC-72 interface across all minichannels. These results offer insight into interfacial heat transfer in multilayer minichannel systems and support the design of compact, high-performance devices.

Keywords: Countercurrent flow; Flow boiling; Heat transfer coefficient; Minichannel; Working fluids

Vol. 47(2026), No. 3, 187–197; doi: 10.24425/ather.2026.7517

Cite this manuscript as: Strąk, K., & Strąk, D. (2026). Experimental investigation of flow boiling heat transfer in a minichannel heat exchanger with countercurrent hot and cold fluid circuits. *Archives of Thermodynamics*, 47(3), 187–197.

1. Introduction

Modern technological demands related to efficient thermal energy management and the intensification of heat transfer processes necessitate the optimisation of heat exchanger design. Small-sized heat exchangers represent a promising solution, as they provide a large heat transfer surface area while maintaining low mass and compact dimensions. Owing to their enhanced thermal efficiency and reduced size, such structures are widely used in electronic cooling systems, photovoltaic/thermal (PV/T) solar modules and server cooling applications. Advances in microchannel technology have led to the development of high-performance liquid-cooling devices that offer significantly higher heat transfer coefficients than conventional air-cooling systems and enabling further system miniaturisation.

The development of hybrid PV/T solar systems and the continuous improvement of their efficiency make effective thermal management a critical issue. Abdelrazik et al. [1] reviewed recent advances in PV/T technology, including various

Nomenclature

A – surface area, m^2
c_p – specific heat, J/(kg K)
d_h – hydraulic diameter, m
E – the radiation intensity for the copper heated plate, W/m^2
k – overall heat transfer coefficient, $W/(m^2 K)$
L – length of the minichannel, m
MRE – mean relative error
p – pressure, Pa
q – heat flux density, W/m^2
Q – heat flux, W
Q_m – mass flow rate, kg/s
Re – Reynolds number
T – temperature, K
x – coordinates in the direction of flow, m

Greek symbols

α – heat transfer coefficient, $W/(m^2 K)$
δ – thickness, depth, m
Δ – difference
ε – emissivity coefficient
λ – thermal conductivity, W/(m K)
ν – kinematic viscosity, m^2/s
ρ – density, kg/m^3
σ – surface tension, N/m

Subscripts and Superscripts

c – closing plate
Cu – copper plate
f – fluid
FC – FC-72 fluid
H – heated plate
in – inlet
IR – infrared camera
lin – linear
TC – thermocouple
out – outlet
s – ambient
w – distilled water

Abbreviations and Acronyms

AM – additive manufacturing
1D – one-dimensional
CFD – computational fluid dynamics
CHF – critical heat flux
GCI – grid convergence index
HTC – heat transfer coefficient
MCHS– microchannel heat sink
PCM – phase change material
PPMC– porous parallel minichannel
PV/T – photovoltaic/thermal
TIM – thermal interface material
VOF – volume of fluid

heat exchanger design solutions, and the application of nanofluids and phase change nanomaterials (nanoPCM) as alternatives to conventional cooling and thermal energy storage methods. The modified PV/T system reduced PV cell temperature by 13°C, increased electrical efficiency from 10.5% to 11.9%, and improved thermal efficiency by approximately 9% compared to a conventional PV/T system. These findings highlight the effectiveness of enhanced cooling and optimised heat collection techniques. In [2], Dubey and Tiwari presented a mathematical model for a flat-plate collector, and the calculated results were compared with experimental data. The study demonstrated a significant increase in instantaneous efficiency, from 33% to 64%, resulting from an increase in the glazing area.

During research on flow boiling heat transfer, systems in which the working fluid flows through multiple parallel channels of small dimensions are of particular importance, as they enable an increase in heat flux density while simultaneously reducing the volume of the heat exchanger, whether using mini- [3] or microchannels [3,4]. Kandlikar [3] highlighted the importance of the configuration of single- and multichannel heat exchangers in determining heat transfer and pressure drop. Flow boiling in mini- and microchannels is characterised by isolated bubble, slug and annular flow regimes. In microchannels, nucleating bubbles as small as 10–20 μm have been observed, while surface tension has been found to strongly influence flow behaviour. Significant pressure-drop fluctuations and flow reversals occur in multichannel evaporators. Heat transfer can be approximated using conventional flow boiling correlations; however, flow instabilities and pressure drop oscillations remain insufficiently understood. Small diameter evaporators generally operate with higher acceptable pressure drops to achieve enhanced heat transfer performance. The intensification of flow boiling is also influenced by the available heat transfer area, fluid stagnation zones, channel distribution and microchannel topology, as reported in the work of Lu et al. [4]. Optimisation of microchannel heat sink (MCHS) geometry significantly improves thermal performance. Biomimetic channel designs maintain temperature differences below 2°C, while ribbed microchannels enhance heat transfer by about 50% compared to smooth rectangular channels. Triangular/trapezoidal cross-sections and triangular cavity structures exhibit the best thermal characteristics. Additionally, diamond/copper composites and nanofluids are promising solutions for further heat transfer enhancement. Harirchian and Garimella [5] presented the characteristics of two-phase flow structures and the enhancement of flow boiling heat transfer of dielectric liquid FC-77 in parallel microchannels with widths ranging from 100 μm to 5850 μm. Experimental studies showed that channels of widths ≥ 400 μm exhibit conventional nucleate boiling over a wide range of heat fluxes. In contrast, smaller channels (< 400 μm) suppress wall bubble nucleation at relatively low heat fluxes, indicating a strong influence of channel size on flow boiling regimes and regime transitions. Mihai [6] discussed the analysis of the cooling process in micro- and nanochannels using a one-dimensional (1D) mathematical approach. The 1D approach simplifies analysis and is useful for determining effective heat transfer coefficients. The CPU cooling systems showed that efficient heat removal depends strongly on channel geometry and the thermal interface material (TIM). Microscope analyses revealed micro/nanochannels in the TIM with widths of 0.01–0.05 μm and depths up to 1000 Å, which

can disrupt heat transfer and contribute to overheating. Experimental studies also identified thermal expansion ('pump-out' effect) at the CPU–cooler interface, while surface roughness remained largely unchanged with increasing temperature, indicating good thermal stability of the TIM. Studies reported in the article by Prończuk and Krzanowska [7] on a shell-and-tube heat exchanger with a minichannel system of 0.8 mm internal diameter confirmed high heat transfer efficiency and highlighted the importance of precise pressure drop measurements. The transition from laminar to transitional flow was identified at a critical Reynolds number of Re = 1160. The authors developed a correlation for the tested heat exchanger, which showed good agreement with both the experimental data and correlations available in the literature. In contrast, Lan et al. [8] presented experimental studies of boiling heat transfer in a minichannel heat sink equipped with twisted tapes inducing swirling flow. The optimal configuration (twist ratio R = 3, tape length = 150 mm) reduced the wall superheat required for boiling onset by 34.4%, increased the heat transfer coefficient by up to 80.9%, and decreased inlet pressure fluctuations by 44.4% compared with a plain minichannel. Additionally, longer twisted tapes generated stronger swirl flow and more effective heat transfer enhancement. Ye et al. [9] presented studies on flow boiling heat transfer of R134a refrigerant in open minichannels, both ordinary and etched, at mass fluxes of 60.5–187.4 kg/(m^2 s) and heat fluxes up to 151 kW/m^2. The authors observed that surfaces with high nucleation site density exhibit the strongest hysteresis effect, leading to up to a 120% increase in the average heat transfer coefficient due to sequential activation of nucleation sites with increasing heat flux. Hysteresis is reduced in channels with limited nucleation sites or vapour backflow, and is influenced by inlet subcooling and mass flow rate. In the subsequent work, Yaghoubi et al. [10] analysed various geometric configurations of channels with rectangular side-wall cavities to enhance the R141b flow boiling heat transfer. The introduction of these cavities led to a six-fold increase in the heat transfer coefficient compared to a plain channel. The cavities act as nucleation sites, reducing the onset of boiling and enhancing heat transfer in bubbly flow. However, in slug flow and near outlet regions, they may reduce HTC (heat transfer coefficient) due to higher wall temperatures. Ye et al. [11] investigated minichannels produced by additive manufacturing (AM) with microengineered surfaces for R134a flow boiling. These channels achieved a 210% increase in heat transfer coefficient compared to conventionally machined channels, achieving values up to 54.9 kW/(m^2 K). Enhancement factors reached 2.5–3.0, confirming that engineered microstructures provide abundant nucleation sites and significantly improve boiling heat transfer performance. Another type of surface enhancement was applied in integrated server cooling circuits during HFE-7100 flow boiling by Shang et al. [12]. Radiators made of 6061 aluminium alloy with a hydraulic diameter of 2 mm were used, where etching created a porous parallel minichannel (PPMC) structure. Such porous surfaces acted as effective nucleation sites and significantly reduced wall temperature (the maximum wall-temperature reduction reached 2.39% at 181.4 kg/(m^2 s) and ~70 kW/m^2) during flow boiling. Titanium carbide nanowires with thicknesses of 4 μm and 12 μm were also employed to intensify flow boiling by Sun et al. [13]. The results showed that a nanowire surface of 12 μm thickness increased the heat transfer coefficient by 19.84% under single-phase flow, whereas a 4 μm nanowire surface increased the coefficient by 27.9% under two-phase flow conditions. Li et al. [14] examined flow stability during boiling in minichannels with phase-separated configurations using porous membranes for vapour–liquid separation. In tests with multiple-pore, phase-separated configurations, a 24.71% reduction in pressure drop was observed in two-phase flow compared to conventional poreless structures. Hsu et al. [15] employed minitubes with diameters of 30 mm and 10 mm, featuring hydrophilic and hydrophobic surfaces, to enhance thermal efficiency during flow boiling. The results showed that hydrophilic surfaces (5° contact angle) significantly improved heat transfer performance, while hydrophobic surfaces (150° contact angle) stabilised the vapour layer, reducing overall pressure drop to 698.4 Pa and minimising fluctuations.

Comprehensive reviews of the literature on heat transfer have been presented in studies [16,17]. Pereira et al. [16] summarised active pool-boiling enhancement techniques beyond surface modification, including fluid additives, external fields, mechanical interventions and thermal-geometric optimisation. These methods aim to improve the heat transfer coefficient, increase critical heat flux (CHF), and reduce boiling hysteresis. The review also highlights the lack of comprehensive datasets and standardised reporting, which limits the development of predictive models and practical cooling system designs. Etminan et al. [17] examined gas-liquid and liquid-liquid two-phase flows in microchannels, focusing on flow-regime transitions, liquid-film behaviour and pressure drop characteristics. The authors highlighted the lack of a universal flow-regime classification and emphasised the key role of liquid-film thickness and contact angle in determining flow patterns, pressure drop, and heat and mass transfer. Existing correlations for slug length, film thickness, and pressure drop are based on dimensionless numbers, flow rate ratios and thermophysical properties.

In the previous study [18], a comparison between one-dimensional and two-dimensional approaches for estimating the heat transfer coefficient was performed using the Trefftz method. The analysis was based on energy equations for the copper plate and FC-72, supported by appropriate boundary conditions. Experiments were conducted on a test module with two rectangular minichannels (1.5 mm×24 mm×240 mm). Although heat transfer in minichannel systems has been widely studied, few works combine infrared heat flux measurements with CFD (computational fluid dynamics) validation for separate hot and cold channel groups. In this study, the heat transfer coefficient was determined experimentally for 12 minichannels (six hot and six cold) using a 1D approach and validated based on STAR-CCM+ simulations under countercurrent flow conditions [19].

The available data for the considered configuration remain limited in the literature, which highlights the need for dedicated experimental and numerical analysis. The main novelties of this study include: (i) a redesigned test module with two groups of minichannels and copper plates replacing previous materials (e.g. glass, solar cells, Haynes-230), (ii) channel dimensions of

140 mm×20 mm×1.5 mm (d_h = 2.77 mm), (iii) heating of a copper plate using a 1000 W halogen lamp, (iv) experiments at heat flux of 6000 W/m^2 under countercurrent flow conditions at the hot channel ($Q_{m,FC}$ = 0.006 kg/s), cold channel ($Q_{m,W}$ = 0.0087 kg/s), and a 165° inclination, and (v) combined experimental, 1D analytical and CFD analysis of FC-72 refrigerant and distilled water flow in a steady-state multi-minichannel system.

This paper presents innovative experimental studies on flow boiling heat transfer of two working fluids: FC-72 in the hot minichannel circuit and distilled water in the cold minichannel circuit under subcooled boiling conditions. Temperature distributions of the copper heated plate, the central copper plate, and the working fluids were measured at the inlets and outlets of both minichannel circuits. Local heat transfer coefficients at the interfaces between each partition of the working fluid plate were calculated using a one-dimensional computational approach based on the experimental data. Previous studies on flow boiling in minichannels have predominantly focused on heat exchangers with a single working fluid circuit. However, data on the heat transfer coefficients of individual partitions, as well as studies employing minichannel arrays with two fluid circuits (additionally cooled with water), are lacking. The presented test module, featuring two countercurrent fluid circuits, has potential applications in cooling systems for high-performance computer processors.

2. Research stand and research procedure

2.1. Research stand

Figure 1 shows a schematic of the test rig with its main components. The experimental setup comprises a test module with a group of minichannels (1), magnetic circulation pumps (2a,2b), pressure transmitter (3), heat exchangers (4a,4b), filters (5a,5b), electromagnetic flow metres (6a,6b) and air separators (7a,7b). The primary flow circuits consist of two closed circulation loops for the working fluids: a low-boiling refrigerant FC-72 circuit (referred to as 'hot') and a distilled water circuit (referred to as 'cold'). The output of magnetic circulation pumps (type GZD.Q57.JDS-B380 (BLDC), MICROPUMP INC., USA) was regulated using three-phase electric inverters. The main components of the measurement data acquisition system include an infrared camera (8), a data acquisition station (9), and a personal computer (10). The heat source for the copper heated plate consisted of two halogen lamps (11), and the illuminance on the heated plate was measured using a luxmeter (12).

The key component of the test rig is the test module containing a group of rectangular minichannels (1), which share a common wall. This wall is a central copper plate with a thickness of 0.5 mm. The dimensions of a single minichannel (from each of the two groups of six minichannels) are 1.5 mm in depth, 20 mm in width, and 140 mm in length.

The outer walls of minichannels are formed by copper plates: a 3 mm thick heated plate and an outer plate, referred to as the module 'closing' plate, with a thickness of 0.5 mm.

Figure 2 shows the characteristic dimensions of the test module.

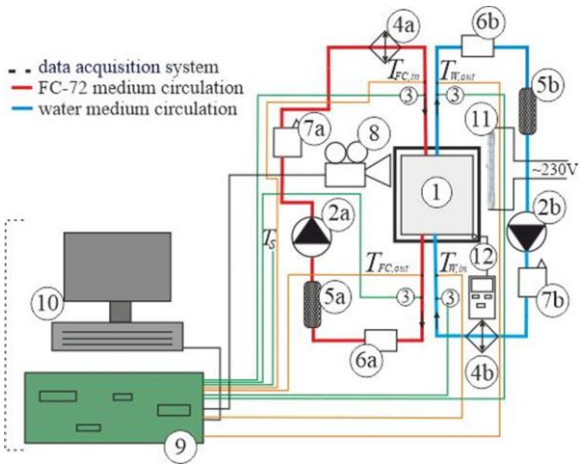


Fig. 1. Schematic of the test rig and its main components: 1 – test module, 2a, 2b – magnetic circulation pump, 3 – pressure transmitter, 4a, 4b – heat exchanger, 5a, 5b – filter, 6a, 6b–- electromagnetic flowmeter, 7a, 7b – air separator, 8 – infrared camera, 9 – data acquisition station, 10 – personal computer, 11 – halogen lamp, 12 – luxmeter.

In one group of six minichannels (referred to as 'hot'), the FC-72 refrigerant flows, and its outer wall is heated by halogen lamps (11 in Fig. 1). In the second group of six minichannels (referred to as 'cold'), distilled water flows in the countercurrent direction. After exiting the channels, both working fluids are cooled with tap water via heat exchangers (4a and 4b in Fig. 1).

The temperature of the heated outer surface of the copper plate was measured using a Flir E60 infrared camera. This surface, which is in direct contact with the surrounding environment, was coated with a thin layer of black paint with a known emissivity of 0.97. The temperature of the central copper plate was measured point-wise at its ends on the side where the FC-72 fluid flows, using K-type thermocouples. The temperatures of the working fluids (measured with K-type thermocouples) and the pressures (measured with pressure transmitters)

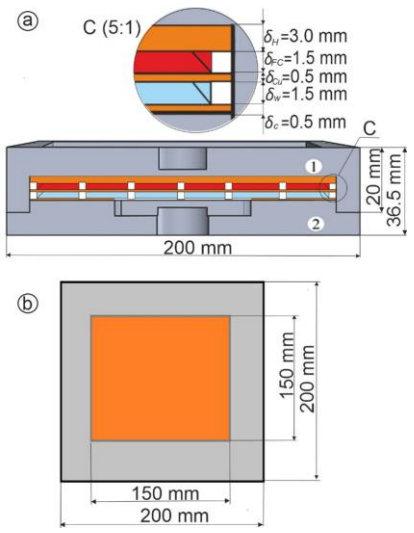


Fig. 2. Characteristic dimensions of the test module: a) cross section, b) view from the heated plate side.

were recorded at the inlet and outlet of each minichannel group.

Figure 3 shows views of the test rig and its main components. The basic physicochemical properties of the low-boiling FC-72 refrigerant and distilled water are summarised in Table 1. The specifications of the main components of the experimental apparatus, along with the maximum measurement errors, are provided in Table 2 and in [18,20,21].

2.2. Research procedure

Prior to the main experimental investigations, several working fluids, including HFE-649 and FC-72, were examined in the hot channel. FC-72 was ultimately selected owing to its higher boiling point, enhanced flow stability and greater volumetric heat capacity. An optimal channel configuration was subsequently defined, consisting of minichannels with a hydraulic diameter below 3 mm, with the channels distributed over the entire active area of the module. The working fluid flow rates were adjusted to ensure uniform coolant distribution across all channels and to achieve appropriate pressure conditions within the system. The higher the mass flow rates of the working fluids in both circuits, the greater the amount of heat removed from the solar cell, resulting in a reduction of the cell temperature. The imposed heat flux was specified to be representative of realistic operating conditions of the collector. An inclination angle of 165° was identified as optimal, representing a minor departure from the horizontal configuration. Optimisation-related issues can be found in the literature [22–24].

After degassing the two flow circuits (hot and cold) and stabilising the pressures and fluid flow rates, the heat flux supplied to the copper heated plate was gradually increased using two

Table 1. Basic physicochemical properties of the FC-72 refrigerant and distilled water.

Properties of the working fluids	FC-72 refrigerant	Distilled water
Boiling point temperature (K)	329	373
Critical temperature (K)	722	647
Kinematic viscosity (m^2/s)	0.38×10^3	1.00×10^3
Density (kg/m^3)	1680.0	998.2
Vapour pressure (Pa)	30.9×10^3	2.3×10^3
Specific heat (J/(kg K))	1100	4187
Thermal conductivity (W/(m·K))	0.057	0.591
Surface tension (N/m)	0.01	0.06

Table 2. Basic data of control and measurement equipment and sensors.

Parameter	Apparatus/ Measuring sensor	Type/ Model, Manufacturer	Measuring range	Measurement error
Heated plate temperature	Infrared camera	E60, Flir	20 – 120°C 0 – 650°C	±1 °C or ±1% in the range 0–120°C*
Temperature at the inlet/ outlet of FC-72 and distilled water; ambient temperature	Thermocouples	Type K (221 b), Czaki Thermo-Product	–40 – 375°C	1.5°C in the range –40–375°C*
Pressure at the channel inlet/ outlet, atmospheric pressure	Pressure transmitter	A-10, Wika	0 – 2.5 bar	0.5% of full scale*
Mass flow rate of fluids	Electromagnetic mass flowmeter	SM6004, IFM	6 – 1500 kg/s	±0.2% of reading*
Light intensity	Luxmeter	OHM-HD2102.1, Delta	0 – 1999.9 W/m^2	±0.02 W/m^2 or ± 2%*

*According to the manufacturer's specifications.

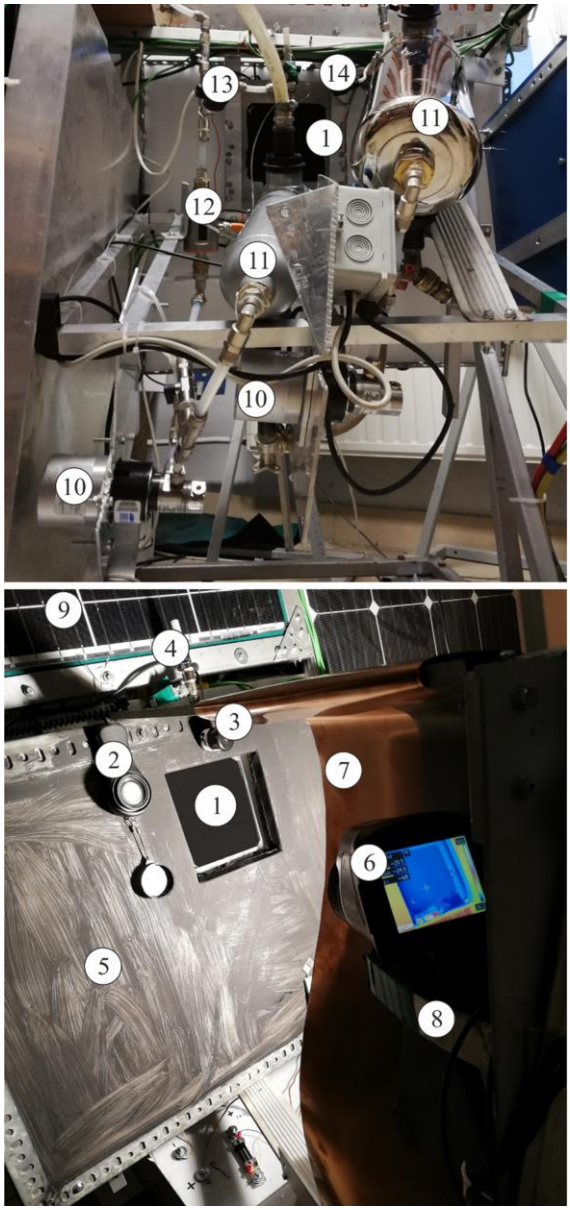


Fig. 3. Views of the test rig and its main components at the test module position angled 165° from the horizontal: 1 – test module, 2 – luxmeter, 3 – luxmeter probe, 4 – hot circuit vent valve, 5 – aluminium heat shield, 6 – infrared camera, 7 – copper heat shield, 8 – infrared camera mounting bracket, 9 – solar panel, 10 – magnetic circulation pump, 11 – heat exchangers, 12 – electromagnetic flowmeter, 13 and 14 – pressure transducers.

halogen lamps. The lamps had a total power of 2000 W and were positioned 330 mm from the surface of the heated plate, at a 90° angle. The infrared (IR) camera was positioned at a 30° angle on the thermal shield on the left side of the test module. The experiments were conducted under steady-state conditions for 3 min at various heat flux densities. Due to the extensive dataset obtained, the results presented herein are limited to a representative case corresponding to a single heat flux density and the thermal and flow parameters listed in Table 3.

Experimental data were recorded using DaqView software (version 9.1.35) in conjunction with the data acquisition station. Data corresponding to a heat flux density of 6000 W/m^2 applied to the heated plate surface were selected for detailed analysis. All tests were performed with a constant mass flow rate in both minichannel circuits (hot, $Q_{m,FC}$ = 0.006 kg/s, and cold, $Q_{m,w}$ = 0.0087 kg/s) under laminar flow conditions with a slight overpressure (see Table 3).

Table 3. Experimental parameters and their ranges of variation.

Experimental parameters	Range of variation
FC-72 refrigerant temperature, T_{FC} (K)	298.46–300.95
Distilled water temperature, T_W (K)	290.45–291.95
Surface temperature of the copper heated plate, $T_{H,IR}$ (K)	299.75–306.95
Temperature of the copper plate central to the minichannels, T_{Cu} (K)	290.65–291.65
Inlet pressure to the hot minichannel, p_{in} (kPa)	110–116
Inlet pressure to the cold minichannel, p_{out} (kPa)	99.1–104
Mass flow rate for the hot channel, $Q_{m,FC}$ (kg/s)	0.006
Mass flow rate for the cold channel, $Q_{m,W}$ (kg/s)	0.0087
Heat flux density, q (kW/m²)	6

Throughout each experimental series, subcooled liquid entered the minichannels and was heated as it flowed along the heated wall toward the outlet. The heat flux applied to the heated surface of the minichannel was gradually increased during the experiments. Consequently, the heat transfer regime evolved from single-phase forced convection at the lowest heat flux densities to subcooled flow boiling at higher heat flux levels. In the subcooled boiling regime, the fluid layer adjacent to the heated surface reached locally superheated conditions, whereas the bulk liquid remained subcooled. As a result, a two-phase liquid–vapour mixture was formed near the channel outlet and subsequently directed to an auxiliary heat exchanger (condenser), where the vapour phase was condensed.

Due to the design of the heat exchanger integrated with the photovoltaic (PV) panel, direct observation of the two-phase flow structures was not feasible. Consequently, the identification of boiling flow regimes was limited to inferences based on the available experimental data, and only the flow regimes likely to occur within the exchanger could be considered.

3. One-dimensional approach

This paper proposes a simplified one-dimensional (1D) computational approach, which considers heat flow in a single direction, perpendicular to both the fluid flow and the width of the minichannel. A linear temperature distribution along the minichannel is assumed under steady-state heat transfer through a flat wall, with only one direction of heat flow considered (perpendicular to the fluid flow and the minichannel width). Heat losses along the channel axis are assumed negligible, no internal heat sources are present, and the thermal conductivity is considered constant. To provide clarification, the heat flux is indicative of the conductive heat flux within the copper heated plate, as determined by the surface's IR measurement. In our experiment, the copper plate (156 mm × 156 mm) was coated with a high-emissivity paint (ε = 0.97), and the measured radiation intensity from the heated plate was E_{IR} = 6000 W/m^2. The heat flux density was then estimated using the methodology presented in [19]:

$$q \approx \frac{E_{IR}}{\varepsilon}, \tag{1}$$

where: E_{IR} – radiation intensity of the copper heated plate, ε – emissivity coefficient.

The heat transfer coefficient α_1 at the interface between the copper heated plate and the FC-72 refrigerant was determined based on the known temperature distribution of the outer surface of the heated plate, following the methodology of [18,20,21,25]:

$$\alpha_1(x) = \frac{q\lambda_H}{\lambda_H(T_{H,IR}(x) - T_{FC,lin}(x) - q\,\delta_H)}, \tag{2}$$

where: δ_H – thickness of the heated plate, λ_H – thermal conductivity of the heated plate, $T_{H,IR}(x)$ – surface temperature of the heated plate, $T_{FC,lin}(x)$ – the temperature of the FC-72 refrigerant, assumed to vary linearly from the inlet to the outlet of the minichannel, x – the distance from the minichannel inlet.

The heat transfer coefficient α_2 at the interface between the FC-72 refrigerant and the central copper plate was estimated using the formula, as in [18,20,21,25]:

$$\alpha_2(x) = \frac{Q_{m,FC}c_{p,FC}(T_{FC,in} - T_{FC,out})}{A(T_{FC,lin(x)} - T_{Cu,lin(x)})}, \tag{3}$$

where: A – surface area of the central plate, $Q_{m,FC}$ – mass flow rate of the FC-72 refrigerant, $c_{p,FC}$ – specific heat of FC-72, $T_{Cu,lin}(x)$ – temperature of the central copper plate approximated linearly based on the known temperature recorded by two K-type thermocouples ($T_{TC,1}$, $T_{TC,2}$) located at the ends of the side of the copper plate on the FC-72 refrigerant side.

Figure 4 shows a general schematic of the test module with minichannels, illustrating the adopted 1D approach for countercurrent flow.

To determine the heat transfer coefficient at the interface between the central copper plate and distilled water, the relationship for the overall heat transfer coefficient (k) was used:

$$\frac{1}{k} = \frac{1}{\alpha_1(x)} + \frac{1}{\alpha_2(x)} + \frac{\delta_{Cu}}{\lambda_{Cu}} + \frac{1}{\alpha_3(x)}, \tag{4}$$

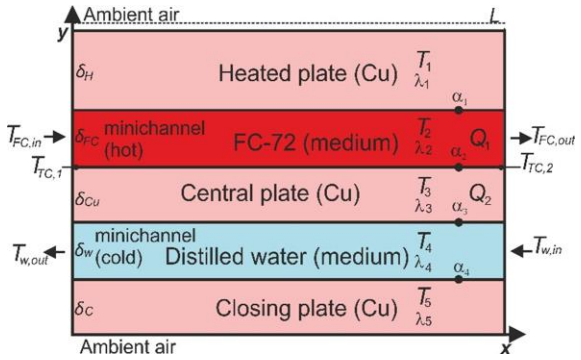


Fig. 4. General schematic of the test module with minichannels, illustrating the one-dimensional approach for countercurrent flow.

where δ_{Cu} is the central plate thickness and λ_{Cu} is the thermal conductivity of the central plate. The overall heat transfer coefficient was calculated for countercurrent flow, similarly to [19,26]:

$$k = \frac{Q_{FC}+Q_w}{2A\,\Delta T}, \tag{5}$$

where ΔT denotes the logarithmic mean temperature difference of the liquids, and Q stands for the heat flux transferred to/from the medium. The heat transfer coefficient α_3 at the interface between the central copper plate and the distilled water was determined according to the methodology applied in [19–21]:

$$\alpha_3(x) = \left[\frac{1}{k} - \frac{1}{\alpha_1(x)} - \frac{1}{\alpha_2(x)} - \delta_{Cu}\frac{1}{\lambda_{Cu}}\right]^{-1}. \tag{6}$$

Finally, the heat transfer coefficient α_4 at the distilled water–copper plate was estimated, following the procedures presented in [19,21]:

$$\alpha_4(x) = -\left[\frac{1}{\alpha_1(x)} + \frac{1}{\alpha_2(x)} + \delta_{Cu}\frac{1}{\lambda_{Cu}} - \frac{1}{k} + \frac{1}{\alpha_3(x)}\right]^{-1}. \tag{7}$$

The mean relative error (MRE) of the heat transfer coefficient α_1 (at the interface between the copper heated plate and the FC-72 refrigerant) using a one-dimensional approach was determined from the formula [18]:

$$\mathrm{MRE} = \sqrt{\begin{array}{c}\left(\frac{\partial\alpha(x)}{\partial q}\Delta q\right)^2 + \left(\frac{\partial\alpha(x)}{\partial T_{H,IR}}\Delta T_{H,IR}(x)\right)^2 + \\ + \left(\frac{\partial\alpha(x)}{\partial T_{FC,l\_in}}\Delta T_{FC,l\_in}(x)\right)^2 + \left(\frac{\partial\alpha(x)}{\partial T_{\lambda_H}}\Delta\lambda_H\right)^2 + \left(\frac{\partial\alpha(x)}{\partial T_{\lambda_H}}\Delta\delta_H\right)^2\end{array}}. \tag{8}$$

Furthermore, the individual contributions to the mean relative error of the calculated heat transfer coefficient are presented below:

- heated plate surface temperature measured by an IR camera, $\Delta T_{H,IR}(x)$ = 1.0 K;
- fluid temperature measured by a thermocouple, $\Delta T_{FC,lin}(x)$ = 0.34 K;
- thermal conductivity of the heated plate $\Delta\lambda_H$ = 0.1 W/(m·K);
- thickness of the heated plate, $\Delta\delta_H = 5\times10^{-5}$ m.

The estimated total measurement error was 2% for the heat flux density (q), and the mean relative error was 14.53% for the heat transfer coefficient (MRE).

The mean relative errors in the 1D approach were low and showed decreasing values with increasing heat flux supplied to the heated plate. As reported by Piasecka et al. [18], the maximum mean relative error of the heat transfer coefficient was 12.93% and occurred at the lowest applied heat flux density q = 12.26 kW/m^2. For the same operating conditions, the mean relative error associated with the heat flux density was significantly lower, reaching only 1.41%.

4. Results

4.1. Results of one-dimensional approach

Based on the experimental data, the surface temperature of the copper heated plate was analysed under laboratory conditions at an ambient temperature of 26°C, a relative humidity of 34% and an atmospheric pressure of 1017 hPa. A luxmeter was used to measure the illuminance on the surface of the heated plate.

Figure 5 shows a thermogram of the outer surface of the copper heated plate, captured using a Flir E60 infrared camera, for a heat flux density of 6000 W/m^2, with the test module inclined at 165° to the horizontal. The six lines marked in the figure (#1 to #6) correspond to the central axes of each of the six minichannels.

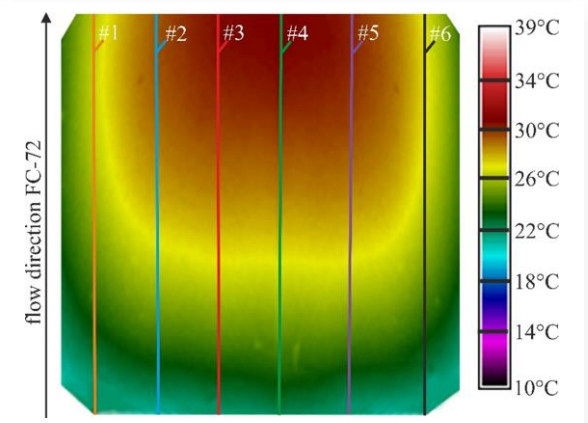


Fig. 5. Thermogram of the copper heated plate surface obtained from a Flir E60 infrared camera for a heat flux density of 6000 W/m^2, module orientation 165°.

On the outer surface of the copper heated plate, the highest temperature was recorded at the outlet section (33.8°C), while the lowest temperature (19.4°C) was observed near the inlet of the minichannels. The temperature distribution across the individual layers of the module, as a function of the distance from the minichannel inlet for the six channels (#1 to #6), is presented in Figs. 6 and 7.

The temperature of the individual layers of the module increased with the distance from the minichannel inlet. The highest temperatures on the surface of the copper heated plate were observed in the centrally located channels (Fig. 6a, channels #3 and #4), reaching approximately 33.8°C, while the lowest temperatures occurred near the side walls (Fig. 6a, channel #1). In the FC-72 minichannels (Fig. 6b), on the central copper plate

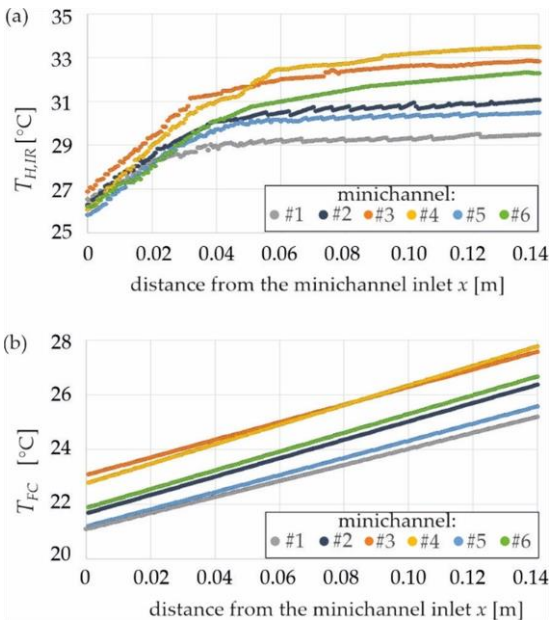


Fig. 6. Temperature distribution across the individual layers of the module as a function of distance from the minichannel inlet for six channels (marked #1 to #6): (a) on the surface of the heated plate, and (b) within the minichannels with FC-72 refrigerant.

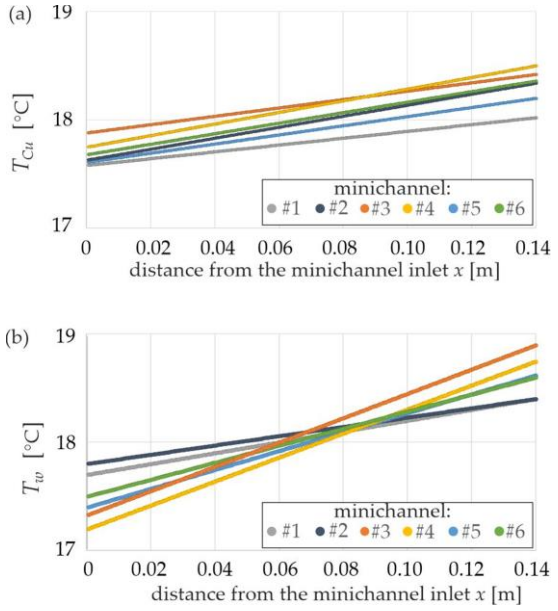


Fig. 7. Temperature distribution across the individual layers of the module as a function of distance from the minichannel inlet for six channels (marked #1 to #6): (a) on the central plate, and (b) within the minichannels with distilled water.

(Fig. 7a) and in the distilled water minichannels (Fig. 7b), the temperature increased approximately linearly with the distance from the channel inlet. The highest temperatures were consistently observed in the central channels (Figs. 6b and 7, channels #3 and #4), with maximum values of 27.8°C (Fig. 6b), 18.4°C (Fig. 7a), and 18.7°C (Fig. 7b).

Figures 8 and 9 present the distributions of local heat transfer coefficients as a function of the distance from the minichannel inlet for a selected heat flux density, corresponding to the experimental parameters listed in Table 3. The coefficients were calculated using the proposed one-dimensional computational approach at the interfaces of the individual layers:

- copper heated plate – FC-72 refrigerant (Fig. 8a),
- FC-72 refrigerant – central copper plate (Fig. 8b),
- central copper plate – distilled water (Fig. 9a),
- distilled water – closing copper plate (Fig. 9b).

The local heat transfer coefficient α_1 at the interface between the copper heated plate and the FC-72 refrigerant exhibited increasing values from one-third of the distance from the inlet toward the channel outlet. The highest value, 1.6 kW/(m^2 K), was observed at the channel outlet near the side walls (Fig. 8a, channel #1), corresponding to the location where the lowest temperature was recorded (Fig. 6a). The remaining coefficients from α_2 to α_4, representing the interfaces FC-72 refrigerant – central copper plate, central copper plate – distilled water, and distilled water – closing plate, respectively, showed decreasing values from the inlet to the outlet of the minichannel. This behaviour is likely related to an increase in the local temperature of the central plate in this region. The highest values of heat transfer coefficients at the channel entrances were approximately 1.55 kW/(m^2 K) (Fig. 8, channels #2, #4 and #6), while a maximum of 1.58 kW/(m^2 K) was obtained at the channel exit (Fig. 8a, channel #1).

Halogen lamps generate a heat flux that unevenly heats the upper surface of the copper plate (Fig. 5). Copper, as a material with high thermal conductivity (400 W/(m·K)), effectively distributes heat throughout the entire surface of the heated plate. In the vicinity of the central channels (Fig. 5, channels #3 and #4), local overheating of the heated plate wall occurs.

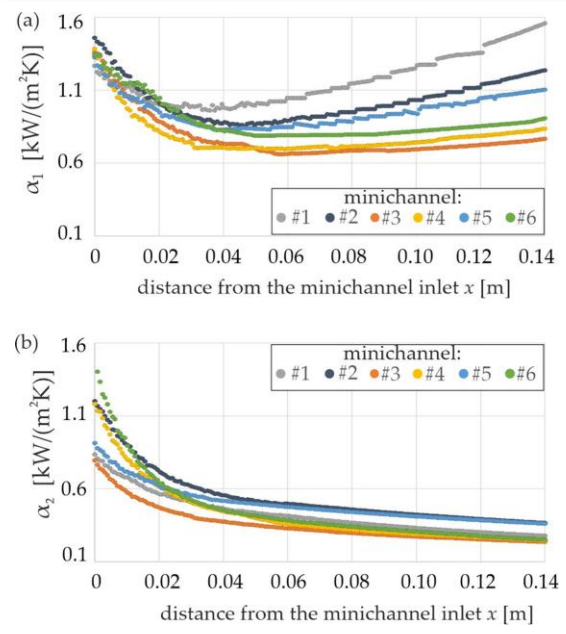


Fig. 8. Heat transfer coefficient as a function of distance from the minichannel inlet for six channels (marked #1 to #6) determined using the 1D approach at the interfaces: a) copper heated plate – FC-72 refrigerant, b) FC-72 refrigerant – copper central plate; heat flux density 6000 W/m^2, module inclined at 165°.

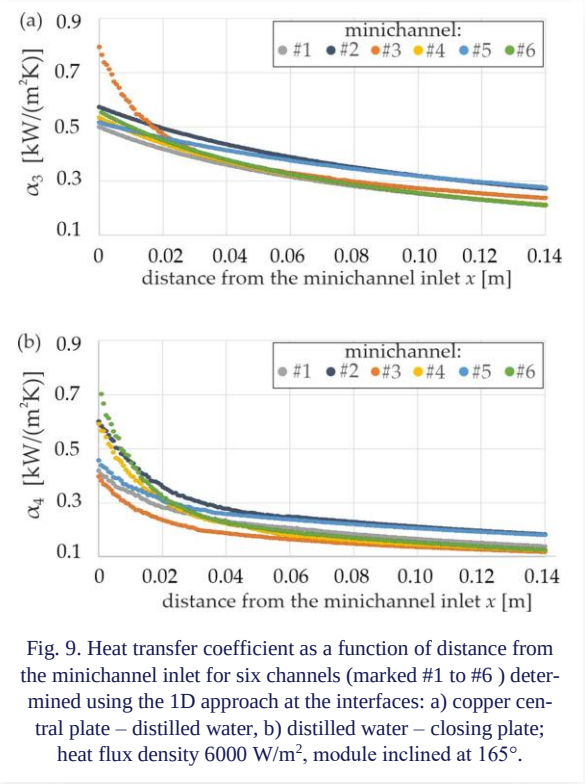


Fig. 9. Heat transfer coefficient as a function of distance from the minichannel inlet for six channels (marked #1 to #6) determined using the 1D approach at the interfaces: a) copper central plate – distilled water, b) distilled water – closing plate; heat flux density 6000 W/m^2, module inclined at 165°.

The FC-72 refrigerant, characterised by a low boiling point, undergoes intense heating already at the channel inlet, particularly in the central minichannels, where local subcooled boiling occurs. In these central channels (Fig. 5, channels #3 and #4), the onset of subcooled boiling is observed in the outlet sections, accompanied by an increase in the heat transfer coefficient α_1, reaching values of 0.8–1.6 kW/(m^2 K), and a corresponding rise in temperature toward the channel outlet.

Minichannels near the side walls (Fig. 6a, #1 and #5) exhibit lower surface temperatures on the heated plate, yet they present the highest local values of α_1 at the interface between the heated plate and the FC-72 refrigerant (Fig. 8a). The countercurrent flow of the working fluids amplifies the local temperature difference in the central plate, further enhancing the heat transfer process.

The central copper plate serves as a thermal bridge between the two working fluid circuits, maintaining an average temperature of approximately 18.5°C (Fig. 7a). Distilled water acts as the cooling medium, removing heat from the central plate. In this closed system, subcooled boiling occurs on the FC-72 side of the central plate, while forced single-phase convection dominates on the water side.

The local subcooled boiling may have occurred at the channel walls, particularly within the adjacent near-wall boundary layer. The liquid in the vicinity of the heated surface reached a superheated state, whereas the bulk fluid remained subcooled (in the hot minichannel with FC-72). In the cold minichannel, heat transfer was governed exclusively by single-phase convection, leading to low temperature gradients between the channel wall and the distilled water.

Consistent with findings reported in the literature [28] for flow boiling in small channels, forced convection boiling is primarily governed by mass flux and vapour quality, whereas nucleate boiling is mainly influenced by heat flux and saturation pressure. Furthermore, nucleate boiling was identified as the dominant heat transfer mechanism throughout the investigated heat flux range.

4.2. Validation of the proposed 1D approach against STAR-CCM+ simulations

The experimental results were validated through comparison with the corresponding CFD predictions. Numerical simulations were conducted using Simcenter STAR-CCM+ (version 2020.2.1, Build 15.04.010) on a workstation equipped with two Intel Xeon E5-2698v4 processors (40 cores total, 3.6 GHz) and 128 GB of RAM. Additionally, the quality of the computational meshes used in the numerical analysis was assessed. Mesh convergence and discretisation errors were evaluated using the grid convergence index (GCI) method, following the procedure and boundary conditions described in [19]. A multiphase volume of fluid (VOF) model was employed to simulate the flow of immiscible fluids and track the phase interface. The governing equations for fluid flow and heat transfer were adopted from [19]. Mesh quality was assessed using the GCI method for three base mesh sizes (2, 3 and 5 mm). The obtained GCI values (0.14% for the fine mesh and 0.35% for the coarse mesh) confirmed mesh convergence and solution reliability. Therefore, the 5 mm mesh was adopted for subsequent simulations, with an estimated discretisation error below 1%.

A comparison of the heat transfer coefficient values obtained using the 1D approach and STAR-CCM+ simulations was conducted for a representative case, involving the heat transfer coefficient α_1 (at the interface between the copper heated plate and the FC-72 refrigerant), at a heat flux density of 6000 W/m^2. Figure 10 shows the maximum relative differences between α_1 values calculated using Eq. (2) and the corresponding values determined from STAR-CCM+ simulations. The results indicate that the highest maximum relative differences in the heat transfer coefficient were observed for minichannels #3 and #6, reaching 30%, whereas the lowest value was recorded for minichannel #1 (19.5%). Furthermore, the average of the maximum relative differences across all minichannels was found to be 26.6%.

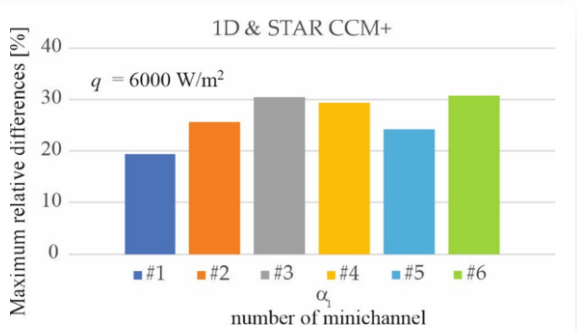


Fig. 10. Maximum relative differences between the values of heat transfer coefficient α_1, calculated using Eq. (2) and those obtained from STAR-CCM+ simulations, based on the average across all minichannels at a heat flux density of 6000 W/m^2.

The heat transfer coefficient at the interface between the heated copper plate and the FC-72 refrigerant (α_1) exhibited the highest maximum relative differences compared to the other calculated heat transfer coefficients ($\alpha_2 - \alpha_4$). Similar values were reported in a previous study [19], where the highest maximum relative difference was also observed for α_1 at a medium heat flux density of 2000 W/m^2, reaching 35.7%. These discrepancies can be attributed primarily to the limitations of the one-dimensional approach, which relies on spatially averaged parameters and does not capture local variations in velocity and temperature fields within the near-wall region. In contrast, the CFD approach resolves three-dimensional flow structures, including boundary layer development and local thermal non-uniformities, which play a significant role in heat transfer within minichannels.

An additional source of discrepancy may be the occurrence of localised subcooled boiling in the hot minichannel, which can enhance heat transfer through intermittent bubble nucleation and collapse. Such phenomena are not represented in the 1D approach. Nevertheless, the cold minichannel remains within the single-phase forced convection regime.

Further discrepancies may also arise from model idealisations, including the simplified treatment of inlet and outlet regions, neglect of surface roughness, manufacturing tolerances and local flow non-uniformities. Moreover, the CFD simulations assumed idealised thermophysical properties and steady-state operating conditions, whereas the experimental system may experience local fluctuations and unavoidable external heat losses.

A grid independence study confirmed mesh adequacy, with variations below 1%. CFD results were extracted along the channel centreline to ensure direct comparison with the 1D approach and experimental data.

The present findings are in agreement with results reported by other authors [28], confirming that channel geometry and flow arrangement strongly influence fluid flow and heat transfer in minichannel systems. The referenced study combined experimental measurements with CFD simulations to investigate fluid flow in mini cooling channels.

5. Conclusions

The main conclusions of this study can be summarised as follows:

- Experimental investigations were conducted on a countercurrent minichannel heat exchanger consisting of two groups of six rectangular minichannels carrying FC-72 refrigerant and distilled water. A heat flux density of 6000 W/m^2 was supplied to the heated copper wall. The test module consisted of twelve parallel rectangular minichannels, separated by a central copper plate, and inclined at 165° to the horizontal.
- A simplified one-dimensional approach was developed to determine local heat transfer coefficients at the interfaces: the copper heated plate – FC-72 refrigerant, FC-72 refrigerant – central copper plate, central copper plate – distilled water, and distilled water – closing plate.
- The results demonstrated a progressive increase in temperature along the flow direction in all regions of the heat exchanger. The local heat transfer coefficient increased at the heated plate – FC-72 interface and decreased at the remaining interfaces along the heat transfer path.
- The results indicate the likely occurrence of local subcooled boiling in the FC-72 minichannels, while heat transfer in the water minichannels remained within the single-phase forced convection regime.
- Validation of the one-dimensional approach against CFD simulations showed satisfactory agreement (average discrepancy of 26.6% across all analysed minichannels). The observed differences were mainly associated with model simplifications and local flow and heat transfer phenomena that cannot be fully represented by the one-dimensional approach.
- The application of a copper heated plate ensured effective heat spreading within the module, while the use of parallel minichannels increased the heat transfer area and intensified heat exchange processes.
- The proposed heat exchanger configuration shows potential for thermal management systems and photovoltaic–thermal applications, where efficient cooling and heat recovery are required.

References

[1] Abdelrazik, A.S., Al-Sulaiman, F.A., Saidur, R., & Ben-Mansour, R. (2018). A review on recent development for the design and packaging of hybrid photovoltaic/thermal (PV/T) solar systems. *Renewable and Sustainable Energy Reviews*, 95(C), 110–129. doi: 10.1016/j.rser.2018.07.013

[2] Dubey, S., & Tiwari, G.N. (2008). Thermal modeling of a combined system of photovoltaic thermal (PV/T) solar water heater. *Solar Energy*, 82(7), 602–612. doi: 10.1016/j.solener.2008.02.005

[3] Kandlikar, S.G. (2002). Fundamental issues related to flow boiling in minichannels and microchannels. *Experimental Thermal and Fluid Science*, 26(2–4), 389–407. doi: 10.1016/S0894-1777(02)00150-4

[4] Lu, K., Wang, C., Wang, C., Fan, X., Qi, F., & He, H. (2023). Topological structures for microchannel heat sink applications – a review. *Manufacturing Review*, 10(2). doi: 10.1051/mfreview/2022035

[5] Harirchian, T., & Garimella, S.V. (2009). Effects of channel dimension, heat flux, and mass flux on flow boiling regimes in microchannels. *International Journal of Multiphase Flow*, 35(4), 349–362. doi: 10.1016/j.ijmultiphaseflow.2009.01.003

[6] Mihai, I.C. (2009). Heat transfer in minichannels and microchannels CPU cooling systems. *Advanced Topics in Optoelectronics, Microelectronics, and Nanotechnologies* IV, 72971N, 7 Jan. Constanta, Romania. doi: 10.1117/12.823670

[7] Prończuk, M., & Krzanowska. A. (2021). Experimental investigation of the heat transfer and pressure drop inside tubes and the shell of a minichannel shell and tube type heat exchanger. *Energies*, 14(24). doi: 10.3390/en14248563

[8] Lan, Y., Feng, Z., Hu, Z., Zheng, S., Zhou, J., Zhang, Y., Huang, Z., Zhang, J., & Lu, W. (2023). Experimental investigation on the effects of swirling flow on flow boiling heat transfer and instability in a minichannel heat sink. *Applied Thermal Engineering*, 219(B), 119512. doi: 10.1016/j.applthermaleng.2022.119512

[9] Ye, H., Zhao, H., Yong, L., Lum, X., & Yao, J. (2025). Unveiling flow boiling hysteresis mechanisms and characteristics of R134a within minichannels. *International Journal of Heat and Mass Transfer*, 249, 127244. doi: 10.1016/j.ijheatmasstransfer.2025.127244

[10] Yaghoubi, M.S., Ahmadpour, A., & Saffar-Avval, M. (2025). Geometrical design of minichannels with rectangular wall cavities for flow boiling heat transfer enhancement. *Results in Engineering*, 25, 103989. doi: 10.1016/j.rineng.2025.103989

[11] Ye, H., Lum, L.Y.X., Kandasamy, R., Zhao, H., & Ho, J.Y. (2024). Flow boiling heat transfer enhancement of R134a in additively manufactured minichannels with microengineered surfaces. *Applied Thermal Engineering*, 256, 124150. doi: 10.1016/j.applthermaleng.2024.124150

[12] Shang, H., Xia, G., Li, R., & Miao, S. (2025). Experimental study on flow boiling heat transfer of HFE-7100 in minichannel heat sinks for professional-grade server chips cooling. *International Communications in Heat and Mass Transfer*, 164(A), 108825. doi: 10.1016/j.icheatmasstransfer.2025.108825

[13] Sun, J., Lin, Y., Li, J., Tang, W., Li, W., Ahmad, W., & Zhao, J. (2024). Heat transfer and visualization of flow boiling on nanowire surfaces in the microchannel. *Applied Thermal Engineering*, 256, 124064, doi: 10.1016/j.applthermaleng.2024.124064.

[14] Li, T., Luo, X., & Li, G. (2024). Instability analysis of pressure drop and flow characteristics in mini-channel heat sink with phase-separated configuration. *Applied Thermal Engi*neering, 253, 123755. doi: 10.1016/j.applthermaleng.2024.123755

[15] Hsu, H.Y., Kumar, R., & Lin, C.W. (2024). A numerical investigation of the wettability effect on minitube flow boiling using the volume of fluid method. *International Journal of Heat and Mass Transfer*, 225, 125370. doi: 10.1016/j.ijheatmasstransfer.2024.125370

[16] Pereira, J.E., Souza, R.R., & Moita, A.S. (2026). Experimental factors and techniques for pool boiling heat transfer enhancement: A critical review. *Heat Transfer*, 55(4), 2201–2232. doi: 10.1002/ htj.70197

[17] Etminan, A. Muzychka, Y.S., & Pope, K. (2021). A review on the hydrodynamics of Taylor flow in microchannels: Experimental and computational st*udies*. *Processe*s, 9(5), 870. doi: 10.3390/pr9050870

[18] Piasecka, M., Hożejowska, S., Pawińska, A., & Strąk, D. (2022). Heat transfer analysis of a co-current heat exchanger with two rectangular mini-channels. *Energie*s, 15(4), 1340. doi: 10.3390/en15041340

[19] Strąk, K., & Strąk, D. (2025). Experimental analysis of heat transfer in multi-mini-channel module: A comparison with CFD simulations. *Energies*, 18(22), 5992. doi:10.3390/en18225992

[20] Strąk, D., Hożejowska, S., Pawińska, A., & Piasecka, M. (2022). Research on a flow heat exchanger with minichannels. In *Advances in heat and mass transfer studies*. *Proceedings of the 16th Symposium on Heat and Mass Transfe*r (276−286). Oficyna Wydawnicza Politechniki Białostockiej, Białystok (in Polish). doi: 10.24427/978-83-67185-30-1_29

[21] Strąk, D. (2023). Performance investigation of hybrid photovoltaic thermal-heat with mini-channels for application in electric vehicles. *The Archives of Automotive Engineering – Archiwum Motoryzacji*, 100(2), 1–26. doi: 10.14669/AM/166810

[22] Mahmood, H., Freegah, B., Faik, A.M.El-D., & Saleh, Q. (2025). Optimizing minichannel heat sink design: A combined numerical and experimental analysis of inlet/outlet configurations and pin fin enhancements. *Heat Transfer*, 54(3), 1921–1939. doi: 10.1002/htj.23267

[23] Mozafari, M., Lee, A., & Mohammadpour, J. (2021). Thermal management of single and multiple PCMs based heat sinks for electronics cooling. *Thermal Science and Engineering Progress*, 23, 100919. doi: 10.1016/j.tsep.2021.100919

[24] Mahmood, H., & Freegah, B. (2026). Optimizing fluid flow to enhance the hydrothermal performance of multi-mini-channel heat sinks. *Heat Transfer*, 55(2), 1071–1082. doi: 10.1002/htj.70122

[25] Strąk, D., Piasecka, M., Pawińska, A., & Hożejowska, S. (2020). Investigation of heat transfer during flow through minichannels of a compact heat exchanger. In *Contemporary Issues in Thermodynamics* (181−190). *The 24th Congress of Thermodynamicists*, 27-30 Oct., Białobrzegi, Poland. Oficyna Wydawnicza Politechniki Warszawskiej (in Polish).

[26] Madejski, J. (1998). *Theory of heat transfer*. Wydawnictwo Politechniki Szczecińskiej, Szczecin (in Polish).

[27] Tran, T.N., Wambsganss, M.W., & France, D.M. (1996). Small circular- and rectangular-channel boiling with two refrigerants. *International Journal of Multiphase Flow*, 22(3) 485–498. doi: 10.1016/0301-9322(96)00002-X

[28] Olmeda, P., Margot, X., García-Tíscar, J., & Kumar, K. (2026). Numerical and experimental analysis of mini cooling channel flow dynamics. *Journal of the Brazilian Society of Mechanical Sciences and Engineering*, 48(3), 194. doi:10.1007/s40430-025-06161-0

Co-published by
Institute of Fluid-Flow Machinery
Polish Academy of Sciences
Committee on Thermodynamics and Combustion
Polish Academy of Sciences

Copyright©2026 by the Authors under licence CC BY-NC-ND 4.0

http://www.imp.gda.pl/archives-of-thermodynamics/

Safety aspects of the use of ammonia and an ammonia-hydrogen mixture

Katarzyna Stolecka-Antczak*, Andrzej Rusin

Silesian University of Technology, Department of Power Engineering and Turbomachinery, Konarskiego 18, 44-100 Gliwice, Poland
*Corresponding author email: katarzyna.stolecka-antczak@polsl.pl

Received: 27.05.2026; revised: 23.07.2026; accepted: 10.09.2026

Abstract

Ammonia is a well-established raw material in the chemical industry. Among others, it is used to produce fertilisers, synthetic fibres or drugs. Ammonia is also used as a refrigerant, and it is viewed as a future fuel in the power industry. Technologies for its combustion in a mixture with hydrogen or methane (natural gas) are also being developed. The widespread use of ammonia involves the need for its transportation and storage. Both these processes are affected by its physical and chemical properties because ammonia is a toxic and flammable substance. The paper presents an analysis of the hazards posed by an uncontrolled leakage of ammonia and its mixture with hydrogen from a 10 m^3 tank. The range of hazard zones due to the toxic effects of ammonia is a few dozen metres. In the case of ammonia-hydrogen mixtures, a fire hazard appears, and the range of hazard zones due to thermal radiation is several metres. The total risk presented by an uncontrolled release of ammonia-hydrogen mixtures stored in 10 m^3 tanks is 10^{-7} and occurs in an area of up to 40 m.

Keywords: Ammonia; Hazards; Ammonia-hydrogen mixture; Risk

Vol. 47(2026), No. 3, 199–211; doi: 10.24425/ather.2026.7518

Cite this manuscript as: Stolecka-Antczak, K., & Rusin, A. (2026). Safety aspects of the use of ammonia and an ammonia-hydrogen mixture. *Archives of Thermodynamics*, 47(3), 199–211.

1. Introduction

Many industries, including power generation, chemicals, petrochemicals and agriculture produce, store and transport numerous hazardous substances. If mishandled or if there is a failure of the installation components, their properties can pose a significant hazard to people and the environment.

Ammonia, produced globally on a large scale, belongs to such hazardous substances. It is a key product in the production of fertilisers, and it is also used in the food industry and refrigeration. Research is also being pursued on the use of ammonia as a fuel for engines and gas turbines. Indeed, considering its properties, ammonia is viewed as an alternative and emission-free future fuel that does not emit carbon dioxide during combustion. It can therefore be a good substitute for hydrocarbon fuels. The research on the use of ammonia as a potential fuel or as an additive to other fuels is currently the subject of many scientific publications.

In [1], the authors present a comprehensive review of ammonia as a fuel. The paper presents the principles of combustion reactions of ammonia and discusses their implications for practical energy applications, thereby supporting the development of ammonia as a carbon-free emission fuel. In [2], the authors review the use of ammonia as an alternative fuel in internal combustion engines, with a perspective on the future of possible applications and practical solutions to related problems. The main

goal of the authors of [3] was to show potential alternative fuels within their applications and present prospective alternative routes for their production. Chemicals like hydrogen and ammonia were tested as an alternative fuel for utilisation technologies. The objective in [4] was to show the prospects and challenges of ammonia as a fuel and suggest significant topics that could benefit from additional studies. The authors of [5] systematically summarise the fundamentals of ammonia-based combustion and its practical application. The comparative study presented in [6], based on a selected design, summarises the operating principles, together with the advantages and disadvantages of direct ammonia fuel cells. A model of a direct ammonia-fed solid oxide fuel cell was presented in [7]. The effect of selected parameters on the cell's efficiency was also studied in the paper. In [8], the authors provide a review of ammonia applications in various fields, including energy systems, fuel cells, gas turbines and propulsion technologies. These studies discuss the use of ammonia as a fuel in industrial applications, highlighting its potential as well as the challenges associated with its various application methods. The presented analyses indicate that ammonia combustion is a challenging process, primarily due to its low reactivity, which results in a low laminar burning velocity. Other limitations also include high ignition energy and combustion instability. To improve the process characteristics, mixtures of ammonia with flammable gases, such as methane and hydrogen, are used. The process of co-combustion of ammonia with other fuels is therefore also the subject of extensive research and analysis. In [9], the structure of hydrogen and ammonia flames and their combustion mechanisms were investigated. A comprehensive summary and review of research progress on the combustion characteristics and reaction mechanisms of ammonia and ammonia-hydrogen mixtures is presented in [10]. In [11], a numerical analysis of the combustion of ammonia-hydrocarbon mixtures under high-pressure dual-fuel conditions in large engines is presented. It was shown that mixtures of methanol and ammonia improve ignition stability and reduce the risk of excessive post-injection after burning. Experimental studies on an engine fuelled with diesel and 40% ammonia by energy fraction are presented in [12]. In subsequent stages, ammonia was gradually replaced with hydrogen, up to 28% by energy fraction. The effect of adding hydrogen to ammonia on combustion characteristics and stability was investigated. Experimental studies of the non-premixed gas turbine model combustor using ammonia fuel or fuel mixtures were presented in [13].

The widespread use of ammonia, which is a toxic and flammable substance, also involves an increasing number of accidents triggered by its uncontrolled release [14]. The spread of an ammonia cloud depends on the physical properties of the compound, the source of the release and the atmospheric environment. Ammonia vapours are flammable in the air, but they catch fire with difficulty, among others, due to their high minimum ignition energy. An explosion of ammonia vapours, on the other hand, occurs primarily in confined spaces (buildings). The hazard related to the spreading of a cloud of ammonia, in addition to the fire hazard, results from its toxicity. In the range of lower concentrations, the gas causes irritation, whereas at higher concentrations, it can cause death [15]. Recent studies based on computational fluid dynamics (CFD) have investigated ammonia leakage and dispersion in confined and semi-confined industrial environments. In [16], the authors analysed ammonia dispersion in closed industrial engine rooms with forced ventilation and demonstrated that ventilation configuration and obstacle distribution strongly influence ammonia accumulation and hazardous zones. An analysis of the effects of ammonia release is also presented in [17]. The authors analyse the hazard zones for various ammonia release scenarios and the influence of selected conditions on the range of impact. The fire-related and toxic consequences of a failure of major equipment and facilities intended for ammonia production are worked out in [18]. In the article [19], based on existing calculation formulas of the probability of explosion risk, analyses were performed in which the influence of the position and height of spatial obstacles and the time of the flammable refrigerant leak on the distribution of the flammable refrigerant concentration was fully considered.

In the paper [20], a comprehensive review of existing research on hydrogen and ammonia diffusion processes and explosion mechanisms is made. Prevention and detection techniques are discussed, providing theoretical support for the effective development of an energy system using hydrogen and ammonia. In the paper [21], a series of experiments conducted within a standard 20-L spherical combustion chamber to investigate the explosion characteristics of ammonia/hydrogen/air premixed gases under diverse conditions, spanning from low to high pressures (0.02–0.3 MPa) and from fuel-lean to fuel-rich scenarios (0.7–1.5), are discussed. The results reveal that the explosion characteristics are pronouncedly enhanced by hydrogen addition. Hydrogen addition remarkably increases the hydrodynamic instability and thermal-diffusion instability of the reactive mixture, enhances the thermal-mass diffusion on the flame front, and promotes flame deformation and cellular structure formation, resulting in an improvement of the flame propagation and compression effect on the unburnt reactant before the flame. In turn, the influence of variable ammonia concentrations on the self-ignition of hydrogen under high pressure during accidental release into a pipe is presented in [22]. Among other things, it was noted that as NH_3 concentration increases, the intensity and speed of shock-wave propagation within the pipe decrease. In [23], the authors analysed the explosion behaviour of ammonia, hydrogen and air mixtures in a closed duct. Both experiments and CFD modelling were used to reproduce, among other aspects, flame dynamics. The study focused on explosion parameters such as flame structure, flame propagation velocity, and overpressure. It was shown that when the ammonia blending ratio in the fuel ranged from 25% to 50%, the premixed flame underwent four distinct stages. It was also found that increasing the ammonia blending ratio in the fuel can significantly alter the explosion behaviour. The work [24] explores the flame evolution and pressure dynamics of NH_3/H_2/air mixtures in a closed duct. Flame instability parameters were calculated, and the NH_3/H_2/air flames on flame propagation were also assessed. Numerical studies of the characteristics of the ammonia, hydrogen and air flame in a micro combustor are presented in [25]. The effects of adding N_2 and CO_2 on the explosion behaviour of premixed hydrogen/ammonia/air mixtures were investigated in [26]

through experiments and analysis of reaction kinetics. The effects of N_2 and CO_2 on the evolution of the flame structure, flame front speed, pressure and reaction kinetics were analysed. The results indicated that increasing the hydrogen fraction in the fuel can accelerate the premixed flame, leading to higher flame front speeds and increased pressure. Conversely, the addition of N_2 and CO_2 has a suppressive effect.

Regardless of the application of ammonia and its mixtures with hydrocarbons, the safety of processes related to its production, storage and transport remains a significant issue. The authors of numerous publications note that due to its toxicity, flammability and the risk of explosions and leaks, ammonia requires a detailed hazard analysis and risk assessment. In [27], the authors presented an overview of current regulations and potential technologies proving the safety of the ammonia bunkering process. They also highlighted the critical issue of determining safety distances from the release site in order to minimise the consequences of hazardous events. The effect of ammonia on human health in the event of a release during a ship collision is discussed in [28]. The analyses included various release scenarios and types of storage tanks. The study showed, among other things, that semi-pressurised tanks may pose a higher toxic risk than refrigerated tanks, and that the use of water curtains and spill containment systems can significantly reduce the environmental impact of an accident.

This article presents an analysis of the hazards and risks associated with the uncontrolled release of ammonia and its mixtures with hydrogen, supplementing issues related to the safety of the processes using this type of fuel. Many studies indicate that adding hydrogen to ammonia improves combustion parameters, including flame propagation speed and reaction stability, making ammonia-hydrogen mixtures a promising direction for research into low-emission fuels and energy carriers. It should be emphasised, however, that both ammonia and hydrogen are hazardous substances, which implies the need for comprehensive process safety analyses as an integral part of research on their practical application. This study considers scenarios involving the release of ammonia in a gaseous state. The effect of the composition of the mixtures on the size of the hazard zones arising due to the toxic effects of ammonia, as well as to the impact of heat flux resulting from a fire of the mixtures, was studied. The novel aspect of this study is the integrated assessment of the consequences and risks related to the uncontrolled release of ammonia and mixtures of ammonia and hydrogen. The proposed approach combines modelling of the impact, including the determination of toxic and thermal hazard zones, with a quantitative risk assessment based on the probability of tank failure. The analysis allows for a comparison of safety levels related to the storage of ammonia and ammonia-hydrogen mixtures with varying proportions of the two gases.

2. Use of ammonia

Ammonia is used primarily as a fertiliser in agriculture. This is due to its rapid reaction with clay particles or organic matter and hydrogen ions. Other industries using ammonia include pharmaceuticals, food production and storage, metallurgical processes, pulp and paper production and textiles [29]. Ammonia is also used as a refrigerant, with benefits such as high efficiency, lower costs or no interaction with the ozone layer [30]. Moreover, ammonia has better heat transfer properties compared to other chemical refrigerants, which makes it possible to use devices with a smaller surface area [31].

There is also a chance of a wider use of ammonia in the power industry. It is expected that by applying the catalytic combustion method, it will be possible to burn ammonia at a lower temperature without emitting unnecessary pollutants. The high temperature of ammonia combustion favours the formation of nitrogen oxides, which are harmful to the environment.

Ammonia can be used as a fuel in various types of internal combustion engines, gas turbines and direct fuel cells, which is a significant advantage over other types of fuel. Using ammonia as a fuel, there will be no CO_2 or SO_x emissions. No soot will be produced either [30]. Fig. 1 presents the ways of using ammonia in industry for different types of generators. Ammonia can be used, for example, in spark-ignited ICEs, diesel ICEs with H_2, combustion turbines, ICEs powered with petrol or an ethanol mixture, transformed biogas generators and direct ammonia fuel cells [32].

Current research results indicate that ammonia has great potential to be used as a primary fuel in spark-ignition engines. The use of ammonia in an internal combustion engine may cause increased NO_x emissions compared to gasoline. The main problem with this use of ammonia is also the fact that its ignition energy is approximately 16 times higher compared to hydrocarbon fuels. The low combustion rate of ammonia makes combustion non-uniform at the low engine loads and/or high rpm values. Therefore, in order to ensure the combustion process stability, it is necessary to mix it, for example, with gasoline, diesel oil or hydrogen [30].

The use of ammonia as a fuel in gas turbines is still quite limited. Current studies concentrate primarily on ammonia-hydrogen and ammonia-natural gas mixtures. The use of ammonia as a fuel involves combustion instability and low combustion efficiency – current research takes account of the use of a swirler and a flame holder, for example [33], which could stabilise combustion and increase its efficiency, as well as reduce nitrogen oxide emissions. In [34], the authors show the possibility of adding ammonia to the gas turbine.

Ammonia can also be used in direct fuel cells, which generate electricity based on electrochemical reactions. Depending on the applied electrolytic materials or the operating conditions, these devices are divided into several types [35], including alkaline fuel cells (AFC), alkaline membrane fuel cells (AMFC), phosphoric acid fuel cells (PAFC), molten carbonate fuel cells (MCFC), proton exchange membrane fuel cells (PEMFC), direct methanol fuel cells (DMFC) and solid oxide fuel cells (SOFC). Solid oxide fuel cells are considered as the most energy-effective, and the gas which is most often used in fuel cells to produce electricity is hydrogen. Research is currently being conducted on the use of ammonia, where it can be used directly as a fuel in AFC, AMFC and SOFC technologies. The use of ammonia ensures that the efficiency of the cells remains relatively high. In the case of fuel cells, the concept of reverse fuel cells (RFCs), currently in development, it is also worth noting.

They enable clean conversion of nitrogen and water to ammonia under the influence of electricity obtained from renewable sources [36].

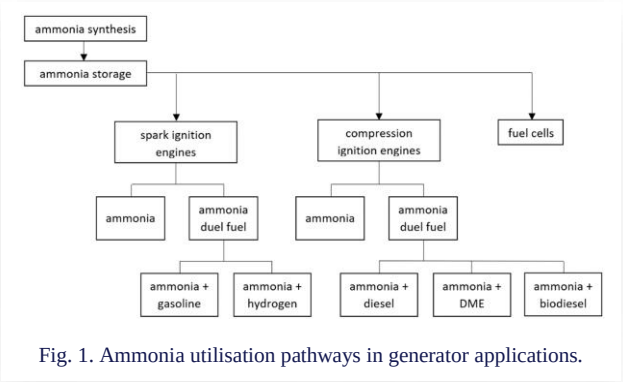


Fig. 1. Ammonia utilisation pathways in generator applications.

A consequence of the need to increase the combustion efficiency of ammonia is that it is often mixed with other agents that upgrade the fuel, such as methane, propane, petrol, kerosene or hydrogen. Mixing ammonia with hydrogen strengthens the combustion flame. In addition, hydrogen can be produced from ammonia, which contributes to the practical benefits of transporting this mixture. Such mixtures have been tested, among others, in spark-ignition engines and gas turbines. The high reactivity of hydrogen contributes to an increase in laminar combustion velocity compared to pure ammonia. On the other hand, mixing ammonia with other hydrocarbon fuels generally leads to a higher flame speed and to an increase in the intensity of radiation and heat release rate. It also results in lower CO_2 emissions [30].

3. Effects of an uncontrolled release of ammonia

The use of ammonia presents various challenges due to its properties. This raw material is used directly or indirectly in a number of industrial processes, and its use requires storage and/or transportation to sites of its final utilisation.

Two methods are generally used for ammonia storage. One, with no refrigeration, involves increasing pressure while maintaining the ambient temperature, e.g. to 0.99 MPa at 25°C. The other method, with refrigeration, involves maintaining atmospheric pressure while lowering the temperature to approximately –33°C. Large volumes of ammonia are most often stored using refrigerated tanks, which minimises the potential leakage rate in the case of failure (compared to pressure tanks). Ammonia tanks should have an appropriate structure and be equipped with, among other things, a system of protection against an excessive increase or drop in pressure.

Ammonia is considered a toxic and flammable substance. Exposure to ammonia can therefore occur under conditions of industrial use or as a result of an accidental leakage during storage or transport. In recent years, a number of incidents involving ammonia spills have occurred around the world. For example, in the USA in 2010, an ammonia release led to the poisoning of more than 120 people [31]. One of the worst accidents involving ammonia occurred in 1992. A cloud of released ammonia caused 129 deaths and 1150 injuries as a result of inhaling high concentrations of the substance [28]. Ammonia tanks, installations and pipelines are therefore potentially dangerous elements of the industrial infrastructure which can fail, for example, due to corrosion or an accidental impact [37]. A leak can pose a fire hazard, or it can have a toxic effect. Depending on the location of the damage, the storage/transport conditions and the type of installation, ammonia may be released in a gaseous or liquid form. A release of liquid ammonia into the environment leads to the immediate formation of a cloud of gaseous ammonia (Fig. 2). This is due to its low boiling point.

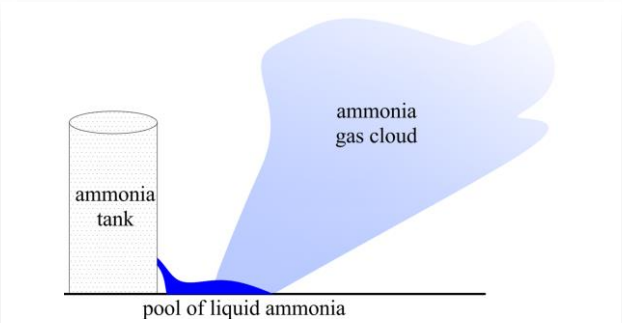


Fig. 2. Release of ammonia.

3.1. Ammonia toxicity

Ammonia is a colourless substance that is lighter than air. It can be smelt in the air at very low concentrations as it has a characteristic pungent and acrid odour. If released into the atmosphere, the gas rises in the air. Contact with ammonia can cause skin burns and changes in the respiratory tract. If inhaled, ammonia can even cause blindness. Ammonia poisoning through the alimentary tract causes disorder in intestinal peristalsis, and in extreme cases, it can even lead to death. The greatest risk of ammonia poisoning is for people working in industries where ammonia is used in large quantities. The gas is also released during the decomposition of matter, for example, in animal faeces.

At concentrations of 5 ppm, ammonia becomes noticeable by smell [38]. Concentration levels of 100 ppm cause violent irritation of the respiratory tract, bronchi and eyes (especially conjunctivitis). Immediate irritation to the eyes, nose and throat will occur for concentrations of 400–700 ppm. Pulmonary oedema, cough and laryngospasm will occur at concentrations higher than 1500 ppm. A concentration higher than 4650 ppm means a lethal dose [39].

As for ammonia interaction with the soil, toxicity is non-existent as the substance evaporates from the surface. The ammonia remaining in the soil is a source of nitrogen fertiliser. Part of the ammonia undergoes photolytic decomposition in the air, and the rest returns to the soil surface through dry or wet deposition.

The toxicity of ammonia in the aqueous environment, where it is very harmful to many aquatic organisms, is a different matter.

3.2. Ammonia explosivity and flammability

The problem of ammonia explosivity arises in confined spaces when very specific conditions are met. For the phenomenon of explosion to occur, the following have to coincide: an oxidiser,

an external source of ignition (explosion trigger), the mixing of ammonia with air within the limits of explosiveness and a spatial limitation, for example in the form of the walls of the room.

The occurrence of an explosion depends on whether the flammable ammonia-air mixture will reach the appropriate temperature due to external energy (minimum ignition energy). This value is about 40 mJ and is significantly higher than the ignition energy of hydrogen, which totals 0.02 mJ. The range of explosivity limits of ammonia is the concentration of 15 to 28% (with oxygen: 14 to 79%), and it changes under the influence of hydrogen contained, for example, in water. When water enters the surface of liquid ammonia, there follows a reaction of intense heat release from the process of ammonia combining with water (exothermic reaction) and due to the evaporation of significant amounts of ammonia, which produces an ignitable and explosive mixture. In addition, the presence of other substances, such as chlorine, bromine, iodine, mercury, sodium and calcium, favours the formation of explosive mixtures [30].

Ammonia is considered a substance which is flash resistant and slow burning. The prerequisite that triggers the combustion process of ammonia in the liquid form is the supply of a sufficient amount of heat (energy) that enables the formation of ammonia-air vapours above the surface of the liquid. The vapours must be in the concentration range between the lower and the upper flammability limit, i.e. 15–28% in the air.

In the event of damage to tanks storing ammonia or its mixtures in the gaseous form, the leaking gas may ignite, and this may result in a jet fire. Another consequence of damage to ammonia storage tanks is the BLEVE phenomenon, i.e. an explosion of rapidly expanding vapours of a boiling liquid, and the formation of a fireball. This phenomenon usually occurs due to the tank being heated by an external flame. As a result, the pressure inside the tank rises considerably, and the tank ruptures violently. The contents of the tank are ejected abruptly through the cracks, a cloud is formed, and a violent ignition follows. The hazards to humans and the environment related to the event of fire are the direct impact of the resulting flame and the heat flux generated by the fire. A heat flux of 4–5 kW/m^2 will not cause injury to humans over a long exposure time. A heat flux of 12.5 kW/m^2 will cause first-degree burns in humans, and a value above 25 kW/m^2 will cause significant injury within 10 seconds. The lethal heat flux for humans is 35–37.5 kW/m^2 [40].

The conditions of flammability and explosivity change when other gases, such as hydrogen, are added to ammonia. This is analysed in the sections below.

4. Methods of calculation

The technical risk related to a failure of a system of transport and storage of dangerous substances can be understood as the product of the probability of the occurrence of a hazardous event and its consequences. Denoting the risk as *R*, the following can be written [41]:

$$R = \sum C_i P_i. \tag{1}$$

where: P_i – probability or frequency of occurrence of a hazardous event *i*, C_i – consequences of the occurrence of event *i*.

Depending on the event under consideration, the consequences can be expressed in monetary units or in the number of potential casualties. In order to determine the risk value according to the above formula, it is necessary to identify possible hazard scenarios, estimate the probabilities of the occurrence of the hazards and assess the consequences [42].

The hazards related to the use of ammonia are due to its physicochemical properties, especially its toxicity and flammability. Ammonia is characterised by a narrow range of flammability and a high temperature of autoignition, which results in its low flammability. In the gaseous form, it can quickly disperse in atmospheric air because its density is lower than the air density. This feature reduces the risk of a possible fire and explosion. However, ammonia is also classified as a toxic substance. Even a small leak of ammonia in a residential area can cause very serious consequences.

The paper presents an analysis of the risks associated with the uncontrolled release of ammonia and its mixtures with hydrogen from the storage tanks of these gases. The considerations involved different sizes of damage. Both the size of the tank and the size of the hole through which a gas is released affect the amount of gas released into the atmosphere, as well as the duration of the leakage. Due to the mentioned properties of ammonia and hydrogen, hazard scenarios related to the toxic effects of the gases and fire of the mixture of these gases were considered.

The risk of occurrence of a hazardous event, for example, in the form of an ammonia tank rupture or puncture, is related to a potential release of ammonia into the atmosphere. This, in turn, can lead to the formation of an ammonia cloud with concentrations hazardous to humans and the environment. Among others, the hazard level will depend on the atmospheric conditions, the size of the damage, the gas parameters and the duration of the leakage.

The analyses of the consequences of such scenarios were conducted using the PHAST v6.7 software package [42]. The program makes use of the unified dispersion model (UDM) [42], which makes it possible to calculate the quantities describing the outflow and transport of the created cloud in the atmosphere, taking account of all the cloud stages, such as the release, the touchdown, the pool formation or evaporation, for example.

Another scenario considered in the risk analysis is the hazardous effects of heat radiation resulting from a fire in the ammonia-hydrogen mixture. A jet fire is possible with the release of flammable gas at a high pressure. The quantities related to this type of fire were calculated using the PHAST v6.7 software [42] with implementation of the Chamberlain model. The model assumes the flame to be a spatial solid in the form of a truncated cone (cone frustum) with dimensions depending, among other things, on the wind speed.

Another type of fire that can occur due to the unsealing of tanks with flammable substances is a fireball, which may be due to the BLEVE phenomenon. This phenomenon is an effect of a sudden and complete rupture of a tank.

For each of the above mentioned scenarios, the probability of its occurrence is estimated. In the article, this probability will be calculated by using the event tree. In the next step, the calculated probability of each scenario and the corresponding proba-

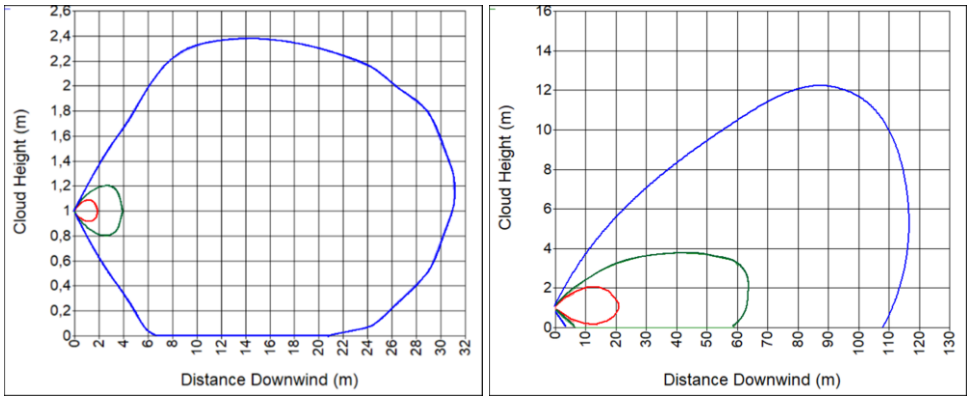
bilities of death of people within the range of negative effects of radiation from a potential fire or toxic properties of gases are presented in risk diagrams. The risk level is also calculated according to Eq. (1).

5. Results of analysis of hazards presented by an uncontrolled release of ammonia and an ammonia-hydrogen mixture

The figures below show the range of clouds with an elevated concentration of ammonia formed when the tank with a capacity of 10 m^3 becomes unsealed. The gaseous form of ammonia was considered. A 10 m^3 tank holds 44.3 kg of ammonia. In the calculations, the air temperature, the wind speed and the atmospheric stability class are assumed at 20°C, 2 m/s and D, respectively. The relative humidity is assumed to be 85 %. The ammonia was released in an open, undeveloped area. The different cloud ranges correspond to different ammonia concentrations of 1000, 10 000 and 25 000 ppm. These are the concentrations that cause severe breathing difficulty, eye and skin irritation in humans (1000 ppm – blue), death after several minutes (10 000 ppm – green) and immediate human death (25 000 ppm – red).

The ranges of a cloud with elevated concentrations of ammonia released due to damage to a tank containing ammonia in the gaseous form with a pressure of 0.5 MPa and temperature of 20°C are shown in Fig. 3. An analysis was conducted of the outflow of the gas through damage with an equivalent diameter of 0.5 cm and 5 cm located at a height of 1 metre above the ground. The hole with the smaller diameter could be the result of corrosion processes in the tank walls. The bigger hole could correspond to damage due to a mechanical effect, e.g. an impact against the tank. The cloud ranges shown in the figure from the side view of the cloud show the concentration of ammonia at a specific time during the process of the outflow from the tank.

Analysing the above graphs, it can be noticed that the most dangerous zone with a lethal level of ammonia concentration for humans will not touch the ground surface. However, it can be seen from the side view that it will cover a range of about 2 and 20 metres for the hole diameters of 0.5 cm and 5 cm, respectively. The zone with the lethal concentration for humans after several minutes of exposure, i.e. 10 000 ppm, will reach a range of about 60 metres on the ground surface only for the larger diameter of the damage (5 cm). The second factor with a significant impact on the death hazard is the time of exposure to the toxic effects of ammonia. This time depends, among other things, on the volume of the released gas. In the case of the tank with a capacity of 10 m^3, the zone with the highest concentration of 25 000 ppm will keep for about 30 seconds, while in the case of the smaller tank, e.g. with a volume of 1 m^3, this time is 5s.



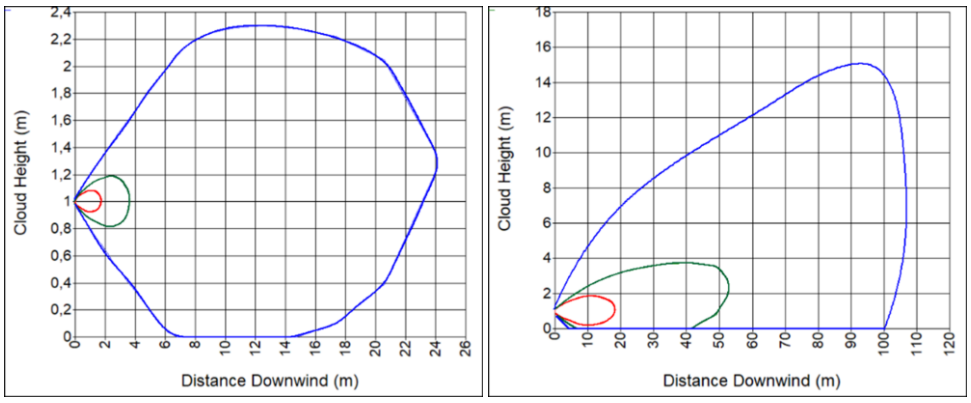
a) b)

Fig. 3. Range of the cloud with an elevated concentration of ammonia (side view, blue – 1000 ppm; green – 10 000 ppm; red – 25 000 ppm): a) hole (damage) with the diameter of 0.5 cm, tank volume: 10 m^3 (time: 14.7 s); b) hole (damage) with the diameter of 5 cm, tank volume: 10 m^3 (time: 23.9 s).

As already mentioned, apart from its widespread use in the chemical industry or agriculture, ammonia can be used as an alternative fuel. Research on the combustion process of this substance in engines has been pursued for many years. In addition to the possibility of using ammonia itself, the combustion of ammonia-hydrogen and ammonia-methane mixtures is also investigated in those works. The addition of hydrogen and methane improves the conditions of ammonia combustion. It will also have an impact on the safety of the use of these mixtures. By adding hydrogen in a mixture with ammonia, the toxicity of the mixture is reduced, which thus reduces the hazard zones in the event of an uncontrolled release of this type of mixture. The effect of hydrogen content in the mixture on the size of areas with high ammonia concentrations of 1000 ppm, 10 000 ppm and 25 000 ppm is shown in the figures below.

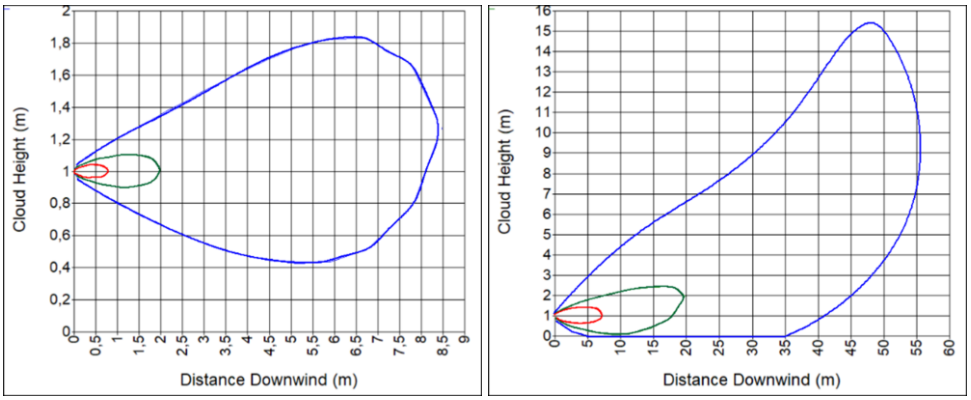
Fig. 4 and Fig. 5 show the size of these zones for an uncontrolled release of ammonia-hydrogen mixtures at the volume ratios of 80/20 and 20/80 from a 10 m^3 tank. Punctures with equivalent diameters of 0.5 cm and 5 cm were analysed. The mixture parameters are the pressure of 0.5 MPa and the temperature of 20°C. The wind speed is assumed at 2 m/s.

Analysing the graphs in Fig. 4, it can be seen that the zones related to the impact of the elevated concentration of ammonia contained in the mixture and causing immediate human death will not touch the ground surface. The range of about 2 and 20 metres will be reached for damage with the diameters of



a) b)

Fig. 4. Range of the cloud with an elevated concentration of ammonia for a gaseous 80/20 (v/v) ammonia-hydrogen mixture (side view, blue – 1000 ppm; green – 10 000 ppm; red – 25 000 ppm): a) hole (damage) with the diameter of 0.5 cm, tank volume: 10 m^3 for the time of 10.9 s; b) hole (damage) with the diameter of 5 cm, tank volume: 10 m^3 for the time of 21 s.



a) b)

Fig. 5. Range of the cloud with an elevated concentration of ammonia for a gaseous 20/80 (v/v) ammonia-hydrogen mixture (side view, blue – 1000 ppm; green – 10 000 ppm; red – 25 000 ppm): a) hole (damage) with the diameter of 0.5 cm, tank volume: 10 m^3 for the time of 2.8 s; b) hole (damage) with the diameter of 5 cm, tank volume: 10 m^3 for the time of 12.6 s.

0.5 cm and 5 cm, respectively, for different times. The zones with the concentration of 10 000 ppm already reach a distance exceeding 50 metres for the larger diameter of the tank damage. The zone with the highest concentration of 25 000 ppm disappears after 25 seconds if the mixture is released from the tank.

Figure 5 shows the range of the areas with an elevated concentration of ammonia at an uncontrolled release of the ammonia-hydrogen mixture with the volume ratio of 20/80. Like before, a tank volume of 10 m^3 was considered, as well as two sizes of damage with the diameters of 0.5 cm and 5 cm. The mixture parameters remain unchanged.

The hazard zones related to the concentration of ammonia, causing immediate death of humans, will occur in an area with a range of about 7 metres. The concentration of 10 000 ppm can reach a distance of about 20 metres from the failure site. High concentrations in the air last for 18 seconds.

The maximum ranges of hazard zones related to the toxic effects of ammonia and its mixture with hydrogen are presented in Tables 1 and 2.

Table 1. Maximum range of toxic hazard zones for varying portions of gases (hole (damage) with the diameter of 0.5 cm).

H_2/NH_3	1000 ppm	10 000 ppm	25 000 ppm
0/100	31.5 m	4.0 m	2.0 m
20/80	24.0 m	3.7 m	1.7 m
80/20	8.4 m	2.0 m	0.7 m

Table 2. Maximum range of toxic hazard zones for varying portions of gases (hole (damage) with the diameter of 5 cm).

H_2/NH_3	1000 ppm	10 000 ppm	25 000 ppm
0/100	116.0 m	64.0 m	21.0 m
20/80	108.5 m	53.5 m	18.0 m
80/20	55.5 m	20.0 m	7.5 m

As already mentioned, another (though less likely) consequence of a release of ammonia is a fire, provided that the conditions for it are favourable. A fire hazard applies primarily to gaseous ammonia and its mixtures with another flammable gas, such as hydrogen, because the ignition of liquid ammonia is difficult.

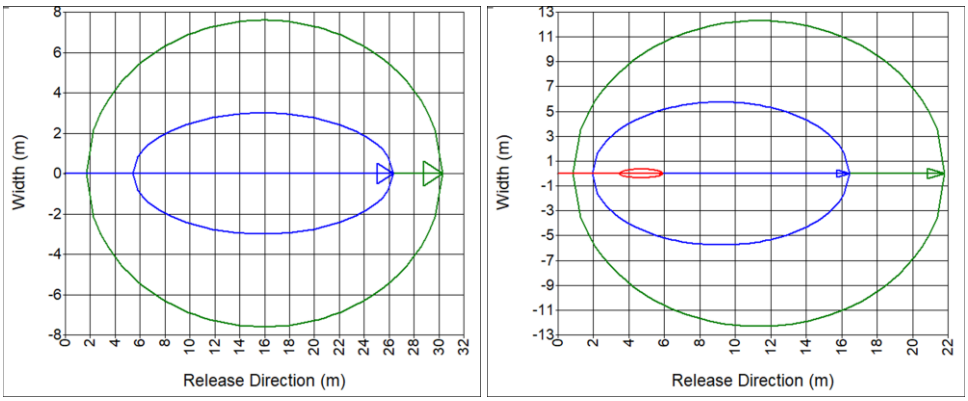
The physical properties of such a mixture differ from those of pure ammonia, which means that the quantities that decide the dimensions of the negative consequences of its uncontrolled release will also vary. Adding hydrogen to ammonia results, among other things, in a change in the lower and the upper flammability limits of the mixture. It also affects the heat of combustion, as shown in Table 3. It should be noted that the addition of ammonia to hydrogen raises the lower flammability limit and lowers the upper flammability limit, thus narrowing the range of concentrations at which ignition and explosion of the mixture are possible. Mixing ammonia with other flammable gases also affects the combustion process parameters, including the value of the heat flux generated during mixture combustion.

The figures show example hazard zones arising due to the ignition of ammonia, hydrogen and ammonia-hydrogen mixtures. The analysis concerns effects of a jet fire and a fireball.

Table 3. Lower and upper limits of mixture flammability.

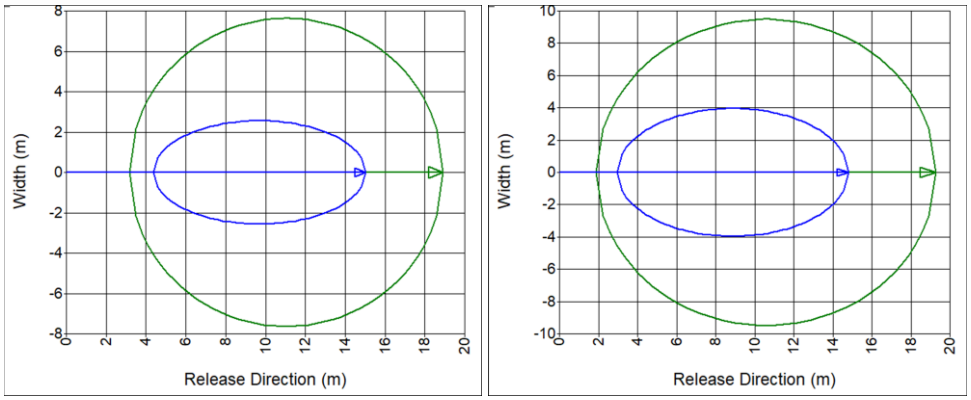
H_2/NH_3	LFL	UFL	Heat of combustion
100/0	4.00 %	75.00 %	241820 kJ/kmol
90/10	4.32 %	62.50 %	242794 kJ/kmol
80/20	4.71 %	53.57 %	243976 kJ/kmol
70/30	5.16 %	46.88 %	245441 kJ/kmol
60/40	5.71 %	41.67 %	247306 kJ/kmol
50/50	6.40 %	37.50 %	249759 kJ/kmol
40/60	7.27 %	34.10 %	253130 kJ/kmol
30/70	8.42 %	31.25 %	258054 kJ/kmol
20/80	10.00 %	28.85 %	265923 kJ/kmol
10/90	12.30 %	26.79 %	280511 kJ/kmol
0/100	15.00 %	28.00 %	316830 kJ/kmol

A jet fire (Fig. 6 and Fig. 7) is a fire resulting from the leakage and ignition of a jet of a pressurised substance flowing out of a hole (damage) formed in the tank wall. The hazard zones shown in the figure refer to the fire-generated heat flux of 4, 12.5 and 37.5 kW/m^2 (green, blue and red, respectively). Exceeding



a) b)

Fig. 6. Heat flux generated by a jet fire of ammonia and hydrogen; hole (damage) with the diameter of 5 cm, tank volume: 10 m^3 (green – 4 kW/m^2, blue – 12.5 kW/m^2, red – 37.5 kW/m^2): a) ammonia (mass: 44.3 kg, mass flow at the hole outlet 1.82 kg/s); b) hydrogen (mass: 4.95 kg, mass flow at the hole outlet 0.62 kg/s).



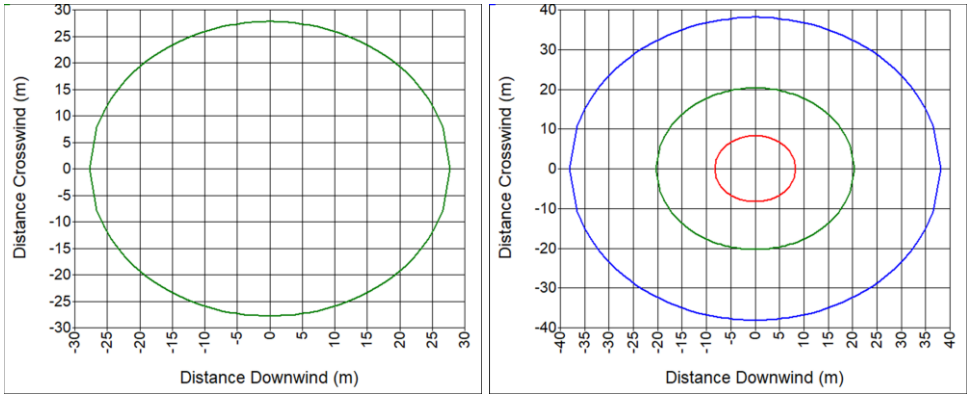
a) b)

Fig. 7. Heat flux generated by a jet fire of ammonia and hydrogen; hole (damage) with the diameter of 5 cm, tank volume: 10 m^3 (green – 4 kW/m^2, blue – 12.5 kW/m^2, red – 37.5 kW/m^2):
a) ammonia-hydrogen mixture (80/20) mass: 35.73 kg, mass flow at the hole outlet 1.64 kg/s;
b) ammonia-hydrogen mixture (20/80) mass: 12.36 kg, mass flow at the hole outlet 0.98 kg/s.

the value of 4 kW/m^2 causes noticeable effects for humans; the value of 12.5 kW/m^2 causes first-degree burns, and the value of 37.5 kW/m^2 causes immediate death. The areas indicated by the red line, which correspond to human deaths, occurred only in the case of a hydrogen release. The presented results relate to the leakage and ignition of ammonia, hydrogen and an ammonia-hydrogen gaseous mixture with the pressure of 0.5 MPa and temperature of 20°C, released from tanks with the volume of 10 m^3. The analysis concerns the larger diameter of the damage, i.e. 5 cm. Two values of the ammonia-hydrogen mixture volumetric ratio are assumed for the considerations: 20/80 and 80/20. In the case of the smaller diameter of the damage, the hazard zones will not occur.

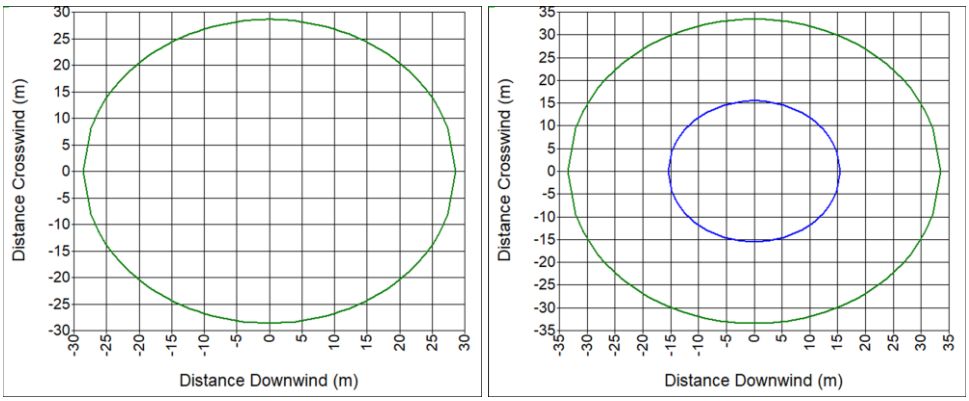
The ranges of the radiation zones shown in the above figures depend, among other things, on the amount of the stored gas and the mass flow through the hole. For pure ammonia, the mass flow is 1.82 kg/s, whereas for pure hydrogen it totals 0.62 kg/s. Figures 8 and 9 show the range of the areas of thermal radiation due to the formation of a fireball. The ranges are shown for the failure of the 10 m^3 tank and two different compositions of the ammonia-hydrogen mixture. Like for the jet fire, the zones illustrate the range of the fireball-generated heat flux values of 4, 12.5 and 37.5 kW/m^2.

Table 4 and Table 5 present the maximum ranges of hazard zones associated with the effects of the heat flux generated by fires of ammonia and its mixture with hydrogen. Table 4 refers



a) b)

Fig. 8. Heat flux generated by a fireball for the ammonia-hydrogen mixture; tank volume: 10 m^3 (green – 4 kW/m^2, blue – 12.5 kW/m^2, red – 37.5 kW/m^2): a) ammonia (mass: 44.3 kg); b) hydrogen (mass: 4.95 kg).



a) b)

Fig. 9. Heat flux generated by a fireball for the ammonia-hydrogen mixture; tank volume: 10 m^3 (green – 4 kW/m^2, blue – 12.5 kW/m^2, red – 37.5 kW/m^2): a) ammonia-hydrogen (80/20), mass: 35.73 kg; b) ammonia-hydrogen mixture (20/80) mass: 12.36 kg.

Table 4. Maximum range of radiation hazard zones for varying portions of gases (hole (damage) with the diameter of 5 cm).

H_2/NH_3	4 kW/m^2	12.5 kW/m^2	37.5 kW/m^2
0/100	30.0 m	26.0 m	–
20/80	19.0 m	14.8 m	–
80/20	19.2 m	15.0 m	–
100/0	21.8 m	16.3 m	6.0 m

Table 5. Maximum range of radiation hazard zones for varying portions of gases (hole (damage) with the diameter of 5 cm).

H_2/NH_3	4 kW/m^2	12.5 kW/m^2	37.5 kW/m^2
0/100	27.5 m	-	–
20/80	28.0 m	-	–
80/20	34.0 m	15.0 m	–
100/0	37.5 m	20.0 m	7.5 m

to the case of a jet fire, while Table 5 refers to the case of a fireball.

If pure ammonia is ignited, the maximum radiation due to the fire totals 4 kW/m^2. With the addition of hydrogen, higher values of radiation will appear, including the zone posing a death hazard. The range of radiation depends on the proportion of hydrogen in the mixture, but it does not exceed several metres.

6. Risk of the occurrence of undesirable effects of an uncontrolled release of ammonia and an ammonia-hydrogen mixture

The following is an estimation of the risk arising due to the failure of an example storage tank of gaseous ammonia and of the ammonia-hydrogen 80/20, 50/50 and 20/80 mixture. The analysed tank storing gas with a pressure of 0.5 MPa and a temperature of 20°C has a volume of 10 m^3; the equivalent diameter of the damage is 5 cm.

6.1. Estimation of the probability of occurrence of dangerous events triggered by tank damage

An uncontrolled release of ammonia or an ammonia-hydrogen mixture can cause a jet fire, a fireball, the movement of a cloud with a toxic concentration, or the gas can disperse in the atmosphere without causing negative effects. The event tree in Fig. 10 presents various possible scenarios for subsequent events triggered by damage to a tank containing hazardous substances [43]. The probability of the occurrence of the triggering event in the form of damage to the gas tank was assumed at 2×10^{-6} according to [44]. The probability of further events is assumed based on the estimations given, for example, in [43].

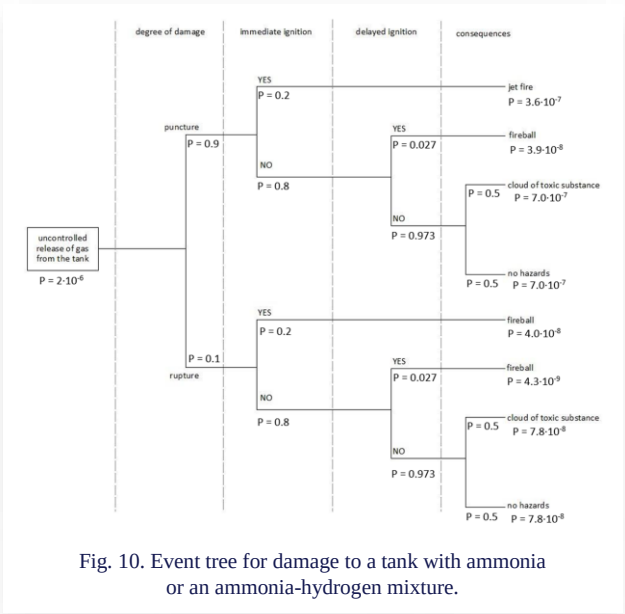


Fig. 10. Event tree for damage to a tank with ammonia or an ammonia-hydrogen mixture.

6.2. Assessment of the consequences of a release of ammonia

The probability of human injuries due to the impact of the negative effects of an accident caused by an uncontrolled release of ammonia and ammonia-hydrogen mixture can be estimated using probit functions. The negative factors affecting humans and the environment in the event of an ammonia release are those analysed above: heat flux, in the case of a fire, and the impact of toxic concentrations, if the released gas cloud does not ignite. For these cases, the probit function can take the form presented in [45]. Based on the analyses presented above of areas with elevated thermal radiation, caused by a fire of ammonia and an ammonia-hydrogen mixture, and areas with elevated ammonia concentrations in the released gas cloud, it is possible to determine the probability of death of humans being within the range of the impact of elevated thermal radiation or elevated toxic gas concentration. The results of such analyses are presented in the figure below.

The graphs shown in the figures below were obtained using probit functions. Different values of the ammonia-hydrogen mixture volumetric ratio and different exposure times were assumed for the considerations. Analysing the graphs presented in Fig. 11, it can be seen that the maximum area will occupy a range of about 30 metres for 5 minutes of exposure. The next figures show the probabilities of death due to the toxic effects of released ammonia. Analysing the graphs presented in Fig. 12, it can be noticed that the concentration of ammonia for the assumed times of exposure does not result in deaths at the level of 100%. The highest probability of death is about 55% and occurs in the area with a radius of about 15 m from the site of the release of pure ammonia. This probability decreases with an increasing proportion of hydrogen in the mixture.

6.3. Estimation of the risk of death due to damage to a tank containing ammonia and an ammonia-hydrogen mixture

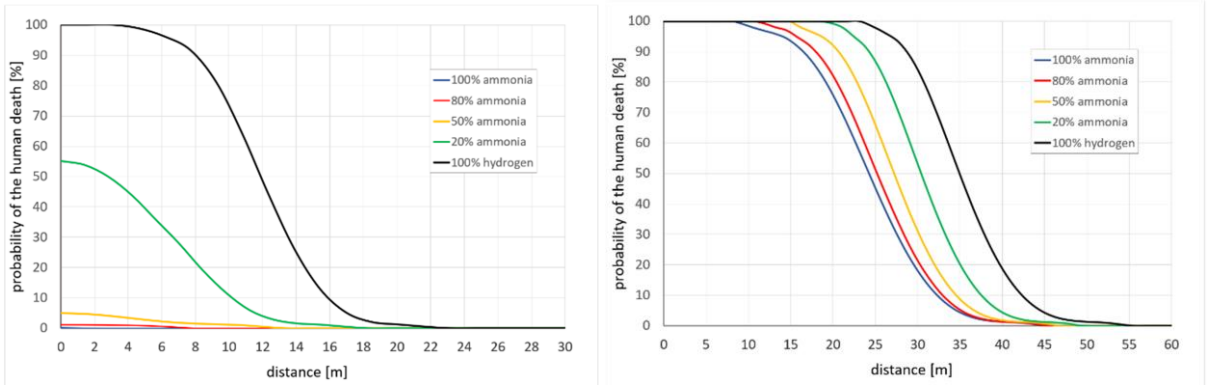
The total risk of death due to the release of ammonia, hydrogen and the ammonia-hydrogen mixtures with the proportions of 80/20, 50/50 and 20/80 resulting from the occurrence of undesirable events following damage to the storage tank is shown in Fig. 13. The calculations were carried out for a tank with a capacity of 10 m^3. The graph shows the risk for the longer analysed time of exposure to negative factors, i.e. 5 minutes.

The total risk level is of the order of 10^{-7} and similar for the analysed compositions of the mixtures. However, the range of the risk varies. The risk due to the release of pure ammonia is the highest, but it occurs in a small area about 10 metres from the tank. The risk posed by the release of the mixture with hydrogen is slightly lower but extends over a larger area.

Figure 14 shows risk diagrams with selected scenarios of uncontrolled release of ammonia and its mixture with hydrogen. For each scenario, both related to toxic hazards and fire hazards, the probability of occurrence and the probability of causing human death are given. The following figure refers to different distances from the accident site and gas release, i.e. risk at a distance of 20 m and 40 m from the gas leak site.

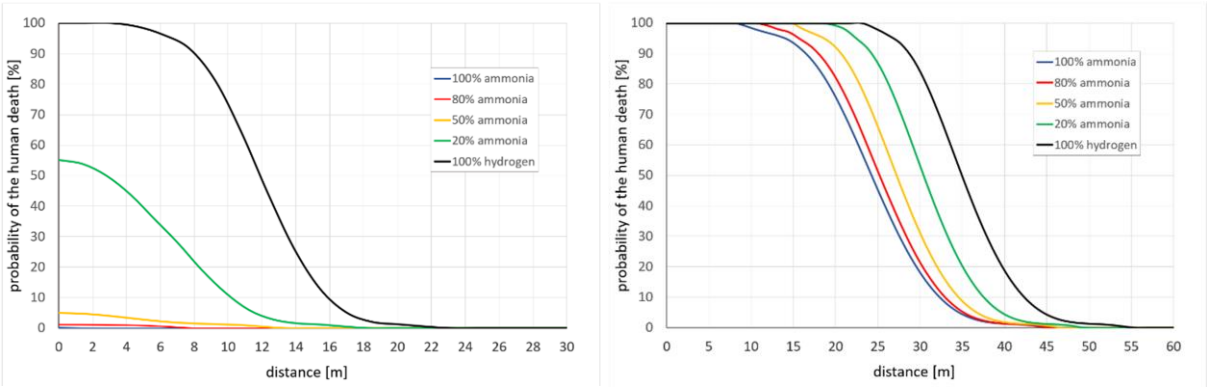
7. Summary

The intensive search for new fuels that can effectively replace hydrocarbon fuels, the combustion of which is considered a ma-



a) b)

Fig.11. Probability of death from exposure to heat radiation generated by a fireball for different compositions of the ammonia-hydrogen mixture and for different exposure times (tank volume 10 m^3): a) 0.5 minutes of exposure; b) 5 minutes of exposure.



a) b)

Fig.12. Probability of death due to the impact of toxic concentrations of ammonia for different compositions of the ammonia-hydrogen mixture and for different exposure times (tank volume 10 m^3): a) 0.5 minutes of exposure; b) 5 minutes of exposure.

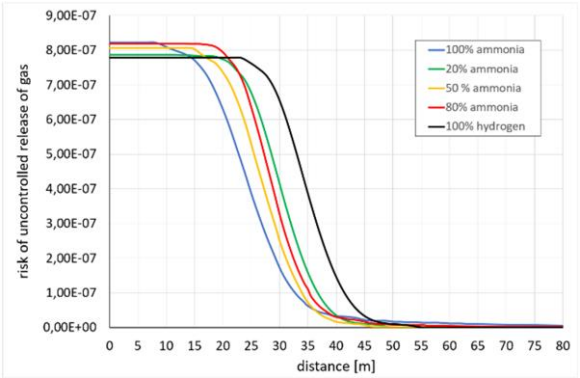


Fig. 13. Risk of death due to the impact of toxic concentrations and heat flux for released ammonia and the ammonia-hydrogen mixture.

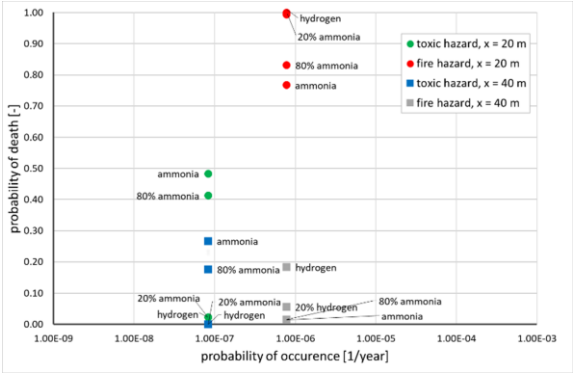


Fig. 14. Risk diagram at 20 meters and 40 metres for ammonia and ammonia-hydrogen mixture leak scenarios.

jor cause of climate changes, indicates that hydrogen fuels could be the solution. In addition to pure hydrogen, the use of ammonia as a stand-alone fuel or as an additive to other gases, such as hydrogen, is also being considered. The paper presents an analysis of the safety of storing such fuels, with a special emphasis on the toxic hazard posed by ammonia, the fire hazard posed by hydrogen and the mutual contribution of these hazards in mixtures of the two gases. Two sizes of damage and different ammonia-to-hydrogen ratios in the mixture were analysed in detail. At a release of gaseous ammonia, the zones with a concentration of 10 000 ppm, i.e. those that can cause death to people, reach a distance of several metres for a small diameter of the damage

and about 60 metres if the damage diameter is large. The capacity of the tank itself, i.e. the amount of the stored gas, affects the time of duration of high concentrations, which is about a few minutes for the 10 m^3 tank.

Ammonia-hydrogen mixtures present a smaller toxic hazard, but the fire hazard becomes more real. A 20% share of hydrogen in the mixture reduces the toxic zone range by several per cent. An 80% share of hydrogen reduces the hazard zones by more than three times. The addition of hydrogen results in the appearance of hazard zones due to the potential impact of thermal radiation from fires of the released mixture. The range of the zones for the analysed volumes of the gases totals several metres. The total risk determined for the effects of toxic concentrations and the fire-generated heat flux has values of the order of 10^{-7}. This level of risk is considered acceptable. Depending on the composition of the mixture, it extends over an area of 30 to 40 m.

The above conclusions concern the leakage of the analysed gases from a 10 m^3 tank under the assumed atmospheric conditions. Leakages from tanks of smaller volume will generally pose a hazard to a relatively smaller area, while tanks of larger volume or diameter of damage may increase both the range and duration of the hazard. Similarly, different meteorological conditions will influence the dispersion of the analysed gases and, consequently, the expected ranges of the hazard zones and levels of risk. Therefore, quantitative results should not be directly applied to other scenarios without calculating the relevant input parameters again, although the general trends observed for different compositions of the ammonia-hydrogen mixture remain valid. It was indeed the aim of the study to compare risk levels for different gas mixture compositions.

Acknowledgements

The presented work was supported by the Silesian University of Technology within statutory research funds.

References

[1] Berwal, P., Kumar, S., & Khandelwal, B. (2021). A comprehensive review on synthesis, chemical kinetics, and practical application of ammonia as future fuel for combustion. *Journal of the Energy Institute*, 99, 273–298. doi: 10.1016/j.joei.2021.10.001

[2] Tornatore, C., Marchitto, L., Sabia, P., & De Joannon, M. (2022). Ammonia as green fuel in internal combustion engines: State-of-the-art and future perspectives. *Frontiers in Mechanical Engineering*, 8, 944201. doi: 10.3389/fmech.2022.944201

[3] Stančin, H., Mikulčić, H., Wang, X., & Duić, N. (2020). A review on alternative fuels in future energy system. *Renewable and Sustainable Energy Reviews*, 128, 109927. doi: 10.1016/j.rser.2020.109927

[4] Herbinet, O., Barocci, P., & Grinberg-Dana, A. (2022). On the use of ammonia as a fuel – A perspective. *Fuel Communications*, 11, 100064. doi: 10.1016/j.jfueco.2022.100064

[5] Elbaz, A.M., Wang, S., Guiberti, T.F., & Roberts, W.L. (2022). Review on the recent advances on ammonia combustion from the fundamentals to the applications. *Fuel Communications*, 10, 100053. doi: 10.1016/j.jfueco.2022.100053

[6] Jeerh, G., Zhang, M., & Tao, S. (2021). Recent progress in ammonia fuel cells and their potential applications. *Journal of Materials Chemistry A*, 9(2), 727–752. doi: 10.1039/D0TA08810B

[7] Song, H., Lu, Z., Ma, Z., Guo, X., & Guo, Q. (2024). Thermodynamic analysis of the performance of an irreversible ammonia-fed solid oxide fuel cell. *Archives of Thermodynamics*, 45(2), 279–290. doi: 10.24425/ather.2024.150872

[8] Valera-Medina, A., Vigueras-Zuniga, M.O., Shi, H., Mashruk, S., Alnajideen, M., Alnasif, A., Davies, J., Wang, Y., Zhu, X., Yang, W., & Cheng, Y.B. (2024). Ammonia combustion in furnaces: A review. *International* Journal *of Hydrogen Energy*, 49(Part B), 1597–1618. doi: 10.1016/j.ijhydene.2023.10.241

[9] Yang, F., Liu, J., Abdellatief, T.M.M., Liu, H., & Duan, X. (2026). Combustion characteristics of the hydrogen and ammonia co-combustion under engine-relevant conditions. *Results in Engineering*, 30, 110724. doi: 10.1016/j.rineng.2026.110724

[10] Zhang, Z., Pan, J., Fan, B., Fu, W., Quaye, E.K., Lu, Q., & Yang, W. (2026). Combustion characteristics and mechanisms of ammonia and ammonia-hydrogen blends: A review and future pathways in the big data era. *International Journal of Hydrogen Energy*, 235, 155230. doi: 10.1016/j.ijhydene.2026.155230

[11] Wakasugi, T., Tsuru, D., & Watanabe, H. (2025). Spray combustion of ammonia–hydrocarbon blended fuels under high-pressure dual-fuel conditions in large engines: Numerical investigation. *Applications in Energy and Combustion Science*, 24, 100425. doi: 10.1016/j.jaecs.2025.100425

[12] Tutak, W., Jamrozik, A., Grab-Rogaliński, K., Pyrc, M., & Gruca, M. (2026). Effect of ammonia-hydrogen fuel ratio on combustion stability, performance and emissions of an industrial diesel engine. *International Journal of Hydrogen Energy*, 205, 153373. doi: 10.1016/j.ijhydene.2026.153373

[13] Mardani, A., Kim, H., Oh, S., Kim, K.C., Xia, X., & Qi, F. (2026). Experimental investigation of an ammonia-hydrogen-methane non-premixed high swirl model combustor for preheated and diluted air regime. *International Journal of Hydrogen Energy*, 207, 153430. doi: 10.1016/j.ijhydene.2026.153430

[14] Eckart, S., Salzano, E., Richter, A., Alnajideen, M., Valera-Medina, A., Shrestha, K.P., Yasiry, A., Wang, J., Bauer, F., Yu, C., Krause, H., & Pio, G. (2026). Exploring the potential of ammonia as a fuel: Advances in combustion understanding and large-scale furnace applications. *Fuel*, 403, 136746. doi: 10.1016/j.fuel.2025.136746

[15] Padappayil, R.P., & Borger, J. (2023). *Ammonia toxicity*. StatPearls. https://www.ncbi.nlm.nih.gov/books/NBK546677/ [accessed 30 Jan. 2026].

[16] Salamonowicz, Z., Majder-Łopatka, M., Dmochowska, A., Rogula-Kozłowska, W., Piechota-Polanczyk, A., & Polanczyk, A. (2022). Ammonia dispersion in the closed space of an ammonia engine room with forced ventilation in an industrial plant. *Atmosphere*, 13(7), 1062. doi: 10.3390/atmos13071062

[17] Yang, M., & Lam, J.S.L. (2024). Risk assessment of ammonia bunkering operations: Perspectives on different release scales. *Journal of Hazardous Materials*, 468, 133757. doi: 10.1016/j.jhazmat.2024.133757

[18] Schmitz, P., Reniers, G., & Swuste, P. (2021). Determining a realistic ranking of the most dangerous process the ammonia production process: A practical approach. *Journal of Loss Prevention in the Process Industries*, 70, 104395. doi: 10.1016/j.jlp.2021.104395

[19] Ge, Y., Yang, Z., He, H., Wu, X., Chen, Y., Lv, Z., & Zhang, Y. (2023). Risk evaluation of ammonia leakage based on modified probability calculation formulas. *Journal of Thermal Science*, 32(2), 854–865. doi: 10.1007/s11630-023-1781-3

[20] Zhang, Z., Zhang, Z., Zhou, Y., Ouyang, Y., Sun, J., Zhang, J., Li, B., Zhang, D., Wang, Y., Yao, J., Xing, H., & Xie, L. (2025). Review of the diffusion process, explosion mechanism, and det-

ection technology of hydrogen and ammonia. *Energies*, 18(10), 2526. doi: 10.3390/en18102526

[21] Cheng, J., & Zhang, B. (2024). Experimental study on the explosion characteristics of ammonia-hydrogen-air mixtures. *Fuel*, 363, 131046. doi: 10.1016/j.fuel.2024.131046

[22] Wang, J., Li, Q., Chen, B., Lu, H., Wu, J., Jiang, J., Yang, Z., & Duan, Q. (2026). Self-ignition characteristics and shock wave dynamics in high-pressure hydrogen-ammonia mixtures: A computational study. *International Journal of Hydrogen Energy*, 198, 152641. doi: 10.1016/j.ijhydene.2025.152641

[23] Zheng, K., Song, Z., Song, C., Jia, Q., Ren, J., & Chen, X. (2024). Investigation on the explosion of ammonia/hydrogen/air in a closed duct by experiments and numerical simulations. *International Journal of Hydrogen Energy*, 79, 1267–1277. doi: 10.1016/j.ijhydene.2024.07.124

[24] Liang, H., Yan, X., Shi, E., Wang, X., Qi, C., Ding, J., Zhang, L., Chen, L., Lv, X., & Yu, J. (2024). Effect of hydrogen blending on ammonia/air explosion characteristics under wide equivalence ratio. *Energy*, 297, 131334. doi: 10.1016/j.energy.2024.131334

[25] Mandal, A., Roy, S., Sarkar, S., & Mukhopadhyay, A. (2026). Flame stabilization in a non-premixed ammonia-hydrogen-air micro-combustor with a 1 mm channel. *International Journal of Hydrogen Energy*, 197, 152650. doi: 10.1016/j.ijhydene.2025.152650

[26] Zheng, K., Chen, Y., Zhang, S., Jia, Q., & Peng, M. (2025). Explosion behavior of premixed hydrogen/ammonia/air mixtures with the addition of N_2 and CO_2. *International Journal of Hydrogen Energy*, 117, 50–61. doi: 10.1016/j.ijhydene.2025.03.148

[27] Duong, P.A., Ryu, B.R., Song, M.K., Nguyen, H.V., Nam, D., & Kang, H. (2023). Safety assessment of the ammonia bunkering process in the maritime sector: A review. *Energies*, 16(10), 4019. doi: 10.3390/en16104019

[28] Masia, B., Yang, M., & Cozzani, V. (2024). Risk assessment of ammonia fueled ships: Consequences on human health of ammonia releases from damaged fuel storage tanks. *ACS Chemical Health & Safety*, 31(6), 503–520. doi: 10.1021/acs.chas.4c00044

[29] Ghavam, S., Vahdati, M., Wilson, I. A. G., & Styring, P. (2021). Sustainable ammonia production processes. *Frontiers in Energy Research*, 9, 580808. doi: 10.3389/fenrg.2021.580808

[30] Aziz, M., Wijayntana, A.T., & Nandiyanto, A.B.D. (2020). Ammonia as effective hydrogen storage: A review on production, storage and utilization. *Energies*, 13(12), 3062. doi: 10.3390/en13123062

[31] Tan, W., Dong, L., Guo, X., Du, H., Liu, L., & Wang, Y. (2020). Accident consequence calculation of ammonia dispersion in factory area. *Journal of Loss Prevention in the Process Industries*, 67, 104271. doi: 10.1016/j.jlp.2020.104271

[32] Bicer, Y., & Dincer, I. (2017). Evaluation of renewable and conventional ammonia as a potential solution. In *Towards 100% Renewable Energy. Springer Proceedings in Energy* (pp. 69–86). Springer Nature. doi: 10.1007/978-3-319-45659-1_7

[33] Ilbas, M., Kumuk, O., & Karyeyen, S. (2021). Numerical study of a swirl gas turbine combustor for turbulent air and oxy-combustion of ammonia/kerosene fuels. *Fuel*, 304, 121359. doi: 10.1016/j.fuel.2021.121359

[34] Ito, S., Uchida, M., Suda, T., & Fujimori, T. (2020). Development of ammonia gas turbine co-generation technology. *IHI Engineering Review*, 53(1), 1–6.

[35] Shang, A., Song, H., & Ma, Z. (2025). Exergetic performance analysis of a direct ammonia-fed solid oxide fuel cell. *Archives of Thermodynamics*, 46(1), 193–200. doi: 10.24425/ather.2025.154193

[36] Portarapillo, M., Bellucci Sessa, A., Russo, D., & di Benedetto, A. (2025). Ammonia as a hydrogen carrier: Energetic assessment of processes integrated with fuel cells for power generation. *Energy & Fuels, 39*(5), 2843–2853. doi: 10.1021/acs.energyfuels.4c04626

[37] Rusin, A., Stolecka-Antczak, K., Kapusta, K., Rogoziński, K., & Rusin, K. (2021). Analysis of the effects of failure of a gas pipeline caused by mechanical damage. *Energies*, 14(22), 7686. doi: 10.3390/en14227686

[38] Hansen, O.R., & Martini, R. (2020). Hydrogen and ammonia infrastructure safety and risk information and guidance. *Report for: Ocean Hyway Cluster*, Report No: PRJ11100256122r1.

[39] AmmoniaKnowHow (2015). *Ammonia – Toxicological overview* AmmoniaKnowHow Website. https://www.ammoniaknowhow.com/ammonia-toxicological-overview/ [accessed 30 Jan. 2026]

[40] Wang, B., Lv, H., Shi, Z., Shen, Y., & He, P. (2025). A device perspective study on hydrogen safety for 70 MPa hydrogen dispenser. *Process Safety and Environmental Protection*, 202(B), 107809. doi: 10.1016/j.psep.2025.107809

[41] Stolecka, K., & Rusin, A. (2020). Analysis of hazards related to syngas production and transport. *Renewable Energy*, 146, 2535–2555. doi: 10.1016/j.renene.2019.08.102

[42] DNV. (2011). *PHAST* (Version 6.7).

[43] Vílchez, J.A., Espejo, V., & Casal, J. (2011). Generic event trees and probabilities for the release of different types of hazardous materials. *Journal of Loss Prevention in the Process Industries*, 24, 281–287. doi: 10.1016/j.jlp.2011.01.005

[44] Rosa, A.C., de Souza, I.T., Terra, A., Hammad, A.W.A., Di Gregório, L.T., Vazquez, E., & Haddad, A. (2021). Quantitative risk analysis applied to refrigeration industry using computational modelling. *Results in Engineering*, 9, 100202. doi: 10.1016/j.rineng.2021.100202

[45] Duijm, N.J., Markert, F., & Paulsen, J.L. (2005). *Safety assessment of ammonia as a transport fuel* (Risø-R-1504(EN)). Risø National Laboratory. DTU Orbit repository

Co-published by
Institute of Fluid-Flow Machinery
Polish Academy of Sciences
Committee on Thermodynamics and Combustion
Polish Academy of Sciences

Copyright©2026 by the Authors under licence CC BY-NC-ND 4.0

http://www.imp.gda.pl/archives-of-thermodynamics/

Experimental test and simulation of properties from ternary Bi-Ni-Pb system: microstructural, mechanical, electrical properties, Scheil and Lever simulation

Veljko Minic[a], Nikola Bojanic[a], Milena Zecevic[a*], Aleksandar Djordjevic[a], Dragan Manasijevic[b], Milan Kolarevic[c]

[a]Faculty of Technical Science, Department of Technological Engineering, University of Prishtina in Kosovska Mitrovica, Kneza Milosa 7, Kosovska Mitrovica, Kosovo[**]
[b]Technical Faculty in Bor, University of Belgrade, VJ 12, 19210 Bor, Serbia
[c]Faculty of Mechanical and Civil Engineering in Kraljevo,University of Kragujevac, Kraljevo, Serbia
[*]Corresponding author email: milena.premovic@gmail.com, [**]UNSCR 1244

Received: 24.04.2026; revised: 14.08.2026; accepted: 10.09.2026

Abstract

Due to the wide application of nickel alloys, the ternary Bi-Ni-Pb system was experimentally investigated. The microstructure, Brinell hardness, and electrical conductivity of 15 ternary alloys were examined. The prepared alloys were selected from three vertical sections: Bi-NiPb, Ni-BiPb and Pb-BiNi. The observed microstructures were compared with the calculated isothermal section at 25°C, and good agreement was achieved. Brinell hardness was measured at three different points on each sample, and the mean values were used to predict hardness across the entire composition range. Hardness prediction was performed using a mathematical model developed through ANOVA analysis. Among the investigated ternary alloys, $Bi_{40}Ni_{40}Pb_{20}$ and $Bi_5Ni_{90}Pb_5$ exhibited the highest hardness values. Electrical conductivity was measured at four different points on each sample, and the mean values were used to predict electrical conductivity throughout the composition range. The $Bi_5Ni_{90}Pb_5$ alloy showed the highest electrical conductivity among all tested ternary alloys. Furthermore, Scheil and Lever simulations were performed for the $Bi_5Ni_{90}Pb_5$ alloy, which exhibited the most favourable combination of mechanical and electrical properties.

Keywords: Mechanical properties; Electrical properties; Microstructural properties; Scheil and Lever simulation; Ternary Bi-Ni-Pb system

Vol. 47(2026), No. 3, 213–232; doi: 10.24425/ather.2026.7520

Cite this manuscript as: Minic, V., Bojanic, N., Zecevic, M., Djordjevic, A., Manasijevic, D., & Kolarevic, M. (2026). Experimental test and simulation of properties from ternary Bi-Ni-Pb system: microstructural, mechanical, electrical properties, Scheil and Lever simulation. *Archives of Thermodynamics*, 47(3), 213–232.

1. Introduction

Nickel and nickel-based alloys have been extensively studied in the literature [1–3] due to their wide range of industrial applications, including lead wires, battery components, transducers, spark electrodes and heat exchangers. In addition to nickel, both bismuth [4] and lead [5] have attracted considerable scientific interest because of their unique physical and chemical properties. Bismuth-based alloys are widely recognised as environmentally friendly alternatives to lead-containing materials because of their low toxicity, low melting temperature and favourable casting behaviour. The addition of nickel to Bi-Pb alloys

may significantly modify the phase constitution, mechanical properties, electrical conductivity and solidification behaviour, making these ternary alloys attractive for applications requiring tailored combinations of physical and mechanical properties.

Previous investigations of the Bi-Ni-Pb system and related ternary alloy systems have primarily focused on phase equilibria, thermodynamic assessment and microstructural characterisation. Reliable knowledge of phase relationships is essential for understanding alloy behaviour and for predicting the formation of equilibrium and non-equilibrium phases during solidification. However, considerably less attention has been devoted to correlating alloy composition and phase constitution with mechanical and electrical properties, although these characteristics are of primary importance for the practical application and optimisation of multicomponent alloys.

The ternary Bi-Ni-Pb system was previously investigated by our research group [6]. The reported results focused on the experimental determination of phase equilibria. The studied alloys were used to establish phase relationships along three vertical sections (x(Bi) = 0.75, x(Ni) = 0.10, and x(Pb) = 0.90) as well as two isothermal sections at 100°C and 300°C. Based on these results, a reliable thermodynamic description of the ternary Bi-Ni-Pb system was developed in Ref. [6], and this thermodynamic database was employed in the present study.

In recent years, statistical approaches such as response surface methodology (RSM) and mixture experimental designs have become valuable tools in materials science for establishing quantitative relationships between alloy composition and material properties. Unlike conventional factorial designs, mixture designs explicitly account for the compositional constraint that the sum of all components is constant. These methods enable efficient optimisation of multicomponent alloy systems, reduce the number of required experiments and provide predictive mathematical models for engineering applications. Their application has been successfully demonstrated for the optimisation of mechanical, electrical, thermal and corrosion properties of metallic materials.

In the current work, fifteen ternary alloys were prepared and subjected to various experimental investigations. Their microstructures were characterised using light optical microscopy (LOM) and scanning electron microscopy (SEM). The chemical compositions of the alloys and their constituent phases were determined by energy-dispersive spectroscopy (EDS), while phase identification was performed using X-ray diffraction (XRD) analysis.

The experimental SEM-EDS and XRD results were compared with the calculated isothermal section at 25°C, showing good agreement between the experimental observations and thermodynamic predictions. The isothermal section at 25°C was calculated using the Pandat software [7].

Hardness and electrical conductivity were measured on the same set of alloys. Since these properties are strongly influenced by alloy composition, phase distribution and microstructure, predictive modelling can provide valuable guidance for alloy design while reducing experimental effort. The average values obtained from the experimental measurements were therefore used for mathematical modelling based on response surface methodology and mixture design. In addition, Scheil and Lever simulations were performed for the $Bi_5Ni_{90}Pb_5$ alloy using Pandat software to evaluate their solidification behaviour and to compare equilibrium and non-equilibrium solidification paths with the experimentally observed microstructures.

The novelty of the present work lies in the combined experimental, thermodynamic and statistical investigation of the Bi-Ni-Pb ternary system. By integrating phase-equilibria calculations, microstructural characterisation, mechanical and electrical property measurements, response surface modelling and solidification simulations, the study establishes quantitative composition-structure-property relationships that may facilitate the design and optimisation of Bi-Ni-Pb alloys for future engineering applications.

2. Materials and methods

2.1. Experimental procedure

A total of fifteen ternary and three binary alloy samples were prepared from high-purity elemental materials (Bi, Ni and Pb, 99.999 at. %) supplied by Alfa Aesar, Germany. The experimental compositions were selected to achieve the broadest possible coverage of the ternary compositional space, thereby ensuring representative sampling of the system. The mass of each ternary alloy sample was approximately 5 g. The accurately weighed amounts of the constituent elements were melted using an arc-melting furnace under a high-purity argon atmosphere with a non-consumable tungsten electrode. To ensure sufficient mixing and chemical homogeneity, each sample was remelted five times. After the final melting step, the alloys were slowly cooled to room temperature. The average mass loss during the melting process was approximately 0.5% of the initial sample mass. The nominal compositions of the prepared alloys are listed in Table 1.

The nominal compositions of the investigated alloys were chosen along three vertical sections of the Bi-Ni-Pb ternary system. Specifically, samples 1–5 were located on the Bi-NiPb section, samples 6–11 on the Ni-BiPb section, and samples 12–15 on the Pb-BiNi section, enabling systematic investigation of the influence of composition on the microstructure and measured properties.

The prepared samples were divided into two groups according to the planned characterisation methods. The first group was subjected to XRD analysis for phase identification, while the second group was used for microstructural characterisation by LOM and SEM-EDS, as well as for electrical conductivity and hardness measurements.

For X-ray diffraction (XRD) analysis, the selected samples were mechanically crushed and ground into fine powders. Powder XRD patterns were collected using a D2 PHASER diffractometer (Bruker, Karlsruhe, Germany) equipped with a dynamic scintillation detector and a ceramic Cu X-ray tube (KFL-Cu-2K). The measurements were performed in the 2θ range from 5° to 75° with a step size of 0.02°. Phase identification was carried out using the TOPAS 4.2 software package and the ICDD PDF-2 database (2013). The diffractometer was calibrated using the Bruker standard Korundprobe A26-B26-S. In addition, ten high-purity elemental powders purchased from

Table 1. Nominal composition of Bi-Ni-Pb alloys used for experimental tests.

Number (mark of sample)	Alloy nominal composition (mole fraction)		
	Bi	Ni	Pb
B1	0	0.5	0.5
1	0.2	0.4	0.4
2	0.4	0.3	0.3
3	0.5	0.25	0.25
4	0.6	0.2	0.2
5	0.8	0.1	0.1
B2	0.5	0	0.5
6	0.45	0.1	0.45
7	0.4	0.2	0.4
8	0.35	0.3	0.35
9	0.3	0.4	0.3
10	0.1	0.8	0.1
11	0.05	0.9	0.05
B3	0.5	0.5	0
12	0.4	0.4	0.2
13	0.3	0.3	0.4
14	0.2	0.2	0.6
15	0.1	0.1	0.8

Alfa Aesar were used as reference materials during the calibration procedure to ensure accurate phase identification and reliable diffraction data analysis.

The samples from the second group were prepared for metallographic examination following a standard preparation procedure. The samples were initially embedded in a polymer resin, followed by sequential grinding using SiC abrasive papers and polishing with diamond paste to obtain a smooth and scratch-free surface. After polishing, the samples were cleaned in an ultrasonic bath to remove any residual contaminants. The prepared specimens were subsequently used for LOM, Brinell hardness and electrical conductivity measurements. For SEM-EDS analysis, the polymer resin was carefully removed after metallographic preparation to expose the sample surface and enable accurate microstructural observation and chemical composition analysis.

The microstructures of the prepared alloys were examined using a light optical microscope (Olympus GX23, Olympus Corporation, Japan). The observations were performed on metallographically prepared surfaces after grinding, polishing, and ultrasonic cleaning.

Hardness measurements were performed using a Brinell hardness tester (INNOVATEST, model NEXUS 3001) according to the ISO 6506 standard. A spherical carbide indenter with a diameter of 2.5 mm was used, and the applied indentation load was 306.4 N for 10 s. The measurements were carried out on metallographically prepared surfaces under controlled conditions. For each alloy, hardness was measured at three different locations to account for possible microstructural heterogeneity, and the average value was calculated and used for further analysis and mathematical modelling. The distance between individual indentations was selected to minimise the influence of neighbouring imprints and to ensure reliable hardness measurements. The Brinell hardness values were determined automatically by the instrument based on the measured indentation diameter.

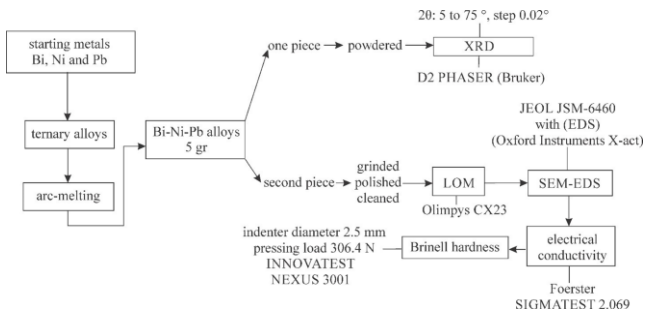


Fig. 1. Scheme of the experimental procedure with the conditions and type of used devices.

Electrical conductivity measurements were carried out using a Foerster SIGMATEST 2.069 eddy current instrument. The measurements were performed at room temperature on metallographically prepared samples with a flat and clean surface to ensure good contact between the probe and the sample. For each alloy, the electrical conductivity was measured at four different positions, and the average value was calculated and used for further analysis and mathematical modelling. Before measurements, the instrument was calibrated using the appropriate reference standards according to the manufacturer's recommendations. The results were expressed in MS/m, and the measurement procedure was performed under identical conditions for all investigated samples to ensure reliable comparison of the electrical conductivity values.

SEM–EDS analysis was performed using a JEOL JSM-6460 scanning electron microscope equipped with an Oxford Instruments X-act EDS detector. Before the measurements, the EDS system was calibrated using a pure copper (Cu) standard to ensure accurate elemental identification and quantitative chemical analysis.

EDS elemental mapping was initially performed to evaluate the compositional homogeneity of the investigated samples and to identify possible elemental segregation. Subsequently, the overall chemical compositions of the alloys and the compositions of individual coexisting phases were determined by EDS point and area analyses. The compositions of the coexisting phases were obtained by analysing several regions corresponding to the same phase in different areas of each sample, providing more reliable compositional values and reducing the influence of local microstructural variations.

A schematic overview of the complete experimental procedure, including sample preparation and subsequent characterisation steps, is presented in Fig. 1.

Experimental results from Brinell hardness and electrical conductivity measurements were used to develop mathematical models describing these properties across the entire compositional range.

2.2. Statistical methodology

The statistical methodology adopted for developing and validating the predictive mixture models is summarised in Fig. 2. The

workflow consisted of five consecutive stages: (i) model selection, (ii) statistical evaluation, (iii) diagnostic analysis, (iv) model visualisation and (v) model validation. This procedure was applied independently to both investigated responses, hardness and electrical conductivity, ensuring a consistent statistical treatment throughout the study [8–10].

The experimental data were analysed using Design-Expert® software (Version 9.0.6, Stat-Ease Inc., Minneapolis, MN, USA) [11]. Scheffé mixture models of increasing complexity (linear, quadratic, special cubic, cubic, special quartic and quartic) were fitted to the experimental data [10,12–14]. For a three-component mixture satisfying the constraint $x_1+x_2+x_3=1$, the investigated Scheffé mixture models can be written as follows [10,12,14]:

Linear: $$\hat{y} = \sum_{i=1}^{q} \beta_i x_i, \quad (1)$$

Quadratic: $$\hat{y} = \sum_{i=1}^{q} \beta_i x_i + \sum_{i<j}^{q-1} \sum_{j}^{q} \beta_{ij} x_i x_j, \quad (2)$$

Special Cubic: $$\hat{y} = \sum_{i=1}^{q} \beta_i x_i + \sum_{i<j}^{q-1} \sum_{j}^{q} \beta_{ij} x_i x_j + \sum_{i<j}^{q-2} \sum_{j<k}^{q-1} \sum_{k}^{q} \beta_{ijk} x_i x_j x_k, \quad (3)$$

Full Cubic: $$\hat{y} = \sum_{i=1}^{q} \beta_i x_i + \sum_{i<j}^{q-1} \sum_{j}^{q} \beta_{ij} x_i x_j + \sum_{i<j}^{q-1} \sum_{j}^{q} \delta_{ij} x_i x_j (x_i - x_j) + \sum_{i<j}^{q-2} \sum_{j<k}^{q-1} \sum_{k}^{q} \beta_{ijk} x_i x_j x_k, \quad (4)$$

Special Quartic:

$$\hat{y} = \sum_{i=1}^{q} \beta_i x_i + \sum_{i<j}^{q-1} \sum_{j}^{q} \beta_{ij} x_i x_j + \sum_{i<j}^{q-2} \sum_{j<k}^{q-1} \sum_{k}^{q} \beta_{iijk} x_i^2 x_j x_k + \sum_{i<j}^{q-2} \sum_{j<k}^{q-1} \sum_{k}^{q} \beta_{ijjk} x_i x_j^2 x_k + \sum_{i<j}^{q-2} \sum_{j<k}^{q-1} \sum_{k}^{q} \beta_{ijkk} x_i x_j x_k^2, \quad (5)$$

Full Quartic:

$$\hat{y} = \sum_{i=1}^{q} \beta_i x_i + \sum_{i<j}^{q-1} \sum_{j}^{q} \beta_{ij} x_i x_j + \sum_{i<j}^{q-1} \sum_{j}^{q} \delta_{ij} x_i x_j (x_i - x_j) + \sum_{i<j}^{q-1} \sum_{j}^{q} \gamma_{ij} x_i x_j (x_i - x_j)^2 + \sum_{i<j}^{q-2} \sum_{j<k}^{q-1} \sum_{k}^{q} \beta_{iijk} x_i^2 x_j x_k +$$
$$+ \sum_{i<j}^{q-2} \sum_{j<k}^{q-1} \sum_{k}^{q} \beta_{ijjk} x_i x_j^2 x_k + \sum_{i<j}^{q-2} \sum_{j<k}^{q-1} \sum_{k}^{q} \beta_{ijkk} x_i x_j x_k^2 + \sum_{i<j}^{q-3} \sum_{j<k}^{q-2} \sum_{k<l}^{q-1} \sum_{l}^{q} \beta_{ijkl} x_i x_j x_k x_l. \quad (6)$$

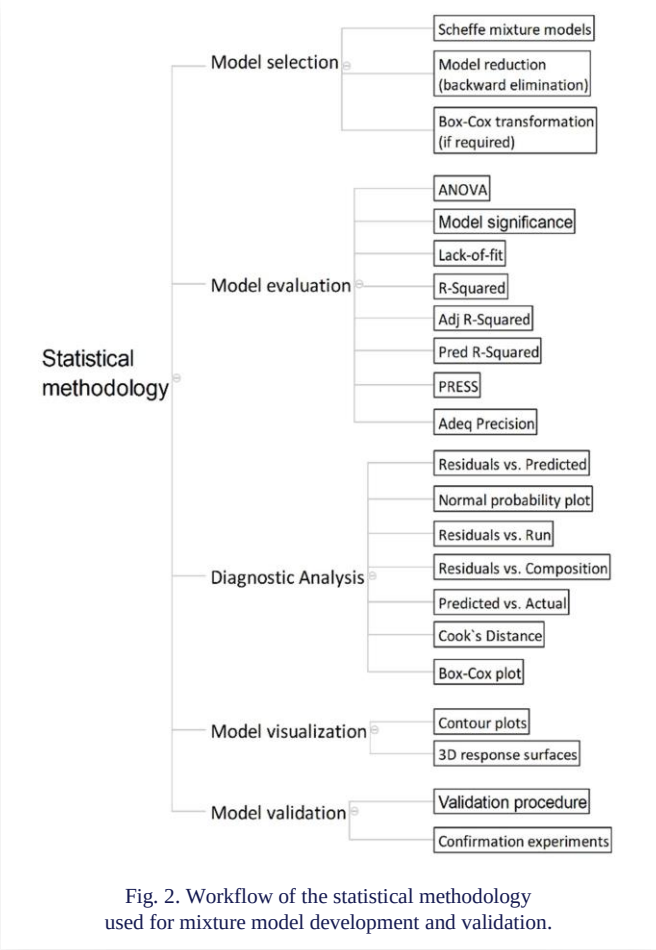


Fig. 2. Workflow of the statistical methodology used for mixture model development and validation.

The candidate Scheffé mixture models were fitted sequentially, and only hierarchical models were considered during model selection. Model reduction was performed using backward elimination with a significance level of $\alpha = 0.05$ while preserving model hierarchy [9,15]. Whenever necessary, a Box-Cox transformation was considered to improve model adequacy; however, no transformation was required for the final models [9,12].

The candidate models were statistically evaluated using analysis of variance (ANOVA) [9,15]. Model significance was assessed by the F-test and associated p-values, whereas goodness-of-fit was evaluated using the coefficient of determination (R^2), adjusted coefficient of determination (Adj. R^2), predicted coefficient of determination (Pred. R^2), predicted residual sum of squares (PRESS), adequate precision and the lack-of-fit test [8,9,11]. The final model for each response was selected by considering both statistical significance and predictive capability rather than relying on a single statistical criterion.

Model adequacy was further examined through residual diagnostics [9,11,15]. Diagnostic plots included predicted versus actual values, residuals versus predicted values, normal probability plots of residuals, residuals versus run order, residuals versus alloy composition, Cook's distance and Box-Cox plots. These analyses were used to verify the assumptions of normality, homoscedasticity, independence of residuals and the absence of influential observations.

The selected models were subsequently visualised using contour plots to illustrate the effects of alloy composition on the investigated responses and to identify regions exhibiting desirable combinations of properties within the experimental design space [8,9,12].

Finally, model validation was carried out by comparing predicted values with independent confirmation experiments performed at selected alloy compositions that were not included in model construction [8,9,11]. The agreement between experimental and predicted values was evaluated using the relative

prediction error, thereby demonstrating the predictive accuracy and practical applicability of the developed mixture models.

3. Results and discussion

Based on the thermodynamic assessment of the ternary Bi-Ni-Pb system reported in Ref. [6], six solid phases and one liquid phase are expected to exist. The identified solid phases and their corresponding crystallographic information are listed in Table 2.

Samples 2–4, 7, and 8 were found to contain the equilibrium phases Bi_3Ni, BiNi and (Pb), as identified by XRD and confirmed by EDS analysis. Their positions in the calculated isothermal section (Fig. 3) are consistent with the BiNi+Bi_3Ni+(Pb) three-phase equilibrium region. Sample 5 was characterised by the equilibrium phases Bi_3Ni, (Pb) and (εPb).

Table 2. Considered phase and their crystal structure data.

Phase names	Common names	Temperature, °C	Composition range in at. %	Strukturbericht symbol and Pearson symbol	Space group	Lattice parameters, Å	Ref.
RHOMBO_A7	(Bi)	0–271	100 Bi	*A7* *hR2*	$R\bar{3}m$	*a*=*b*=4.548, *c*=11.852	[16]
FCC_A1	(Ni) (Pb)	0–1455 0–327	97.80–100 Ni 96.88–100 Pb	*A1* *cF4*	$Fm\bar{3}m$	*a*=*b*=*c*=3.5243 *a*=*b*=*c*=4.9496	[17] [18]
HCP_A3	(εPb)	0–183.64	57.30–75.60 Pb	*A3*	$P6_3/mmc$	*a*=*b*=3.265 *c*=5.387	[19]
BI3NI	Bi_3Ni	0–464.83	25 Ni, 75Bi	*C4* *oP16*	*Pnma*	*a*=8.879 *b*=4.0998 *c*=11.483	[20]
BINI	BiNi	0–645.8	48.47–49.95 Ni	$B8_1$ *mC64*	*F*12/*m*1	*a*=14.124 *b*=8.1621 *c*=21.429	[21]

3.1. Microstructural properties

Fifteen slowly cooled ternary alloys (samples 1–15, listed in Table 1) were experimentally characterised. Their microstruc-tures were examined by LOM and SEM. The chemical compo-sitions of both the bulk alloys and the coexisting phases were determined using EDS. Phase identification was performed by XRD, and the combined EDS and XRD results are summarised in Table 3. The experimental findings were further validated by comparison with the calculated isothermal section of the Bi-Ni-Pb system at 25°C, shown in Fig. 3.

The experimentally determined alloy compositions obtained by EDS are superimposed on the calculated isothermal section as square markers. Excellent agreement was observed between the nominal alloy compositions and those measured by EDS, confirming the reliability of the alloy preparation procedure. To distinguish the three investigated vertical sections, different marker colours were used in Fig. 3. Red squares represent samples 1–5 from the Bi-NiPb vertical section, orange squares correspond to samples 6–11 from the Ni-BiPb vertical section, and green squares denote samples 12–15 from the Pb-BiNi vertical section.

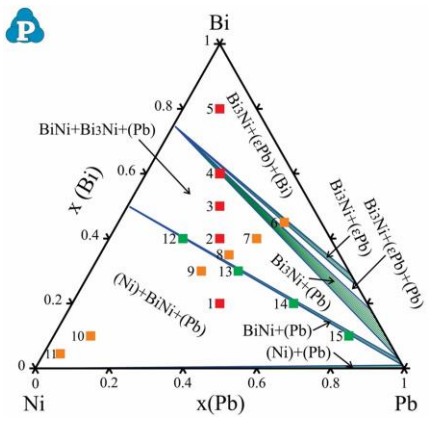


Fig. 3. Predicted isothermal section at 25°C with marked compositions of tested alloys.

The calculated isothermal section at 25°C comprises eight phase fields, including four two-phase and four three-phase equilibrium regions. The experimentally identified phase constitutions are fully consistent with the calculated phase equilibria, demonstrating good agreement between the thermodynamic predictions and the experimental observations.

XRD analysis showed that samples 1 and 9–15 consisted of the three equilibrium phases (Ni), BiNi and (Pb). The phase identification was confirmed by EDS analysis, and the corresponding phase compositions are listed in Table 3. As shown in Fig. 3, these samples are located within the three-phase equilibrium region (Ni)+BiNi+(Pb).

The experimental phase assemblage determined by XRD and EDS is in excellent agreement with the calculated isothermal section, confirming that the alloy belongs to the Bi_3Ni+(Pb)+(εPb) three-phase region.

Similarly, sample 6 was found to consist of the equilibrium phases Bi_3Ni, (Pb) and (εPb). The phases predicted by the calculated isothermal section were confirmed by both XRD and EDS analyses, demonstrating excellent agreement between the experimental observations and thermodynamic calculations.

Consequently, all four predicted three-phase equilibrium regions were experimentally validated. Moreover, the measured phase compositions closely matched the equilibrium compositions predicted by the thermodynamic calculations, further confirming the reliability of the thermodynamic description of the Bi-Ni-Pb system.

Table 3. EDS and XRD results of the ternary Bi-Ni-Pb samples.

Number	Composition of samples in at. %	Predicted phases	Determined phases		Compositions of phases in at. % determined by EDS		
			EDS	XRD	x(Bi)	x(Ni)	x(Pb)
1	20.19 Bi 39.86 Ni 39.95 Pb	(Ni) BiNi (Pb)	(Ni) BiNi (Pb)	(Ni) BiNi (Pb)	0.13 49.53 1.10	99.85 50.43 0.66	0.02 0.04 98.24
2	39.81 Bi 30.19 Ni 30.00 Pb	Bi_3Ni BiNi (Pb)	Bi_3Ni BiNi (Pb)	Bi_3Ni BiNi (Pb)	74.65 49.18 3.14	25.17 50.79 0.72	0.18 0.03 96.14
3	50.21 Bi 25.13 Ni 24.66 Pb	Bi_3Ni BiNi (Pb)	Bi_3Ni BiNi (Pb)	Bi_3Ni BiNi (Pb)	75.12 50.01 3.41	24.79 49.88 0.07	0.09 0.11 96.52
4	59.59 Bi 20.52 Ni 19.89 Pb	Bi_3Ni BiNi (Pb)	Bi_3Ni BiNi (Pb)	Bi_3Ni BiNi (Pb)	75.67 49.32 3.09	24.22 50.59 0.37	0.11 0.09 96.54
5	80.13 Bi 9.81 Ni 10.06 Pb	(Bi) BiNi (εPb)	(Bi) BiNi (εPb)	(Bi) BiNi (εPb)	98.72 50.92 29.87	1.13 48.99 1.00	0.15 0.09 69.13
6	45.12 Bi 9.91 Ni 44.97 Pb	Bi_3Ni (Pb) (εPb)	Bi_3Ni (Pb) (εPb)	Bi_3Ni (Pb) (εPb)	74.25 18.82 25.18	25.72 0.09 0.02	0.03 81.09 74.80
7	39.18 Bi 20.81 Ni 40.01 Pb	Bi_3Ni BiNi (Pb)	Bi_3Ni BiNi (Pb)	Bi_3Ni BiNi (Pb)	74.65 49.97 3.28	25.15 49.88 0.02	0.20 0.15 96.70
8	35.23 Bi 30.17 Ni 34.60 Pb	Bi_3Ni BiNi (Pb)	Bi_3Ni BiNi (Pb)	Bi_3Ni BiNi (Pb)	75.62 49.74 3.19	24.36 50.15 0.04	0.02 0.11 96.77
9	29.81 Bi 40.15 Ni 30.04 Pb	(Ni) BiNi (Pb)	(Ni) BiNi (Pb)	(Ni) BiNi (Pb)	0.18 50.13 0.92	99.70 49.79 0.05	0.12 0.08 99.03
10	9.83 Bi 80.54 Ni 9.63 Pb	(Ni) BiNi (Pb)	(Ni) BiNi (Pb)	(Ni) BiNi (Pb)	0.07 50.23 1.03	99.75 49.72 0.26	0.18 0.05 98.71
11	5.12 Bi 90.03 Ni 4.85 Pb	(Ni) BiNi (Pb)	(Ni) BiNi (Pb)	(Ni) BiNi (Pb)	0.18 49.87 0.98	99.65 50.08 0.37	0.17 0.05 98.65
12	40.71 Bi 39.58 Ni 19.71 Pb	(Ni) BiNi (Pb)	(Ni) BiNi (Pb)	(Ni) BiNi (Pb)	0.15 49.93 0.84	99.77 49.98 0.74	0.08 0.09 98.42
13	30.64 Bi 30.02 Ni 39.34 Pb	(Ni) BiNi (Pb)	(Ni) BiNi (Pb)	(Ni) BiNi (Pb)	0.03 50.07 1.01	99.92 49.82 0.21	0.05 0.11 98.78
14	20.66 Bi 19.82 Ni 59.52 Pb	(Ni) BiNi (Pb)	(Ni) BiNi (Pb)	(Ni) BiNi (Pb)	0.12 49.42 0.97	99.81 50.52 0.50	0.07 0.06 98.53
15	9.92 Bi 10.11 Ni 79.97 Pb	(Ni) BiNi (Pb)	(Ni) BiNi (Pb)	(Ni) BiNi (Pb)	0.15 49.87 0.89	99.79 50.04 0.70	0.06 0.09 98.41

The microstructures of samples 1 and 3 are presented in Fig. 4. Three distinct phases can be clearly distinguished in both micrographs, and the corresponding phases are labelled directly on the images. In both microstructures, the (Pb) phase forms the continuous matrix in which the other two phases are dispersed.

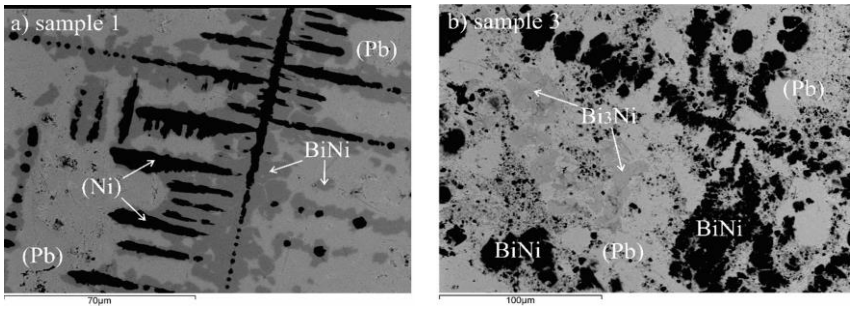


Fig. 4. SEM micrographs of the samples: a) 1; b) 3.

In the microstructure of sample 1, the (Ni) phase appears as a dark contrast phase with clearly defined boundaries, while the BiNi phase exhibits a light-gray contrast and is mainly located in the vicinity of the (Ni) phase. Such a phase arrangement indicates a close spatial relationship between the intermetallic BiNi phase and the Ni-rich regions formed during solidification.

In the microstructure of sample 3, the Bi_3Ni and BiNi phases exhibit similar morphologies and distribution patterns within the (Pb) matrix. The Bi_3Ni phase appears with a dark-gray contrast, whereas the BiNi phase is observed as a darker phase, which can be attributed to the higher Ni content and differences in chemical composition between these intermetallic compounds. The observed phase morphology and distribution are consistent with the phase equilibria predicted by the calculated isothermal section and contribute to the differences in the measured mechanical and electrical properties of the investigated alloys.

3.2. Mechanical properties

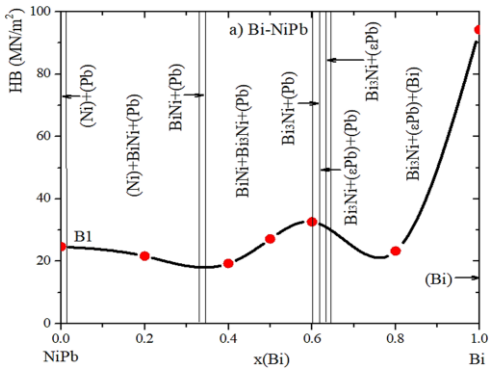
3.2.1. Experimental results

Brinell hardness measurements were performed at three different locations on each sample, and the results are summarised in Table 4. The table provides the sample identification numbers, the calculated phase fractions of the investigated alloys, the individual hardness values obtained from the three measurements and the corresponding average Brinell hardness values. For comparison, the hardness values of the pure constituent elements reported in the literature [22] are also included. The phase fractions of all investigated alloys at room temperature were determined using the thermodynamic database.

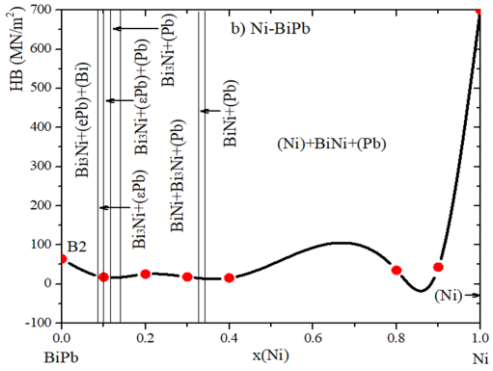
Figure 5 presents the mean Brinell hardness values listed in Table 4 as a function of alloy composition. The graphical representation provides a clear overview of the variation in hardness across the investigated composition ranges and facilitates the analysis of the relationship between alloy composition, phase constitution and the resulting mechanical response.

The measured Brinell hardness values show a clear dependence on the phase constitution of the investigated Bi-Ni-Pb alloys. As presented in Table 4 and Fig. 5, the hardness variation along the three investigated vertical sections is closely associated with changes in the relative fractions of the constituent phases. In particular, the results demonstrate that the mechanical response of the alloys cannot be described solely by their nominal chemical composition, but rather by the phase assemblage developed at room temperature.

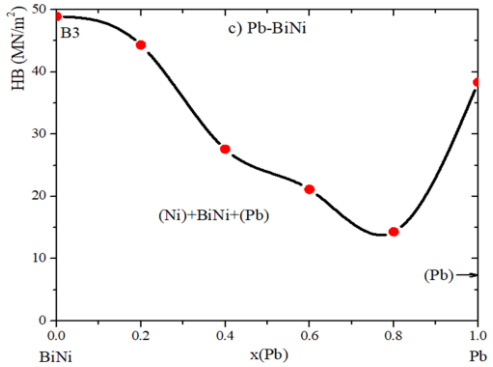
For the Bi-NiPb section (samples 1–5), the Brinell hardness values of the investigated alloys range from 19.3 to 32.6 MN/m^2. The observed variation in hardness can be associated with changes in the relative fractions of the constituent phases. Along this section, three different three-phase regions are encountered. Notably, samples 2–4 belong to the same three-phase region; however, their hardness values differ considerably, indicating that the hardness is influenced not only by the type of phases present but also by their relative proportions.



a).



b).



c).

Fig. 5. Graphical presentation of Brinell hardness dependence of composition and phase fraction: a) vertical section Bi-NiPb; b) vertical section Ni-BiPb; c) vertical section Pb-BiNi.

Sample 2 exhibits the lowest hardness among samples 2–4, with a value of 19.3 MN/m^2. Its phase constitution consists of approximately 17.9% Bi_3Ni, 51.3% BiNi and 30.8% (Pb). In sample 3, the fraction of Bi_3Ni increases substantially to approximately 48.4%, while the BiNi fraction decreases to 25.9%, and the (Pb) fraction remains approximately 25.7%. This change in phase fractions is accompanied by an increase in hardness to 27.1 MN/m^2. For sample 4, the Bi_3Ni fraction increases further to approximately 78.9%, while the fractions of the BiNi and (Pb) phases decrease considerably. Correspondingly, the hardness reaches 32.6 MN/m^2.

Table 4. Calculated phase fractions at room temperature and related Brinell hardness values of B1, B2, B3 and ternary Bi-Ni-Pb alloys.

Number	Calculated fraction of a phase (%)	Measured value (MN/m²)			Mean value (MN/m²)
		1	2	3	
B1	50.0 % (Pb), 50.0 % (Ni)	24.8	25.6	23.7	24.7
1	20.5 % (Ni), 39.1 % BiNi, 40.4 % (Pb)	20.1	22.5	22.3	21.63
2	17.9 % Bi_3Ni, 51.3 % BiNi, 30.8 % (Pb)	18.9	19.4	19.5	19.3
3	48.4 % Bi_3Ni, 25.9 % BiNi, 25.7 % (Pb)	25.5	26.2	29.6	27.1
4	78.9 % Bi_3Ni, 0.6 % BiNi, 20.5 % (Pb)	32.0	33.2	32.6	32.6
5	45.9 % (Bi), 40.0 % BiNi, 14.1 % (εPb)	20.4	24.4	25.1	23.3
Bi	100.0 % (Bi)				94.2 [22]
B2	70.4 % (εPb), 29.6 % (Bi)	64.1	62.8	65.7	64.2
6	40.0 % Bi_3Ni, 1.0 % (Pb), 59.0 % (εPb)	15.5	19.6	17.7	17.6
7	37.6 % Bi_3Ni, 21.3 % BiNi, 41.1 % (Pb)	23.5	26.6	25.4	25.2
8	7.6 % Bi_3Ni, 56.4 % BiNi, 36.0 % (Pb)	16.9	18.5	19.4	18.2
9	10.4 % (Ni), 30.3 % (Pb), 59.3 % BiNi	15.1	13.5	18.3	15.6
10	70.1 % (Ni), 10.1 % (Pb), 19.8 BiNi	34.1	35.1	35.7	34.9
11	85.1 % (Ni), 5.0 % (Pb), 9.9 % BiNi	49.8	52.7	57.1	53.2
Ni	100 % (Ni)				700 [22]
B3	99.9 % BiNi, 0.1 % (Ni)	50.8	47.1	48.9	48.9
12	79.5 % BiNi, 20.2 % (Pb), 0.3 % (Ni)	43.1	43.3	46.5	44.3
13	59.1 % BiNi, 40.4 % (Pb), 0.5 % (Ni)	27.0	28.1	27.7	27.6
14	38.8 % BiNi, 60.6 % (Pb), 0.6 % (Ni)	21.7	20.8	20.7	21.1
15	18.4 % BiNi, 80.8 % (Pb), 0.8 % (Ni)	14.0	14.7	14.3	14.3
Pb	100 % (Pb)				38.3 [22]

Table 5. Mixture model. Model summary statistics used for model selection.

Source	Std. dev.	R^2	Adjusted R^2	Predicted R^2	PRESS	
Linear	1.075535	0.228267	0.198003	0.134089	66.19505	
Quadratic	0.940062	0.445116	0.387316	0.249458	57.37556	
Special Cubic	0.71964	0.681598	0.640951	0.608051	29.96273	
Cubic	0.731591	0.684938	0.628926	0.587455	31.53719	Aliased
Special Quartic	0.698647	0.712674	0.661593	0.619531	29.08518	Suggested
Quartic	0.553781	0.831511	0.787382	0.774756	17.21889	Aliased

The progressive increase in hardness from sample 2 to sample 4 is therefore closely associated with the increasing fraction of the Bi_3Ni phase and the simultaneous reduction in the fractions of the BiNi and Pb-rich constituents. The Bi_3Ni frac-tion increases from 17.9% in sample 2 to 48.4% in sample 3 and 78.9% in sample 4, accompanied by an increase in hardness of approximately 41% and 69%, respectively, relative to sample 2. This trend suggests that Bi_3Ni makes a significant contribution to the overall hardness of the alloys, while the decreasing fraction of the softer Pb-rich constituent further promotes the increase in hardness. These results demonstrate that, even within the same three-phase region, changes in the relative phase fractions can produce a pronounced variation in Brinell hardness.

For the Ni-BiPb section represented by samples 6–11, the Brinell hardness values show a pronounced variation with alloy composition and phase constitution. The investigated compositions are located within three different three-phase regions, indicating that changes in hardness are associated both with changes in the phase assemblage and with variations in the relative fractions of the individual phases.

A more detailed comparison can be made for samples 9–11, which belong to the same three-phase region. Despite having the same type of three-phase phase assemblage, these samples exhibit significant differences in Brinell hardness, demonstrating that the mechanical response is strongly affected by the relative phase fractions. The hardness increases progressively toward sample 11, reaching the highest value of 53.2 MN/m^2. This increase can be associated with the changing proportions of the constituent phases, particularly the increasing fraction of the harder Ni-rich phase (Ni) and the corresponding reduction in the softer constituents.

The comparison of samples 9–11 is particularly important because the phase assemblage remains unchanged, while the phase fractions vary with composition. Therefore, the observed change in hardness cannot be attributed to the appearance of a new phase, but rather to the changing relative contribution of the phases already present. The higher hardness observed for

sample 11 indicates that its phase constitution is more favourable for strengthening, with the larger fraction of the Ni-rich constituent contributing significantly to the overall mechanical response. Conversely, the lower hardness of samples 9 and 10 can be related to their higher proportions of the softer constituents.

Overall, the results for samples 6–11 demonstrate that Brinell hardness is governed by both the type of three-phase region and, importantly, the relative fractions of the constituent phases. The comparison of samples 9–11 shows that substantial changes in hardness can occur even within the same three-phase region, highlighting the significant influence of phase fraction on the mechanical properties of the investigated alloys.

For samples 12–15, all compositions belong to the same three-phase region, allowing the effect of changing phase fractions on Brinell hardness to be evaluated without a change in the phase assemblage. The hardness decreases progressively from 44.3 MN/m^2 for sample 12 to 14.3 MN/m^2 for sample 15. This decrease is associated with a reduction in the fraction of the harder Bi_3Ni phase, from approximately 79.5% in sample 12 to 18.4% in sample 15, accompanied by an increase in the Pb-rich constituent to approximately 80.8%. The results therefore indicate that, even within the same three-phase region, variations in the relative phase fractions have a pronounced effect on hardness, with a higher Bi_3Ni fraction contributing to increased hardness, while an increasing Pb-rich fraction promotes softening.

Among all investigated alloys, the highest Brinell hardness value was recorded for sample 11, reaching 53.2 MN/m^2. The lowest Brinell hardness value was determined for sample 15.

The experimental data given in Table 4 were further used to develop a mathematical model for predicting Brinell hardness across the entire composition range.

3.2.2. Development and validation of the mixture model for Brinell hardness

The hardness model was developed using all experimentally measured Brinell hardness values obtained for the investigated alloy compositions. Three independent hardness measurements were performed for each of the eighteen alloy compositions, resulting in a total of fifty-four experimental observations. In contrast to the previous preliminary analysis based on composition averages, all individual measurements were retained in the regression analysis in order to provide an unbiased estimate of the experimental (pure) error and to enable a statistically valid lack-of-fit test.

Model selection

To describe the influence of the Bi-Ni-Pb composition on Brinell hardness (HB), several Scheffé mixture models of increasing complexity (linear, quadratic, special cubic and special quartic) were evaluated using Design-Expert® software. Model selection was based on standard statistical criteria including the determination (R^2), adjusted coefficient of determination (Adj. R^2), predicted coefficient of determination (Pred. R^2), prediction error sum of squares (PRESS) and adequate precision. In accordance with the principle of parsimony, the simplest hierarchical model providing satisfactory predictive performance was selected (Table 5).

The special cubic mixture model was selected because it provides an adequate balance between goodness of fit and model simplicity. Although the special quartic model produced slightly lower residual error and slightly higher coefficients of determination, the improvement was relatively small, while requiring additional higher-order interaction terms. Since the objective was to obtain a statistically sound and physically interpretable model, the hierarchical special cubic model was adopted for subsequent analyses.

Analysis of variance

The analysis of variance (ANOVA) for the selected special cubic model is presented in Table 6. The overall regression model was highly significant ($F = 16.77$, $p < 0.0001$), indicating that the selected polynomial adequately describes the relationship between alloy composition and Brinell hardness. Among the regression terms, the Bi-Ni (AB), Bi-Pb (AC) and ternary interaction (ABC) were statistically significant ($p < 0.05$), whereas the Ni-Pb interaction (BC) was not statistically significant (Table 7).

The obtained coefficient of determination ($R^2 = 0.682$) indicates that approximately 68% of the total variation in hardness is explained by the selected model. The adjusted coefficient of determination (Adj. $R^2 = 0.641$) remained close to R^2, indicat-

Table 6. ANOVA for special cubic mixture model.

Source	Sum of squares	Degrees of freedom	Mean square	F-value	p-value Prob > F	
Model	52.10509	6	8.684182	16.76866	3.15E–10	significant
Linear mixture	17.44998	2	8.724992	16.84747	3.04E–06	
AB	4.607531	1	4.607531	8.896881	0.004518	
AC	14.32134	1	14.32134	27.6537	3.49E–06	
BC	0.16212	1	0.16212	0.313045	0.578474	
ABC	18.07794	1	18.07794	34.90747	3.7E–07	
Residual	24.34043	47	0.517882			
Lack of fit	23.39639	11	2.126944	81.10836	5.33E–22	significant
Pure error	0.944046	36	0.026223			
Corrected total	76.44552	53				

Table 7. Summary statistics for the selected special cubic mixture model.

Std. dev.	0.71964	**R-squared**	0.681598
Mean	5.314471	**Adj. R-squared**	0.640951
Coeff. var. %	13.54114	**Pred. R-squared**	0.608051
PRESS	29.96273	**Adeq. Precision**	13.32147

ing that unnecessary model terms were not introduced. Likewise, the predicted coefficient of determination (Pred. R^2 = 0.608) differed from Adj. R^2 by less than 0.2, indicating moderate but acceptable predictive capability within the investigated experimental domain. The Adeq. Precision ratio reached 13.32, which is considerably higher than the recommended minimum value of 4, indicating an adequate signal-to-noise ratio for navigation throughout the investigated composition space. The residual standard deviation (std. dev. = 0.720) and PRESS value (29.96) provide additional measures of the model prediction error and should be considered together with the moderate Pred. R^2 value when assessing its predictive performance.

Although the lack-of-fit test was statistically significant, this result is primarily attributed to the very small pure experimental error obtained from the replicated measurements, which makes residual standard deviation, coefficient of determination and the lack-of-fit test highly sensitive even to relatively small deviations between the fitted model and the experimental data. Nevertheless, the residual diagnostic plots showed no systematic patterns or violations of the underlying regression assumptions, while the model retained acceptable predictive capability (Pred. R^2 = 0.608). Therefore, the model was considered adequate for describing the overall compositional trends within the investigated experimental domain, although its predictive accuracy should be regarded as moderate rather than high.

Regression equation and interpretation of the transformed response

The final regression equation describing the square-root transformed Brinell hardness is:

$$(HB)^{0.5}=3.002415(Bi) + 6.917359(Ni) + 2.143854(Pb) + 9.336419(Bi)(Ni) + 18.39945(Bi)(Pb) + \\ + 1.751249(Ni)(Pb) - 71.2602(Bi)(Ni)(Pb). \quad (7)$$

where Bi, Ni and Pb denote the corresponding component fractions in the alloy. The component fractions are expressed in mass fraction and satisfy Bi+Ni+Pb=1.

The linear coefficients do not represent the hardness of the pure components. Instead, they correspond to the linear contribution of each component within the constrained Scheffé mixture model and should therefore be interpreted only together with the interaction terms.

The positive coefficients associated with the Bi-Ni and Bi-Pb interactions indicate positive interaction effects on the square-root transformed hardness response, which are reflected in increased predicted hardness in the corresponding compositional regions after back-transformation, whereas the large negative coefficient of the ternary interaction suggests that the simultaneous presence of all three components reduces hardness relative to that expected from the binary interactions alone.

For practical application, the predicted Brinell hardness is obtained by applying the inverse transformation,

$$HB=[(HB)^{0.5}]^2. \quad (8)$$

Accordingly, the regression equation is first used to calculate the transformed response, after which the predicted Brinell hardness is obtained by squaring the calculated value.

Model diagnostics

Figure 6 shows the diagnostic plots used to validate the regression model. The normal probability plot confirms approximate normality of residuals. Residuals are randomly distributed around zero without systematic trends, indicating homoscedasticity. No influential observations were detected based on externally studentised residuals and Cook's distance. None of the observations exceeded the commonly accepted influence limits. Likewise, the residuals showed no dependence on experimental run order, confirming statistical independence of the observations.

The Box-Cox analysis suggested an optimum transformation close to λ = –0.1. However, the square-root transformation (λ = 0.5) was retained because it lies within the 95% confidence interval of acceptable transformations while providing a simpler and more physically interpretable response transformation. The selected transformation also resulted in satisfactory residual diagnostics and stable prediction performance (Fig. 7).

Response surface analysis

The predicted variation of Brinell hardness throughout the investigated Bi-Ni-Pb composition space is illustrated in Fig. 8.

The contour plot reveals a distinctly nonlinear response surface, indicating pronounced interaction effects among the alloying elements. The highest predicted hardness values are observed in the Bi-Ni-rich region with moderate Pb content, whereas increasing Pb content generally leads to lower hardness. The curvature of the contour lines reflects the contribution of the binary Bi-Ni and Bi-Pb interactions as well as the ternary Bi-Ni-Pb interaction included in the selected special cubic model. This behaviour is consistent with the regression analysis, particularly with the positive Bi-Ni interaction and the negative ternary interaction.

Although the regression analysis was performed using the transformed response, all graphical presentations of the response surface and all reported optimum hardness values are expressed on the original Brinell hardness scale after back-transformation, thereby facilitating engineering interpretation of the results.

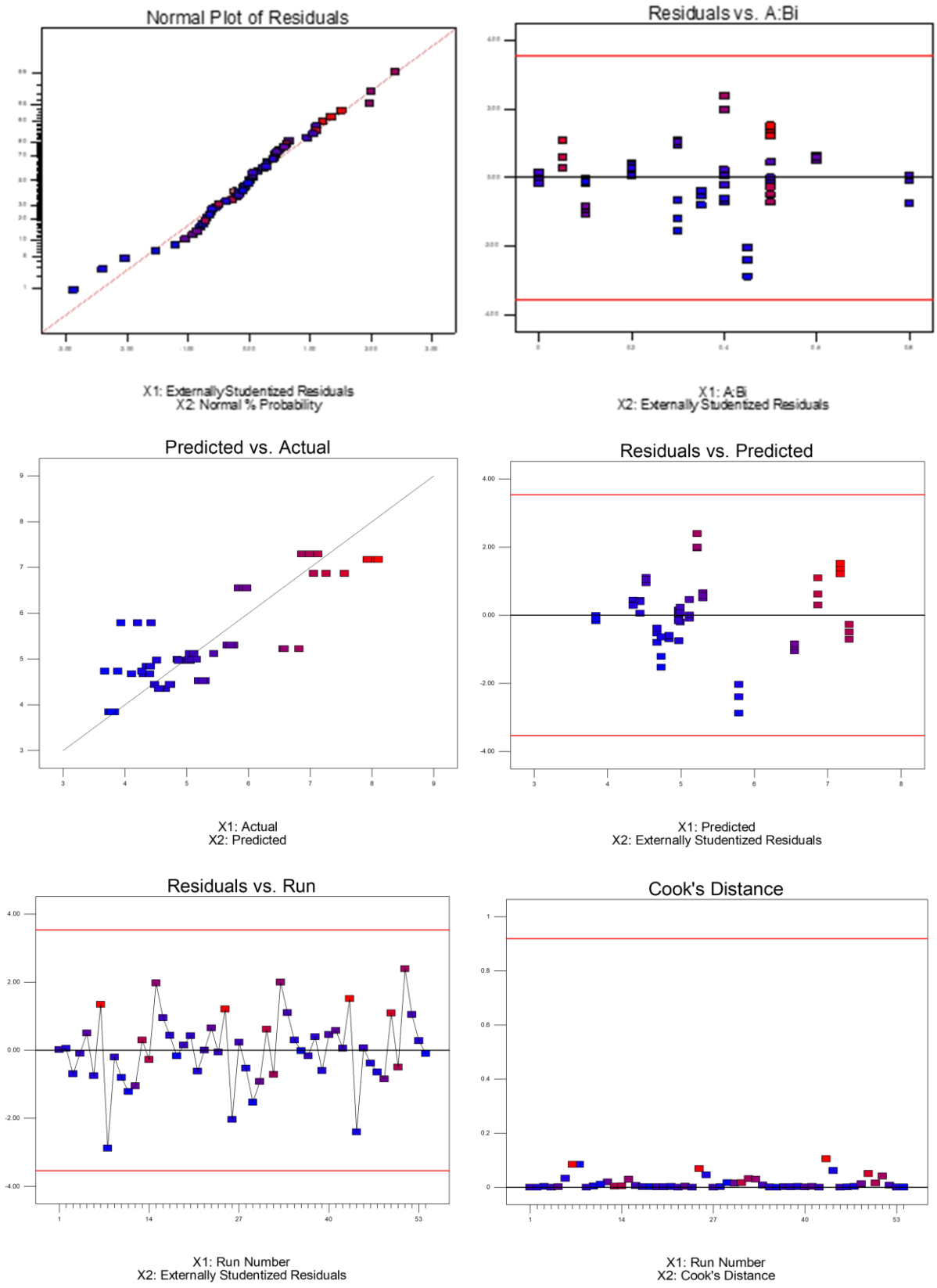


Fig. 6. Diagnostic plots used to evaluate the adequacy of the Brinell hardness regression model.

Based on the statistical evaluation, diagnostic analysis and predictive performance, the special cubic Scheffé mixture model with square-root transformation was selected as the final mathematical model for describing the influence of Bi-Ni-Pb composition on Brinell hardness. Although more complex quartic models yielded only marginal improvements in goodness-of-fit sta-

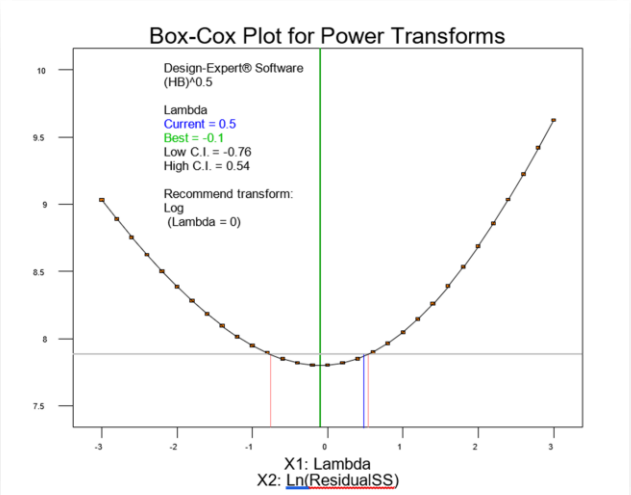


Fig. 7. Box–Cox plot for the Brinell hardness response showing the selected square-root transformation ($\lambda = 0.5$).

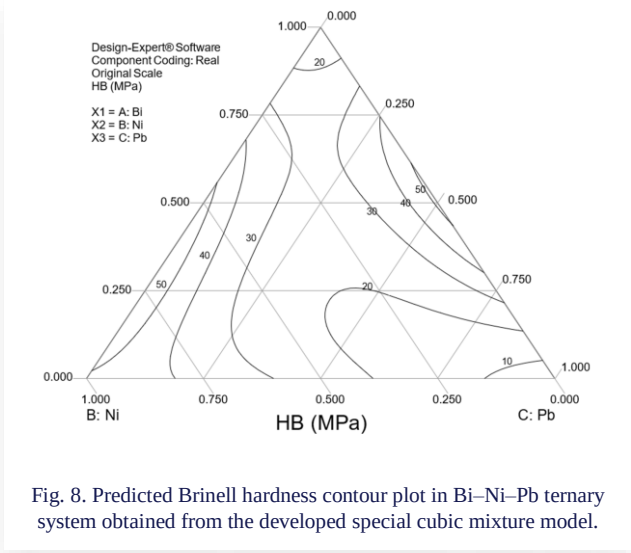


Fig. 8. Predicted Brinell hardness contour plot in Bi–Ni–Pb ternary system obtained from the developed special cubic mixture model.

tistics, they introduced additional higher-order interaction terms without substantially improving predictive capability. Therefore, the selected special cubic model represents the most appropriate compromise between statistical quality, physical interpretability and model simplicity for describing compositional trends and graphical analysis within the investigated experimental domain.

Confirmation of model predictions

The predictive performance of the developed special cubic Scheffé model was further evaluated by confirmation experiments at three selected compositions within the investigated composition space. For each confirmation point, Brinell hardness was measured at three different locations, and the arithmetic mean of the three measurements was used as the observed response. The experimental mean values were compared with the corresponding model predictions and the 95% prediction intervals, as summarised in Table 8.

Good agreement between the experimental and predicted responses was obtained for the first two confirmation points. At point 1, the experimentally determined mean hardness was 21.733 HB compared with the predicted value of 20.264 HB, while at point 2 the experimental and predicted values were 25.167 and 25.152 HB, respectively. A larger deviation was observed at point 3, where the experimental mean hardness (35.267 HB) exceeded the predicted value (27.790 HB). Nevertheless, the experimental mean values for all three confir-mation points were within their corresponding 95% prediction intervals. These results confirm that the developed model pro-vides an acceptable representation of Brinell hardness within the investigated composition domain, while the larger deviation ob-served at point 3 indicates locally increased uncertainty in model prediction.

The larger deviation observed at point 3 may be associated with increased local microstructural heterogeneity and variations in phase distribution at this composition. Since Brinell hardness is sensitive to the local microstructure within the indentation region, such heterogeneity may contribute to greater experimental variability and consequently to the observed difference between the experimental and predicted mean value.

Table 8. Results of confirmation experiments for the developed Brinell hardness model.

Point	Bi	Ni	Pb	Observed mean (HB)	Predicted mean (HB)	95% prediction interval	Validation
1	0.20	0.40	0.40	21.733	20.264	12.536–28.588	Confirmed
2	0.40	0.20	0.40	25.167	25.152	16.864–34.558	Confirmed
3	0.40	0.40	0.20	35.267	27.790	18.686–37.475	Confirmed

3.3. Electrical properties

3.3.1. Experimental results

Electrical conductivity measurements were performed on the samples listed in Table 1. For each sample, four measurements of electrical conductivity were carried out, and the results are presented in Table 9 and Fig. 9.

In addition to the experimental values, Table 9 also includes the calculated phase fractions, the mean values obtained from the four measurements and literature values of electrical conductivity for the pure elements [25].

The measured electrical conductivity of the investigated Bi-Ni-Pb alloys show a pronounced dependence on phase composition and phase fraction. The results indicate that the electrical transport properties cannot be described solely in terms of the nominal elemental composition, since the formation of intermetallic phases significantly modifies the conductivity of the alloys. This is particularly evident when comparing the conduc-

tivity of the individual constituents with that of the multiphase samples. The reference values are approximately 14.0 MS/m for (Ni), 4.8 MS/m for (Pb), and 0.77 MS/m for (Bi), whereas most of the multiphase alloys exhibit substantially lower conductivities.

The alloys containing a high fraction of Ni-rich phases (Ni), generally show the highest electrical conductivity among the investigated multiphase compositions. For example, samples 10 and 11, containing 70.1% and 85.1% (Ni), respectively, together with BiNi and Pb-containing (Pb) phases, exhibit conductivities of 5.5260 and 6.1861 MS/m. The relatively high conductivity of these samples can be attributed to the dominant contribution of the Ni-rich constituent, which provides comparatively efficient electron transport. Nevertheless, their conductivity remains considerably lower than that of pure Ni, indicating that the presence of Bi-containing and intermetallic phases introduces additional scattering and interrupts the continuous conductive Ni-rich paths.

A markedly different behaviour is observed for compositions dominated by BiNi and other Bi-Ni intermetallic phases. The reference sample B3, consisting of 99.9% BiNi, exhibits a conductivity of 2.108 MS/m, which is substantially lower than that of pure Ni and Pb. Furthermore, samples 12–15, in which the BiNi phase is combined predominantly with Pb, show conductivities ranging from 0.4169 to 2.7025 MS/m. An increase in the Pb fraction from 20.2% to 80.8% is accompanied by a general increase in conductivity. This trend suggests that, despite the relatively high intrinsic conductivity of Pb compared with BiNi, the overall electrical response is strongly influenced by the connectivity and spatial distribution of the phases. Increasing the Pb fraction may promote the formation of more continuous Pb-rich conductive regions.

The lowest conductivities are generally observed in alloys containing substantial fractions of Bi-rich and Bi-Ni inter-metallic phases. Samples 1–5 and 7–8 exhibit conductivities between approximately 0.47 and 0.96 MS/m, despite considerable differences in their phase fractions. For instance, sample 5, containing 45.9% (Bi), 40.0% BiNi and 14.1% (εPb), has a conductivity of only 0.4742 MS/m. Similarly, sample 2, containing 17.9% Bi_3Ni, 51.3% BiNi and 30.8% Pb, exhibits a conductivity of 0.5918 MS/m. These results demonstrate that a high proportion of Bi-rich or Bi-Ni intermetallic phases can strongly suppress electrical transport. The relatively low conductivity of Bi compared with Pb and Ni, combined with the intrinsically lower conductivity of the intermetallic phases, is likely responsible for this behaviour.

The comparison of samples 6–9 further demonstrates the importance of phase connectivity. Sample 6, containing 59.0% (εPb) and 40.0% Bi_3Ni, exhibits a conductivity of 1.2167 MS/m, while sample 9, with a high fraction of BiNi (59.3%) and a lower Bi fraction, reaches 1.6670 MS/m. Thus, the conductivity does not follow a simple linear relationship with the fraction of any single phase. Instead, it reflects the combined effects of phase fraction, intrinsic conductivity, interfacial scattering, and the continuity of electrically conductive paths through the microstructure.

The binary Pb-Ni alloy B1, containing 50% (Pb) and 50% (Ni), exhibits a conductivity of 3.1862 MS/m, which is

Table 9. Calculated phase fractions at room temperature and related electrical conductivity values of B1, B2, B3 and ternary Bi-Ni-Pb alloys.

Number	Calculated fraction of a phase (%)	Measured value (MS/m)				Mean value (MS/m)
		1	2	3	4	
B1	50.0% (Pb), 50.0% (Ni)	3.1876	3.1872	3.1845	3.1856	3.1862
1	20.5 % (Ni), 39.1 % BiNi, 40.4 % (Pb)	0.8726	0.8706	0.8614	0.8648	0.8673
2	17.9 % Bi_3Ni, 51.3 % BiNi, 30.8 % (Pb)	0.5869	0.5876	0.5963	0.5964	0.5918
3	48.4 % Bi_3Ni, 25.9 % BiNi, 25.7 % (Pb)	0.6536	0.6502	0.6635	0.6630	0.6575
4	78.9 % Bi_3Ni, 0.6 % BiNi, 20.5 % (Pb)	0.6816	0.6762	0.6796	0.6794	0.6792
5	45.9 % (Bi), 40.0 % BiNi, 14.1 % (εPb)	0.4737	0.4751	0.4769	0.4711	0.4742
Bi	100.0 % (Bi)					0.77 [23]
B2	70.4 % (εPb), 29.6 % (Bi)	0.5532	0.5454	0.5563	0.5481	0.5507
6	40.0 % Bi_3Ni, 1.0 % (Pb), 59.0 % (εPb)	1.2230	1.2100	1.2200	1.2140	1.2167
7	37.6 % Bi_3Ni, 21.3 % BiNi, 41.1 % (Pb)	0.9635	0.9621	0.9646	0.9643	0.9636
8	7.6 % Bi_3Ni, 56.4 % BiNI, 36.0 % (Pb)	0.6105	0.6082	0.6188	0.6089	0.6116
9	10.4 % (Ni), 30.3 % (Pb), 59.3 % BiNi	1.6687	1.6661	1.6690	1.6643	1.6670
10	70.1 % (Ni), 10.1 % (Pb), 19.8 % BiNi	5.5249	5.5251	5.5293	5.5250	5.5260
11	85.1 % (Ni), 5.0 % (Pb), 9.9 % BiNi	6.1873	6.1832	6.1843	6.1898	6.1861
Ni	100 % (Ni)					14.0 [23]
B3	99.9 % BiNi, 0.1 % (Ni)	2.1090	2.1078	2.1098	2.1068	2.108
12	79.5 % BiNi, 20.2 % (Pb), 0.3 % (Ni)	0.3871	0.4765	0.3986	0.4056	0.4169
13	59.1 % BiNi, 40.4 % (Pb), 0.5 % (Ni)	0.7950	0.7947	0.7963	0.7930	0.7947
14	38.8 % BiNi, 60.6 % (Pb), 0.6 % (Ni)	1.3860	1.3900	1.3820	1.3760	1.3835
15	18.4 % BiNi, 80.8 % (Pb), 0.8 % (Ni)	2.6970	2.7200	2.6950	2.6980	2.7025
Pb	100 % (Pb)					4.8 [23]

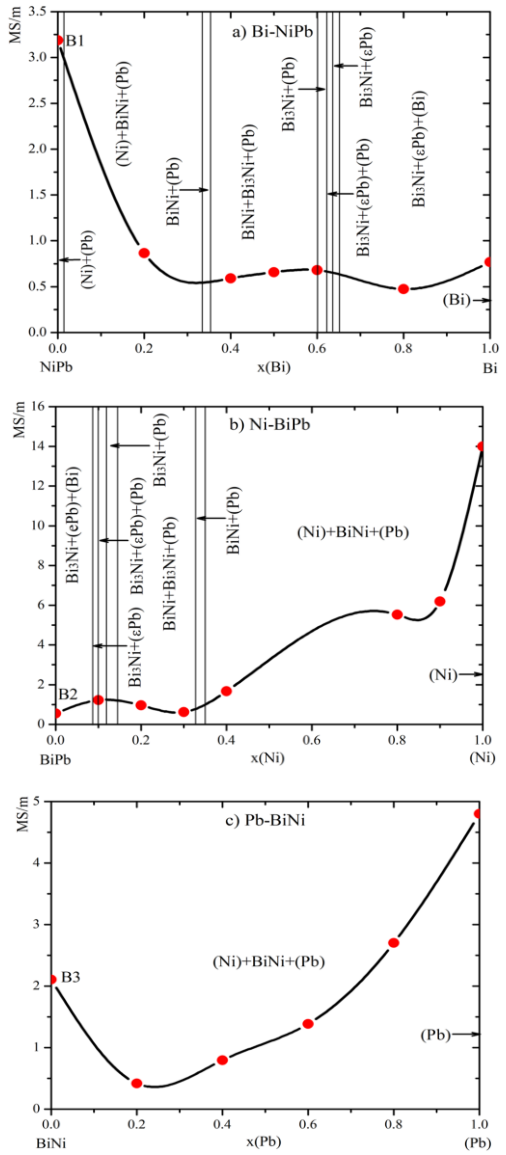


Fig. 9. Graphical presentation of electrical conductivity dependence of composition and phase fraction: a) vertical section Bi-NiPb; b) vertical section Ni-BiPb; c) vertical section Pb-BiNi.

considerably lower than would be expected from the conductivity of the pure constituents based solely on their volume fractions. This reduction can be associated with the formation of additional phases and with the disruption of continuous metallic conduction paths. Consequently, the experimental results confirm that phase transformations and intermetallic-phase formation play a crucial role in determining the electrical properties of the investigated alloys.

Overall, the results demonstrate that increasing the fraction of highly conductive Ni-rich regions tends to increase electrical conductivity, whereas increasing the proportion of Bi-rich and Bi-Ni intermetallic phases generally lead to lower conductivity. The results show that sample 11 exhibits the highest electrical conductivity among all investigated ternary alloys. This is attributed to the high fraction of the (Ni) solid solution in the alloy (85.1%), while the remaining phases are 9.9% BiNi and 5.0% (Pb).

Figure 9 presents a graphical representation of the mean values given in Table 9, providing a clearer overview of the results.

3.3.2. Response surface model for electrical conductivity

Model selection

The relationship between the chemical composition of the Bi-Ni-Pb alloys and electrical conductivity (EP) was analysed using a quadratic Scheffé mixture model. The model was selected based on the sequential model sum of squares, statistical significance of the regression terms, model hierarchy and predictive capability. Although higher-order models slightly improved the coefficient of determination, they were either aliased or non-hierarchical and therefore unsuitable for practical application. Consequently, the quadratic model was selected as the most appropriate compromise between statistical performance, interpretability and predictive capability.

Model development using alloy compositions

The experimental values corresponding to the pure components (100 wt.% Bi, 100 wt.% Ni and 100 wt.% Pb) were excluded from the regression analysis used to construct the response surface model. These compositions represent the vertices of the simplex and exhibit electrical conductivity values that differ markedly from those of the investigated ternary alloys.

Their inclusion produced pronounced leverage effects, resulting in poor regression diagnostics and a statistically significant lack of fit. Consequently, these extreme compositions prevented the construction of a predictive response surface representative of the investigated alloy system.

Since the objective of the mixture design was to model the electrical conductivity within the practical composition region of the Bi-Ni-Pb alloys rather than the pure constituents, the regression model was developed using only the alloy compositions.

Preliminary analyses performed with all experimental points included produced substantially poorer diagnostic statistics and pronounced systematic deviations in the residual plots, indicating that the extreme responses of the pure components dominated the regression. Therefore, these points were omitted from the final model.

Model summary statistics

The statistical indicators summarised in Table 10 demonstrate that the selected quadratic Scheffé model provides a good balance between goodness of fit, predictive capability and model robustness.

ANOVA

The ANOVA results confirmed that the developed model was highly significant ($p < 0.0001$). The coefficient of determination was $R^2 = 0.9522$, indicating that more than 95% of the variability in electrical conductivity was explained by the alloy composition. The adjusted and predicted coefficients of determination were Adj. $R^2 = 0.9486$ and Pred. $R^2 = 0.9451$, respectively, demonstrating excellent agreement between model fitting and

Table 10. Model summary statistics used for selection of the quadratic Scheffé mixture model.

Statistic	Value	Interpretation
R^2	0.9522	Excellent model fit; 95.22% of the variability explained
Adjusted R^2	0.9486	High explanatory capability after accounting for model complexity
Predicted R^2	0.9451	High predictive capability for new observations
Std. dev.	0.3787	Low residual variability around the fitted model
PRESS	10.883	Low prediction error, indicating robust model performance
Adeq. Precision	55.89	Far above the recommended value of 4, indicating an excellent signal-to-noise ratio

predictive performance. Furthermore, the Adeq. Precision ratio of 55.89 was substantially higher than the recommended minimum value of 4, indicating an adequate signal-to-noise ratio and confirming that the model can be reliably used to navigate the design space.

The significance of the individual model terms is summarised in Table 11. All linear mixture components and binary interaction terms were statistically significant ($p < 0.0001$), indicating that both the individual alloy constituents and their interactions significantly affected electrical conductivity. Among the interaction terms, the Ni-Pb interaction exhibited the largest F-value, indicating that this binary interaction had the strongest influence on electrical conductivity.

Table 11. ANOVA for the quadratic Scheffé mixture model of electrical conductivity.

Source	Sum of squares	df	Mean square	F-value	p-value
Model	188.7243	5	37.7449	263.20	<0.0001
Linear mixture	142.8060	2	71.4030	497.90	<0.0001
AB	16.8962	1	16.8962	117.82	<0.0001
AC	7.8048	1	7.8048	54.42	<0.0001
BC	24.3914	1	24.3914	170.08	<0.0001
Residual	9.4650	66	0.1434		
Lack of fit	9.4589	12	0.7882	7004.36	<0.0001
Pure error	0.0061	54	0.0001		

Regression equation

The final quadratic Scheffé mixture equation describing the dependence of electrical conductivity on alloy composition is expressed as:

$$EP = 1.4588(\mathrm{Bi}) + 8.2429(\mathrm{Ni}) + 4.6059(\mathrm{Pb}) + \\ - 11.7571(\mathrm{Bi})(\mathrm{Ni}) - 8.7015(\mathrm{Bi})(\mathrm{Pb}) - 14.1497(\mathrm{Ni})(\mathrm{Pb}) \quad (9)$$

where Bi, Ni and Pb denote the mass fractions of the corresponding alloy components.

Interpretation of coefficients

Among the linear blending coefficients, Ni has the largest positive coefficient, indicating that increasing the relative contribution of Ni is associated with higher electrical conductivity within the investigated mixture domain. Pb exhibits an intermediate contribution, whereas Bi has the lowest linear blending coefficient. The negative interaction coefficients for Bi-Ni, Bi-Pb, and Ni-Pb indicate antagonistic deviations from linear blending, meaning that the conductivity of the corresponding binary mixtures is lower than would be expected from the linear contributions of the individual components.

The magnitude of the interaction coefficients indicates that the Ni-Pb interaction exerts the strongest negative influence on electrical conductivity, followed by the Bi-Ni and Bi-Pb interactions. This suggests that the electrical conductivity cannot be predicted by a simple rule of mixtures but is strongly affected by interactions among the alloy constituents.

Diagnostic plots

Diagnostic plots of the selected model are presented in Fig. 10. The normal probability plot of residuals showed an approximately linear distribution, indicating that the residuals were close to normally distributed. The residuals versus predicted values plot revealed no systematic pattern, confirming homoscedasticity of the residuals. Likewise, the residuals plotted against the experimental run order showed random scatter, suggesting the absence of time-dependent effects or systematic experimental errors. The predicted versus actual values exhibited excellent agreement, confirming the high predictive capability of the developed model.

Finally, the Box-Cox analysis indicated that the original response scale was appropriate, as the current transformation parameter ($\lambda = 1$) lay within the confidence interval around the optimum value in Fig. 11.

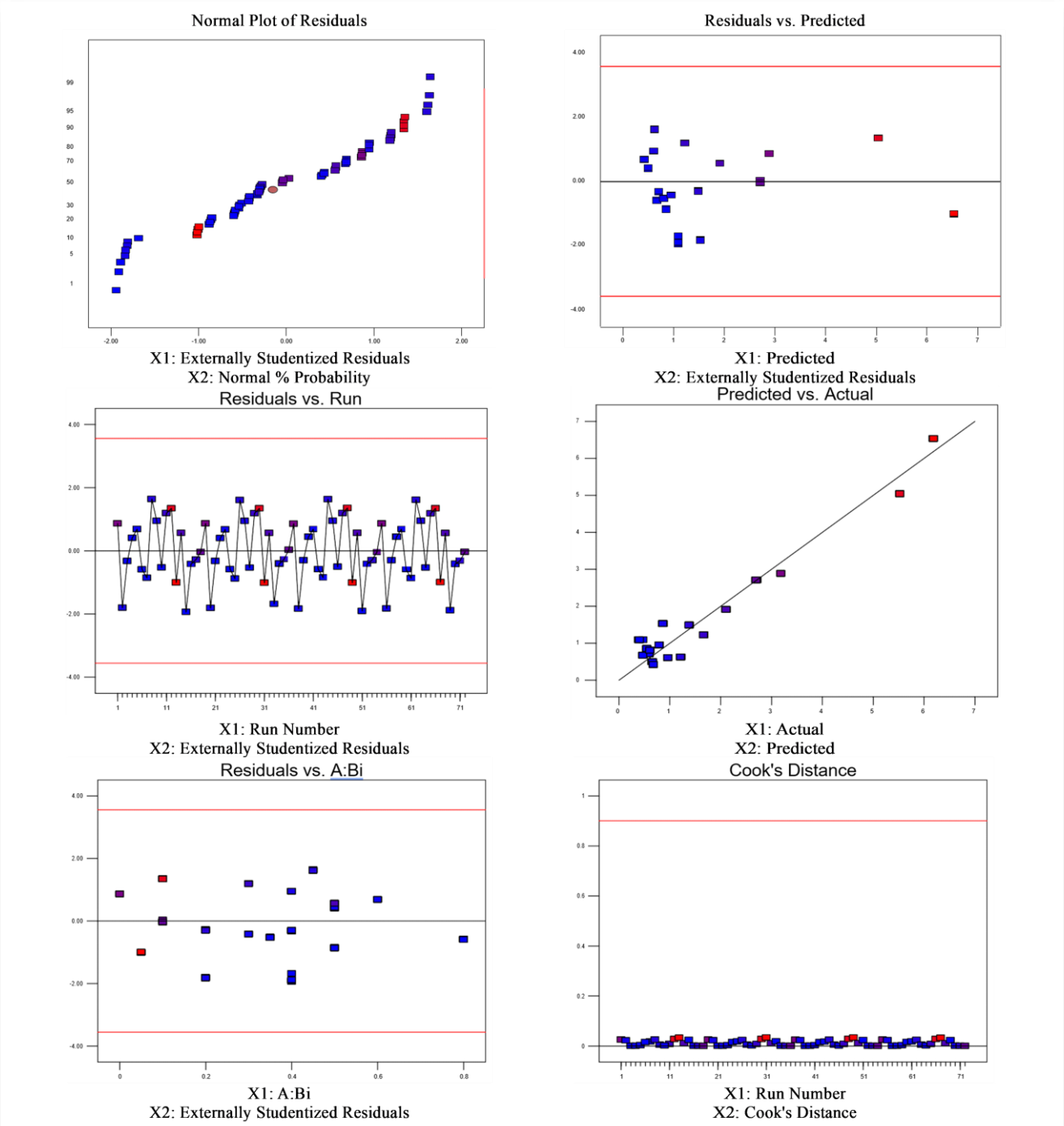


Fig. 10. Diagnostic plots for the selected quadratic Scheffé mixture model of electrical conductivity.

Although the lack-of-fit test was statistically significant, the pure experimental error was exceptionally low because of the excellent repeatability of the electrical conductivity measurements. Consequently, the lack-of-fit test became highly sensitive, such that even relatively small deviations between the fitted model and the experimental observations resulted in a statistically significant lack-of-fit. Nevertheless, the diagnostic plots revealed no systematic deviations, and the model exhibited excellent predictive capability (Pred. R^2 = 0.9451). Therefore, the quadratic model was considered adequate for prediction within the investigated experimental domain. Overall, these diagnostic results demonstrate that the quadratic Scheffé mixture model provides an adequate and statistically reliable description of the relationship between alloy composition and electrical conductivity within the investigated experimental region.

Contour plot

The contour plot generated from the quadratic Scheffé mixture model is presented in Fig. 12. This graphical representation illustrates the combined influence of Bi, Ni and Pb contents on

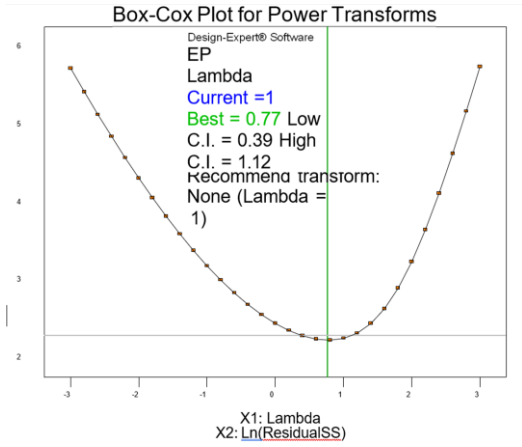


Fig. 11. Box–Cox plot for the electrical conductivity response.

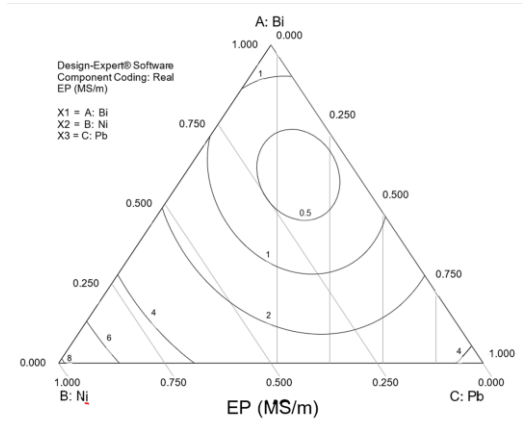


Fig. 12. Predicted electrical conductivity contour plot in the Bi-Ni-Pb ternary system obtained from the developed quadratic Scheffé mixture model.

the electrical conductivity of the investigated alloys and provides a clear visualisation of the predicted response throughout the composition domain.

The contour plot reveals a pronounced compositional dependence of electrical conductivity. The highest conductivity values are predicted in the Ni-rich region of the ternary diagram, where the nickel content approaches its upper limit within the investigated experimental domain. In contrast, conductivity decreases markedly with the increasing Bi content, reaching its minimum in the Bi-rich corner of the composition triangle. Alloys containing intermediate amounts of Pb exhibit conductivity values between these two extremes, indicating that the influence of Pb is less pronounced than that of Ni but considerably more favourable than that of Bi.

The curved contour lines demonstrate that the relationship between alloy composition and electrical conductivity is nonlinear. The absence of abrupt changes in the contour pattern indicates that the developed quadratic model provides a smooth description of the composition–property relationship within the investigated domain. Instead of varying according to a simple linear mixing rule, conductivity changes progressively across the composition triangle, reflecting significant interactions among the alloying elements. This behaviour is consistent with the significant interaction terms (Bi×Ni, Bi×Pb and Ni×Pb) identified in the quadratic mixture model. The negative interaction coefficients indicate that simultaneous increases in two components reduce the conductivity relative to the value expected from their individual linear contributions.

Overall, the contour plot demonstrates that nickel is the dominant component associated with higher electrical conductivity in the Bi-Ni-Pb system, whereas increasing bismuth content is associated with lower conductivity. Lead exhibits an intermediate effect, while the curvature of the contour lines reflects the significant binary interactions identified by the quadratic Scheffé mixture model. The graphical analysis therefore supports the compositional trends identified by the statistical evaluation of the model.

Confirmation of model predictions

To verify the predictive capability of the developed quadratic Scheffé mixture model, three additional binary alloy compositions that were not included in the model fitting procedure were experimentally prepared and tested. The investigated compositions were Bi-Ni (0.5-0.5-0), Bi-Pb (0.5-0-0.5) and Ni-Pb (0-0.5-0.5). For each composition, electrical conductivity was measured four times, and the average value was calculated.

Table 12 compares the experimentally measured electrical conductivity values with those predicted by the quadratic mixture model. The measured average electrical conductivities were 2.1045, 0.6982 and 3.1158 MS/m for the Bi-Ni, Bi-Pb and Ni-Pb alloys, respectively, whereas the corresponding model predictions were 1.9116, 0.8570 and 2.8870 MS/m.

Although small differences between the predicted and experimental values were observed, all measured values were located within the corresponding 95% prediction intervals generated by the model. This indicates that the deviations are within the expected prediction uncertainty and confirms the satisfactory predictive capability of the developed quadratic mixture model.

The confirmation experiments therefore demonstrate that the quadratic Scheffé model reliably predicts the electrical conductivity of Bi-Ni-Pb alloys within the investigated composition region and can therefore be confidently used for interpolation and alloy composition optimization within this domain.

Table 12. Results of confirmation experiments for the developed electrical conductivity model.

Composition (Bi-Ni-Pb)	Predicted (MS/m)	Experimental (MS/m)	95% Prediction interval (MS/m)	Validation
0.5-0.5-0.0	1.9116	2.1045	1.4257–2.3975	within PI
0.5-0.0-0.5	0.8570	0.6982	0.3949–1.3191	within PI
0.0-0.5-0.5	2.8870	3.1158	2.3995–3.3745	within PI

3.4. Scheil and Lever solidification simulations

Sample 11, $Bi_5Ni_{90}Pb_5$, exhibited a favourable combination of both hardness and electrical conductivity among all investigated ternary alloys. This sample was selected for solidification simulations. The simulations were performed using Scheil and Lever models, and the results are presented in Fig. 13.

The non-equilibrium (Scheil) simulation is shown as a blue curve, while the equilibrium (Lever) simulation is represented by a red curve. During non-equilibrium solidification, seven phases are predicted to form, whereas five phases are formed under equilibrium conditions.

Figure 14 presents the calculated solidification behaviour of the $Bi_5Ni_{90}Pb_5$ alloy using the Scheil and Lever models. Both simulations predict a very similar overall solidification sequence, indicating that the alloy solidifies predominantly through the formation of a Ni-rich solid solution (Ni), followed by the appearance of Bi-Ni intermetallic phases and, at lower temperatures, Pb-rich and Bi-containing constituents.

At the beginning of solidification, the alloy remains in the liquid + (Ni) region, with the first solid phase being an Ni-rich solid solution. The calculated liquidus temperatures are almost identical for the two models, 1344.37°C for the Scheil simulation and 1344.33°C for the Lever simulation. This close agreement confirms that the initial solidification temperature is essentially insensitive to the assumed equilibrium/non-equilibrium solidification conditions.

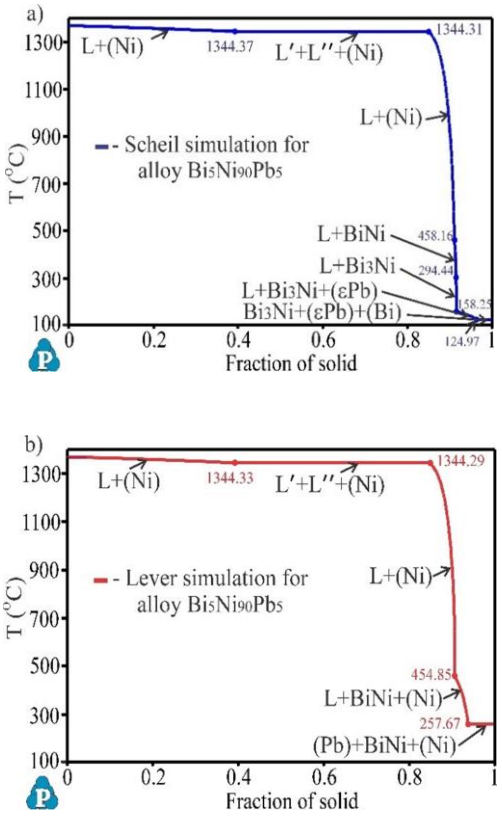


Fig. 13. Scheil (a) and Lever (b) simulation results for alloy $Bi_5Ni_{90}Pb_5$.

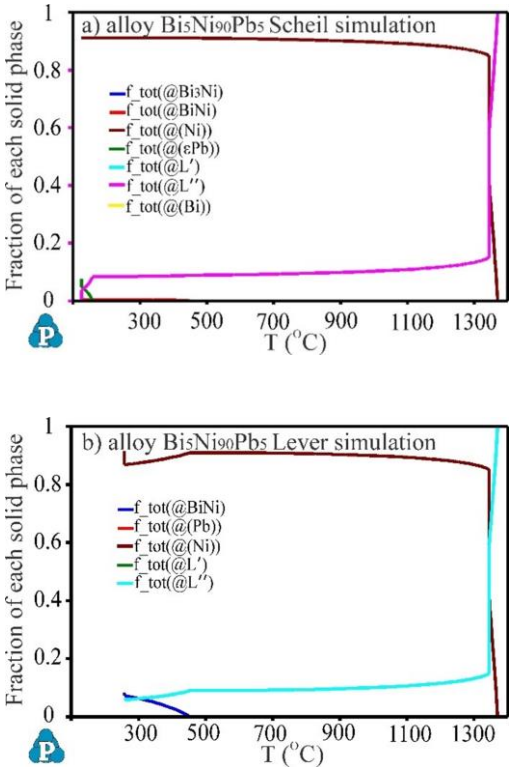


Fig. 14. Fraction of each solid phase as a function of temperature for alloy $Bi_5Ni_{90}Pb_5$: a) Scheil simulation; b) Lever simulation.

As solidification proceeds, the fraction of solid increases rapidly while the temperature remains relatively high. The first significant difference between the two calculations appears at the transition involving the BiNi phase. In the Scheil model, the corresponding temperature is approximately 458.16°C, whereas the Lever model predicts 454.85°C. The Scheil calculation therefore predicts a slightly higher temperature for the onset of this transformation. This difference is associated with the fundamental assumptions of the two models: the Scheil model assumes complete mixing in the liquid and negligible diffusion in the solid, whereas the Lever model represents an equilibrium solidification condition with redistribution between the solid and liquid phases.

A more pronounced difference is observed at lower temperatures. The transition associated with the formation of the BiNi-containing region occurs at approximately 294.44°C in the Scheil calculation, compared with 257.67°C in the Lever calculation. This indicates that the assumed degree of solute redistribution has a significant influence on the final stages of solidification. Under Scheil conditions, solute enrichment in the remaining liquid is enhanced because diffusion in the already formed solid is neglected. Consequently, the residual liquid becomes progressively enriched in elements that are rejected by the primary Ni-rich solid, promoting the formation of secondary and low-temperature constituents.

In the final stage of solidification, both models predict a multiphase microstructure containing BiNi, Ni-rich solid solution, and Pb-rich/Bi-containing phases. The Scheil simulation indicates the formation of a final constituent at approximately

124.97°C, while the Lever calculation terminates at approximately 257.67°C. This difference highlights the stronger segregation predicted by the Scheil approach and suggests that the non-equilibrium model is more sensitive to the enrichment of the residual liquid during the last stages of solidification.

Overall, the two simulations show good agreement in the general solidification path and in the formation of the primary Ni-rich phase. However, their differences become increasingly evident as the fraction of solid approaches unity. The Scheil model predicts stronger chemical segregation and a more complex evolution of the residual liquid, whereas the Lever model provides a more equilibrium-like description of phase formation. Considering that the experimental alloy is expected to undergo limited solid-state diffusion during relatively rapid cooling, the Scheil simulation may provide a more realistic representation of the actual solidification path, particularly with respect to the formation of the final Bi-, Pb- and BiNi-rich constituents.

Additional thermodynamic properties can be derived from the solidification simulations, as illustrated in Figs. 14 and 15.

Figure 14 shows the fraction of each solid phase as a function of temperature, while Fig. 15 presents the latent heat and total heat evolution as a function of temperature. Fig. 14 compares the predicted phase evolution of the $Bi_5Ni_{90}Pb_5$ alloy obtained using Scheil and Lever simulations. Both approaches show similar overall phase evolution, with the Ni-rich, (Ni) solid phase remaining dominant over most of the temperature range. The main differences are observed near the solidification end, where the phase fractions change rapidly. Overall, the two simulations exhibit good qualitative agreement. Fig. 15 presents the heat evolution of the $Bi_5Ni_{90}Pb_5$ alloy as a function of temperature,

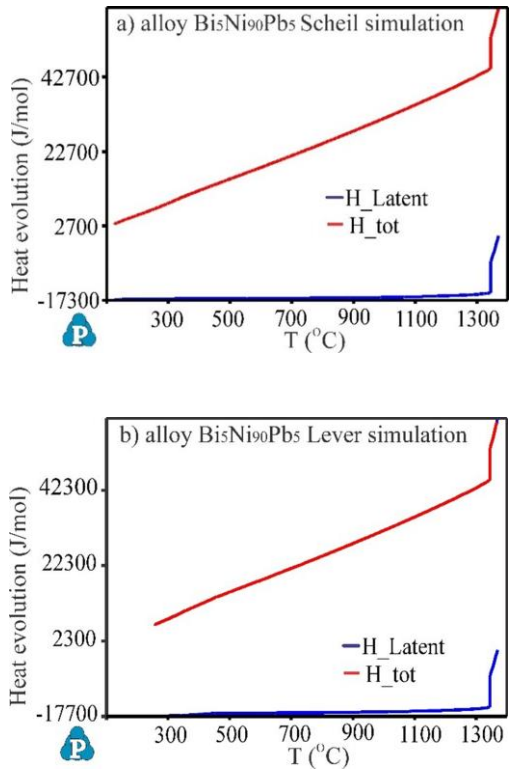


Fig. 15. Heat evolution as a function of temperature for alloy $Bi_5Ni_{90}Pb_5$: a) Scheil simulation; b) Lever simulation.

calculated using Scheil and Lever simulations. Both approaches show a similar trend in the total heat evolution, with a pronounced increase near the end of solidification. The latent heat contribution remains relatively low over most of the temperature range and increases sharply at high temperatures. Overall, the Scheil and Lever simulations exhibit comparable thermal evolution behaviour.

6. Conclusions

Fifteen Bi-Ni-Pb ternary alloys were experimentally investigated using XRD, LOM, SEM–EDS, hardness and electrical conductivity measurements. The experimentally determined phase constitutions showed very good agreement with the calculated 25°C isothermal section, confirming the reliability of the thermodynamic description of the system.

The results demonstrated that both Brinell hardness and electrical conductivity are strongly influenced by phase constitution and phase fractions. The developed Scheffé mixture models provided satisfactory predictive capability, with the special cubic model describing hardness and the quadratic model describing electrical conductivity. The obtained models enable quantitative prediction of the investigated properties within the studied composition range.

Among the investigated alloys, $Bi_5Ni_{90}Pb_5$ exhibited the most favourable combination of hardness and electrical conductivity and was therefore selected for solidification analysis. Scheil and Lever simulations showed similar overall solidification paths, with a primary Ni-rich phase followed by the formation of Bi-Ni intermetallic and Pb-/Bi-rich phases, while the Scheil model predicted stronger segregation during the final stages of solidification.

Overall, the combined thermodynamic, experimental and statistical approach provides a useful basis for understanding composition–phase–property relationships and for further optimisation of Bi-Ni-Pb alloys.

Acknowledgements

The authors would like to thank the Ministry of Science, Technological Development and Innovation of the Republic of Serbia for funding the scientific research work, contract no. 451-03-65/2024-03/200155, realised by the Faculty of Technical Sciences in Kosovska Mitrovica, University of Pristina.

References

[1] Kaňa, V., Krutiš, V., Bořil, P., Záděra, A., & Rimko, M. (2021). Influence of Heat Treatment and Nickel Content on the Properties of the GX4CrNi13-4 Steel. *Archives of Metallurgy and Materials*, 66(1), 37–41. doi: 10.24425/amm.2021.134756

[2] Samui, P., & Agarwal, R. (2022). Thermodynamic Assessment and Solubility of Ni in LBE Coolants. *Thermo*, 2(4), 371–382. doi: 10.3390/thermo2040025

[3] Zeng, Y., Liu, Y., Min, Q., Wen, S., Du, C., Zheng, Z., Liu, H., Du, Y., Premovic, M., & Wang, J. (2020). Diffusion coefficients and atomic mobilities in fcc Ni–Cu–Mo alloys: Experiment and modelling. *Calphad*, 71, 102209. doi: 10.1016/j.calphad.2020.102209

[4] ZaiMi, N.S.M., Salleh, M., BaSer, M., Baharin, N.A.I., Aziz, M.S.A., Abdullah, M.A.B., & Nabiałek, M. (2025). Impact of bismuth as microalloying element in Sn-0.7Cu lead-free solder alloys. *Archives of Metallurgy and Materials*, 70(4), 1753–1758. doi: 10.24425/amm.2025.156258

[5] Milosavljevic, M., Premovic, M., Minic, D., Manasijevic, D., Todic, A., & Tomovic, M. (2021). Thermodynamic description of the Cu-Ge-Pb system: experiment and modeling. *Calphad*, 72, 102216. doi: 10.1016/J.Calphad.2020.102216

[6] Minić, D., Premović, M., Tošković, N., Manasijević, D., Ćosović, V., Janaćković, M., & Tomović, M. (2019). Experimental investigation and thermodynamic calculations of the Bi-Ni-Pb phase diagram. *Journal of Mining and Metallurgy, Section B: Metallurgy*, 55(2), 157–166. doi: 10.2298/JMMB181128024M

[7] Cao, W., Chen, S.L., Zhang, F., Wu, K., Yang, Y., Chang, Y.A., Schmid-Fetzer, R., & Oates, W.A. (2009). PANDAT software with panengine, panoptimizer and panprecipitation for multi-component phase diagram calculation and materials property simulation. *Calphad*, 33(2), 328–342. doi: 10.1016/J.Calphad.2008.08.004

[8] Anderson, M.J., & Whitcomb, P.J. (2016). *RSM simplified: optimizing processes using response surface methods for design of experiments* (2nd ed.). CRC Press.

[9] Myers, R.H., Montgomery, D.C., & Anderson-Cook, C.M. (2016). *Response Surface Methodology, Process and Product Optimization Using Designed Experiments* (4th ed.). Wiley.

[10] Cornell, J.A. (2002). *Experiments with mixtures: designs, models, and the analysis of mixture data* (3rd ed.). Wiley & Sons.

[11] Stat-Ease, (2018). *Handbook for Experimenters*. Stat-Ease. https://cdnm.statease.com/pubs/Handbook%20for%20Experimenters.pdf [accessed 30 Jan. 2025].

[12] Box, G.E.P., & Draper, N.R. (2007). *Response Surfaces, Mixtures, and Ridge Analyses* (2nd ed.). John Wiley & Sons.

[13] Lazić, Ž.R. (2004). *Design of Experiments in Chemical Engineering: A Practical Guide*. Wiley-VCH.

[14] Kang, L., Salgado, J.C., & Brenneman, W.A. (2016). Comparing the Slack-Variable Mixture Model with Other Alternatives. *Technometrics*, 58(2), 255–268. doi: 10.1080/00401706.2014. 985389

[15] Montgomery, D.C. (2017). *Design and Analysis of Experiments* (9th ed.). Wiley.

[16] Davey, W.P. (1925). Precision measurements of the lattice constants of twelve common metals. *Physical Review*, 25(6), 753–761. doi: 10.1103/Physrev.25.753

[17] Owen, E.A. & Yates, E.L. (1936). LXVI. X-Ray measurement of the thermal expansion of pure nickel. *The London, Edinburgh, and Dublin Philosophical Magazine and Journal of Science*, 21(142), 809–819. doi: 10.1080/14786443608561628

[18] Owen, E.A. & Yates, E.L. (1933). XLI. Precision measurements of crystal parameters, *The London, Edinburgh, and Dublin Philosophical Magazine and Journal of Science*, 15(98), 472–488. doi: 10.1080/14786443309462199

[19] Takahashi, T., Mao, H.K., & Bassett, W.A. (1969). Lead: X-ray diffraction study of a high-pressure polymorph. *Science*, 165(3900), 1352–1353. doi: 10.1126/Science.165.3900.13

[20] Martinez Piñeiro, E.L., Ruiz Herrera, B.L., Escudero, R., & Bucio, L. (2011). Possible coexistence of superconductivity and magnetism in intermetallic $Nibi_3$. *Solid State Communications*, 151(6), 425–429. doi: 10.1016/J.Ssc.2011.01.005

[21] Ruck, M. (1999). Die kristallstruktur von BiNi: eine komplexe Ausdünnungsvariante des $InNi_2$-Typs. *Journal of Inorganic and General Chemistry*, 625, 2050–2054. doi: 10.1002/(SICI)1521-3749(199912)625:12<2050::AID-ZAAC2050>3.0.CO;2-R

[22] https://periodictable.com/Properties/A/BrinellHardness.v.html, [accessed 14 Sep. 2019].

[23] https://periodictable.com/Properties/A/ElectricalConductivity.v.html, [accessed 13 Sep. 2019].

Co-published by
Institute of Fluid-Flow Machinery
Polish Academy of Sciences
Committee on Thermodynamics and Combustion
Polish Academy of Sciences

Copyright©2026 by the Authors under licence CC BY-NC-ND 4.0

http://www.imp.gda.pl/archives-of-thermodynamics/

Experimental Investigation of Microplastic Removal from Drinking Water Using Aluminium Electrocoagulation: Process Performance and Operating Parameters

Salma Seham Jameel, Ali Rahim Ali, Hussein Fawzi Hussein*,
Alaa Hussein Ali, Shaalan Bdaiwi Ahmed

Scientific Research Commission, Baghdad, Iraq
*Corresponding author email: hussein.f.hussein@src.edu.iq

Received: 11.01.2026; revised: 09.04.2026; accepted: 16.09.2026

Abstract

Microplastic contamination in drinking water has emerged as a growing environmental concern due to its persistence and potential health risks. In this study, an aluminium-based electrocoagulation process was experimentally evaluated for the removal of microplastic particles from real drinking water samples. A bench-scale reactor equipped with parallel aluminium electrodes was used to investigate the influence of key operating parameters, including pH, current density, electrolyte concentration, and treatment time. The results demonstrated that removal efficiency strongly depended on electrochemical conditions, with optimal performance observed at near-neutral pH and moderate current density. Rapid removal was achieved during the initial treatment stage, followed by stabilisation as the system approached an equilibrium. The removal mechanism was governed by the formation of aluminium hydroxide flocs, enabling particle aggregation through adsorption, sweep flocculation and flotation processes. Under optimised conditions, removal efficiencies of approximately 80% were obtained. The findings indicate that electrocoagulation can serve as an effective supplementary treatment for reducing microplastic contamination in drinking water. However, the results should be interpreted considering the use of real water samples and the limitations of gravimetric estimation, highlighting the need for further validation using controlled synthetic systems.

Keywords: Microplastics; Electrocoagulation; Aluminium electrodes; Drinking water treatment; Operating parameters

Vol. 47(2026), No. 3, 233–240; doi: 10.24425/ather.2026.7521

Cite this manuscript as: Jameel, S.S., Ali, A.R., Hussein, H.F., Ali, A.H., & Ahmed, S.B. (2026). Experimental Investigation of Microplastic Removal from Drinking Water Using Aluminium Electrocoagulation: Process Performance and Operating Parameters. *Archives of Thermodynamics*, 47(3), 233–240.

1. Introduction

The widespread use of plastic materials over the past decades has led to a continuous increase in plastic residues in natural and engineered water systems. Due to their durability and resistance to degradation, plastics undergo gradual physical and chemical fragmentation, resulting in the formation of microplastics with characteristic dimensions below a few millimetres [1,2]. These particles have been detected in rivers, lakes, wastewater treatment plants, and even in drinking water supplies, raising concerns regarding their persistence, transport behaviour and potential interactions with biological and chemical systems [3,4].

Microplastics exhibit complex behaviour in aquatic environments owing to their diverse polymer composition, surface properties and size distribution. Their tendency to aggregate, adsorb contaminants and interact with natural colloids enhances

their mobility and persistence within water systems [5]. Several studies have reported the presence of microplastic particles in treated drinking water, indicating that conventional treatment processes are not always sufficient to ensure their complete removal. As a result, microplastics are increasingly regarded as an emerging class of contaminants that require targeted mitigation strategies [6,7].

From a health and environmental perspective, the concern associated with microplastics extends beyond their physical presence. These particles may act as carriers for organic pollutants, heavy metals and microorganisms, potentially increasing exposure risks for aquatic organisms and humans [8]. Their long-term stability and resistance to biodegradation further complicate their management within water treatment systems [9]. Consequently, the development and evaluation of effective removal techniques for microplastics have become an active area of research [10,11].

A wide range of treatment technologies has been investigated for microplastic removal, including membrane filtration, adsorption, magnetic separation, biological processes and advanced oxidation techniques [12–15]. While some of these approaches demonstrate high removal efficiencies under controlled conditions, their practical implementation is often limited by high energy demand, operational complexity, fouling issues, or chemical consumption [16,17]. In recent years, coagulation-based methods have gained attention due to their ability to destabilise suspended particles and promote aggregation through relatively simple operational schemes [18].

Electrocoagulation represents a hybrid electrochemical-physical treatment process in which sacrificial metal electrodes are dissolved in situ under an applied electric field, generating coagulant species without the direct addition of chemicals. The process has been widely applied in wastewater treatment for the removal of suspended solids, oils, dyes and heavy metals [19,20]. From a thermodynamic and electrochemical standpoint, electrocoagulation involves a balance between electrical energy input, metal dissolution kinetics, hydrolysis reactions and gas evolution, all of which influence treatment performance [21].

Recent investigations have explored the applicability of electrocoagulation for microplastic removal from wastewater and drinking water matrices [22,23]. Aluminium electrodes, in particular, have been shown to generate amorphous aluminium hydroxide species with high surface activity, capable of adsorbing and entrapping microplastic particles through charge neutralisation and sweep flocculation mechanisms [24]. However, reported removal efficiencies vary significantly depending on operating conditions such as pH, current density, electrolyte concentration and hydraulic residence time [25].

Despite the growing body of literature, several aspects of microplastic removal by electrocoagulation remain insufficiently understood. Many studies focus primarily on wastewater matrices, while fewer investigations address drinking water systems under controlled laboratory conditions [26]. In addition, the combined influence of electrochemical parameters on process stability and removal efficiency has not been consistently evaluated within a unified experimental framework [27,28]. From a thermodynamic perspective, understanding how operating parameters govern coagulant formation, particle aggregation and separation behaviour is essential for optimising process performance and ensuring reliable operation [29–31].

Therefore, the present study investigates the applicability of aluminium-based electrocoagulation for reducing microplastic contamination in real drinking water samples collected from Baghdad. The objective was not to simulate an idealised synthetic suspension, but rather to examine the process behaviour under realistic drinking-water conditions, where microplastic concentrations are expected to be relatively low and variable. This approach provides practical insight into the feasibility of electrocoagulation as a supplementary treatment step for real water matrices. However, it also introduces limitations related to sample heterogeneity and the absence of a controlled synthetic baseline. Accordingly, the results should be interpreted as an experimental feasibility assessment under realistic conditions, while future work should include synthetic microplastic-spiked water to improve reproducibility, mass balance evaluation and mechanistic interpretation.

2. Materials and methods

2.1. Water samples and sampling procedure

Drinking water samples were collected from Baghdad city to represent typical conditions of local supply and consumption. Two categories were considered: (i) tap water collected from different locations, and (ii) commercially bottled drinking water from different manufacturers. For tap water, the faucet was allowed to run for 1 min before sampling to reduce the influence of stagnant water in household plumbing. Each sample was collected in 1 L dark glass containers that had been pre-cleaned and rinsed with distilled water. Bottled water samples were kept in their original containers until analysis and treatment. The selection of local drinking water matrices is consistent with regional observations reporting microplastics occurrence in Baghdad drinking-water-related systems [12].

The use of real tap and bottled drinking water was intended to reflect practical exposure conditions rather than an idealised laboratory matrix. It is acknowledged, however, that natural drinking water generally contains relatively low and variable microplastic concentrations compared with synthetic suspensions. Therefore, the present study should be interpreted as a feasibility-oriented assessment of electrocoagulation performance in real drinking-water matrices. Future investigations should incorporate synthetic water spiked with known microplastic concentrations to provide a more controlled baseline and improve reproducibility.

2.2. Reagents and materials

Analytical-grade sodium chloride (NaCl) was used as supporting electrolyte to adjust electrical conductivity. The solution pH was adjusted using diluted sulfuric acid (H_2SO_4) and sodium hydroxide (NaOH). Cellulose nitrate (or equivalent) membrane filters with pore size 0.45 μm were used for post-treatment filtration. All solutions were prepared using distilled water.

2.3. Electrocoagulation reactor and electrode configuration

Electrocoagulation (EC) experiments were performed in a bench-scale batch reactor consisting of a 1 L Pyrex glass beaker. Two parallel aluminium plate electrodes were vertically installed in the reactor. Each electrode had dimensions of 80 × 130 × 1 mm. The inter-electrode spacing was varied between 1 and 5 cm depending on the experiment. A DC power supply (0–30 V, maximum current 5 A) was used to provide constant-current operation (galvanostatic mode), which is commonly recommended for reproducible EC performance assessment [1]. To maintain uniform mixing and reduce concentration gradients near the electrode surfaces, the reactor contents were stirred using a magnetic stirrer at 250 rpm throughout treatment. After each experiment, the reactor was switched off and the suspension was allowed to settle for 2 h prior to filtration and analytical measurements.

2.3.1. Electrode preparation and cleaning

Before each run, aluminium electrodes were rinsed with distilled water. To remove surface residues and maintain consistent electrode activity, the plates were immersed in diluted H_2SO_4 for 2 min, then thoroughly rinsed with distilled water, dried and weighed. This routine cleaning step is frequently used to minimise passivation and improve repeatability in EC studies [1].

2.4. Experimental design and operating conditions

A parametric experimental plan was adopted to examine the influence of operating variables on microplastic removal, focusing on factors known to affect EC performance through coagulant generation rate, hydrolysis pathways and gas evolution behaviour [1]. The main investigated variables were:

- pH: 3, 5, 7, 8, 9 and 10.
- Supporting electrolyte (NaCl): 1, 2, 3 and 4 g/L.
- Current density (CD): 5, 10, 20, 30 and 40 mA/cm^2.
- Electrode spacing: 1–5 cm.
- Treatment time: 15, 30, 45, 60, 75 and 90 min.

Unless otherwise stated, each set of tests was conducted at room temperature under constant stirring. Samples were withdrawn at 15 min intervals for analysis.

The chosen ranges were guided by previous studies on EC operation and microplastic removal behaviour, where pH and current density strongly control aluminium hydrolysis species and separation efficiency [6].

2.5. Electrochemical reactions and process description

The EC process was conducted using sacrificial aluminium electrodes. The primary reactions can be represented as follows [1]:

Anode: $Al\ (s) \rightarrow Al^{+3}\ (aq) + 3e.$ (1)

Cathode: $3H_2O\ (l) + 3e^- \rightarrow 3/2\ H_2\ (g) + 3OH^-\ (aq).$ (2)

In solution: $Al^{+3}\ (aq) + 3OH^-\ (aq) \rightarrow Al(OH)_3\ (s).$ (3)

The in-situ formation of amorphous $Al(OH)_3$ flocs provides active surfaces for particle destabilisation, adsorption and sweep flocculation, while hydrogen evolution contributes to flotation of aggregated particles [1,6,9]. These mechanisms are particularly relevant to microplastic removal, where aggregation and capture into larger flocs is typically the dominant separation pathway [6,13].

2.6. Sample handling, filtration and drying

After the settling step, the treated suspension was filtered using a vacuum filtration unit equipped with 0.45 µm membrane filters. Filters were dried in an oven at 45°C for 48 h before gravimetric measurements and microscopic inspection. This approach aligns with established workflows used in microplastic separation and EC-related microplastic studies, while recognising that polymer confirmation requires spectroscopic verification [6].

2.7. Microplastic analysis methods

2.7.1. Gravimetric estimation of retained solids and apparent microplastic removal

Retained solids on the membrane were quantified by filter mass difference before and after filtration. The removal efficiency was estimated based on the relative reduction in retained mass compared to the initial concentration, following approaches commonly reported in electrocoagulation-based microplastic studies [6].

Because electrocoagulation with aluminium electrodes produces $Al(OH)_3$ flocs and may also capture other suspended matter, the gravimetric result does not represent a direct measurement of pure microplastic mass alone. Instead, it provides an apparent estimate of microplastic-associated retained solids after treatment. For this reason, gravimetric measurements were supported by fluorescence microscopy and Fourier transform infrared spectroscopy (FTIR) analysis to strengthen the interpretation that the retained material included polymeric particles. Accordingly, the reported removal efficiencies should be interpreted as estimated values under the adopted analytical procedure rather than absolute polymer-specific removal.

2.7.2. Fluorescence microscopy (visual inspection)

Dried filters were examined using a fluorescence microscope (MEIJI MX, Japan). Microplastic particles were identified by visual sorting under magnification, and categorised according to morphology (e.g. fragments, pellets/fibres) following a practical classification approach used in field and drinking-water-related microplastic screening studies [15]. Representative images were recorded for documentation.

2.7.3. FTIR spectroscopy

To confirm polymeric signatures, selected retained material on dried filters was analysed by FTIR using an IRPrestige-21 (Shimadzu). Spectra were recorded and compared qualitatively to known polymer functional-group regions reported in the microplastics literature [37]. FTIR confirmation was used as the pri-

mary evidence to support microplastic presence before treatment and reduction after EC, consistent with widely adopted identification practices [35].

It should be noted that no independent chemical digestion or density-separation step was applied to completely isolate polymer particles from aluminium hydroxide flocs prior to gravimetric assessment. Therefore, microscopy and FTIR were used as confirmatory tools to support the presence of polymeric material on the filters. This analytical limitation should be considered when interpreting the absolute magnitude of the reported removal efficiencies.

2.8. Quality assurance and contamination control

Because microplastic measurements can be affected by airborne fibres and secondary contamination, practical contamination-reduction measures were adopted during sampling and analysis. Glass containers were preferred over plastic during sampling and storage, and filters were handled using clean metal tweezers. Work surfaces were cleaned prior to filtration and microscopy. These precautions are consistent with the general recommendations in microplastic analytical studies aiming to minimise false positives [15].

2.9. Energy-related process indicators

Electrical energy consumption can be reported using a specific energy consumption (SEC) metric, widely used in electrochemical water treatment analysis [1]:

$$\mathrm{SEC}\ (\mathrm{kWh/m^3}) = \frac{U\ I\ t}{V} 10^{-3}, \qquad (4)$$

where U is voltage (V), I current (A), t operating time (h) and V treated volume (m^3). This indicator allows comparison between operating cases and supports optimisation discussions based on energy demand, not only removal percentage.

2.10. Methodological limitations

The present work was designed to assess electrocoagulation performance in real drinking-water samples rather than in synthetic microplastic suspensions. While this improves practical relevance, it limits strict reproducibility because the initial microplastic content in natural samples is inherently low and variable. In addition, gravimetric filtration may include aluminium hydroxide flocs and other retained solids in addition to microplastic particles. Therefore, the reported removal efficiencies should be interpreted together with the supporting microscopy and FTIR observations. Future work should include synthetic microplastic-spiked water, polymer-specific quantification and additional water-quality indicators such as turbidity, total suspended solids (TSS), conductivity and total dissolved solids (TDS).

3. Results and discussion

3.1. Identification of microplastics in drinking water samples

3.1.1. Visual inspection using fluorescence microscopy

Prior to electrocoagulation treatment, microplastic particles were visually identified on the filtered membranes using fluorescence microscopy. Irregular fragments as well as spherical plastic-like particles were observed, indicating the presence of different microplastic morphologies in drinking water samples. After electrocoagulation, the number of visually distinguishable plastic particles on the membrane surface was noticeably reduced, suggesting aggregation and removal during the treatment process. Representative microscopy images are presented in Fig. 1.

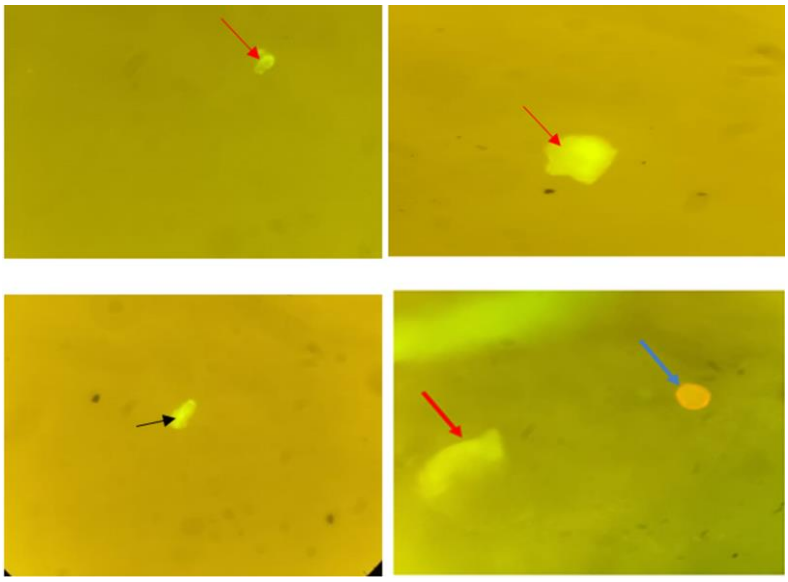


Fig. 1. Fluorescence microscopy images of microplastic particles in drinking water samples before electrocoagulation, showing the presence of irregular fragments and spherical particles.

3.1.2. FTIR confirmation of polymeric material

Because the study relied on real drinking-water samples, the detected microplastic content and retained solids should be interpreted within the natural variability of the sampled matrices. FTIR analysis was performed to confirm the polymeric nature of retained particles before and after electrocoagulation treatment. The untreated water samples exhibited characteristic absorption bands associated with common polymer functional groups, while several of these bands were absent or significantly reduced after treatment. The observed reduction in oxygenated and aromatic functional groups indicates preferential removal of polymers such as polyethylene terephthalate (PET) and polystyrene (PS), whereas nonpolar polymers showed lower sensitivity to electrocoagulation. The corresponding FTIR spectra are presented in Fig. 2.

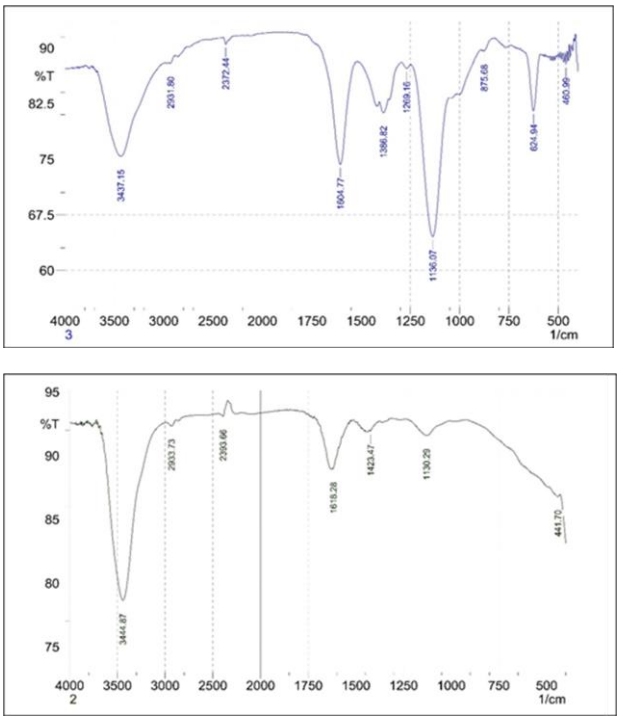


Fig. 2. FTIR spectra of retained particles before and after electrocoagulation treatment, indicating the reduction of characteristic polymer functional groups.

3.1.3. Observation of floc formation during electrocoagulation

During the electrocoagulation process, the formation of visible flocs was clearly observed in the treated water samples. As the treatment progressed, the initially transparent or slightly turbid water gradually developed suspended whitish, gelatinous aggregates characteristic of aluminium hydroxide formation. These flocs increased in size and density with time, leading to noticeable settling at the bottom of the reactor after the treatment was stopped.

The observed flocs exhibited typical behaviour associated with sweep flocculation, where suspended particles are enmeshed within growing aluminium hydroxide structures. In addition, fine gas bubbles generated at the cathode contributed to the flotation of aggregated particles toward the water surface. This combined sedimentation–flotation behaviour was consistently observed under optimal operating conditions, particularly at near-neutral pH and moderate current density.

Although photographic documentation is not included, the consistent reduction in measured retained solids and the corresponding decrease in visually identifiable microplastic particles (as confirmed by microscopy) strongly support the occurrence of effective floc formation and particle aggregation during electrocoagulation.

3.2. Effect of electrocoagulation time on microplastic removal

The influence of treatment time on microplastic removal efficiency was investigated under constant operating conditions. A rapid increase in removal efficiency was observed during the first 15 min of operation, reaching approximately 70%. Extending the treatment time to 30 min resulted in an increase in removal efficiency to about 80%, while further prolongation produced only marginal improvement. This trend suggests that most microplastic aggregation occurs during the early stages of electrocoagulation. The variation of removal efficiency with time is illustrated in Fig. 3, and the corresponding concentrations are summarised in Table 1.

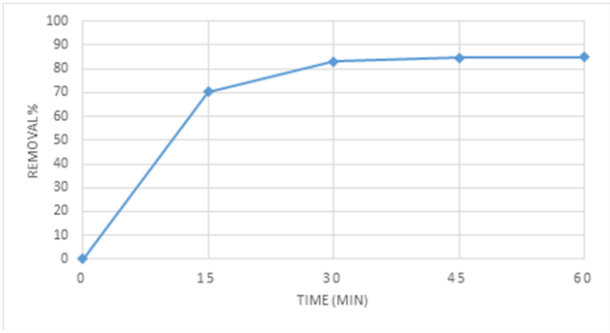


Fig. 3. Variation of microplastic removal efficiency with treatment time, showing rapid initial removal followed by stabilization due to floc saturation and reduced particle availability.

Table 1. Variation of microplastic concentration with treatment time during electrocoagulation.

Time (min)	0	15	30	45	60
Concentration (ppm)	101	30	15.1	15	15

This behaviour is consistent with the progressive formation and growth of aluminium hydroxide flocs during electrocoagulation, which enhance particle aggregation and facilitate their removal through sedimentation and flotation.

The experimental setup was constructed following standard bench-scale electrocoagulation configurations commonly reported in the literature [1], including parallel aluminium electrodes, controlled current supply and continuous mixing. Although a photographic image of the setup is not included, all op-

erational parameters and reactor configurations are described in sufficient detail to ensure reproducibility.

The rapid increase in removal efficiency during the initial 15 minutes indicates that the early stage of electrocoagulation is dominated by availability of active adsorption sites on freshly formed aluminium hydroxide flocs, which facilitates the rapid capture of microplastic particles. As the treatment progresses, the system gradually approaches a quasi-equilibrium condition, where removal efficiency stabilises due to the partial saturation of available adsorption sites and the reduction in the number of remaining particles in the solution. This behaviour is consistent with coagulation mechanisms governed by mass transfer and surface interaction processes.

3.3. Effect of pH on microplastic removal efficiency

Solution pH had a pronounced effect on electrocoagulation performance. The highest removal efficiencies were achieved under near-neutral conditions (pH 7–8), while acidic and alkaline conditions resulted in lower efficiency. This behaviour is attributed to the formation of amorphous aluminium hydroxide species at neutral pH, which enhances aggregation and flocculation of microplastic particles. The effect of pH on removal efficiency is shown in Fig. 4.

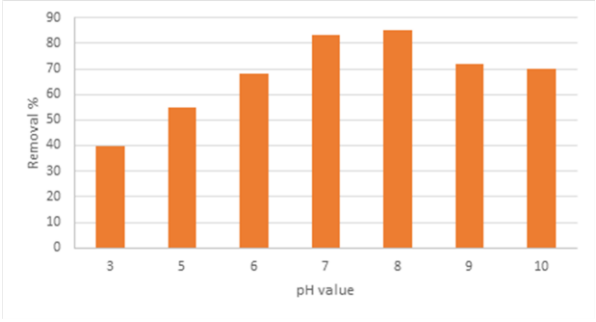


Fig. 4. Influence of initial pH on microplastic removal efficiency, highlighting optimal performance under near-neutral conditions due to favourable aluminium hydroxide speciation.

The improved removal efficiency at near-neutral pH further supports the formation of amorphous $Al(OH)_3$ flocs with high adsorption capacity, which play a dominant role in microplastic capture through sweep flocculation mechanisms.

The dependence of removal efficiency on pH can be interpreted based on aluminium speciation. At near-neutral pH, the dominant species are amorphous $Al(OH)_3$ with high surface area, which enhances adsorption and sweep flocculation. In contrast, under acidic conditions, soluble Al^{3+} species dominate, reducing floc formation, while at high pH, negatively charged $Al(OH)_4^-$ species limit particle aggregation due to electrostatic repulsion.

3.4. Influence of electrolyte (NaCl) concentration

Increasing sodium chloride concentration improved microplastic removal efficiency due to enhanced solution conductivity and more stable current flow. Removal efficiency increased with electrolyte concentration up to 4 g/L, beyond which excessive

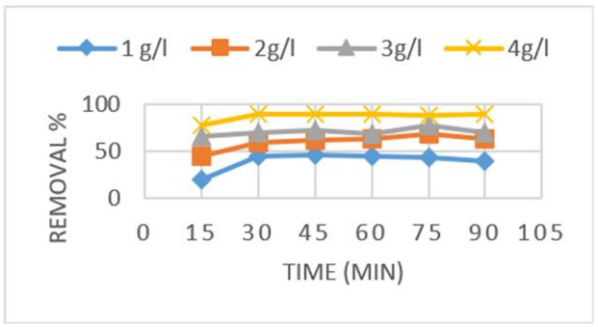


Fig. 5. Effect of electrolyte (NaCl) concentration on microplastic removal efficiency, illustrating the role of solution conductivity and its impact on electrocoagulation performance.

gas evolution and sludge formation were observed, negatively affecting operational stability. The influence of electrolyte concentration on removal efficiency is presented in Fig. 5.

The improvement in removal efficiency with increasing NaCl concentration is primarily attributed to enhanced electrical conductivity, which reduces ohmic resistance and promotes uniform current distribution. However, excessive electrolyte concentration leads to intensified gas evolution and turbulence, which may disrupt floc structure and reduce separation efficiency.

3.5. Effect of current density

Current density controlled the rate of aluminium dissolution and gas evolution within the reactor. Removal efficiency increased with current density up to 20 mA/cm^2. Further increases led to reduced efficiency and operational instability, including short-circuiting between electrodes. The effect of current density on removal efficiency and final concentration is shown in Fig. 6 and Table 2.

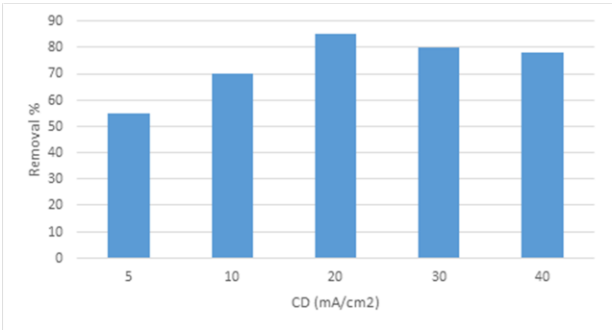


Fig. 6. Influence of current density on microplastic removal efficiency, showing the existence of an optimal value governed by coagulant generation and system stability.

The removal of microplastic particles during electrocoagulation can be attributed to multiple simultaneous mechanisms. Initially, charge neutralisation reduces electrostatic repulsion between particles, promoting aggregation. Subsequently, the in situ generated aluminium hydroxide flocs act as a sweep flocculant, entrapping microplastic particles within a growing three-

dimensional network. In addition, hydrogen gas bubbles produced at the cathode enhance flotation by carrying aggregated particles toward the surface. Therefore, the overall removal process is governed by a combination of adsorption, sweep flocculation and electroflotation mechanisms.

Table 2. Effect of current density on microplastic-associated solids concentration after electrocoagulation.

Current density (mA/cm^2)	5	10	20	30	40
Concentration (ppm)	45	30	15	30	45

The existence of an optimal current density indicates a balance between coagulant generation and system stability. At low current densities, insufficient Al^{3+} ions are generated, limiting floc formation. Conversely, at high current densities, excessive gas evolution and electrode passivation may reduce the effective contact between flocs and microplastic particles, resulting in a decrease in removal efficiency.

Overall, the results obtained from varying operating parameters consistently indicate that electrocoagulation performance is governed by the interplay between aluminium hydroxide floc formation, solution chemistry and electrochemical operating conditions. The observed trends across different parameters reinforce the role of adsorption, sweep flocculation and flotation as the dominant removal mechanisms.

4. Conclusions

This study demonstrated the potential of aluminium-based electrocoagulation as a supplementary treatment for microplastic removal from drinking water. The process efficiency was strongly influenced by operating parameters, particularly pH, current density and treatment time. Optimal removal was achieved under near-neutral conditions and moderate current density, where aluminium hydroxide flocs effectively promoted particle aggregation and separation. The removal mechanism was governed by a combination of adsorption, sweep flocculation and flotation processes.

Despite the promising results, the findings should be interpreted in light of the use of real drinking water samples and the limitations associated with gravimetric estimation of retained solids. Further investigations using controlled synthetic microplastic suspensions and advanced analytical techniques are recommended to enhance accuracy and reproducibility.

References

[1] Mao, Y., Zhao, Y., & Cotterill, S. (2023). Examining current and future applications of electrocoagulation in wastewater treatment. *Water*, 15(8), 1455. doi: 10.3390/w15081455

[2] Alimi, O., Budarz, J., Hernandez, L., & Tufenkji, N. (2018). Microplastics and nanoplastics in aquatic environments: Aggregation, deposition, and enhanced contaminant transport. *Environmental Science & Technology*, 52(4), 1704–1724. doi: 10.1021/acs.est.7b05559

[3] Al-Rubaiey, N.A., & Al-Barazanjy, M.G. (2018). Electrocoagulation treatment of oily wastewater in the oil industry. *Journal of Petroleum Research and Studies*, 8(3), 274–289. doi: 10.52716/jprs.v8i3.285

[4] Amjad, M., Intisar, A., Afzal, A., & Hussain, N. (2023). Biological methods for the removal of microplastics from water. *Advances in Chemical Pollution, Environmental Management and Protection*, 9, 65–78. doi: 10.1016/bs.apmp.2022.10.003

[5] Akarsu, C., Kumbur, H., & Kideys, A.E. (2021). Removal of microplastics from wastewater through electrocoagulation – electroflotation and membrane filtration processes. *Water Science and Technology*, 84(7), 1648–1662. doi: 10.2166/wst. 2021.356

[6] Lin, B., & Wu, R. (2021). The dilemma of paraxylene plants in China: Real trouble for the environment. *Science of the Total Environment*, 779, 146456. doi: 10.1016/j.scitotenv.2021.146456

[7] Elkhatib, D., Oyanedel-Craver, V., & Carissimi, E. (2021). Electrocoagulation applied for the removal of microplastics from wastewater treatment facilities. *Separation and Purification Technology*, 276, 118877. doi.: 10.1016/j.seppur.2021.118877

[8] Ghosh, S., Sinha, J.K., Ghosh, S., Vashisth, K., Han, S., & Bhaskar, R. (2023). Microplastics as an emerging threat to the global environment and human health. *Sustainability*, 15(14), 10821. doi: 10.3390/su151410821

[9] H Sultan, H., Abdul Wahab Shaker Al-Aadhami, M., & Nihad Baqer, N. (2023). Detection of microplastics in drinking water treatment plants in Baghdad City/Iraq. *Pollution*, 9(4), 1838–1849. doi: 10.22059/poll.2023.359382.1913

[10] Khan, M.T., Ahmad, M., Hossain, M.F., Nawab, A., Ahmad, I., Ahmad, K., & Panyametheekul, S. (2023). Microplastic removal by coagulation: a review of optimizing the reaction conditions and mechanisms. *Water Emerging Contaminants & Nanoplastics*, 2023, 2(22), 1–29. doi: 10.20517/wecn.2023.39

[11] Lu, Y., Li, M.C., Lee, J., Liu, C., & Mei, C. (2023). Microplastic remediation technologies in water and wastewater treatment processes: Current status and future perspectives. *Science of the Total Environment*, 868, 161618. doi: 10.1016/j.scitotenv.2023.161618

[12] Shen, M., Zhang, Y., Eydhah, A., Hu, T., Zhang, C., Sun, B., & Zhang, Z. (2022). Efficient removal of microplastics from wastewater by an electrocoagulation process. *Chemical Engineering Journal*, 428, 131161. doi: 10.1016/j.cej.2021.131161

[13] Batros, S.S., Saeed, F.R., & Hussein, H.F. (2025). Antibacterial activity and microstructure properties of cadmium-doped copper oxide particles prepared by chemical precipitation. *Iranian Journal of Materials Science and Engineering*, 22(1), 107–117. doi: 10.22068/ijmse.3864

[14] Nabi, I., Li, K., Cheng, H., Wang, T., Liu, Y., Ajmal, S., Yang, Y., Feng, Y., & Zhang, L. (2020). Complete photocatalytic mineralization of microplastic on TiO_2 nanoparticle film. *iScience*, 23(7), 101326. doi: 10.1016/j.isci.2020.101326

[15] Pandey, B., Pathak, J., Singh, P., Kumar, R., Kumar, A., Kaushik, S., & Thakur, T.K. (2023). Microplastics in the ecosystem: an overview on detection, removal, toxicity assessment, and control release. *Water*, 15(1), 51. doi: 10.3390/w15010051

[16] Perren, W., Wojtasik, A., & Cai, Q. (2018). Removal of microbeads from wastewater using electrocoagulation. *ACS Omega*, 3(3), 3357–3364. doi: 10.1021/acsomega.7b02037

[17] Rajala, K., Grönfors, O., Hesampour, M., & Mikola, A. (2020). Removal of microplastics from secondary wastewater treatment plant effluent by coagulation/flocculation. *Water Research*, 183, 116045. doi: 10.1016/j.watres.2020.116045

[18] Ramadani, A.I., Fardiyah, Q., & Rumhayati, B. (2024). The Study of Removal of Polyvinyl Chloride (PVC) Particles from Wastewater through Electrocoagulation. *Indonesian Journal of Chemistry*, 24(5), 1498–1513. doi: 10.22146/ijc.87924

[19] Tampubolon, D.R.S., & Rosariawari, F. (2023). Kombinasi elektrokoagulasi dan oksidasi lanjut berbasis O3/GAC dalam mengolah limbah industri batik. Envirous, 1(2), 1–9. doi: 10.33005/envirous.v1i2.29

[20] Ahmed, S.B., Al-Naemi, A.N.A., Kamar, F.H., Hussein, H.F., & Nawar, M.S. (2024). Adsorption of phenol from aqueous solution using graphene nanoparticles. *AIP Conference Proceedings*, 3105(1), 070003. doi: 10.1063/5.0212296

[21] Salahuddin, U., Sun, J., Zhu, C., & Gao, P. (2023). Filtration methods for microplastic removal in wastewater streams. *International Journal of High Speed Electronics and Systems*, 32(02n04), 2350019. doi: 10.1142/S0129156423500192

[22] Shalaby, A., Nassef, E., Mubark, A., & Hussein, M. (2014). Phosphate removal from wastewater by electrocoagulation using aluminum electrodes. *American Journal of Environmental Engineering and Science*, 1(5), 90–98.

[23] Shi, X., Zhang, X., Gao, W., Zhang, Y., & He, D. (2022). Removal of microplastics from water by magnetic nano-Fe_3O_4. *Science of the Total Environment*, 802, 149838. doi: 10.1016/ j.scitotenv.2021.149838

[24] Srirangsan, A., Ongwandee, M., & Chavalparit, O. (2009). Treatment of biodiesel wastewater by electrocoagulation process. *Environment Asia*, 2(2), 15–19. doi: 10.14456/ea.2009.11

[25] Wang, J., Sun, C., Huang, Q.X., Chi, Y., & Yan, J.H. (2021). Adsorption and thermal degradation of microplastics from aqueous solutions by Mg/Zn-modified magnetic biochars. *Journal of Hazardous Materials*, 419, 126486. doi: 10.1016/j.jhazmat.2021.126486

[26] Yao, Z., Seong, H.J., & Jang, Y.S. (2022). Environmental toxicity and decomposition of polyethylene. *Ecotoxicology and Environmental Safety*, 242, 113933. doi: 10.1016/j.ecoenv.2022. 113933

[27] Zhang, K., Shi, H., Peng, J., Wang, Y., Xiong, X., Wu, C., & Lam, P.K.S. (2018). Microplastic pollution in China's inland water systems. *Science of the Total Environment*, 630, 1641–1653. doi: 10.1016/j.scitotenv.2018.02.300

[28] Saeed, F.R., Abdulkader, J.G., & Hussein, H.F. (2025). Advanced analysis of aluminum alloy welded joints microstructure. *Discover Materials*, 6(1), 27. doi: 10.1007/s4393 9-025-00491-5

[29] Zhang, Y., Diehl, A., Lewandowski, A., Gopalakrishnan, K., & Baker, T. (2020). Removal efficiency of micro- and nanoplastics during drinking water treatment. *Science of the Total Environment*, 720, 137383. doi: 10.1016/j.scitotenv.2020.137383

[30] Zhou, C., Bi, R., Su, C., Liu, W., & Wang, T. (2022). The emerging issue of microplastics in the marine environment: A bibliometric analysis from 2004 to 2020. *Marine Pollution Bulletin*, 179, 113712. doi: 10.1016/j.marpolbul.2022.113712

[31] Singh, S., Chakma, S., Alawa, B., & Diwan, V. (2022). Identification, characterization, and implications of microplastics in soil – A case study of Bhopal, central India. *Journal of Hazardous Materials Advances*, 9, 100225. doi: 10.1016/j.hazadv.2022.100225

Co-published by
Institute of Fluid-Flow Machinery
Polish Academy of Sciences
Committee on Thermodynamics and Combustion
Polish Academy of Sciences

Copyright©2026 by the Authors under licence CC BY-NC-ND 4.0

http://www.imp.gda.pl/archives-of-thermodynamics/

Impact of activation energy and Deborah number on heat and mass transfer of three dimensional rotating magnetic nanofluid over a stretching surface

P. Sudarsana Reddy*, P. Sreedevi

Department of Mathematics, Rajeev Gandhi Memorial College of Engineering & Technology, Nandyal-518501, A.P, India
*Corresponding author email: suda1983@gmail.com

Received: 26.07.2025; revised: 27.04.2026; accepted: 10.08.2026

Abstract

The influence of activation energy and thermal Biot number on MHD (magnetohydrodynamic) mass and heat transport analysis of rotating Maxwell nanoliquid flow over an elongating surface with radiation is examined in the present study by considering both suction and non-suction cases. Momentum equations in both directions of x and y, energy and species equations are transformed into the a of ODEs (ordinary differential equations) by utilising similarity conversions. These transformed equations supplemented with boundary conditions are solved numerically with the use of the finite element method. Velocities in both x and y directions, concentration and temperature sketches are plotted for various values of Deborah parameter, activation energy, Biot number, magnetic parameter, thermophoresis, Brownian motion, radiation and rotation parameters. The rates of mass transport, heat transport and dimensionless gradient of velocity are also calculated. Key findings reveal that an increase in activation energy significantly enhances the concentration of the nanoliquid in both suction and non-suction cases. Furthermore, it was observed that the magnetic parameter induces a Lorentz force that retards fluid motion while simultaneously elevating the liquid's temperature. Results also demonstrate that the rotation parameter has a more pronounced effect on temperature degradation in the presence of suction.

Keywords: Rotating fluid; Maxwell nanofluid; MHD; Convective boundary condition; Finite element method; Radiation

Vol. 47(2026), No. 3, 241–252; doi: 10.24425/ather.2026.7524

Cite this manuscript as: Sudarsana Reddy, P., & Sreedevi, P. (2026). Impact of activation energy and Deborah number on heat and mass transfer of three dimensional rotating magnetic nanofluid over a stretching surface. *Archives of Thermodynamics*, 47(3), 241–252.

1. Introduction

Cancer therapy, energy production, cooling of nuclear reactors, power generation, thermal insulation, food processing, storage of foodstuffs, increasing the efficiency of engines, etc., are a few industrial and environmental applications of nanoliquids. Limited thermal conductivity is the major drawback of common liquids like engine oil, kerosene, water and ethylene glycol. Their thermal conductivities may amplify by adding a kind of metal particles known as “nanoparticles”. The thermal conductivity of such nanoliquids is enhanced compared to normal liquids. Recently, many authors worked on and calculated the heat transport performance of dissimilar kinds of nanoliquids and observed considerable augmentation of heat transfer in nanofluids [1–10].

Mass and heat transport features of Maxwell nanoliquid have also received highest priority by the research community, as it has good applications in electronic devices. Recent advancements in renewable energy systems have highlighted the critical role of nanofluids in enhancing the efficiency of photovoltaic-

Nomenclature

B_0 – magnetic field strength, T
B1 – Biot number
C_f – skin-friction coefficient
Cr – chemical reaction parameter
D_B – Brownian diffusion coefficient, m^2/s
D_T – thermophoretic diffusion coefficient, m^2/s
$E1$ – activation energy parameter
$f(\eta)$– dimensionless stream function
g – gravitational acceleration, m/s^2
k_{nf} – thermal conductivity of nanofluid, W/(m·K)
k_o^2 – chemical reaction rate
k_s – thermal conductivity, W/(m·K)
K – porous parameter
K^* – mean absorption coefficient
Le – Lewis number
M – magnetic parameter
Nb – Brownian motion parameter
Nt – thermophoresis parameter
Nu_x– Nusselt number
Pr – Prandtl number
q_r – radiative heat flux, W/m^2
q_w – wall heat flux, W/m^2
R – radiation parameter
T – fluid temperature, K
T_w – surface temperature, K
T_∞ – ambient temperature, K
u, v– velocity components in x- and y-axis, m/s
$V0$ – suction parameter
x, y – Cartesian coordinates, m

Greek symbols

α – thermal diffusivity of base fluid, m^2/s
β – thermal expansion coefficient, 1/K
ε – pressure parameter
η – similarity variable
θ_η – dimensionless temperature
λ – Maxwell parameter
μ – fluid viscosity, Pa·s
μ_{nf} – kinematic viscosity of the nanofluid, Pa·s
ν_f – kinematic viscosity of the base fluid, m^2/s
ρ_f – density of the base fluid, kg/m^3
ρ_{nf} – density of the nanofluid, kg/m^3
ρ_p – nanoparticle mass density, kg/m^3
σ – electrical conductivity, S/m
σ^* – Stephan-Boltzmann constant, $W/(m^2 \cdot K^4)$
τ_w – shear stress, Pa
φ – volume fraction of nanoparticles
ϕ_η – dimensionless concentration
ψ – stream function
Ω – rotation parameter

Subscripts and Superscripts

f – base fluid
nf – nanofluid
w – at the cone surface
∞ – far away from the cone surface

Abbreviations and Acronyms

FEM – finite element method
MHD– magnetohydrodynamics
ODE – ordinary differential equation

thermal (PVT) systems. Advanced configurations, such as the use of nanofluid spectral splitters to improve concentrated solar PV thermal efficiency and the integration of thermoelectric generators supported by nanofluid filters, have shown great promise for sustainable energy production. Furthermore, the inclusion of vortex generators in the presence of heat sinks has been shown to significantly influence the performance of concentrated solar modules. Ahmed et al. [11] investigated heat transport and flow features of a Buongiorno modelled Maxwell nanoliquid over a shrinking/stretching radially rotating disk by taking variable thermal conductivity into account and observed that the thermophoresis parameter deteriorates heat transport in the nanoliquid. Ijaz et al. [12] investigated the authority of double stratification and activation energy on species and energy transport topographies of Maxwell nanoliquid over an inclined non-linear stretching cylinder and professed that the velocity profiles of the Maxwell nanoliquid decrease with the increasing values of the Deborah parameter. Ahmed et al. [13] presented Buongiorno typed nanoliquid concentration and temperature features over a revolving disk with uniform injection/suction and observed that the rate of mass transport magnifies with magnifying values of the thermophoresis number. Ahmed et al. [14,15] deliberated the Buongiorno modelled Maxwell nanoliquid flow behaviour over a disk/cylinder in which the resulting non-linear fluid flow equations are numerically examined by utilising MATLAB built in function bvp4c. Sharma et al. [16] discussed the sway of viscous dissipation and Joule heating on flow analysis of graphene Maxwell nanoliquid over a non-linearly extending sheet and observed that the rate of heat transport augments as the values of thermal slip number amplify. Khan et al. [17] professed non-Newtonian Maxwell nanoliquid flow over an exponential widening surface and observed that the rate of heat transport values decreases with the increasing values of time relaxation number. Abro et al. [18] analysed SWCNTs (single-walled carbon nanotubes) and MWCNTs (multi-walled carbon nanotubes), ethylene glycol type Maxwell nanoliquid heat transport features and observed magnification in the rates of energy transport of Maxwell nanoliquid with amplifying nanoparticle volume fraction values. Ali et al. [19] deliberated copper/alumina typed Maxwell hybrid nanoliquid flow features through a vertical channel and intuited that amplification in the values of volume fraction of both considered nanoparticles elevates the temperature scatterings of the nanofluid. Jamshed et al. [20] investigated the sway of MHD and entropy generation on energy and flow features of Maxwell nanoliquid, prepared with copper–H_2O/titanium oxide–H_2O, over a horizontal infinite plate and detected a noticeable increase in the thermal conductivity of the nanofluid compared with the base liquid. Gowda et al. [21] deliberated Maxwell-Casson modelled nanoliquid heat transport and flow analysis between double elongated disks. Zhou et al. [22] analysed fluid flow topographies of Maxwell thermally radiative nanoliquid over a rotating stretchable porous disk.

Mustafa et al. [23] pondered the influence of Christov-Cattaneo energy flux on heat transport and flow examination over a stretching surface and observed that as the values of thermal relaxation number increase, the temperature of the liquid decreases. Ahuja et al. [24] analysed the influence of magnetic field and rotation parameter on fluid flow of rotating Maxwell nanofluid. Hayat et al. [25] implemented the optimal homotopy analysis method to investigate mass and energy transport in rotating Maxwell nanoliquid over a spreading exponential surface, and observed that the nanoliquid temperature magnifies with the increasing values of Deborah number. Rashid et al. [26] investigated the power of chemical reaction and Arrhenius energy on three-dimensional rotating Maxwell nanofluid heat transport performance over an exponentially widening porous surface and observed amplification in the sketches of temperature with magnifying values of heat sink/source number. Ali et al. [27] investigated mass and heat transport of three-dimensional rotating Maxwell nanoliquid flow over a stretchable surface with activation energy and Christov-Cattaneo double diffusion and observed that the temperature scattering of the nanoliquid magnifies with amplifying values of the Deborah parameter. Ahmed et al. [28] perceived the sway of Christov-Cattaneo double diffusion on solutal and thermal energy transport of rotating Maxwell nanoliquid flow over a revolving disk. Khalid et al. [29] pondered the impact of thermophoresis and Brownian motion on Rayleigh-Benard convective rotating Maxwell nanoliquid flow saturated with permeable media. Ramaiah et al. [30] examined the transport of mass and flow of revolving Maxwell nanoliquid over a stretchable sheet with activation energy and Christov-Cattaneo heat flux, and observed denigration in the scatterings of temperature as the Deborah number values amplify. Khan et al. [31], in their work on flow analysis of revolving Maxwell nanoliquid over an exponential/linear stretched sheet, scrutinised that as the values of rotation parameter magnifies, the heat flux of the nanoliquid is increased. Ali et al. [32] investigated solutal and heat energy transport features of bio-convective Maxwell revolving nanoliquid over a Riga plate with Christov-Cattaneo heat flux and observed magnification in the temperature of the liquid with the growing value of rotation parameter. Chu et al. [33] professed the sway of Newtonian heating and gyrotactic microorganisms on heat transport and flow investigation of revolving Maxwell nanoliquid over an elongated surface. Alzahrani et al. [34] pondered radiative Maxwell nanoliquid flow behaviour over a revolving frame by captivating microorganisms and activation energy into consideration and observed a magnification in the liquid temperature with the enhanced rotation parameter values. Very recently, Cao et al. [35], Wei et al. [36] and Ali et al. [37] studied the thermophysical properties of rotating Maxwell nanoliquid flow over various configurations and observed that the effect of Deborah number is considerably high on the velocity and rates of heat transport in the liquid. Very recently, several authors [38–41] studied heat and mass transport of tri-nanoliquids over different geometries and noticed considerable augmentation in the rates of heat transfer after adding nanoparticles to the base fluid.

Careful examination of the aforementioned literature [11–37] reveals that while several researchers have explored rotating Maxwell nanoliquid flows, a comprehensive analysis of mass and energy transport in a three-dimensional rotating Maxwell radiative nanoliquid over an exponentially stretching sheet, specifically incorporating the combined effects of activation energy and the thermal Biot number, is currently missing. This study aims to fill this significant gap by investigating these coupled phenomena. The governing non-linear equations are conversed using similarity transformations and solved numerically using the finite element method (FEM). The novelty of this work lies in providing a detailed understanding of how activation energy and convective boundary conditions influence the performance of rotating non-Newtonian systems, with results presented for both suction and non-suction cases.

2. Mathematical modelling of the problem

Consider the steady, three-dimensional, rotating, viscous, incompressible, laminar, MHD boundary layer Maxwell nanofluid flow past an exponentially stretching surface. The coordinate system is chosen such that *u*, *v* and *w* are the velocity components along the *x*-, *y*- and *z*- directions, respectively, as shown in Fig. 1. We also consider a constant magnetic field of strength in the *z*-direction. The flow is caused by the stretching of the sheet, which moves in its own plane with the surface velocity. The stretching surface is maintained at a uniform temperature and concentration, and these values are assumed to be greater than the ambient temperature and concentration, respectively. Under the above assumptions and with reference to the work of Hayat et al. [25], the governing equations describing the momentum, energy and concentration in the presence of thermal radiation, activation energy and chemical reaction take the following form:

$$\frac{\partial u}{\partial x}+\frac{\partial v}{\partial y}+\frac{\partial w}{\partial z}=0, \tag{1}$$

$$u\frac{\partial u}{\partial x}+v\frac{\partial u}{\partial y}+w\frac{\partial u}{\partial z}-2\Omega v=\frac{\mu}{\rho}\frac{\partial^2 u}{\partial z^2}-\lambda_1\left(u^2\frac{\partial^2 u}{\partial x^2}+v^2\frac{\partial^2 u}{\partial y^2}+w^2\frac{\partial^2 u}{\partial z^2}+2uv\frac{\partial^2 u}{\partial x\,\partial y}+2vw\frac{\partial^2 u}{\partial y\,\partial z}+\right.$$
$$\left.+2uw\frac{\partial^2 u}{\partial x\,\partial z}-2\Omega\left(u\frac{\partial v}{\partial x}+v\frac{\partial v}{\partial y}+w\frac{\partial v}{\partial z}\right)+2\Omega\left(v\frac{\partial u}{\partial x}-u\frac{\partial u}{\partial y}\right)\right)-\frac{\sigma}{\rho}{B_0}^2u, \tag{2}$$

$$u\frac{\partial v}{\partial x}+v\frac{\partial v}{\partial y}+w\frac{\partial v}{\partial z}+2\Omega u=\frac{\mu}{\rho}\frac{\partial^2 v}{\partial z^2}-\lambda_1\left(u^2\frac{\partial^2 v}{\partial x^2}+v^2\frac{\partial^2 v}{\partial y^2}+w^2\frac{\partial^2 v}{\partial z^2}+2uv\frac{\partial^2 v}{\partial x\,\partial y}+2vw\frac{\partial^2 v}{\partial y\,\partial z}+\right.$$
$$\left.+2uw\frac{\partial^2 v}{\partial x\,\partial z}+2\Omega\left(u\frac{\partial u}{\partial x}+v\frac{\partial u}{\partial y}+w\frac{\partial u}{\partial z}\right)+2\Omega\left(v\frac{\partial v}{\partial x}-u\frac{\partial u}{\partial y}\right)\right)-\frac{\sigma}{\rho}{B_0}^2v, \tag{3}$$

$$u\frac{\partial T}{\partial x}+v\frac{\partial T}{\partial y}+w\frac{\partial T}{\partial z}=\alpha\frac{\partial^2 T}{\partial z^2}+\tau\left[D_B\frac{\partial C}{\partial z}\frac{\partial T}{\partial z}+\left(\frac{D_T}{T_\infty}\right)\left(\frac{\partial T}{\partial z}\right)^2\right]-\frac{1}{\rho c_p}\frac{\partial q_r}{\partial z}, \quad (4)$$

$$u\frac{\partial C}{\partial x}+v\frac{\partial C}{\partial y}+w\frac{\partial C}{\partial z}=D_B\frac{\partial^2 C}{\partial z^2}-k_o^2\left(\frac{T}{T_0}\right)^n(C-C_\infty)e^{\frac{-E1}{\kappa T}}. \quad (5)$$

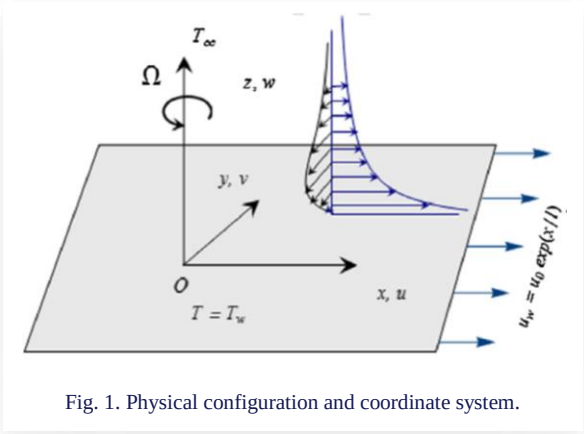


Fig. 1. Physical configuration and coordinate system.

The associated boundary conditions are:

$$C=C_w,\ -k\frac{\partial T}{\partial y}=h_f\left(T_f-T\right),\ u=u_w(x)=U_0e^{(x/L)},$$

$$v=0,\ w=-U_0 \text{ at } z=0;$$

$$C\to C_\infty,\ v\to 0,\ T\to T_\infty,\ u\to 0 \text{ at } z\to\infty. \quad (6)$$

By utilising the Rosseland diffusion approximation, the radiative heat flux is defined as:

$$q_r=-\frac{4\sigma^*}{3K^*}\frac{\partial T^4}{\partial y}. \quad (7)$$

We assume that the temperature variations within the fluid region are sufficiently small so that T^4 can be approximated as a linear function of T; therefore, this term can be expanded in a Taylor series. After neglecting higher-order terms in the expansion of the Taylor series of T^4 about T_∞, we obtain:

$$T^4\cong 4T_\infty{}^3T-3T_\infty^4. \quad (8)$$

After replacing Eq. (8) in Eq. (7), we obtain:

$$q_r=-\frac{16T_\infty{}^3\sigma^*}{3K^*}\frac{\partial T}{\partial z}. \quad (9)$$

The subsequent similarity transformations are considered to convert the above non-linear PDEs (partial differential equations) into ODEs.

$$v=U_0e^{\left(\frac{x}{L}\right)}\omega(\eta),\ u=U_0e^{\left(\frac{x}{L}\right)}f'(\eta),$$

$$w=-\left(\frac{U_0\nu}{2L}\right)^{\frac{1}{2}}e^{\left(\frac{x}{2L}\right)}\left(f(\eta)+\omega(\eta)\right),$$

$$\phi(\eta)=\frac{C-C_\infty}{C_w-C_\infty},\ \theta(\eta)=\frac{T-T_\infty}{T_w-T_\infty},\ \eta=\left(\frac{U_0}{2\nu L}\right)^{\frac{1}{2}}e^{\left(\frac{x}{2L}\right)}z. \quad (10)$$

Substituting Eqs. (9) and (10) into Eqs. (1)–(5), we get the subsequent non-linear ODEs:

$$f'''+ff''-2f'^2-\frac{\beta}{2}(f^2f'''-6ff'f''-\eta f'^2f''+4f'^3)-Mf'+\lambda(4\omega-2\beta(f\omega'+\eta f''\omega)=0, \quad (11)$$

$$\omega''+f\omega'-2f'\omega-\frac{\beta}{2}\left(f^2\omega''-6ff'^{\omega'}-\eta f'^2\omega'+4f'^2\omega\right)-Mf'+4\lambda\left(-f'+\beta\left(-f'^2-\omega^2-\frac{\eta}{2}\omega\omega'+\frac{1}{2ff''}\right)\right)=0, \quad (12)$$

$$(1+R)\theta''+\mathrm{Pr}f\theta'-\mathrm{Pr}Af'\theta+Nb\theta'\phi'+Nt(\theta')^2=0, \quad (13)$$

$$\phi''+\mathrm{Le}f\phi'-\mathrm{Le}Bf'\phi-Cr(1+\delta\theta)^ne^{\left(\frac{-E1}{(1+\delta\theta)}\right)}\phi+\frac{Nt}{Nb}\theta''=0. \quad (14)$$

The transformed boundary conditions are:

$$\eta=0,\ f=V0,\ \omega=0,\ f'=1,\ \theta'=-\mathrm{B1}(1-\theta),\ \phi=1;$$

$$\eta\longrightarrow\infty,\ \theta=0,\ f'=0,\ \omega=0,\ \phi=0, \quad (15)$$

where

$$\beta=\frac{\lambda_1U_w}{L},\ Nt=\frac{\tau D_T(T_w-T_\infty)}{\alpha T_\infty},\ Nb=\frac{\tau D_B(C_w-C_\infty)}{\alpha},\ \lambda=\frac{\Omega L}{U_w},$$

$$\delta=\frac{T_w-T_\infty}{T_\infty},\ V0=\frac{-V_wx}{\alpha(U_0/2\nu L)^{0.5}},\ \mathrm{Le}=\frac{\gamma}{D_B},\ Cr=\frac{k^2{}_o}{\alpha},\ \mathrm{Pr}=\frac{\gamma}{\alpha},$$

$$R=\frac{16T_\infty{}^3\sigma^*}{3K^*k_f},\ M=\frac{\sigma\beta_0^2}{\rho\,\alpha},\ \mathrm{B1}=\frac{h_f}{k(U_0/2\nu L)^{0.5}}. \quad (16)$$

Quantities of practical interest in this problem are the skin-friction coefficient (C_f), local Nusselt number (Nu_x), and the local Sherwood number (Sh_x), which are defined as:

$$\mathrm{C_f}=\frac{2\tau_w}{\rho},\ \mathrm{Nu_x}=\frac{xq_w}{k(T_w-T_\infty)},\ \mathrm{Sh_x}=\frac{xJ_w}{D_B(c_w-c_\infty)}. \quad (17)$$

3. Method of solution

The set of non-linear ODEs Eqs. (11)–(14) together with boundary conditions Eq. (15) are solved using the finite element method [42–46], which is highly efficient for boundary layer problems. The procedure involves the following steps:

Discretization: The entire domain [0, $\eta_{\max}$] is divided into a finite number of linear or quadratic sub-elements. We selected $\eta_{\max}$ = 4 as the infinity boundary, ensuring that all profiles asymptotically reach their required values.

Weighted residuals: The Galerkin method is applied to the governing equations to derive the weak form.

Shape functions: Linear interpolation functions are used to approximate the primary variables (velocity, temperature, concentration).

Assembly and iterations: The element stiffness matrices are assembled into a global matrix. Since the system is non-linear, an iterative approach is used with convergence criterion of 10^{-6} for all variables.

The 0.01 size taken refers to the dimensionless element length ($\Delta\eta$). Within the domain $\eta = [0,4]$, this results in 500 equal elements, providing high resolution for the boundary layer.

4. Results and discussion

This section presents the comparison of concentration, temperature and velocity scatterings for dissimilar values of pertinent parameters with ($V0 \neq 0$) or without ($V0 = 0$) suction. The values of the species concentration gradient, gradient of temperature and velocity are also investigated and presented in the form of Tables. The current calculations were validated by comparing the present results with the existing results, as shown in Table 1. To verify the convergence of the numerical solution, the grid independence test is performed and demonstrated in Table 2.

Table 1. Comparison of Nusselt number and Sherwood number values with existing results.

Parameter		Hayat et al. [25]		Present results	
β	λ	$-\theta'(0)$	$-\phi'(0)$	$-\theta'(0)$	$-\phi'(0)$
0.0	**0.1**	0.5323	0.5040	0.5328	0.5043
0.1	**0.1**	0.5239	0.4943	0.5232	0.4946
0.2	**0.1**	0.5172	0.4858	0.5174	0.4854
0.1	**0.0**	0.5358	0.5107	0.5355	0.5102
0.1	**0.1**	0.5239	0.4943	0.5231	0.4945
0.1	**0.2**	0.4988	0.4609	0.4986	0.4607

Table 2. Grid independence analysis of the problem.

Number of elements	Step size ($\Delta\eta$)	$f''(0)$	$-\theta'(0)$	$-\phi'(0)$
100	0.05	1.23456	0.45678	0.78901
250	0.02	1.23561	0.45712	0.78955
500	0.01	1.23565	0.45715	0.78958
1000	0.005	1.23565	0.45715	0.78958

The impact of magnetic number (M) on the sketches of velocity in x-direction (f'), velocity in y-direction (ω), temperature (θ) and concentration (ϕ) with suction ($V0 \neq 0$) and without ($V0 = 0$) is exposed in Figs. 2–5. The velocity profiles in the x- and y-directions both decrease with the increasing values of M, and this diminishing nature is more pronounced in the case of $V0 = 0$ than in the case of $V0 \neq 0$, as shown in Figs. 2 and 3. Both temperature and concentration sketches magnify with intensifying values of M and this magnification is considerably higher in the case of $V0 \neq 0$ than in the case of $V0 = 0$, as depicted in Figs. 4 and 5. This occurs because the application of a magnetic field to the fluid flow generates a Lorentz force. This force opposes the fluid motion, thereby reducing the velocity of the liquid. To dominate this force, fluid has to perform additional work, which causes an increase in temperature of the liquid.

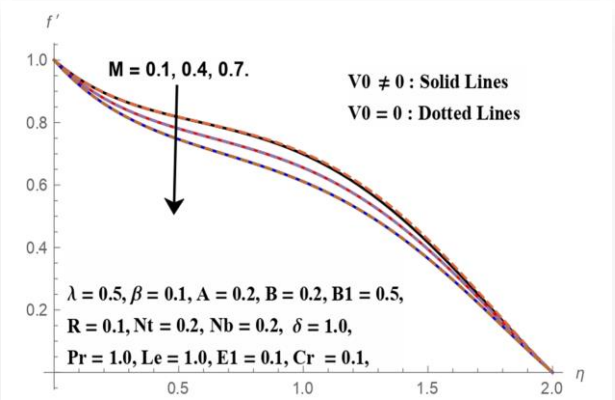


Fig. 2. Effect of M on f'.

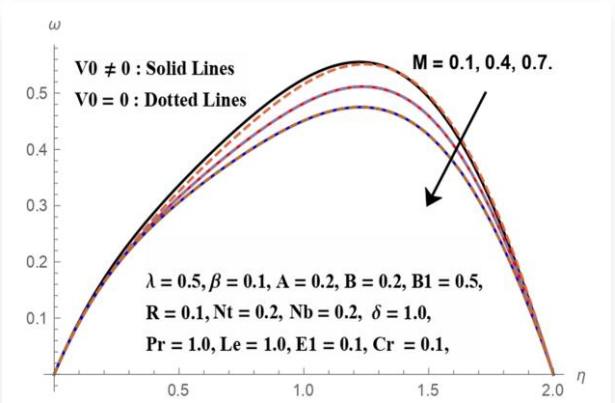


Fig. 3. Effect of M on ω.

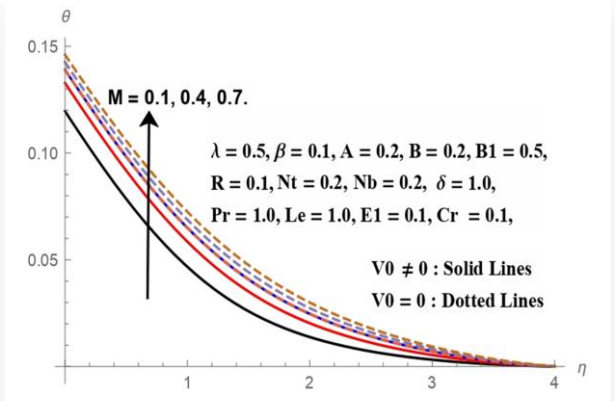


Fig. 4. Effect of M on θ.

Temperature and concentration profiles, in both cases $V0 \neq 0$ and $V0 = 0$, for dissimilar values of rotation number (λ) are illustrated in Figs. 6 and 7. The sketches of temperature of rotating nanoliquid decrease with the amplifying values of λ, and this decreasing trend is more pronounced in the case of $V0 \neq 0$ than in the case of $V0 = 0$. Furthermore, the concentration profiles of the nanoliquid also decrease as λ increases, and this decrease is more pronounced for $V0 \neq 0$ than for $V0 = 0$.

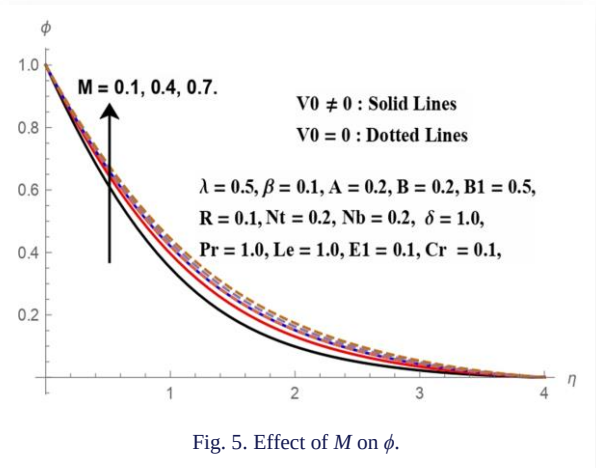


Fig. 5. Effect of M on ϕ.

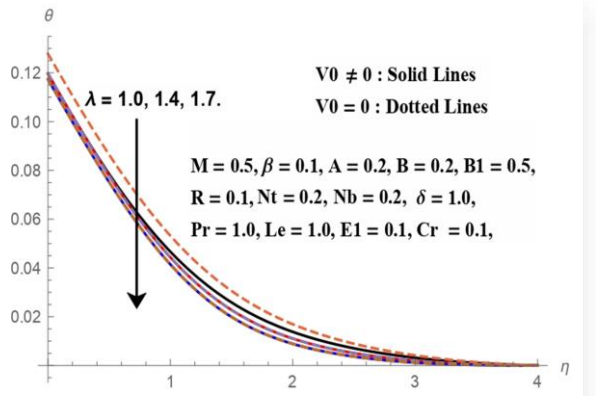


Fig. 6. Effect of λ on θ.

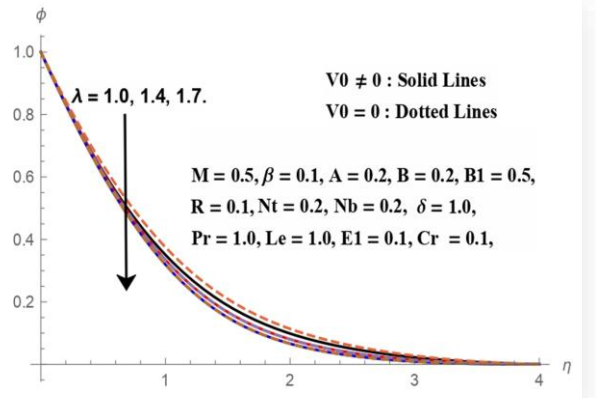


Fig. 7. Effect of λ on ϕ.

The Deborah parameter (β) influence on the distributions of velocity (f') in x-direction, velocity (ω) in y-direction, temperature (θ) and concentration (ϕ) with suction ($V0 \neq 0$) and without suction ($V0 = 0$) is disclosed in Figs. 8–11. Both components of velocity distributions of rotating nanoliquid diminish with the magnifying values of β in both cases of $V0 \neq 0$ and $V0 = 0$. This is true, generally because the Deborah number (β) is contingent on the relaxation time, and values of the Maxwell nanofluid relaxation time upsurge with the rising Deborah number values; therefore, the velocity of the rotating nanoliquid declines in the liquid area. However, the temperature and concentration of the rotating nanoliquid both magnify with the increasing values of β as revealed in Figs. 10 and 11.

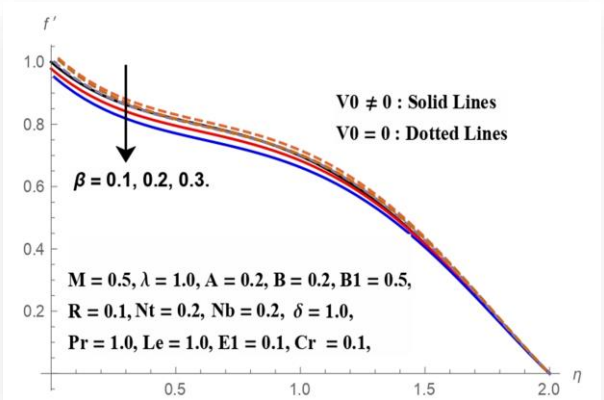


Fig. 8. Effect of β on f'.

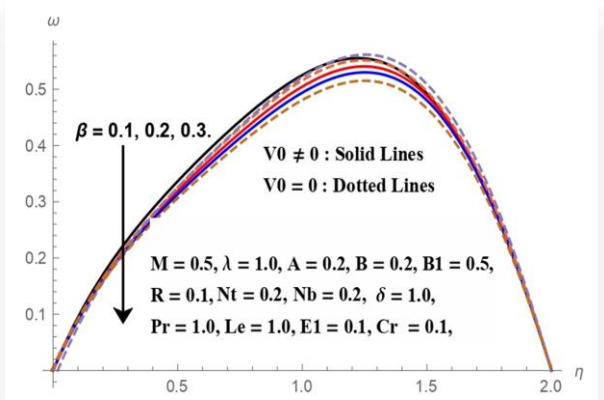


Fig. 9. Effect of β on ω.

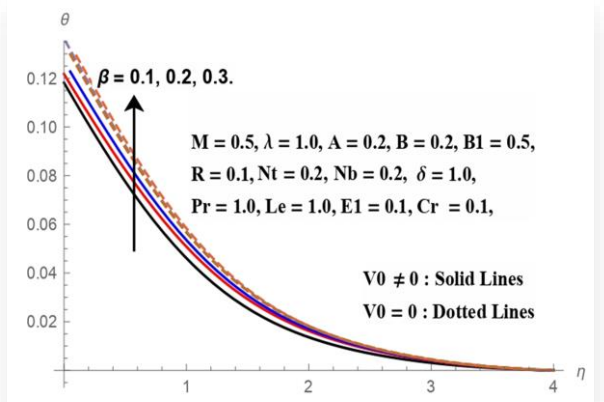


Fig. 10. Effect of β on θ.

The thermal radiation number (R) increases the temperature of the rotating Maxwell nanofluid in both cases of $V0 \neq 0$ and $V0 = 0$, as illustrated in Fig. 12. Generally, the inclusion of thermal radiation increases the fluid temperature. This increase in temperature profiles is slightly greater for the case of $V0 = 0$ than in the case of $V0 \neq 0$. Furthermore, the distributions of concent-

ration also increase with the rising R values in both cases of suction and without suction (Fig. 13).

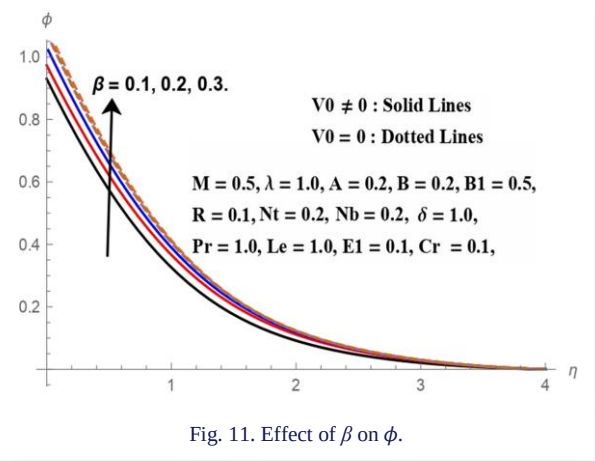


Fig. 11. Effect of β on ϕ.

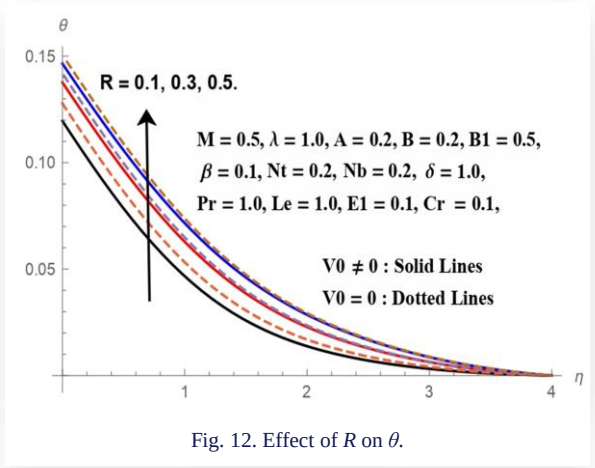


Fig. 12. Effect of R on θ.

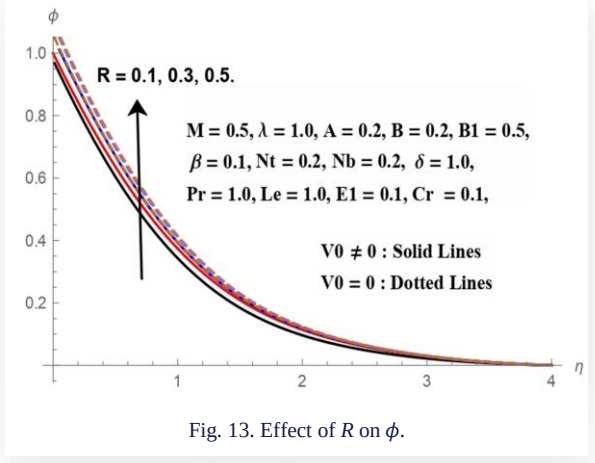


Fig. 13. Effect of R on ϕ.

The temperature and concentration fields of the rotating Maxwell nanoliquid for different values of the Brownian motion parameter Nb are shown in Figs. 14–15 for both $V0 \neq 0$ and $V0 = 0$. The temperature profiles increase with the increasing Nb, and this increase is slightly greater for $V0 = 0$ than for $V0 \neq 0$. In contrast, the concentration profiles decrease as Nb increases. Generally, nanoparticles undergo random motion in the fluid region (Brownian motion), which increases the fluid temperature and is also associated with nanoparticle agglomeration and size.

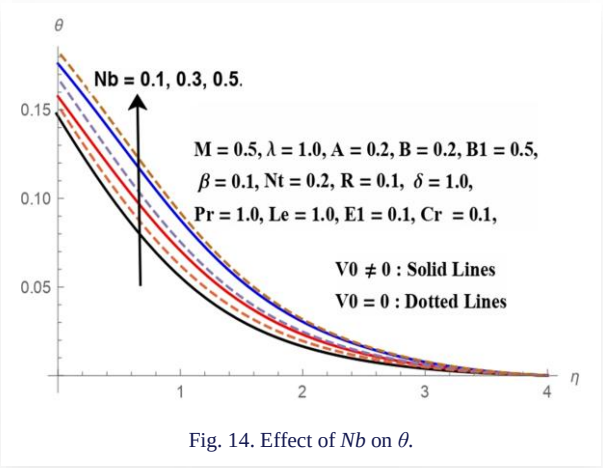


Fig. 14. Effect of Nb on θ.

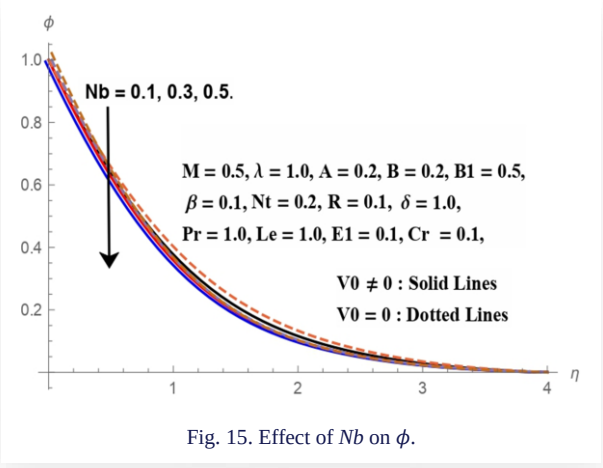


Fig. 15. Effect of Nb on ϕ.

Figs. 16–17 illustrate that both temperature and concentration profiles of rotating Maxwell nanoliquid increase with the rising thermophoretic parameter (Nt) values in both cases with and without suction. This is because the thermophoretic forces influentially thrust the particles present at the hot surface towards the cold surface; as a consequence, both the temperature and concentration of the rotating Maxwell nanoliquid magnify.

The chemical reaction parameter (Cr) impact on species outlines of rotating Maxwell nanofluid is depicted in Fig.18 in both cases with and without suction. The concentration profiles of the rotating Maxwell nanoliquid decrease with the increasing Cr, and this decrease is slightly greater for $V0 \neq 0$ than for $V0 = 0$. The effect of the Lewis number Le on the concentration profiles is illustrated in Fig. 19. The concentration distributions decrease in both cases with the increasing values of Le.

The concentration profiles of the rotating Maxwell nanofluid increase with the increasing values of the activation energy parameter ($E1$), as shown in Fig. 20, for both $V0 \neq 0$ and $V0 = 0$. Figure 21 shows that the concentration profiles of the rotating Maxwell nanoliquid increase as the temperature ratio parameter (δ) increases in both the suction and non-suction cases.

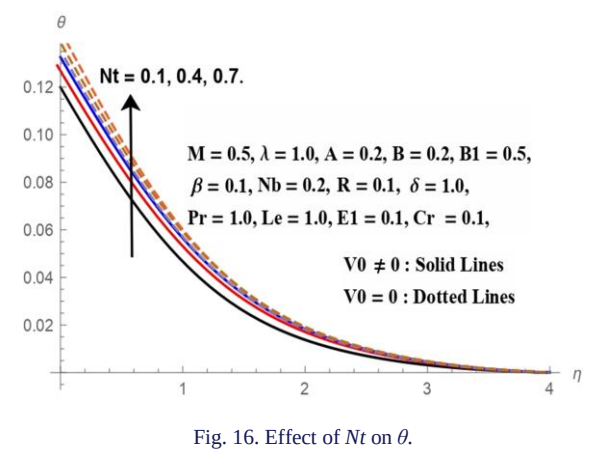


Fig. 16. Effect of *Nt* on θ.

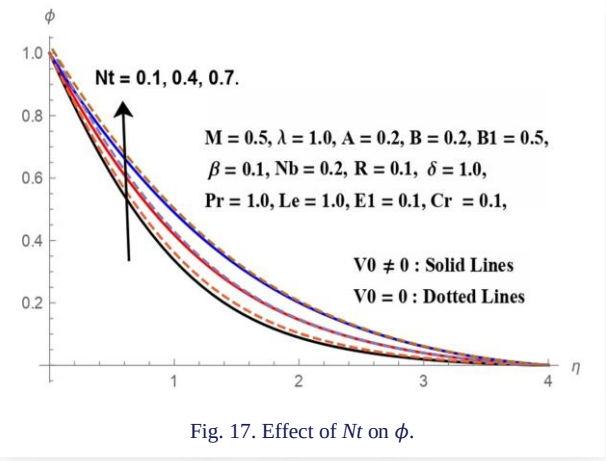


Fig. 17. Effect of *Nt* on ϕ.

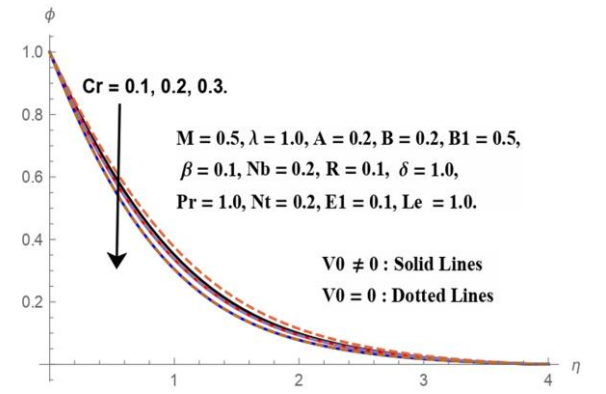


Fig. 18. Effect of *Cr* on ϕ.

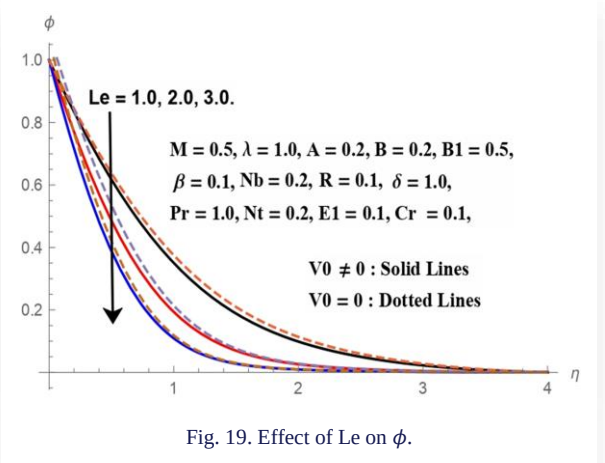


Fig. 19. Effect of Le on ϕ.

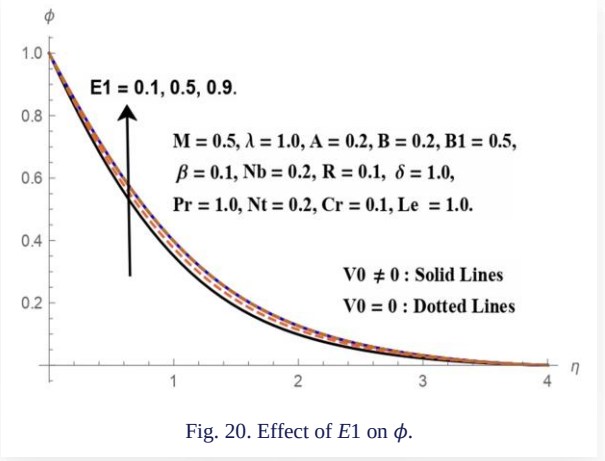


Fig. 20. Effect of *E*1 on ϕ.

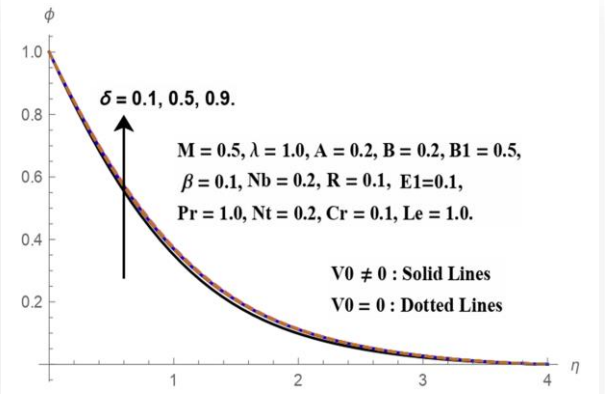


Fig. 21. Effect of δ on ϕ.

As the temperature exponent parameter (*A*) increases, the temperature profiles of the rotating Maxwell nanoliquid decrease, and this decrease is more pronounced for $V0 \neq 0$ than for $V0 = 0$, as illustrated in Fig. 22. Figure 23 shows that the concentration profiles of the rotating Maxwell nanoliquid decrease as the concentration exponent parameter (*B*) increases, with a slightly greater decrease for $V0 \neq 0$ than for $V0 = 0$.

The effect of the thermal Biot number B1 on the temperature and concentration profiles of the rotating Maxwell nanoliquid is illustrated in Figs. 24–25 for both $V0 \neq 0$ and $V0 = 0$. The temperature profiles increase with the increasing B1, and this increase is more pronounced for $V0 = 0$ than for $V0 \neq 0$. Furthermore, the concentration distributions increase with the increasing B1 in both cases.

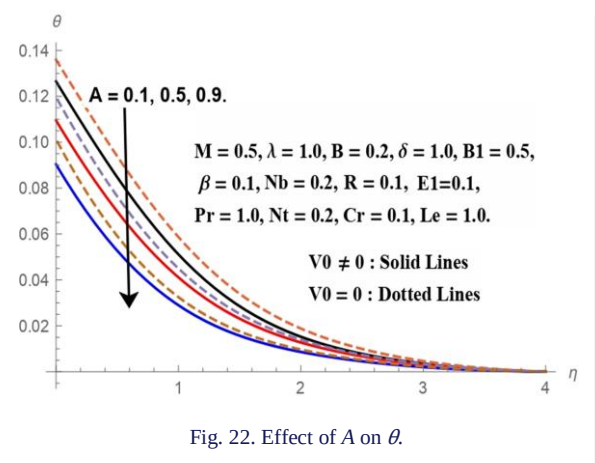


Fig. 22. Effect of A on θ.

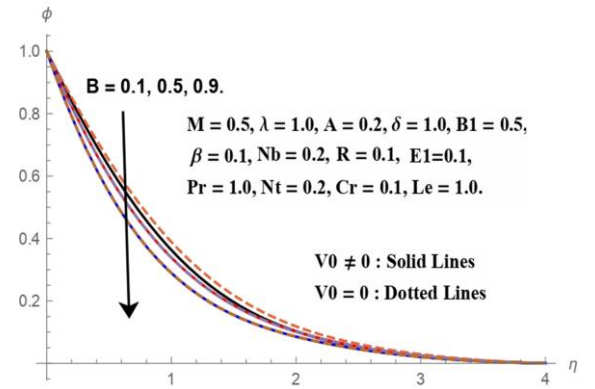


Fig. 23. Effect of B on ϕ.

The effects of various pertinent parameters on the velocity gradient, Sherwood number, and heat transfer under both suction and non-suction conditions are presented in Tables 3 and 4. It is observed that the dimensionless rates of mass, heat, and momentum transfer of the rotating Maxwell nanoliquid decrease with the increasing values of M in both the suction and non-suction cases. Furthermore, the concentration gradient and velocity gradient of the Maxwell nanoliquid increase with increasing rotation number (λ) in both the suction and non-suction cases. The heat transfer rate decreases for $V0 \neq 0$ but increases for $V0 = 0$ as λ increases. The mass transfer rate, heat transfer rate and velocity gradient of the rotating Maxwell nanoliquid decrease with the increasing β for both $V0 = 0$ and $V0 \neq 0$. The dimensionless value of $-\theta'(0)$ decreases as R increases in both the suction and non-suction cases. However, $-\phi'(0)$ and $f''(0)$ increase with the increasing R in both cases. The dimensionless values of $-\phi'(0)$ and $f''(0)$ increase with the increasing Nb for both $V0 = 0$ and $V0 \neq 0$. The heat-transfer rate decreases with the increasing Nb.

The dimensionless velocity gradient increases for $V0 \neq 0$ but decreases for $V0 = 0$ as Nt increases. The Sherwood number and temperature gradient decrease in both cases with the increasing Nt. For $V0 \neq 0$, the velocity gradient increases, whereas it decreases for $V0 = 0$ as Cr increases. The value of $-\theta'(0)$ decreases, whereas $-\phi'(0)$ increases in both cases with the increasing Cr. The increasing $E1$ increases $f''(0)$ for $V0 \neq 0$ but decreases it for $V0 = 0$. The Nusselt number decreases in the suction case and increases in the non-suction case as $E1$ increases. The species concentration gradient decreases in both cases with the increasing $E1$. The velocity gradient increases for $V0 \neq 0$ but decreases for $V0 = 0$ as δ increases. The value of $-\theta'(0)$ decreases, whereas $-\phi'(0)$ increases in both cases with the increasing δ. The skin friction coefficient increases for $V0 \neq 0$ but decreases for $V0 = 0$ as B1 increases. Finally, $-\theta'(0)$ increases, whereas $-\phi'(0)$ decreases in both cases as B1 increases.

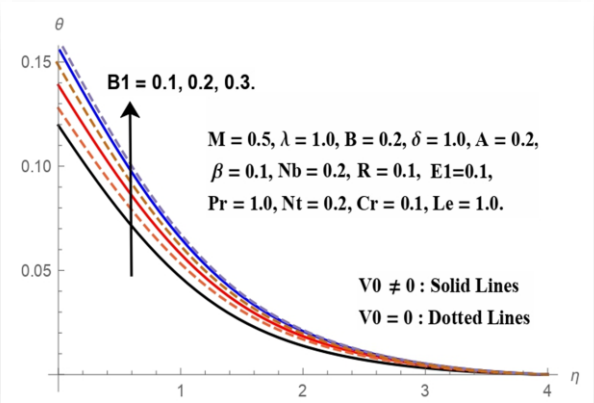


Fig. 24. Effect of B1 on θ.

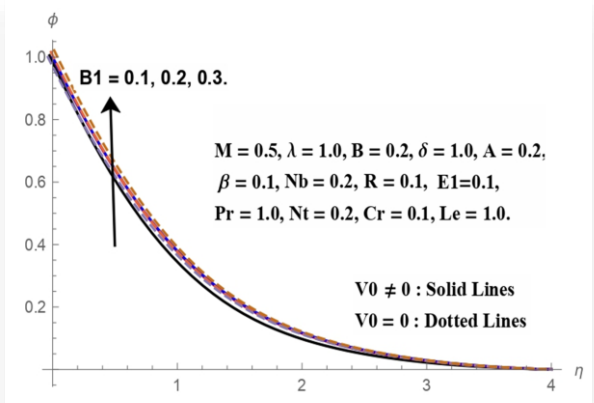


Fig. 25. Effect of B1 on ϕ.

5. Conclusions

A comparative analysis of the diffusion of species and energy transport features of rotating Maxwell nanoliquid flow over an elongating exponential surface with and without suction, by taking boundary condition of convective type into account, is presented in this article. The finite element method is utilised to solve the dimensionless equations of mass, heat and momentum. Velocity sketches in x and y directions, concentration and temperature sketches for dissimilar values of parameters are examined in detail and important summaries are mentioned below.

(i) An increase in the activation energy parameter leads to a significant magnification in the concentration profiles of the nanoliquid for both suction ($V0 \neq 0$) and non-suction ($V0 = 0$) cases.

Table 3. The effect of various parameters on skin-friction coefficient $f''(0)$, local Nusselt number $-\theta'(0)$ and local Sherwood number $-\phi'(0)$.

Parameter					$f''(0)$		$-\theta'(0)$		$-\phi'(0)$	
M	λ	β	R	Nb	$V0 \neq 0$	$V0 = 0$	$V0 \neq 0$	$V0 = 0$	$V0 \neq 0$	$V0 = 0$
0.1	1.0	0.2	0.1	0.2	−0.70118	−1.14140	0.08804	0.08615	0.87140	0.74857
0.4	1.0	0.2	0.1	0.2	−0.90632	−1.26921	0.08671	0.08574	0.78171	0.73018
0.7	1.0	0.2	0.1	0.2	−1.14140	−1.38860	0.08610	0.08540	0.74857	0.71433
0.5	1.0	0.2	0.1	0.2	−0.70118	−0.69482	0.08804	0.08721	0.86407	0.81146
0.5	1.4	0.2	0.1	0.2	−0.55695	−0.54695	0.08802	0.08802	0.87490	0.86490
0.5	1.7	0.2	0.1	0.2	−0.53901	−0.53901	0.08801	0.08826	0.88205	0.88205
0.5	1.0	0.1	0.1	0.2	−0.70118	−0.69482	0.08804	0.08721	0.87140	0.81146
0.5	1.0	0.2	0.1	0.2	−0.70809	−0.70809	0.08719	0.08719	0.80971	0.80970
0.5	1.0	0.3	0.1	0.2	−0.72105	−0.72105	0.08716	0.08716	0.80796	0.80796
0.5	1.0	0.2	0.1	0.2	−0.70118	−0.69482	0.08804	0.08721	0.81140	0.81146
0.5	1.0	0.2	0.3	0.2	−0.69482	−0.69325	0.08623	0.08623	0.81445	0.81445
0.5	1.0	0.2	0.5	0.2	−0.68542	−0.69215	0.08534	0.08534	0.81717	0.81717
0.5	1.0	0.2	0.1	0.1	−0.70119	−0.68452	0.08851	0.08771	0.82079	0.76432
0.5	1.0	0.2	0.1	0.3	−0.69482	−0.67548	0.08559	0.08559	0.84055	0.84055
0.5	1.0	0.2	0.1	0.5	−0.68452	−0.66584	0.08239	0.08239	0.85183	0.85183

Table 4. The effect of various parameters on skin-friction coefficient $f''(0)$, local Nusselt number $-\theta'(0)$ and local Sherwood number $-\phi'(0)$.

Parameter					$f''(0)$		$-\theta'(0)$		$-\phi'(0)$	
Nt	Cr	$E1$	δ	B1	$V0 \neq 0$	$V0 = 0$	$V0 \neq 0$	$V0 = 0$	$V0 \neq 0$	$V0 = 0$
0.1	0.1	0.1	1.0	0.5	−0.70118	−0.69482	0.08807	0.08725	0.89504	0.83330
0.4	0.1	0.1	1.0	0.5	−0.69482	−0.69587	0.08709	0.08706	0.74664	0.74668
0.7	0.1	0.1	1.0	0.5	−0.65842	−0.70154	0.08688	0.08682	0.64094	0.64494
0.2	0.1	0.1	1.0	0.5	−0.70118	−0.69482	0.08804	0.08721	0.87140	0.81146
0.2	0.2	0.1	1.0	0.5	−0.69482	−0.69524	0.08801	0.08716	0.92748	0.92768
0.2	0.3	0.1	1.0	0.5	−0.67542	−0.70123	0.08711	0.08711	1.03152	1.03159
0.2	0.1	0.1	1.0	0.5	−0.70118	−0.69498	0.08804	0.08721	0.87140	0.81146
0.2	0.1	0.5	1.0	0.5	−0.69471	−0.70809	0.08729	0.08724	0.75819	0.75819
0.2	0.1	0.9	1.0	0.5	−0.67533	−0.72105	0.08725	0.08725	0.74797	0.74799
0.2	0.1	0.1	0.1	0.5	−0.70118	−0.69482	0.08804	0.08721	0.81140	0.81146
0.2	0.1	0.1	0.5	0.5	−0.69482	−0.70215	0.08721	0.08712	0.82706	0.82706
0.2	0.1	0.1	0.9	0.5	−0.68542	−0.75242	0.08720	0.08602	0.84254	0.84254
0.2	0.1	0.1	1.0	0.1	−0.70118	−0.68452	0.08804	0.08721	0.87407	0.81146
0.2	0.1	0.1	1.0	0.2	−0.69482	−0.69521	0.09472	0.09472	0.80817	0.80817
0.2	0.1	0.1	1.0	0.3	−0.68321	−0.70215	0.10203	0.10203	0.80496	0.80496

(ii) The magnetic parameter induces a Lorentz force that retards fluid motion (decreasing velocity) while simultaneously elevating the liquid's temperature due to the additional work required to overcome the force.

(iii) Higher values of the rotation parameter led to a degradation in temperature distributions, a trend that is more pronounced in the presence of suction.

(iv) The temperature of the rotating Maxwell nanoliquid magnifies with the magnifying values of β both without and with suction.

(v) With the amplifying values of thermal Biot number (B1), the temperature profiles of the Maxwell nanoliquid increase.

References

[1] Choi, S.U.S., Zhang, Z.G., Yu, W., Lockwood, F.E., & Grulke, E.A. (2001). Anomalous thermal conductivity enhancement in nanotube suspensions. *Applied Physics*, 79(14), 2252–2254. doi: 10.1063/1.1408272

[2] Ghalambaz, M., Behseresht, A., Behseresht, J., & Chamkha, A.J. (2015). Effects of nanoparticles diameter and concentration on natural convection of the Al_2O_3-water nanofluids considering variable thermal conductivity around a vertical cone in porous media. *Advanced Powder Technology*, 26(1), 224–235. doi: 10.1016/j.apt.2014.10.001

[3] Ghalambaz, M., Doostani, A., Chamkha, A.J., & Ismael, M.A. (2017). Melting of nanoparticles-enhanced phase-change materials in an enclosure: effect of hybrid nanoparticles. *International journal of Mechanical Sciences*, 134, 85–97. doi: 10.1016/j.ijmecsci.2017.09.045

[4] Saha, S., Raut, S., & Das, A.N. (2021). Thermal enhancement and entropy generation of laminar water-Al_2O_3 nanofluid flow through a sudden expansion channel with bell-shaped surface. *International Journal of Fluid Mechanics Research*, 48(4), 65–78. doi: 10.1615/InterJFluidMechRes.2021039636

[5] Sudarsana Reddy, P., Sreedevi, P., & Chamkha, A.J. (2018). MHD boundary layer heat and mass transfer characteristics of

nanofluid over a vertical cone under convective boundary condition. *Propulsion and Power Research*, 7(4), 308–319. doi: 10.1016/j.jppr.2018.11.004

[6] Fadodun, O.G., Amosun, A.A., Salau, A.O., Olaloye, D.O., Ogundeji, J.A., Ibitoye, F.I., & Balogun, F.A. (2020). Numerical investigation and sensitivity analysis of turbulent heat transfer and pressure drop of Al_2O_3/H_2O nanofluid in straight pipe using response surface methodology. *Archives of Thermodynamics*. 41(1), 3–30. doi: 10.24425/ather.2020.132948

[7] Iweka, S.C., & Fadodun, O.G. (2021). Numerical modeling of heat transfer in Al_2O_3/H_2O nanofluid flowing through a Bessel-like converging pipe. *Archives of Thermodynamics*, 42(2), 121–153. doi: 10.24425/ather.2021.137557

[8] Rashad, A.M., & Mansour, M.A. (2022). Natural Bioconvective Flow Through a Vertical Cylinder in Porous Media Drenched with a Nanofluid. *Journal of Nanofluids*, 11(3), 340–349. doi: 10.1166/jon.2022.1854

[9] Chamkha, A.J., Nabwey, H.A., Abdelrahman, Z.M.A., & Rashad, A.M. (2020). Mixed Bioconvective Flow Over a Wedge in Porous Media Drenched with a Nanofluid. *Journal of Nanofluids*, 9(1), 24–35. doi: 10.1166/jon.2020.1728

[10] Sreedevi, P., Sudarsana Reddy, P., & Sheremet, M.A. (2020). Impact of homogeneous-heterogeneous reactions on heat and mass transfer flow of Au-Eg and Ag-Eg Maxwell nanofluid past a horizontal stretched cylinder. *Journal of Thermal Analysis and Calorimetry*, 141(1), 533–546. doi: 10.1007/s10973-020-09581-3

[11] Ahmed, J., Khan, M., & Ahmad, L. (2019). Stagnation point flow of Maxwell nanofluid over a permeable rotating disk with heat source/sink. *Journal of Molecular Liquids*, 287, 110853. doi: 10.1016/j.molliq.2019.04.130

[12] Ijaz, M., & Ayub, M. (2019). Nonlinear convective stratified flow of Maxwell nanofluid with activation energy. *Heliyon*, 5(1), e01121. doi: 10.1016/j.heliyon.2019.e01121

[13] Ahmed, J., Khan, M., Ahmad, L., Alzahrani, A.K., & Alghamdi, M. (2019). Thermally radiative flow of Maxwell nanofluid over a permeable rotating disk. *Physica Scripta*, 94(12), 125016. doi: 10.1088/1402-4896/ab3b9a

[14] Ahmed, A., Khan, M., Ahmed, J., Hafeez, A., & Iqbal, Z. (2020). Unsteady stagnation point flow of Maxwell nanofluid over stretching disk with Joule heating. *Arabian Journal for Science and Engineering*, 45(7), 5529–5540. doi: 10.1007/s13369-020-04468-9

[15] Ahmed, A., Khan, M., & Ahmed, J. (2020). Mixed convective flow of Maxwell nanofluid induced by vertically rotating cylinder. *Applied Nanoscience*, 10(12), 5179–5190. doi: 10.1007/s13204-020-01320-2

[16] Sharma, R., Hussain, S.M., Raju, C.S.K., Seth, G.S., & Chamkha, A.J. (2020). Study of graphene Maxwell nanofluid flow past a linearly stretched sheet: A numerical and statistical approach. *Chinese Journal of Physics*, 68, 671–683. doi: 10.1016/j.cjph.2020.10.013

[17] Khan, M.N., & Nadeem, S. (2020). Theoretical treatment of bioconvective Maxwell nanofluid over an exponentially stretching sheet. *Canadian Journal of Physics*, 98(8), 732–741. doi: 10.1139/cjp-2019-0380

[18] Abro, K.A., Soomro, M., Atangana, A., & Gómez-Aguilar, J.F. (2022). Thermophysical properties of Maxwell nanofluids via fractional derivatives with regular kernel. *Journal of Thermal Analysis and Calorimetry*, 147(1), 449–459. doi: 10.1007/s10973-020-10287-9

[19] Ali, R., Asjad, M.I., Aldalbahi, A., Rahimi-Gorji, M., & Rahaman, M. (2021). Convective flow of a Maxwell hybrid nanofluid due to pressure gradient in a channel. *Journal of Thermal Analysis and Calorimetry*, 143(2), 1319–1329. doi: 10.1007/s10973-020-10304-x

[20] Jamshed, W. (2021). Numerical investigation of MHD impact on Maxwell nanofluid. *International Communications in Heat and Mass Transfer*, 120, 104973. doi: 10.1016/j.icheatmasstransfer.2020.104973

[21] Gowda, R.J.P., Rauf, A., Naveen Kumar, R., Prasannakumara, B.C., & Shehzad, S.A. (2022). Slip flow of Casson–Maxwell nanofluid confined through stretchable disks. *Indian Journal of Physics*, 96(7), 2041–2049. doi: 10.1007/s12648-021-02153-7

[22] Zhou, S.S., Bilal, M., Khan, M.A., & Muhammad, T. (2021). Numerical analysis of thermal radiative Maxwell nanofluid flow over-stretching porous rotating disk. *Micromachines*, 12(5), 540. doi: 10.3390/mi12050540

[23] Mustafa, M. (2015). Cattaneo-Christov heat flux model for rotating flow and heat transfer of upper-convected Maxwell fluid. *AIP Advances*, 5(4), 047109. doi: 10.1063/1.4917306

[24] Ahuja, J., & Gupta, U. (2016). MHD effects for a rotating nanofluid layer for LTNE model. *International Journal of Technology*, 6(2), 209. doi: 10.5958/2231-3915.2016.00032.8

[25] Hayat, T., Muhammad, T., Shehzad, S.A., & Alsaedi, A. (2017). Three dimensional rotating flow of Maxwell nanofluid. *Journal of Molecular Liquids*, 229, 495–500. doi: 10.1016/j.molliq.2016.12.095

[26] Rashid, S., Khan, M.I., Hayat, T., Ayub, M., & Alsaedi, A. (2020). Darcy–Forchheimer flow of Maxwell fluid with activation energy and thermal radiation over an exponential surface. *Applied Nanoscience*, 10(8), 2965–2975. doi: 10.1007/s13204-019-01008-2

[27] Ali, B., Nie, Y., Hussain, S., Manan, A., & Sadiq, M.T. (2020). Unsteady magneto-hydrodynamic transport of rotating Maxwell nanofluid flow on a stretching sheet with Cattaneo–Christov double diffusion and activation energy. *Thermal Science and Engineering Progress*, 20, 100720. doi: 10.1016/j.tsep.2020.100720

[28] Ahmed, A., Khan, M., Ahmed, J., & Hafeez, A. (2020). Von Kármán rotating flow of Maxwell nanofluids featuring the Cattaneo-Christov theory with a Buongiorno model. *Applied Mathematics and Mechanics*, 41(8), 1195–1208. doi: 10.1007/s10483-020-2632-8

[29] Khalid, I.K., Mokhtar, N.F.M., Ibrahim, Z.B., & Siri, Z. (2020). Rayleigh–Bénard convection in Maxwell nanofluids layer saturated in a rotating porous medium with feedback control subjected to viscosity and thermal conductivity variations. *Applied Nanoscience*, 10(8), 3085–3095. doi: 10.1007/s13204-020-01302-4

[30] Ramaiah, K.D., Surekha, P., Kotha, G., & Thangavelu, K. (2020). MHD rotating flow of a Maxwell fluid with Arrhenius activation energy and non-Fourier heat flux model. *Heat Transfer*, 49(4), 2209–2227. doi: 10.1002/htj.21717

[31] Khan, M.N., & Nadeem, S. (2021). A comparative study between linear and exponential stretching sheet with double stratification of a rotating Maxwell nanofluid flow. *Surfaces and Interfaces*, 22, 100886. doi: 10.1016/j.surfin.2020.100886

[32] Ali, B., Pattnaik, P.K., Naqvi, R.A., Waqas, H., & Hussain, S. (2021). Brownian motion and thermophoresis effects on bioconvection of rotating Maxwell nanofluid over a Riga plate with Arrhenius activation energy and Cattaneo-Christov heat flux theory. *Thermal Science and Engineering Progress*, 23, 100863. doi: 10.1016/j.tsep.2021.100863

[33] Chu, Y.M., Ramzan, M., Shaheen, N., Dong Chung, J., Kadry, S., Howari, F., Malik, M.Y., & Ghazwani, H.A.S. (2021). Analysis of Newtonian heating and higher-order chemical reaction on a Maxwell nanofluid in a rotating frame with gyrotactic microor-

ganisms and variable heat source/sink. *Journal of King Saud University-Science*, 33(8), 101645. doi: 10.1016/j.jksus.2021.101645

[34] Alzahrani, F., & Ijaz Khan, M. (2021). Applications of Darcy-Forchheimer 3D reactive rotating flow of rate type nanoparticles with non-uniform heat source and sink and activation energy. *Chemical Physics Letters*, 783, 139054. doi: 10.1016/j.cplett.2021.139054

[35] Cao, L., Zhang, P., & Si, X. (2022). Electroosmotic flow of two-layer fluid containing Oldroyd-B fluid with fractional derivative in a rotating microparallel channel. *Microfluidics and Nanofluidics*, 26(5), 34. doi: 10.1007/s10404-022-02539-x

[36] Wei, Y., Rehman, S.U., Fatima, N., Ali, B., Ali, L., Chung, J.D., & Shah, N.A. (2022). Significance of dust particles, nanoparticles radius, coriolis and lorentz forces: The case of Maxwell dusty fluid. *Nanomaterials*, 12(9), 1512. doi: 10.3390/nano12091512

[37] Ali, B., Thumma, T., Habib, D., Salamat, N., & Riaz, S. (2022). Finite element analysis on transient MHD 3D rotating flow of Maxwell and tangent hyperbolic nanofluid past a bidirectional stretching sheet with Cattaneo-Christov heat flux model. *Thermal Science and Engineering Progress*, 28, 101089. doi: 10.1016/j.tsep.2021.101089

[38] Raza, J., Mustafa, F., Lund, L.A., Shah, Z., Alshehri, M.H., & Vrinceanu, N. (2024). Optimization of heat transfer rate of trihybrid nanofluid embedded between two horizontal coaxial cylinders by RSM. *Case Studies in Thermal Engineering*, 60, 104637. doi: 10.1016/j.csite.2024.104637

[39] Shutaywi, M., Raza, J., Lund, L.A., Shah, Z., Vrinceanu, N., & Deebani, W. (2024). Optimization of heat transfer in a channel with stretching walls using a magnetized tetra-hybrid nanofluid. *Advances in Mechanical Engineering*, 16(11). doi: 10.1177/16878132241293959

[40] Shutaywi, M., Raza, J., Abualnaja, K.M., Shah, Z., Vrinceanu, N., & Deebani, W. (2025). Integrated Taguchi-GRA-PCA for optimizing the heat transfer performance of trihybrid Casson nanofluid flow over stretching sheet with quadratic velocity. *Journal of Radiation Research and Applied Sciences*, 18(3), 101570. doi: 10.1016/j.jrras.2025.101570

[41] Raza, J., & Ashfaq, A. (2025). Optimization of heat transfer in two-phased nanofluid flow over a biaxial sheet using Taguchi-GRA method. *Multiscale and Multidisciplinary Modeling Experiments and Design*, 8(1), 124. doi: 10.1007/s41939-024-00712-z

[42] Sudarsana Reddy, P., & Chamkha, A.J. (2016). Soret and Dufour Effects on unsteady MHD heat and mass transfer over a stretching sheet with thermophoresis and non-uniform heat generation/absorption. *Journal of Applied Fluid Mechanics*, 9(5), 2443–2455. doi: 10.18869/acadpub.jafm.68.236.25171

[43] Sreedevi, P., Sudarsana Reddy, P., & Chamkha, A.J. (2017). Heat and Mass transfer analysis of nanofluid over linear and non- linear stretching surface with thermal radiation and chemical reaction. *Powder Technology*, 315, 194–204. doi: 10.1016/j.powtec.2017.03.059

[44] Sudarsana Reddy, P., Chamkha, A.J., & Al-Mudhaf, A. (2017). MHD heat and mass transfer flow of a nanofluid over an inclined vertical porous plate with radiation and heat generation/absorption. *Advanced Powder Technology*, 28(3), 1008–1017. doi: 10.1016/j.apt.2017.01.005

[45] Sudarsan Reddy, P., & Prasada Rao, V. (2012). Thermo-diffusion and diffusion –thermo effects on convective heat and mass transfer through a porous medium in a circular cylindrical annulus with quadratic density temperature variation – Finite element study. *Journal of Applied Fluid Mechanics*, 5(4), 139–144. doi: 10.36884/jafm.5.04.19472

[46] Sudrsana Reddy, P., Sreedevi, P., & Chamkha, A.J. (2017). MHD boundary layer flow, heat and mass transfer analysis over a rotating disk through porous medium saturated by Cu-water and Ag-water nanofluid with chemical reaction. *Powder Technology*, 307, 46–55. doi: 10.1016/j.powtec.2016.11.017

Co-published by
Institute of Fluid-Flow Machinery
Polish Academy of Sciences
Committee on Thermodynamics and Combustion
Polish Academy of Sciences

Copyright©2026 by the Authors under licence CC BY-NC-ND 4.0

http://www.imp.gda.pl/archives-of-thermodynamics/

Analysis of phase behaviour of R1243zf/lubricant oil mixtures and its impact on the performance of vapour-compression refrigeration cycle

Heyu Jia, Wenzhe Dang, Xiaopo Wang*

Key Laboratory of Thermo-Fluid Science and Engineering, Ministry of Education, School of Energy and Power Engineering, Xi'an Jiaotong University, Xi'an, 710049, China
*Corresponding author email: wangxp@xjtu.edu.cn

Received: 21.11.2025; revised: 07.05.2026; accepted: 10.08.2026

Abstract

Due to the extremely low ozone depletion potential and global warming potential, 3,3,3-trifluoropropene (R1243zf) is considered a good substitute for traditional hydrofluorocarbons used in vapour-compression refrigeration cycles. The phase behaviour of refrigerant with lubricant oil is a critical factor affecting the performance of the cycle. However, comprehensive analysis of phase behaviour of R1243zf/lubricant oil mixture and quantitative assessment of its impact on the cycle efficiency is still lacking. Therefore, this work employs the Soave-Redlich-Kwong (SRK) equation of state, combined with the modified van der Waals-Berthelot mixing rule and hypothetical oil model proposed by Yokozeki, to investigate the phase equilibrium data of R1243zf/oil mixtures and the phase behaviour of R1243zf with different lubricant oils. Furthermore, the impact of oils on the performance of the vapour-compression refrigeration cycle is quantitatively analysed. Results show that polyolester (POE)-type lubricant oils exhibit superior performance in R1243zf-based refrigeration systems.

Keywords: R1243zf; SRK equation; Lubricant oils; Phase behaviour; Coefficient of performance

Vol. 47(2026), No. 3, 253–260; doi: 10.24425/ather.2026.7526

Cite this manuscript as: Jia, H., Dang, W., & Wang, X. (2026). Analysis of phase behaviour of R1243zf/lubricant oil mixtures and its impact on the performance of vapour-compression refrigeration cycle. *Archives of Thermodynamics*, 47(3), 253–260.

1. Introduction

Environmental issues have become a common challenge for the world. The Paris Agreement and the subsequent Glasgow Climate Pact (COP26) have set clear targets for global temperature control and emission reduction. By 2023, COP28 further advanced these efforts by adopting the "Global Cooling Pledge" which explicitly aims to reduce the cooling-related emissions by 68% by 2050 compared to 2022 levels, demonstrating the international community's firm commitment to mitigating climate change. In the refrigeration industry, the refrigerant plays a critical role in environmental protection, and the development and application of low-global warming potential (GWP) refrigerants have become a key direction for technological innovation [1–3].

In the past decade, hydrofluoroolefins (HFOs) have attracted significant attention due to their unique molecular structures and environmentally friendly characteristics. The C=C double bond in HFO molecules promotes rapid reaction with atmospheric OH radicals, substantially shortening their atmospheric lifetime [4]. Among the various HFOs proposed, 3,3,3-trifluoropropene (R1243zf) garnered widespread interest due to its excellent properties. R1243zf has an ODP of 0 and GWP of 0.82, and extremely short atmospheric lifetime of only 6 days [5,6]. From a thermodynamic perspective, the properties of R1243zf are

very similar to those of R134a, indicating strong replacement compatibility and application potential. Experimental studies have confirmed that, in air conditioning systems, R1243zf exhibits a higher coefficient of performance (COP) and operates with lower suction and exhaust pressures compared to conventional refrigerants [7], making it a promising candidate for the next generation of refrigerants.

It is well known that the thermo-physical properties of R1243zf as well as R1243zf/lubricant oil mixture are essential for the design and optimisation of the vapour compression refrigeration cycle. A series of studies have been reported on the properties of R1243zf, such as critical properties, density, vapour pressure, specific heat capacity and surface tension [8–11]. In addition, the vapour-liquid equilibrium data of R1243zf with lubricant oils were also reported [12–14]. However, a comprehensive analysis of phase behaviour of R1243zf/lubricant oil is still lacking in the literature.

Furthermore, the selection of lubricant oil significantly affects the performance of a refrigeration system because it directly influences oil circulation and refrigerant distribution within the cycle. For example, Chen et al. [15] experimentally compared the effects of different lubricant oils, including polyalkylene glycol (PAG) and mineral oil (MO), in a 1.5 HP R290 split-type room air conditioner. They found that the use of PAG can reduce the amount of R290 in the compressor and improve heating capacity. However, due to the increased viscosity of R290/lubricant oil mixture in the oil sump, the coefficient of performance (COP) under heating conditions is relatively low. Li et al. [16] experimentally analysed the flow characteristics and the impact of lubricant oil in heat pump systems and heat exchangers, pointing out that the oil circulation rate is directly affected by the compressor oil charge. At the same time, oil retention in the evaporator and condenser increases the amount of oil held in the system, impairing heat transfer capacity and consequently degrading overall system performance. Naseri et al. [17] identified that for a modified revolving vane expander in a micro-scale organic Rankine cycle, an oil circulation rate (OCR) of about 1% represents an optimal compromise. Albà et al. [18] employed the Statistical Associating Fluid Theory (SAFT) equation of state to evaluate the performance of lubricants such as PEC5 (pentaerythritol tetrapentanoate) and TrEGDME (triethylene glycol dimethyl ether) in a low-GWP R513A refrigeration cycle, demonstrating that PEC5 had the least impact on cycle efficiency and is more suitable for this system. Therefore, it is necessary to conduct a performance analysis of R1243zf and lubricant oils for the purpose of selecting an appropriate lubricant oil.

In this work, based on the experimental vapour-liquid equilibrium (VLE) data of R1243zf with two mineral oils (3GS and 4GS) and one polyol ester oil (RL68H) [14] mixtures, the SRK equation of state, the modified van der Waals-Berthelot mixing rule, and the hypothetical oil (UniOIL) model proposed by Yokozeki [19] were employed to correlate the data. The phase behaviour of R1243zf with lubricant oils was investigated, and the impact of oil type on the performance of the vapour-refrigeration cycle was evaluated. This work provides a theoretical foundation for deepening the understanding of phase behaviour in R1243zf/lubricant oils and for optimising the refrigeration system.

2. Modelling

In this work, the SRK equation of state along with the van der Waals-Berthelot mixing rule was employed to correlate the experimental VLE data. In addition, due to the lack of critical parameters for the lubricant oil, the hypothetical oil (UniOIL) model proposed by Yokozeki [19] was used. In the UniOIL model, the oil is treated as a single pseudo-pure component with fixed critical temperature and pressure. The SRK equation is defined as follows [20]:

$$P = \frac{RT}{v-b} - \frac{a(T)}{v(v+b)}, \tag{1}$$

where a(T) is the attraction parameter and b is the co-volume parameter. The two parameters are calculated by:

$$a(T) = 0.427480\frac{(RT_c)^2}{P_c}\alpha(T), \tag{2}$$

$$b = 0.08664\frac{RT_c}{P_c}, \tag{3}$$

where R is the gas constant (8.31445 J/(mol·K)), T_c and P_c are the critical temperature (in K) and critical pressure (in Pa) of the R1243zf or lubricant oils, respectively. For R1243zf, the critical temperature and pressure are obtained from REFPROP [21]. Based on the UniOil model, the critical temperature and pressure of the lubricant oils are set to 800 K and 0.95 MPa [19], respectively. a(T) is a temperature-dependent term, defined by the following expressions:

$$\alpha(T) = \sum_{k=0}^{\leq 3}\beta_k(1/T_r - T_r)^k, \quad \text{for } T_r \leq 1, \tag{4}$$

$$\alpha(T) = \beta_0 + \beta_1[\exp(2(1-T_r)) - 1], \quad \text{for } T_r \geq 1. \tag{5}$$

where T_r is the reduced temperature ($T_r = T/T_c$). The value of $\beta(k)$ for R1243zf was determined from regression of vapour density data, and the values for the refrigerant and lubricant oil are provided in Table 1.

Table 1. Values of coefficient $\beta(k)$ in Eq. (4).

Components	β_1	β_2	β_3	β_4
R1243zf	1.0	0.48044	-0.11435	0.04702
Lubricant oil	1.0	1.0	0.0	0.0

In the modified van der Waals-Berthelot mixing rule, the attraction parameter $a(T)$ and co-volume parameter b of the mixtures are obtained by combining the pure-component parameters $a_i(T)$ and b_i through binary interaction parameters. The expressions are given as follows [19]:

$$a = \sum_{i,j=1}^{N}\sqrt{a_i a_j}\, f_{ij}(T)(1-k_{ij})x_i x_j, \tag{6}$$

$$b = \frac{1}{2}\sum_{i,j=1}^{N}(b_i + b_j)\,(1-k_{ij})(1-m_{ij})x_i x_j, \tag{7}$$

$$f_{ij}(T) = \tau_{0,ij} + \tau_{1,ij}/T + \tau_{2,ij}T, \quad (8)$$

$$k_{ij} = \frac{l_{ij}l_{ji}(x_i+x_j)}{l_{ji}x_i+l_{ij}x_j}, \quad (9)$$

where the m_{ij}, l_{ij}, l_{ji}, $\tau_{0,ij}$, $\tau_{1,ij}$ and $\tau_{2,ij}$ are binary interaction parameters, whose values were regressed from binary VLE data. The other parameters obey the relations: $f_{ij} = f_{ji}$, $f_{ii} = 1$, $m_{ij} = m_{ji}$, $m_{ii} = 0$, $k_{ij} = k_{ji}$, $k_{ii} = 0$.

In phase equilibrium calculations, the fugacity coefficient is indispensable – for component i, it is given by Eq. (10); a'_i and b'_i represent the partial derivatives of the attraction and co-volume terms with respect to the mole number of component i, respectively. The expressions are defined in Eqs. (11) and (12).

$$\ln\phi_i = \ln\frac{RT}{P(V-b)} + b'_i\left(\frac{1}{V-b} - \frac{a}{RTb(V+b)}\right) + \frac{a}{RTb}\left(\frac{a'_i}{a} - \frac{b'_i}{b} + 1\right)\ln\frac{V}{V+b}, \quad (10)$$

$$a'_i = 2\sum_{j=1}^{N}\sqrt{a_i a_j}\, f_{ij}x_j\left\{1 - k_{ij} - \frac{l_{ij}l_{ji}(l_{ij}-l_{ji})x_i x_j}{(l_{ji}x_i - l_{ij}x_j)^2}\right\} - a, \quad (11)$$

$$b'_i = \sum_{j=1}^{N}(b_i + b_j)(1 - m_{ij})\, x_j\left\{1 - k_{ij} - \frac{l_{ij}l_{ji}(l_{ij}-l_{ji})x_i x_j}{(l_{ji}x_i - l_{ij}x_j)^2}\right\} - b. \quad (12)$$

The phase equilibrium of the components is defined by the following equation:

$$x_i^{\alpha}\phi_i^{\alpha} = x_i^{\beta}\phi_i^{\beta} = x_i^{\gamma}\phi_i^{\gamma} = \ldots\ldots, (i = 1, \ldots, N), \quad (13)$$

where i is a component, and α, β, γ denote the coexisting phases.

The accuracy of the model was assessed by average absolute relative deviation (AARD) and maximum absolute relative deviation (MARD), which are given by:

$$\mathrm{AARD}/\% = \frac{100}{N}\sum_{i=1}^{N}\left|\frac{p_i^{\mathrm{cal}} - p_i^{\mathrm{exp}}}{p_i^{\mathrm{exp}}}\right|, \quad (14)$$

$$\mathrm{MARD}/\% = \max\left(100\left|\frac{p_i^{\mathrm{cal}} - p_i^{\mathrm{exp}}}{p_i^{\mathrm{exp}}}\right|\right), \quad (15)$$

where N denotes the total number of experimental points; p_i^{cal} and p_i^{exp} represent the calculated and experimental equilibrium pressures of R1243zf, respectively.

3. Results and analysis

3.1. VLE correlation results for R1243zf and three lubricant oils

The optimised binary interaction parameters are summarised in Table 2. Figure 1 illustrates the relative deviations between the calculated and experimental equilibrium pressures.

Table 2. Correlated binary interaction parameters for R1243zf/lubricant oils.

Parameters	R1243zf + 3GS	R1243zf + 4GS	R1243zf + RL68H
m_{ij}	-1.1224×10^{-2}	-1.0934×10^{-1}	-6.6252×10^{-3}
l_{ij}	-4.3360×10^{-3}	1.2181×10^{-1}	7.2919×10^{-2}
l_{ji}	-1.4472×10^{-2}	8.7517×10^{-2}	6.4677×10^{-4}
$\tau_{0,ij}$	4.3596×10^{-1}	4.9923×10^{-1}	7.1982×10^{-1}
$\tau_{1,ij}$	77.4473	72.7367	31.0292
$\tau_{2,ij}$	7.3489×10^{-4}	7.2135×10^{-4}	3.5786×10^{-4}
AARD/%	1.02	1.52	1.49
MARD/%	4.80	7.01	8.24

The AARD for R1243zf mixtures with 3GS, 4GS and RL68H is 1.02%, 1.52% and 1.49%, respectively, demonstrating a good overall quantitative agreement between the SRK model and experimental data.

It can be observed from Fig. 1 that the maximum relative deviations consistently occur at low liquid-phase mole fractions of R1243zf. The MARD for the equilibrium pressure of R1243zf+3GS, R1243zf+4GS and R1243zf+RL68H mixtures is 4.80%, 7.01%, and 8.24%, respectively.

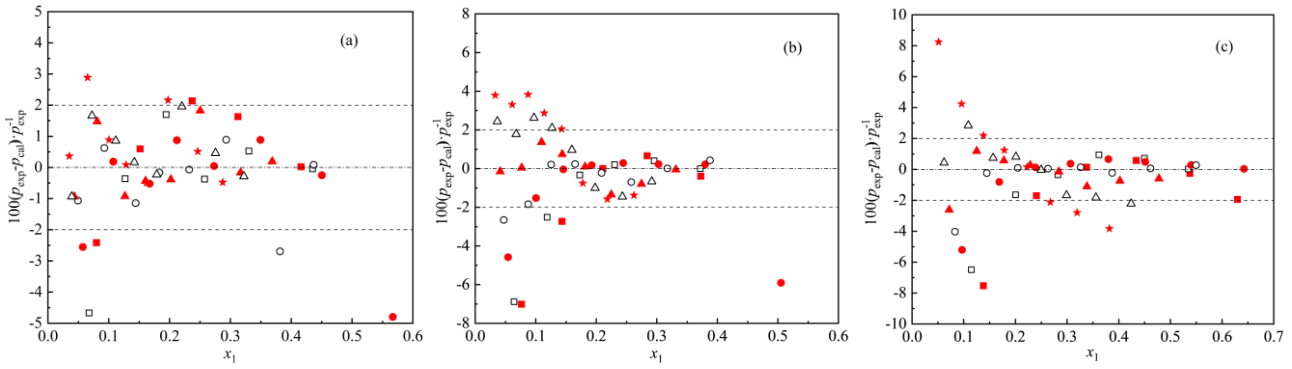


Fig. 1. Relative deviation between experimental data and model calculations of (a) R1243zf/3GS, (b) R1243zf/4GS and (c) R1243zf/RL68H. ■ 283.15 K; □ 293.15 K; ● 303.15 K;○ 313.15 K; ▲ 323.15 K; △ 333.15 K; □ 343.15 K.

3.2. Phase behaviour analysis of R1243zf/lubricant oils

The developed model for the studied R1243zf/oil mixtures was employed to analyse the phase diagrams and critical properties. Initially, the model was used to predict the vapour-liquid-liquid phase equilibrium (VL_1L_2E) and immiscibility regions (L_1L_2E). It should be noted that, due to the significant difference in molar mass between R1243zf and lubricant oils, using the mole fraction x as the abscissa in the phase diagram may result in overly compressed changes in the peripheral regions. Therefore, the mass fraction w was adopted for plotting the phase diagrams.

Figure 2 presents the pressure-temperature-composition ($P-T-w$) phase diagrams for R1243zf mixed with 3GS, 4GS and RL68H oils. Within the temperature range of 283.15−343.15 K, the binary mixtures of R1243zf with three lubricant oils present consistent phase behaviour. The diagrams show two vapour-liquid equilibrium regions (VL_1E and VL_2E), one liquid-liquid equilibrium region (L_1L_2E), and one vapour-liquid-liquid phase equilibrium region (VL_1L_2E), as indicated in Fig. 2. Here, V denotes the vapour phase of R1243zf; L_1 and L_2 represent the oil-rich liquid phase and the R1243zf-rich liquid phase, respectively.

To further investigate the temperature-dependent phase behaviour of the R1243zf/lubricant oils, the phase diagrams of R1243zf/3GS mixture were predicted at three representative temperatures: 343.15 K, 373.15 K and 383.15 K. The three temperatures correspond to conditions below, near and above the critical point of R1243zf. Figure 3 presents the pressure composition ($P-w$) and pressure-molar density ($P-\rho$) diagrams for the binary mixture at 343.15 K. In both diagrams, the L_1L_2E region exhibits a "chimney" shape. However, the width of this chimney shows opposite trends with the increasing pressure in the two types of diagrams. In the $P-w$ diagram, the narrowing of the chimney width is attributed to pressure-induced changes in the mixture's composition distribution. Conversely, in the $P-\rho$ diagram, the broadening of the L_1L_2E region suggests that the increased pressure enhances molecular interactions, thereby expanding the composition range for the liquid-liquid phase region.

Figure 4 presents the $P-w$ and $P-\rho$ diagrams of the R1243zf/3GS mixture at 373.15 K. A clear transformation is observed in the L_1L_2E region compared to 343.15 K. In the $P-w$ diagram, the L_1L_2E region no longer exhibits the upright chimney shape; instead, the L_1 and L_2 phases converge with rising pressure and merge near 10.1 MPa. In the $P-\rho$ diagram,

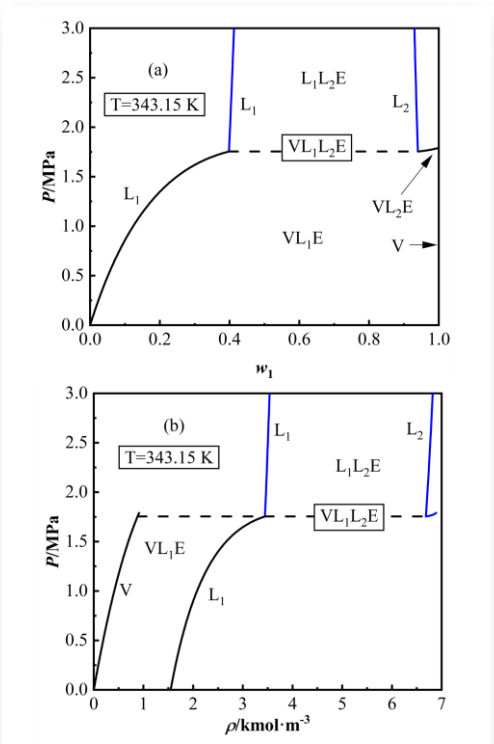


Fig. 3. (a) $P-w$ diagram and (b) $P-\rho$ diagram of the R1243zf/3GS mixture at 343.15 K.

the L_2 phase displays a distinctly different trend in molar density. At low liquid-phase mole fractions of R1243zf, the L_2 curve initially shifts toward higher density before reversing direction. This behaviour becomes particularly evident upon entering the VL_2E region, where the L_2 phase shows a strong tendency to approach the V phase.

Figure 5 shows the $P-w$ and $P-\rho$ diagrams for R1243zf/3GS mixture at 383.15 K. At this condition, the VL_1L_2E and VL_2E phase regions are no longer present. Only the VL_1E vapour-liquid equilibrium and the L_1L_2E liquid-liquid equilibrium persist in the diagrams. These regions are separated by an isopleth located at approximately 3.2 MPa. Below this pressure, the system exhibits vapour-liquid equilibrium, comprising the vapour phase V and the liquid phase L_1. Above 3.2 MPa, liquid-liquid equilibrium prevails, where the L_1 and L_2 phases gradually converge with increasing pressure and eventually merge at the critical point located near 7.98 MPa.

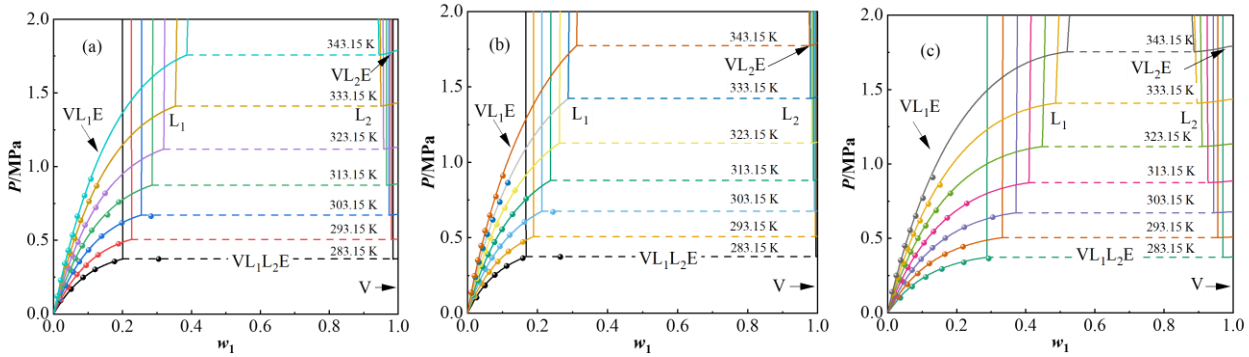


Fig. 2. $P-T-w$ diagrams for R1243zf with three lubricant oils including (a) R1243zf/3GS, (b) R1243zf/4GS and (c) R1243zf/RL68H.

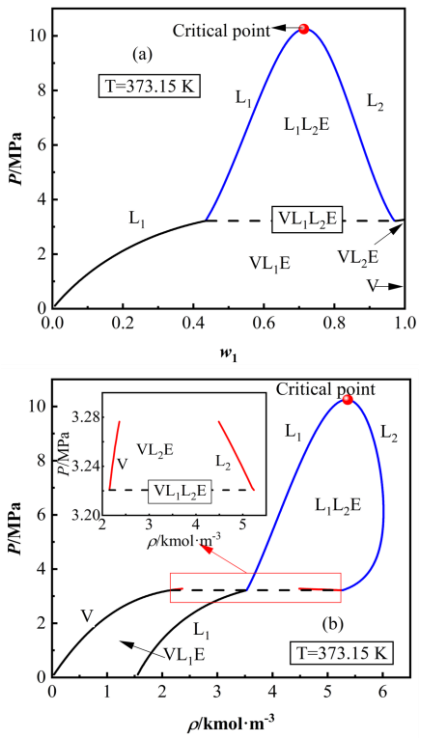


Fig. 4. (a) *P*–*w* diagram and (b) *P*–*ρ* diagram of the R1243zf/3GS mixture at 373.15 K.

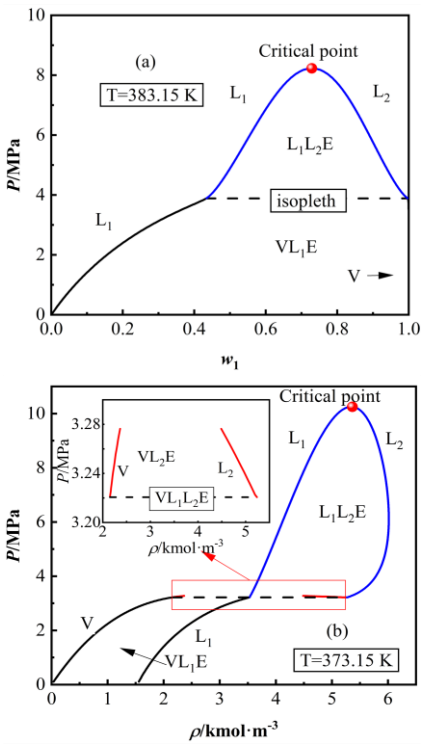


Fig. 5. (a) *P*–*w* diagram and (b) *P*–*ρ* diagram of the R1243zf/3GS mixture at 383.15 K.

Van Konynenburg and Scott [22,23] pioneered the classification of phase behaviour types in binary mixtures, identifying five of the six major phase behaviours. Among these, type III mixture is one of the most extensively studied. Type III mixture is characterised by features including a three-phase equilibrium region, an upper critical solution temperature, and the absence of a lower critical solution temperature. Based on the analysis of *P*–*w* and *P*–*ρ* diagrams at different temperatures, the R1243zf/3GS can be classified as a type III mixture. It should be noted that the mixtures of R1243zf/4GS and R1243zf/RL68H exhibit similar trends with that of R1243zf/3GS and are also categorised as type III mixtures, therefore, the phase diagram of R1243zf/4GS and R1243zf/RL68H mixtures was not discussed here.

The classification of all three R1243zf/oil systems as type III mixtures implies the existence of a three-phase (VL_1L_2) region and a liquid-liquid immiscibility gap under conditions relevant to refrigeration cycles. Among the studied oils, the phase diagrams indicate that RL68H exhibits an immiscibility region that is relatively narrower and shifted compared to the mineral oils 3GS and 4GS. This suggests a lower tendency for phase separation.

3.3. Performance analysis of vapour-compression refrigeration cycle with lubricant oil

In this part, the influence of lubricant oil on the performance of the vapour-compression refrigeration cycle was analysed. The cycle incorporated superheating and subcooling, each set to 2.5 K, to secure a fully condensed liquid after the condenser and to prevent liquid entrainment in the vapour stream entering the compressor. Figure 6 presents the pressure-enthalpy (*P*–*h*) and temperature-entropy (*T*–*s*) diagrams of the vapour-compression refrigeration cycle.

In this study, the coefficient of performance (COP) of the refrigeration cycle was simulated by maintaining a fixed condensing temperature of 330 K. To facilitate quantitative analysis, pressure drops during evaporation and condensation were assumed to be negligible. Table 3 summarises the process conditions of the cycle adopted in this work. In Table 3, P_i and T_i denote the pressure and temperature at state point *i*, respectively; T_{evap} and T_{cond} represent the evaporating and condensing temperatures of the cycle; $w_{i,oil}$ indicates the liquid-phase mass fraction of the lubricant oil at state point *i*.

COP of the cycle is calculated by the following equation:

$$\mathrm{COP} = \frac{\sum q_{in}}{\sum W_{net,in}} = \frac{h_1 - h_4}{h_2 - h_1} = \frac{h_1 - h_3}{h_2 - h_1}, \tag{16}$$

where q_{in} denotes the evaporator heat absorption, $W_{net,in}$ denotes the net compressor work input, and h_i is the specific enthalpy at state *i*. The expansion process is assumed isenthalpic, giving $h_3 = h_4$.

The specific enthalpy of the R1243zf/lubricant oil mixture at state *i* is determined using the thermodynamic model of Youbi-Idrissi [24], and is given by:

Table 3. Process conditions of the vapour-compression refrigeration cycle for refrigerant/lubricant oil mixture.

Operating point	1	2	3
Degrees of freedom	2	2	2
Fixed variables	P_1, T_{evap}	P_3, S_2	P_3, T_{cond}
Obtained variables	$w_{1,oil}$	T_2, $w_{2,oil}$	$w'_{3,oil}$, $w''_{3,oil}$

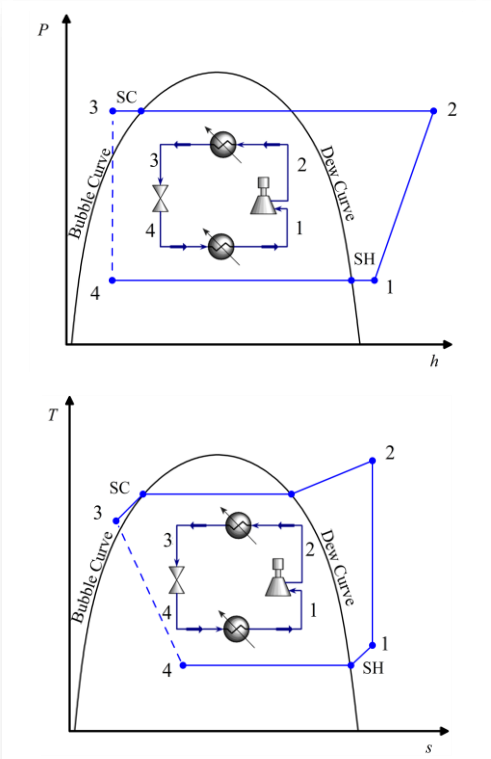


Fig. 6. $P-h$ and $T-s$ diagrams |of the vapour-compression refrigeration cycle.

$$h_i = \left(\frac{m_{L,r}}{m_{L,r}+m_{oil}+m_V}\right) h_{L,r} + \left(\frac{m_V}{m_{L,r}+m_{oil}+m_V}\right) h_V + \left(\frac{m_{oil}}{m_{L,r}+m_{oil}+m_V}\right) h_{oil}, \quad (17)$$

where h_i is the specific enthalpy at state point i (J/kg), $h_{L,r}$ and h_V are the specific enthalpies of the liquid and vapour refrigerant (J/kg), and h_{oil} is the specific enthalpy of the lubricate oil (J/kg). The liquid refrigerant enthalpy $h_{L,r}$ and vapour refrigerant enthalpy h_V were obtained from REFPROP [21]. The specific enthalpy of the lubricating oil (h_{oil}) is expressed as:

$$h_{oil} = h_{ref} + \int_{T_{ref}}^{T} C_{P,oil}\, \mathrm{d}T, \quad (18)$$

where h_{ref} is the reference specific enthalpy (J/kg), T_{ref} is the reference temperature (K), and $C_{p,oil}$ is the specific heat capacity of the lubricate oil (J/(kg·K)). Since only enthalpy differences between state points are relevant for efficiency calculations, it is sufficient to maintain consistent values of T_{ref} and h_{ref} for the lubricant across all states. Here, T_{ref} is taken as 273.15 K and h_{ref} as 0 J/kg. The specific heat capacity of the lubricate oil, $C_{p,oil}$ can be calculated using the model proposed by Liley et al. [25]:

$$C_{p,oil} = 4.186\left[\frac{0.388+0.00045(1.8T+32)}{\sqrt{\rho_{oil}/998.5}}\right] = \frac{(1.684+0.0034T)}{\sqrt{\rho_{oil}/998.5}}, \quad (19)$$

where ρ_{oil} is the density of the lubricate oil (kg/m^3) at 288.71 K.

To investigate the influence of lubricant oil content on cycle performance, COP was evaluated at varying oil circulation rates (OCR), defined as the mass ratio of lubricant oil to the total circulating fluid. Calculations were performed at OCR levels of 1%, 2% and 3%, representing conditions of oil deficiency, normal operation and potential mild compressor leakage, respectively.

Figure 7 presents the calculated COP values for mixtures of R1243zf with 3GS, 4GS and RL68H under different OCR values. It indicates that at a constant evaporation temperature, the COP exhibits a clear decreasing trend as OCR increases. For example, at an evaporation temperature of 278 K, as OCR increases from 1% to 3%, the COP for the R1243zf/3GS mixture decreases from 3.92 to 3.34, representing a reduction of 14.80%. These findings are consistent with the results reported by Albà et al. [18] for R513A/lubricant systems, where COP was also found to decrease with increasing oil circulation rate.

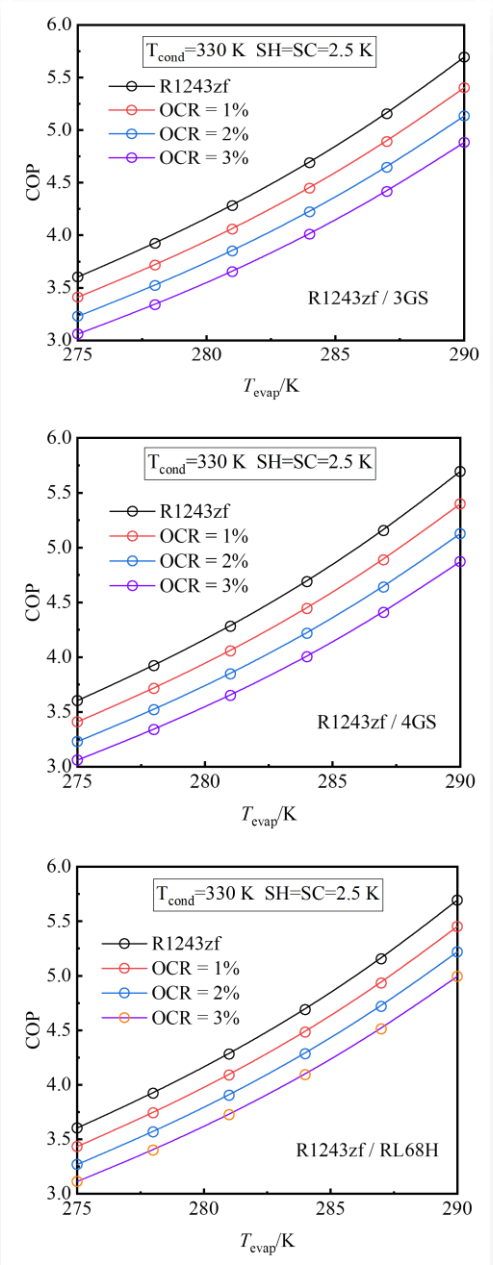


Fig. 7. COP of R1243zf/3GS, R1243zf/4GS and R1243zf/RL68H mixtures under different OCR.

Figure 8 shows the reduction in COP of the refrigeration cycle using R1243zf/oil mixture compared to that of pure R1243zf. As shown in the figure, the COP reduction exhibits a clear increasing trend with rising OCR. At a low OCR of 1% and evaporation temperature of 278 K, the COP reductions are 0.207, 0.208 and 0.180 for 3GS, 4GS and RL68H, respectively. At a high OCR of 3% under the same evaporation temperature, the corresponding reductions are 0.582, 0.583 and 0.522. This trend occurs because a higher OCR increases the proportion of lubricant in the system, which correspondingly displaces the refrigerant and reduces the effective mass flow rate contributing to refrigeration, thereby diminishing the cooling capacity.

At a fixed OCR, the negative impact of the lubricant oil on the system efficiency becomes more pronounced as the evaporation temperature increases, as indicated in Fig. 8. For example, at an OCR of 3% for R1243zf/3GS mixture, the COP reduction increases from 0.542 at 275 K to 0.81 at 290 K. Moreover, the extent of COP reduction varies among different lubricants. Particularly, under lower evaporation temperature, RL68H shows the smallest adverse effect on cycle efficiency compared to the other two lubricants.

At OCR of 3% and evaporation temperature of 278 K, the COP reduction for RL68H is 10.4% lower than that for 3GS, and 10.6% lower than that for 4GS. Therefore, from a system performance perspective, RL68H is identified as the most suitable lubricant for R1243zf refrigeration systems among the three candidates. This conclusion is consistent with the work of Albà et al. [18], who employed the polar soft-SAFT equation of state to evaluate lubricants for R513A, and identified PEC5 (a pure component of POE oil) as the optimal choice, with a COP decrease of less than 3% across the studied range.

RL68H is a POE type lubricant, whereas 3GS and 4GS are mineral oils. The superior performance of R1243zf/RL68H mixture can be attributed to its molecular structure. The oxygen-containing ester linkages in POE lubricant provide favourable polar interactions with fluorinated R1243zf molecules, enhancing miscibility, giving more stable thermodynamic behaviour.

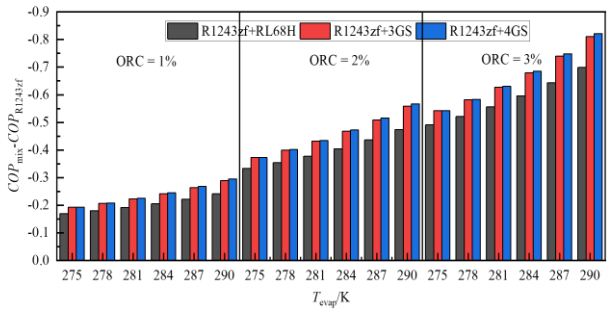


Fig. 8. Reduction in COP for R1243zf/3GS, R1243zf/4GS and R1243zf/RL68H mixtures compared to pure R1243zf.

4. Conclusions

This study correlated the experimental phase equilibrium data of R1243zf with three lubricant oils using the SRK equation of state, modified van der Waals-Berthelot mixing rule and the UniOIL model proposed by Yokozeki. The relative deviations between calculated and experimental values were predominantly within ±2%. The correlated model was subsequently applied to predict and analyse phase behaviour, including vapour-liquid and liquid-liquid equilibrium of R1243zf/lubricant oils. Phase diagram analysis confirmed that the binary systems of R1243zf with 3GS, 4GS and RL68H are classified as type III mixtures. Furthermore, the coefficient of performance (COP) of the cycle was comprehensively evaluated. By comparing the effects of different lubricants on cycle performance, it can be concluded that RL68H is the most suitable lubricant among the three lubricants for R1243zf refrigeration systems. The modelling framework and COP evaluation methodology developed in this work can be extended to a broader range of refrigerant/lubricant combinations, providing a useful basis for lubricant screening.

Acknowledgements

This work was supported by National Natural Science Foundation of China (Grant No. 52276165).

References

[1] Esen, M. (2004). Thermal performance of a solar cooker integrated vacuum-tube collector with heat pipes containing different refrigerants. *Solar Energy*, 76(6), 751–757. doi: 10.1016/j.solener.2003.12.009

[2] Esen, M., Hazar, H., & Esen, H. (2005). Experimental investigation of a solar cooker using collector with heat pipes. *Sigma Journal of Engineering and Natural Sciences*, 23(1), 114–122.

[3] Esen, M., & Esen, H. (2005). Experimental investigation of a two-phase closed thermosyphon solar water heater. *Solar Energy*, 79(5), 459–468. doi: 10.1016/j.solener.2005.01.001

[4] Wallington, T.J., Andersen, M.S., & Nielsen, O.J. (2015). Atmospheric chemistry of short-chain haloolefins: Photochemical ozone creation potentials (POCPs), global warming potentials (GWPs), and ozone depletion potentials (ODPs). *Chemosphere*, 129, 135–141. doi: 10.1016/j.chemosphere.2014.06.092

[5] Bobbo, S., Di Nicola, G., Zilio, C., Brown, J.S., & Fedele, L. (2018). Low GWP halocarbon refrigerants: A review of thermophysical properties. *International Journal of Refrigeration*, 90, 181–201. doi: 10.1016/j.ijrefrig.2018.03.027

[6] McLinden, M.O., Kazakov, A.F., Brown, J.S., & Domanski, P.A. (2014). A thermodynamic analysis of refrigerants: Possibilities and tradeoffs for low-GWP refrigerants. *International Journal of Refrigeration*, 38, 80–92. doi: 10.1016/j.ijrefrig.2013.09.032

[7] Lai, N.A. (2014). Thermodynamic properties of HFO-1243zf and their application in study on a refrigeration cycle. *Applied Thermal Engineering*, 70(1), 1–6. doi: 10.1016/j.applthermaleng.2014.04.042

[8] Brown, J.S., Di Nicola, G., Fedele, L., Bobbo, S., & Zilio, C. (2013). Saturated pressure measurements of 3,3,3-trifluoroprop-1-ene (R1243zf) for reduced temperatures ranging from 0.62 to 0.98. *Fluid Phase Equilibria*, 351, 48–52. doi: 10.1016/j.fluid.2012.09.036

[9] Higashi, Y., & Sakoda, N. (2018). Measurements of PvT properties, saturated densities, and critical parameters for 3,3,3-trifluoropropene (HFO1243zf). *Journal of Chemical and Engineering Data*, 63(10), 3818–3822. doi: 10.1021/acs.jced.8b00452

[10] Di Nicola, G., Brown, J.S., Fedele, L., Securo, M., Bobbo, S., & Zilio, C. (2013). Subcooled liquid density measurements and PvT measurements in the vapor phase for 3,3,3-trifluoroprop-1-ene (R1243zf). *International Journal of Refrigeration*, 36(8), 2209–2215. doi: 10.1016/j.ijrefrig.2013.08.004

[11] Kondou, C., Nagata, R., Nii, N., Koyama, S., & Higashi, Y. (2015). Surface tension of low GWP refrigerants R1243zf, R1234ze(Z), and R1233zd(E). *International Journal of Refrigeration*, 53, 80–89. doi: 10.1016/j.ijrefrig.2015.01.005

[12] Luo, Y., Liu, Z., Lu, C., & Wang, X. (2022). Vapor-liquid equilibrium measurements of 3,3,3-trifluoropropene with pentaerythritol tetraheptanoate and pentaerythritol tetranonanoate. *The Journal of Chemical Thermodynamic*s, 174, 106874. doi: 10.1016/j.jct.2022.106874

[13] Luo, Y., Wang, X., & Wang, X. (2023). Solubilities of 3,3,3-trifluoropropene in pentaerythritol tetrahexanoate and pentaerythritol tetraoctanoate from 278.15 K to 343.15 K at pressures to 1 MPa. *Fluid Phase Equilibria*, 566, 113699. doi: 10.1016/j.fluid.2022.113699

[14] Jia, H., Wang, X., & Wang, X. (2023). Vapor-liquid equilibrium of 3,3,3-trifluoropropene with mineral oils and POE lubricant between 283.15 K and 343.15 K. *International Journal of Refrigeration*, 146, 375–380. doi: 10.1016/j.ijrefrig.2022.11.027

[15] Chen, R., Wu, J., & Duan, J. (2019). Performance and refrigerant mass distribution of a R290 split air conditioner with different lubricating oils. *Applied Thermal Engineering*, 162, 114225. doi: 10.1016/j.applthermaleng.2019.114225

[16] Li, K., Kong, F., Luo, S., Liu, N., Zhang, H., Dou, B., Zhao, Y., Zhou, X., Tu, R., Su, L., & He, Q. (2024). Influence of lubricating oil circulation characteristics on the performance of electric vehicle heat pump system under low temperature conditions. *Applied Thermal Engineering*, 236, 121601. doi: 10.1016/j.applthermaleng.2023.121601

[17] Naseri, A., Moradi, R., Cioccolanti, L., & Subiantoro, A. (2023). Impact of the lubricant on a modified revolving vane expander (M-RVE) in an organic Rankine cycle system. *Energies*, 16(14), 5340. doi: 10.3390/en16145340

[18] Albà, C.G., Llovell, F., & Vega, L.F. (2021). Searching for suitable lubricants for low global warming potential refrigerant R513A using molecular-based models: Solubility and performance in refrigeration cycles. *International Journal of Refrigeration*, 128, 252–263. doi: 10.1016/j.ijrefrig.2021.04.010

[19] Yokozeki, A. (2001). Solubility of refrigerants in various lubricants. *International Journal of Thermophysics*, 22(4), 1057–1071. doi.: 10.1023/A:1010695705260

[20] Soave, G. (1972). Equilibrium constants from a modified Redlich-Kwong equation of state. *Chemical Engineering Science*, 27(6), 1197–1203. doi: 10.1016/0009-2509(72)80096-4

[21] Lemmon, E.W., Bell, I.H., Huber, M.L., & McLinden, M.O. (2019). *NIST Standard Reference Database 23: Reference fluid thermodynamic and transport properties-REFPROP* (*Version 10.0*). National Institute of Standards and Technology. https://pages.nist.gov/REFPROP-docs/ [accessed 10 Oct. 2025].

[22] Scott, R.L., & Van Konynenburg, P.H. (1970). Static properties of solutions. Van der Waals and related models for hydrocarbon mixtures. *Discussions of the Faraday Society*, 49, 87–97. doi: 10.1039/DF9704900087

[23] Van Konynenburg, P.H., & Scott, R.L. (1980). Critical lines and phase equilibria in binary van der Waals mixtures. *Philosophical Transactions of the Royal Society A: Mathematical, Physical and Engineering Sciences*, 298(1442), 495–540. doi: 10.1098/rsta.1980.0266

[24] Youbi-Idrissi, M., Bonjour, J., Marvillet, C., & Meunier, F. (2003). Impact of refrigerant–oil solubility on an evaporator performance working with R-407C. *International Journal of Refrigeration*, 26(3), 284–292. doi: 10.1016/S0140-7007(02) 00129-9

[25] Mermond, Y., Feidt, M., & Marvillet, C. (1999). Thermodynamic and physical properties of mixtures of refrigerants and oils. *International Journal of Refrigeration*, 22(7), 569–579. doi: 10.1016/S0140-7007(99)00015-8